INNOVATORS IN CHEMICAL BIOLOGY

EDITED BY: John D. Wade, Olivier Renaudet and Matthew A. Coleman
PUBLISHED IN: Frontiers in Chemistry

frontiers Research Topics

ISSN 1664-8714
ISBN 978-2-83250-069-9
DOI 10.3389/978-2-83250-069-9

About Frontiers

Frontiers is more than just an open-access publisher of scholarly articles: it is a pioneering approach to the world of academia, radically improving the way scholarly research is managed. The grand vision of Frontiers is a world where all people have an equal opportunity to seek, share and generate knowledge. Frontiers provides immediate and permanent online open access to all its publications, but this alone is not enough to realize our grand goals.

Frontiers Journal Series

The Frontiers Journal Series is a multi-tier and interdisciplinary set of open-access, online journals, promising a paradigm shift from the current review, selection and dissemination processes in academic publishing. All Frontiers journals are driven by researchers for researchers; therefore, they constitute a service to the scholarly community. At the same time, the Frontiers Journal Series operates on a revolutionary invention, the tiered publishing system, initially addressing specific communities of scholars, and gradually climbing up to broader public understanding, thus serving the interests of the lay society, too.

Dedication to Quality

Each Frontiers article is a landmark of the highest quality, thanks to genuinely collaborative interactions between authors and review editors, who include some of the world's best academicians. Research must be certified by peers before entering a stream of knowledge that may eventually reach the public - and shape society; therefore, Frontiers only applies the most rigorous and unbiased reviews.
Frontiers revolutionizes research publishing by freely delivering the most outstanding research, evaluated with no bias from both the academic and social point of view. By applying the most advanced information technologies, Frontiers is catapulting scholarly publishing into a new generation.

What are Frontiers Research Topics?

Frontiers Research Topics are very popular trademarks of the Frontiers Journals Series: they are collections of at least ten articles, all centered on a particular subject. With their unique mix of varied contributions from Original Research to Review Articles, Frontiers Research Topics unify the most influential researchers, the latest key findings and historical advances in a hot research area! Find out more on how to host your own Frontiers Research Topic or contribute to one as an author by contacting the Frontiers Editorial Office: frontiersin.org/about/contact

INNOVATORS IN CHEMICAL BIOLOGY

Topic Editors:
John D. Wade, University of Melbourne, Australia
Olivier Renaudet, Université Grenoble Alpes, France
Matthew A. Coleman, University of California, Davis, United States

Citation: Wade, J. D., Renaudet, O., Coleman, M. A., eds. (2022). Innovators in Chemical Biology. Lausanne: Frontiers Media SA.
doi: 10.3389/978-2-83250-069-9

Table of Contents

frontiers | Frontiers in Chemistry

TYPE Editorial
PUBLISHED 04 November 2022
DOI 10.3389/fchem.2022.1074759

OPEN ACCESS

EDITED AND REVIEWED BY
Boris Vauzeilles,
Institut de Chimie des Substances Naturelles CNRS-ICSN, France

*CORRESPONDENCE
John D. Wade,
john.wade@florey.edu.au
Olivier Renaudet,
olivier.renaudet@univ-grenoble-alpes.fr
Matthew A. Coleman,
coleman16@llnl.gov

SPECIALTY SECTION
This article was submitted to Chemical Biology, a section of the journal Frontiers in Chemistry

RECEIVED 19 October 2022
ACCEPTED 24 October 2022
PUBLISHED 04 November 2022

CITATION
Wade JD, Renaudet O and Coleman MA (2022), Editorial: Innovators in chemical biology.
Front. Chem. 10:1074759.
doi: 10.3389/fchem.2022.1074759

Editorial: Innovators in chemical biology

John D. Wade[1,2]*, Olivier Renaudet[3]* and Matthew A. Coleman[4,5]*

[1]Florey Institute of Neuroscience and Mental Health, Parkville, VIC, Australia, [2]School of Chemistry, University of Melbourne, Melbourne, VIC, Australia, [3]Universite Grenoble Alpes, Grenoble, France, [4]Physical and Life Sciences Directorate, Lawrence Livermore National Laboratory, Livermore, CA, United States, [5]Radiation Oncology, University of California, Davis, Sacramento, CA, United States

KEYWORDS

amyloid, antimicrobial, biomaterials, GPCRs, natural products, polyketides, peptides, photoreceptors

Editorial on the Research Topic
Innovators in chemical biology

The science of chemical biology has matured greatly in the past decade to provide enormous insights into the chemical basis of cellular and biological processes and to exploit the resulting knowledge for the development of novel research tools and compounds in across fields such as medicine, agriculture, veterinary science and biology. Such advances have been made possible by not only the acquisition of new chemical and biophysical techniques and instrumentation including cryo-electron microscopy but also superbly skilled application of these.

In this dedicated Research Topic, eleven leading international researchers of chemical biology together with their teams present their latest results across a wide spectrum of research. These showcase the contribution that current or novel chemical biological methods and technology make towards the better understanding of the chemical basis of biology. Application of such expertise and resources is wide and varied as exemplified by the following examples. Avalon et al. report the use of bioinformatic tools to develop predictive models of the biosynthesis of the marine polyketide natural product, palmerolide A. Enzymatic reactions and organic synthesis interpretations were based on homology analyses. Together, these led to the identification of a biosynthetic gene cluster from an Antarctic microbial species that is ultimately responsible for the stepwise synthesis of the polyketide.

The development of new antibiotics is essential given the increasing development of antimicrobial resistance (AMR). Here, Fang et al. focus on the design and synthesis of a series of calix (4) arene derivatives as antimicrobial agents that biomimic the structural properties and biological activities of antimicrobial peptides (Fang et al.). Following the introduction of cationic hydrophilic moieties and after further structural optimization, a lead compound was obtained with potent activity against Gram-positive bacteria while having low toxicity towards mammalian cells. Such rational peptide drug design on novel natural product templates affords a promising path towards addressing AMR.

The reported studies of Wodzanowski et al. were an attempt to better understand the molecular mechanisms whereby the human immune system can differentiate between pathogenic bacteria and the commensal bacteria of the microbiome (Wodzanowski et al.). A comprehensive chemical biology platform was established in which biorthogonal chemistry was used to differentially label the cell walls of two different species of bacteria. Then, a hydrogel-based synthetic matrix was developed and employed to encapsulate monocytes and macrophages for subsequent measurement of the invading bacteria and a reflection of pathogen invasion and homeostatic maintenance.

The fourth manuscript, by Mackinnon et al., in this special Research Topic describes an effort to develop novel inhibitors of hydroxy acid oxidase 1 (HOA1) as an alternative approach to treat primary hyperoxaluria (Mackinnon et al.). They report the use of X-ray crystallography for the discovery and optimization of six low-molecular-weight active site fragments. Two of these were shown by biophysical analyses to be of suitable potency while devoid of substrate competition that make them suitable for further possible drug development.

Lin et al. report their ongoing efforts to develop novel glucose-responsive insulin analogues which represent a primary goal in the better management of fluctuating blood glucose levels in type 1 diabetes and some type 2 diabetes (Lin et al.). Using elegant chemical peptide synthesis, they prepared an insulin analogue that contains two fluorophenylboronic acid (FPBA) moieties at the C-terminus of the A-chain of insulin glargine. In turn, they showed that this led to an increase in the baseline glucose-dependent solubility of insulin without potency reduction. This finding augurs well for the development of novel insulin-based therapies for diabetes. Crystal Chan et al. also use chemical peptide synthesis to prepare a series of analogues of Peptide5, a connexin43 inhibitor, that regulates both cellular communication with the cytoplasm and cell to cell communication (Crystal Chan et al.). The goal was to develop greater *in vivo* stability as well as to increase the peptide's potency. From these studies, design criteria were established which enabled the production of improved analogues that were suitable for further optimization.

G-coupled receptors are a fascinating and important class of cellular signal transducers which are also primary drug targets for many therapeutic interventions. The review by de Grip and Ganapathy focuses upon rhodopsin proteins, a superfamily of photoreceptors that are essential to multiple elements of light-sensitive animal physiology (de Grip and Ganapathy). Discussions include spectral and structural properties of these proteins together with the current and future applications of engineered rhodopsins in fields as diverse as bioelectronic and biomimic nanotechnology, optogenetics, and cell factories.

Post-translational modifications (PTMs) of peptides and proteins is a key cellular process that adds significant structural and functional diversity. Glycosylation is probably the most common PTM but is highly complex and difficult to study. The manuscript by Zhao et al. review the use of chemoenzymatic synthesis strategies to prepare homogenous complex-type N-glycans for use in the preparation of well-characterized glycopeptides (Zhao et al.). Despite significant gains in synthetic efficiency, much more remains to be done to achieve higher, reliable and reproducible yields of these essential core oligosaccharides.

In another review, Landrieu et al. provide a comprehensive treatise on the putative role of protein aggregation (amyloidosis) in neurological disease or systemic diseases such as type 2 diabetes (Landrieu et al.). The biophysical study of the ultrastructural organization of such aggregates has provided sophisticated and discriminating detail of the molecular features that govern the development and features of fibril (amyloid) formation. The role of chemical biology tools in such studies is highlighted with several examples including of protein engineering methods and biorthogonal chemistry for the introduction of protein chemical modifications. Amyloid-beta oligomers (AβO) are one of the most-studied protein aggregates given its still-unconfirmed role in Alzheimer's disease onset and development. Hilt et al. report the synthesis of a class of bifunctional stilbenes and of measurements *via* a range of sophisticated chemical biology tools of their ability to modulate the conformational toxicity of the aggregates (Hilt et al.). They show that the ability of these designed small molecules to intervene with neuronal AβO strongly suggests a potential therapeutic application for Alzheimer's disease.

The final paper in this Research Topic, by Zhou et al., describes the isolation and chemical characterization of six novel bibenzyl small molecules (three pairs of enantiomers), blestrinsD-F, from the tubers of *Bletilla striata*. Use of a range of analytical techniques including 1D/2D NMR led to their structural elucidation (Zhou et al.). One of the compounds showed prominent inhibitory activity against three different Gram-positive bacteria which augurs well for further development as a novel antibiotic.

Together this excellent collection of manuscripts highlights the continuing and powerful role chemical biology makes in our understanding of complex cellular processes. The contributions that the development and utility of novel chemical biology research tools produce are amply illustrated. The work described in the manuscripts also shows the acceleration towards translation to the design and production of research diagnostics and potential medicinal therapeutics and agricultural applications. It is hoped that the reader will enjoy and appreciate this Research Topic.

Author contributions

All authors listed have made a substantial, direct, and intellectual contribution to the work and approved it for publication.

Funding

JW thanks the National Health and Medical Research Council (NHMRC) of Australia for an Idea research grant (APP2010781). Work was also performed under the auspices of the U.S. Department of Energy by the Lawrence Livermore National Laboratory under contract DE-AC52-07NA27344.

Acknowledgments

The editors thank all the contributing authors for their considerable efforts in producing the enclosed articles.

Conflict of interest

The authors declare that the research was conducted in the absence of any commercial or financial relationships that could be construed as a potential conflict of interest.

Publisher's note

frontiers in Chemistry

ORIGINAL RESEARCH
published: 24 December 2021
doi: 10.3389/fchem.2021.802574

Bioinformatic and Mechanistic Analysis of the Palmerolide PKS-NRPS Biosynthetic Pathway From the Microbiome of an Antarctic Ascidian

Nicole E. Avalon[1], Alison E. Murray[2], Hajnalka E. Daligault[3], Chien-Chi Lo[3], Karen W. Davenport[3], Armand E. K. Dichosa[3], Patrick S. G. Chain[3]* and Bill J. Baker[1]**

[1]Department of Chemistry, University of South Florida, Tampa, FL, United States, [2]Division of Earth and Ecosystem Sciences, Desert Research Institute, Reno, NV, United States, [3]Los Alamos National Laboratory, Los Alamos, NM, United States

OPEN ACCESS

Edited by:
Matthew A. Coleman, University of California at Davis, United States

Reviewed by:
Olivier Berteau, Université Paris-Saclay, France
Geoff Horsman, Wilfrid Laurier University, Canada

***Correspondence:**
Alison E. Murray
alison.murray@dri.edu
Patrick S. G. Chain
pchain@lanl.gov
Bill J. Baker
bjbaker@usf.edu

Specialty section:
This article was submitted to Chemical Biology, a section of the journal Frontiers in Chemistry

Received: *26 October 2021*
Accepted: *23 November 2021*
Published: *24 December 2021*

Citation:
Avalon NE, Murray AE, Daligault HE, Lo C-C, Davenport KW, Dichosa AEK, Chain PSG and Baker BJ (2021) Bioinformatic and Mechanistic Analysis of the Palmerolide PKS-NRPS Biosynthetic Pathway From the Microbiome of an Antarctic Ascidian. Front. Chem. 9:802574. doi: 10.3389/fchem.2021.802574

Complex interactions exist between microbiomes and their hosts. Increasingly, defensive metabolites that have been attributed to host biosynthetic capability are now being recognized as products of host-associated microbes. These unique metabolites often have bioactivity targets in human disease and can be purposed as pharmaceuticals. Polyketides are a complex family of natural products that often serve as defensive metabolites for competitive or pro-survival purposes for the producing organism, while demonstrating bioactivity in human diseases as cholesterol lowering agents, anti-infectives, and anti-tumor agents. Marine invertebrates and microbes are a rich source of polyketides. Palmerolide A, a polyketide isolated from the Antarctic ascidian *Synoicum adareanum,* is a vacuolar-ATPase inhibitor with potent bioactivity against melanoma cell lines. The biosynthetic gene clusters (BGCs) responsible for production of secondary metabolites are encoded in the genomes of the producers as discrete genomic elements. A candidate palmerolide BGC was identified from a *S. adareanum* microbiome-metagenome based on a high degree of congruence with a chemical structure-based retrobiosynthetic prediction. Protein family homology analysis, conserved domain searches, active site and motif identification were used to identify and propose the function of the ~75 kbp *trans*-acyltransferase (AT) polyketide synthase-non-ribosomal synthase (PKS-NRPS) domains responsible for the stepwise synthesis of palmerolide A. Though PKS systems often act in a predictable co-linear sequence, this BGC includes multiple *trans*-acting enzymatic domains, a non-canonical condensation termination domain, a bacterial luciferase-like monooxygenase (LLM), and is found in multiple copies within the metagenome-assembled genome (MAG). Detailed inspection of the five highly similar *pal* BGC copies suggests the potential for biosynthesis of other members of the palmerolide chemical family. This is the first delineation of a biosynthetic gene cluster from an Antarctic microbial species, recently proposed as *Candidatus* Synoicihabitans palmerolidicus. These findings have relevance for fundamental knowledge of PKS combinatorial biosynthesis and could

enhance drug development efforts of palmerolide A through heterologous gene expression.

Keywords: marine natural products, macrolide, biosynthetic gene clusters, Antarctic microbiology, *trans*-AT type I polyketide synthase, secondary metabolites

1 INTRODUCTION

Marine invertebrates such as corals, sponges, mollusks, and ascidians are known to be a rich source of bioactive compounds (Carroll et al., 2019). Due to their sessile or sluggish nature, chemical defenses such as secondary metabolites are often key to their survival. Many compound classes are represented among benthic invertebrates including terpenes, nonribosomal peptide synthetase (NRPS) products, ribosomally synthesized and post-translationally modified peptides (RiPPs), and polyketides. It is estimated that over 11,000 secondary metabolites from marine and terrestrial environments understood to be products of polyketide synthase (PKS) and NRPS origin have been isolated and described (Dejong et al., 2016). BGCs exist as a series of genomic elements that encode for the biosynthetic machinery responsible for production of these secondary metabolites. BGCs can have distinct nucleotide composition properties such as codon usage and guanine-cytosine content that do not match the remainder of the genome (Lawrence et al., 2002; Ravenhall et al., 2015), suggesting a mechanism of horizontal gene transfer from organisms that are distantly related, including across different kingdoms (Schmidt, 2008; Schmitt and Lumbsch, 2009). Interestingly, the BGCs for many natural products isolated from marine invertebrates are found in the host-associated microbiota, reflecting the role of these compounds in symbiosis (Schmidt, 2015).

Polyketides are a complex family of natural products produced by a variety of PKS enzymes that are related to, but evolutionarily divergent from, fatty acid synthases (Helfrich and Piel, 2016). They often possess long carbon chains with varied degrees of oxidation, can contain aromatic components, and may be either cyclic or linear. It is estimated that of the polyketides that have been isolated and characterized, 1% have potential biological activity against human diseases, making this class of compounds particularly appealing from a drug discovery and development standpoint (Koskinen and Karisalmi, 2005). This potential for use as pharmaceuticals is approximately five times greater than for compounds of all other natural product classes (Koskinen and Karisalmi, 2005). Many polyketides are classified as macrolides, which are large-ring lactones that are pharmaceutically relevant due to a number of biological actions, including, targeting the cytoskeleton, ribosomal protein biosynthesis, and vacuolar type V-ATPases (Bordeleau et al., 2005; Nishimura et al., 2005; Napolitano et al., 2012; Ueoka et al., 2015). V-ATPases are responsible for acidification of cells and organelles via proton transport across membranes, including those of lysosomes, vacuoles, and endosomes. These enzymes appear to have an impact on angiogenesis, apoptosis, cell proliferation, and tumor metastasis (Napolitano et al., 2012). A number of marine macrolides inhibit V-ATPases, including lobatamides, chondropsins, iejimalides, and several of the palmerolides (Bowman et al., 2003; Shen et al., 2003; Diyabalanage et al., 2006; Kazami et al., 2006; Noguez et al., 2011).

There are three types of PKS systems. Type I PKS systems in bacteria are primarily comprised of non-iteratively acting multimodular enzymes that lead to progressive elongation of a polyketide chain, though these megaenzymes can also include "stuttering" modules that may act iteratively (Wilkinson et al., 2000; Shen et al., 2007; Tatsuno et al., 2007). In addition, some bacterial Type I PKS systems are comprised solely of iteratively acting monomodular enzymes that catalyze a series of chain elongation steps for polyketide formation (Wang et al., 2020). Type II PKS systems typically contain separate, iteratively acting enzymes that biosynthesize polycyclic aromatic polyketides, while Type III PKS systems possess iteratively-acting homodimeric enzymes that often result in monocyclic or bicyclic aromatic polyketides (Shen et al., 2007). Type I PKS systems can be subdivided into two groups, depending upon whether the acyl transferase (AT) modules are encoded within each module at the site that is parallel to the functional role of the ATs, referred to as *cis*-AT Type I PKS, or physically distinct from the megaenzyme, which are referred to as *trans*-AT Type I PKS. In both cases, there are often parallel relationships between the genome order, the action of enzymatic modules, and the functional groups present in the growing polyketide chain, though in *trans*-AT systems deviations from these parallel relationships is more likely to be observed (Nguyen et al., 2008). In *trans*-AT systems, AT domains may be incorporated in a mosaic fashion through horizontal gene transfer (Nguyen et al., 2008). This introduces greater molecular architectural diversity over evolutionary time, as one clade of *trans*-ATs may select for a malonyl-CoA derivative, while the *trans*-AT domains in another clade may select for unusual or functionalized subunits (Haydock et al., 1995; Jenke-Kodama et al., 2005). Additionally, recombination, gene duplication, and conversion events can lead to further diversification of the resultant biosynthetic machinery (Nivina et al., 2019). Predictions regarding the intrinsic relationship between a secondary metabolite of interest, the biosynthetic megaenzyme, and the biosynthetic gene cluster (BGC) can be harnessed for natural product discovery and development (Kim et al., 2012; Videau et al., 2016; Greunke et al., 2018).

In the search for new and bioactive chemotypes as inspiration for the next generation of drugs, underexplored ecosystems hold promise as biological and chemical hotspots (McClintock et al., 2005). The vast Southern Ocean comprises one-tenth of the total area of Earth's oceans and is largely

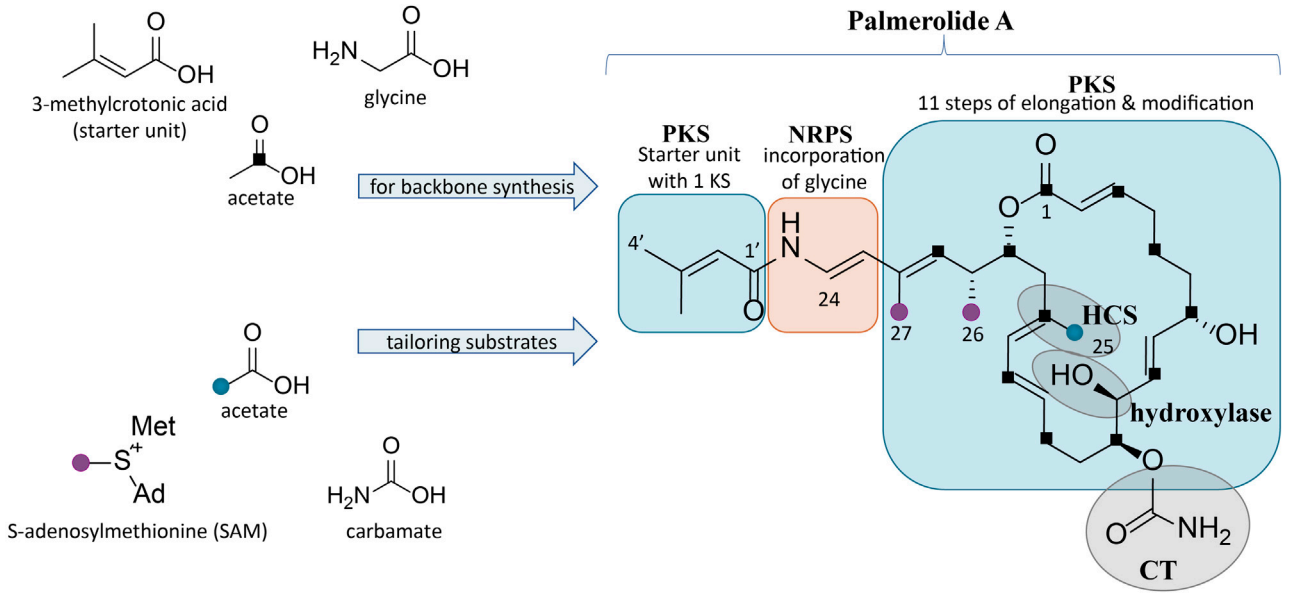

FIGURE 1 | Structure of palmerolide A with notations for the proposed retrobiosynthesis. Backbone synthesis is a result of incorporation of the starter unit, a glycine residue, and acetate subunits (C1 indicated by black squares). Structural features from *trans*-acting tailoring enzymes (indicated by grey ovals) utilize additional substrates: methyl transfers from SAM (purple dots), installation of C-25 methyl from acetate (blue dot) via an HCS cassette, and carbamoyl transfer to the secondary alcohol on C-11. The α-hydroxy group on C-10 is predicted to arise from incorporation of hydroxymalonic acid or a *trans*-acting hydroxylase.

unstudied for its chemodiversity. The coastal marine environment of Antarctica experiences seasonal extremes in, for example, ice cover, light field, and food resources. Taken with the barrier to migration imposed by the Antarctic Circumpolar Current and the effects of repeated glaciation events on speciation, a rich and endemic biodiversity has evolved, with consequent potential for new chemodiversity (McClintock et al., 2005; Clarke and Crame, 2010; Young et al., 2013).

Palmerolide A (**Figure 1**) is the principal secondary metabolite isolated from *Synoicum adareanum*, an ascidian which can be found in abundance at depths of 10–40 m in the coastal waters near Palmer Station, Antarctica (Diyabalanage et al., 2006). Palmerolide A is a macrolide polyketide that possesses potent bioactivity against malignant melanoma cell lines, while demonstrating minimal cytotoxicity against other cell lines (Diyabalanage et al., 2006). The National Cancer Institute's COMPARE algorithm was used to correlate experimental findings with a database for prediction of the biochemical mechanism of action by identifying the mechanism of action of palmerolide A as a V-ATPase inhibitor (Paull et al., 1995). Downstream effects of V-ATPase inhibition include an increase in both hypoxia induction factor-1α and autophagy (Diyabalanage et al., 2006; Von Schwarzenberg et al., 2013). Increased expression of V-ATPase on the surface of metastatic melanoma cells (Von Schwarzenberg et al., 2013) perhaps explains palmerolide A's selectivity for UACC-62 cell lines over the other cell types (Diyabalanage et al., 2006). Despite the relatively high concentrations of palmerolide A in the host tissue (0.49–4.06 mg palmerolide A x g^{-1} host dry weight) (Murray et al., 2020), isolation of palmerolide A from its Antarctic source in mass sufficient for drug development it is neither ecologically nor logistically feasible. Although synthetic strategies for palmerolide A have been reported (Jiang et al., 2007; Kaliappan and Gowrisankar, 2007; Nicolaou et al., 2008b; Penner et al., 2009; Lebar and Baker, 2010; Pujari et al., 2011; Pawar and Prasad, 2012; Lisboa et al., 2013), a clear pathway to achieve sufficient quantities needed for drug development has been elusive. Therefore, there is substantial interest in identifying the BGC responsible for palmerolide A production as this would pave a way for future drug development efforts.

Our approach to identify the palmerolide BGC (*pal* BGC) began with the characterization of the ascidian host-associated microbiome (Riesenfeld et al., 2008). Next, a persistent cohort of bacteria present across many individual ascidians – a core microbiome – for *Synoicum adareanum* was identified through analysis of occurrence of distinct amplicon sequence variants (ASV) from iTag sequencing of the Variable 3–4 regions of the bacterial 16S rRNA (Murray et al., 2020). This work ultimately led to the evaluation of the microbiome metagenome and the subsequent assembly of a nearly 4.3 Mbp metagenome assembled genome (MAG) of *Candidatus* Synoicihabitans palmerolidicus, a verrucomicrobium in the family *Opitutaceae* (Murray et al., 2021). Contained within the genome are five non-identical copies of a candidate *pal* BGC. Here, we report on a detailed bioinformatic analysis of the *pal* BGCs and conclude that at least three of the candidate BGCs likely are responsible for the biosynthesis

of palmerolides with structures that have been previously reported from Antarctic *S. adareanum* in this macrolide family (Diyabalanage et al., 2006; Noguez et al., 2011).

2 MATERIALS AND METHODS

The methods employed in this study used bioinformatic tools to develop predictive models of palmerolide biosynthesis. Enzymatic reactions and organic synthetic interpretations were based on homology analyses. Automated annotation and manual bioinformatic tools were used to discern the details of palmerolide A biosynthesis in addition to generating predictions for the other *pal* BGCs. The *Ca*. Synoicihabitans palmerolidicus MAG was annotated using antiSMASH (v. 5.0) (Blin et al., 2019) using the full complement of annotation options available. Then we predicted the gene cluster responsible for palmerolide A biosynthesis using retrobiosynthetic predictions focused on the 5' end of the BGCs (**Figure 1**). The annotation predictions were integrated and validated with results of additional protein family homology analysis, conserved domain searches, active site and motif identification to predict the step-wise biosynthesis of palmerolide A. Manual annotation of the *pal* BGC sequences included BLASTP searches to confirm enzymatic identities, then protein family alignments were used to identify active site residues key for stereochemical outcomes, confirm substrate affinities, and other biochemical synthesis details.

Additional manual bioinformatic efforts included obtaining BGCs from public NCBI databases for basiliskamide, bryostatin 1, calyculin, corallopyronin, mandelalide, onnamide, oxazolamycin, pederin, phormidolide, psymberin, sorangicin, and myxoviricin (**Supplementary Table S1**). ClustalO alignment tool in the CLC Genome Workbench (QIAGEN v. 20.0.3) was used for multiple sequence alignments of enzymatic domains with HMM Pfam Seeds obtained from EMBL-EBI and the amino acid sequences from the other PKS BGCs. MIBiG (Kautsar et al., 2020) was used to acquire the KS amino acid sequence from the type III PKS BGC responsible for 3-(2′-hydroxy-3′-oxo-4′-methylpentyl)-indole biosynthesis from *Xenorhabdus bovienii SS-2004* (GenBank Accession: FN667741.1), which was used for an outgroup. The *pal* BGC ACPs and PCPs were numbered according to their position in the proposed biosynthesis of palmerolide A. The BGC KSs were numbered according to their position in their proposed biosynthesis in the literature. Prior to the construction of the phylogenetic tree for the KS domains, the sequences in the alignment were manually inspected and trimmed. Phylogenetic trees were created in CLC Genome Workbench (QIAGEN v. 20.0.3) with Neighbour Joining (NJ) as a distance method and Bayesian estimation for ACP and PCP comparisons as well as for KS analysis. Jukes-Cantor was selected for the genetic distance model and bootstrapping was performed with 100 replicates. Additionally, the sequence of each KS in the *pal* BGCs was queried using the *trans*-AT PKS Polyketide Predictor (*trans*ATor) to help define the specificity of KS domains. The software is based on phylogenetic analyses of fifty-four *trans*-AT type I PKS systems with 655 KS sequences and the resulting clades are referenced to help predict the KS specificity for the upstream unit (Helfrich et al., 2019).

3 RESULTS AND DISCUSSION

3.1 Retrobiosynthetic Scheme for Palmerolide

A retrobiosynthetic scheme of the *pal* BGC was developed based on the chemical structure for palmerolide A, including modules consistent with a hybrid PKS-NRPS and tailoring enzymes for key functional groups (**Figure 1**). We hypothesized that the initial module would be PKS-like in nature to utilize 3-methylcrotonic acid as the starter unit followed by a NRPS domain for the incorporation of glycine. PKS elongation was predicted to be an 11-step sequence resulting in 22 contiguous carbons. Modifying enzymes that are encoded co-linearly were predicted to create the architectural diversity with olefin placement, reduction of certain carbonyl groups to secondary alcohols, and full reduction of other subunits. In addition, incorporation of methylmalonyl CoA or enzymatic activity of carbon methyltransferases (cMTs) were predicted to be responsible for the placement of methyl groups C-26 and C-27 from *S*-adenosylmethionine (SAM).

Several key structural features proposed to result from the action of *trans*-acting enzymes are present. For example, as seen in the kalimantacins (Mattheus et al., 2010), the carbamate on C-11 was hypothesized to be installed by a carbamoyl transferase (CT). The C-25 methyl group located on C-17 in the β-position to the carbonyl suggests the origin of this branch is likely from hydroxymethylglutaryl-CoA synthase (HCS) catalysis, rather than SAM-mediated methylation, which occurs at the α-position to the carbonyl. Methylation at the site of the β-carbonyl is unusual, but represented in a number of notable BGCs, such as those of the jamaicamides, bryostatins, curacin A, oocydin, pederin, and psymberin, among others; in biochemically characterized Type I PKS BGCs, HCS-mediated β-branch formation is the common mechanism (Chang et al., 2004; Edwards et al., 2004; Sudek et al., 2007; Fisch et al., 2009; Matilla et al., 2012). SAM-mediated methylation does, however, appear to be the origin of the C-26 and C-27 methyl groups. Lastly, the hydroxy group on C-10 in the α-position was hypothesized to arise by elongation resulting from hydroxymalonyl-CoA incorporation or by the action of a hydroxylase at a later stage of biosynthesis.

3.2 Proposed Architecture of the Putative *pal* Biosynthetic Gene Cluster and Biosynthesis of Palmerolide A

The *Ca.* Synoicihabitans palmerolidicus MAG (GenBank accession number JAGGDC000000000; NCBI BioProject accession number PRJNA662631) included candidate hybrid PKS-NRPS biosynthetic gene clusters that were present in

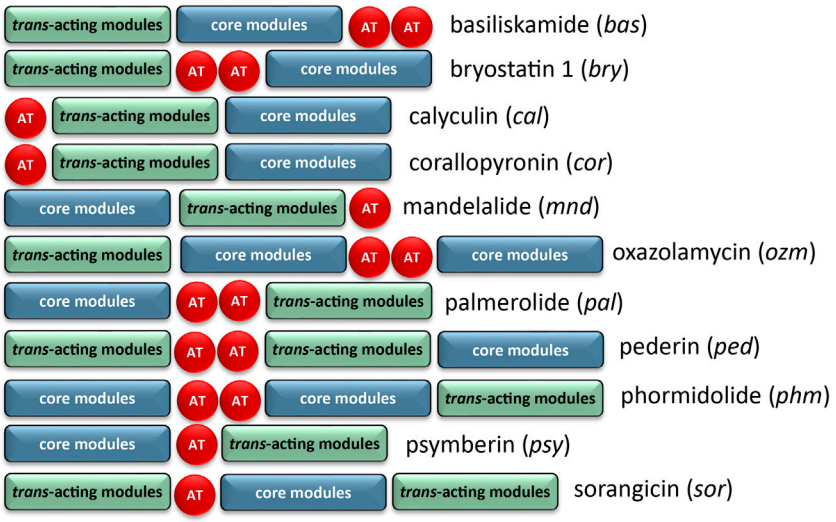

FIGURE 2 | Comparison of BGC organization of select *trans*-AT systems. There is significant variability in the order of the core modules, AT modules, and modules which contain *trans*-acting tailoring enzymes. There is also variability in the number of encoded AT modules, though the AT modules are typically encoded on separate, but tandem genes if more than one is present.

multiple, non-identical copies (Murray et al., 2021). Detailed inspection of one of these clusters (specifically contig 9 which corresponds to *pal* BGC 4, the first to be interrogated here) has excellent congruence with the retrobiosynthetic predictions outlined above (**Figure 1**). The results here in which we integrated BGC annotations predicted using AntiSMASH (Blin et al., 2019) with information from protein family homology analysis, conserved domain searches, active site and motif identification, together support the hypothesis that this ~75 kbp BGC is putatively responsible for palmerolide A production.

The architecture of the BGC reveals core biosynthetic domains followed by 2 ATs, and finally, a series of trans-acting domains (**Figure 2**). The structural backbone is explained by the NRPS and *trans*-AT PKS hybrid system. In addition, each of the tailoring enzymes that are expected for biosynthesis of the distinct chemical features (**Figure 1**) are encoded in the *Ca.* Synoicihabitans palmerolidicus genome. Comparisons of this overall modular architecture with 11 other *trans*-AT systems suggests a significant amount of flexibility in the organization of these BGCs (**Figure 2**). The psymberin BGC (Fisch et al., 2009) most closely resembles that of palmerolide in which the core modules are followed in line by AT modules, and *trans*-acting modules are encoded at the end of the cluster except that there is only a single AT reported in the case of mandelalide. The proposed BGC for palmerolide A is comprised of 14 core biosynthetic modules and 25 genes in a single operon of 74,655 bases (**Figure 3**). The 14 modules are co-linear and two *trans*-AT domains (modules 15 & 16) follow the core biosynthetic genes. Additional *trans*-acting genes contribute to backbone modifications with at least one gene contributing to post-translational tailoring (**Figure 3**).

3.2.1 An Unusual Starter Unit and Nonribosomal Peptide Synthetase Domains of *palA*

Bioinformatic analysis of the gene sequence suggests that the initial core biosynthetic domains of *palA* (modules 1 and 2) encode for the requisite acyl carrier proteins (ACP) (**Figure 3**). ACPs are typically responsible for tethering the acyl subunits to a phosopantetheine arm via thioester bond formation. Encoded in module 1 are three ACPs in tandem, which could serve to promote an increase in metabolite production (Gulder et al., 2011). The second in series is an ACP-β containing the conserved domain sequence GXDS (Bertin et al., 2016) which is likely the acceptor of a starter unit containing a β-branch. This is consistent with our proposed starter unit for palmerolide A, 3-methylcrotonic acid. While both *trans*-acting ATs, PalE and PalF, (**Figure 3**) possess the catalytic active site serine which is key for the proper positioning of the selected subunit within the hydrophobic cleft of the active site (Reeves et al., 2001; Helfrich and Piel, 2016), only the first AT, PalE, has a characteristic motif that includes an active site phenylalanine, conferring specificity for malonate selection (Yadav et al., 2003). The AT selecting the methylcrotonic acid starter unit is likely the second of the two *trans*-AT domains (PalF), which lacks definitive specificity for malonyl-CoA. In support of this hypothesis, some *trans*-acting ATs have demonstrated affinity for a wider range of substrates than their *cis*-acting counterparts (Dunn et al., 2014; Nivina et al., 2019). 3-Methylcrotonyl-CoA is an intermediate of branched-chain amino acid catabolism in leucine degradation; intermediates of this pathway can be diverted to secondary metabolite production (Díaz-Pérez et al., 2016). The subsequent NRPS module (module 2) contains condensation (C) and adenylation (A) domains as well as a carrier protein. Signature sequence information and NRPSPredictor2 analysis

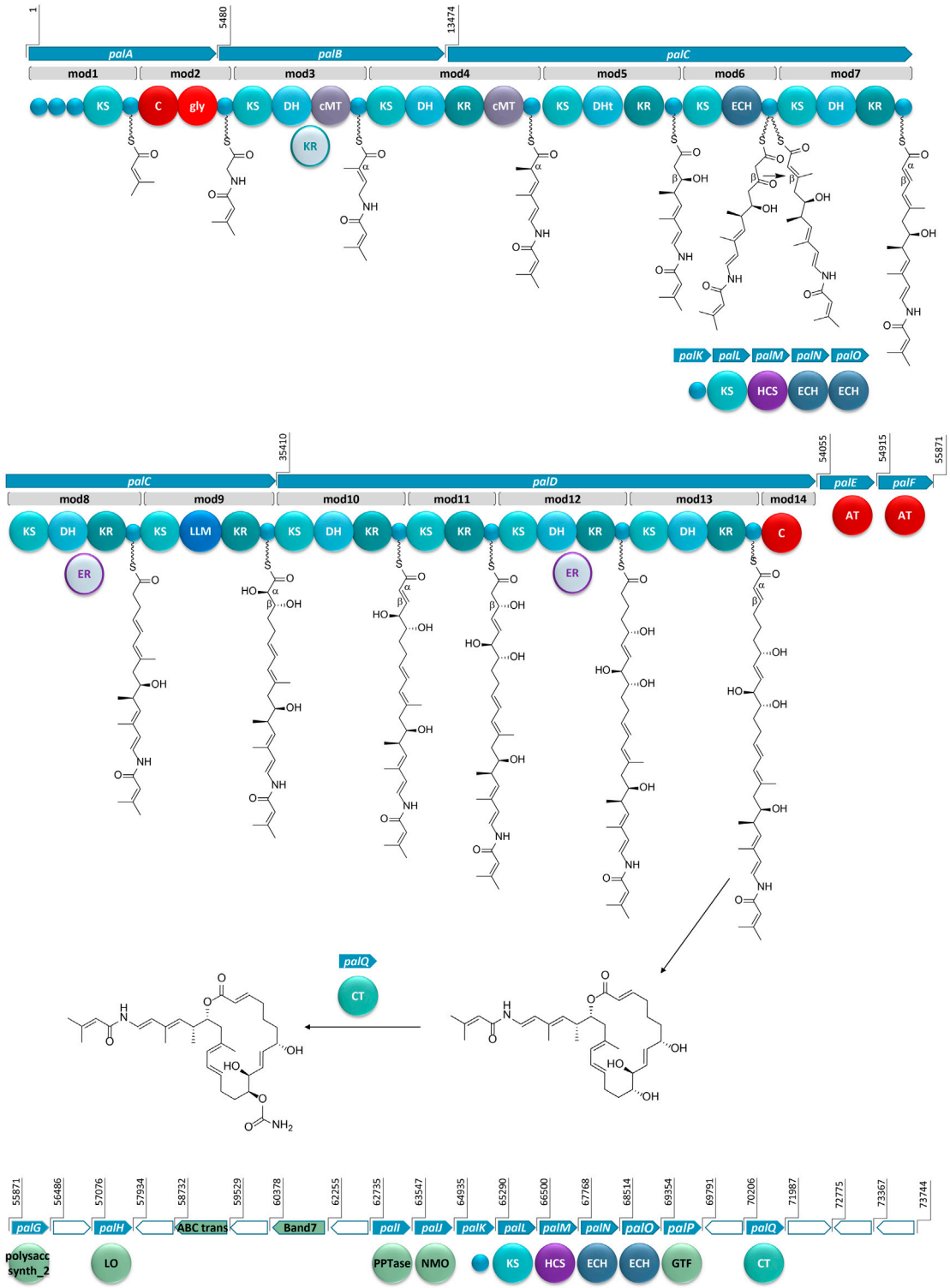

FIGURE 3 | The proposed BGC for palmerolide A, showing the hybrid PKS-NRPS system. KS: ketosynthase domain, C: condensation domain, gly: adenylation domain for glycine incorporation, DH: dehydratase domain, cMT: carbon methyl transferase domain, KR: ketoreductase domain, DHt: dehydratase variant; ECH: enoyl-CoA hydratase, LLM: luciferase-like monooxygenase, AT: acyl transferase; polysacc synt_2: polysaccharide biosynthesis protein, LO: lactone oxidase, ABC trans: ATP-binding cassette transporter, Band7: stomatin-like integral membrane, PPTase: phosphopantetheinyl transferase, NMO: nitronate monooxygenase, HCS: hydroxymethylglutaryl-CoA synthase, GTF: glycosyl transferase ER: enoyl reductase, CT: carbamoyl transferase, small blue circles represent acyl- or peptidyl-carrier proteins. Ppant arms are symbolized by wavy lines. The grey domains (the KR in mod3 and ERs in mod8 and mod12) indicate domains that would be expected to perform an enzymatic transformation; however, are not encoded in the BGC. Blue arrows indicate biosynthetic genes. Green arrows indicate genes that encode for non-biosynthetic proteins. White arrows reflect genes that encode for hypothetical proteins. The BGC is displayed in reverse compliment.

(Röttig et al., 2011; Blin et al., 2019) of the A domain are consistent with selection of a glycine residue. These domains incorporate the amino acid residue, resulting in the addition of a nitrogen and two carbons in this step of the biosynthesis of palmerolide A.

In a non-canonical fashion, the carrier proteins flanking the NRPS domains do not appear to be the expected ACP and peptidyl-carrier protein (PCP) for module 1 and 2, respectively. The carrier protein following the KS domain in module 1 was initially annotated as a non-β-branching ACP; however, phylogenetic analysis with the amino acid sequences of carrier proteins from other hybrid PKS-NRPS systems demonstrates that this carrier protein is in the same clade as PCPs (**Supplementary Figure S1**). The carrier protein associated with module 2, which was initially annotated simply as a phosphopantetheine attachment site (Pfam00550.24), is found to be more phylogenetically-related to ACPs within PKS-NRPS systems (**Supplementary Figure S1**). Notably, it possesses the (D/E)xGxDSL motif for phosphopantetheine arm attachment (Keatinge-Clay, 2012) with the exception of an isoleucine rather than leucine in the final position of the motif, which is a residue common to other ACPs from hybrid PKS-NRPS systems (**Supplementary Figure S2**). Typically, a PCP would follow the domains in NRPS-like modules, however, there are exceptions in the literature. For example, the BGCs for both corallopyronin and oxazolamycin contain ACPs following an A domain (Erol et al., 2010; Zhao et al., 2010). This non-canonical finding could point to the acquisition of these domains over evolutionary time, as the carrier protein for module 1 is encoded in *palA*, the same gene encoding the proteins for both modules 1 and 2, whereas the carrier protein for module 2 is encoded at the beginning of *palB*, a gene which encodes for only PKS domains (**Figure 3**).

3.2.2 Contiguous Polyketide Synthase Chain and *Trans*-Acting Enzymes at Site of Action for *palB* – *palD*

The contiguous carbon backbone of palmerolide A is proposed to arise from 11 cycles of elongation in which the synthesis proceeds through a series of modules with a variety of enzymatic domains that include an ACP, KS, and associated genes that establish the oxidation state of each subunit (**Figure 3**). The first module of *palB* (module 3) includes a dehydratase (DH) and cMT domains, a sequence which results in a chain extension modification to an α,β-unsaturated thioester, a result of the action of the encoded DH. The expected KR domain that would be responsible for the Δ^{22} olefin (**Figure 3**) is not present. The BGCs for bryostatin 1, corallopyronin, and sorangicin also lack an accompanying KR domain to work in concert with an encoded DH. The unaccompanied DH in the bryostatin 1 and corallopyronin systems are deemed inactive; however, an olefin results from the DH in the absence of an accompanying KR in both modules 9 and 11 of the sorangicin BGC (Sudek et al., 2007; Erol et al., 2010; Irschik et al., 2010). The subsequent cMT methylation is consistent with an *S*-adenosylmethionine (SAM)-derived methyl group, as expected for C-27 in palmerolide A. Module 4, spanning the end of *palB* and beginning of *palC*, includes a DH, a ketoreductase (KR), and another cMT domain. This cluster of domains is predicted to result in the methyl-substituted conjugated diene of the macrolide tail (C-19 through C-24, C-26 on palmerolide A).

The substrate critical for macrolactonization of the polyketide is the C-19 hydroxy group, a result of the action of the KS and KR domains encoded in module 5 (**Figure 3**). Interestingly, a domain initially annotated as a dehydratase (DHt) at this location may contribute to the final cyclization and release of the molecule from the megaenzyme by assisting the terminal C domain with ring closure (Bertin et al., 2016). The DHt sequence does not possess the hotdog fold that is indicative of canonical dehydratases (Cantu et al., 2010), and therefore, may not truly represent a DH. Alternatively, this domain could be responsible for the olefin shifts to the β,γ-positions, as seen in bacillaene and ambruticin biosynthesis (Moldenhauer et al., 2010; Berkhan et al., 2016).

In addition to a standard ACP and KS encoded in module 6, which would lead to a ketone function, an enoyl-CoA hydratase (ECH) is also encoded. Based on our retrobiosynthetic analysis, the ketone at C-17 is the necessary substrate for HCS-catalyzed β-branch formation, resulting in the C-25 methyl group on C-17. We propose that the ECH encoded in module 6 works in concert with the HCS cassette. The HCS cassette (PalK through PalO) is comprised of a series of *trans*-acting domains, including an ACP, an HCS, a free KS, and 2 additional ECH modules (**Figure 3**). The HCS cassette can act while the elongating chain is tethered to an ACP module, rather than after cyclization and release (Moldenhauer et al., 2007; Hertweck, 2009). The two ECHs in the HCS cassette along with the ECH encoded in-line with the core biosynthetic genes would be responsible for isomerization of a terminal methylene to the observed internal olefin. An HCS cassette formed by the combination of a *trans*-KS and at least one ECH module with an HCS domain is reported in several other bacterial BGCs such as bryostatin 1, calyculin A, jamaicamide, mandelalide, phormidolide, and psymberin (Sudek et al., 2007; Wakimoto et al., 2014; Edwards et al., 2004; Lopera et al., 2017; Bertin et al., 2016; Fisch et al., 2009; respectively). The domain structure for the HCS cassettes has a remarkably high degree of synteny across these diverse BGCs (Buchholz et al., 2010), however, the presence of a *cis*-ECH domain in these biosynthetic systems may vary. There is precedence for a similar domain architecture in oocydin, pederin, onnamide, psymberin, phormidolide, and mandelalide, though the presence of the additional ECH domain in-line with the core biosynthetic genes does not necessarily correlate with the formation of an internal versus terminal olefin (Piel et al., 2004; Fisch et al., 2009; Matilla et al., 2012; Bertin et al., 2016; Lopera et al., 2017).

There is substantial similarity in the domain structure of module 7, module 10, and module 13, whereby each includes a KS, DH, and KR (**Figure 3**). The olefin that arises from the action of module 7, concomitant with carbon chain elongation, is conjugated with the Δ^{16} olefin adjacent to the C-17 β-branch. Modules 10 and 13 have similar enzymatic composition to 7 and are likely responsible for Δ^{8} and Δ^{2} olefins. The combination of KR and DH domains are also found in modules 8 and 12; however, in concert with an as of yet unidentified *trans*-acting

enoyl reductase domain (ER), these olefins would be reduced to fully saturated monomeric subunits. There are some examples of *trans*-acting ER domains carrying out this function, including OocU in oocydin, SorN in sorangicin, and MndM in mandelalide (Irschik et al., 2010; Matilla et al., 2012; Lopera et al., 2017), while in other systems, such as corallopyronin and leinamycin, the reductions of the olefins are largely unexplained (Cheng et al., 2003; Erol et al., 2010). The reduction by a *trans*-acting enzyme often occurs while the elongating polyketide is tethered to the megaenzyme, as evidenced by the downstream specificity of the KS module for Claisen-type condensation with subunits containing single or double bonds (Irschik et al., 2010).

The genetic architecture for the biosynthesis of two functional groups essential for bioactivity is encoded in module 9 (**Figure 3**). Structure-activity relationship studies demonstrate the importance of the C-10 hydroxyl group and the C-11 carbamate (Nicolaou et al., 2008a). The KR domain predicting the C-11 alcohol function serves as the substrate for the carbamoyl transferase (*palQ*) in a post-translational modification (Haydock et al., 2005; Chen et al., 2009; Mihali et al., 2011). Intriguingly, a domain annotated as a luciferase-like monooxygenase (LLM) in module 9 initially seemed out of place. However, palmerolide A has a hydroxy group at C-10, which represents an α-hydroxylation. LLMs associated with BGCs may not serve as true luciferases, but, instead, demonstrate oxidizing effects on polyketides and peptides without evidence of corresponding bioluminescence (El-Sayed et al., 2001; Maier et al., 2015). For example, there is an overrepresentation of LLMs in *Candidatus* Entotheonella BGCs without known bioluminescence (Lackner et al., 2017). As demonstrated through individual inactivation of the LLM in the BGC of mensacarin, a Type II PKS system, Msn02, Msn04, and Msn08 have key activity as epoxidases and hydroxlases (Maier et al., 2015). There are several examples of LLMs in modular Type I PKS systems. OnnC from onnamide and NazB from nazumamide are two LLMs in *Candidatus* Endotheonella that are proposed to serve biosynthetically as hydroxylases (Lackner et al., 2017). In calyculin and mandelalide, the CalD and MndB LLMs catalyze chain shortening reactions through α-hydroxylation and Baeyer-Villiger-type oxidation reactions (Wakimoto et al., 2014; Lopera et al., 2017). Phormidolide has a LLM that adds a hydroxy group, which is hypothesized to attack an olefin through a Michael-type addition for cyclization with enzymatic assistance from a pyran synthase (Bertin et al., 2016). The hydroxylation that is key in cyclization of oocydin A is likely installed by OocK or OocM, flavin-dependent monooxygenases that are contiguous to the PKS genes and are thought to act while the substrate is bound to a portion of the PKS megaenzyme (Matilla et al., 2012). It is this hydroxylase activity that we propose for the LLM in module 9. Since the producing bacteria is yet to be cultured, it is not established whether this LLM may also serve a role in bioluminescence and/or quorum sensing. Further evidence for the role of the LLM is provided through alignment against other LLMs. In addition to the annotation within Pfam00296, which includes the bacterial LLMs, the sequence aligns with the hidden Markov models of the TIGR subfamily 04020, which contains natural product biosynthesis LLMs (Lackner et al., 2017). The subfamily occurs in both NRPS and PKS systems as well as small proteins with binding of either flavin mononucleotide or coenzyme F420. Alignment of the LLMs from multiple PKS systems, including palmerolide A, shows homology with model sequences from the TIGR subfamily 04020 (**Supplementary Figure S3**).

The addition of C-5 and C-6 and the reduction of the β-carbonyl to form the C-7 hydroxy group of palmerolide A, is due to module 11, which possesses a KR domain in addition to elongating KS (**Figure 3**). In the structure of palmerolide A this is followed by the fully reduced subunit from module 12 as discussed above. The final elongation results from module 13, which includes DH and KR domains that contribute to the conjugated ester found as palmerolide A's C-1 through C-3, completing the palmerolide A C_{24} carbon skeleton.

3.2.3 Noncanonical Termination Condensation Domain in *palD* for Product Cyclization and Release

Typically, PKS systems terminate with a thioesterase (TE) domain, leading to release of the polyketide from the megaenzyme (Piel, 2002; Gu et al., 2009; Gehret et al., 2011; Lopera et al., 2017). This canonical domain is not present in the *pal* cluster. Instead, the final module in the *cis*-acting biosynthetic gene cluster includes a truncated condensation domain comprised of 133 amino acid residues, compared to the approximately 450 residues that comprise a standard condensation domain (Stachelhaus et al., 1998) (**Figure 3**). Condensation domains catalyze cyclization through ester formation in free-standing condensation domains that act in *trans* as well as in NRPS systems (Zaleta-Rivera et al., 2006; Lin et al., 2009). In addition, this non-canonical termination domain is not without precedent in hybrid PKS-NRPS and in PKS systems as both basiliskamide and phormidolide include condensation domains for product release (Theodore et al., 2014; Bertin et al., 2016). Though the terminal condensation domain in the *pal* BGC is shortened, it maintains much of the HHXXDDG motif (**Supplementary Figure S3**), most notably the second histidine, which serves as the catalytic histidine in the condensation reaction (Stachelhaus et al., 1998).

3.2.4 Stereochemical and Structural Confirmation Based on Sequence Information

KR domains are NADPH-dependent enzymes that belong to the short-chain dehydrogenase superfamily, with Rossman-like folds for co-factor binding (Keatinge-Clay and Stroud, 2006; Keatinge-Clay, 2012). Enzymatically, the two KR subtypes, A-Type and B-type, are responsible for stereoselective reduction of β-keto groups and can also determine the stereochemistry of α-substituents. C-type KRs, however, lack reductase activity and often serve as epimerases. A-Type KRs have a key tryptophan residue in the active site, do not possess the LDD amino acid motif, and result in the reduction of β-carbonyls to L-configured hydroxy groups (Keatinge-Clay, 2012). B-Type, which are identified by the presence of an LDD amino acid motif, result in formation of D-configured hydroxy groups (Keatinge-Clay, 2012). The stereochemistry observed in palmerolide A is reflected in the active site sequence

information for the L-configured hydroxy group from module 5 and D-configured hydroxy group from module 11 (**Figures 1**, **3**). When an enzymatically active DH domain is within the same module, the stereochemistry of the *cis*- versus *trans*-olefin can be predicted, as the combination of an A-Type KR with a DH results in a *cis*-olefin formation and the combination of a B-Type KR with a DH results in *trans*-olefin formation. The *trans*-α,β-olefins arising from module 7 (Δ^{14}), module 10 (Δ^{8}), and module 13 (Δ^{2}) stem from B-Type KRs and active DHs. The other three olefins present in the structure of palmerolide A, as noted above, likely have positional and stereochemical influence during the enzymatic shifts to the β,γ-positions (Δ^{21} and Δ^{23}) or from the ECH domain (module 6).

Additional insights into the structural features of the resulting compound were obtained through defining the specificity of KS domains using phylogenetic analysis and the *trans*-AT PKS Polyketide Predictor (*trans*ATor) bioinformatic tool (Helfrich et al., 2019). KS domains catalyze the sequential two-carbon elongation steps through a Claisen-like condensation with a resulting β-keto feature (Khosla et al., 2007). Additional domains within a given module can modify the β-carbonyl or add functionality to the adjacent α- or γ-positions (Keatinge-Clay, 2012). Specificity of KSs, based on the types of modification located on the upstream acetate subunit were determined and found to be mostly consistent with our retrobiosynthetic predictions (**Supplementary Figure S4**, **Supplementary Table S2**). For example, the first KS, KS1 (module 1), is predicted to receive a subunit containing a β-branch. KS3 (module 4) and KS4 (module 5) are predicted to receive an upstream monomeric unit with α-methylation and an olefinic shift, consistent with the structure of palmerolide A and with the enzymatic transformations resulting from module 3 and module 4, respectively. Interestingly, the KS associated with the HCS cassette branches deeply compared to all others upon phylogenetic analysis (**Supplementary Figure S4**). *Trans*ATor also aided in confirming the stereochemical outcomes of the hydroxy groups and olefins, which occur through reduction of the β-carbonyls. The predictions for the D-configured hydroxy groups were consistent with not only the presence of the LDD motif, indicative of B-type KR as outlined above, but also with stereochemical determination based on the clades of the KS domains of the receiving modules, KS5 (module 6) and KS11 (module 12). They are also consistent with the structure of palmerolide A. The KS predictions, however, did not aid in confirming reduction of the upstream olefins for KS8 (module 9) and KS12 (module 13).

3.2.5 Additional *Trans*-Acting Domains and Domains Between Genes Responsible for Biosynthesis

A glycosyl transferase (PalP) and lactone oxidase (PalH) that are often associated with glycosylation of polyketides are encoded in the palmerolide A BGC following the AT domains and preceding the HCS cassette (**Figure 3**). Though glycosylated palmerolides have not been observed, glycosylation as a means of self-resistance in *Streptomyces* has been described (Quirós et al., 1998; Wencewicz, 2019) and is hypothesized as a role for these observed domains in the BGC. Glycosyl transferases are found in other macrolide- and non-macrolide-producing organisms as a means to inactivate hydroxylated polyketides (Jenkins and Cundliffe, 1991; Gourmelen et al., 1998). Though prokaryotic V-ATPases tend to be more structurally simple than those of eukaryotes, there is homology in the active sites of prokaryotic and eukaryotic V-ATPases making the pro-drug hypothesis for self-resistance a reasonable hypothesis in palmerolide A biosynthesis (Yokoyama and Imamura, 2005). The D-arabinono-1,4-lactone oxidase (*palH*) is a FAD-dependent oxidoreductase that likely works in concert with the glycosyltransferase. An ATP-binding cassette (ABC) transporter is encoded between the core biosynthetic genes and the genes for the *trans*-acting enzymes (Murray et al., 2021). This transporter, which has homology to SryD and contains the key nucleotide-binding domain GGNGSGKST, may be responsible for the translocation of the macrolide out of the cell, since it is housed within the BGC, it is likely under the same regulatory control. Additionally, a few hypothetical proteins of unknown function are present downstream of the core biosynthetic genes. Together these genes encoding potential macrolide glycosylation and transport functions may play a role in the bioactivity and export of palmerolide A from the producing organism. Future integrated studies will be needed to decipher the functions of these genes *in situ*.

3.3 Multiple Copies of the *pal* Biosynthetic Gene Cluster Explain Structural Variants in the Palmerolide Family

Careful assembly of the *Ca*. Synoicihabitans palmerolidicus MAG revealed the *pal* BGC was present in multiple copies (**Figure 4** and **Supplementary Figures S5–S7**) (Murray et al., 2021), evidenced by their independent anchoring loci within the MAG and supported by a five-fold increase in depth of coverage relative to the rest of the genome. The structural complexity of the multicopy BGCs represents a biosynthetic system that is similar to that found in *Ca*. Didemnitutus mandela, another ascidian-associated verrucomicrobium in the family *Opitutaceae* (Lopera et al., 2017). The five distinct Type I PKS BGCs with significant regions of overlap are likely responsible for much of the structural diversity in the family of palmerolides (Diyabalanage et al., 2006; Noguez et al., 2011) (**Figure 4**). Palmerolide A, which is the predominant secondary metabolite isolated from *Synoicum adareanum* (Murray et al., 2020), is hypothesized to arise from the BGC designated as *pal* BGC 4 with additional compounds also arising from this cluster. The other clusters designated as *pal* BGC 1, *pal* BGC 2, *pal* BGC 3, and *pal* BGC 5 and their potential biosynthetic products of each are described below. It is hypothesized that there are three levels of diversity introduced to create the family of palmerolides: 1) differences in the site of action for the *trans*-acting domains (with additional *trans*-acting domains at play as well), 2) promiscuity of the initial selection of the starter subunit, and 3) differences in the core biosynthetic genes with additional PKS domains or stereochemical propensities within a module.

There are several palmerolides that likely arise from the same BGC encoding the megaenzyme responsible for palmerolide A

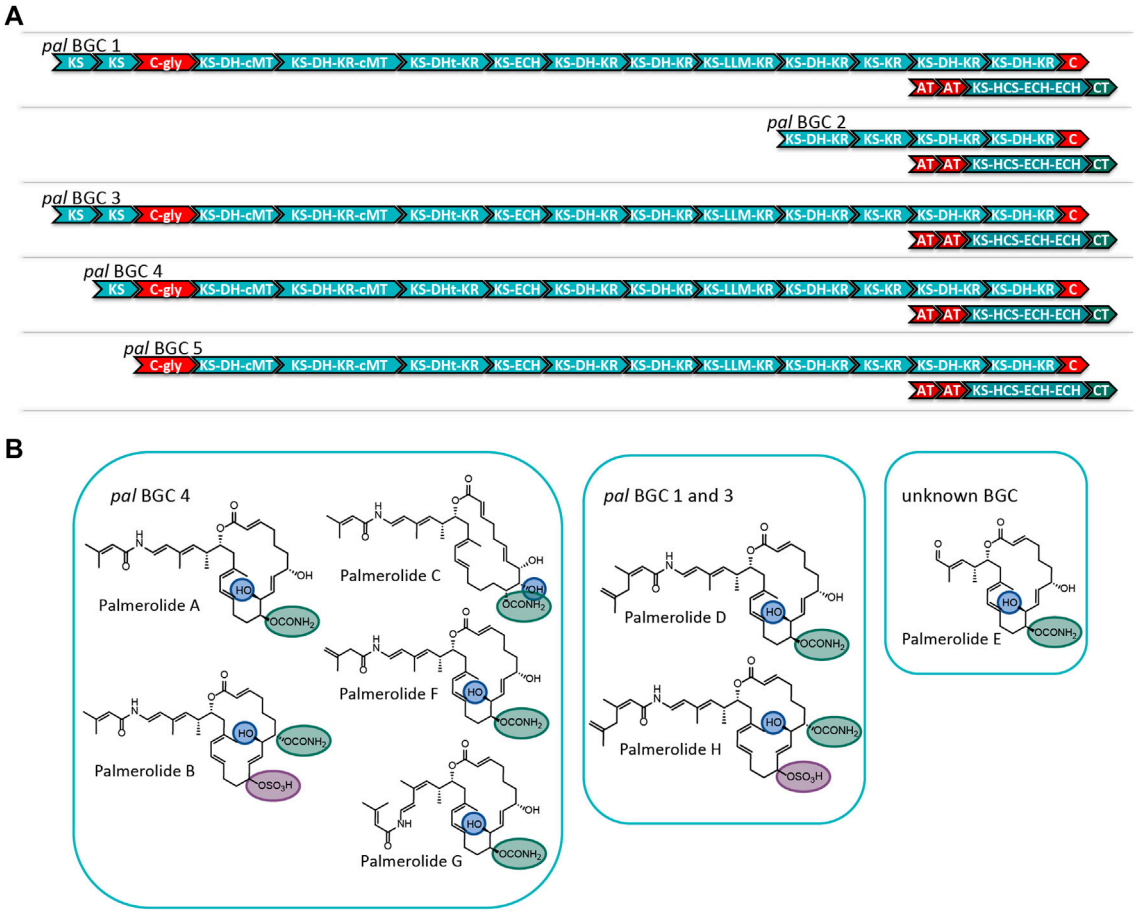

FIGURE 4 | (A) Comparison of the modular structure of the 5 *pal* BGCs. **(B)** Family of palmerolides. Much of the structural diversity can be explained by differences due to starter unit promiscuity, sites of action for the *trans*-acting tailoring enzymes, and differences in the core modules of the multiple *pal* BGCs. It is proposed that *pal* BGC 4 is responsible for not only palmerolide A, but also palmerolide B, palmerolide C, palmerolide F, and palmerolide G. It is interesting to note that the modular structure of the domains responsible for biosynthesis are equivalent for *pal* BGC 1 and *pal* BGC 3. These two BGCs contain an additional KS domain as compared to *pal* BGC 4 and are likely responsible for the biosynthesis of palmerolide D and palmerolide H.

(*pal* BGC 4). We hypothesize that the *trans*-acting domains have different sites of action than what is seen in palmerolide A biosynthesis. For example, the chemical scaffold of palmerolide B (**Figure 4**) is similar to palmerolide A, though the carbamate transfer occurs on the C-7 hydroxy group. Palmerolide B instead bears a sulfate group on the C-11 hydroxy group; proteins with homology to multiple types of sulfatases from the UniProtKB database (P51691, P15289, O69787, Q8ZQJ2) are found in the genome of *Ca.* Synoicihabitans palmerolidicus (Murray et al., 2021), but are not encoded within the BGCs. One of these *trans*-acting sulfatases likely modifies the molecule post-translationally. Other structural differences including the hydroxylation on C-8 instead of C-10 (as observed in palmerolide A) and the Δ^9 olefin that differs from palmerolide A's Δ^8 olefin, are either due to a difference of the site of action of the LLM (module 9) or a *trans*-acting hydroxylase. Another member of the compound family, palmerolide C, has structural differences attributable to *trans*-acting enzymes as well. Again, a *trans*-acting hydroxylase or the LLM is proposed to be responsible for hydroxylation on C-8. A hydroxy group on C-9 occurs through reduction of the carbonyl. The carbamate installation occurs on C-11 after *trans*-acting hydroxylation or LLM hydroxylation. In addition, the Δ^8 olefin in palmerolide A is not observed, but rather a Δ^6 olefin.

Additional levels of structural variation are seen at the site of the starter unit, likely due to a level of enzymatic promiscuity of the second AT (PalF). This, combined with differences in the sites of action for the *trans*-acting domains, is likely responsible for the structural differences observed in palmerolide F (**Figure 4**). The terminal olefin on the tail of the macrolide, which perhaps is a product of promiscuity of the selection of the starter unit, the isomeric 3-methyl-3-butenoic acid, is consistent with the aforementioned lack of consensus for malonate selection by the AT. In addition, the KS that receives the starter unit is phylogenetically distinct from the other KS in the *pal* clusters (**Supplementary Figure S4**).

The retrobiosynthetic hypothesis for palmerolide G (**Figure 4**) has much similarity to what is present in *pal* BGC 4; however, the presence of a *cis*-olefin rather than a *trans*-olefin could arise from

a difference in the enzymatic activity of module 4. This olefin subsequently undergoes an olefinic shift and, therefore, the stereochemistry is not solely reliant upon the action of the associated KR. Although this difference has not been identified in the BGCs in the samples sequenced, this could be present in other environmental samples that have been batched for processing and compound isolation. Currently, the biosynthetic mechanism is unknown.

The modular structure of two palmerolide BGCs (*pal* BGC 1 and *pal* BGC 3) are identical to one another (**Supplementary Figure S5**) and possess an additional elongation module when compared to *pal* BGC 4. In fact, there are only two single nucleotide polymorphisms (SNPs) and a single deletion between these two BGCs. Palmerolide D (**Figure 4**) is structurally very similar to palmerolide A with the exception of elongation in the carboxylate tail of the macrolide by an isopropyl group. This could arise from one additional round of starter unit elongation via a KS and methylation. These two identical BGCs are consistent with the additional elongation module found in *pal* BGC 1 and *pal* BGC 3. The overall architecture and stereochemistry are otherwise maintained. Palmerolide H (**Figure 4**) also likely arises from these two BGCs although it includes the structural differences of both palmerolide B and palmerolide D in which it contains the extended carboxylate tail with a terminal olefin and incorporates hydroxylation on C-8 rather than C-10. Again, there is no genomic evidence that this hydroxylation in the α-position is due to incorporation of hydroxymalonate to explain this but is instead likely due to a *trans*-acting hydroxylase. The carbamate installation occurs on C-7, while sulfonation occurs on C-11 and α-hydroxy placement is on C-8.

The final two *pal* BGCs are shorter with a reduced number of biosynthetic modules found compared to *pal* BGC 4. The gene structure of *pal* BGC 5 (**Supplementary Figure S6**) shows preservation of many of the core biosynthetic genes; however, there are no pre-NRP PKS modules noted in the BGC. The HCS cassette, glycosyl transferase, and CT are all present downstream. The predicted product of this cluster does not correspond with a known palmerolide, though post-translational hydrolysis of the C-24 amide may result in a structure similar to palmerolide E (**Figure 4**), which maintains much of the structure of palmerolide A; however, it is missing the initial polyketide starter unit and the glycine subunit. The final *pal* BGC in *Ca.* Synoicihabitans palmerolidicus, *pal* BGC 2 (**Supplementary Figure S7**), includes only five elongating modules, which would result in a 10-carbon structure that has not been isolated. Interestingly, despite the shortened BGC, the HCS cassette, glycosyl transferase, and CT are all present downstream, and the sequence itself aligns perfectly with few SNPs to the other BGCs (Murray et al., 2021). There would only be a single hydroxy group serving as a substrate for the CT, glycosyl transferase, and sulfatase to act. The 2-carbon site of action for the β-branch introduced in the palmerolide A structures would not be present. The structure-based retrobiosynthesis of the eight known palmerolides (A-F) can be hypothesized to arise from differences in the core biosynthetic genes of these non-identical copies of the *pal* BGC, starter unit promiscuity, and differing sites of action in the *trans*-acting enzymes.

4 CONCLUSION

The putative *pal* BGC has been described and represents the first BGC elucidated from an Antarctic organism (Murray et al., 2021). As outlined in this retrobiosynthetic strategy, the *pal* BGC represents a *trans*-AT Type I PKS-NRPS hybrid system with compelling alignment to the predicted biosynthetic steps for palmerolide A. The *pal* BGC is proposed to begin with PKS modules resulting in the incorporation of an isovaleric acid derivative, 3-methylcrotonic acid, as a starter unit, followed by incorporation of a glycine residue with NRPS-type modules. Thereafter, eleven rounds of progressive polyketide elongation likely occur and leading to varying degrees of oxidation introduced with each module. There are several interesting non-canonical domains encoded within the BGC, such as an HCS, CT, LLM, and a truncated condensation termination domain. Additionally, a glycosylation domain may be responsible for reversible, pro-drug formation to produce self-resistance to the V-ATPase activity of palmerolide A. There are several additional domains, the function of which have yet to be determined.

A combination of modular alterations, starter unit differences, and activity of *trans*-acting enzymes contributes to Nature's production of a suite of palmerolide analogues. There are a total of five distinct *pal* BGCs in the MAG of *Ca.* Synoicihabitans palmerolidicus, predicted to yield the known eight palmerolides, with genetic differences that explain some of the structural variety seen within this family of compounds. These include differences in modules that comprise the core biosynthetic genes. Additionally, it is proposed that some of the architectural diversity of palmerolides arises from different sites of action of the *trans*-acting, or non-colinear, modules. Starter unit promiscuity is another potential source of the structural differences observed in the compounds. Analysis of the *pal* BGC not only provides insight into the architecture of this Type I PKS-NRPS hybrid BGC with unique features, but also lays the foundational groundwork for drug development studies of palmerolide A via heterologous expression.

DATA AVAILABILITY STATEMENT

The BGC data presented in the study are deposited in the MIBiG database (https://mibig.secondarymetabolites.org/), accession numbers: BGC0002118 (for *pal* BGC 4) and BGC0002119 (for *pal* BGC 3).

AUTHOR CONTRIBUTIONS

This work was the result of a team effort in which the following contributions are recognized: conceptualization, AM, PC, and BB; methodology, NA, AM, PC, and BB; data analysis, NA, AM, HD, C-CL, KD, AD, PC, and BB; data curation, NA, AM, HD, C-CL, PC, and BB; original draft preparation, NA, BB, AM, and HD; review and editing, NA, BB, AM, C-CL, HD, PC, and AD; funding acquisition, AM, PC, and BB. All authors have read and agreed to the published version of the manuscript.

FUNDING

Support for this research was provided in part by the National Institutes of Health award (CA205932) to AM, BB, and PC, with additional support from National Science Foundation awards (ANT-0838776, and PLR-1341339 to BB, ANT-0632389 to AM).

ACKNOWLEDGMENTS

The authors acknowledge the assistance of field team members, including William Dent, Charles D. Amsler, James B. McClintock, Margaret O. Amsler, and Katherine Schoenrock. This work would not have been possible without the outstanding logistical support of the United States Antarctic Program. Lucas Bishop, Robert Read, and Mary L. Higham are also recognized for their contributions.

SUPPLEMENTARY MATERIAL

The Supplementary Material for this article can be found online at: https://www.frontiersin.org/articles/10.3389/fchem.2021.802574/full#supplementary-material

REFERENCES

Berkhan, G., Merten, C., Holec, C., and Hahn, F. (2016). The Interplay between a Multifunctional Dehydratase Domain and a C-Methyltransferase Effects Olefin Shift in Ambruticin Biosynthesis. *Angew. Chem. Int. Ed.* 55, 13589–13592. doi:10.1002/anie.201607827

Bertin, M. J., Vulpanovici, A., Monroe, E. A., Korobeynikov, A., Sherman, D. H., Gerwick, L., et al. (2016). The Phormidolide Biosynthetic Gene Cluster: A *Trans*-AT PKS Pathway Encoding a Toxic Macrocyclic Polyketide. *ChemBioChem* 17, 164–173. doi:10.1002/cbic.201500467

Blin, K., Shaw, S., Steinke, K., Villebro, R., Ziemert, N., Lee, S. Y., et al. (2019). antiSMASH 5.0: Updates to the Secondary Metabolite Genome Mining Pipeline. *Nucleic Acids Res.* 47, W81–W87. doi:10.1093/nar/gkz310

Bordeleau, M.-E., Matthews, J., Wojnar, J. M., Lindqvist, L., Novac, O., Jankowsky, E., et al. (2005). Stimulation of Mammalian Translation Initiation Factor eIF4A Activity by a Small Molecule Inhibitor of Eukaryotic Translation. *Proc. Natl. Acad. Sci.* 102, 10460–10465. doi:10.1073/pnas.0504249102

Bowman, E. J., Gustafson, K. R., Bowman, B. J., and Boyd, M. R. (2003). Identification of a New Chondropsin Class of Antitumor Compound that Selectively Inhibits V-ATPases. *J. Biol. Chem.* 278, 44147–44152. doi:10.1074/jbc.M306595200

Buchholz, T. J., Rath, C. M., Lopanik, N. B., Gardner, N. P., Håkansson, K., and Sherman, D. H. (2010). Polyketide β-Branching in Bryostatin Biosynthesis: Identification of Surrogate Acetyl-ACP Donors for BryR, an HMG-ACP Synthase. *Chem. Biol.* 17, 1092–1100. doi:10.1016/j.chembiol.2010.08.008

Cantu, D. C., Chen, Y., and Reilly, P. J. (2010). Thioesterases: A New Perspective Based on Their Primary and Tertiary Structures. *Protein Sci.* 19, 1281–1295. doi:10.1002/pro.417

Carroll, A. R., Copp, B. R., Davis, R. A., Keyzers, R. A., and Prinsep, M. R. (2019). Marine Natural Products. *Nat. Prod. Rep.* 36, 122–173. doi:10.1039/c8np00092a

Chang, Z., Sitachitta, N., Rossi, J. V., Roberts, M. A., Flatt, P. M., Jia, J., et al. (2004). Biosynthetic Pathway and Gene Cluster Analysis of Curacin A, an Antitubulin Natural Product from the Tropical Marine Cyanobacterium *Lyngbya majuscula*. *J. Nat. Prod.* 67, 1356–1367. doi:10.1021/np0499261

Chen, W., Huang, T., He, X., Meng, Q., You, D., Bai, L., et al. (2009). Characterization of the Polyoxin Biosynthetic Gene Cluster from *Streptomyces cacaoi* and Engineered Production of Polyoxin H. *J. Biol. Chem.* 284, 10627–10638. doi:10.1074/jbc.M807534200

Cheng, Y.-Q., Tang, G.-L., and Shen, B. (2003). Type I Polyketide Synthase Requiring a Discrete Acyltransferase for Polyketide Biosynthesis. *Proc. Natl. Acad. Sci.* 100, 3149–3154. doi:10.1073/pnas.0537286100

Clarke, A., and Crame, J. A. (2010). Evolutionary Dynamics at High Latitudes: Speciation and Extinction in Polar Marine Faunas. *Phil. Trans. R. Soc. B* 365, 3655–3666. doi:10.1098/rstb.2010.0270

Dejong, C. A., Chen, G. M., Li, H., Johnston, C. W., Edwards, M. R., Rees, P. N., et al. (2016). Polyketide and Nonribosomal Peptide Retro-Biosynthesis and Global Gene Cluster Matching. *Nat. Chem. Biol.* 12, 1007–1014. doi:10.1038/nchembio.2188

Díaz-Pérez, A. L., Díaz-Pérez, C., and Campos-García, J. (2016). Bacterial L-Leucine Catabolism as a Source of Secondary Metabolites. *Rev. Environ. Sci. Biotechnol.* 15, 1–29. doi:10.1007/s11157-015-9385-3

Diyabalanage, T., Amsler, C. D., McClintock, J. B., and Baker, B. J. (2006). Palmerolide A, a Cytotoxic Macrolide from the Antarctic Tunicate *Synoicum adareanum*. *J. Am. Chem. Soc.* 128, 5630–5631. doi:10.1021/ja0588508

Dunn, B. J., Watts, K. R., Robbins, T., Cane, D. E., and Khosla, C. (2014). Comparative Analysis of the Substrate Specificity of *Trans*- versus *Cis*-Acyltransferases of Assembly Line Polyketide Synthases. *Biochemistry* 53, 3796–3806. doi:10.1021/bi5004316

Edwards, D. J., Marquez, B. L., Nogle, L. M., McPhail, K., Goeger, D. E., Roberts, M. A., et al. (2004). Structure and Biosynthesis of the Jamaicamides, New Mixed Polyketide-Peptide Neurotoxins from the Marine Cyanobacterium *Lyngbya majuscula*. *Chem. Biol.* 11, 817–833. doi:10.1016/j.chembiol.2004.03.030

El-Sayed, A. K., Hothersall, J., and Thomas, C. M. (2001). Quorum-sensing-dependent Regulation of Biosynthesis of the Polyketide Antibiotic Mupirocin in *Pseudomonas fluorescens* NCIMB 10586. *Microbiology* 147, 2127–2139. doi:10.1099/00221287-147-8-2127

Erol, Ö., Schäberle, T. F., Schmitz, A., Rachid, S., Gurgui, C., El Omari, M., et al. (2010). Biosynthesis of the Myxobacterial Antibiotic Corallopyronin A. *Chem. Eur. J. Chem. Bio.* 11, 1253–1265. doi:10.1002/cbic.201000085

Esquenazi, E., Coates, C., Simmons, L., Gonzalez, D., Gerwick, W. H., and Dorrestein, P. C. (2008). Visualizing the Spatial Distribution of Secondary Metabolites Produced by marine Cyanobacteria and Sponges via MALDI-TOF Imaging. *Mol. Biosyst.* 4, 562–570. doi:10.1039/b720018h

Fisch, K. M., Gurgui, C., Heycke, N., Van Der Sar, S. A., Anderson, S. A., Webb, V. L., et al. (2009). Polyketide Assembly Lines of Uncultivated Sponge Symbionts from Structure-Based Gene Targeting. *Nat. Chem. Biol.* 5, 494–501. doi:10.1038/nchembio.176

Gehret, J. J., Gu, L., Gerwick, W. H., Wipf, P., Sherman, D. H., and Smith, J. L. (2011). Terminal Alkene Formation by the Thioesterase of Curacin A Biosynthesis. *J. Biol. Chem.* 286, 14445–14454. doi:10.1074/jbc.M110.214635

Gourmelen, A., Blondelet-Rouault, M.-H., and Pernodet, J.-L. (1998). Characterization of a Glycosyl Transferase Inactivating Macrolides, Encoded by gimA from *Streptomyces ambofaciens*. *Antimicrob. Agents Chemother.* 42, 2612–2619. doi:10.1128/aac.42.10.2612

Greunke, C., Duell, E. R., D'Agostino, P. M., Glöckle, A., Lamm, K., and Gulder, T. A. M. (2018). Direct Pathway Cloning (DiPaC) to Unlock Natural Product Biosynthetic Potential. *Metab. Eng.* 47, 334–345. doi:10.1016/j.ymben.2018.03.010

Gu, L., Wang, B., Kulkarni, A., Geders, T. W., Grindberg, R. V., Gerwick, L., et al. (2009). Metamorphic Enzyme Assembly in Polyketide Diversification. *Nature* 459, 731–735. doi:10.1038/nature07870

Gulder, T. A. M., Freeman, M. F., and Piel, J. (2011). The Catalytic Diversity of Multimodular Polyketide Synthases: Natural Product Biosynthesis beyond Textbook Assembly Rules. *Top. Curr. Chem.* 1–53. https://link.springer.com/chapter/10.1007%2F128_2010_113

Haydock, S. F., Aparicio, J. F., Molnár, I., Schwecke, T., Khaw, L. E., König, A., et al. (1995). Divergent Sequence Motifs Correlated with the Substrate Specificity of (Methyl)malonyl-CoA:acyl Carrier Protein Transacylase Domains in Modular Polyketide Synthases. *FEBS Lett.* 374, 246–248. doi:10.1016/0014-5793(95)01119-Y

Haydock, S. F., Appleyard, A. N., Mironenko, T., Lester, J., Scott, N., and Leadlay, P. F. (2005). Organization of the Biosynthetic Gene Cluster for the Macrolide Concanamycin A in *Streptomyces neyagawaensis* ATCC 27449. *Microbiology* 151, 3161–3169. doi:10.1099/mic.0.28194-0

Helfrich, E. J. N., and Piel, J. (2016). Biosynthesis of Polyketides by *Trans*-AT Polyketide Synthases. *Nat. Prod. Rep.* 33, 231–316. doi:10.1039/c5np00125k

Helfrich, E. J. N., Ueoka, R., Dolev, A., Rust, M., Meoded, R. A., Bhushan, A., et al. (2019). Automated Structure Prediction of *Trans*-acyltransferase Polyketide Synthase Products. *Nat. Chem. Biol.* 15, 813–821. doi:10.1038/s41589-019-0313-7

Hertweck, C. (2009). The Biosynthetic Logic of Polyketide Diversity. *Angew. Chem. Int. Ed.* 48, 4688–4716. doi:10.1002/anie.200806121

Irschik, H., Kopp, M., Weissman, K. J., Buntin, K., Piel, J., and Müller, R. (2010). Analysis of the Sorangicin Gene Cluster Reinforces the Utility of a Combined Phylogenetic/retrobiosynthetic Analysis for Deciphering Natural Product Assembly by *Trans*-AT PKS. *Chem. Eur. J. Chem. Bio.* 11, 1840–1849. doi:10.1002/cbic.201000313

Jenke-Kodama, H., Sandmann, A., Müller, R., and Dittmann, E. (2005). Evolutionary Implications of Bacterial Polyketide Synthases. *Mol. Biol. Evol.* 22, 2027–2039. doi:10.1093/molbev/msi193

Jenkins, G., and Cundliffe, E. (1991). Cloning and Characterization of Two Genes from *Streptomyces lividans* that Confer Inducible Resistance to Lincomycin and Macrolide Antibiotics. *Gene* 108, 55–62. doi:10.1016/0378-1119(91)90487-V

Jiang, X., Liu, B., Lebreton, S., and De Brabander, J. K. (2007). Total Synthesis and Structure Revision of the marine Metabolite Palmerolide A. *J. Am. Chem. Soc.* 129, 6386–6387. doi:10.1021/ja0715142

Kaliappan, K., and Gowrisankar, P. (2007). Synthetic Studies on a marine Natural Product, Palmerolide A: Synthesis of C1-C9 and C15-C21 Fragments. *Synlett* 2007, 1537–1540. doi:10.1055/s-2007-982539

Kautsar, S. A., Blin, K., Shaw, S., Navarro-Muñoz, J. C., Terlouw, B. R., van der Hooft, J. J. J., et al. (2020). MIBiG 2.0: A Repository for Biosynthetic Gene Clusters of Known Function. *Nucleic Acids Res.* 48, D454–D458. doi:10.1093/nar/gkz882

Kazami, S., Muroi, M., Kawatani, M., Kubota, T., Usui, T., Kobayashi, J. i., et al. (2006). Iejimalides Show Anti-osteoclast ActivityviaV-ATPase Inhibition. *Biosci. Biotechnol. Biochem.* 70, 1364–1370. doi:10.1271/bbb.50644

Keatinge-Clay, A. T., and Stroud, R. M. (2006). The Structure of a Ketoreductase Determines the Organization of the β-Carbon Processing Enzymes of Modular Polyketide Synthases. *Structure* 14, 737–748. doi:10.1016/j.str.2006.01.009

Keatinge-Clay, A. T. (2012). The Structures of Type I Polyketide Synthases. *Nat. Prod. Rep.* 29, 1050. doi:10.1039/c2np20019h

Khosla, C., Tang, Y., Chen, A. Y., Schnarr, N. A., and Cane, D. E. (2007). Structure and Mechanism of the 6-Deoxyerythronolide B Synthase. *Annu. Rev. Biochem.* 76, 195–221. doi:10.1146/annurev.biochem.76.053105.093515

Kim, E. J., Lee, J. H., Choi, H., Pereira, A. R., Ban, Y. H., Yoo, Y. J., et al. (2012). Heterologous Production of 4-O-Demethylbarbamide, a Marine Cyanobacterial Natural Product. *Org. Lett.* 14, 5824–5827. doi:10.1021/ol302575h

Koskinen, A. M. P., and Karisalmi, K. (2005). Polyketide Stereotetrads in Natural Products. *Chem. Soc. Rev.* 34, 677–690. doi:10.1039/b417466f

Lackner, G., Peters, E. E., Helfrich, E. J. N., and Piel, J. (2017). Insights into the Lifestyle of Uncultured Bacterial Natural Product Factories Associated with marine Sponges. *Proc. Natl. Acad. Sci. USA* 114, E347–E356. doi:10.1073/pnas.1616234114

Lawrence, J. G., Ochman, H., and Ragan, M. A. (2002). Reconciling the many Faces of Lateral Gene Transfer. *Trends Microbiol.* 10, 1–4. doi:10.1016/S0966-842X(01)02282-X

Lebar, M. D., and Baker, B. J. (2010). Synthesis of the C3-14 Fragment of Palmerolide A Using a Chiral Pool Based Strategy. *Tetrahedron* 66, 1557–1562. doi:10.1016/j.tet.2009.12.007

Lin, S., Van Lanen, S. G., and Shen, B. (2009). A Free-Standing Condensation Enzyme Catalyzing Ester Bond Formation in C-1027 Biosynthesis. *Proc. Natl. Acad. Sci.* 106, 4183–4188. doi:10.1073/pnas.0808880106

Lisboa, M. P., Jones, D. M., and Dudley, G. B. (2013). Formal Synthesis of Palmerolide A, Featuring Alkynogenic Fragmentation and *Syn*-Selective Vinylogous Aldol Chemistry. *Org. Lett.* 15, 886–889. doi:10.1021/ol400014e

Lopera, J., Miller, I. J., McPhail, K. L., and Kwan, J. C. (2017). Increased Biosynthetic Gene Dosage in a Genome-Reduced Defensive Bacterial Symbiont. *mSystems* 2(6), e00096–17. doi:10.1128/mSystems.00096-17

Maier, S., Heitzler, T., Asmus, K., Brötz, E., Hardter, U., Hesselbach, K., et al. (2015). Functional Characterization of Different ORFs Including Luciferase-like Monooxygenase Genes from the Mensacarcin Gene Cluster. *ChemBioChem* 16, 1175–1182. doi:10.1002/cbic.201500048

Matilla, M. A., Stöckmann, H., Leeper, F. J., and Salmond, G. P. C. (2012). Bacterial Biosynthetic Gene Clusters Encoding the Anti-cancer Haterumalide Class of Molecules. *J. Biol. Chem.* 287, 39125–39138. doi:10.1074/jbc.M112.401026

Mattheus, W., Gao, L.-J., Herdewijn, P., Landuyt, B., Verhaegen, J., Masschelein, J., et al. (2010). Isolation and Purification of a New Kalimantacin/Batumin-Related Polyketide Antibiotic and Elucidation of its Biosynthesis Gene Cluster. *Chem. Biol.* 17, 149–159. doi:10.1016/j.chembiol.2010.01.014

McClintock, J. B., Amsler, C. D., Baker, B. J., and Van Soest, R. W. M. (2005). Ecology of Antarctic marine Sponges: An Overview. *Integr. Comp. Biol.* 45, 359–368. doi:10.1093/icb/45.2.359

Mihali, T. K., Carmichael, W. W., and Neilan, B. A. (2011). A Putative Gene Cluster from a *Lyngbya wollei* Bloom that Encodes Paralytic Shellfish Toxin Biosynthesis. *PLoS One* 6, e14657. doi:10.1371/journal.pone.0014657

Moldenhauer, J., Chen, X.-H., Borriss, R., and Piel, J. (2007). Biosynthesis of the Antibiotic Bacillaene, the Product of a Giant Polyketide Synthase Complex of The *trans*-AT Family. *Angew. Chem. Int. Ed.* 46, 8195–8197. doi:10.1002/anie.200703386

Moldenhauer, J., Götz, D. C. G., Albert, C. R., Bischof, S. K., Schneider, K., Süssmuth, R. D., et al. (2010). The Final Steps of Bacillaene Biosynthesis in Bacillus Amyloliquefaciens FZB42: Direct Evidence for β,γ Dehydration by a *Trans*-acyltransferase Polyketide Synthase. *Angew. Chem.* 122, 1507–1509. doi:10.1002/ange.200905468

Murray, A. E., Avalon, N. E., Bishop, L., Davenport, K. W., Delage, E., Dichosa, A. E. K., et al. (2020). Uncovering the Core Microbiome and Distribution of Palmerolide in *Synoicum adareanum* across the Anvers Island Archipelago, Antarctica. *Mar. Drugs* 18, 298. doi:10.3390/md18060298

Murray, A. E., Lo, C.-C., Daligault, H. E., Avalon, N. E., Read, R. W., Davenport, K. W., et al. (2021). Discovery of an Antarctic Ascidian-Associated Uncultivated Verrucomicrobia with Antimelanoma Palmerolide Biosynthetic Potential. *mSphere*. doi:10.1128/mSphere.00759-21

Napolitano, J. G., Daranas, A. H., Norte, M., and Fernandez, J. J. (2009). Marine Macrolides, a Promising Source of Antitumor Compounds. *Acamc* 9, 122–137. doi:10.2174/187152009787313800

Nguyen, T., Ishida, K., Jenke-Kodama, H., Dittmann, E., Gurgui, C., Hochmuth, T., et al. (2008). Exploiting the Mosaic Structure of *Trans*-acyltransferase Polyketide Synthases for Natural Product Discovery and Pathway Dissection. *Nat. Biotechnol.* 26, 225–233. doi:10.1038/nbt1379

Nicolaou, K. C., Leung, G. Y. C., Dethe, D. H., Guduru, R., Sun, Y.-P., Lim, C. S., et al. (2008a). Chemical Synthesis and Biological Evaluation of Palmerolide A Analogues. *J. Am. Chem. Soc.* 130, 10019–10023. doi:10.1021/ja802803e

Nicolaou, K. C., Sun, Y.-P., Guduru, R., Banerji, B., and Chen, D. Y.-K. (2008b). Total Synthesis of the Originally Proposed and Revised Structures of Palmerolide A and Isomers Thereof. *J. Am. Chem. Soc.* 130, 3633–3644. doi:10.1021/ja710485n

Nishimura, S., Matsunaga, S., Yoshida, S., Nakao, Y., Hirota, H., and Fusetani, N. (2005). Structure-activity Relationship Study on 13-deoxytedanolide, a Highly Antitumor Macrolide from the marine Sponge *Mycale adhaerens*. *Bioorg. Med. Chem.* 13, 455–462. doi:10.1016/j.bmc.2004.10.014

Nivina, A., Yuet, K. P., Hsu, J., and Khosla, C. (2019). Evolution and Diversity of Assembly-Line Polyketide Synthases. *Chem. Rev.* 119, 12524–12547. doi:10.1021/acs.chemrev.9b00525

Noguez, J. H., Diyabalanage, T. K. K., Miyata, Y., Xie, X.-S., Valeriote, F. A., Amsler, C. D., et al. (2011). Palmerolide Macrolides from the Antarctic Tunicate

Synoicum adareanum. *Bioorg. Med. Chem.* 19, 6608–6614. doi:10.1016/j.bmc.2011.06.004

Paull, K. D., Hamel, E., and Malspeis, L. (1995). Prediction of Biochemical Mechanism of Action from the *In Vitro* Antitumor Screen of the National Cancer Institute. *Cancer Chemother. Agents*, 9–45. Available at: https://dtp.cancer.gov/databases_tools/docs/compare/compare.htm (Accessed October 10, 2018).

Pawar, A. B., and Prasad, K. R. (2012). Formal Total Synthesis of Palmerolide A. *Chem. Eur. J.* 18, 15202–15206. doi:10.1002/chem.201202324

Penner, M., Rauniyar, V., Kaspar, L. T., and Hall, D. G. (2009). Catalytic Asymmetric Synthesis of Palmerolide a via Organoboron Methodology. *J. Am. Chem. Soc.* 131, 14216–14217. doi:10.1021/ja906429c

Piel, J. (2002). A Polyketide Synthase-Peptide Synthetase Gene Cluster from an Uncultured Bacterial Symbiont of Paederus Beetles. *Proc. Natl. Acad. Sci.* 99, 14002–14007. doi:10.1073/pnas.222481399

Piel, J., Hui, D., Wen, G., Butzke, D., Platzer, M., Fusetani, N., et al. (2004). Antitumor Polyketide Biosynthesis by an Uncultivated Bacterial Symbiont of the marine Sponge *Theonella swinhoei*. *Proc. Natl. Acad. Sci.* 101, 16222–16227. doi:10.1073/pnas.0405976101

Pujari, S. A., Gowrisankar, P., and Kaliappan, K. P. (2011). A Shimizu Non-aldol Approach to the Formal Total Synthesis of Palmerolide A. *Chem. Asian J.* 6, 3137–3151. doi:10.1002/asia.201100429

Quiros, L. M., Aguirrezabalaga, I., Olano, C., Mendez, C., and Salas, J. A. (1998). Two Glycosyltransferases and a Glycosidase Are Involved in Oleandomycin Modification during its Biosynthesis by *Streptomyces antibioticus*. *Mol. Microbiol.* 28, 1177–1185. doi:10.1046/j.1365-2958.1998.00880.x

Ravenhall, M., Škunca, N., Lassalle, F., and Dessimoz, C. (2015). Inferring Horizontal Gene Transfer. *Plos Comput. Biol.* 11, e1004095–16. doi:10.1371/journal.pcbi.1004095

Reeves, C. D., Murli, S., Ashley, G. W., Piagentini, M., Hutchinson, C. R., and McDaniel, R. (2001). Alteration of the Substrate Specificity of a Modular Polyketide Synthase Acyltransferase Domain through Site-specific Mutations. *Biochemistry* 40, 15464–15470. doi:10.1021/bi015864r

Riesenfeld, C. S., Murray, A. E., and Baker, B. J. (2008). Characterization of the Microbial Community and Polyketide Biosynthetic Potential in the Palmerolide-Producing Tunicate *Synoicum adareanum*. *J. Nat. Prod.* 71, 1812–1818. doi:10.1021/np800287n

Röttig, M., Medema, M. H., Blin, K., Weber, T., Rausch, C., and Kohlbacher, O. (2011). NRPSpredictor2-a Web Server for Predicting NRPS Adenylation Domain Specificity. *Nucleic Acids Res.* 39, W362–W367. doi:10.1093/nar/gkr323

Schmidt, E. W. (2015). The Secret to a Successful Relationship: Lasting Chemistry between Ascidians and Their Symbiotic Bacteria. *Invertebr. Biol.* 134, 88–102. doi:10.1111/ivb.12071

Schmidt, E. W. (2008). Trading Molecules and Tracking Targets in Symbiotic Interactions. *Nat. Chem. Biol.* 4, 466–473. doi:10.1038/nchembio.101

Schmitt, I., and Lumbsch, H. T. (2009). Ancient Horizontal Gene Transfer from Bacteria Enhances Biosynthetic Capabilities of Fungi. *PLoS One* 4, e4437–8. doi:10.1371/journal.pone.0004437

Shen, B., Cheng, Y.-Q., Christenson, S. D., Jiang, H., Ju, J., Kwon, H.-J., et al. (2007). Polyketide Biosynthesis beyond the Type I, II, and III Polyketide Synthase Paradigms: A Progress Report. *ACS Symp. Ser.* 955, 154–166. doi:10.1021/bk-2007-0955.ch011

Shen, R., Lin, C. T., Bowman, E. J., Bowman, B. J., and Porco, J. A. (2003). Lobatamide C: Total Synthesis, Stereochemical Assignment, Preparation of Simplified Analogues, and V-ATPase Inhibition Studies. *J. Am. Chem. Soc.* 125, 7889–7901. doi:10.1021/ja0352350

Stachelhaus, T., Mootz, H. D., Bergendahl, V., and Marahiel, M. A. (1998). Peptide Bond Formation in Nonribosomal Peptide Biosynthesis. *J. Biol. Chem.* 273, 22773–22781. doi:10.1074/jbc.273.35.22773

Sudek, S., Lopanik, N. B., Waggoner, L. E., Hildebrand, M., Anderson, C., Liu, H., et al. (2007). Identification of the Putative Bryostatin Polyketide Synthase Gene Cluster from "*Candidatus* Endobugula sertula", the Uncultivated Microbial Symbiont of the Marine Bryozoan *Bugula neritina*. *J. Nat. Prod.* 70, 67–74. doi:10.1021/np060361d

Tatsuno, S., Arakawa, K., and Kinashi, H. (2007). Analysis of Modular-Iterative Mixed Biosynthesis of Lankacidin by Heterologous Expression and Gene Fusion. *J. Antibiot.* 60, 700–708. doi:10.1038/ja.2007.90

Theodore, C. M., Stamps, B. W., King, J. B., Price, L. S. L., Powell, D. R., Stevenson, B. S., et al. (2014). Genomic and Metabolomic Insights into the Natural Product Biosynthetic Diversity of a Feral-Hog-Associated *Brevibacillus laterosporus* Strain. *PLoS One* 9, e90124–12. doi:10.1371/journal.pone.0090124

Ueoka, R., Uria, A. R., Reiter, S., Mori, T., Karbaum, P., Peters, E. E., et al. (2015). Metabolic and Evolutionary Origin of Actin-Binding Polyketides from Diverse Organisms. *Nat. Chem. Biol.* 11, 705–712. doi:10.1038/nchembio.1870

Videau, P., Wells, K. N., Singh, A. J., Gerwick, W. H., and Philmus, B. (2016). Assessment of *Anabaena* sp. Strain PCC 7120 as a Heterologous Expression Host for Cyanobacterial Natural Products: Production of Lyngbyatoxin A. *ACS Synth. Biol.* 5, 978–988. doi:10.1021/acssynbio.6b00038

Von Schwarzenberg, K., Wiedmann, R. M., Oak, P., Schulz, S., Zischka, H., Wanner, G., et al. (2013). Mode of Cell Death Induction by Pharmacological Vacuolar H+-ATPase (V-ATPase) Inhibition. *J. Biol. Chem.* 288, 1385–1396. doi:10.1074/jbc.M112.412007

Wakimoto, T., Egami, Y., Nakashima, Y., Wakimoto, Y., Mori, T., Awakawa, T., et al. (2014). Calyculin Biogenesis from a Pyrophosphate Protoxin Produced by a Sponge Symbiont. *Nat. Chem. Biol.* 10, 648–655. doi:10.1038/nchembio.1573

Wang, B., Guo, F., Huang, C., and Zhao, H. (2020). Unraveling the Iterative Type I Polyketide Synthases Hidden in Streptomyces. *Proc. Natl. Acad. Sci. USA* 117, 8449–8454. doi:10.1073/pnas.1917664117

Wencewicz, T. A. (2019). Crossroads of Antibiotic Resistance and Biosynthesis. *J. Mol. Biol.* 431, 3370–3399. doi:10.1016/j.jmb.2019.06.033

Wilkinson, B., Foster, G., Rudd, B. A., Taylor, N. L., Blackaby, A. P., Sidebottom, P. J., et al. (2000). Novel Octaketide Macrolides Related to 6-deoxyerythronolide B Provide Evidence for Iterative Operation of the Erythromycin Polyketide Synthase. *Chem. Biol.* 7, 111–117. doi:10.1016/S1074-5521(00)00076-4

Yadav, G., Gokhale, R. S., and Mohanty, D. (2003). Computational Approach for Prediction of Domain Organization and Substrate Specificity of Modular Polyketide Synthases. *J. Mol. Biol.* 328, 335–363. doi:10.1016/S0022-2836(03)00232-8

Yokoyama, K., and Imamura, H. (2005). Rotation, Structure, and Classification of Prokaryotic V-ATPase. *J. Bioenerg. Biomembr.* 37, 405–410. doi:10.1007/s10863-005-9480-1

Young, R., Von Salm, J., Amsler, M., Lopez-Bautista, J., Amsler, C., McClintock, J., et al. (2013). Site-specific Variability in the Chemical Diversity of the Antarctic Red Alga *Plocamium cartilagineum*. *Mar. Drugs* 11, 2126–2139. doi:10.3390/md11062126

Zaleta-Rivera, K., Xu, C., Yu, F., Butchko, R. A. E., Proctor, R. H., Hidalgo-Lara, M. E., et al. (2006). A Bidomain Nonribosomal Peptide Synthetase Encoded by FUM14 Catalyzes the Formation of Tricarballylic Esters in the Biosynthesis of Fumonisins. *Biochemistry* 45, 2561–2569. doi:10.1021/bi052085s

Zhao, C., Coughlin, J. M., Ju, J., Zhu, D., Wendt-Pienkowski, E., Zhou, X., et al. (2010). Oxazolomycin Biosynthesis in *Streptomyces albus* JA3453 Featuring an "Acyltransferase-Less" Type I Polyketide Synthase that Incorporates Two Distinct Extender Units. *J. Biol. Chem.* 285, 20097–20108. doi:10.1074/jbc.M109.090092

Conflict of Interest: The authors declare that the research was conducted in the absence of any commercial or financial relationships that could be construed as a potential conflict of interest.

Publisher's Note: All claims expressed in this article are solely those of the authors and do not necessarily represent those of their affiliated organizations, or those of the publisher, the editors and the reviewers. Any product that may be evaluated in this article, or claim that may be made by its manufacturer, is not guaranteed or endorsed by the publisher.

frontiers in Chemistry

ORIGINAL RESEARCH
published: 08 February 2022
doi: 10.3389/fchem.2022.816741

Membrane-Active Antibacterial Agents Based on Calix[4]arene Derivatives: Synthesis and Biological Evaluation

Shanfang Fang†, Yuan-Ye Dang†, Haizhou Li, Hongxia Li, Jiayong Liu, Rongcui Zhong, Yongzhi Chen, Shouping Liu and Shuimu Lin**

The Fifth Affiliated Hospital and Key Laboratory of Molecular Target and Clinical Pharmacology and the State Key Laboratory of Respiratory Disease, School of Pharmaceutical Sciences, Guangzhou Medical University, Guangzhou, China

Bacteria have developed increasing resistance to currently used antimicrobial agents. New classes of antimicrobial drugs are urgently required to fight drug-resistant pathogens. Here, we designed and synthesized a series of calix[4]arene derivatives as antibacterial agents by biomimicking the structural properties and biological functions of antibacterial peptides. After introducing cationic hydrophilic moieties and preliminary structural optimization, we obtained a lead compound (**16**) that exhibited excellent antibacterial activity against Gram-positive bacteria, low toxicity toward mammalian cells and poor hemolytic activity. The antibacterial mechanism studies showed that compound **16** can destroy bacterial cell membrane directly, leading to bacterial death and a low tendency to develop bacterial resistance.

Keywords: antimicrobial agents, Calix[4]arene derivatives, membrane-active, peptidomimetics, bacterial resistance, gram-positive bacteria

OPEN ACCESS

Edited by:
Wenshe Ray Liu,
Texas A&M University, United States

Reviewed by:
Margherita De Rosa,
University of Salerno, Italy
Lorenzo Stella,
University of Rome Tor Vergata, Italy

****Correspondence:***
Shouping Liu
liushouping2018@163.com
Shuimu Lin
linshuimu020@163.com

†These authors have contributed equally to this work

Specialty section:
This article was submitted to Chemical Biology, a section of the journal Frontiers in Chemistry

Received: *17 November 2021*
Accepted: *07 January 2022*
Published: *08 February 2022*

Citation:
Fang S, Dang Y-Y, Li H, Li H, Liu J, Zhong R, Chen Y, Liu S and Lin S (2022) Membrane-Active Antibacterial Agents Based on Calix[4]arene Derivatives: Synthesis and Biological Evaluation. Front. Chem. 10:816741. doi: 10.3389/fchem.2022.816741

INTRODUCTION

The development of multi-drug resistant bacteria and the decrease in the discovery of new antibiotics pose a major threat to public health in the 21st century (Lyddiard et al., 2016; Woolhouse et al., 2016; Monserrat-Martinez et al., 2019). In addition, due to the rapid development of antimicrobial resistance, short medication cycle, and low profits of antimicrobial agents, many pharmaceutical companies have greatly reduced their investment in the development of antimicrobial agents, which could slow the discovery of new antibiotics (Livermore, 2011; Rogers et al., 2012). The ESKAPE pathogens, including E*nterococcus faecium*, *Staphylococcus aureus*, *Klebsiella pneumoniae*, *Acinetobacter baumannii*, *Pseudomonas aeruginosa*, and *Enterobacter* spp., are spreading and becoming more resistant to many commonly used antibacterial agents (Rice, 2008). Currently, most newly approved antibiotics are likely to develop rapid resistance as most of them belong to known classes of antibiotics, based on the molecular scaffolds of traditional antibiotics (Molchanova et al., 2017). In 2017, the World Health Organization (WHO) released a priority list of drug-resistant pathogens to guide the development of new antibiotics and warned that there was a serious lack of new antibiotics to treat the growing number of drug-resistant infections (Kmietowicz, 2017). Antimicrobial resistance causes increases in mortality, morbidity, length of hospitalization and cost of healthcare (Maragakis et al., 2008). If effective measures are not taken to combat antibiotic resistance, we will return to the "pre-antibiotic era," and most surgical procedures will not be safe to implement.

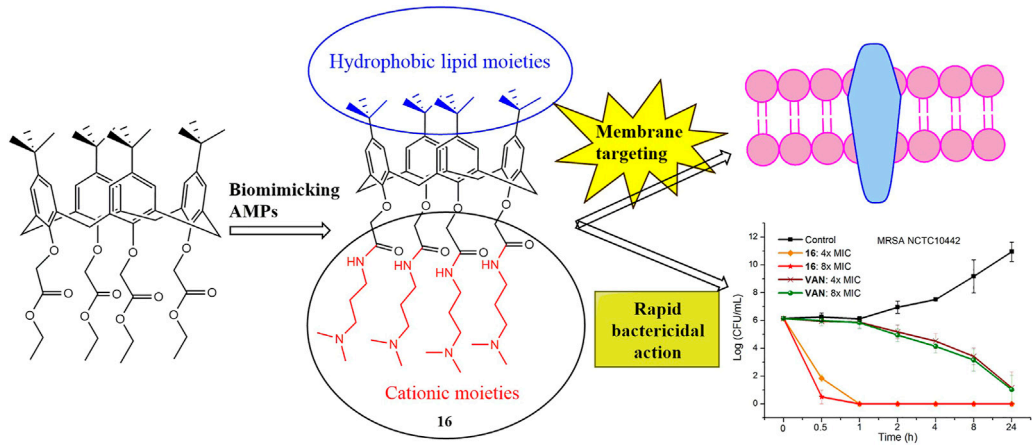

Graphical Abstract |

Antimicrobial peptides (AMPs), also known as host defense peptides, exist in various life forms from microorganisms to humans. Most of them are positively charged and possess broad-spectrum antimicrobial activity against bacteria, viruses and fungi (Koh et al., 2015; Lázár et al., 2018; Arbour et al., 2020; Thapa et al., 2020). Compared with conventional antibiotics, AMPs have several obvious advantages, such as rapid bactericidal action (Li et al., 2017), immunomodulatory activity (Jenssen et al., 2006), synergistic effects with antibacterial agents (Zasloff, 2002), and low probability of developing bacterial resistance (Wimley and Hristova, 2011). However, the progress in the clinical application of AMPs has been hindered by the sensitivity to proteolytic enzymes, poor *in vivo* efficacy and poor pharmacokinetic properties (Adessi and Soto, 2002; Marr et al., 2006; Costa et al., 2019). Small peptidomimetics that mimic the chemical structure and biological function of AMPs can avoid most of the defects of AMPs (Hickey et al., 2015; Nizalapur et al., 2017). Several small peptidomimetics have shown great application potential, such as Brilacitine and LTX-109 that have successfully entered or completed Phase II clinical trials (Isaksson et al., 2011; Mensa et al., 2014; Kowalski et al., 2016; Kuppusamy et al., 2019).

Calixarene derivatives have been found to contain various biological activities, such as antiviral, antibacterial, antifungal and

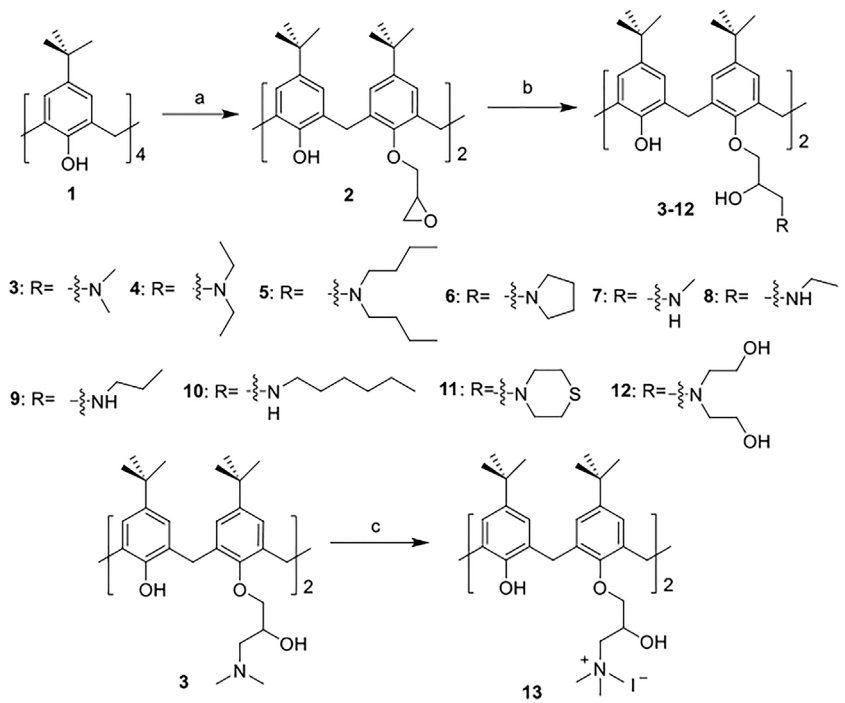

SCHEME 1 | Synthesis of cationic amphiphilic calix[4]arene derivatives **2–13**. Reagents and conditions: (a) epibromohydrin, KI, K_2CO_3, acetonitrile, 85°C, reflux, 10–12 h (b) corresponding amines, CH_3OH, 65°C, reflux, 3 h. (c) Iodomethane, CH_3OH, room temperature (RT), overnight.

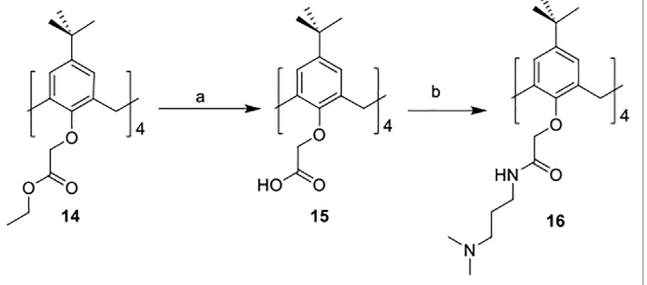

SCHEME 2 | Synthesis of cationic amphiphilic calix[4]arene derivatives **15–16.** Reagents and conditions: (a) LiOH, THF/water, RT, 1.5 h (b) 3-dimethylaminopropylamine, DMTMM, DIPEA, DMF, RT, 12 h.

anticancer activities (Yousaf et al., 2015; Nasuhi Pur, 2016). In addition, they do not display obvious cytotoxicity and immunogenicity (Ma and Zhao, 2015; Pur, 2021). Due to their versatility, low cost and unique three-dimensional structures, calixarene could serve as an ideal molecular scaffold for the design and optimization of drug molecules (Hanna et al., 2003; Mokhtari and Pourabdollah, 2013). Calix[4]arene derivatives have attracted special attention owing to the cheap and easy availability, unique structural characteristics and easy modification (Naseer et al., 2017; Bono et al., 2018). The functionalized basket cavity of calix[4]arene is suitable for small ions and neutral molecules, and calix[4]arene can provide excellent conditions for the incorporation of other moieties via the hydroxyl groups (Naseer et al., 2017). The antitumor agent calix[4]arene compound OTX008 that targets human galectin-1 is being evaluated in phase I clinical trial, indicating that calixarene has great potential as a molecular skeleton of drugs (Läppchen et al., 2015). However, to our knowledge, there are no other calixarene-based drugs have entered clinical trials at present (Nimse and Kim 2013). As reported, calixarene derivatives have great potential as antibacterial agents and could avoid cross-

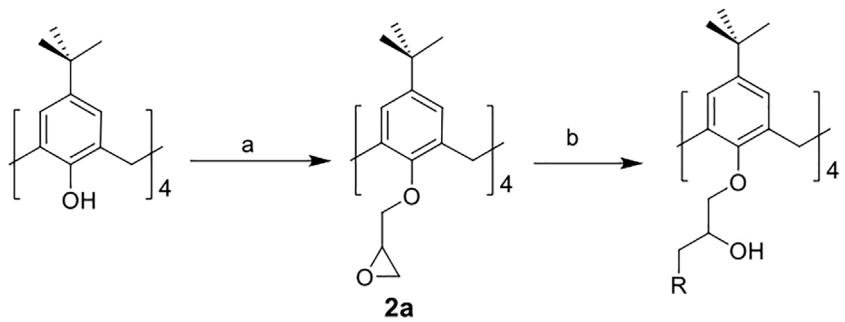

SCHEME 3 | Synthesis of calix[4]arene derivative **2a.** Reagents and conditions: (a) epibromohydrin, KI, K_2CO_3 or potassium tert-butoxide, acetonitrile, 85°C, reflux. (b) corresponding amines, CH_3OH, 65°C, reflux.

TABLE 1 | *In vitro* anti-Gram-positive bacterial activities and hemolytic activities of calix[4]arene derivatives **1–16.**

Compound	MIC, μg/ml (μM)			HC_{50}, μg/ml (μM)
	***S. aureus* ATCC29213**	**MRSA N315**	**MRSA NCTC10442**	
1	>50 (>77)	>50 (>77)	>50 (>77)	>200 (>308)
2	>50 (>66)	>50 (>66)	>50 (>66)	>200 (>263)
3	13 (15)	13 (15)	13 (15)	>200 (>235)
4	25 (28)	13 (14)	25 (28)	>200 (>220)
5	>50 (>49)	>50 (>49)	>50 (>49)	>200 (>196)
6	50 (55)	50 (55)	>50 (>55)	>200 (>221)
7	4.7 ± 2 (5.7 ± 2)	1.6 (1.9)	3.1 (3.8)	151 ± 5 (183 ± 6)
8	1.6 (1.8)	1.2 ± 0.4 (1.4 ± 0.5)	1.6 (1.8)	123 ± 8 (144 ± 9)
9	2.3 ± 0.8 (2.6 ± 0.9)	2.3 ± 0.8 (2.6 ± 0.9)	4.7 ± 2 (5.3 ± 2)	191 ± 2 (217 ± 3)
10	>50 (>52)	>50 (>52)	>50 (>52)	>200 (>208)
11	>50 (>52)	>50 (>52)	>50 (>52)	>200 (>207)
12	>50 (>52)	>50 (>52)	>50 (>52)	>200 (>206)
13	3.1 (2.8)	3.1 (2.8)	3.1 (2.8)	16 ± 1 (14 ± 1)
14	>50 (>50)	>50 (>50)	>50 (>50)	>200 (>201)
16	1.6 (1.3)	1.6 (1.3)	3.1 (2.6)	>200 (>164)
vancomycin	0.78 (0.50)	1.6 (1.1)	1.6 (1.1)	ND[a]

[a]*Not determined.*

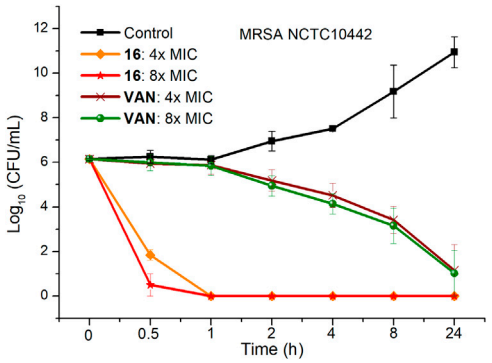

FIGURE 1 | Time-kill kinetics of compound **16** and vancomycin against MRSA NCTC10442.

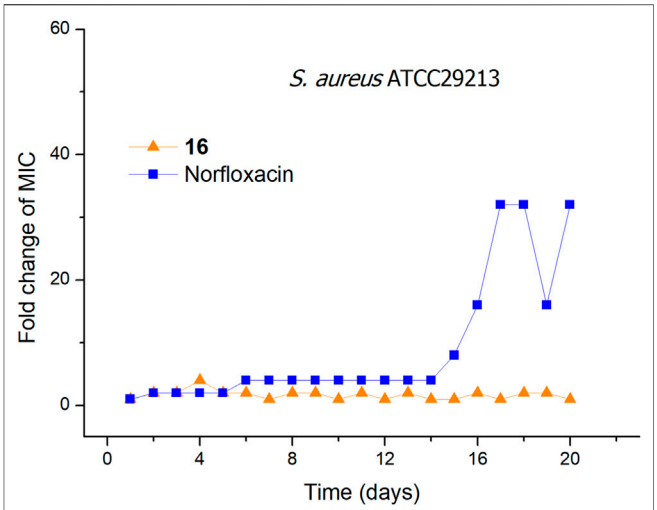

FIGURE 2 | Bacterial resistance studies of compound **16** and norfloxacin against *S. aureus* ATCC29213.

resistance with existing antibacterial agents due to their different molecular structures from existing antibacterial agents (Shurpik et al., 2020).

In this work, by biomimicking AMPs, we designed and synthesized a series of calix[4]arene derivatives as membrane-active antibacterial agents. The most promising compound **16** showed potent antibacterial activity against Gram-positive bacteria, including methicillin-resistant *Staphylococcus aureus* (MRSA). No bacterial resistance was observed for compound **16** in the laboratory simulation of the drug resistance study. The commercial reagents 4-tert-butylcalix[4]arene, and tetraethyl 4-tert-butylcalix[4]arene-O,O′,O″,O‴-tetraacetate were used as the starting materials, and then cationic moieties were introduced to the calix[4]arene scaffold to form cationic amphiphilic structures. The introduced cationic moieties are beneficial to identify bacterial cells, which can promote the interaction between cationic calix[4]arene compounds and negatively charged bacterial membranes via electrostatic action, while the hydrophobic tert-butyl groups can facilitate the insertion of calix[4]arene compounds into bacterial phospholipid bilayer membranes, leading to the change in the permeability of bacterial cell membranes and the death of bacteria. The difference in cell membrane composition between eukaryotes and bacteria is very conducive to improving the selectivity of cationic amphiphilic calix[4]arene derivatives. Bacterial membranes are rich in anionic lipids (Malmsten, 2014), while the membrane surfaces of eukaryotes mainly contain zwitterionic phospholipids including phosphatidylethanolamine, phosphatidylcholine, and sphingomyelin (Pasupuleti et al., 2012). After a series of structural modifications, the cationic hydrophilic moieties of calix[4]arene derivatives were fine-tuned to obtain potent antibacterial agents with good antibacterial activity and low toxicity. Finally, the time-kill kinetics, drug resistance development, *in vitro* cytotoxicity toward mammalian cells, and the antibacterial mechanism were studied. These findings suggest that this design strategy for calix[4]arene-based AMPs mimics is very conducive to developing new antibacterial agents to fight drug-resistant bacteria.

RESULTS AND DISCUSSION

Design and Synthesis of Calix[4]arene-Based Antibacterial Derivatives

The synthetic routes for synthesizing various amphiphilic calix[4]arene analogs are shown in **Schemes 1**, **2**. The starting material 4-tert-butylcalix[4]arene was treated with epibromohydrine together with K_2CO_3 to yield intermediate compound **2**. Compounds **3–12** were then obtained by the treatment of compound **2** with corresponding amines. Polyamine compounds often become polycations at physiological pH and then exert their biological activity. The Nitrogen atoms containing lone pairs of electrons in polyamines are easily protonated to be positively charged. Compound **3** was coupled with iodomethane to afford compound **13**. The starting materials tetraethyl 4-tert-butylcalix[4]arene-O,O′,O″,O‴-tetraacetate was hydrolyzed by LiOH to produce compound **15**. Then the acid **15** was reacted with 3-dimethylaminopropylamine in the presence of 4-(4,6-dimethoxy-1,3,5-triazin-2-yl)-4-methylmorpholinium chloride (DMTMM) to provide compound **16**. In fact, we initially planned to design and synthesize a four-arm modified intermediate epoxy compound **2a** (**Scheme 3**), and then **2a** reacted with the corresponding amines to prepare a series of amphiphilic cationic four-arm modified calixarene derivatives as antibacterial compounds (**Scheme 3**). We tried many different conditions, but failed to synthesize **2a**. All synthesized compounds were characterized by H NMR, C NMR, and HRMS.

In Vitro Antibacterial and Hemolytic Activity

The *in vitro* antibacterial activity of the calix[4]arene derivatives was evaluated against three Gram-positive bacteria, including *S. aureus* ATCC29213, MRSA NCTC10442 and MRSA N315. The *in vitro* antibacterial activity was assessed by minimum inhibitory concentrations (MICs). The HC_{50} value (concentration of compounds required to lyse 50% of rabbit red blood cells) was

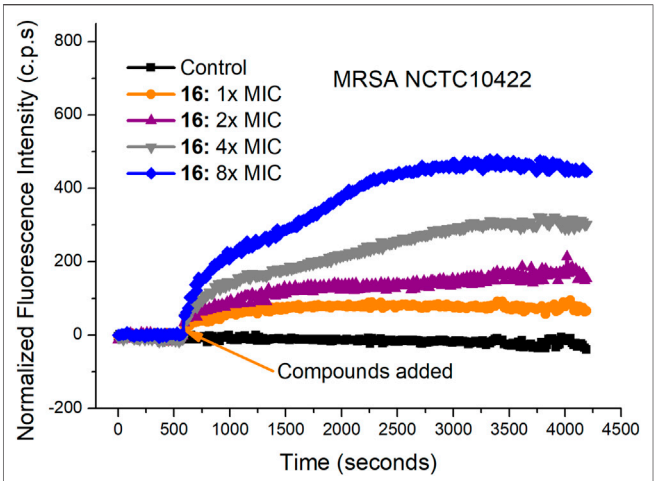

FIGURE 3 | Cytoplasmic membrane permeabilization of compounds **16** against MRSA NCTC10442.

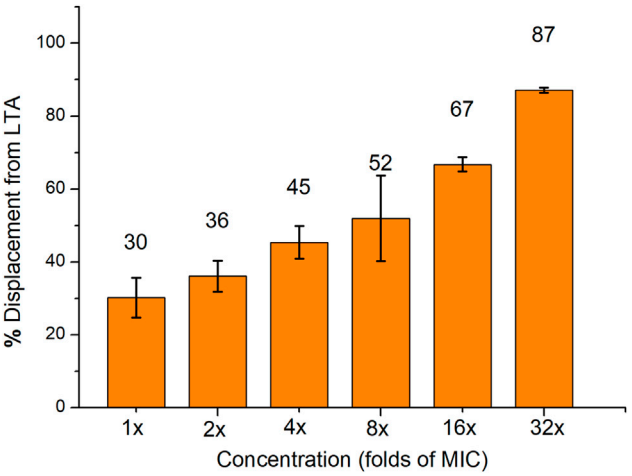

FIGURE 4 | The displacement of BODIPY-TR-cadaverine from LTA was caused by compound **16**. Data are presented as the average value of two independent experiments.

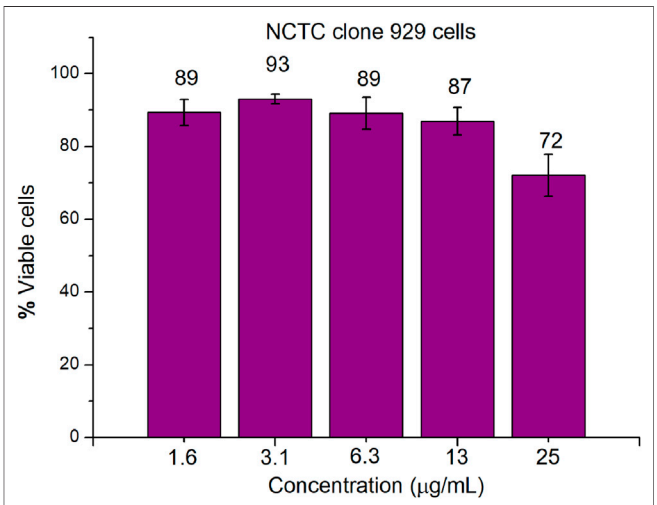

FIGURE 5 | Cytotoxicity of compound **16** against mouse NCTC clone 929 cells using CCK-8 assays.

used to evaluate the hemolytic activity of the synthesized compounds toward rabbit red blood cells (**Table 1**).

To investigate the effects of different secondary amine substituents on the antibacterial and hemolytic activities of the calix[4]arene derivatives, compounds **7–10** were synthesized. Compounds **7–9** displayed good antibacterial activities against Gram-positive bacterial strains tested (MICs = 1.2–4.7 μg/ml) and weak hemolytic activity, with HC_{50} values in the range of 123–191 μg/ml. However, n-hexylamine-coupled compound **10**, a more hydrophobic compound, showed very poor antibacterial activity (MICs > 50 μg/ml) and very poor hemolytic activities (HC_{50} > 200 μg/ml). The anti-Gram-positive bacterial activities of these compounds are determined by the hydrophobic side chains connected to positive charge centers. These results suggested that the secondary amine substituents with short hydrophobic side chains can greatly improve the antibacterial activity of calix[4]arene derivatives, and also slightly increase the hemolytic activity of calix[4]arene derivatives.

Next, compounds **3–6**, **11–12**, and **16** were used to explore the effects of different types of tertiary amine substitutions on the hemolytic and antibacterial activity of amphiphilic calix[4]arene derivatives. Dimethylamine-coupled compound **3** and diethylamine-coupled compound **4** showed moderate antibacterial activity (MICs = 13–25 μg/ml). However, dibutylamine-coupled compound **5** did not display any antibacterial activities even at the highest tested concentration of 50 μg/ml. This result indicated that tertiary amine substituted calix[4]arene derivatives with long alkyl side chains would lead to a significant decrease or even loss in biological activity. When introducing pyrrolidine (**6**), very weak antibacterial activity was observed (MICs ≥ 50 μg/ml). 3-Dimethylaminopropylamine-containing compound **16** with four-arm functionalization displayed enhanced antibacterial activity, with MICs in the range of 1.6–3.1 μg/ml. Compound **16** was also used to investigate the effect of four-arm modification and two-arm modification on the biological activity of amphiphilic cationic calixarene derivatives. We found that the membrane selectivity of four-arm modified compound **16** was higher than that of two-arm modified calixarene derivatives. Owing to the low pKa value of the introduced cationic group, compound **11** containing thiomorpholine (pKa of free thiomorpholine = 9.0) (Jones et al., 2017), and compound **12** containing diethanolamine (pKa of free diethanolamine = 8.9) (Singh et al., 2011), exhibited very poor antibacterial activity against Gram-positive bacteria (MICs > 50 μg/ml). It manifested that the amine substituents with low pKa value were harmful to the antibacterial activity of calix[4]arene derivatives. No hemolytic activity (HC_{50} > 200 μg/ml) was observed for these eight compounds, suggesting that tertiary amine substitutions had little effect on the hemolytic activity of calix[4]arene derivatives. Tertiary amine **3** was reacted with iodomethane to

yield quaternary ammonium salt **13** that was used to investigate the effect of quaternary ammonium salt substitution on the antibacterial and hemolytic activities of amphiphilic calix[4]arene derivatives. Compared with the precursor compound **3**, both the activity against Gram-positive bacteria and the hemolytic activity of compound **13** increased obviously, with MICs of 3.1 μg/ml and HC_{50} of 16 ± 1 μg/ml. These results suggested that quaternary ammonium salt substitutions had a significant effect on the antibacterial activity and hemolytic activity of calix[4]arene derivatives.

From the preliminary structure-activity relationship (SAR) study of amphiphilic calix[4]arene derivatives, we found that several structural parameters have significant effects on the antibacterial and hemolytic activities, including the types of amine substituents, the length of the carbon chain connected to the positive charge center and the pKa value of the cationic group. The introduction of amine groups with long hydrophobic side chains would lead to the loss in antibacterial activity of calix[4]arene compounds (MIC > 50 μg/ml). In addition, poor antibacterial activity was observed when low pKa amine groups were incorporated. 3-Dimethylaminopropylamine coupled compound **16** displayed excellent anti-Gram-positive bacterial activity (MICs = 1.6–3.1 μg/ml) and very weak hemolytic activity (HC_{50} > 200 μg/ml). The cationic moieties play an important role in the interaction with negatively charged bacterial membranes. The incorporation of cationic groups enables the cationic calix[4]arene derivatives to act on negatively charged bacterial cell membranes through electrostatic interaction, which is helpful for calix[4]arene derivatives to distinguish bacterial cell membranes from mammalian cell membranes. Among all the synthesized compounds, only compound **16** with four-arm tertiary amines functionalized showed excellent antimicrobial activity and very poor hemolytic activity.

Time-Kill Kinetics

To investigate the bactericidal performance of calix[4]arene derivatives, we determined the time-kill kinetics curves of compound **16** against MRSA NCTC10442 at different concentrations (4× and 8× MIC). As shown in **Figure 1**, compound **16** reduced 4.3 and 5.6 log bacteria (killing > 99.99% of MRSA NCTC10442) within 0.5 h at 4× and 8× MIC, respectively, indicating that compound **16** exhibited rapid bactericidal activity. In contrast, the commercial vancomycin only achieved 1.6 and 2.0 log bacterial reductions within 4 h at 4× and 8× MIC, respectively. These findings indicated that compound **16** showed rapid bactericidal action that will help to reduce the treatment time of bacterial infection and the probability of developing bacterial resistance.

Resistance Development Study

The ability to overcome bacterial resistance has become an important criterion to evaluate a new antibacterial drug (Gajdács, 2019). The rapid development of bacterial resistance to antimicrobials is a major threat to public health in the 21st century (Walsh, 2000; O'Neill, 2008; Piddock, 2012). The membrane-targeting antibacterial agents can effectively avoid or slow down the development of bacterial resistance. To evaluate the tendency of bacterial resistance of compound **16**, a laboratory simulation study on the drug resistance of compound **16** was carried out. In the presence of a sublethal concentration of compound **16** or norfloxacin, *S. aureus* ATCC29213 was consecutively passaged for 19 days. As shown in **Figure 2**, after 19 passages, no more than a 4-fold increase in the MIC values was observed for compound **16**. In contrast, the MIC value of norfloxacin was increased by 32-fold after 17 passages, indicating that norfloxacin could rapidly induce bacterial resistance. The reason may be that the bacterial membrane is a conservative component in the evolution of bacterial cells and determines the phenotype, it is difficult for bacteria to keep alive with great changes in the composition of the cell membranes (Zasloff, 2002; Yeaman and Yount, 2003). These results demonstrated that compound **16** has obvious advantages over conventional antibacterial drugs, and can avoid the occurrence of developing bacterial resistance.

Antibacterial Mechanism Studies

The rapid bactericidal action of compound **16** may be based on the membrane-active mode of action. To verify this hypothesis, SYTOX Green dye was used to study the effect of compound **16** on the bacterial cell membrane. SYTOX Green is a green nucleic acid dye that can easily penetrate the damaged bacterial cell membrane but cannot penetrate the living cell membrane with a complete membrane structure (Roth et al., 1997; Thakur et al., 2015). After binding with intracellular nucleic acid, its fluorescence intensity will be significantly enhanced. As shown in **Figure 3**, when MRSA NCTC10442 were treated with compound **16** at four different concentrations (1×, 2×, 4× and 8× MIC), the fluorescence intensity increased notably. The results indicated that compound **16** could increase the permeability of Gram-positive bacterial cell membrane, and then destroy the integrity of bacterial cell membranes, causing the leakage of the cellular contents and bacterial cell death.

The interaction between compound **16** and lipoteichoic acid (LTA) which was one of the main components of Gram-positive bacteria was also explored. The binding affinity between compound **16** and LTA was determined using the BODIPY-TR-cadaverine displacement assay. The fluorescence intensity of the probe was quenched when it was bound to LTA (Swain et al., 2019). When the probe is replaced by compound **16** and dissolved in solution, the fluorescence will be significantly enhanced. As shown in **Figure 4**, a proper amount of BODIPY-TR-cadaverine (30 ± 5%) was replaced by 1× MIC compound **16** from LTA. And compound **16** can replace a considerable amount of BODIPY-TR-cadaverine from LTA at 16× MIC (67 ± 2%), indicating that compound **16** could interact with LTA on the bacterial surface *via* a concentration-dependent manner.

In Vitro Cytotoxicity Evaluation

An important parameter in the development of antimicrobial drugs is their ability to selectively act on microbial cells rather than mammalian cells. CCK-8 assay was used to evaluate the *in vitro* cytotoxicity of compound **16** toward mammalian cells (mouse fibroblast NCTC clone 929). As shown in **Figure 5**,

compound **16** showed very low cytotoxicity toward mouse fibroblast NCTC clone 929 cells at the concentration of ≤ 25 μg/ml (8–16× MIC). 72 ± 6% viability of mouse fibroblasts was observed for compound **16** at 25 μg/ml. In general, when considering the low MIC values of compound **16** against Gram-positive bacterial strains, these cytotoxicity results are very encouraging.

CONCLUSION

In summary, we have designed and synthesized a series of calix[4]arene-based antibacterial agents, and have evaluated the *in vitro* antibacterial and hemolytic activity of these synthesized compounds. The incorporation of different cationic groups can effectively improve the antibacterial activity of calix[4]arene derivatives. The most promising compound **16** showed excellent activity against all tested Gram-positive bacterial strains. The antibacterial mechanism studies have shown that compound **16** could destroy the integrity of Gram-positive bacteria, causing the leakage of cell contents and leading to bacterial cell deaths. Membrane active mode of action and rapid bactericidal ability can effectively reduce the probability of bacterial drug resistance. In general, we have synthesized a class of calix[4]arene derivatives as membrane-active antibacterial agents, which provided a new design idea for the development of new membrane-active antibacterial agents.

MATERIALS AND METHODS

Chemistry

All chemicals and solvents were purchased from commercial suppliers and used directly without further purification. 4-Tert-butylcalix[4]arene, and tetraethyl 4-tert-butylcalix[4]arene-O,O′,O″,O‴-tetraacetate were purchased from Aladdin Biochemical Technology Co., Ltd. The completion of all reactions was monitored by thin-layer chromatography (Merck silica gel 60 F254). ^{1}H and ^{13}C NMR spectra were recorded on the JEOL 400 MHz spectrometer operating at frequencies of 400 and 100 MHz, respectively. Chemical shifts (δ) are given in ppm, and coupling constants (J) are given in Hz. HRMS spectra were recorded on a Thermo DFS mass spectrometer. The final products were purified by preparative high-performance liquid chromatography on an Agilent 1260 Integrated system (C18 column, YMC-Pack, 20 mm × 150 mm, 5 μm), using methanol and distilled water (both containing 0.1% formic acid) as the gradient elution.

$1^5,3^5,5^5,7^5$-Tetra-tert-butyl-$3^2,7^2$-bis(oxiran-2-ylmethoxy)-1,3,5,7(1,3)-tetrabenzenacyclooctaphane-$1^2,5^2$-diol (2)

4-Tert-butylcalix[4]arene (200 mg, 0.31 mmol) was dissolved in anhydrous acetonitrile by ultrasonic, and then epibromohydrin (202 μl, 2.5 mmol), potassium iodide (20 mg, 0.12 mmol) and potassium carbonate (170 mg, 1.2 mmol) were added. The reaction mixture was refluxed at 85°C overnight. After completion of the reaction, the mixture was diluted with ethyl acetate and washed twice with water. The organic phase was concentrated under reduced pressure, and the crude product was purified by silica gel chromatography (petroleum ether: ethyl acetate, 4:1, v:v) to give compound **2** as a white solid (141 mg, 70%). ^{1}H NMR (400 MHz, $CDCl_3$) δ 7.18–7.09 (m, 2H), 7.08–7.03 (m, 4H), 6.81 (s, 4H), 4.37–4.21 (m, 6H), 4.10–4.03 (m, 2H), 3.55 (s, 2H), 3.37–3.28 (m, 4H), 3.11–2.89 (m, 4H), 1.30–1.26 (m, 18H), 1.02–0.92 (m, 18H). ^{13}C NMR (100 MHz, $CDCl_3$) δ 150.55, 150.50, 149.56, 149.52, 147.25 (2×C), 141.64, 141.61, 141.58, 132.78, 132.66, 132.62, 132.48, 127.93, 127.79, 127.73, 127.64, 125.80, 125.71, 125.59, 125.22, 125.19, 125.15, 125.10, 76.04, 75.75, 60.47, 50.28, 44.77, 44.73, 34.02, 34.01, 33.89 (2×C), 31.75 (6×CH_3), 31.62 (2×CH_2), 31.59 (2×CH_2), 31.07 (6×CH_3). HRMS (ESI+): calculated for $C_{50}H_{65}O_6$ $[M + H]^+$ 761.4781, found 761.4762.

$1^5,3^5,5^5,7^5$-Tetra-tert-butyl-$3^2,7^2$-bis(3-(dimethylamino)-2-hydroxypropoxy)-1,3,5,7(1,3)-tetrabenzenacyclooctaphane-$1^2,5^2$-diol (3)

To a solution of **2** (38 mg, 0.050 mmol) in methanol (5.0 ml), dimethylamine (1.0 ml) was added, and the reaction mixture was refluxed at 65°C for 3 h. After completion of the reaction, the reaction mixture was directly distilled under reduced pressure. The crude product was purified by HPLC to give compound **3** as a white solid (22 mg, 59%). ^{1}H NMR (400 MHz, CD_3OD) δ 7.19–7.11 (m, 8H), 4.61–4.37 (m, 2H), 4.35–4.24 (m, 4H), 4.23–4.08 (m, 3H), 4.06–3.92 (m, 2H), 3.65–3.36 (m, 6H), 3.22–3.13 (m, 1H), 2.82 (s, 12H), 1.23 (s, 18H), 1.14–1.10 (m, 18H). ^{13}C NMR (100 MHz, $CDCl_3$) δ 149.93, 149.88, 149.04, 148.89, 147.85, 147.71, 142.57, 142.51, 132.80, 132.64, 132.56, 132.47, 127.84, 127.81, 127.79, 127.43, 126.24, 125.96, 125.82, 125.62, 125.49, 125.45, 125.36, 100.00, 78.36, 78.29, 66.13, 65.73, 61.26, 61.17, 44.62 (2×CH_3), 44.55 (2×CH_3), 34.16, 34.10, 33.95 (2×C), 31.72 (2×CH_2), 31.71 (2×CH_2), 31.10 (6×CH_3), 31.07 (6×CH_3). HRMS (ESI+): calculated for $C_{54}H_{79}N_2O_6$ $[M + H]^+$ 851.5938, found 851.5923.

$1^5,3^5,5^5,7^5$-Tetra-tert-butyl-$3^2,7^2$-bis(3-(diethylamino)-2-hydroxypropoxy)-1,3,5,7(1,3)-tetrabenzenacyclooctaphane-$1^2,5^2$-diol (4)

Compound **4** was prepared from **2** (37 mg, 0.049 mmol) and diethylamine (1.0 ml), following the procedure used to prepare **3.** The product was obtained as a white solid (28 mg, 75%). ^{1}H NMR (400 MHz, $CDCl_3$) δ 8.20 (s, 1H), 7.82–7.72 (m, 1H), 7.10–6.99 (m, 4H), 6.98–6.89 (m, 2H), 6.88 (s, 2H), 4.55–3.87 (m, 10H), 3.45–3.30 (m, 6H), 2.94–2.76 (m, 12H), 1.27–1.24 (m, 18H), 1.18–1.12 (m, 12H), 1.07 (s, 9H), 1.02 (s, 9H). ^{13}C NMR (100 MHz, $CDCl_3$) δ 150.15, 150.00, 149.96, 149.32, 149.20, 147.64, 147.50, 142.44, 142.39, 142.30, 132.52, 132.41, 132.35, 132.26, 128.03, 127.88, 127.86, 127.66, 126.10, 125.86, 125.73, 125.52, 125.39, 125.33, 78.83, 78.60, 66.10, 65.81, 56.32, 55.95, 47.96 (2×CH_2), 47.94 (2×CH_2), 34.08, 34.04, 33.96 (2×C), 31.75 (2×CH_2), 31.73 (2×CH_2), 31.07 (6×CH_3), 31.04 (6×CH_3), 9.76 (2×CH_3), 9.55 (2×CH_3). HRMS (ESI+): calculated for $C_{58}H_{87}N_2O_6$ $[M + H]^+$ 907.6564, found 907.6556.

$1^5,3^5,5^5,7^5$-tetra-tert-butyl-$3^2,7^2$-bis(3-(dibutylamino)-2-hydroxypropoxy)-1,3,5,7(1,3)-tetrabenzenacyclooctaphane-$1^2,5^2$--diol (5)

Compound **5** was prepared from **2** (39 mg, 0.051 mmol) and di-n-butylamine (1.0 ml), following the procedure used to prepare **3**. The product was obtained as a brown solid (27 mg, 70%). ^{1}H NMR (400 MHz, $CDCl_3$) δ 8.21 (s, 1H), 7.77–7.66 (m, 1H), 7.09–7.00 (m, 4H), 6.99–6.86 (m, 4H), 4.59–4.52 (m, 2H), 4.50–3.88 (m, 10H), 3.46–3.26 (m, 4H), 3.05–2.82 (m, 4H), 2.80–2.65 (m, 8H), 1.64–1.46 (m, 8H), 1.39–1.30 (m, 8H), 1.29–1.24 (m, 18H), 1.08 (s, 9H), 1.02 (s, 9H), 0.92 (t, J = 7.3 Hz, 12H). ^{13}C NMR (100 MHz, $CDCl_3$) δ 150.23, 149.93, 149.77, 149.48, 149.21, 147.77, 147.47, 142.55, 142.34, 142.17, 133.25, 132.88, 132.80, 132.70, 128.21, 127.87, 127.74, 127.50, 126.42, 125.92, 125.77, 125.69, 125.47, 125.39, 79.76, 79.28, 67.54, 67.06, 57.38, 56.59, 54.38 (2×CH_2), 54.30 (2×CH_2), 34.20, 34.12, 33.95, 33.93, 32.51, 32.04, 31.94, 31.74, 31.72 (3×CH_3), 31.68 (3×CH_3), 31.18 (3×CH_3), 31.13 (3×CH_3), 28.36 (2×CH_2), 28.17 (2×CH_2), 20.61 (2×CH_2), 20.58 (2×CH_2), 14.08 (2×CH_3), 14.04 (2×CH_3). HRMS (ESI+): calculated for $C_{66}H_{103}N_2O_6$ $[M + H]^+$ 1,019.7816, found 1,019.7791.

$1^5,3^5,5^5,7^5$-Tetra-tert-butyl-$3^2,7^2$-bis(2-hydroxy-3-(pyrrolidin-1-yl)propoxy)-1,3,5,7(1,3)-tetrabenzenacyclooctaphane-$1^2,5^2$-diol (6)

Compound **6** was prepared from **2** (35 mg, 0.046 mmol) and tetrahydropyrrole (1.0 ml), following the procedure used to prepare **3**. The product was obtained as a white solid (27 mg, 78%). ^{1}H NMR (400 MHz, $CDCl_3$) δ 7.59 (s, 1H), 7.41–7.35 (m, 1H), 7.08–6.97 (m, 4H), 6.89–6.76 (m, 4H), 5.78 (br, 4H), 4.64–4.51 (m, 2H), 4.28–3.74 (m, 8H), 3.46–3.15 (m, 16H), 2.11–1.99 (m, 8H), 1.29–1.24 (m, 18H), 1.00 (s, 9H), 0.97 (s, 9H). ^{13}C NMR (100 MHz, $CDCl_3$) δ 150.10, 150.05, 149.96, 149.14, 149.10, 147.67, 147.64, 142.51, 142.36, 132.69, 132.54, 132.51, 132.36, 127.88, 127.79, 127.76, 127.46, 126.16, 125.94, 125.88, 125.73, 125.50, 125.38, 125.26, 78.64, 78.31, 66.68, 66.44, 59.41, 59.11, 54.88 (2×CH_2), 54.82 (2×CH_2), 34.11, 34.08, 33.95, 33.94, 31.99, 31.76 (2×CH_2), 31.72 (6×CH_3), 31.58, 31.08 (3×CH_3), 31.06 (3×CH_3), 23.31 (4×CH_2). HRMS (ESI+): calculated for $C_{58}H_{83}N_2O_6$ $[M + H]^+$ 903.6251, found 903.6240.

$1^5,3^5,5^5,7^5$-Tetra-tert-butyl-$3^2,7^2$-bis(2-hydroxy-3-(methylamino)propoxy)-1,3,5,7(1,3)-tetrabenzenacyclooctaphane-$1^2,5^2$-diol (7)

Compound **7** was prepared from **2** (35 mg, 0.046 mmol) and methylamine (1.0 ml), following the procedure used to prepare **3**. The product was obtained as a brown solid (18 mg, 51%). ^{1}H NMR (400 MHz, $CDCl_3$) δ 8.64 (s, 1H), 8.08 (s, 1H), 7.08–7.00 (m, 4H), 6.98–6.90 (m, 4H), 5.62 (s, 4H), 4.60 (d, J = 19.3 Hz, 2H), 4.30–4.06 (m, 6H), 3.99–3.77 (m, 2H), 3.49–3.20 (m, 8H), 2.75 (d, J = 5.5 Hz, 6H), 1.23 (s, 18H), 1.07 (s, 18H). ^{13}C NMR (100 MHz, $CDCl_3$) δ 149.87, 149.82, 149.68, 148.73, 148.56, 148.11, 147.97, 142.76, 142.55, 133.12, 133.01, 132.85, 132.67, 127.68, 127.60, 127.30, 127.08, 126.39, 126.15, 126.08, 125.91, 125.79, 125.64, 125.51, 78.42, 78.04, 66.75, 66.16, 52.82, 52.51, 34.24, 34.22, 33.95, 33.94, 33.89, 33.78, 32.24, 32.07, 32.02, 31.78, 31.69 (3×CH_3), 31.67 (3×CH_3), 31.16 (3×CH_3), 31.14 (3×CH_3). HRMS (ESI+): calculated for $C_{52}H_{75}N_2O_6$ $[M + H]^+$ 823.5625, found 823.5591.

$1^5,3^5,5^5,7^5$-Tetra-tert-butyl-$3^2,7^2$--bis(3-(ethylamino)-2-hydroxypropoxy)-1,3,5,7(1,3)-tetrabenzenacyclooctaphane-$1^2,5^2$-diol (8)

Compound **8** was prepared from **2** (37 mg, 0.048 mmol) and ethylamine (1.0 ml), following the procedure used to prepare **3**. The product was obtained as a white solid (22 mg, 58%). ^{1}H NMR (400 MHz, $CDCl_3$) δ 8.64 (s, 1H), 8.53 (s, 1H), 7.07–6.96 (m, 8H), 5.80 (br, 4H), 4.81–4.65 (m, 2H), 4.41–4.10 (m, 6H), 3.95–3.80 (m, 2H), 3.47–3.02 (m, 12H), 1.44–1.34 (m, 6H), 1.26–1.18 (m, 18H), 1.16–1.06 (m, 18H). ^{13}C NMR (100 MHz, $CDCl_3$) δ 149.99, 149.61, 149.47, 148.73, 148.52, 148.30, 148.07, 142.84, 142.48, 142.38, 133.57, 133.50, 133.21, 133.08, 127.82, 127.14, 127.07, 126.64, 126.18, 125.95, 125.85, 125.74, 125.62, 125.50, 78.23, 77.89, 67.08, 66.87, 50.50, 49.89, 43.60, 43.35, 34.32, 34.29, 33.94, 33.91, 32.65, 32.31, 32.22, 31.99, 31.67, 31.65, 31.63 (3×CH_3), 31.23 (3×CH_3), 31.21 (3×CH_3), 29.78, 11.59, 11.46. HRMS (ESI+): calculated for $C_{54}H_{79}N_2O_6$ $[M + H]^+$ 851.5938, found 851.5928.

$1^5,3^5,5^5,7^5$-Tetra-tert-butyl-$3^2,7^2$-bis(2-hydroxy-3-(propylamino)propoxy)-1,3,5,7(1,3)-tetrabenzenacyclooctaphane-$1^2,5^2$-diol (9)

Compound **9** was prepared from **2** (35 mg, 0.046 mmol) and *N*-propylamine (1.0 ml), following the procedure used to prepare **3**. The product was obtained as a white solid (26 mg, 74%). ^{1}H NMR (400 MHz, $CDCl_3$) δ 8.64 (s, 1H), 8.55 (s, 1H), 7.07–7.03 (m, 2H), 7.03–7.00 (m, 4H), 7.00–6.96 (m, 2H), 4.83–4.64 (m, 2H), 4.41–4.10 (m, 6H), 3.94–3.77 (m, 2H), 3.47–3.09 (m, 8H), 3.03–2.87 (m, 4H), 1.92–1.76 (m, 4H), 1.25–1.20 (m, 18H), 1.16–1.11 (m, 18H), 1.01 (t, J = 7.4 Hz, 6H). ^{13}C NMR (100 MHz, $CDCl_3$) δ 150.04, 149.65, 149.54, 148.77, 148.59, 148.25, 148.04, 142.76, 142.44, 142.34, 133.56, 133.27, 133.14, 127.82, 127.78, 127.16, 127.11, 126.60, 126.18, 125.92, 125.86, 125.72, 125.60, 125.50, 78.23, 77.94, 67.01, 66.89, 50.91, 50.36, 50.27, 50.04, 34.32, 34.29, 33.93, 33.91, 32.66, 32.31, 32.24, 32.01, 31.67, 31.65, 31.64 (3×CH_3), 31.23 (3×CH_3), 31.22 (3×CH_3), 29.78, 19.79, 19.63, 11.42, 11.41. HRMS (ESI+): calculated for $C_{56}H_{83}N_2O_6$ $[M + H]^+$ 879.6251, found 879.6237.

$1^5,3^5,5^5,7^5$-Tetra-tert-butyl-$3^2,7^2$-bis(3-(hexylamino)-2-hydroxypropoxy)-1,3,5,7(1,3)-tetrabenzenacyclooctaphane-$1^2,5^2$-diol (10)

Compound **10** was prepared from **2** (47 mg, 0.062 mmol) and n-hexylamine (1.0 ml), following the procedure used to prepare **3** and purified by HPLC to give compound **10** as a brown solid (25 mg, 53%). ^{1}H NMR (400 MHz, $CDCl_3$) δ 8.63–8.60 (m, 2H), 7.07–6.96 (m, 8H), 4.96–4.66 (m, 3H), 4.40–4.04 (m, 7H), 3.88–3.78 (m, 2H), 3.51–2.84 (m, 14H), 1.91–1.68 (m, 4H), 1.40–1.28 (m, 12H), 1.22 (s, 18H), 1.14 (s, 18H), 0.90–0.86 (m, 6H). ^{13}C NMR (100 MHz, $CDCl_3$) δ 149.56, 149.47, 148.75, 148.55, 148.29, 148.06, 142.79, 142.44, 133.66, 133.58, 133.31, 133.15, 127.83, 127.10, 127.04, 126.66, 126.19, 126.17, 125.96, 125.83, 125.75, 125.61, 125.49, 100.00, 78.19, 77.84, 67.03, 66.81, 50.84, 50.17, 48.84, 48.47, 34.32, 34.30, 33.93, 33.92, 33.90, 32.71,

32.35, 32.25, 32.01, 31.66, 31.62 (3×CH_3), 31.38, 31.36, 31.24 (3×CH_3), 31.22 (3×CH_3), 31.00, 26.61, 26.58, 26.18, 26.00, 22.54, 22.52, 14.04 (2×CH_3). HRMS (ESI+): calculated for $C_{62}H_{95}N_2O_6$ $[M + H]^+$ 963.7190, found 963.7176.

$1^5,3^5,5^5,7^5$-Tetra-tert-butyl-$3^2,7^2$-bis(2-hydroxy-3-thiomorpholinopropoxy)-1,3,5,7(1,3)-tetrabenzenacyclooctaphane-$1^2,5^2$-diol (11)

Compound **11** was prepared from **2** (44 mg, 0.058 mmol) and thiomorpholine (1.0 ml), following the procedure used to prepare **3**. The product was obtained as a white solid (27 mg, 61%). ^{1}H NMR (400 MHz, $CDCl_3$) δ 8.76 (s, 1H), 8.33–8.23 (m, 1H), 7.09–6.95 (m, 8H), 4.58–3.89 (m, 10H), 3.49–3.28 (m, 4H), 2.94–2.84 (m, 8H), 2.78–2.60 (m, 12H), 1.26–1.21 (m, 18H), 1.16–1.08 (m, 18H). ^{13}C NMR (100 MHz, $CDCl_3$) δ 149.93, 149.66, 149.50, 149.17, 148.93, 148.08, 147.82, 142.76, 142.59, 142.53, 133.72, 133.21, 133.20, 128.18, 127.76, 127.59, 127.29, 126.64, 126.12, 125.96, 125.78, 125.65, 125.61, 125.52, 79.63, 78.95, 68.06, 67.67, 61.13, 60.88, 55.78 (2×CH_2), 55.73 (2×CH_2), 34.31, 34.25, 33.95, 33.94, 32.88, 32.34, 32.19, 32.02, 31.69, 31.67, 31.64 (6×CH_3), 31.25 (3×CH_3), 31.21 (3×CH_3), 28.19, 28.16. HRMS (ESI+): calculated for $C_{58}H_{84}N_2O_6S_2$ $[M + 2H]^{2+}$ 484.2880, found 484.2874.

$3^2,7^2$-Bis(3-(bis(2-hydroxyethyl)amino)-2-hydroxypropoxy)-$1^5,3^5,5^5,7^5$-tetra-tert-butyl-1,3,5,7(1,3)-tetrabenzenacyclooctaphane-$1^2,5^2$-diol (12)

Compound **12** was prepared from **2** (49 mg, 0.064 mmol) and diethanolamine (1.0 ml), following the procedure used to prepare **3.** The product was obtained as a white solid (29 mg, 59%). ^{1}H NMR (400 MHz, $CDCl_3$) δ 8.54–7.85 (m, 2H), 7.09–6.98 (m, 4H), 6.97–6.81 (m, 4H), 4.95 (s, 10H), 4.58 (s, 2H), 4.38–4.16 (m, 4H), 4.04–3.65 (m, 10H), 3.44–3.26 (m, 4H), 3.18–3.04 (m, 4H), 3.00–2.54 (m, 6H), 1.26–1.19 (m, 18H), 1.11–1.00 (m, 18H). ^{13}C NMR (100 MHz, $CDCl_3$) δ 150.05, 149.58, 149.37, 149.14, 147.85, 147.73, 147.70, 142.72, 133.39, 133.26, 133.09, 132.82, 128.42, 128.13, 127.62, 127.42, 126.69, 126.26, 126.03, 125.85, 125.77, 125.43, 78.89, 78.28, 68.45, 67.74, 59.01 (2×CH_2), 58.73 (2×CH_2), 57.99 (2×CH_2), 57.67 (2×CH_2), 34.23, 34.21, 33.92, 33.91, 33.89, 32.84, 32.51, 32.20, 31.68 (3×CH_3), 31.63 (3×CH_3), 31.20 (3×CH_3), 31.18 (3×CH_3). HRMS (ESI+): calculated for $C_{58}H_{88}N_2O_{10}$ $[M + 2H]^{2+}$ 486.3214, found 486.3207.

3,3′-((1^5,3^5,5^5,7^5-Tetra-tert-butyl-3^2,7^2-dihydroxy-1,3,5,7(1,3)-tetrabenzenacyclooctaphane-1^2,5^2-diyl) bis(oxy))bis(2-hydroxy-*N,N,N*-trimethylpropan-1-aminium) Iodide (13)

A mixture of compound **3** (54 mg, 0.063 mmol) and methyl iodide (1.0 ml) was dissolved in methanol and was stirred overnight at room temperature. After completion of the reaction, the mixture was directly concentrated under reduced pressure. Then the crude product was purified by HPLC to provide compound **13** as a white solid (26 mg, 48%). ^{1}H NMR (400 MHz, CD_3OD) δ 7.28–7.14 (m, 6H), 7.06–7.02 (m, 2H), 4.56–3.90 (m, 12H), 3.85–3.78 (m, 2H), 3.69–3.45 (m, 8H), 3.45–3.34 (m, 14H), 1.29 (s, 12H), 1.22 (s, 6H), 1.19 (s, 6H), 1.06–1.03 (m, 12H). ^{13}C NMR (100 MHz, CD_3OD) δ 150.75, 150.70, 150.66, 150.56, 149.38, 149.34, 144.05, 144.00, 143.98, 134.08, 134.03, 133.97, 129.47, 129.43, 129.34, 129.20, 127.33, 127.16, 127.07, 126.93, 126.55, 126.45, 126.36, 126.34, 79.44, 79.39, 69.62, 69.50, 66.77 (2×CH_3), 65.25 (2×CH_2), 55.23 (2×CH_3), 43.20 (2×CH_3), 35.01, 35.00, 34.76, 32.46, 32.32, 32.06 (3×CH_3), 31.54 (3×CH_3), 31.25, 30.25, 24.40, 24.15, 14.47, 11.44. HRMS (ESI+): calculated for $C_{56}H_{84}I_2N_2O_6$ $[M - 2I]^{2+}$ 440.3159, found 440.3152.

2,2′,2″,2‴-((1^5,3^5,5^5,7^5-Tetra-tert-butyl-1,3,5,7(1,3)-tetrabenzenacyclooctaphane-1^2,3^2,5^2,7^2-tetrayl) tetrakis(oxy))tetrakis(*N*-(3-(dimethylamino)propyl) acetamide) (16)

Tetraethyl 4-tert-butylcalix[4]arene-O,O′,O″,O‴-tetraacetate (100 mg, 0.10 mmol) was dissolved in tetrahydrofuran, and then lithium hydroxide (48 mg, 2.0 mmol) dissolved in water (2.0 ml) was added. After the mixture was stirred at room temperature for 1.5 h, acetic acid was added to adjust its acidity, then the mixture was diluted with n-butanol and washed twice with water. The organic phase was concentrated under reduced pressure to give crude product **15**, which was directly used for the next step without further purification. Subsequently, **15** was dissolved in DMF (5.0 ml), and then 4-(4,6-dimethoxy-1,3,5-triazin-2-yl)-4-methylmorpholinium chloride (223 mg, 0.81 mmol), DIPEA (0.27 ml, 1.6 mmol) and 3-(dimethylamino)-1-propylamine (203 μl, 0.016 mmol) were added. After stirring overnight at room temperature, the reactant mixture was diluted with n-butanol and washed twice with water. The organic phase was concentrated under reduced pressure, and the crude product was purified by HPLC to yield compound **16** as a brown solid (12 mg, 12%). ^{1}H NMR (400 MHz, CD_3OD) δ 6.92 (s, 8H), 4.85–4.78 (m, 8H), 4.61 (s, 8H), 3.39 (t, J = 6.8 Hz, 8H), 2.91–2.77 (m, 8H), 2.72–2.58 (m, 24H), 1.99–1.84 (m, 8H), 1.11 (s, 36H). ^{13}C NMR (100 MHz, CD_3OD) δ 172.09 (4×C), 134.96 (4×C), 134.94 (4×C), 134.88 (4×C), 134.82 (4×C), 127.15 (8×CH), 75.44 (4×CH_2), 56.71 (4×CH_2), 43.75 (8×CH_3), 37.42 (4×CH_2), 34.98 (4×CH, 4×CH_2), 31.85 (12×CH_3), 26.37 (4×CH_2). HRMS (ESI+): calculated for $C_{72}H_{114}N_8O_8$ $[M + 2H]^{2+}$ 609.4374, found 609.4359.

Antibacterial Activity Evaluation

MIC values were determined by the broth microdilution method according to the guidelines established by the Clinical and Laboratory Standards Institute (CLSI). Bacterial cells were prepared on Mueller-Hinton agar (MHA) plates at 37°C for 24 h and adjusted to approximately 1.0 × 10^6 CFU/ml. Compounds were dissolved in DMSO and water to prepare stock solution, and then diluted to the required concentration in Mueller-Hinton Broth (MHB) medium. The bacterial suspension (100 μl) was added to each well of the 96-well plate and mixed with an equal volume of the two-fold serial dilutions of the compounds (100 μl), then the 96-well plates were incubated at 37°C for 24 h. The MIC values were determined by measuring OD600 and visual inspection. Compared with the negative control group, the MIC value was determined as the

lowest sample concentration without bacterial growth. All reported MIC values have been determined repeatedly.

Hemolytic Activity Evaluation

Fresh rabbit red blood cells (RBCs) were washed three times with PBS, centrifuged at 2,500 rpm for 3 min, and then diluted with PBS to prepare 8% (v/v) suspension. The compounds were dissolved in DMSO (final DMSO concentration of ≤ 0.50%) or PBS, and then diluted with PBS. Two-fold serial dilutions of compounds (100 μl) were incubated for 1 h at 37°C with 100 μl of RBC suspension (~5.0×10^8 cells/ml) in a 96-well plate. Then, the mixture was centrifuged at 2,500 rpm for 5 min, 100 μl supernatant was transferred into a 96-well plate and measured the absorbance at 576 nm using BioTek multi-detector microplate reader. RBCs treated with PBS were used as a negative control, and RBCs treated with 2.0% Triton X-100 solution were used as a positive control. The hemolysis percentage was calculated by the following formula: % hemolysis = $[(Abs_{sample} - Abs_{negative\ control})/(Abs_{positive\ control} - Abs_{negative\ control})] \times 100$. All values have been determined at least twice independently with biologically replicates.

Cytotoxicity Assay

Mouse NCTC clone 929 cells (~2.0×10^4 cells/well) were incubated in a 96-well plate, and treated with different concentrations of compound **16** at 37°C with 5% CO_2 for 24 h. Then, 10 μl of CCK-8 reagent was added to each well and incubated at 37°C with 5.0% CO_2 for 1 h. The absorbance at 450 nm was detected by BioTek multi-detector microplate reader, and the cell viability was calculated by the ratio of OD450 value of compound-treated cells to OD450 value of untreated cells. The experiments were carried out at least twice with biologically replicates.

SYTOX Green Assay

Bacteria were cultured on MHA plates overnight, then the bacterial cells were washed twice with PBS buffer (10 mM, pH = 7.2) and resuspended in PBS. The absorbance of the suspension at 600 nm was adjusted to 0.20. After mixing with 0.30 μM SYTOX Green, the suspension was cultured in dark. The change of fluorescence intensity was monitored by the BioTek multi-detector microplate reader (excitation wavelength: 504 nm, emission wavelength: 523 nm). After the fluorescence signal was stable, compound **16** dissolved in DMSO was immediately added to the SYTOX Green-treated bacterial suspension, and the change of fluorescence intensity was recorded for about 1 h. All experiments were conducted at least twice with biologically replicates.

BODIPY™-TR-Cadaverine Displacement Assay

BODIPY™-TR-cadaverine replacement test was used to determine the binding affinity between compound **16** and lipoteichoic acid (LTA). BODIPY™-TR-cadaverine was purchased from ThermoFisher, LTA from *S. aureus* was purchased from Sigma-Aldrich. When the probe binds to LTA, the fluorescence intensity of the probe is quenched. The fluorescence will be significantly enhanced when the probe is replaced and re-dissolved in solution. BODIPY™-TR-cadaverine (final concentration of 5.0 μM) and LTA (final concentration of 10 μg/ml) were mixed in the 24 well plates with Tris buffer (50 mM, pH = 7.4). After 15 min, compound **16** (1×, 2×, 4×, 8×, 16× and 32× MIC) dissolved in DMSO was added, and then the mixture was placed in the dark for 30 min at room temperature. Finally, the fluorescence intensity (excitation wavelength 580 nm, emission wavelength 620 nm) was measured using a Biotek multiple detector microplate reader. These experiments were performed at least twice with biological replications. The percentage of displacement from LTA was obtained according to the following formula: % displacement from LTA = $[(F_{sample} - F_0)/(F_{max} - F_0)] \times 100$. F_0 is the fluorescence intensity of the probe with LTA, and F_{max} is the fluorescence intensity of the probe without LTA and compound **16**.

Time-Kill Study

Bacterial cells were incubated on MHA plates at 37°C for 24 h, and then adjusted to approximately 1.0×10^6 CFU/ml. The bacterial suspensions were treated with compound **16** at different concentrations (4× and 8× MIC) and were incubated at 37°C. Then, the culture samples (100 μl) were respectively taken from the mixture at 0.5, 1, 2, 4, 8 and 24 h and were serially diluted 10-fold in PBS. The dilutions were plated onto MHA plates and incubated at 37°C for 24 h, then the bacterial colonies were counted. The experiments were repeated at least twice and with biological replicates.

DATA AVAILABILITY STATEMENT

The original contributions presented in the study are included in the article/supplementary material, further inquiries can be directed to the corresponding authors.

AUTHOR CONTRIBUTIONS

SF, Y-YD, SML, and SPL conceived and designed the experiments. SML and SPL coordinated the whole study. The experiments were carried out by SF, HZL, HXL, JL, RZ, and YC. Y-YD, SF, and SML analyzed the data. The manuscript was written through contributions from all authors. All authors listed have made a substantial, direct, and intellectual contribution to the work and approved it for publication.

FUNDING

This work was supported by the National Natural Science Foundation of China (21907019), the Talent Fund for High-Level University Construction of Guangzhou (B195002009029 and B195002009030), Educational Commission of Guangdong Province (2019KQNCX118), Medical Scientific Research Foundation of Guangdong Province (A2020396), College Student Laboratory Opening Project of Guangzhou Medical University (01-408-2102053), and High-level University Construction Fund of Guangdong Province (06-410-2107207; 06-410-2107286).

REFERENCES

Abd Hamid, S., M Bunnori, N., Adekunle, I. A., and Ali, Y. (2015). Applications of Calixarenes in Cancer Chemotherapy: Facts and Perspectives. *Dddt* 9, 2831–2838. doi:10.2147/DDDT.S83213

Adessi, C., and Soto, C. (2002). Converting a Peptide into a Drug: Strategies to Improve Stability and Bioavailability. *Cmc* 9, 963–978. doi:10.2174/0929867024606731

Arbour, C. A., Mendoza, L. G., and Stockdill, J. L. (2020). Recent Advances in the Synthesis of C-Terminally Modified Peptides. *Org. Biomol. Chem.* 18, 7253–7272. doi:10.1039/d0ob01417f

Bono, N., Pennetta, C., Sganappa, A., Giupponi, E., Sansone, F., Volonterio, A., et al. (2018). Design and Synthesis of Biologically Active Cationic Amphiphiles Built on the Calix[4]arene Scaffold. *Int. J. Pharmaceutics* 549, 436–445. doi:10.1016/j.ijpharm.2018.08.020

Costa, F., Teixeira, C., Gomes, P., and Martins, M. C. L. (2019). Clinical Application of AMPs. *Adv. Exp. Med. Biol.* 1117, 281–298. doi:10.1007/978-981-13-3588-4_15

Gajdács, M. (2019). The Concept of an Ideal Antibiotic: Implications for Drug Design. *Molecules* 24, 892. doi:10.3390/molecules24050892

Hanna, T. A., Liu, L., Angeles-Boza, A. M., Kou, X., Gutsche, C. D., Ejsmont, K., et al. (2003). Synthesis, Structures, and Conformational Characteristics of Calixarene Monoanions and Dianions. *J. Am. Chem. Soc.* 125, 6228–6238. doi:10.1021/ja0289797

Hickey, S. M., Ashton, T. D., Khosa, S. K., Robson, R. N., White, J. M., Li, J., et al. (2015). Synthesis and Evaluation of Cationic Norbornanes as Peptidomimetic Antibacterial Agents. *Org. Biomol. Chem.* 13, 6225–6241. doi:10.1039/c5ob00621j

Isaksson, J., Brandsdal, B. O., Engqvist, M., Flaten, G. E., Svendsen, J. S. M., and Stensen, W. (2011). A Synthetic Antimicrobial Peptidomimetic (LTX 109): Stereochemical Impact on Membrane Disruption. *J. Med. Chem.* 54, 5786–5795. doi:10.1021/jm200450h

Jenssen, H., Hamill, P., and Hancock, R. E. W. (2006). Peptide Antimicrobial Agents. *Clin. Microbiol. Rev.* 19, 491–511. doi:10.1128/CMR.00056-05

Jones, M. R., Mathieu, E., Dyrager, C., Faissner, S., Vaillancourt, Z., Korshavn, K. J., et al. (2017). Multi-target-directed Phenol-Triazole Ligands as Therapeutic Agents for Alzheimer's Disease. *Chem. Sci.* 8, 5636–5643. doi:10.1039/c7sc01269a

Kmietowicz, Z. (2017). Few Novel Antibiotics in the Pipeline, WHO Warns. *Bmj* 358, j4339. doi:10.1136/bmj.j4339

Koh, J.-J., Lin, H., Caroline, V., Chew, Y. S., Pang, L. M., Aung, T. T., et al. (2015). N-lipidated Peptide Dimers: Effective Antibacterial Agents against Gram-Negative Pathogens through Lipopolysaccharide Permeabilization. *J. Med. Chem.* 58, 6533–6548. doi:10.1021/acs.jmedchem.5b00628

Kowalski, R. P., Romanowski, E. G., Yates, K. A., and Mah, F. S. (2016). An Independent Evaluation of a Novel Peptide Mimetic, Brilacidin (PMX30063), for Ocular Anti-infective. *J. Ocul. Pharmacol. Ther.* 32, 23–27. doi:10.1089/jop.2015.0098

Kuppusamy, R., Willcox, M., Black, D. S., and Kumar, N. (2019). Short Cationic Peptidomimetic Antimicrobials. *Antibiotics* 8, 44. doi:10.3390/antibiotics8020044

Läppchen, T., Dings, R. P. M., Rossin, R., Simon, J. F., Visser, T. J., Bakker, M., et al. (2015). Novel Analogs of Antitumor Agent Calixarene 0118: Synthesis, Cytotoxicity, Click Labeling with 2-[18F]fluoroethylazide, and *In Vivo* Evaluation. *Eur. J. Med. Chem.* 89, 279–295. doi:10.1016/j.ejmech.2014.10.048

Lázár, V., Martins, A., Spohn, R., Daruka, L., Grézal, G., Fekete, G., et al. (2018). Antibiotic-Resistant Bacteria Show Widespread Collateral Sensitivity to Antimicrobial Peptides. *Nat. Microbiol.* 3, 718–731. doi:10.1038/s41564-018-0164-0

Li, J., Koh, J.-J., Liu, S., Lakshminarayanan, R., Verma, C. S., and Beuerman, R. W. (2017). Membrane Active Antimicrobial Peptides: Translating Mechanistic Insights to Design. *Front. Neurosci.* 11, 73. doi:10.3389/fnins.2017.00073

Livermore, D. M., Blaser, M., Carrs, O., Cassell, G., Fishman, N., Guidos, R., et al. (2011). Discovery Research: the Scientific Challenge of Finding New Antibiotics. *J. Antimicrob. Chemother.* 66, 1941–1944. doi:10.1093/jac/dkr262

Lyddiard, D., Jones, G. L., and Greatrex, B. W. (2016). Keeping it Simple: Lessons from the Golden Era of Antibiotic Discovery. *FEMS Microbiol. Lett.* 363, fnw084. doi:10.1093/femsle/fnw084

Ma, X., and Zhao, Y. (2015). Biomedical Applications of Supramolecular Systems Based on Host-Guest Interactions. *Chem. Rev.* 115, 7794–7839. doi:10.1021/cr500392w

Malmsten, M. (2014). Antimicrobial Peptides. *Upsala J. Med. Sci.* 119, 199–204. doi:10.3109/03009734.2014.899278

Maragakis, L. L., Perencevich, E. N., and Cosgrove, S. E. (2008). Clinical and Economic Burden of Antimicrobial Resistance. *Expert Rev. Anti-infective Ther.* 6, 751–763. doi:10.1586/14787210.6.5.751

Marr, A., Gooderham, W., and Hancock, R. (2006). Antibacterial Peptides for Therapeutic Use: Obstacles and Realistic Outlook. *Curr. Opin. Pharmacol.* 6, 468–472. doi:10.1016/j.coph.2006.04.006

Mensa, B., Howell, G. L., Scott, R., and DeGrado, W. F. (2014). Comparative Mechanistic Studies of Brilacidin, Daptomycin, and the Antimicrobial Peptide LL16. *Antimicrob. Agents Chemother.* 58, 5136–5145. doi:10.1128/AAC.02955-14

Mokhtari, B., and Pourabdollah, K. (2013). Applications of Nano-Baskets in Drug Development: High Solubility and Low Toxicity. *Drug Chem. Toxicol.* 36, 119–132. doi:10.3109/01480545.2011.653490

Molchanova, N., Hansen, P., and Franzyk, H. (2017). Advances in Development of Antimicrobial Peptidomimetics as Potential Drugs. *Molecules* 22, 1430. doi:10.3390/molecules22091430

Monserrat-Martinez, A., Gambin, Y., and Sierecki, E. (2019). Thinking outside the Bug: Molecular Targets and Strategies to Overcome Antibiotic Resistance. *Ijms* 20, 1255. doi:10.3390/ijms20061255

Naseer, M. M., Ahmed, M., and Hameed, S. (2017). Functionalized Calix[4]arenes as Potential Therapeutic Agents. *Chem. Biol. Drug Des.* 89, 243–256. doi:10.1111/cbdd.12818

Nasuhi Pur, F. (2016). Calixdrugs: Calixarene-Based Clusters of Established Therapeutic Drug Agents. *Mol. Divers.* 20, 781–787. doi:10.1007/s11030-016-9667-x

Nimse, S. B., and Kim, T. (2013). Biological Applications of Functionalized Calixarenes. *Chem. Soc. Rev.* 42, 366–386. doi:10.1039/c2cs35233h

Nizalapur, S., Kimyon, O., Yee, E., Ho, K., Berry, T., Manefield, M., et al. (2017). Amphipathic Guanidine-Embedded Glyoxamide-Based Peptidomimetics as Novel Antibacterial Agents and Biofilm Disruptors. *Org. Biomol. Chem.* 15, 2033–2051. doi:10.1039/c7ob00053g

O'Neill, A. (2008). New Antibacterial Agents for Treating Infections Caused by Multi-Drug Resistant Gram-Negative Bacteria. *Expert Opin. Investig. Drugs* 17, 297–302. doi:10.1517/13543784.17.3.297

Pasupuleti, M., Schmidtchen, A., and Malmsten, M. (2012). Antimicrobial Peptides: Key Components of the Innate Immune System. *Crit. Rev. Biotechnol.* 32, 143–171. doi:10.3109/07388551.2011.594423

Piddock, L. J. (2012). The Crisis of No New Antibiotics-What Is the Way Forward? *Lancet Infect. Dis.* 12, 249–253. doi:10.1016/S1473-3099(11)70316-4

Pur, F. N. (2021). Calix[4]API-s: Fully Functionalized Calix[4]arene-Based Facial Active Pharmaceutical Ingredients. *Mol. Divers.* 25, 1247–1258. doi:10.1007/s11030-020-10042-0

Rice, L. B. (2008). Federal Funding for the Study of Antimicrobial Resistance in Nosocomial Pathogens: No ESKAPE. *J. Infect. Dis.* 197, 1079–1081. doi:10.1086/533452

Rogers, G. B., Carroll, M. P., and Bruce, K. D. (2012). Enhancing the Utility of Existing Antibiotics by Targeting Bacterial Behaviour? *Br. J. Pharmacol.* 165, 845–857. doi:10.1111/j.1476-5381.2011.01643.x

Roth, B. L., Poot, M., Yue, S. T., and Millard, P. J. (1997). Bacterial Viability and Antibiotic Susceptibility Testing with SYTOX Green Nucleic Acid Stain. *Appl. Environ. Microbiol.* 63, 2421–2431. doi:10.1128/aem.63.6.2421-2431.1997

Shurpik, D. N., Padnya, P. L., StoikovII, and Cragg, P. J. (2020). Antimicrobial Activity of Calixarenes and Related Macrocycles. *Molecules* 25, 5145. doi:10.3390/molecules25215145

Singh, P., van Swaaij, W. P. M., and Brilman, D. W. F. (2011). Kinetics Study of Carbon Dioxide Absorption in Aqueous Solutions of 1,6-hexamethyldiamine (HMDA) and 1,6-hexamethyldiamine, N,N′ Di-methyl (HMDA, N,N′). *Chem. Eng. Sci.* 66, 4521–4532. doi:10.1016/j.ces.2011.06.008

Swain, J., El Khoury, M., Flament, A., Dezanet, C., Briée, F., Van Der Smissen, P., et al. (2019). Antimicrobial Activity of Amphiphilic Neamine Derivatives: Understanding the Mechanism of Action on Gram-Positive Bacteria. *Biochim. Biophys. Acta (Bba) - Biomembranes* 1861, 182998. doi:10.1016/j.bbamem.2019.05.020

Thakur, S., Cattoni, D. I., and Nöllmann, M. (2015). The Fluorescence Properties and Binding Mechanism of SYTOX Green, a Bright, Low Photo-Damage DNA Intercalating Agent. *Eur. Biophys. J.* 44, 337–348. doi:10.1007/s00249-015-1027-8

Thapa, R. K., Diep, D. B., and Tønnesen, H. H. (2020). Topical Antimicrobial Peptide Formulations for Wound Healing: Current Developments and Future Prospects. *Acta Biomater.* 103, 52–67. doi:10.1016/j.actbio.2019.12.025

Walsh, C. (2000). Molecular Mechanisms that Confer Antibacterial Drug Resistance. *Nature* 406, 775–781. doi:10.1038/35021219

Wimley, W. C., and Hristova, K. (2011). Antimicrobial Peptides: Successes, Challenges and Unanswered Questions. *J. Membr. Biol* 239, 27–34. doi:10.1007/s00232-011-9343-0

Woolhouse, M., Waugh, C., Perry, M. R., and Nair, H. (2016). Global Disease burden Due to Antibiotic Resistance - State of the Evidence. *J. Glob. Health* 6, 010306. doi:10.7189/jogh.06.010306

Yeaman, M. R., and Yount, N. Y. (2003). Mechanisms of Antimicrobial Peptide Action and Resistance. *Pharmacol. Rev.* 55, 27–55. doi:10.1124/pr.55.1.2

Zasloff, M. (2002). Antimicrobial Peptides of Multicellular Organisms. *Nature* 415, 389–395. doi:10.1038/415389a

Conflict of Interest: The authors declare that the research was conducted in the absence of any commercial or financial relationships that could be construed as a potential conflict of interest.

Publisher's Note: All claims expressed in this article are solely those of the authors and do not necessarily represent those of their affiliated organizations, or those of the publisher, the editors and the reviewers. Any product that may be evaluated in this article, or claim that may be made by its manufacturer, is not guaranteed or endorsed by the publisher.

frontiers in Chemistry

ORIGINAL RESEARCH
published: 15 February 2022
doi: 10.3389/fchem.2022.842602

Multiscale Invasion Assay for Probing Macrophage Response to Gram-Negative Bacteria

Kimberly A. Wodzanowski[1], *Jeffrey L. Caplan*[2,3], *April M. Kloxin*[4,5*†] and *Catherine L. Grimes*[1,2*†]

[1]Department of Chemistry and Biochemistry, University of Delaware, Newark, DE, United States, [2]Department of Biological Sciences, University of Delaware, Newark, DE, United States, [3]Bioimaging Center, Delaware Biotechnology Institute, Newark, DE, United States, [4]Department of Chemical and Biomolecular Engineering, University of Delaware, Newark, DE, United States, [5]Department of Materials Science and Engineering, University of Delaware, Newark, DE, United States

The immune system is a complex network of various cellular components that must differentiate between pathogenic bacteria and the commensal bacteria of the human microbiome, where misrecognition is linked to inflammatory disorders. Fragments of bacterial cell wall peptidoglycan bind to pattern recognition receptors within macrophages, leading to immune activation. To study this complex process, a methodology to remodel and label the bacterial cell wall of two different species of bacteria was established using copper (I) catalyzed azide-alkyne cycloaddition (CuAAC) and strain-promoted azide-alkyne cycloaddition (SPAAC). Additionally, an approach for three-dimensional (3D) culture of human macrophages and their invasion with relevant bacteria in a well-defined hydrogel-based synthetic matrix inspired by the microenvironment of the gut was established. Workflows were developed for human monocyte encapsulation and differentiation into macrophages in 3D culture with high viability. Bacteria invaded into macrophages permitted *in situ* peptidoglycan labeling. Macrophages exhibited biologically-relevant cytokine release in response to bacteria. This molecularly engineered, multi-dimensional bacteria-macrophage co-culture system will prove useful in future studies to observe immunostimulatory, bacterial fragment production and localization in the cell at the carbohydrate level for insights into how the immune system properly senses bacteria.

Keywords: biomaterials, bioorthogonal chemistry, invasion model, bacteria-macrophage interactions, click chemistry, live cell imaging, 3D cell culture, synthetic extracellular matrix

OPEN ACCESS

Edited by:
John D. Wade,
University of Melbourne, Australia

Reviewed by:
Ralf Hoffmann,
Leipzig University, Germany
Sander Izaak Van Kasteren,
Leiden University, Netherlands

***Correspondence:**
April M. Kloxin
akloxin@udel.edu
Catherine L. Grimes
cgrimes@udel.edu

[†]These authors have contributed equally to this work and share senior authorship

Specialty section:
This article was submitted to Chemical Biology, a section of the journal Frontiers in Chemistry

Received: *23 December 2021*
Accepted: *27 January 2022*
Published: *15 February 2022*

Citation:
Wodzanowski KA, Caplan JL, Kloxin AM and Grimes CL (2022) Multiscale Invasion Assay for Probing Macrophage Response to Gram-Negative Bacteria. Front. Chem. 10:842602. doi: 10.3389/fchem.2022.842602

INTRODUCTION

The innate immune system is the body's first line of defense against invading pathogens. It is armed with sophisticated molecular mechanisms to sense and differentiate between pathogenic bacteria and the over 39 trillion bacteria constituting the human microbiome. Macrophages have many roles in the innate immune system, including ingesting pathogens by phagocytosis, scavenging dead cells and cell debris, and remodeling tissues after injury (Galli et al., 2011). Based on their tissue location and specialization in various microenvironments, macrophages take on a variety of names including alveolar macrophages (lung), microglia (brain and central nervous system), osteoclasts (bone), and Kupffer cells (liver) to name a few (Italiani and Boraschi, 2014). Macrophages are derived from monocytes, which circulate in the blood stream until entering the tissue and differentiating into

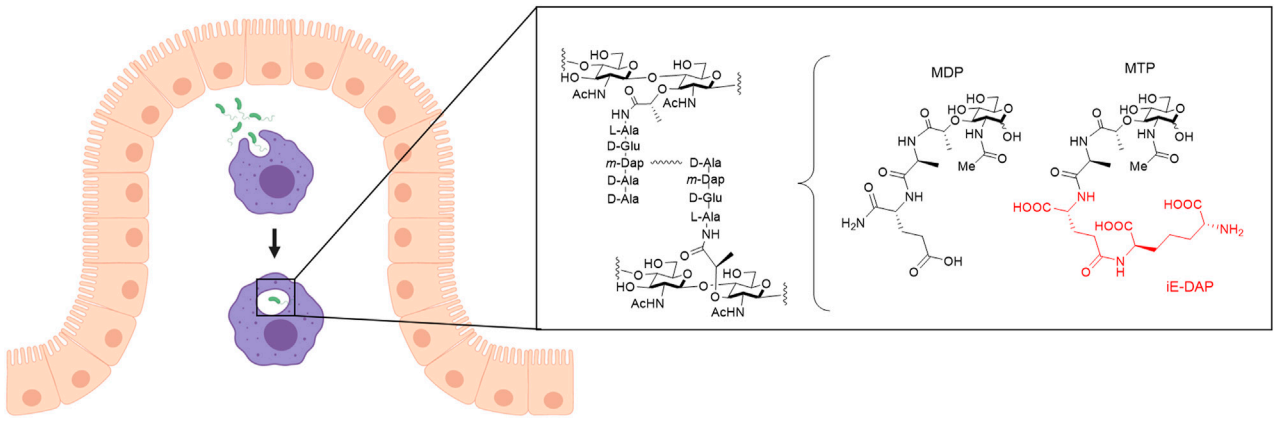

FIGURE 1 | Invasion of bacteria into macrophages. Macrophages (purple) that arise from monocytes reside in the connective tissue underlying the intestinal epithelium (beige). Macrophages phagocytose pathogens such as bacteria (green) and break them down into smaller fragments to determine what type of signaling for an immune response is needed. One recognition element of bacteria, peptidoglycan (PG), is composed of alternating *N*-acetyl glucosamine (NAG) and *N*-acetyl muramic acid (NAM) sugars with a pentapeptide chain off the 3-position of the NAM that is further crosslinked to form mature PG. Out of this larger structure, smaller synthetic fragments, muramyl dipeptide (MDP) and muramyl tripeptide (MTP), can be teased out with the core NAM sugar, which are known to elicit an immune response. D-glutamyl-meso-diaminopimelic acid (iE-DAP), shown in red, is a specific muropeptide in Gram-negative bacteria that activates the NLR, NOD1, to initiate an immune response. Figure created with Biorender.

macrophages, based on release of activating lymphokines from T lymphocytes present in the area of infection (Johnston, 1988). Mature macrophages express receptors that identify pathogens, allowing their proper uptake into the cell for degradation and response (Galli et al., 2011). These receptors include membrane-associated Toll-like receptors (TLRs) and cytosolic NOD-like receptors (NLRs), which are known to bind to fragments of the bacterial peptidoglycan (PG), a component of the bacterial cell wall. Peptidoglycan structure generally contains alternating sugars *N*-acetyl glucosamine (NAG) and *N*-acetyl muramic acid (NAM) with a pentapeptide chain off of the NAM sugar (**Figure 1**). Chemists have developed synthetic PG mimics of smaller fragments such as muramyl dipeptide (MDP) and muramyl tripeptide (MTP), which bind to NLRs and therefore have been used to study immune responses (**Figure 1**). Misrecognition of various PG fragments by the immune system is hypothesized to lead to diseases including Crohn's disease, inflammatory bowel disease, asthma, and gastrointestinal cancers (Geddes et al., 2009; Thaiss et al., 2016). Although MDP and MTP serve as important tools in studying immune responses in humans, the true identity of naturally produced immunostimulatory fragments, how they are generated, and how they interact with innate immune receptors in macrophages is not well known (Hasegawa et al., 2006; Herskovits et al., 2007; Humann and Lenz, 2009). Recently, underlying inflammation has been suggested to have other fundamental roles in biology that have yet to be discovered (Medzhitov, 2021). Therefore, there is a need for development of physiologically-relevant co-culture systems to model invasion of bacteria within human macrophages and begin probing these complex interactions toward addressing these important questions. Moreover, these systems should be amenable to downstream chemical biology labeling techniques of both the host and invading bacterial species.

In a typical experiment to study macrophage-bacteria interactions, macrophages are cultured on two-dimensional (2D) surfaces such as tissue culture polystyrene (TCPS). While this approach provides a well-defined environment, the material is unnaturally polarizing and has mechanical properties (Young's modulus (E) ~ 3 GPa) a million times stiffer than those of the native soft tissue of the intestines (E ~ 2–20 kPa) (Simon-Assmann et al., 1995; Rehmann and Kloxin, 2013). Seminal works have demonstrated how the function of many different cell types (e.g., stem cells, epithelial cells, cancer cells) is influenced by the dimensionality and stiffness of the culture environment (Petersen et al., 1992; Tanaka et al., 2004; Engler et al., 2006). Soft three-dimensional (3D) culture systems have been shown to be particularly effective for probing cell differentiation and migration in a physiologically relevant manner (Tibbitt and Anseth, 2009). As macrophages reside within connective tissue underneath the epithelium in the gut and respond to bacteria that breach this layer, 3D migration and interactions with the extracellular matrix (ECM) play an important role in infection clearing, suggesting the potential importance of studying macrophage response to bacterial invasion in multi-dimensional systems (Wodzanowski et al., 2020).

For studies of the gut in 3D, recent progress has been made in the development of organoids cultures, amongst other approaches (Snyder et al., 2020; Wodzanowski et al., 2020). Organoids are 3D cell clusters formed *in vitro*, with stem cells or cells derived from primary tissues, and are capable of self-organization and self-renewal, exhibiting similar function to *in vivo* organs (de Souza, 2018). However, organoids lack immune cells, in addition to requiring lengthy timescales with intensive maintenance to fully generate (e.g., 1–3 months) (Clevers, 2016; de Souza, 2018). Animal models have also provided insights in the context of inflammatory bowel disorders (IBD) by allowing study

of mucosal inflammation. However, these models can have reproducibility issues and do not sufficiently capture human IBD as they cannot accurately control for intestinal pathology, inflammation, and bacteria related to IBD (Blumberg et al., 1999; Goyal et al., 2014; Webb, 2014; Wodzanowski et al., 2020). Currently, a gap remains in physiologically-relevant, multi-dimensional systems for studying specific bacteria-immune cell interactions, where few immune cells, particularly macrophages, have been cultured in three dimensions (Sun et al., 2011; Blasioli et al., 2014; Peck et al., 2014; Samavedi et al., 2017). There is a need for robust hybrid systems with well-defined 3D properties that can be manipulated to reflect aspects of the native tissue and are suitable for co-culture of macrophages and bacteria.

Hydrogels, crosslinked water-swollen networks of hydrophilic polymers, have emerged as good candidates for mimicking a variety of soft tissue microenvironments for 3D cell culture applications. In particular, synthetic hydrogels can be engineered to mimic key properties of the native ECM, including mechanical properties and biochemical content, and permit 3D cell encapsulation and culture (Caliari and Burdick, 2016). These systems include multi-arm polymers (e.g., biologically-inert poly (ethylene glycol) (PEG)) that have been functionalized with reactive handles (e.g., (meth)acrylates, norbornenes, vinyl sulfones, thiols) for crosslinking with functionalized cell-degradable and integrin-binding peptides inspired by native tissues for a range of applications (Caliari and Burdick, 2016). Studies of macrophages with such synthetic materials often have focused on probing the foreign body response in 2D culture studies (Blakney et al., 2012; Witherel et al., 2019), given its importance in the design of implanted materials, with recent efforts demonstrating feasibility of macrophage 3D culture (Samavedi et al., 2017; Kim et al., 2019). More recently, matrix-metalloproteinase (MMP) degradable synthetic hydrogels have been utilized to encapsulate human epithelial-mesenchymal intestinal organoids for coculture studies (Jowett et al., 2021). Additionally, 3D cocultures are beginning to be developed to study bacterial infections such as the case of the oral microbiome and the lung (Montefusco-Pereira et al., 2020; Mountcastle et al., 2020). These versatile materials provide significant opportunities for creating multi-dimensional culture systems with well-defined and tunable properties for probing macrophage-bacteria interactions to test hypotheses in more physiologically-relevant environments related to the gut.

In parallel, novel methods have emerged to study the bacterial cell wall. Work has been done previously to label various aspects of PG including small fluorophores coupled to D-amino acids, NAG and NAM sugar probes, and near-infrared radiation (NIR) fluorogenic probes (Wodzanowski et al., 2020; Banahene et al., 2021). Because synthetic fragments MDP and MTP both contain the NAM sugar, it is believed that NAM plays an important structural role in fragment identification and subsequent infection clearing by macrophages. NAM probes developed have had a variety of functional groups including bioorthogonal handles, fluorescent dyes, biotin, and photoactivatable crosslinker (DeMeester et al., 2018). Of particular interest are the click handles, especially the bioorthogonal azide at the 2-acetyl position, providing versatility in what is 'clicked' onto the handle for various assays (Liang et al., 2017; DeMeester et al., 2019). Another advantage of the NAM probes is that under a lethal dose of the antibiotic fosfomycin, the first enzyme in the PG biosynthetic pathway, Mur A, can be selectively inhibited, which prevents first committed PG biosynthetic pathway steps from occurring, and cells only survive if they uptake supplemented NAM sugar provided through alternative recycling machinery if present in the cell (Kahan et al., 1974). Instrumental work by Mayer and coworkers showed that certain *Pseudomonas* species contain recycling machinery involving the enzymes anomeric NAM/NAG kinase (AmgK) and α-1-phosphate uridylyl transferase (MurU) that under a lethal dose of Fosfomycin can recycle NAM into uridine diphosphate (UDP)-NAM, which is then incorporated into mature PG (Gisin et al., 2013). Therefore, utilizing these NAM probes can allow visualization of the bacterial PG core and have potential downstream applications as an affinity handle for purifying naturally produced PG fragments from breakdown in macrophages.

In this work, we aimed to establish a well-defined, bio-inspired co-culture system that enabled encapsulation and culture of immune cells relevant to the human gut, and to study their response to invasion by Gram-negative bacteria in three dimensions. First, we utilized the biorthogonal azide NAM probe to remodel and label bacterial PG, including for the first time the pathogen *P. aeruginosa*, through copper (I) azide alkyne cycloaddition (CuAAC) and strain-promoted azide-alkyne cycloaddition (SPAAC) click reactions. Next, we developed a PEG-peptide hydrogel composition inspired by aspects of the microenvironment of the healthy gut. We established workflows for the successful encapsulation of human monocytes and their differentiation into human macrophages within these hydrogel-based synthetic matrices where cells can be facilely recovered by digestion of the hydrogel with collagenase for downstream assays. Utilizing the fluorescent bacteria, we visualized macrophage engulfment of bacteria in real time and in both 2D and 3D culture. Further, we probed macrophage cytokine expression in these systems with contrasting dimensionality, elucidating key differences in macrophage response. These studies provide new tools, such as an expansion of previous fluorescent labeling strategies of bacteria and a new 3D model system, for insights into the interactions between bacteria and immune cells and how our immune system recognizes bacteria in a variety of physiologically relevant settings.

MATERIALS AND METHODS

See supplemental information (SI) for general materials and methods.

Bacterial Labeling and Remodeling With SPAAC

Overnight pre-cultured *E. coli ΔMurQ-KU* cells (Liang et al., 2017) or *P. aeruginosa* were inoculated into fresh LB medium and were incubated until the OD_{600nm} was about 0.600. 1.2 ml of cell

suspension were collected by centrifugation at 8,000 rpm (6,000 g) for 5 min. *E. coli ΔMurQ-KU* cells were resuspended in 190 µl LB medium. 6 mM NAM sugar (NAM (Sigma-Aldrich) or AzNAM (synthesized in house based on established protocols) (Liang et al., 2017)), 1 mM isopropyl-1-thio-β-D-galactoside (*E. coli* only) and 200 µg/ml fosfomycin were added into cell samples. Cells were incubated while shaking at 37 °C for 60 min. Cells were then collected (10,000 rpm, 2 min) and washed with 2 × 600 µl 1xPBS. Cells were resuspended in 194 µl LB and then 30 µM DBCO-488 (AZDye™ 488 DBCO; Click Chemistry Tools) was added. Cells were covered and incubated at 37°C for 40 min while shaking. Cells were then collected (10,000 rpm, 2 min) and washed with 2 × 600 µl 1xPBS. Cells were fixed in 4% paraformaldehyde in PBS for 20 min. Cells were washed with 2 × 600 µl 1xPBS. Cells were washed 2 × 600 µl 1xPBS, 1 × 200 µl 1xPBS, 1 × 200 µl 1xPBS for 45 min in the dark, and 1 × 200 µl 1xPBS. The cells were resuspended in 100 µl 1xPBS. 15 µl of cells were added to pre-treated coverslips for confocal microscopy. The rest of the cells were stored at 4°C until flow cytometry analysis.

Bacterial Labeling and Remodeling With CuAAC

Bacterial remodeling and labeling was achieved based on established protocols for *E. coli* (Liang et al., 2017; DeMeester et al., 2019). Briefly, overnight pre-cultured *E. coli ΔMurQ-KU* (EQKU) cells or *P. aeruginosa* were inoculated into fresh LB medium and were incubated until the OD_{600nm} was about 0.600. 1.2 ml of cell suspension were collected by centrifugation at 8,000 rpm (6,000 g) for 5 min. Cells were resuspended in 190 µl LB medium. 6mM NAM sugar 1 or 2 (NAM, AzNAM), 1 mM isopropyl-1-thio-β-D-galactoside (*E. coli* only) and 200 µg/ml fosfomycin were added into cell samples. Cells were incubated while shaking at 37°C for 60 min. Cells were then collected (10,000 rpm, 2 min) and washed with 2 × 600 µl 1xPBS. Cells were fixed in 4% paraformaldehyde in PBS for 20 min. Cells were washed with 2 × 600 µl 1xPBS. Cells were resuspended in 190 µl PBS to prepare for the click reaction. To the bioorthogonally tagged bacterial cells was sequentially added 1 mM $CuSO_4$ solution, 140 µM BTTAA, 1.2 mM freshly prepared (+)−sodium (L) ascorbate (Sigma-Aldrich) and 20 µM of Alk488. Cells were incubated at room temperature for 30 min. Cells were washed 2 × 600 µl 1xPBS, 1 × 200 µl 1xPBS, 1 × 200 µl 1xPBS for 45 min in the dark, and 1 × 200 µl 1xPBS. The cells were resuspended in 100 µl 1xPBS and prepared for imaging.

Flow Cytometry for Bacterial Labeling

Flow cytometry was performed on ACEA Novocyte Flow Cytometer. Samples were briefly vortexed before each run. 100,000 cell counts were collected for each sample and were analyzed in triplicate, and fluorescence intensities (height) were generated and overlaid.

Growth Curve Assay With Plate Reader

Overnight pre-cultured *E. coli ΔMurQ-KU* or *P. aeruginosa* cells were inoculated into fresh LB medium (supplemented with kanamycin and chloramphenicol for *E. coli* cells only) to an OD_{600nm} of approximately 0.200. Cells were incubated at 37°C shaking for ~1 h 1 ml of cell suspension were added to new sterile Eppendorf tubes and spun at 8,000 rpm for 5 min to pellet the cells. The cells were resuspended in 190 µl of LB and supplemented with 200 µg/ml fosfomycin, 1 mM IPTG for *E. coli* cells only, and 6 mM NAM or AzNAM probe. The cells were then incubated for an additional hour to remodel. Then, the cells were pelleted to remove excess probe at 10,000 rpm for 2 min and resuspended in 100 µl of fresh LB. 100 µl of cell solution was added into each well of a white, clear bottom 96 well plate in triplicate for each probe concentration. 30 µl of DBCO-488 was added to appropriate wells. The plate was incubated at 37°C in the plate reader where it was shaken for 2 min, scanned at 600 nm, and then repeated every 20 min for 6 h (Brown et al., 2021a). Cell growth curves were formulated with Origin 2019.

Synthesis and Characterization of Norbornene-Functionalized PEG

Multi-arm (Herskovits et al., 2007) PEG (M_n ~ 40,000 g/mol) was functionalized with norbornene end groups according to established protocols (Rehmann et al., 2016; Ovadia et al., 2018). Briefly, in a 250 ml round bottom flask, PEG-8-NH_2·HCl (5 g, Jenkem) was dissolved in anhydrous *N,N*-dimethylformamide (DMF, ThermoFisher) and stirred at room temperature. In a second 250 ml round bottom flask, 5-norbornene-2-carboxylic acid (Nb-COOH) (17.6 M equivalent; 2.2 excess relative to amine groups on the PEG), 4-methylmorpholine (4-MMP) (36 M equivalent), and HATU (16 M equivalent; 2 excess) were dissolved in 10 ml of DMF stirring at room temperature. Once the individual flask components were dissolved, they were combined into one flask and stirred at room temperature overnight. The solution was then precipitated twice in cold diethyl ether (500 ml, 14x excess diethyl ether relative to DMF), and the resulting suspension was filtered with a Buchner funnel with filter paper to recover the precipitated polymer product. The solid PEG product was dried in the vacuum oven overnight. The PEG was purified by dialysis (MWCO 1000 g/mol, Spectrum Laboratories)) in mqH_20 for 48 h according to manufacturer's instructions followed by freezing and lyophilization. Product purity was confirmed by ^{1}H NMR in DMSO-d_6. Norbornene functionality was determined to be approximately 75% on average (**Supplementary Figure S13**), and PEG-8-Nb was stored at −20°C following lyophilization.

Synthesis and Characterization of Peptides

All peptides were synthesized using solid phase peptide synthesis based on established protocols (Ovadia et al., 2018). The difunctional linker peptide (GCRDVPMSMRGGDRCG) and the monofunctional pendant peptide (CGKGYIGSR) were synthesized using standard FMOC-chemistry on an automated peptide synthesizer (PS3 Peptide Synthesizer; Protein Technologies, Inc, Tucson, AZ and Liberty Blue; CEM, Matthews, NC). The peptides were built on Rink Amide MBHA resin. All amino acids were double coupled. The peptides were cleaved from the resin for 2–3 h in 95%

trifluoroacetic acid, 2.5% water, and 2.5% triisopropylsilane supplemented with 50 mg/ml dithiothreitol. Following cleavage, all peptides were precipitated in cold diethyl ether at 4°C and let air dry overnight. The peptides were purified by reverse-phase high performance liquid chromatography (HPLC; XBridge BEH C18 OBD 5 µm column; Waters, Milford, MA) with a linear 95%/5 to 5%/95% linear water-acetonitrile (ACN) gradient over 15–30 min. Purified peptides were subsequently lyophilized. Their molecular weights were verified by mass spectrometry (**Supplementary Figure S11**, **Supplementary Figure S12**), and the thiol concentration of each peptide upon reconstitution for stock solution preparation was determined using Ellman's assay. Purified peptides were dissolved in phosphate buffered saline (PBS) and stored at −80°C.

Synthesis and Rheological Characterization of Hydrogels

Monomer stocks were prepared by dissolving each component in sterile phosphate buffered saline (PBS): PEG-8-Nb (40 mM Nb functionality); lithium phenyl-2,4,6-trimethylbenxoylphospohinate (LAP) (30 mM) sterile filtered with 0.2 µM filter; and each peptide (~200 mM). PEG-8-Nb and LAP stocks were stored at −20°C, and peptide stocks were stored at −80°C.

A bulk hydrogel precursor solution was prepared using 7 mM PEG-8-Nb, 5 mM peptide crosslinker, 2 mM pendant peptide, and 2 mM LAP in PBS. Rheology measurements were conducted as previously reported (Italiani and Boraschi, 2014) on AR-G2 rheometer with UV-visible light attachment (TA instruments) in tandem with an Omnicure Series 2000 light source (Excelitas) with a 365 nm bandpass filter and light guide (Exfo). Briefly, 10 µl of hydrogel precursor solution was pipetted onto the quartz plate of the UV-vis light attachment on the rheometer with a 8 mm flat plate geometry installed, and the gap was set to 150 µm. Hydrogel crosslinking and gelation were monitored by measuring storage (G′) and loss (G") moduli at 0.5% applied strain and 2 rad/s frequency upon irradiation (10 mW/cm^2 at 365 nm). The gelation time was determined to be less than 2 min based on the change in G' being within 5% between two consecutive points (Geddes et al., 2009). Frequency sweeps at 1% strain were performed after the irradiation was complete to measure the final moduli of hydrogels formed *in situ*. All of the rheometric measurements were performed within the linear viscoelastic regime. Final equilibrium swollen moduli at physiological temperature were calculated as previously reported (Johnston, 1988; Thaiss et al., 2016) using the *in situ* measured modulus and the following equations:

$$G_{final} = G_0\left(\frac{T_{final}}{T_0}\right)\left(\frac{Q_{final}}{Q_0}\right)^{-\frac{1}{3}} \quad (1)$$

$$Q_{final} = (1-2\chi)N^{0.57}\phi^{-0.38} \quad (2)$$

where G_0 is the *in situ* measured shear modulus; T_{final} is 310 K; T_0 is 298 K; Q_0 is the initial volumetric swelling ratio of the hydrogels; χ is 0.426, the PEG–water interaction parameter; N is 304, the number of PEG repeats between crosslinks; and ϕ is the initial volume fraction of polymer. Lastly, the Young's modulus (E) was estimated by rubber elasticity theory:

$$E = 2G_{final}(1+\nu) \quad (3)$$

where ν is Poisson's ratio and is taken to be 0.5 for these incompressible, elastic PEG hydrogels.

Mammalian Cell Culture

THP-1, HEK293T, and CCL151 cells were purchased from the American Type Culture Collection (ATCC) and cultured under sterile conditions at 37°C with 5% CO_2. THP1 cells were grown in RPMI media; HEK293T cells were grown in DMEM media; and CCL151 cells were grown in F12K media. All media was supplemented with 10% FBS (Atlantic Biologicals), 2 mM L-glutamine, and 2 mM penicillin-streptomycin. THP-1 cells were stimulated with 200 nM PMA for 72 h to differentiate into macrophages (Zhang et al., 2008; Daigneault et al., 2010; Lund et al., 2016).

Cell Encapsulation

THP-1 cells were encapsulated as a single cell suspension at a density of 5 × 10^6 cells per ml in 20 µl of hydrogel precursor solution (250,000 cells/hydrogel). Precursor solution was prepared using 7 mM PEG-8-Nb, 5 mM linker peptide, 2 mM pendant peptide, 2 mM lithium phenyl-2,4,6-trimethylbenzoylphosphinate (LAP), and THP-1 cell suspension in PBS, where all concentrations noted are for the functional handle. Hydrogels were formed in 10 mm × 0.5 mm sterile gasket molds unless otherwise noted (43 µl precursor solution/mold) upon irradiation with a cytocompatible dose of long wavelength UV light (10 mW/cm^2, 365 nm, 2 min; Omnicure 2000 with light guide and collimating lens). Two replicates were formed at a time and then placed in a 24 well plate with 500 µl of RPMI media. 200 nM PMA was added to the media in each well for differentiation into macrophages. Cell-hydrogel constructs were incubated under sterile conditions at 37°C with 5% CO_2.

Live/Dead Viability Assay on Encapsulated Cells

THP-1 monocyte and macrophage cell viability following encapsulation in the hydrogels was assessed on days 1, 3, and 7 using a LIVE/DEAD® Viability/Cytotoxicity Kit (ThermoFisher Scientific). THP-1 monocytes were encapsulated as a single cell suspension at a density of 5 × 10^6 cells per ml in 20 µl of hydrogel precursor solution (250,000 cells/hydrogel). Precursor solution was prepared using 7 mM PEG-8-Nb, 5 mM linker peptide, 2 mM pendant peptide, 2 mM LAP, and THP-1 cell suspension in PBS. Hydrogels were formed in 10 mm × 0.5 mm sterile gasket molds (43 µl precursor solution/mold) upon irradiation with a cytocompatible dose of long wavelength UV light (10 mW/cm^2, 365 nm, 2 min; Omnicure 2000 with light guide and collimating lens). Two replicates were formed at a time and then placed in a 24 well plate with 500 µl of RPMI media. 200 nM TPA was added to the media in each well

for differentiation into macrophages. Cell-hydrogel constructs were incubated under sterile conditions at 37°C with 5% CO_2. Hydrogels ($n = 3$) were removed from incubator on days 1, 3, and 7, and washed 2 × 5 min with 500 µl of PBS followed by a 20-min incubation (37°C at 5% CO_2) with 500 µL of PBS containing calcein AM (2 µM) and ethidium homodimer-1 (4 µM). After staining, hydrogels were again washed (2 × 5 min with 500 µl of PBS) before imaging. Hydrogels were transferred to a chamber slide (Nunc Lab-Tek™ II Chamber Slide, Glass, 1 well) and imaged with confocal microscopy (Zeiss LSM ×800, ×10 objective at a zoom of ×0.6 and frame size of 1,024 × 1,024 for each image, 200 µm z-stack, three images per hydrogel sample). Orthogonal projections were made of each z-stack, and live (green) and dead (red) cells were counted using ImageJ.

Flow Cytometry for THP-1 Cell Differentiation

To confirm differentiation of THP-1 cells into macrophages within 3D culture, hydrogels with encapsulated THP-1 cells treated with PMA (for differentiation into macrophages) or untreated THP-1 monocytes were washed twice in 2 ml in 1xPBS for 5 min each. Hydrogels were put into 1.5 ml Eppendorf tubes (4 hydrogels per tube), and a 1 ml solution of collagenase (300 U/ml) (Sigma Aldrich) was added to degrade the hydrogel. Tubes were placed in a CO_2 incubator at 37°C. The solution was triturated every 10 min for up to 30 min until the solution could be pipetted freely. The now-digested hydrogel solution was centrifuged (150 g, 5 min) to pellet the cells. Monocytes (THP-1 cells) or macrophages (differentiated THP-1 cells) from 2D culture (1×10^6 cells) were removed from plates and similarly centrifuged in 1.5 ml Eppendorf tubes. Pelleted cell samples were washed with 2% bovine serum albumin (BSA) in PBS and resuspended in 100 µl of 2% BSA in PBS, and 5 µl of CD11 b antibody was added. Samples were placed on ice in the dark for 30 min and then centrifuged followed by washing with 2% BSA in PBS. Cells were then fixed in 4% paraformaldehyde in 1xPBS for 15 min at room temperature, centrifuged, and washed 2 × 100 µl in Intracellular Staining Permeabilization Wash Buffer (BioLegend). Cells were resuspended in 100 µl of Intracellular Staining Permeabilization Wash Buffer, and 5 µl of CD68 was added to each sample followed by incubation on ice for 30 min. Cells were washed 1 × 100 µl of Intracellular Staining Permeabilization Wash Buffer. Flow cytometry was performed on ACEA Novocyte Flow Cytometer. Samples were briefly vortexed before each run. 100,000 cell counts were collected for each sample and were analyzed in triplicate, and fluorescence intensities (height) were generated and overlaid.

DBCO Fluorophore Staining for Fixed Samples

THP-1 cells as monocytes, THP-1 cells differentiated into macrophages using PMA, and HEK293T cells were seeded onto pre-treated coverslips. Cells were fixed with 4% PFA for 10 min at room temperature, and then washed 3 × 5 min with 1x PBS. Cells were then incubated with 30 µM DBCO-488 or an equivalent volume of water as a control for 40 min at 37°C. Cells were washed 3 × 5 min with 1xPBS at room temperature on a rocker. Coverslips were mounted with mounting media with DAPI and imaged using confocal microscopy.

DBCO Fluorophore Staining for Live Samples

THP-1 cells as monocytes, THP-1 cells differentiated into macrophages using PMA, HEK cells, and CCL151 fibroblast cells were seeded onto pre-treated coverslips. Cells were then incubated with 30 µM DBCO-488 or an equivalent volume of water as a control for 40 min at 37°C. Cells were washed. Cells were fixed with 4% PFA for 10 min at room temperature, and then washed 3 × 5 min with 1x PBS. Coverslips were mounted with mounting media with DAPI and imaged using confocal microscopy.

Invasion Assay in 2D Culture for Imaging With CuAAC Bacteria

UV sterilized cover glasses (Fisher Scientific, catalogue number 12-545-80) were coated with 500 µl of 0.1 mg/ml poly-L-ornithine (Sigma-Aldrich) in 24-well plate overnight. The poly-L-ornithine was removed, and the cover glasses were washed with PBS twice. THP-1 cells were seeded on the cover glasses in 24-well plates with RPMI media (1×10^5 cells/well). THP-1 cells were differentiated into macrophages through stimulation with PMA for 3 days. Cells were then washed with RPMI media without antibiotics twice. For invasion, *E. coli ΔMurQ-KU* was grown and remodeled following the protocols above for CuAAC. 20 µl of bacterial suspension ($OD_{600nm} = 2.0$) was added to each well, and the samples were incubated at 37°C and 5% CO_2 for 30 min. After incubation, the media was removed, and fresh media with gentamycin (1:1,000) was added to kill extracellular bacteria, incubating for 30 min at 37°C and 5% CO_2. The media then was removed, and the cells were rinsed twice with 1xPBS at room temperature. Cells were fixed 4% paraformaldehyde in 1xPBS for 10 min at room temperature and rinsed twice with 1xPBS. Then, cells were permeabilized with 1% Triton-X in PBS for 10 min at room temperature and washed 3 × 5 min with 1xPBS with 0.2% Tween-20 and 1.5% BSA at room temperature on a rocker. PBS (500 µl) with 0.2% Tween-20 and 0.1% Triton-X was added to each well to prepare for the click reaction. To each well was sequentially added 1 mM $CuSO_4$ solution, 140 µM BTTAA, 1.2 mM freshly prepared (+)−sodium (L) ascorbate (Sigma-Aldrich), and 20 µM of Alk488. The click reaction was performed at room temperature for 30 min while shaking. The cells were washed 3 × 5 min with 1xPBS with 0.2% Tween-20 and 1.5% BSA at room temperature on a rocker. The cells were then stained with 1:200 Phalloidin-TRITC (F-actin stain) in 1.5% BSA in 1xPBS for 1 h at room temperature. The cells were washed 3 × 5 min with 1xPBS with 0.2% Tween and 1.5% BSA at room temperature on a rocker and then were mounted on glass slides with 4,6-diamidino-2-phenylindole (Invitrogen) for super resolution imaging.

Invasion Assay in 2D Culture for Imaging With SPAAC Bacteria

Sterile cover glasses (Fisher Scientific, catalogue number 12-545-80) were coated with 500 µl of 0.1 mg/ml poly-L-ornithine (Sigma-Aldrich) in 24-well plate overnight. The poly-L-ornithine was removed, and the cover glasses were washed with PBS twice. THP-1 cells were seeded on the cover glasses in 24-well plates with RPMI media (1×10^5 cells/well). THP-1 cells were differentiated into macrophages through stimulation with PMA for 3 days. Cells were then washed with RPMI media without antibiotics twice. For invasion, *E. coli ΔMurQ-KU* was grown and remodeled following the protocols above for SPAAC. Following remodeling and labeling with DBCO-488, 20 µl of bacteria (OD_{600nm} = 2.0) was added to each well, and the samples were incubated at 37°C and 5% CO_2 for 30 min. After incubation, the media was removed, and fresh media with gentamycin (1:1,000) was added to kill extracellular bacteria, incubated for 30 min at 37°C and 5% CO_2. The media then was removed, and the cells were rinsed twice with 1xPBS at room temperature. Cells were fixed 4% paraformaldehyde in 1xPBS for 10 min at room temperature and rinsed twice with 1xPBS. Then, cells were permeabilized with 1% Triton-X in PBS for 10 min at room temperature and washed 3 × 5 min with 1xPBS with 0.2% Tween-20 and 1.5% BSA at room temperature on a rocker. The cells were then stained with 1:200 Phalloidin-TRITC (F-actin stain) in 1.5% BSA in 1xPBS for 1 h at room temperature. The cells were washed 3 × 5 min with 1xPBS with 0.2% Tween and 1.5% BSA at room temperature on a rocker and then were mounted on glass slides with 4,6-diamidino-2-phenylindole (Invitrogen) for confocal microscopy imaging.

Invasion Assay in 3D Culture for Imaging With CuAAC Bacteria

THP-1 cells were encapsulated with an adapted version of the protocol described above. Here, cells suspended in hydrogel precursor solution were prepared as before, and then 20 µl of hydrogel precursor solution was pipetted onto a 1 ml syringe mold (instead of a gasket mold) resulting in 100,000 cells per hydrogel. Hydrogels were formed by photopolymerization and placed into 24-well plates for 3D cell culture and differentiation with PMA for 3 days as before. Samples were then washed with RPMI media without antibiotics twice. For invasion, 20 µl of *E. coli ΔMurQ-KU* (OD_{600nm} = 2.0), grown and remodeled as noted above for the CuAAC protocol, was added to each well for 60 min, and the samples were incubated at 37°C and 5% CO_2. After incubation, the media was removed, and fresh media with gentamycin (1:1,000) was added to kill extracellular bacteria for 60 min at 37°C and 5% CO_2. After 60 min, the media was removed, and the cells were rinsed twice with 1 x PBS at room temperature. Cells were fixed 4% paraformaldehyde in 1xPBS for 15 min at room temperature. Fixed cells were rinsed 3 × 5 min with 1xPBS, and were permeabilized with 1% Triton-X in PBS for 30 min at room temperature. Cells were washed 3 × 5 min with 1xPBS with 0.2% Tween-20 and 1.5% BSA at room temperature on a rocker. PBS (500 µl) with 0.2% Tween-20 and 0.1% Triton-X was added to each well to prepare for the click reaction. To each well was sequentially added 1 mM $CuSO_4$ solution, 128 µM Tris [(1-benzyl-1H-1,2,3-triazol-4-yl)methyl] amine, 1.2 mM freshly prepared (+)−sodium (L) ascorbate (Sigma-Aldrich), and 20 µM of Alk488. The click reaction was performed at room temperature for 1 h while shaking. The cells were washed 2 × 30 min with 1xPBS with 0.2% Tween-20 and 1.5% BSA at room temperature on a rocker. The cells were washed overnight in 1xPBS with 0.2% Tween-20 and 1.5% BSA at 4°C. The next day, the cells were washed 2 × 30 min with 1xPBS with 0.2% tween-20 and 1.5% BSA at room temperature on a rocker. Cells were stained with 4,6-diamidino-2-phenylindole (DAPI) for 30 min and were washed 3 × 10 min with 0.2% Tween-20 and 1.5% BSA at room temperature on a rocker. Hydrogels were moved to glass chamber well slides for confocal imaging.

Invasion Assay in 3D Culture for Imaging With SPAAC Bacteria

THP-1 cells were encapsulated as described above. Hydrogels were formed by photopolymerization and placed into 24-well plates for 3D cell culture and differentiation with PMA for 3 days as before. Samples were then washed with RPMI media without antibiotics twice. For invasion, 20 µl of *E. coli ΔMurQ-KU* (OD_{600nm} = 2.0), grown and remodeled as noted above with the SPAAC protocol, was added to each well for 60 min, and the samples were incubated at 37°C and 5% CO_2. After incubation, the media was removed, and fresh media with gentamycin (1:1,000) was added to kill extracellular bacteria for 60 min at 37°C and 5% CO_2. After 60 min, the media was removed, and the cells were rinsed twice with 1xPBS at room temperature. Cells were fixed 4% paraformaldehyde in 1xPBS for 15 min at room temperature. Fixed cells were rinsed 3 × 5 min with 1xPBS, and were permeabilized with 1% Triton-X in PBS for 30 min at room temperature. Cells were washed 3 × 5 min with 1xPBS with 0.2% tween-20 and 1.5% BSA at room temperature on a rocker Cells were stained with DAPI for 30 min and were washed 3 × 10 min with 0.2% Tween-20 and 1.5% BSA at room temperature on a rocker. Hydrogels were moved to glass chamber well slides for confocal imaging.

Live Cell Imaging

THP-1 cells were seeded into 8-well chamber slides and treated with 20 nM PMA to differentiate for 3 days. Media was replaced to RPMI without antibiotics. Cells were then incubated with Cell Mask Orange for 15 min. The media was changed and SPAAC labeled bacteria (see Bacterial Labeling and Remodeling) with strain promoted azide-alkyne cycloaddition (SPAAC) was added to the appropriate wells. The cells were imaged using the Andor Dragonfly 505 spinning disk confocal microscope with a Plan-Apochromat 63x/1.47 oil objective to visualize the engulfment of bacteria cells in real time. Excitation of labeled bacteria and Cell Mask Orange was achieved with a 637 nm laser at 2% power and a 561 nm laser at 0.2% power. 3D volumes were acquired every 1 min for 2 min.

Confocal Microscopy for 2D Samples

P. aeruginosa images and 2D invasion images were taken on a Zeiss LSM 800 microscope with Plan-Apochromat 63x/1.4 Oil differential interference contrast (DIC) M27 objective. Excitation of DBCO-488 was achieved with 488 nm, 2% laser excitations. Excitation of phalloidin-TRITC was achieved with 562 nm, 0.2% laser excitations. Excitation of DAPI was achieved with 405 nm, 1% laser excitation. Scan mode was frame and bidirectional. Program Carl Zeiss ZEN 2012 was used to process the raw data to construct the images. Processing and filtering settings were kept constant and image intensity was preserved with the raw image scale option in Zen 2012. Two-dimensional (2D) images were generated. Scale bars were made with the line measurement tool function.

Structured Illumination Microscopy (SIM) for 2D Samples

Bacterial labeling of EQKU cells was imaged on a Zeiss Elyra PS.1 microscope with Plan-Apochromat 63x/1.4 oil differential interference contrast (DIC) M27 objective. Excitation of Alk488 was achieved with 488 nm laser excitation, and the camera exposure time was set to 100.0 ms. The raw data contained five rotations with 0.110 µm z-stack interval. Images were processed in Carl Zeiss ZEN 2012 to construct SIM images. Processing and filtering settings were kept constant and image intensity was preserved using the raw image scale option. Two-dimensional (2D) SIM images and 2D maximum intensity projection images were generated.

Confocal Microscopy Imaging for 3D Samples

3D culture samples were imaged with confocal microscopy. Images were taken on Zeiss LSM800 with Plan-Apochromat 63X/1.40 Oil DIC M27 objective and frame size of 1,024 × 1,024 pixels. Z-stacks were 200 µm with 0.2 µm slices. Excitation of 4,6-diamidino-2-phenylindole and Alk488 was achieved with 405 and 488 nm lasers, respectively. Pixel, line, and frame time were 1.03 µs, 4.95 ms, and 5.06 s, respectively. Scan direction was bidirectional, and an average of four scans per image was utilized. ZEN 2012 (Zeiss) was used to process the images and prepare z-stack projections.

ELISA Preparation

Three days before stimulation with bacteria, macrophage samples were seeded and encapsulated for 2D and 3D culture, respectively. For 2D culture, cells were seeded at 1×10^6 cells per well in a 6 well plate. For 3D culture, hydrogels were formed in gasket molds as described above, and four hydrogels (250,000 cells per hydrogel) were placed per well in a 6 well plate (total of 1×10^6 cells per well). All cells were differentiated for 3 days with 200 nM PMA. The cells were washed twice with RPMI media without antibiotics. Cells were provided RPMI media without antibiotics after the washes. The day of the stimulation with bacteria, bacterial overnights were diluted to OD = 2.0, and 20 µl; of these bacteria was added to each well. To the control samples, 20 µl of sterile water was added. Plates were incubated for 4 h in an incubator (37°C, 5% CO_2). After 4 h, the supernatant was removed, and it was stored at −20°C until shipment (1 ml total volume per sample) to University of Maryland Cytokine Core for analysis by ELISA.

RESULTS AND DISCUSSION

Bacterial Remodeling and Labeling Utilizing CuAAC and SPAAC

A previously engineered strain of *E. coli*, *E. coli ΔMurQ KU* (EQKU) that expresses recycling enzymes AmgK and MurU was used to specifically label the NAM residue of PG (Liang et al., 2017). Through remodeling with the 2-azido *N*-acetyl muramic acid sugar (AzNAM), we observed fluorescent labeling specifically to the cell wall of the EQKU PG following the copper catalyzed azide-alkyne cycloaddition (CuAAC) click reaction to install an alkyne fluorophore (Alk488) which matches previously reported data from our lab (**Figure 2**).

As the *Pseudomonas* family naturally express AmgK and MurU, we sought to expand our CuAAC labeling methodology beyond EQKU into the pathogenic species *Pseudomonas aeruginosa,* an opportunistic, pathogenic species of bacteria that is known to break through mucosal barriers particularly in hospital infections and is extremely antibiotic resistant (Lister et al., 2009). Previous work has shown success in applying this CuAAC methodology to *P. putida*, *B. subtilis*, and *H. pylori* (Liang et al., 2017; Taylor et al., 2020; Taylor et al., 2021). Once again utilizing the AzNAM probe and a lethal dose of the cell wall targeting antibiotic, fosfomycin, the first steps of PG biosynthesis are inhibited and we observed incorporation of the AzANM probe using AmgK and MurU recycling enzymes into the *P. aeruginosa* cell wall as confirmed by fluorescent microscopy following CuAAC click reaction (**Figure 2**).

Although the CuAAC click reaction allows for the visualization of the cell wall, reaction requires the cells to be fixed due to the toxic nature of copper to cells, eliminating the ability of tracking the bacteria in real time to get engulfed by macrophages. Therefore, we explored another bioorthogonal reaction called the strain promoted azide-alkyne cycloaddition (SPAAC) that does not require a cytotoxic catalyst, allowing for the possibility of live cell imaging (Baskin et al., 2007). Some applications of SPAAC include labeling proteins, lipids, glycans on mammalian cells (Neef and Schultz, 2009; Nikić et al., 2015; Debets et al., 2020), in living animals such as mice (Chang et al., 2010), ribonucleic acid (RNA) (Wang et al., 2020), and more recently, on bacteria using penicillin binding proteins (Brown et al., 2021b). Since we previously remodeled both *E. coli* and *P. aeruginosa* with AzNAM, we utilized a dibenzocyclooctyne (DBCO) 488 dye as our strained alkyne. Through a detailed study of DBCO concentrations and click reaction times, we determined that 40 min at 37°C with 30 µM DBCO-488 was sufficient to label the cell wall in *E. coli* for microscopy (**Figure 2**, **Supplementary Figure S1**), demonstrating that the DBCO dye can cross the outer membrane of the bacterial cell. Flow cytometry revealed that a concentration higher than 30 µM DBCO leads to a secondary population of unlabeled cells in *E. coli*. Interestingly, the SPAAC reaction on AzNAM remodeled *P.*

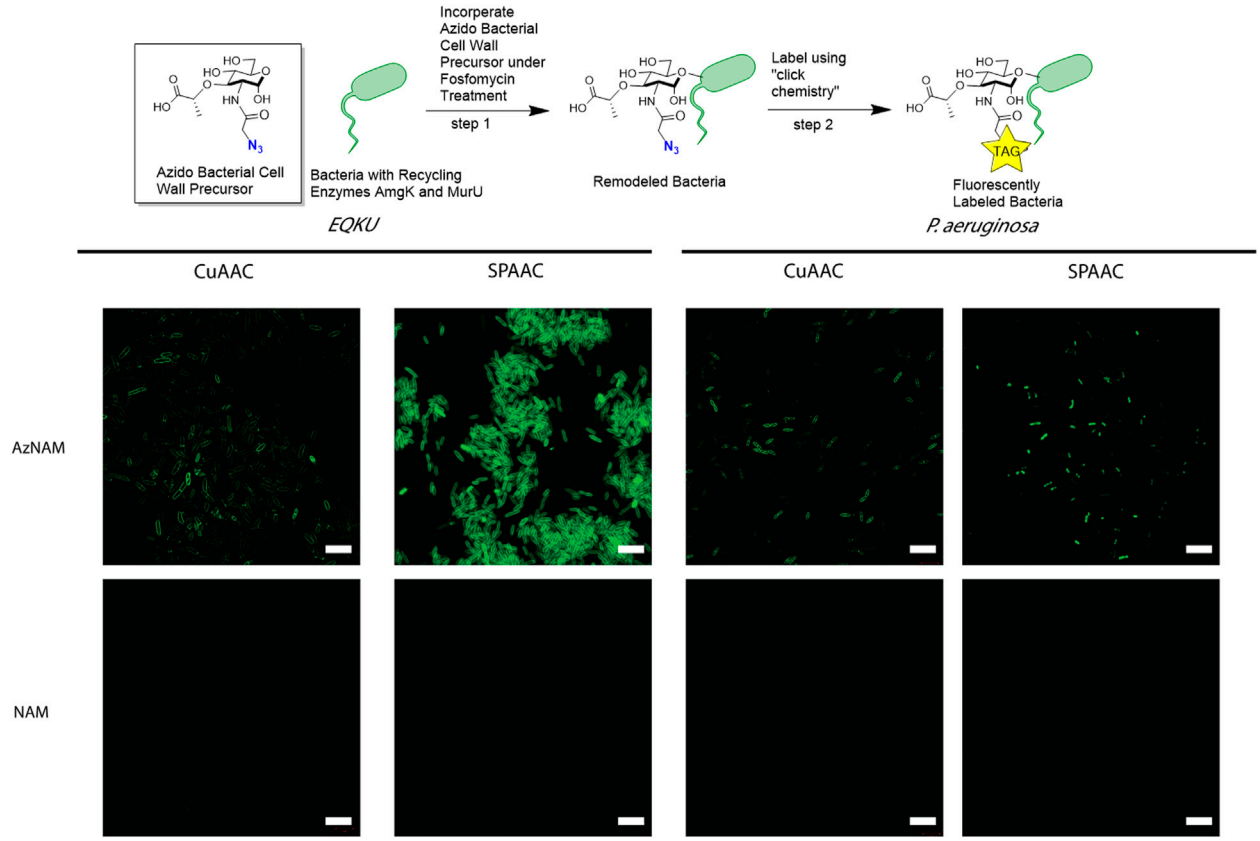

FIGURE 2 | Labeling of Gram-negative bacteria utilizing CuAAC and SPAAC chemistries. *E. coli ΔMurQ KU* (EQKU) and *P. aeruginosa* cells are remodeled by incorporating the azido bacterial cell wall precursor (AzNAM) in the cell wall with recycling enzymes AmgK and MurU. Bacteria are then fluorescently labeled using CuAAC or SPAAC to install a terminal alkyne (CuAAC) or strained alkyne (SPAAC) fluorophores. NAM cells do not have the azide handle and therefore do not react with the fluorophores, leading to no fluorescence. CuAAC images were taken using super resolution microscopy (SIM) and SPAAC images were taken using confocal microscopy. Images are representative of a minimum of three fields viewed per replicate with at least two technical replicates, and experiments were conducted in at least three biological replicates. Scale bars = 10 μM.

aeruginosa appeared to be located predominantly in the poles and leads to a shorter cell length than CuAAC labeled *P. aeruginosa* (**Figure 2**). A plate reader growth curve assay was utilized to observe how growth rates of species were different following the click reaction on the living cells and found that both cell type's growth rates were unaffected by the chemistry occurring on the cell wall (**Supplementary Figure S2**, **Figure 3**). We hypothesize that differences in cell wall architecture between the two species lead to the modification being more permittable in *E. coli* and is causing the probe to get stuck in the poles of the *P. aeruginosa* cells. With the CuAAC and SPAAC reactions working well in *E. coli*, we proceeded with this specific species to visualize engulfment by macrophages in both 2D and 3D invasion models.

Development of 3D Synthetic Matrix for Macrophage Culture

To fabricate a 3D synthetic matrix with tunable properties in the range of those of the healthy gut, we utilized an 8-arm PEG functionalized with norbornene end groups (PEG-8-Nb) linked with a matrix metalloproteinase (MMP) - degradable sequence (GCRDVPMS↓MRGGDRCG) (Ovadia et al., 2018) that is responsive to MMP-2 amongst other enzymes secreted by monocytes and macrophages (Ahmad et al., 2019; Chellat et al., 2005). Additionally, these hydrogels were modified with the integrin binding peptide CGKGYIGSR, derived from the laminin β_1 chain, to promote cell adhesion inspired by the laminin-rich ECM of the basement membrane of the gut (Smithmyer et al., 2014; Yamada et al., 2011; Rezakhani et al., 2021). The hydrogels were formed rapidly through light-triggered thiol-ene click chemistry *via* a step growth mechanism, as the norbornene groups on the PEG are coupled to the thiols presented by the cysteines in the difunctional MMP-degradable linker peptide and monofunctional integrin binding peptide (**Figures 3A,B**) (Fairbanks et al., 2009). The reaction was initiated using the photoinitiator lithium phenyl-2,4,6-trimethylbenzoylphosphinate (LAP) and low, cytocompatible doses of light (10 mW/cm^2 at 365 nm for 2 min). These

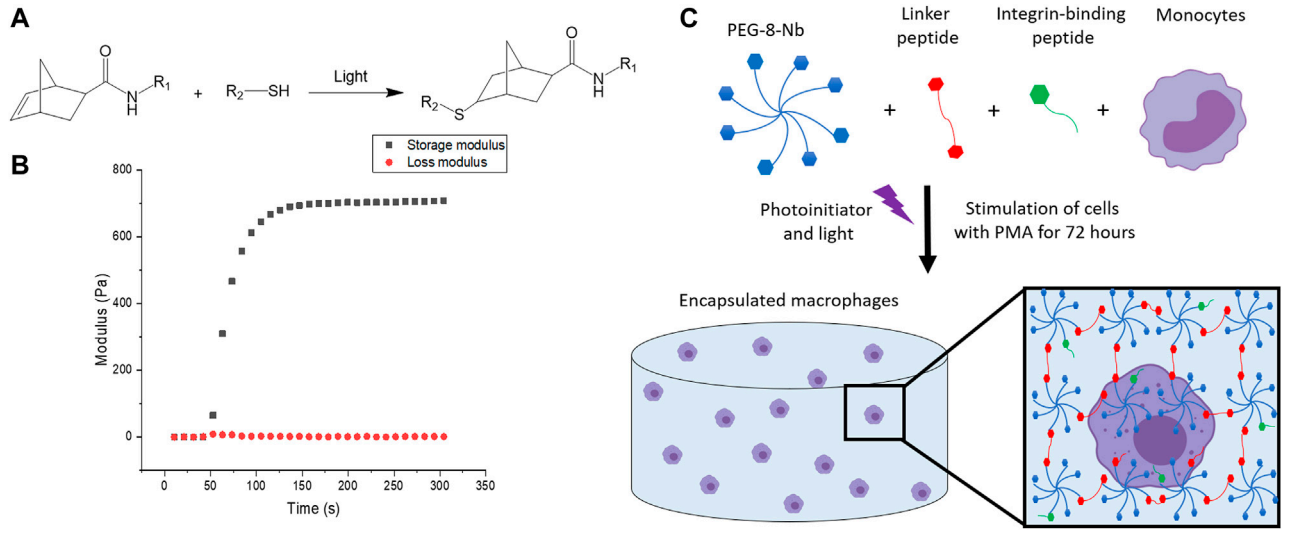

FIGURE 3 | Overview of hydrogel design. **(A)** Hydrogels were formed using thiol-ene click chemistry with norbornenes on the PEG and thiols on the difunctional linker and monofunctional integrin binding peptides. **(B)** Hydrogels are rapidly formed upon the application of light. The increase in storage modulus, monitored with *in situ* rheometry, indicates crosslinking events, and complete hydrogel formation was observed within 2 min. This final modulus, converted to Young's modulus by rubber elasticity theory for ease of comparison to native tissues, is relevant for mimicking the modulus or "stiffness" of the healthy gut. **(C)** The hydrogel network is composed of 8-arm PEG-norbornene (blue), thiol-containing linker peptide (red), and thiol-containing integrin binding peptide (green). Components were photo-polymerized with a low, cytocompatible dose of light (10 mW/cm^2 at 365 nm for 2 min) to form a hydrogel, and the monocyte cells in the hydrogel subsequently were differentiated into macrophages through stimulation with PMA for 72 h. Schematic not to scale.

synthetic bioinspired hydrogels were designed with a Young's modulus (E ~ 2.6 ± 0.8 kPa) to mimic the "stiffness" of the healthy gut (Johnson et al., 2013), as confirmed by shear rheometry (**Figure 3C**).

This type of PEG-peptide hydrogel, formed by a photoinitiated thiol-ene step growth polymerization under similar conditions (10 mW/cm^2 at 365 nm for < 10 min), has been used previously to culture a wide variety of cell types, including human mesenchymal stem cells, induced pluripotent stem cells, and breast cancer cells (Tibbitt and Anseth, 2009; Caliari and Burdick, 2016; Ovadia et al., 2018; Gerecht et al., 2007; Benoit et al., 2008). However, as the mechanism of hydrogel polymerization involves free-radicals, the viability of sensitive cell types can be impacted during cell encapsulation and hydrogel formation (Caliari and Burdick, 2016; Ovadia et al., 2018; Macdougall et al., 2018). Accordingly, we examined cell viability upon encapsulation and during 3D cell culture within these materials. Here, THP-1 cells were selected as a human monocytic cell line that are commonly differentiated into macrophage cells, as human primary tissue macrophages cannot be readily expanded *ex vivo* (Daigneault et al., 2010). We first differentiated monocytes into macrophages on TCPS and subsequently encapsulated these cells. We observed low viability in the hydrogels (**Supplementary Figure S4**). Therefore, we examined encapsulating monocytes and then differentiating them into macrophages within the matrix, which also mimics aspects of the natural process of monocyte arrival and differentiation into macrophages within the native gut. Importantly, monocytes were successfully encapsulated within the hydrogels and exhibited high viability throughout 3D culture (**Figure 4A**, **Supplementary Figure S5**). Based on observations from prior studies with other human cell types, we speculate that the cytotoxic effects of hydrogel formation on macrophages were related to their sensitivity to free radical exposure (Caliari and Burdick, 2016; Macdougall et al., 2018; Ovadia et al., 2018); opportunities for future investigations include examination of the specific cause(s) of macrophage death in this system and related approaches for rescuing human macrophage cell viability (e.g., inclusion of different ligands for promoting cell health (Ovadia et al., 2018), examination of different photoinitiators or irradiation wavelengths (Bryant et al., 2000; Williams et al., 2005; Zeng et al., 2021), or use of a different hydrogel formation mechanism (Macdougall et al., 2018). For the purpose of our studies here, focused on probing bacterial cell-macrophage interactions, the system established functioned well for maintaining monocyte viability and allowing their differentiation into macrophages during 3D culture, which has broad utility for probing not only macrophage-bacteria interactions but also monocyte-bacteria interactions in future studies.

After confirmation of successful culture of THP-1 monocyte cells, monocytes were differentiated into macrophage cells through stimulation with phorbol 12-myristate 13-acetate (PMA) over 3 days based on literature precedent in two dimensions (Zhang et al., 2008; Daigneault et al., 2010; Lund et al., 2016). To probe differentiation, the hydrogels were digested using collagenase and centrifuged to isolate the cells from the materials to study changes in their extracellular and intracellular macrophage markers. Through subsequent staining and flow cytometry, differentiation was confirmed for the recovered

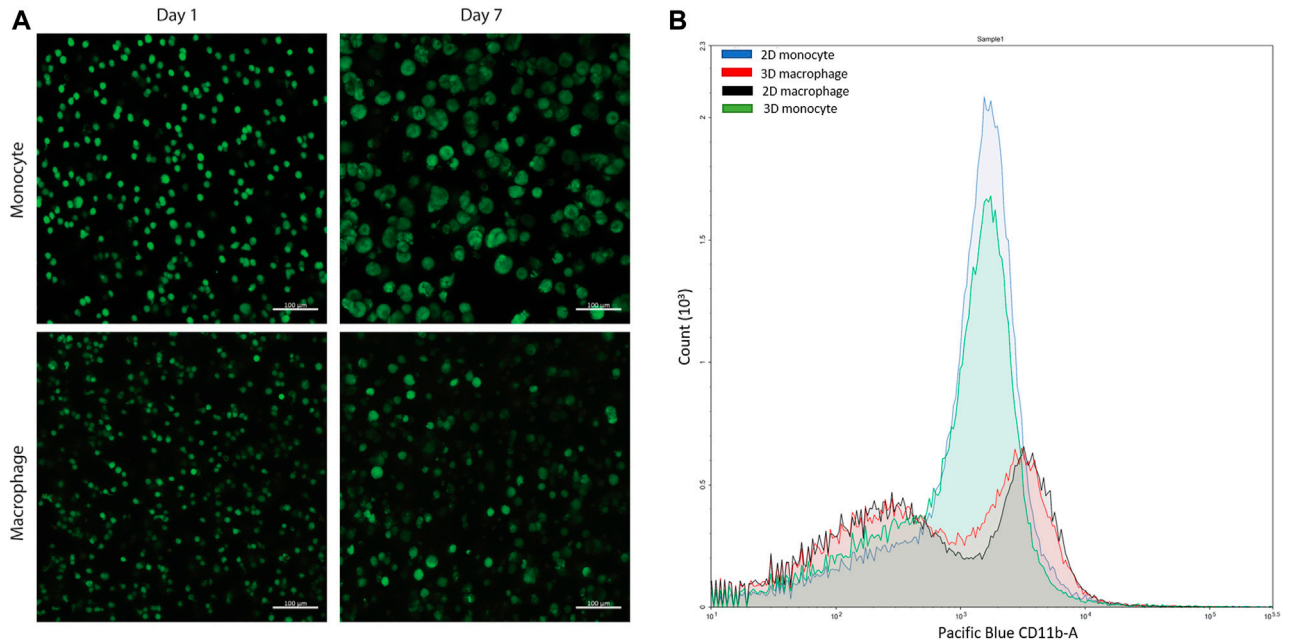

FIGURE 4 | Confirmation of cell viability and cell differentiation in 3D culture. **(A)** Live/dead cytotoxicity results of THP-1 cells (monocytes) and THP-1 cells differentiated with PMA (macrophages) in PEG-peptide hydrogels. Confocal images are representative of a minimum of three fields per view per hydrogel of three biological replicates. **(B)** Flow cytometry data of macrophages and monocytes in 2D or 3D culture stained for extracellular macrophage marker CD11 b. 2D (blue) and 3D monocyte (green) profiles match each other, and 2D (red) and 3D (black) macrophage profiles match each other, showing differentiation is achieved in the 3D hydrogel. Plot is representative of three biological replicates and two technical replicates.

cells using macrophage extracellular and intracellular markers, CD11 b and CD68, respectively (**Figure 4B**, **Supplementary Figure S6**). This hydrogel digestion method can be applied to isolate a wide variety of 3D cultured mammalian cells for downstream flow cytometry analysis. Further, these macrophages also exhibited high viability in the hydrogels (**Figure 4A**, **Supplementary Figure S5**).

Invasion of Fluorescent Bacteria Into Macrophages in 2D and 3D Culture

With the ability to fluorescently label *E. coli* with CuAAC and SPAAC, macrophages were invaded with bacteria on 2D culture on TCPS and into 3D cultures within synthetic hydrogels. For the CuAAC click reactions, EQKU were remodeled with AzNAM and subsequently invaded into macrophages, followed by fixation and the CuAAC reaction. After invasion for 1 h, we observed engulfment of the bacteria by the macrophages in both 2D and 3D culture (**Figure 5**), indicating that this system will have utility in identifying naturally released bacterial peptidoglycan fragments. We also noted that the bacteria in 3D culture invasion assay appeared to be more similar in size to the expected biologically-relevant lengths of 1–2 µm, whereas bacteria were larger in 2D invasion (Ei-Hajj and Newman, 2015). Overall, these observations suggest that the dimensionality of the culture system affects rate of bacterial breakdown to smaller fragments and bacterial growth independently of macrophages in these types of 3D materials. We also remodeled *E. coli* and labeled with SPAAC prior to invasion into macrophages. Following fixation and staining, we can observe EQKU within the macrophages in 2D and 3D culture (**Figure 5**). This pre-labeling method of the bacteria with SPAAC is also advantageous as it allows us to visualize the engulfment in real time. Within 5 minutes in live samples, we can observe engulfment of EQKU by macrophages in 2D culture (**Figure 5**, **Supplementary Videos S1, S2**).

Next, we wanted to determine if remodeled EQKU can be invaded into macrophages and a subsequent SPAAC click chemistry can be performed once the bacteria are already inside of the cell; this would mimic the CuAAC labeling method. Following the engulfment of the bacterial cells, the macrophage cells were fixed and then treated the cells with DBCO-488 to label the bacteria in the system. The confocal microscopy images revealed the labeled of EQKU cells but also significant, non-specific binding of the fluorophore to the cells (**Supplementary Figure S7**) despite rigorous washing steps. To determine the cause of the background dye labeling, macrophage cells were treated as well as monocytes (undifferentiated THP-1 cells) and HEK293T cells with 30 µM DBCO-488 after fixing the cells. We determined that the utilization of a fixative agent causes the DBCO dye to nonspecifically bind to the macrophage cells as well as THP-1 monocyte cells and HEK293T cells; this behavior has been observed in the literature (**Supplementary Figure S8**) (Loebel et al., 2019). Interestingly, when treating live cells with the DBCO dye prior to fixation, only the macrophage cells continue to have nonspecific binding while THP1 monocyte cells, HEK293T, and CCL151 fibroblast cells do not nonspecifically

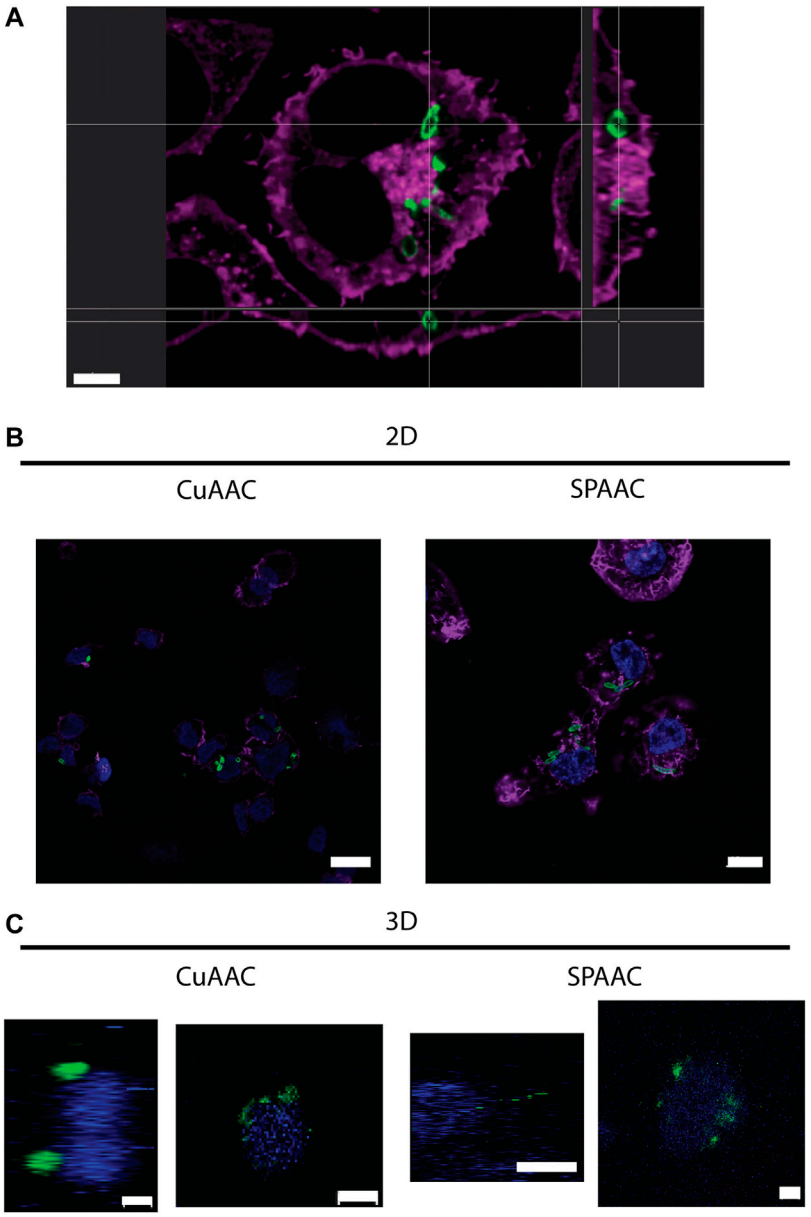

FIGURE 5 | THP-1 macrophage cells invaded by remodeled *E. coli ΔMurQ KU* in 2D and 3D culture. *E. coli ΔMurQ KU* (EQKU) cells are remodeled by incorporating the azido bacterial cell wall precursor in the cell wall with recycling enzymes AmgK and MurU. **(A)** EQKU cells labeled with DBCO-488 using SPAAC were invaded into macrophage cells and observed with Andor Dragonfly microscope. Bacteria (green) can be visualized within macrophages (purple) as shown by ortho view above. Scale bar = 5 μm **(B,C)** The CuAAC condition bacteria were invaded into THP-1 macrophage cells and fixed prior to the CuAAC click labeling (bacteria, green) and subsequent staining with Hoechst (nucleus, blue). The SPAAC condition bacteria were remodeled with the DBCO-488 (bacteria, green) and then invaded into the THP-1 cells. The cells were then fixed and stained with Hoechst (nucleus, blue). The 2D samples **(B)** were also stained with Phalloidin-TRITC (F-actin, purple). Images were taken on a Zeiss LSM800 Confocal Microscope with single plain snaps for 2D images and ortho-projections (XYZ) of Z-stacks of the cells in the synthetic hydrogels. Images are representative of a minimum of three fields viewed per replicate with at least two technical replicates, and experiments were conducted in at least three biological replicates. **(B)** Scale bars = 10 μm **(C)** Scale bars = 5 μm.

label (**Supplementary Figure S9**). We suggest that this is due to the phagocytic and pinocytotic nature of macrophage cells to continuously sense their local environment for possible pathogens. We caution those culturing macrophages to find alternatives to DBCO dyes for fixed SPAAC staining.

Cytokine Screen From Macrophages Following Bacterial Invasion in 2D and 3D

Following successful invasion of macrophages in both 2D and 3D culture, we aimed to probe potential differences in cytokine expression as a measure of macrophage activation upon

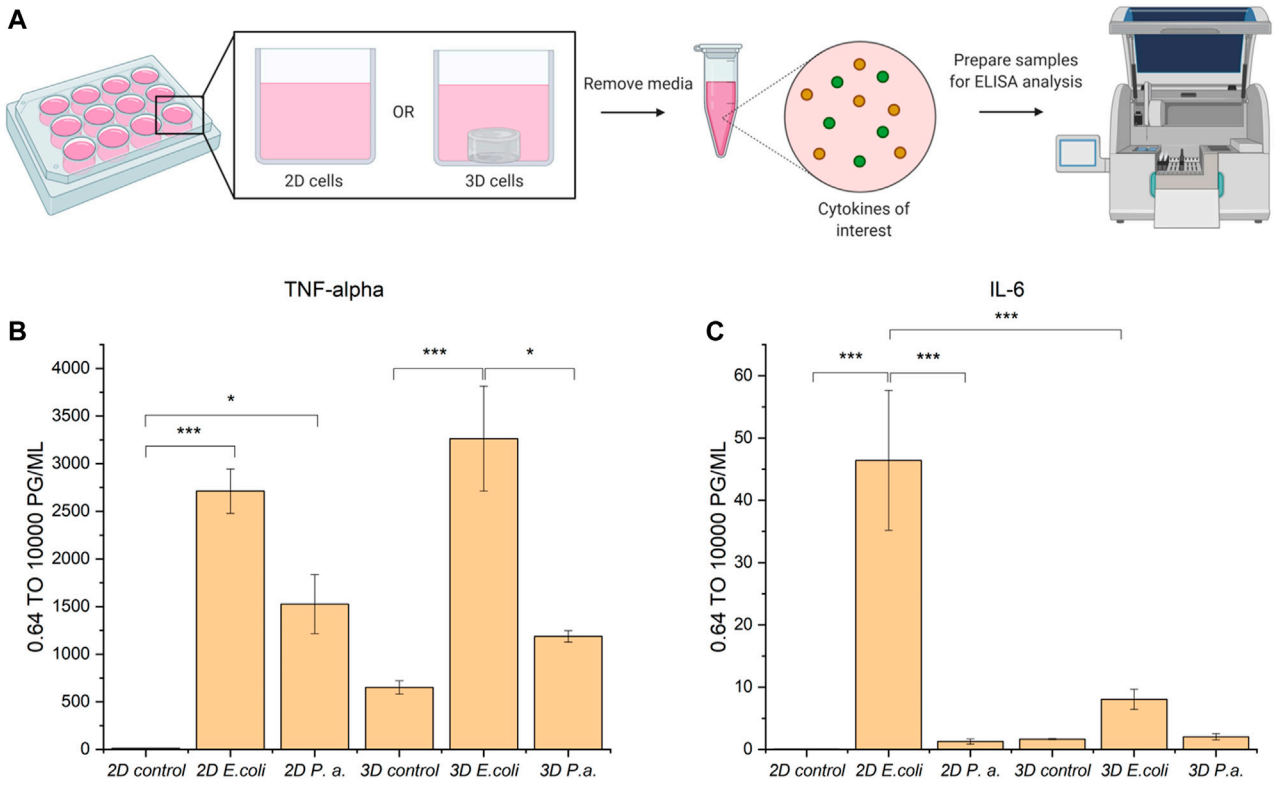

FIGURE 6 | ELISA analysis of TNF-α and IL-6 cytokine production by THP-1 macrophage cells in 2D and 3D culture upon invasion with *E. coli* or *P. aeruginosa*. **(A)** Macrophage cells in 2D or 3D culture were stimulated with bacteria or water for 4 h. Cell culture supernatant was harvested and subjected to ELISA analysis for TNF-alpha and IL-6 cytokines. **(B)** ELISA analysis of TNF-alpha shows cells stimulated with *E. coli* or *P. aeruginosa* exhibited increased secretion of TNF-alpha as compared to the control. **(C)** ELISA analysis of IL-6 shows cells stimulated with *E. coli* in 2D exhibited increased secretion of IL-6 as compared to in 3D culture and the controls. Macrophages in 2D and 3D culture when stimulated with *P. aeruginosa* did not exhibit increased secretion of IL-6 as compared to the control. All samples were analyzed in biological triplicate and technical duplicate and statistically analyzed by ANOVA with Tukey's test (*$p < 0.05$, **$p < 0.01$, ***$p < 0.001$).

invasion, which may be influenced by the dimensionality and complexity of the culture system. Here, we utilized EQKU and *P. aeruginosa,* both unmodified. To assess macrophage response, we examined secretion of cytokines associated with different aspects of macrophage activation. Specifically, an enzyme-linked immunosorbent assay (ELISA) was implemented to observe cytokine output of tumor necrosis factor alpha (TNF-α) and interleukin 6 (IL-6) of cells treated with *E. coli*, *P. aeruginosa*, or no bacteria. TNF-α is a cytokine involved in systemic inflammation and regulates immune cells, induces fever, inhibits viral replication, and induces apoptosis. Dysregulation of TNF-α is implicated in various diseases including IBD. IL-6 is a cytokine involved in stem cell differentiation, antibody synthesis by B cells, and T cell cytotoxicity (Sanceau et al., 1991). IL-6 is produced in response to bacterial and viral infections, and work has shown that dysregulation of IL-6 can be involved in autoimmune disease pathogenesis (Sanceau et al., 1991).

When macrophages were invaded with either *E. coli* or *P. aeruginosa*, an increase in TNF-α expression was observed, which accurately represents known responses that THP-1 macrophages have to lipopolysaccharide (LPS) located on Gram-negative bacteria (**Figure 6**) (Zhang et al., 2008; Schildberger et al., 2013). Further, THP-1 macrophage cells from 2D plates treated with *E. coli* showed statistically significant increased expression of IL-6 as compared to untreated cells and cells treated with *P. aeruginosa*. Notably, THP-1 macrophage cells treated with *E. coli* in 3D culture did not show statistically different expression of IL-6 compared to the control and *P. aeruginosa* samples (**Figure 6**). These data suggest that the 3D invasion model produced a more biologically relevant response of IL-6 to the various bacterial species, as literature precedent shows THP-1 macrophages treated with LPS are known to have little IL-6 response (Schildberger et al., 2013).

CONCLUSION

Overall, we have established a well-defined hydrogel-based system for the 3D culture of monocytes and macrophages in an environment that mimics aspects of the basement membrane of the gut, and a multi-dimensional invasion assay for probing macrophage response to invading bacterial species. The multiscale system allows the integration of probes within the bacterial cell wall at the molecular level, control of bacterial-host interactions at the cellular level, and mimicry of aspects of the ECM

dimensionality, biochemical content, and biophysical properties at the multi-cellular to tissue level initially and over time. This molecularly engineered system is reproducible, robust, and based on the underlying design of the synthetic matrix, provides future opportunities for not only probing the impacts of host-bacterial cell interactions, but also cell-matrix interactions through manipulation of extracellular biochemical and mechanical cues. The system is amenable to bioorthogonal chemistry on bacterial peptidoglycan within the hydrogel and opens the door for further applications in chemical biology involving labeling and study of the bacterial cell wall. This model system can be easily tailored for studying cell-cell and cell-matrix interactions in disease progression and for asking new questions beyond traditional 2D culturing methods that prevail in the field. The use of the NAM probes with the azide bioorthogonal handle embedded in the bacterial peptidoglycan allows for multiple click chemistry to take place, including CuAAC and SPAAC, and will provide opportunities to enrich for biologically produced bacterial cell wall fragments from these invasion systems for further analysis. These studies provide new insights into the interactions between bacteria and immune cells, and this new chemical biology model system provides a platform to examine how our immune system recognizes bacteria in a variety of physiologically relevant settings, including pathogen invasion and homeostatic maintenance.

DATA AVAILABILITY STATEMENT

The raw data supporting the conclusion of this article will be made available by the authors, without undue reservation.

AUTHOR CONTRIBUTIONS

KW, AK, and CG designed experiments. KW conducted experiments with assistance from JC for live cell imaging studies. KW, JC, AK, and CG analyzed data, prepared figures, and wrote and edited the manuscript. AK and CG supervised the studies.

FUNDING

We are thankful for support from the Delaware COBRE program, supported by a grant from the National Institute of General Medical Sciences (NIGMS 1 P30 GM110758 and 1 P20 GM104316-01A1). Microscopy access was supported by the Delaware INBRE program, with a grant from NIGMS (P20 GM103446) and the State of Delaware. This research was supported by grants for related work from the NIH U01 Common Fund program with grant number U01CA221230-01 (CG) and the NIH Director's New Innovator Award with grant number DP2HL152424 (AK). KW would also like to thank the NIH for support through Chemistry-Biology Interface (CBI) training grant, T32GM133395. The authors acknowledge the use of facilities and instrumentation supported by NSF through the University of Delaware Materials Research Science and Engineering Center DMR-2011824.

ACKNOWLEDGMENTS

We thank Lisa Hester, and the University of Maryland Cytokine Core Laboratory, for assistance with ELISA assays. We thank Dr. Catherine Fromen and graduate student Bader Jarai for access and training on flow cytometry. KW would like to thank Dr. Lina Pradhan for initial training and mentorship for hydrogel chemistry and Dr. Kristen DeMeester for initial training and mentorship for bacteria labeling and mammalian cell culture. We would like to thank Liam-Michael Sandles for assistance with the DBCO plate reader assay and Samantha Cassel for culture of the CCL151 fibroblast cells. We would like to thank Cinta Santiago for synthesizing the AzNAM probe. We would like to thank Elizabeth D'Ambrosio and Samantha Cassel for critical reading of this manuscript. **Figure 1** and **Figure 6** were created using BioRender.com.

SUPPLEMENTARY MATERIAL

The Supplementary Material for this article can be found online at: https://www.frontiersin.org/articles/10.3389/fchem.2022.842602/full#supplementary-material

REFERENCES

Ahmad, N., Colak, B., Zhang, D.-W., Gibbs, M. J., Watkinson, M., Becer, C. R., et al. (2019). Peptide Cross-Linked Poly (Ethylene Glycol) Hydrogel Films as Biosensor Coatings for the Detection of Collagenase. *Sensors* 19 (7), 1677. doi:10.3390/s19071677

Banahene, N., Kavunja, H. W., and Swarts, B. M. (2021). Chemical Reporters for Bacterial Glycans: Development and Applications. *Chem. Rev.* doi:10.1021/acs.chemrev.1c00729

Baskin, J. M., Prescher, J. A., Laughlin, S. T., Agard, N. J., Chang, P. V., Miller, I. A., et al. (2007). Copper-free Click Chemistry for Dynamic *In Vivo* Imaging. *Proc. Natl. Acad. Sci.* 104 (43), 16793–16797. doi:10.1073/pnas.0707090104

Benoit, D. S. W., Schwartz, M. P., Durney, A. R., and Anseth, K. S. (2008). Small Functional Groups for Controlled Differentiation of Hydrogel-Encapsulated Human Mesenchymal Stem Cells. *Nat. Mater* 7 (10), 816–823. doi:10.1038/nmat2269

Blakney, A. K., Swartzlander, M. D., and Bryant, S. J. (2012). Student Award winner in the Undergraduate Category for the Society of Biomaterials 9th World Biomaterials Congress, Chengdu, China, June 1-5, 2012. *J. Biomed. Mater. Res.* 100A (6), 1375–1386. doi:10.1002/jbm.a.34104

Blasioli, D. J., Matthews, G. L., and Kaplan, D. L. (2014). The Degradation of Chondrogenic Pellets Using Cocultures of Synovial Fibroblasts and U937 Cells. *Biomaterials* 35 (4), 1185–1191. doi:10.1016/j.biomaterials.2013.10.050

Blumberg, R. S., Saubermann, L. J., and Strober, W. (1999). Animal Models of Mucosal Inflammation and Their Relation to Human Inflammatory Bowel Disease. *Curr. Opin. Immunol.* 11 (6), 648–656. doi:10.1016/s0952-7915(99)00032-1

Brown, A. R., Wodzanowski, K. A., Santiago, C. C., Hyland, S. N., Follmar, J. L., Asare-Okai, P., et al. (2021). Protected N-Acetyl Muramic Acid Probes Improve

Bacterial Peptidoglycan Incorporation via Metabolic Labeling. *ACS Chem. Biol.* 16 (10), 1908–1916. doi:10.1021/acschembio.1c00268

Brown, N. W., Jr., Shirley, J. D., Marshall, A. P., and Carlson, E. E. (2021). Comparison of Bioorthogonal β-Lactone Activity-Based Probes for Selective Labeling of Penicillin-Binding Proteins. *Chembiochem* 22 (1), 193–202. doi:10.1002/cbic.202000556

Bryant, S. J., Nuttelman, C. R., and Anseth, K. S. (2000). Cytocompatibility of UV and Visible Light Photoinitiating Systems on Cultured NIH/3T3 Fibroblasts *In Vitro*. *J. Biomater. Sci. Polym. Edition* 11 (5), 439–457. doi:10.1163/156856200743805

Caliari, S. R., and Burdick, J. A. (2016). A Practical Guide to Hydrogels for Cell Culture. *Nat. Methods* 13 (5), 405–414. doi:10.1038/nmeth.3839

Chang, P. V., Prescher, J. A., Sletten, E. M., Baskin, J. M., Miller, I. A., Agard, N. J., et al. (2010). Copper-free Click Chemistry in Living Animals. *Proc. Natl. Acad. Sci. USA* 107 (5), 1821–1826. doi:10.1073/pnas.0911116107

Chellat, F., Grandjean-Laquerriere, A., Naour, R. L., Fernandes, J., Yahia, L. H., Guenounou, M., et al. (2005). Metalloproteinase and Cytokine Production by THP-1 Macrophages Following Exposure to Chitosan-DNA Nanoparticles. *Biomaterials* 26 (9), 961–970. doi:10.1016/j.biomaterials.2004.04.006

Clevers, H. (2016). Modeling Development and Disease with Organoids. *Cell* 165 (7), 1586–1597. doi:10.1016/j.cell.2016.05.082

Daigneault, M., Preston, J. A., Marriott, H. M., Whyte, M. K. B., and Dockrell, D. H. (2010). The Identification of Markers of Macrophage Differentiation in PMA-Stimulated THP-1 Cells and Monocyte-Derived Macrophages. *PLoS One* 5 (1), e8668. doi:10.1371/journal.pone.0008668

de Souza, N. (2018). A Model Gut Microbiome. *Nat. Methods* 15 (8), 572. doi:10.1038/s41592-018-0094-z

Debets, M. F., Tastan, O. Y., Wisnovsky, S. P., Malaker, S. A., Angelis, N., Moeckl, L. K. R., et al. (2020). Metabolic Precision Labeling Enables Selective Probing of O-linkedN-Acetylgalactosamine Glycosylation. *Proc. Natl. Acad. Sci. USA* 117 (41), 25293–25301. doi:10.1073/pnas.2007297117

DeMeester, K. E., Liang, H., Zhou, J., Wodzanowski, K. A., Prather, B. L., Santiago, C. C., et al. (2019). Metabolic Incorporation of N-Acetyl Muramic Acid Probes into Bacterial Peptidoglycan. *Curr. Protoc. Chem. Biol.* 11 (4), e74. doi:10.1002/cpch.74

DeMeester, K. E., Liang, H., Jensen, M. R., Jones, Z. S., D'Ambrosio, E. A., Scinto, S. L., et al. (2018). Synthesis of Functionalized N-Acetyl Muramic Acids to Probe Bacterial Cell Wall Recycling and Biosynthesis. *J. Am. Chem. Soc.* 140 (30), 9458–9465. doi:10.1021/jacs.8b03304

Zhang, D., Chen, L., Li, S., Gu, Z., and Yan, J. (2008). Lipopolysaccharide (LPS) of Porphyromonas Gingivalis Induces IL-1β, TNF-α and IL-6 Production by THP-1 Cells in a Way Different from that of *Escherichia coli* LPS. *Innate Immun.* 14 (2), 99–107. doi:10.1177/1753425907088244

Ei-Hajj, Z. W., and Newman, E. B. (2015). How Much Territory Can a Single E-Coli Cell Control? *Front. Microbiol.* 6.

Engler, A. J., Sen, S., Sweeney, H. L., and Discher, D. E. (2006). Matrix Elasticity Directs Stem Cell Lineage Specification. *Cell* 126 (4), 677–689. doi:10.1016/j.cell.2006.06.044

Fairbanks, B. D., Schwartz, M. P., Halevi, A. E., Nuttelman, C. R., Bowman, C. N., and Anseth, K. S. (2009). A Versatile Synthetic Extracellular Matrix Mimic via Thiol-Norbornene Photopolymerization. *Adv. Mater.* 21 (48), 5005–5010. doi:10.1002/adma.200901808

Galli, S. J., Borregaard, N., and Wynn, T. A. (2011). Phenotypic and Functional Plasticity of Cells of Innate Immunity: Macrophages, Mast Cells and Neutrophils. *Nat. Immunol.* 12 (11), 1035–1044. doi:10.1038/ni.2109

Geddes, K., Magalhães, J. G., and Girardin, S. E. (2009). Unleashing the Therapeutic Potential of NOD-like Receptors. *Nat. Rev. Drug Discov.* 8 (6), 465–479. doi:10.1038/nrd2783

Gerecht, S., Burdick, J. A., Ferreira, L. S., Townsend, S. A., Langer, R., and Vunjak-Novakovic, G. (2007). Hyaluronic Acid Hydrogel for Controlled Self-Renewal and Differentiation of Human Embryonic Stem Cells. *Proc. Natl. Acad. Sci.* 104 (27), 11298–11303. doi:10.1073/pnas.0703723104

Gisin, J., Schneider, A., Nägele, B., Borisova, M., and Mayer, C. (2013). A Cell wall Recycling Shortcut that Bypasses Peptidoglycan De Novo Biosynthesis. *Nat. Chem. Biol.* 9 (8), 491–493. doi:10.1038/nchembio.1289

Goyal, N., Rana, A., Ahlawat, A., Bijjem, K. R. V., and Kumar, P. (2014). Animal Models of Inflammatory Bowel Disease: a Review. *Inflammopharmacol* 22 (4), 219–233. doi:10.1007/s10787-014-0207-y

Hasegawa, M., Yang, K., Hashimoto, M., Park, J.-H., Kim, Y.-G., Fujimoto, Y., et al. (2006). Differential Release and Distribution of Nod1 and Nod2 Immunostimulatory Molecules Among Bacterial Species and Environments. *J. Biol. Chem.* 281 (39), 29054–29063. doi:10.1074/jbc.m602638200

Herskovits, A. A., Auerbuch, V., and Portnoy, D. A. (2007). Bacterial Ligands Generated in a Phagosome Are Targets of the Cytosolic Innate Immune System. *Plos Pathog.* 3 (3), e51. doi:10.1371/journal.ppat.0030051

Humann, J., and Lenz, L. L. (2009). Bacterial Peptidoglycan-Degrading Enzymes and Their Impact on Host Muropeptide Detection. *J. Innate Immun.* 1 (2), 88–97. doi:10.1159/000181181

Italiani, P., and Boraschi, D. (2014). From Monocytes to M1/M2 Macrophages: Phenotypical vs. Functional Differentiation. *Front. Immunol.* 5, 514. doi:10.3389/fimmu.2014.00514

Johnson, L. A., Rodansky, E. S., Sauder, K. L., Horowitz, J. C., Mih, J. D., Tschumperlin, D. J., et al. (2013). Matrix Stiffness Corresponding to Strictured Bowel Induces a Fibrogenic Response in Human Colonic Fibroblasts. *Inflamm. Bowel Dis.* 19 (5), 891–903. doi:10.1097/mib.0b013e3182813297

Johnston, R. B., Jr. (1988). Monocytes and Macrophages. *N. Engl. J. Med.* 318 (12), 747–752. doi:10.1056/nejm198803243181205

Jowett, G. M., Norman, M. D. A., Yu, T. T. L., Rosell Arévalo, P., Hoogland, D., Lust, S. T., et al. (2021). ILC1 Drive Intestinal Epithelial and Matrix Remodelling. *Nat. Mater.* 20 (2), 250–259. doi:10.1038/s41563-020-0783-8

Kahan, F. M., Kahan, J. S., Cassidy, P. J., and Kropp, H. (1974). The Mechanism of Action of Fosfomycin (Phosphonomycin). *Ann. N. Y Acad. Sci.* 235 (0), 364–386. doi:10.1111/j.1749-6632.1974.tb43277.x

Kim, M., Lee, S., and Ki, C. S. (2019). Cellular Behavior of RAW264.7 Cells in 3D Poly(ethylene Glycol) Hydrogel Niches. *ACS Biomater. Sci. Eng.* 5 (2), 922–932. doi:10.1021/acsbiomaterials.8b01150

Liang, H., DeMeester, K. E., Hou, C.-W., Parent, M. A., Caplan, J. L., and Grimes, C. L. (2017). Metabolic Labelling of the Carbohydrate Core in Bacterial Peptidoglycan and its Applications. *Nat. Commun.* 8, 15015. doi:10.1038/ncomms15015

Lister, P. D., Wolter, D. J., and Hanson, N. D. (2009). Antibacterial-Resistant *Pseudomonas aeruginosa* : Clinical Impact and Complex Regulation of Chromosomally Encoded Resistance Mechanisms. *Clin. Microbiol. Rev.* 22 (4), 582–610. doi:10.1128/cmr.00040-09

Loebel, C., Mauck, R. L., and Burdick, J. A. (2019). Local Nascent Protein Deposition and Remodelling Guide Mesenchymal Stromal Cell Mechanosensing and Fate in Three-Dimensional Hydrogels. *Nat. Mater.* 18 (8), 883–891. doi:10.1038/s41563-019-0307-6

Lund, M. E., To, J., O'Brien, B. A., and Donnelly, S. (2016). The Choice of Phorbol 12-myristate 13-acetate Differentiation Protocol Influences the Response of THP-1 Macrophages to a Pro-inflammatory Stimulus. *J. Immunological Methods* 430, 64–70. doi:10.1016/j.jim.2016.01.012

Macdougall, L. J., Wiley, K. L., Kloxin, A. M., and Dove, A. P. (2018). Design of Synthetic Extracellular Matrices for Probing Breast Cancer Cell Growth Using Robust Cyctocompatible Nucleophilic Thiol-Yne Addition Chemistry. *Biomaterials* 178, 435–447. doi:10.1016/j.biomaterials.2018.04.046

Medzhitov, R. (2021). The Spectrum of Inflammatory Responses. *Science* 374 (6571), 1070–1075. doi:10.1126/science.abi5200

Montefusco-Pereira, C. V., Horstmann, J. C., Ebensen, T., Beisswenger, C., Bals, R., Guzman, C. A., et al. (2020). *P. aeruginosa* Infected 3D Co-culture of Bronchial Epithelial Cells and Macrophages at Air-Liquid Interface for Preclinical Evaluation of Anti-infectives. *J. Vis. Exp.* 160, e61069. doi:10.3791/61069

Mountcastle, S. E., Cox, S. C., Sammons, R. L., Jabbari, S., Shelton, R. M., and Kuehne, S. A. (2020). A Review of Co-culture Models to Study the Oral Microenvironment and Disease. *J. Oral Microbiol.* 12 (1), 1773122. doi:10.1080/20002297.2020.1773122

Neef, A. B., and Schultz, C. (2009). Selective Fluorescence Labeling of Lipids in Living Cells. *Angew. Chem. Int. Ed.* 48 (8), 1498–1500. doi:10.1002/anie.200805507

Nikić, I., Kang, J. H., Girona, G. E., Aramburu, I. V., and Lemke, E. A. (2015). Labeling Proteins on Live Mammalian Cells Using Click Chemistry. *Nat. Protoc.* 10 (5), 780–791. doi:10.1038/nprot.2015.045

Ovadia, E. M., Colby, D. W., and Kloxin, A. M. (2018). Designing Well-Defined Photopolymerized Synthetic Matrices for Three-Dimensional Culture and

Differentiation of Induced Pluripotent Stem Cells. *Biomater. Sci.* 6 (6), 1358–1370. doi:10.1039/c8bm00099a

Peck, Y., Ng, L. Y., Goh, J. Y. L., Gao, C., and Wang, D.-A. (2014). A Three-Dimensionally Engineered Biomimetic Cartilaginous Tissue Model for Osteoarthritic Drug Evaluation. *Mol. Pharmaceutics* 11 (7), 1997–2008. doi:10.1021/mp500026x

Petersen, O. W., Ronnov-Jessen, L., Howlett, A. R., and Bissell, M. J. (1992). Interaction with Basement Membrane Serves to Rapidly Distinguish Growth and Differentiation Pattern of normal and Malignant Human Breast Epithelial Cells. *Proc. Natl. Acad. Sci.* 89 (19), 9064–9068. doi:10.1073/pnas.89.19.9064

Rehmann, M. S., and Kloxin, A. M. (2013). Tunable and Dynamic Soft Materials for Three-Dimensional Cell Culture. *Soft Matter* 9 (29), 6737–6746. doi:10.1039/c3sm50217a

Rehmann, M. S., Luna, J. I., Maverakis, E., and Kloxin, A. M. (2016). Tuning Microenvironment Modulus and Biochemical Composition Promotes Human Mesenchymal Stem Cell Tenogenic Differentiation. *J. Biomed. Mater. Res.* 104 (5), 1162–1174. doi:10.1002/jbm.a.35650

Rezakhani, S., Gjorevski, N., and Lutolf, M. P. (2021). Extracellular Matrix Requirements for Gastrointestinal Organoid Cultures. *Biomaterials* 276, 121020. doi:10.1016/j.biomaterials.2021.121020

Samavedi, S., Diaz-Rodriguez, P., Erndt-Marino, J. D., and Hahn, M. S. (2017). A Three-Dimensional Chondrocyte-Macrophage Coculture System to Probe Inflammation in Experimental Osteoarthritis. *Tissue Eng. Part. A.* 23 (3-4), 101–114. doi:10.1089/ten.TEA.2016.0007

Sanceau, J., Wijdenes, J., Revel, M., and Wietzerbin, J. (1991). IL-6 and IL-6 Receptor Modulation by IFN-Gamma and Tumor Necrosis Factor-Alpha in Human Monocytic Cell Line (THP-1). Priming Effect of IFN-Gamma. *J. Immunol.* 147 (8), 2630–2637.

Schildberger, A., Rossmanith, E., Eichhorn, T., Strassl, K., and Weber, V. (2013). Monocytes, Peripheral Blood Mononuclear Cells, and THP-1 Cells Exhibit Different Cytokine Expression Patterns Following Stimulation with Lipopolysaccharide. *Mediators Inflamm.* 2013, 697972. doi:10.1155/2013/697972

Simon-Assmann, P., Kedinger, M., De Arcangelis, A., Rousseau, V., and Simo, P. (1995). Extracellular Matrix Components in Intestinal Development. *Experientia* 51 (9-10), 883–900. doi:10.1007/BF01921739

Smithmyer, M. E., Sawicki, L. A., and Kloxin, A. M. (2014). Hydrogel Scaffolds Asin Vitromodels to Study Fibroblast Activation in Wound Healing and Disease. *Biomater. Sci.* 2 (5), 634–650. doi:10.1039/c3bm60319a

Snyder, J., Wang, C.-M., Zhang, A. Q., Li, Y., Luchan, J., Hosic, S., et al. (2020). Materials and Microenvironments for Engineering the Intestinal Epithelium. *Ann. Biomed. Eng.* 48 (7), 1916–1940. doi:10.1007/s10439-020-02470-8

Sun, L., Wang, X., and Kaplan, D. L. (2011). A 3D Cartilage - Inflammatory Cell Culture System for the Modeling of Human Osteoarthritis. *Biomaterials* 32 (24), 5581–5589. doi:10.1016/j.biomaterials.2011.04.028

Tanaka, H., Murphy, C. L., Murphy, C., Kimura, M., Kawai, S., and Polak, J. M. (2004). Chondrogenic Differentiation of Murine Embryonic Stem Cells: Effects of Culture Conditions and Dexamethasone. *J. Cel. Biochem.* 93 (3), 454–462. doi:10.1002/jcb.20171

Taylor, J. A., Bratton, B. P., Sichel, S. R., Blair, K. M., Jacobs, H. M., DeMeester, K. E., et al. (2020). Distinct Cytoskeletal Proteins Define Zones of Enhanced Cell wall Synthesis in *Helicobacter pylori*. *Elife* 9, e52482. doi:10.7554/eLife.52482

Taylor, J. A., Santiago, C. C., Gray, J., Wodzanowski, K. A., DeMeester, K. E., Biboy, J., et al. (2021). Localizing Peptidoglycan Synthesis in *Helicobacter pylori* Using Clickable Metabolic Probes. *Curr. Protoc.* 1 (4), e80. doi:10.1002/cpz1.80

Thaiss, C. A., Zmora, N., Levy, M., and Elinav, E. (2016). The Microbiome and Innate Immunity. *Nature* 535 (7610), 65–74. doi:10.1038/nature18847

Tibbitt, M. W., and Anseth, K. S. (2009). Hydrogels as Extracellular Matrix Mimics for 3D Cell Culture. *Biotechnol. Bioeng.* 103 (4), 655–663. doi:10.1002/bit.22361

Wang, D., Zhang, Y., and Kleiner, R. E. (2020). Cell- and Polymerase-Selective Metabolic Labeling of Cellular RNA with 2′-Azidocytidine. *J. Am. Chem. Soc.* 142 (34), 14417–14421. doi:10.1021/jacs.0c04566

Webb, D. R. (2014). Animal Models of Human Disease: Inflammation. *Biochem. Pharmacol.* 87 (1), 121–130. doi:10.1016/j.bcp.2013.06.014

Williams, C. G., Malik, A. N., Kim, T. K., Manson, P. N., and Elisseeff, J. H. (2005). Variable Cytocompatibility of Six Cell Lines with Photoinitiators Used for Polymerizing Hydrogels and Cell Encapsulation. *Biomaterials* 26 (11), 1211–1218. doi:10.1016/j.biomaterials.2004.04.024

Witherel, C. E., Abebayehu, D., Barker, T. H., and Spiller, K. L. (2019). Macrophage and Fibroblast Interactions in Biomaterial-Mediated Fibrosis. *Adv. Healthc. Mater.* 8 (4), e1801451. doi:10.1002/adhm.201801451

Wodzanowski, K. A., Cassel, S. E., Grimes, C. L., and Kloxin, A. M. (2020). Tools for Probing Host-Bacteria Interactions in the Gut Microenvironment: From Molecular to Cellular Levels. *Bioorg. Med. Chem. Lett.* 30 (10), 127116. doi:10.1016/j.bmcl.2020.127116

Yamada, Y., Hozumi, K., and Nomizu, M. (2011). Construction and Activity of a Synthetic Basement Membrane with Active Laminin Peptides and Polysaccharides. *Chem. Eur. J.* 17 (38), 10500–10508. doi:10.1002/chem.201101064

Zeng, B. N., Cai, Z. L., Lalevee, J., Yang, Q. Z., Lai, H. W., Xiao, P., et al. (2021). Cytotoxic and Cytocompatible Comparison Among Seven Photoinitiators-Triggered Polymers in Different Tissue Cells. *Toxicol. Vitro* 72, 105103. doi:10.1016/j.tiv.2021.105103

Conflict of Interest: The authors declare that the research was conducted in the absence of any commercial or financial relationships that could be construed as a potential conflict of interest.

Publisher's Note: All claims expressed in this article are solely those of the authors and do not necessarily represent those of their affiliated organizations, or those of the publisher, the editors, and the reviewers. Any product that may be evaluated in this article, or claim that may be made by its manufacturer, is not guaranteed or endorsed by the publisher.

frontiers in Chemistry

ORIGINAL RESEARCH
published: 16 March 2022
doi: 10.3389/fchem.2022.859133

Synthesis and Characterization of Phenylboronic Acid-Modified Insulin With Glucose-Dependent Solubility

Nai-Pin Lin[1,2†], *Nan Zheng*[2†], *Landa Purushottam*[1], *Yi Wolf Zhang*[1,2] *and Danny Hung-Chieh Chou*[1,2*]

[1]Department of Pediatrics, Division of Diabetes and Endocrinology, Stanford University, Stanford, CA, United States, [2]Department of Biochemistry, University of Utah, Salt Lake City, UT, United States

Glucose-responsive insulin represents a promising approach to regulate blood glucose levels. We previously showed that attaching two fluorophenylboronic acid (FPBA) residues to the C-terminal B chain of insulin glargine led to glucose-dependent solubility. Herein, we demonstrated that relocating FPBA from B chain to A chain increased the baseline solubility without affecting its potency. Furthermore, increasing the number of FPBA groups led to increased glucose-dependent solubility.

Keywords: insulin, glucose responsiveness, peptide, insulin modification, phenylboronate

OPEN ACCESS

Edited by:
John D. Wade,
University of Melbourne, Australia

Reviewed by:
Knud J. Jensen,
University of Copenhagen, Denmark
Thomas Hoeg-Jensen,
Novo Nordisk, Denmark

****Correspondence:***
Danny Hung-Chieh Chou
dannychou@stanford.edu

[†]These authors have contributed equally to this work and share first authorship

Specialty section:
This article was submitted to Chemical Biology, a section of the journal Frontiers in Chemistry

Received: *21 January 2022*
Accepted: *22 February 2022*
Published: *16 March 2022*

Citation:
Lin N-P, Zheng N, Purushottam L, Zhang YW and Chou DH-C (2022) Synthesis and Characterization of Phenylboronic Acid-Modified Insulin With Glucose-Dependent Solubility. Front. Chem. 10:859133. doi: 10.3389/fchem.2022.859133

1 INTRODUCTION

Insulin therapy is essential to the treatment of type I diabetes (T1D) and some type II diabetes (T2D) (Berenson et al., 2011). These diseases present a complete or partial loss of insulin response or insulin sensitivity, resulting in dysregulation of blood glucose levels. Glycemic control currently relies on an accurate dose of insulin drugs according to the measurement of blood glucose and individual response (DeWitt and Hirsch, 2003). All currently US Food and Drug Administration (FDA)-approved insulin still have a narrow therapeutic window: insulin overdoses lead to hypoglycemia and underdoses result in hyperglycemia (Peyrot et al., 2012). Chronic hyperglycemia can lead to cardiovascular diseases, nephropathy, non-healing wounds, and other diabetic complications, whereas hypoglycemia can result in acute coma or even death (McCoy et al., 2012; Frier, 2014). This challenge of optimal glycemic control remains to be addressed. Glucose-responsive insulin (GRI) derivatives have been developed to address this challenge by making the insulin conjugate itself with a higher glucose-lowering effect in response to elevated blood glucose levels (Veiseh et al., 2015; Bakh et al., 2017; Rege et al., 2017; Disotuar et al., 2020; Jarosinski et al., 2021). To date, carbohydrates (Brownlee and Cerami, 1979; Wang et al., 2017; Kaarsholm et al., 2018), hydrazones (Mannerstedt et al., 2021), and phenylboronic acids (PBA) (Hoeg-Jensen et al., 2005a; Hoeg-Jensen et al., 2005b; Chou et al., 2015; Qiu et al., 2019; Chen et al., 2021) have been conjugated to insulin to achieve glucose responsiveness through different mechanisms.

Insulin glargine, marketed as Lantus®, is a long-acting insulin analog with a 24-h dosing regimen. The additional 2 arginine residues on the C-terminus of the B chain increases its isoelectric point (pI) 6.7, which lowers its solubility at physiological pH and leads to precipitation at the subcutaneous injection site (Kohn et al., 2007). Glargine is then released slowly from the precipitate into the bloodstream to establish the long-acting property. We previously hypothesized that this releasing mechanism can also be controlled by the glucose concentration to create a GRI, which had a low solubility under a low glucose environment, and the solubility could increase along with the elevating glucose concentration to release more insulin into the bloodstream. PBA is known to reversibly bind to 1,2- and 1,3-diols including glucose. After binding with a diol, PBA is further negatively charged

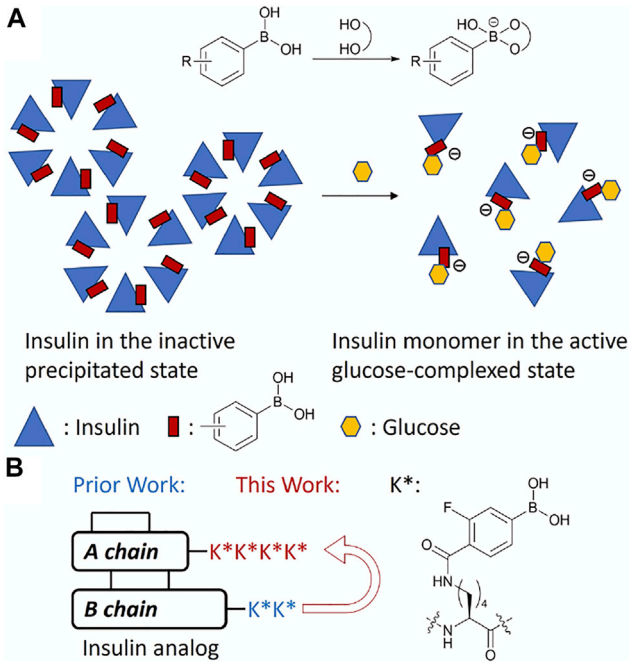

FIGURE 1 | (A) Schematic mechanism of glucose-responsive insulin. **(B)** Design of FPBA-conjugated glucose-responsive insulin.

(Furikado et al., 2014). If insulin is conjugated with PBA, the acquired negative charges after glucose binding can lower the pI away from 7.4 resulting in solubility increase and insulin release to bloodstream. The addition to hydrophilic sugar molecules would also increase overall solubility (**Figure 1A**). We previously reported an insulin analog with two fluorophenylboronic acid (FPBA)-conjugated lysine on the ε-amino group (K*) in the C-terminal B chain with glucose responsiveness through solubility change (Qiu et al., 2019). The electro-withdrawing fluoro substituent can lower the pKa of non-substituted PBA (8.8) to facilitate binding of glucose at physiologic pH (Yan et al., 2004). In this work, we further explore the impacts of the position and numbers of FPBA on glucose-dependent solubility of insulin to optimize the glucose responsiveness (**Figure 1B**).

2 RESULTS AND DISCUSSION

We previously found that addition of FPBA on insulin B chain dramatically decreases the solubility of peptide intermediates and final insulin analogs due to its hydrophobicity (Qiu et al., 2019). During the attempt on the synthesis of human insulin B chain sequence with three FPBA, the solubility of the resulting B chain is too low for purification and subsequent reactions. To circumvent this challenge, we shifted the pI by introducing a Glu to Ala mutation at B21, which was previously shown to have similar insulin receptor affinity (Kristensen et al., 1997). As a result, two additional Arg residues with B21Ala mutation can be synthesized to allow the preparation of the insulin B chain with 3 FPBA on the C-terminus (**Scheme 1**; **Supplementary Material**). Synthesis of these insulin analogs followed previously published methods with slight modifications (Liu et al., 2013; 2014; Qiu et al., 2019). The A chain and B chain were first synthesized separately followed by chain combinations. To construct three disulfide bonds in a controlled manner, four Cys of the A chain were introduced with four orthogonal protecting groups used as previously reported (Liu et al., 2013; 2014; Qiu et al., 2019). After the fully protected A chain was synthesized on resin, A6 Cys (S^tBu) was deprotected by 2-mercaptoethanol and then activated with 2,2′-dithiobis (5-nitropyridine) (DTNP) followed by A11 Cys (Mmt) deprotection under 1% trifluoroacetic acid (TFA) to yield a thiol group. The intramolecular disulfide bond between A6 and A11 was spontaneously formed through a disulfide substitution reaction. The A chain was finally cleaved from the resin to give the A6-A11 disulfide, A7 Cys (Acm), and A20 free Cys A chain **1**. To avoid degradation of FPBA under harsh peptide synthesis reaction conditions, FPBA was introduced at late stage after the whole B chain was synthesized. Fmoc-Lys (Dde)-OH was used for FPBA conjugation with Boc-Phe-OH used for PheB1. After the fully protected B chain was synthesized on resin, all Lys (Dde) residues were deprotected using 5% hydrazine and then coupled with 4-carboxy-3-fluorophenylboronic acid on the ε-amino group to yield the K* residues (Qiu et al., 2019). The B chain was cleaved under a standard cleavage condition in the presence of 2,2′-dithiodipyridine (DTDP) to give the B7 Cys (Acm) and B19 Cys (SPy) B chain **2**. The A and B chain were combined through a disulfide substitution reaction between A20 and B19. The last disulfide bond between A7 and B7 was formed by treatment of iodine. The Thr-Ser isoacyl linkage (to increase solubility of A chain) was finally transformed to an amide bond through an *O*-to-*N* acyl shift under a basic condition to give insulin analogs **4**. We then measured solubilities of insulin analogs at 0–400 mg dl^{-1} glucose solutions to determine their glucose-dependent solubilities (**Figure 2A**). In the absence of glucose (baseline solubility), insulin analog **4b** (with 3 FPBAs on the B chain) was less soluble compared to the 2FPBA analog **4a** due to the hydrophobicity of FPBA (**Figure 2A**). However, both analogs demonstrated similar glucose responsive profiles (**Figure 2B**). Both **4a** and **4b** had comparable EC_{50} with human insulin in activating insulin receptor signaling using pAKT as an indicator (**Figure 2C**).

Another potential approach to circumvent the solubility issue of B chain intermediates is using sortase A (SrtA)-mediated ligation to semi-synthesize insulin analogs with B chain C-terminal modifications (Disotuar et al., 2021). However, SrtA ligation needs a specific recognition sequence around the ligation site, which becomes a functionless region between insulin and the ligated peptide. Instead, we turn to the C-terminal A chain as an alternative strategy to circumvent the solubility issue. Traditionally, very few publications reported modifications on the C-terminal A chain of insulin (Edgerton et al., 2014; 2019). Our recent work on characterizing venom insulins from fish-hunting cone snails suggests that modifications can be introduced to this region without blocking its ability to bind insulin receptor (Ahorukomeye et al., 2019; Xiong et al., 2020; 2021). In the

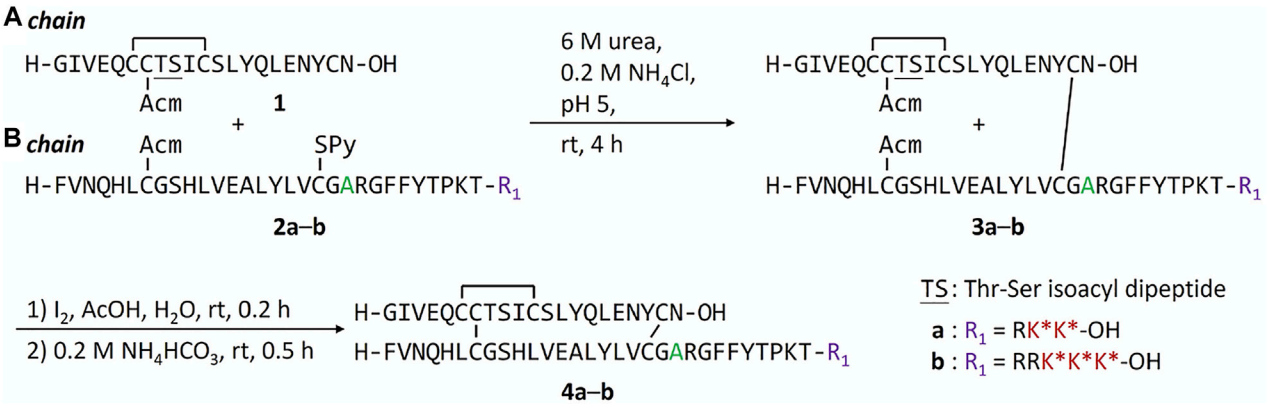

SCHEME 1 | Synthesis of FPBA-conjugated insulin analogs.

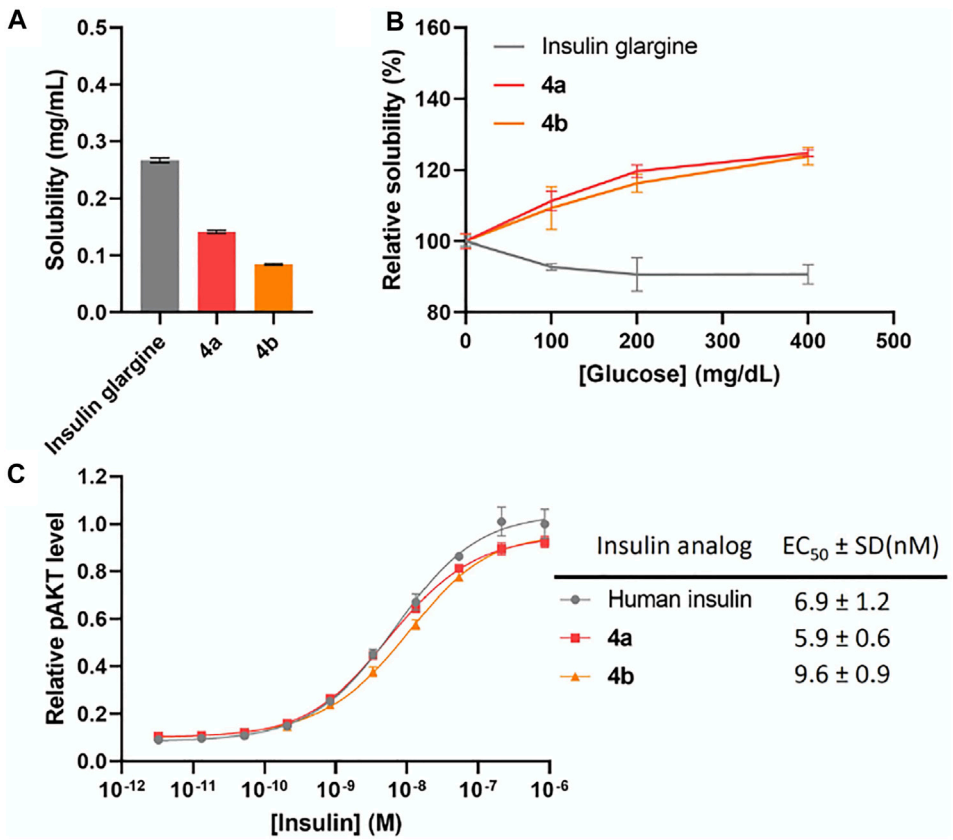

FIGURE 2 | (A) Solubility of insulin analogs in pH 7.4 PBS. Data are expressed as mean ± SD (n = 4 per group). **(B)** Solubility of insulin analogs in pH 7.4 PBS with different glucose concentrations. Data are expressed as mean ± SD (n = 4 per group). **(C)** *In vitro* activity of insulin analogs by using activated pAKT levels as measurements. Data are expressed as mean ± SD (n = 4 per group). EC_{50} was calculated by Prism 9 (GraphPad Software, CA, United States) with nonlinear regression curve fitting of dose-response asymmetric equation.

original synthesis (**Scheme 1**), 1-(4,4-dimethyl-2,6-dioxocyclohex-1-ylidene)ethyl (Dde) was the key protecting group to allow selective coupling with FPBA. However, Thr-Ser isoacyl linkage was crucial to provide the overall solubility of the A chain but it cannot survive the condition for Dde removal (Liu et al., 2014). To address this challenge, we turn to another orthogonal protecting group, allyloxycarbonyl (Alloc), which uses a mild Pd-mediated deprotection condition (**Scheme 2**). In addition, to avoid the interference between the Pd catalyst and the A6-A11 intramolecular disulfide on the A chain, both Cys

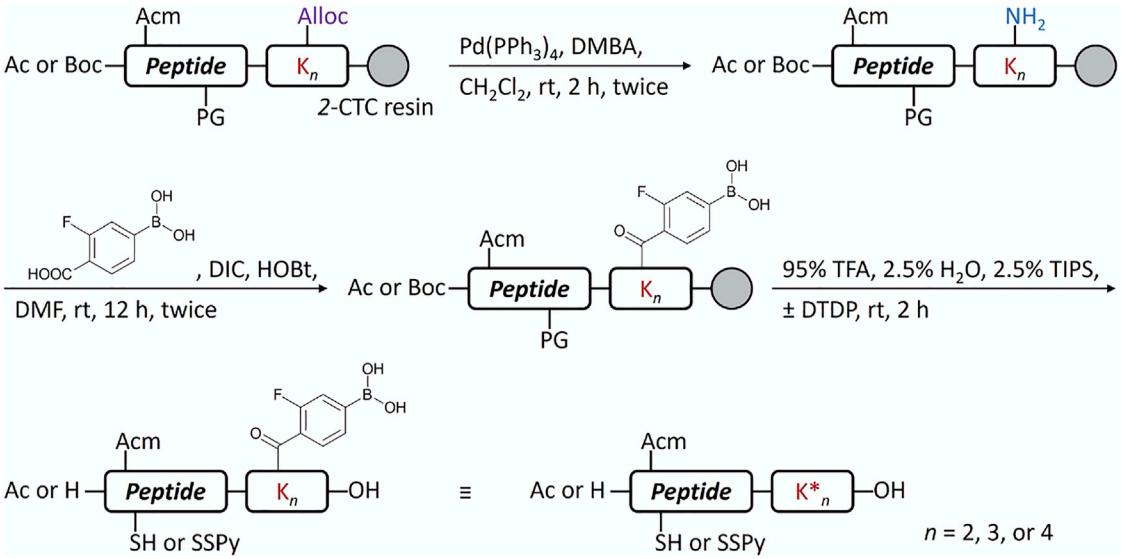

SCHEME 2 | Conjugation of FPBA to peptides by Alloc strategy.

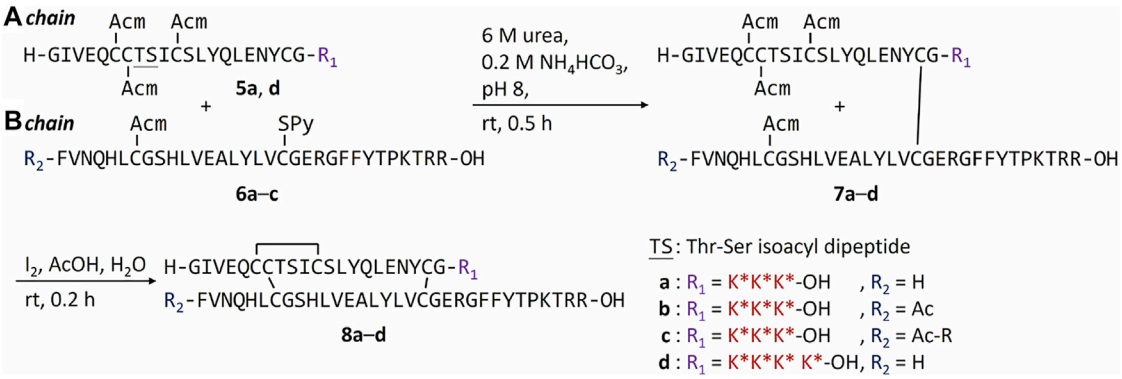

SCHEME 3 | Synthesis of A chain FPBA-conjugated insulin analogs.

were alternatively protected as Cys (Acm) and the disulfide bond was formed later together with the iodine-mediated disulfide formation of A7-B7 (Liu et al., 2013; Xiong et al., 2020). A total of 4 analogs with FPBA groups on the A chain were synthesized and further evaluated (**Scheme 3**; **Supplementary Material**). We found that the solubility of **8a** was improved about 6-fold without a significant change of EC_{50} and glucose responsiveness comparing to the corresponding B chain three FPBA analog **4b** (**Figure 3**). Acetylation on the B chain N-terminus of **8a** (**8b**) can block the N-terminal amino group, which reduces pI and increases solubility at pH 7.4 (**Figure 3A**) but EC_{50} had an about 8-fold decrease (**Figure 3C**). Restoring pI of **8b** by adding an extra Arg on the N-terminal of the B chain (**8c**) decreases the solubility, as expected (**Figure 3A**). Over-modifications of **8c** had deleterious effects on both solubility and EC_{50} to the insulin receptor (**Figure 3C**). All three analogs (**8a**, **8b**, and **8c**) had similar glucose-dependent solubility profiles, consistent with the same number of FPBA groups on each analog (**Figure 3B**).

Due to the increase of overall solubility by relocating FPBAs to the A chain, we were able to synthesize the four FPBA insulin analog **8d**. The baseline solubility of **8d** is comparable to **4a** and **4b**, which have two and three FPBA on B chain respectively (**Figure 3A**). EC_{50} of **8d** was also only reduced by about 4-fold compared to human insulin (**Figure 3C**). On the other hand, the additional FPBA brought a jump of glucose-dependent solubility to 100% increase between 0 and 400 mg dl^{-1}, in which the corresponding three FPBA analog **8a** just had around 20% (**Figure 3B**). This result suggests that increasing the number of FPBA groups led to larger glucose-dependent solubility enhancements.

In summary, we explored the conjugation of FPBA groups on insulin C-terminal A chain through a new Alloc-mediated conjugation strategy. We further discovered that by relocating

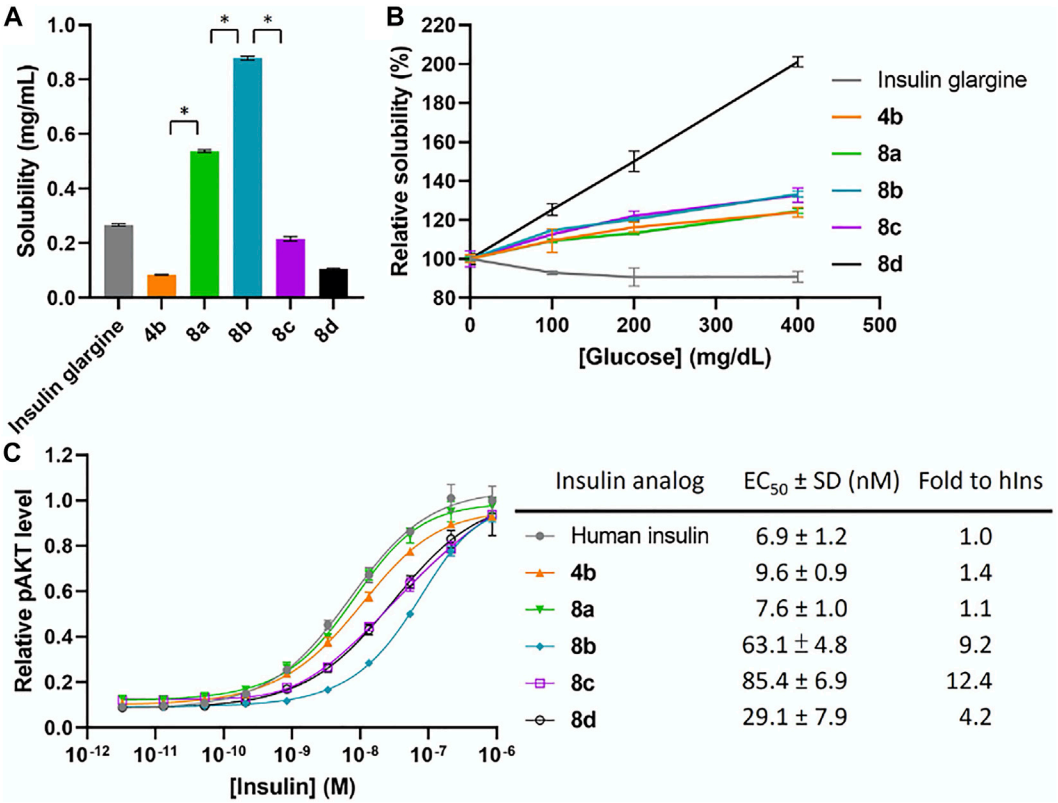

FIGURE 3 | (A) Solubility of insulin analogs in pH 7.4 PBS. Data are expressed as mean ± SD (n = 4 per group). The statistical comparison of the two groups was evaluated by the unpaired two-tailed Student's t-test. *p < 0.001. **(B)** Solubility of insulin analogs in pH 7.4 PBS with different glucose concentrations. Data are expressed as mean ± SD (n = 4 per group). **(C)** *In vitro* activity of insulin analogs by using activated pAKT levels as measurements. Data are expressed as mean ± SD (n = 4 per group). EC_{50} was calculated by Prism 9 (GraphPad Software, CA, United States) with nonlinear regression curve fitting of dose-response asymmetric equation.

the hydrophobic FPBA residues to the A chain, the baseline solubility of insulin is increased without potency reduction. This allowed further demonstration that increasing FPBA groups led to increasing glucose-dependent solubility. With these exciting findings, further *in vivo* properties are being investigated.

3 MATERIALS AND METHODS

3.1 General Information

All Fmoc amino acids, reagents, and solvents were used without purification. Fmoc amino acids and 1-[bis(dimethylamino) methylene]-1*H*-1,2,3-triazolo [4,5-*b*]pyridinium 3-oxid hexafluorophosphate (HATU) were purchase from AAPPTec, Bachem, Chem-Impex, ChemPep, and PurePep. The Rink amide ChemMatrix resin (catalog number: 7-600-1310) was purchased from Biotage. The 2-chlorotrityl chloride (2-CTC) resin (catalog number: 150301) were purchased from ChemPep. *N*,*N*-dimethylformamide (DMF), CH_2Cl_2, MeCN, MeOH, Et_2O, AcOH, Ac_2O, *N*,*N*-diisopropylethylamine (DIPEA), trifluoroacetic acid (TFA), NH_4HCl, NH_4HCO_3, urea, NaOH, 80% hydrazine hydrate, 2-mercaptoethanol were purchased from Fisher Scientific. Piperidine, triisopropylsilane (TIPS), hydroxybenzotriazole (HOBt), *N*,*N*′-diisopropylcarbodiimide (DIC), 2,2′-dithiodipyridine (DTDP), 2,2′-dithiobis (5-nitropyridine) (DTNP), I_2, $Pd(PPh_3)_4$, 1,3-dimethylbarbituric acid (DMBA), glucose, sodium ascorbate were purchased from Sigma Aldrich. 4-carboxy-3-fluorophenylboronic acid was purchased from Alfa Aesar. Agilent 6120 Quadrupole LC–MS system was used to acquire the LC chromatograms and mass spectra of samples with Luna® 5 µm C18 100 Å (50 × 2 mm) column (Phenomenex, CA, United States) at 0.4 ml/min with 5% of a H_2O/MeCN + 0.1% TFA solution for 1 min followed by a linear gradient from 5% to 95% of a H_2O/MeCN + 0.1% TFA solution over 5 min.

3.2 Automated Fmoc/^{t}Bu SPPS

Peptides were synthesized *via* Fmoc/^{t}Bu solid-phase peptide synthesis on Syro I (MultiSynTech GmbH, Germany) in a 10 ml reactor vial with a 0.1 mmol total loading capacity of resin. The first C-terminal amino acid of carboxylic acid C-terminus was coupled manually to the 2-CTC resin: The Fmoc-amino acid (0.1 mmol) and DIPEA (87.1 µl, 0.5 mmol) were dissolved in a solution of DMF and CH_2Cl_2 (1:1, 2.5 ml). This solution was added to the 2-CTC resin (250 mg), which was washed with DMF 3 times and then CH_2Cl_2 3 times before the reaction. The reaction mixture was mixed on a rotator for 2 h at room temperature. The resin was washed with DMF 3 times and

CH_2Cl_2 3 times and then capped with a solution of CH_2Cl_2, MeOH, and DIPEA (17:2:1, 5.0 ml) for 10 s 4 times. The resin was finally washed with CH_2Cl_2 3 times and then DMF 3 times. The first C-terminal amino acid of an amide C-terminus was coupled with Rink Amide resin with the same reaction condition as the typical amino acid coupling as follows. Fmoc was deprotected with 20% piperidine in DMF for 10 min twice at room temperature. Fmoc amino acids were coupled onto resin with a solution of Fmoc-amino acid (0.5 mmol), HATU (0.5 mmol), and DIPEA (1.0 mmol) in DMF (2.5 ml) for 10 min at 50°C (Cys and His) or at 70°C (others). The resin was washed with DMF 3 times between Fmoc deprotection and amino acid coupling.

3.3 Peptide Cleavage From Resin

A peptide was cleaved from resins (0.1 mmol) with a solution of TFA, H_2O, and TIPS (38:1:1, 8 ml) at room temperature for 2 h. Additional DTDP (220 mg, 10 mmol) was added in the cleavage solution to re-protect the thiol group of Cys with thiopyridine (SPy) if required. Peptides were precipitated from the cleavage solutions by adding to cold Et_2O (80 ml). After centrifuge under 3,000 ×g for 3 min, the supernatant was discarded, and the pellet of peptide was resuspended with Et_2O (40 ml) and again centrifuged to pellet 2 more times. Then crude material was dried under reduced pressure.

3.4 On Resin *N*-Terminal Acetylation

The resin (0.1 mmol) was swelled with DMF for 10 min and then DMF was removed by suction. A solution of Ac_2O (94.5 μlL, 1.0 mmol) and DIPEA (174 μl, 1.0 mmol) in DMF (4.0 ml) was added to the resin. The reaction mixture was gently agitated at room temperature for 1 h. The solution was removed by suction and the resin was washed with DMF 3 times.

3.5 On Resin Lys(Dde) Deprotection

The resin (0.1 mmol) was swelled with DMF for 10 min and then DMF was removed by suction. A 50% hydrazine solution in DMF (4 ml, prepared from 80% hydrazine hydrate) was added to the resin. The reaction mixture was gently agitated at room temperature for 30 min. The solution was removed by suction and the resin was washed with DMF 3 times.

3.6 On Resin Lys(Alloc) Deprotection

The resin (0.1 mmol) was swelled with CH_2Cl_2 for 10 min and then CH_2Cl_2 was removed by suction. A solution of $Pd(PPh_3)_4$ (11.6 mg per Alloc, 0.01 mmol per Alloc) and DMBA (31.2 mg per Alloc, 0.2 mmol per Alloc) in CH_2Cl_2 (4 ml) was added to the resin. The reaction mixture was gently agitated at room temperature for 2 h. The solution was removed by suction and the resin was washed with CH_2Cl_2 3 times. The reaction was monitored by LC–MS with microcleavage of the resin. The above treatment was repeated until all Alloc were removed.

3.7 On Resin Conjugation of FPBA to Lys

The resin (0.1 mmol) was swelled with DMF for 10 min and then DMF was removed by suction. A solution of 4-carboxy-3-fluorophenylboronic acid (55.2 mg per Lys, 0.3 mmol per Lys), DIC (47.0 μl per Lys, 0.3 mmol per Lys), and HOBt (40.5 mg per Lys, 0.3 mmol per Lys) in DMF (4 ml) was gently agitated at room temperature for 10 min and then added to the resin. The reaction mixture was gently agitated at room temperature for 12 h. The solution was removed by suction and the resin was washed with DMF 3 times. The reaction was monitored by LC–MS with microcleavage of the resin. The above treatment was repeated until all Lys were conjugated with FPBA.

3.8 General Synthetic Procedure of 1

Peptide **1** was synthesized by following the general procedure of automated Fmoc/^{t}Bu SPPS. Isoacyl-dipeptide Boc-Ser [Fmoc-Thr (^{t}Bu)]-OH was used to create the isoacyl linkage between ThrA8 and SerA9. After the entire sequence was completed on resin, on resin formation of A6-A11 disulfide bond was carried out by following the reported procedure (Liu et al., 2014). The resin was treated with 25% 2-mercaptoethanol in DMF (*v*/*v*, 6 ml) at room temperature for 1.5 h with gentle agitation. This step was repeated once. The resulting resin was washed with DMF 3 times and CH_2Cl_2 3 times. A solution of DTNP (310 mg, 1 mmol) in CH_2Cl_2 (6 ml) was added to the resin. The reaction mixture was gently agitated at room temperature for 1.0 h. The resin was washed with DMF 3 times and CH_2Cl_2 3 times. The resin was and treated with a solution of 1% TFA and 5% TIPS in CH_2Cl_2 (6 ml) for 2 min with 5 repeats. The resin was washed with DMF 3 times and CH_2Cl_2 3 times and gently agitated in CH_2Cl_2 (6 ml) at room temperature for 1 h. The resin was washed with CH_2Cl_2 3 times. The final peptide was cleaved by following the general procedure of peptide cleavage from resin. The crude was purified on Luna® 5 μm C18 100 Å (250 × 21 mm) column (Phenomenex, CA, United States) at 5 ml/min with a linear gradient from 30% to 50% of a H_2O/MeCN + 0.1% TFA solution over 30 min on an Agilent 1260 HPLC system detected at 220, 240, 260, and 280 nm. The fractions containing **1** were flash frozen under liquid N_2 and then lyophilized to give **1** as a white powder.

3.9 General Synthetic Procedure of 2

Peptide **2** was synthesized by following the general procedure of automated Fmoc/^{t}Bu SPPS. Fmoc-Lys (Dde)-OH was used for FPBA conjugation and Boc-Phe-OH was used for PheB1. After the entire sequence was completed on resin, Lys (Dde) was deprotected by following the general procedure of on resin Lys (Dde) deprotection and then FPBA was introduced by following the general procedure of on resin conjugation of FPBA to Lys. The final peptide was cleaved by following the general procedure of peptide cleavage from resin. The crude was purified on Luna® 5 μm C18 100 Å (250 × 21 mm) column (Phenomenex, CA, United States) at 5 ml/min with a linear gradient from 20% to 60% of a H_2O/MeCN + 0.1% TFA solution over 40 min on an Agilent 1260 HPLC system at 220, 240, 260, and 280 nm. The fractions containing **2** were flash frozen under liquid N_2 and then lyophilized to give **2** as a white powder.

3.10 General Synthetic Procedure of 3

The lyophilized A chain powder **1** (1.0 μmol) and the B chain powder **2** (1.0 μmol) were each dissolved in a solution of 6 M urea

and 0.2 M NH_4Cl (pH 5, 0.25 ml). The solutions of **1** and **2** were mixed with equal volumes (0.25 ml). The reaction mixture was gently mixed and left at room temperature for 4 h. The resulting solution was purified on Jupiter® 5 μm C18 300 Å (250 × 10 mm) column (Phenomenex, CA, United States) at 3 ml/min with a linear gradient from 10% to 60% of a H_2O/MeCN + 0.1% TFA solution over 50 min on an Agilent 1260 HPLC system detected at 220, 240, 260, and 280 nm. The fractions containing **3** were flash frozen under liquid N_2 and then lyophilized to give **3** as a white powder.

3.11 General Synthetic Procedure of 4

The lyophilized powder **3** (1.0 μmol) was dissolved in a solution of 20% AcOH in H_2O (*v*/*v*, 0.33 ml). A freshly prepared solution of I_2 (2.54 mg, 10 μmol) in AcOH (0.5 ml) was added into the solution of **3** at room temperature. The reaction mixture was gently agitated at room temperature for 10 min. The reaction was monitored by LC–MS to apply the additional amount of I_2 portionwise if required. After the reaction was completed, a solution of 1 M sodium ascorbate (0.3 ml) was added to the reaction mixture followed by gentle agitation until color of the solution turned to pale yellow. After added with a solution of 0.1% TFA in H_2O (1.5 ml), the reaction mixture was purified on Jupiter® 5 μm C18 300 Å (250 × 10 mm) column (Phenomenex, CA, United States) at 3 ml/min with a linear gradient from 10% to 60% of a H_2O/MeCN + 0.1% TFA solution over 50 min on an Agilent 1260 HPLC system detected at 220, 240, 260, and 280 nm. The fractions with resulting product were flash frozen under liquid N_2 and then lyophilized to give a white powder. The white powder was dissolved in 0.2 M NH_4HCO_3 (pH 8). The reaction mixture was gently agitated at room temperature for 30 min and then purified on Jupiter® 5 μm C18 300 Å (250 × 10 mm) column (Phenomenex, CA, United States) at 3 ml/min with a linear gradient from 10% to 60% of a H_2O/MeCN + 0.1% TFA solution over 50 min on an Agilent 1260 HPLC system detected at 220, 240, 260, and 280 nm. The fractions containing **4** were flash frozen under liquid N_2 and then lyophilized to give **4** as a white powder.

3.12 General Synthetic Procedure of 5

Peptide **5** was synthesized by following the general procedure of automated Fmoc/^{t}Bu SPPS. Isoacyl-dipeptide Boc-Ser [Fmoc-Thr (^{t}Bu)]-OH was used to create the isoacyl linkage between ThrA8 and SerA9. Fmoc-Lys(Alloc)-OH was used for FPBA conjugation and Boc-Gly-OH was used for GlyA1. After the entire sequence was completed on resin, Lys(Alloc) was deprotected by following the general procedure of on resin Lys(Alloc) deprotection and then FPBA was introduced by following the general procedure of on resin conjugation of FPBA to Lys. The final peptide was cleaved by following the general procedure of peptide cleavage from resin. The crude was purified on Luna® 5 μm C18 100 Å (250 × 21 mm) column (Phenomenex, CA, United States) at 5 ml/min with a linear gradient from 30% to 50% of a H_2O/MeCN + 0.1% TFA solution over 30 min on an Agilent 1260 HPLC system detected at 220, 240, 260, and 280 nm. The fractions containing **5** were flash frozen under liquid N_2 and then lyophilized to give **5** as a white powder.

3.13 General Synthetic Procedure of 6

Peptide **6** was synthesized by following the general procedure of automated Fmoc/^{t}Bu SPPS. If required, *N*-terminal acetylation was carried out by following the general procedure of on resin *N*-terminal acetylation. The final peptide was cleaved by following the general procedure of peptide cleavage from resin. The crude was purified on Luna® 5 μm C18 100 Å (250 × 21 mm) column (Phenomenex, CA, United States) at 5 ml/min with a linear gradient from 20% to 60% of a H_2O/MeCN + 0.1% TFA solution over 40 min on an Agilent 1260 HPLC system at 220, 240, 260, and 280 nm. The fractions containing **6** were flash frozen under liquid N_2 and then lyophilized to give **6** as a white powder.

3.14 General Synthetic Procedure of 7

The lyophilized A chain powder **5** (1.0 μmol) and the B chain powder **6** (1.0 μmol) were each dissolved in a solution of 6 M urea and 0.2 M NH_4Cl (pH 8, 0.25 ml). The solutions of **5** and **6** were mixed with equal volumes (0.25 ml). The reaction mixture was gently mixed and left at room temperature for 30 min. The resulting solution was purified on Jupiter® 5 μm C18 300 Å (250 × 10 mm) column (Phenomenex, CA, United States) at 3 ml/min with a linear gradient from 10% to 60% of a H_2O/MeCN + 0.1% TFA solution over 50 min on an Agilent 1260 HPLC system detected at 220, 240, 260, and 280 nm. The fractions containing **7** were flash frozen under liquid N_2 and then lyophilized to give **7** as a white powder.

3.15 General Synthetic Procedure of 8

The lyophilized powder **7** (1.0 μmol) was dissolved in a solution of 20% AcOH in H_2O (*v*/*v*, 0.33 ml). A freshly prepared solution of I_2 (2.54 mg, 10 μmol) in AcOH (0.5 ml) was added into the solution of **3** at room temperature. The reaction mixture was gently agitated at room temperature for 10 min. The reaction was monitored by LC–MS to apply the additional amount of I_2 portion wise if required. After the reaction was completed, a solution of 1 M sodium ascorbate (0.3 ml) was added to the reaction mixture followed by gentle agitation until color of the solution turned to pale yellow. After added with a solution of 0.1% TFA in H_2O (1.5 ml), the reaction mixture was purified on Jupiter® 5 μm C18 300 Å (250 × 10 mm) column (Phenomenex, CA, United States) at 3 ml/min with a linear gradient from 10% to 60% of a H_2O/MeCN + 0.1% TFA solution over 50 min on an Agilent 1260 HPLC system detected at 220, 240, 260, and 280 nm. The fractions containing **8** were flash frozen under liquid N_2 and then lyophilized to give **8** as a white powder.

3.16 Solubility Determination

Lyophilized insulin analogs were dissolved with Milli-Q water in 10 mg/mL as a stock solution. An equal ratio of insulin stock solution and 5× phosphate buffered saline (PBS) were mixed. Then, pH of the mixture was adjusted by 100 and 10 mM NaOH solution to 7.4, the glucose solution (2,000 mg/dl) was added to

target different final concentrations (0, 100, 200, 400 mg/dl), and the mixture was finally diluted to 1× PBS. The mixtures were gently shaken at room temperature for 2 h and then centrifuged under 20,000 ×g for 10 min. Saturated peptide concentrations of supernatants were determined by the measurements of absorption at 280 nm with NanoDrop One (Thermo Fisher Scientific) and the calculated extinction coefficient at 280 nm (ε_{280}). ε_{280} = (number of Trp × 5,500) + (number of Tyr × 1490) + (number of Cystine × 125) + (number of FPBA × 745).

3.17 Cell-Based pAKT (Ser473) Assay

The bioactivities of insulin analogs were measured through cell-based pAKT (Ser473) assay. pAKT levels were measured in a human insulin receptor-B overexpressed R^- NIH 3T3-like cell line, derived from IGF-1R knockout mice (a generous gift from A. Morrione, Thomas Jefferson University). Cells were cultured in DMEM (Sigma Aldrich) with 10% fetal bovine serum (FBS, Gibco), 100 U/ml penicillin-streptomycin (Thermo Fisher Scientific) and 2 mg/ml puromycin (Thermo Fisher Scientific) at 37 °C under 5% CO_2. For each assay, 40,000 cells per well and 100 µl per well, were plated in a 96-well plate with culture media containing 1% FBS. 20 h later, the media was removed followed by adding 50 µl of culture media with different concentrations of recombinant human insulin or insulin analogs into each well. After 30-min at 37°C, the insulin solution was removed and the HTRF pAKT Ser473 kit (Cisbio, MA, United States) was used to measure the intracellular level of pAKT Ser473 by following the manufacturer's protocol. Briefly, cells were first treated with cell lysis buffer (50 µl per well) for 1 h under mild shaking. 16 µl of cell lysate was then added to 4 µl of detecting reagent in a white 384-well plate. After 4-h incubation, the plate was read in a Synergy Neo plate reader (BioTek, VT, United States) or SpectraMax iD5 (Molecular Devices, CA, United States). Each data point was sampled from four replicates. Data were processed according to the manufacturer's protocol. EC_{50} was calculated by Prism 9 (GraphPad Software, CA, United States) with nonlinear regression curve fitting of dose-response asymmetric equation.

DATA AVAILABILITY STATEMENT

The raw data supporting the conclusion of this article will be made available by the authors, without undue reservation.

AUTHOR CONTRIBUTIONS

N-PL performed part of the synthesis, performed the solubility assay, analyzed the data, and wrote the manuscript. NZ performed part of the synthesis. LP performed part of the synthesis. YZ performed the cell-based activity assay. DH-CC conceived and supervised the project.

SUPPLEMENTARY MATERIAL

The Supplementary Material for this article can be found online at: https://www.frontiersin.org/articles/10.3389/fchem.2022.859133/full#supplementary-material

REFERENCES

Ahorukomeye, P., Disotuar, M. M., Gajewiak, J., Karanth, S., Watkins, M., Robinson, S. D., et al. (2019). Fish-Hunting Cone Snail Venoms Are a Rich Source of Minimized Ligands of the Vertebrate Insulin Receptor. *ELife* 8, e41574. doi:10.7554/eLife.41574

Bakh, N. A., Cortinas, A. B., Weiss, M. A., Langer, R. S., Anderson, D. G., Gu, Z., et al. (2017). Glucose-Responsive Insulin by Molecular and Physical Design. *Nat. Chem* 9, 937–944. doi:10.1038/nchem.2857

Berenson, D. F., Weiss, A. R., Wan, Z.-L., and Weiss, M. A. (2011). Insulin Analogs for the Treatment of Diabetes Mellitus: Therapeutic Applications of Protein Engineering. *Ann. N.Y Acad. Sci.* 1243, E40–E54. doi:10.1111/j.1749-6632.2012.06468.x

Brownlee, M., and Cerami, A. (1979). A Glucose-Controlled Insulin-Delivery System: Semisynthetic Insulin Bound to Lectin. *Science* 206, 1190–1191. doi:10.1126/science.505005

Chen, Y.-S., Gleaton, J., Yang, Y., Dhayalan, B., Phillips, N. B., Liu, Y., et al. (2021). Insertion of a Synthetic Switch into Insulin Provides Metabolite-dependent Regulation of Hormone-Receptor Activation. *Proc. Natl. Acad. Sci. USA* 118, e2103518118. doi:10.1073/pnas.2103518118

Chou, D. H.-C., Webber, M. J., Tang, B. C., Lin, A. B., Thapa, L. S., Deng, D., et al. (2015). Glucose-Responsive Insulin Activity by Covalent Modification with Aliphatic Phenylboronic Acid Conjugates. *Proc. Natl. Acad. Sci. USA* 112, 2401–2406. doi:10.1073/pnas.1424684112

DeWitt, D. E., and Hirsch, I. B. (2003). Outpatient Insulin Therapy in Type 1 and Type 2 Diabetes Mellitus. *JAMA* 289, 2254–2264. doi:10.1001/jama.289.17.2254

Disotuar, M. M., Chen, D., Lin, N.-P., and Chou, D. H.-C. (2020). Glucose-Responsive Insulin through Bioconjugation Approaches. *J. Diabetes Sci. Technol.* 14, 198–203. doi:10.1177/1932296819854105

Disotuar, M. M., Smith, J. A., Li, J., Alam, S., Lin, N.-P., and Chou, D. H.-C. (2021). Facile Synthesis of Insulin Fusion Derivatives through Sortase A Ligation. *Acta Pharm. Sin. B* 11, 2719–2725. doi:10.1016/j.apsb.2020.11.011

Edgerton, D. S., Moore, M. C., Winnick, J. J., Scott, M., Farmer, B., Naver, H., et al. (2014). Changes in Glucose and Fat Metabolism in Response to the Administration of a Hepato-Preferential Insulin Analog. *Diabetes* 63, 3946–3954. doi:10.2337/db14-0266

Edgerton, D. S., Scott, M., Farmer, B., Williams, P. E., Madsen, P., Kjeldsen, T., et al. (2019). Targeting Insulin to the Liver Corrects Defects in Glucose Metabolism Caused by Peripheral Insulin Delivery. *JCI Insight* 4, e126974. doi:10.1172/jci.insight.126974

Frier, B. M. (2014). Hypoglycaemia in Diabetes Mellitus: Epidemiology and Clinical Implications. *Nat. Rev. Endocrinol.* 10, 711–722. doi:10.1038/nrendo.2014.170

Furikado, Y., Nagahata, T., Okamoto, T., Sugaya, T., Iwatsuki, S., Inamo, M., et al. (2014). Universal Reaction Mechanism of Boronic Acids with Diols in Aqueous Solution: Kinetics and the Basic Concept of a Conditional Formation Constant. *Chem. Eur. J.* 20, 13194–13202. doi:10.1002/chem.201403719

Hoeg-Jensen, T., Havelund, S., Nielsen, P. K., and Markussen, J. (2005a). Reversible Insulin Self-Assembly under Carbohydrate Control. *J. Am. Chem. Soc.* 127, 6158–6159. doi:10.1021/ja051038k

Hoeg-Jensen, T., Ridderberg, S., Havelund, S., Schäffer, L., Balschmidt, P., Jonassen, I., et al. (2005b). Insulins with Built-In Glucose Sensors for Glucose Responsive Insulin Release. *J. Pept. Sci.* 11, 339–346. doi:10.1002/psc.624

Jarosinski, M. A., Dhayalan, B., Rege, N., Chatterjee, D., and Weiss, M. A. (2021). 'Smart' Insulin-Delivery Technologies and Intrinsic Glucose-Responsive Insulin Analogues. *Diabetologia* 64, 1016–1029. doi:10.1007/s00125-021-05422-6

Kaarsholm, N. C., Lin, S., Yan, L., Kelly, T., van Heek, M., Mu, J., et al. (2018). Engineering Glucose Responsiveness into Insulin. *Diabetes* 67, 299–308. doi:10.2337/db17-0577

Kohn, W. D., Micanovic, R., Myers, S. L., Vick, A. M., Kahl, S. D., Zhang, L., et al. (2007). PI-shifted Insulin Analogs with Extended *In Vivo* Time Action and Favorable Receptor Selectivity. *Peptides* 28, 935–948. doi:10.1016/j.peptides.2007.01.012

Kristensen, C., Kjeldsen, T., Wiberg, F. C., Schäffer, L., Hach, M., Havelund, S., et al. (1997). Alanine Scanning Mutagenesis of Insulin. *J. Biol. Chem.* 272, 12978–12983. doi:10.1074/jbc.272.20.12978

Liu, F., Luo, E. Y., Flora, D. B., and Mayer, J. P. (2013). Concise Synthetic Routes to Human Insulin. *Org. Lett.* 15, 960–963. doi:10.1021/ol400149j

Liu, F., Luo, E. Y., Flora, D. B., and Mezo, A. R. (2014). A Synthetic Route to Human Insulin Using Isoacyl Peptides. *Angew. Chem. Int. Ed.* 53, 3983–3987. doi:10.1002/anie.201310735

Mannerstedt, K., Mishra, N. K., Engholm, E., Lundh, M., Madsen, C. S., Pedersen, P. J., et al. (2021). An Aldehyde Responsive, Cleavable Linker for Glucose Responsive Insulins. *Chem. Eur. J.* 27, 3166–3176. doi:10.1002/chem.202004878

McCoy, R. G., Van Houten, H. K., Ziegenfuss, J. Y., Shah, N. D., Wermers, R. A., and Smith, S. A. (2012). Increased Mortality of Patients with Diabetes Reporting Severe Hypoglycemia. *Diabetes Care* 35, 1897–1901. doi:10.2337/dc11-2054

Peyrot, M., Barnett, A. H., Meneghini, L. F., and Schumm-Draeger, P. M. (2012). Insulin Adherence Behaviours and Barriers in the Multinational Global Attitudes of Patients and Physicians in Insulin Therapy Study. *Diabetic Med.* 29, 682–689. doi:10.1111/j.1464-5491.2012.03605.x

Qiu, Y., Agrawal, R., Chen, D., Zheng, N., Durupt, G., Kim, J. H., et al. (2019). Long-Lasting Designer Insulin with Glucose-Dependent Solubility Markedly Reduces Risk of Hypoglycemia. *Adv. Therap.* 2, 1900128. doi:10.1002/adtp.201900128

Rege, N. K., Phillips, N. F. B., and Weiss, M. A. (2017). Development of Glucose-Responsive 'smart' Insulin Systems. *Curr. Opin. Endocrinol. Diabetes Obes.* 24, 267–278. doi:10.1097/MED.0000000000000345

Veiseh, O., Tang, B. C., Whitehead, K. A., Anderson, D. G., and Langer, R. (2015). Managing Diabetes with Nanomedicine: Challenges and Opportunities. *Nat. Rev. Drug Discov.* 14, 45–57. doi:10.1038/nrd4477

Wang, C., Ye, Y., Sun, W., Yu, J., Wang, J., Lawrence, D. S., et al. (2017). Red Blood Cells for Glucose-Responsive Insulin Delivery. *Adv. Mater.* 29, 1606617. doi:10.1002/adma.201606617

Xiong, X., Blakely, A., Karra, P., VandenBerg, M. A., Ghabash, G., Whitby, F., et al. (2020). Novel Four-Disulfide Insulin Analog with High Aggregation Stability and Potency. *Chem. Sci.* 11, 195–200. doi:10.1039/C9SC04555D

Xiong, X., Blakely, A., Kim, J. H., Menting, J., Schafer, I., Schubert, H., et al. (2021). Visualization of Insulin Receptor Activation by a Novel Insulin Analog with Elongated A Chain and Truncated B Chain. doi:10.21203/rs.3.rs-501661/v1

Yan, J., Springsteen, G., Deeter, S., and Wang, B. (2004). The Relationship Among pKa, pH, and Binding Constants in the Interactions between Boronic Acids and Diols-It Is Not as Simple as it Appears. *Tetrahedron* 60, 11205–11209. doi:10.1016/j.tet.2004.08.051

Conflict of Interest: The authors declare that the research was conducted in the absence of any commercial or financial relationships that could be construed as a potential conflict of interest.

Publisher's Note: All claims expressed in this article are solely those of the authors and do not necessarily represent those of their affiliated organizations, or those of the publisher, the editors and the reviewers. Any product that may be evaluated in this article, or claim that may be made by its manufacturer, is not guaranteed or endorsed by the publisher.

frontiers | Frontiers in Chemistry

ORIGINAL RESEARCH
published: 04 May 2022
doi: 10.3389/fchem.2022.844598

Novel Starting Points for Human Glycolate Oxidase Inhibitors, Revealed by Crystallography-Based Fragment Screening

Sabrina R. Mackinnon[1†], Gustavo A. Bezerra[1], Tobias Krojer[1†], Tamas Szommer[1,2], Frank von Delft[1,3], Paul E. Brennan[1,2] and Wyatt W. Yue[1*†]*

[1]Centre for Medicines Discovery, Nuffield Department of Medicine, University of Oxford, Oxford, United Kingdom, [2]Target Discovery Institute, University of Oxford, Oxford, United Kingdom, [3]Diamond Light Source, Harwell Science and Innovation Campus, Didcot, United Kingdom

OPEN ACCESS

Edited by:
John D. Wade,
University of Melbourne, Australia

Reviewed by:
James Robert Ketudat Cairns,
Suranaree University of Technology, Thailand
Barbara Cellini,
University of Perugia, Italy

***Correspondence:**
Paul E. Brennan
paul.brennan@ndm.ox.ac.uk
Wyatt W. Yue
wyatt.yue@cmd.ox.ac.uk

†Present address:
Sabrina R. Mackinnon
Wyatt W. Yue
Biosciences Institute, Newcastle University, Newcastle, United Kingdom Tobias Krojer
MAX IV Laboratory, Lund University, Lund, Sweden

Specialty section:
This article was submitted to Chemical Biology, a section of the journal Frontiers in Chemistry

Received: 28 December 2021
Accepted: 18 March 2022
Published: 04 May 2022

Citation:
Mackinnon SR, Bezerra GA, Krojer T, Szommer T, von Delft F, Brennan PE and Yue WW (2022) Novel Starting Points for Human Glycolate Oxidase Inhibitors, Revealed by Crystallography-Based Fragment Screening. Front. Chem. 10:844598. doi: 10.3389/fchem.2022.844598

Primary hyperoxaluria type I (PH1) is caused by AGXT gene mutations that decrease the functional activity of alanine:glyoxylate aminotransferase. A build-up of the enzyme's substrate, glyoxylate, results in excessive deposition of calcium oxalate crystals in the renal tract, leading to debilitating renal failure. Oxidation of glycolate by glycolate oxidase (or hydroxy acid oxidase 1, HAO1) is a major cellular source of glyoxylate, and siRNA studies have shown phenotypic rescue of PH1 by the knockdown of HAO1, representing a promising inhibitor target. Here, we report the discovery and optimization of six low-molecular-weight fragments, identified by crystallography-based fragment screening, that bind to two different sites on the HAO1 structure: at the active site and an allosteric pocket above the active site. The active site fragments expand known scaffolds for substrate-mimetic inhibitors to include more chemically attractive molecules. The allosteric fragments represent the first report of non-orthosteric inhibition of any hydroxy acid oxidase and hold significant promise for improving inhibitor selectivity. The fragment hits were verified to bind and inhibit HAO1 in solution by fluorescence-based activity assay and surface plasmon resonance. Further optimization cycle by crystallography and biophysical assays have generated two hit compounds of micromolar (44 and 158 μM) potency that do not compete with the substrate and provide attractive starting points for the development of potent and selective HAO1 inhibitors.

Keywords: glycolate oxidase, glyoxylate metabolism, primary hyperoxaluria, fragment-based drug discovery, substrate reduction therapy

INTRODUCTION

Primary hyperoxalurias are inborn errors of glyoxylate metabolism in the liver (Cochat et al., 2012; Salido et al., 2012). The biochemical hallmark is over-accumulated glyoxylate, which is oxidized to oxalate and deposited as calcium oxalate crystals in renal tissues, leading to progressive renal damage. Once the kidney filtration rate is exceeded, systemic deposition of oxalate ensues causing life-threatening damage to bones, heart, and other tissues (Cochat et al., 2012). The most common and severe form of primary hyperoxaluria is type 1 (PH1, OMIM 259900) (Hopp et al., 2015) with an estimated prevalence of 1–3 per million population and an incidence of 1:100,000 live births in

Europe (Cochat et al., 1995; Kopp and Leumann 1995; van Woerden et al., 2003; Milliner et al., 2017). PH1 is caused by loss-of-function mutations in the *AGXT* gene (Danpure and Jennings 1986), encoding the PLP-dependent enzyme alanine: glycine aminotransferase (AGXT, EC 2.6.1.44) that catalyzes the transamination of glyoxylate and alanine to glycine and pyruvate in the hepatocyte peroxisome.

At present, the only definitive treatment is combined liver-kidney transplantation, since the liver is the source of oxalate, and the kidney is the first organ damaged by it. Organ transplantation entails considerable risks associated with long-term immunosuppression (Danpure 2005), limited organ availability, and increased morbidity and mortality (Harambat et al., 2012). Alternative therapies are needed, such as substrate reduction therapy, aimed at mitigating the toxic accumulation of metabolite(s) due to the defect by inhibiting an enzyme upstream of it (Yue, Mackinnon, and Bezerra 2019).

In the context of PH1, glycolate oxidase (hydroxy acid oxidase 1, HAO1, EC 1.1.3.15) has been proposed as a target for substrate reduction therapy. Accumulation of the substrate of HAO1 is benign as the accumulated glycolate is highly soluble and can be excreted freely. Similarly, there is no damaging deficit of metabolites downstream of HAO1 as sufficient levels of glycine and pyruvate can be obtained through other pathways. The safety of HAO1 inhibition is further supported by reports of asymptomatic loss-of-function *HAO1* mutations in humans (Frishberg et al., 2014; Narasimhan et al., 2016; McGregor et al., 2020). Proof-of-concept rescue by HAO1 inhibition was shown in mouse models of primary hyperoxaluria by genetic knockout (Martin-Higueras, Luis-Lima, and Salido 2016; Zabaleta et al., 2019), RNAi knockdown (Dutta et al., 2016; Li et al., 2016), and small-molecule inhibition (Martin-Higueras, Luis-Lima, and Salido 2016). RNAi targeting HAO1 has also been validated in a non-human primate model (Liebow et al., 2017) and recently approved for the treatment of PH1 patients (Frishberg et al., 2014; Frishberg et al., 2021; Scott and Keam 2021).

HAO1 is a flavin mononucleotide (FMN)-dependent enzyme that oxidizes α-hydroxy acids to the corresponding α-keto acids, with the concomitant reduction of molecular oxygen to H_2O_2. Human HAO1 (hHAO1) exhibits a broad substrate range from the two-carbon glycolate to the 16-carbon 2-hydroxypalmitate, with glycolate being the preferred substrate (Murray et al., 2008). The other human isozyme HAO2 (long-chain hydroxy acid oxidase, or LCHAO) oxidizes only long-chain aliphatic α-hydroxy acids (e.g., 2-hydroxypalmitate, 2-hydroxyoctanoate) *in vitro* (Jones, Morrell, and Gould 2000), but its physiological substrate is not known. The two isozymes share 50% sequence identity (**Supplementary Figure S1**). Two key features differentiate HAO1 from HAO2: the presence of tryptophan (Trp110 in hHAO1) coordinating the glycolate substrate and an inserted "gating loop" (hHAO1 aa169-212, sometimes referred to as loop 4 due to its position between beta-strand 4 and helix 4) predicted to shield the active site during catalysis (**Supplementary Figures S1, S2**). This gating loop is highly flexible, as demonstrated by the variable orientation and degree of disorder observed in crystal structures, and is poorly conserved (in both sequence and length) within the hydroxy acid oxidase family (**Supplementary Figure S2**) (Murray et al., 2008).

Several published inhibitors of hHAO1, largely based on a heterocyclic carboxylic acid chemotype, have been reported from structure-guided design (Stenberg and Lindqvist 1997; Jones, Morrell, and Gould 2000; Murray et al., 2008; Bourhis et al., 2009), *in silico* docking (Bourhis et al., 2009) and phenotypic screens (Wang et al., 2016), although so far none have proceeded to clinical studies. Given the limited diversity of these available starting points, we performed a crystallography-based fragment screen (Cox et al., 2016; Hoffer et al., 2018), to identify new scaffolds and, potentially, novel binding pockets for inhibitor development. We identified and optimized hits bound to a previously uncharacterized non-orthosteric pocket of hHAO1, resulting in hHAO1 inhibition at μM potency. These molecules are dissimilar in chemotype from previously published inhibitors and do not compete with the substrate glycolate.

MATERIALS AND METHODS

Chemicals

All fragments were purchased from Enamine. Follow-up compounds were purchased either from Enamine (active site compounds) or MolPort (gating loop site compounds).

Expression, and Purification of hHAO1

A hHAO1 construct, encoding residues Met1-Ser368, with an engineered N-terminal His6-tag subcloned into the pNIC28-Bsa4 vector (Mackinnon et al., 2018), was transformed into *E. coli* BL21 (DE3) cells. hHAO1 was cultured in auto-induction Terrific Broth (Fox and Blommel, 2009) for 6 h before incubation at 18°C for 40 h. Cell pellets were harvested, homogenized in lysis buffer (50 mM HEPES pH 7.5, 500 mM NaCl, 5% glycerol, 0.5 mM TCEP, 0.1 mM FMN), and centrifuged to remove insoluble material. The supernatant was purified by Nickel affinity (Thermo Fisher Scientific) followed by size exclusion (Superdex 200 Hi-Load 16/60, GE Healthcare) chromatography into crystallization buffer (50 mM HEPES pH 7.5, 500 mM NaCl, 5% glycerol, 0.5 mM TCEP). The purified protein was concentrated to 13.7 mg/ml by cycles of centrifugation (15 min, 4,000 rpm, 4°C) and mixing in a Vivaspin protein concentrator with a molecular weight cut-off of 30 kDa (GE Healthcare).

Crystallography-Based Fragment Screening

To launch the fragment soaking campaign, hundreds of crystals were grown by vapor diffusion at 4°C in 150 nL sitting drops of 13.7 mg/ml protein equilibrated against the well solution containing 25–35% PEG1000, sodium malonate-imidazole-boric acid (MIB) buffer, pH 8.0 (Mackinnon et al., 2018). For soaking, 50 nl of each fragment compound (~500 fragments from the DSi-Poised Library (Cox et al., 2016); from supersaturated stock solutions of 100–500 mM in d6-DMSO, resulting in a final concentration of 25–125 mM fragment) was added to a

crystallization drop using an ECHO acoustic liquid handler dispenser at the Diamond Light Source beamline I04-1 XChem facility. Crystals were soaked for 2 hours with fragments before being harvested using the SHIFTER technology, cryo-cooled in liquid nitrogen, and measured using the "automated unattended" mode of the I04-1 beamline. The XChemExplorer pipeline (Krojer et al., 2017) was used for structure solution with parallel molecular replacement using DIMPLE (Wojdyr et al., 2013), followed by map averaging and statistical modeling to identify weak electron densities generated from low occupancy fragments using PanDDA (Pearce et al., 2017). Model building and refinement were performed using the WinCoot and REFMAC software integrated into the XChemExplorer pipeline (Krojer et al., 2017). Figures were prepared using ICM-Pro software (Molsoft LLC). Coordinates and structure factors for all data sets with bound fragments are deposited in the RCSB Protein Data Bank. PanDDA electron density maps for HAO1 co-structures with fragments 1 - 6 are provided as Data Sheets 2 - 7 in **Supplementary Material**.

Amplex Red Activity Assay

hHAO1 activity *in vitro* was determined using the Amplex Red fluorescence hydrogen peroxide assay (Sigma Aldrich). The Amplex Red assay reagent contained horseradish peroxidase (EC 1.11.1.7, 0.2 U/ml) and its substrate Amplex Red (10-acetyl-3,7-dihydroxyphenoxazine, 100 μM) in assay buffer. The assay buffer contained 50 mM sodium phosphate, pH 7.4, 200 mM KCl, 2 mM $MgCl_2$, and 0.01% TritonX. Determination of suitable assay parameters is described in the **Supplementary Material**. To measure activity and inhibition of hHAO1, 10 μl/well of reaction containing 30 nM of hHAO1 and 30 μM glycolate in assay buffer was incubated with varying concentrations of fragment (1 and 10 mM) or follow-up compounds (0–1 mM, 12 concentrations), and dispensed into 384-well assay plates (Greiner®). Following 10 min incubation at room temperature, 10 μl/well of Amplex Red reagent was added. Fluorescence emission was measured at 585 nm, with excitation at 570 nm, after a further incubation period of 10 min, using a PHERAstar plate reader with a FI 540 590 optics module. All reactions were performed in technical triplicates for two different preparations of hHAO1. Reaction rate, defined as total H_2O_2 produced by the hHAO1 reaction, was determined from the H_2O_2 standard curve. Data were plotted using GraphPad Prism software; curve fitting was performed with nonlinear least-squares regression fit to log (inhibitor) vs response (three parameters) equation (for IC50 determination) and to mixed model, competitive, non-competitive, and uncompetitive inhibition models from the GraphPad Prism Enzyme kinetics–Inhibition equations and the best fit was selected for each ligand by comparison of Akaike's information criterion probability scores and extra sum-of-squares F test *p* values calculated by the software (for inhibition mode determination). An additional parameter calculated when fitting to enzyme kinetics–mixed model inhibition equation was the α value. This value is defined as the difference between the inhibition constant for the free enzyme (K_i) and the inhibition constant for the enzyme-substrate complex (αKi) and can be related to the initial velocity (V_0), substrate concentration ([S]), inhibitor concentration ([I]), and other kinetic parameters (K_m, V_{max}, K_i) as follows: $V_0 = V_{max}\,[S]/(K_m\,(1 + [I]/K_i) + [S](1 + [I]/(\alpha * K_i)))$. When an inhibitor binds with equal affinity to both the enzyme alone and the enzyme-substrate complex, $\alpha = 1$, indicating a non-competitive inhibition mode ($K_i = \alpha K_i$). When an inhibitor preferentially binds to the enzyme alone, $\alpha > 1$, with a very large value indicating an inhibition mode close to competitive inhibition (αK_i cannot be calculated for competitive inhibition as no binding to the enzyme-substrate complex occurs). When inhibitor preferentially binds to the enzyme-substrate complex, $\alpha < 1$, with a very small value indicating an inhibition mode close to uncompetitive inhibition (K_i for the free enzyme cannot be calculated for uncompetitive inhibition as no binding to the free enzyme occurs).

Surface Plasmon Resonance

Purified hHAO1 (30 μg/ml) was attached via the C-terminal His6-tag to a Ni-NTA chip to a density of 5000 RU. The assay buffer was 20 mM HEPES, pH 7.5, 0.05% TWEEN20, 200 mM NaCl, 0.5 mM TCEP, 5% DMSO. A serial dilution (11 concentrations) was prepared in the above buffer for each analyte (small molecule) by 1:1 dilution from 100 to 0.05 μM and the subsequent solutions were passed over the chip at a flow rate of 30 μL/min. Data are from an n = 1 experiment.

RESULTS

Three Fragments Identified by X-Ray Crystallography to Bind HAO1

We applied crystallography-based fragment screening to determine hHAO1 crystal structures with novel ligands bound (Bradley et al., 2017). Among the different constructs tested, hHAO1 Met1-Ser368 (last 2 amino acids truncated) readily yields reproducible crystals with consistent diffraction quality better than 2 Å. Pre-formed hHAO1 crystals were each soaked with an individual fragment from the DSi-Poised fragment library (Cox et al., 2016) and subjected to high throughput X-ray crystallography to identify bound fragments (**Supplementary Table S1**) (Krojer et al., 2017; Pearce et al., 2017). Over 400 structures were determined by automated molecular replacement and refinement (Krojer et al., 2017) to 1.2–2.2 Å resolution. Examination of SigmaA-weighted ($2mF_o$-F_c) electron density maps, with background correction, performed using multi-crystal isomorphous difference density maps (PanDDA method; Pearce et al., 2017) reveal two fragments bound at the active site (**1, 2**) and one fragment at the surface-exposed gating loop, ~12 Å from the active site (**3**) (**Figure 1**; ligand densities in $2F_o$-F_c maps before background (ground state) subtraction and

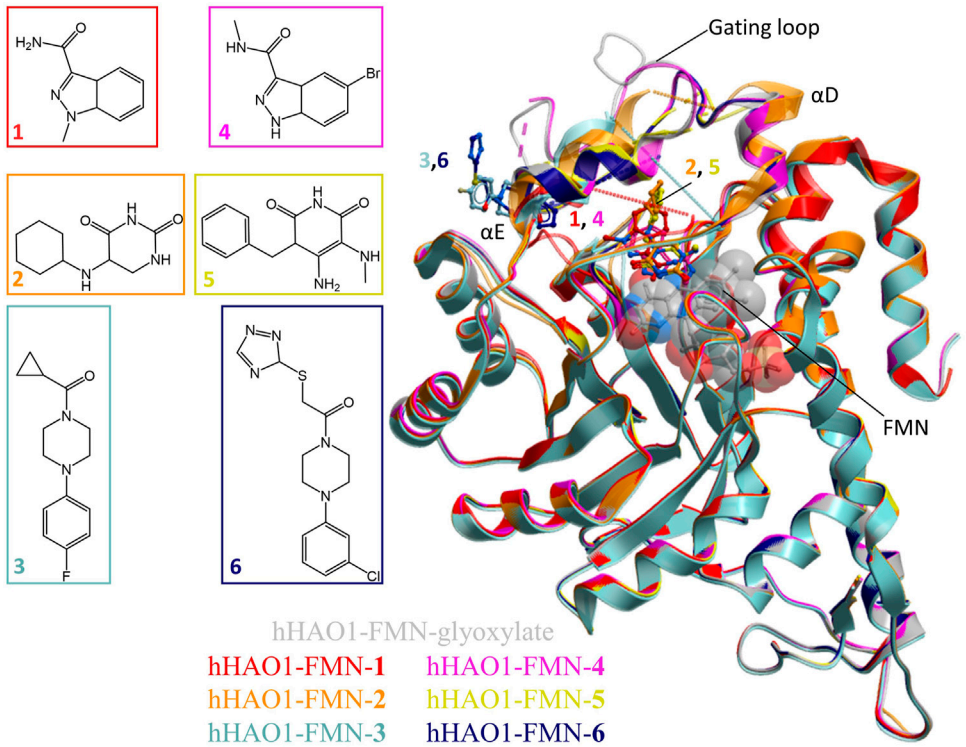

FIGURE 1 | Fragment screening by X-ray crystallography. Superimposition of fragment-bound HAO1 structures. All structures contained FMN, shown as spacefill and sticks. Protein structures are displayed as ribbons and colored in the same scheme as their bound fragments. Dotted lines in structures indicate disordered protein regions. Fragments are displayed as sticks, colored according to the same key. Inset: Chemical structures of fragments bound to HAO1.

$2mF_o$-F_c maps output from PanDDA are shown in **Supplementary Figure S3**). Each original chemotype was expanded by soaking with a structurally related fragment, yielding structures bound with a further two active site fragments (**4, 5**) and one gating loop fragment (**6**).

Active Site Fragments Replicate Known Inhibitor Binding Mode

The active site fragments **1**, **2**, **4**, and **5** occupy the glycolate binding site, stacking with the FMN co-factor (**Figure 2**). Fragments **1** and **4** have an indazole-carboxamide scaffold while fragments **2** and **5** have a 5-aryl-pyrimidine-2,4-dione scaffold. The overall fragment-bound structures are similar except for the region of the gating loop (**Figure 2A**). The variable conformation of the gating loop, as mentioned in the Introduction, is a characteristic feature of hHAO1 structures, observed across ligand-bound states, and reflects the flexibility of this region.

To contextualize the active site fragments, we first analyzed the binding modes of known HAO1 inhibitors, by comparing a 1.2 Å resolution structure of hHAO1 bound with 5-[(4-methylphenyl)sulfanyl]-1,2,3-thiadiazole-4-carboxylic acid (CCPST) determined in this study (PDB code 6gmc; **Supplementary Table S2** and **Figure S4**), with reported structures of triazole, dioxo-pyrroline, benzoic acid, and indazole carboxylic acid inhibitors bound to either spinach glycolate oxidase (sGOX; PDB codes 1al7 and 1al8; Stenberg and Lindqvist, 1997) or hHAO1 (**Supplementary Figure S5**; PDB codes 2rdt (Murray et al., 2008), 2w0u (Bourhis et al., 2009), 6w44, 6w45, 6w4c (Lee et al., 2021) and 7m2o (Ding et al., 2021)), sGOX-FMN-glyoxylate (PDB code 1gox; Lindqvist, 1989) and hHAO1-FMN-glycolate (PDB codes 2nzl (Mackinnon et al., 2018) and 6gmb, determined in this study). These inhibitor-bound structures all demonstrate similar features: displacement of residues lining the substrate-binding pocket (Tyr26, Trp110, Tyr132, Arg167, Arg263) relative to glycolate/glyoxylate-bound hHAO1 structures, interaction with residues involved in substrate turnover (Asp160, Lys236, His260), and disruption of the hydrogen bonding network posited to maintain gating loop conformation during catalysis (Trp110, Tyr134, Leu191, Tyr208; (Murray et al., 2008)) (**Supplementary Table S3** and **Figure S5**).

The active site fragments described in this work maintain similar binding modes to the reported inhibitors with respect to the heterocyclic polar head group that interacts with residues lining the substrate-binding pocket and causes rotation of the Trp110 sidechain outward from the active site, and the attached non-polar group that disrupts the hydrogen bonding network involved in maintaining gating loop conformation for catalysis (**Figure 2**).

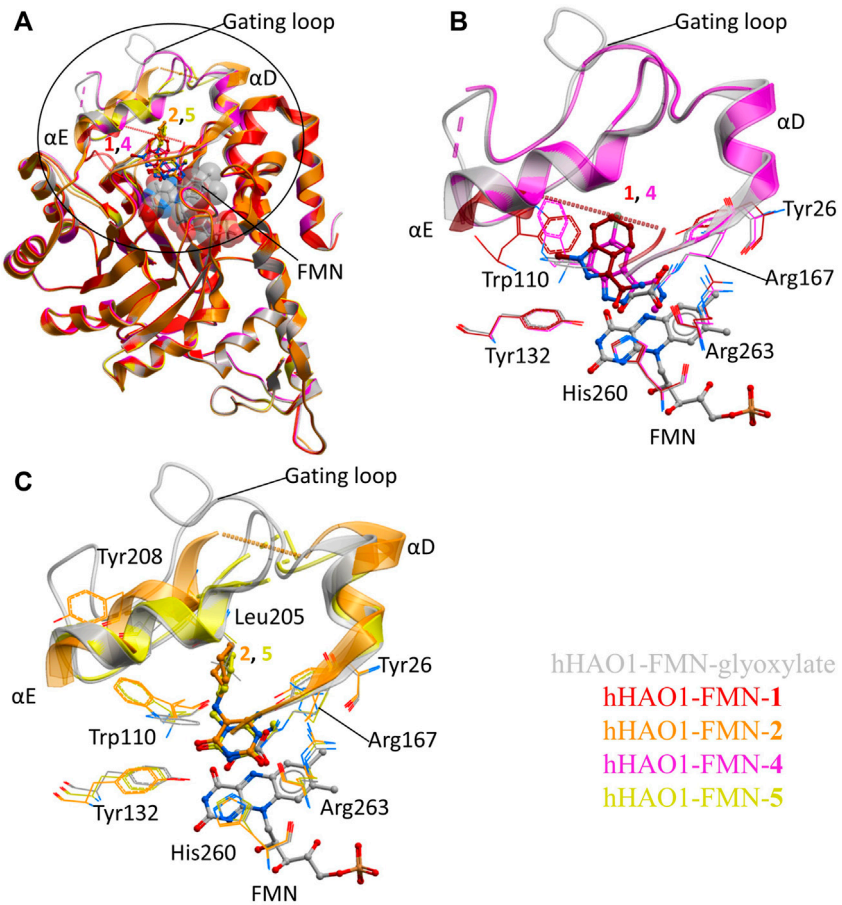

FIGURE 2 | Fragment hits binding to the active site of hHAO1. **(A)** Superimposed structures of fragment-bound HAO1 structures. All structures contained FMN, one copy of which is shown as spacefill. Structures with fragments **1**, **2**, **4**, and **5** are colored red, orange, pink, and yellow respectively. Fragments are displayed as sticks, colored according to the same key. **(B)** Close-up view, showing key structural features and residues involved in binding fragments **1** (red) and **4** (pink) relative to glyoxylate-bound structure (gray). **(C)** Close-up view, showing key structural features and residues involved in binding fragments **2** (orange) and **5** (yellow) relative to glyoxylate-bound structure (gray).

Fragment **1** is less embedded in the active site than the described indazole carboxylic acid inhibitors (**Supplementary Figure S5F**), likely binding less tightly but still causing significant displacement of Trp110 and interacting with His260 and Tyr132 via the carboxamide group (**Figure 2B**). The related, larger fragment, **4**, superimposes well with published indazole and triazole carboxylic acid inhibitors, such as 4-carboxy-5-dodecylsulfanyl-1,2,3-triazole (**Supplementary Figure S5C,F**), with the methyl-carboxamide group in place of the carboxylic acid. The methyl-carboxamide group of **4** interacts with the substrate-binding residues Tyr26, Arg167, and Arg263; the pyrazole nitrogen atoms hydrogen bond with His260 and Tyr132; and the bromo-phenyl group displaces Tyr110, causing it to rotate 180° out from the active site (**Figure 2B**).

Fragments **2** and **5** recapitulate the binding pose seen in the published structure of sGOX bound to a dioxo-pyrroline inhibitor (3-decyl-2,5-dioxo-4-hydroxy-3-pyrroline, TKP, PDB code 1al7, **Supplementary Figure S5E** (Stenberg and Lindqvist 1997)), coordinated by Tyr132, Arg167, His260 and Arg263 in the substrate-binding pocket (**Figure 2C**; **Supplementary Figure S5D**). Binding of **2** and **5** also causes the Trp110 sidechain to rotate 180° out from the active site as seen in other hHAO1-inhibitor complexes (**Figure 2C**). In both fragments, the hydrophobic group attached to the piperidine (cyclohexane in **2** and phenyl in **5**) makes few interactions but in fragment **2** it displaces Tyr208, further disrupting the hydrogen bonding network around the gating loop.

Collectively these four fragments represent embellishment to known inhibitor scaffolds that have not been explored, and we next aimed to characterize their utility as starting points for inhibitor development by characterizing them in solution.

Novel Non-orthosteric Binding Pocket at the Gating Loop

The two non-orthosteric fragments **3** and **6**, bound above the active site where the gating loop would otherwise be, contain a phenylpiperazine scaffold (**Figure 3A**). The phenylpiperazine moiety fits into a hydrophobic groove formed by the regions

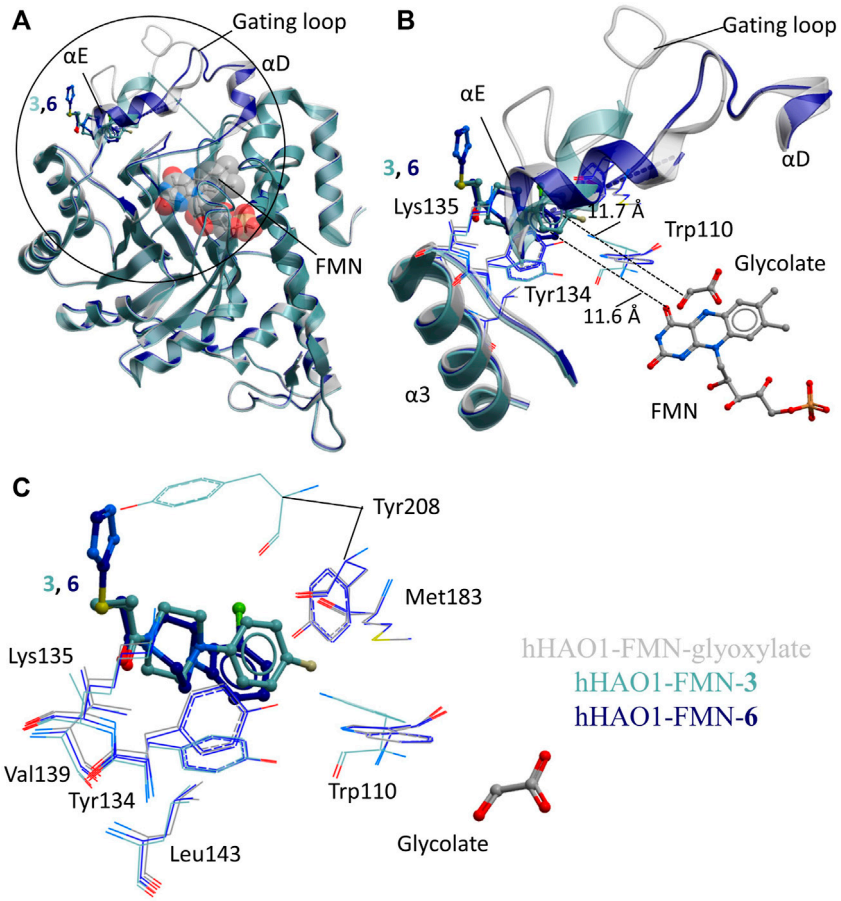

FIGURE 3 | Fragment hits binding to the gating loop site of hHAO1. **(A)** Superimposition of fragment-bound hHAO1 structures. FMN is shown as spacefill and sticks. Structures with fragments **3** and **6** are colored light and dark blue respectively. Fragments are displayed as sticks, colored according to the same key. **(B-C)** Close-up view of HAO1 gating loop site, circled in panel A, showing key structural features and residues involved in binding fragments **3** (light blue) and **6** (dark blue) relative to glyoxylate-bound structure (gray). (B) shows secondary structures forming the gating loop pocket as ribbons, key interacting residues as lines, and fragments, and FMN as sticks. The shortest distance from fragments to glyoxylate is indicated by dotted lines. **(C)** shows interacting residues that interact with fragments **3** and **6** as lines and glycolate and fragments are shown as sticks.

containing loop 3/helix α3 (aa131-150; Tyr134, Val139, Leu143) and gating loop (loop 4)/helix αE (aa171-213; Met183, Tyr208) (**Figure 3B**).

Binding of **3** causes small movements to the sidechain of Tyr134 in loop 3 to avoid clashing with the fluorophenyl group of the fragment. This disrupts the hydrogen bonding network between Tyr134, Trp110, Leu191, and Tyr208, causing additional minor displacement of the Trp110 sidechain (**Figure 3C**). Loss of these hydrogen bonds, combined with the position of the piperidine core in the space usually occupied by the gating loop, causes helix αE to shift so that Tyr208 is now mostly surface exposed and interacting with the fragment. The carbonyl group of **3** also hydrogen bonds with the backbone nitrogen of Lys135.

Binding of **6** also causes movement of the Tyr134 sidechain (both conformations are observed) and maintains the hydrogen bond with the backbone nitrogen of Lys135 but the sulfanyl-triazole extension prevents movement of Tyr208 to the location as seen with **3** and instead the piperazine ring is twisted slightly to avoid clashing (**Figure 3C**).

We next asked whether this gating loop pocket had been observed indirectly in structures of HAO1 (spinach or human) bound to active site inhibitors. We inspected structures of HAO1 bound to active site inhibitors that contained a secondary moiety, away from the heteroaryl-carboxylic acid, that could theoretically reach the gating loop pocket described in this work. Of the seven compounds that could occupy the gating loop pocket (**Supplementary Figure S6**), only one does so. This compound was reported as a dual lactate dehydrogenase (LDH)-HAO1 inhibitor (5-[(5'-{1-(4-carboxy-1,3-thiazol-2-yl)-5-(cyclopropylmethyl)-4-[(3-fluoro-4-sulfamoylphenyl)methyl]-1H-pyrazol-3-yl}-2′-fluoro [1,1′-biphenyl]-4-yl)oxy]-1H-1,2,3-triazole-4-carboxylic acid; PDB code 7m2o (Ding et al., 2021)), and the group occupying this pocket is the thiazole-carboxylic acid component of the LDH-targeting moiety (**Supplementary Figure S6C**).

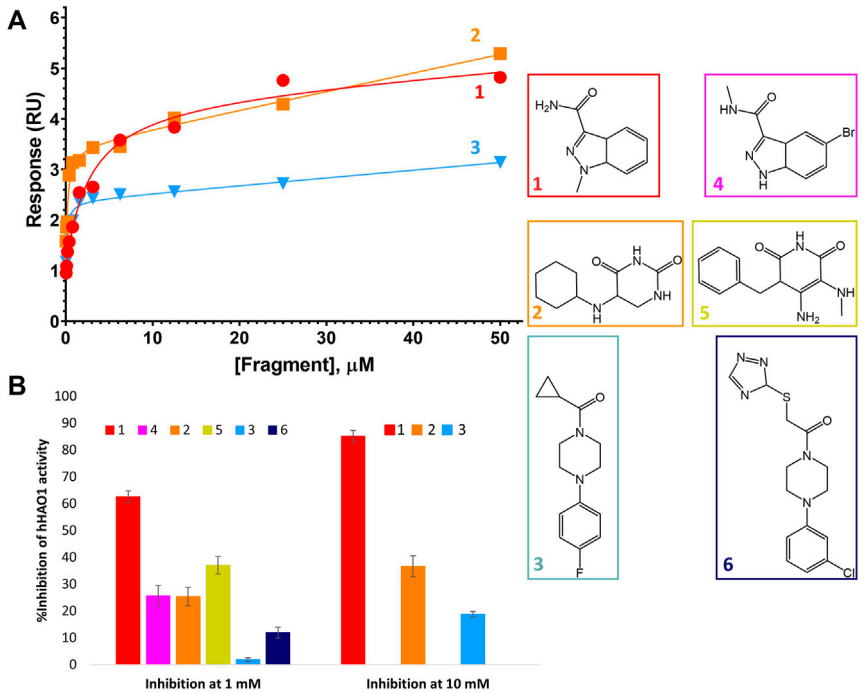

FIGURE 4 | Binding to and inhibition of hHAO1 by fragments. **(A)** Characterization of fragment binding to hHAO1 by surface plasmon resonance. Plot of relative response, in response units (RU), against fragment concentration. Response curves for fragments **1-3** are shown in red, orange, and blue respectively. **(B)** Bar chart showing the observed change in hHAO1 activity in the presence of 1 mM or 10 mM fragment, as measured in the Amplex Red activity assay. Change in activity is reported as %Inhibition. Errors bars are standard deviation of three replicates. *Inset:* Fragment chemical structures.

Fragment Characterization in Solution

After identification of six fragment hits *in crystallo*, we next characterized their binding and inhibition of hHAO1 in solution. We first determined the binding affinity of the control inhibitor CCPST for hHAO1, which has not previously been reported for any HAO enzyme, using surface plasmon resonance (SPR). We immobilized His-tagged hHAO1 to an Ni-NTA coated SPR chip and passed increasing concentrations (0–100 μM, 11 concentrations) of CCPST across it at a flow rate of 30 μl/min. Using this method, we measured a K_D of 47.5 μM for CCPST (**Supplementary Figure S7**), in line with the observed potency, validating our set-up for measuring the affinity of novel fragments and compounds. Here we find that the three original fragments (**1**–**3**) demonstrated measurable, specific binding to hHAO1 in solution at concentrations from 15 to 50 μM, though the binding was too weak to determine K_D values (**Figure 4A**).

We next measured enzyme activity of our hHAO1 preparation, as well as inhibition by CCPST and potentially our fragment hits, using the previously established horseradish peroxidase-coupled assay employing an Amplex Red reporter system (Wang et al., 2016, **Supplementary Figure S8A**). After establishing the incubation period and linear assay window for the reaction (**Supplementary Figure S8B,C**), hHAO1 activity was confirmed by titrations with the favored substrate glycolate (calculated K_m of 18.5 μM; **Supplementary Figure S8D**) and the alternate substrate 2-hydroxypalmitate (100-fold higher K_m; **Supplementary Figure S8E**).

HAO inhibition by CCPST has previously been reported for purified mGO (IC_{50} 43–198 μM) (Martin-Higueras, Luis-Lima, and Salido 2016; Moya-Garzón et al., 2018), rat LCHAO (equivalent to hHAO2) (IC_{50} 3.6 μM), flavin dehydrogenase domain of yeast flavocytochrome b2 (IC_{50} 6 μM), and hHAO1 (IC_{50} 4.5 μM) (Chen et al., 2012). However, puzzlingly, published kinetics of CCPST inhibition against these targets report a non-competitive inhibition mode (Chen et al., 2012; Martin-Higueras, Luis-Lima, and Salido 2016), which would indicate non-orthosteric binding, contradicting the active site binding observed in the three published HAO-CCPST structures (PDB codes 3sgz, 2w0u, and 6gmc). Inhibition of hHAO1 by CCPST observed in this work is consistent with these published values, with an average IC_{50} value of 22 ± 9 μM across three preparations of hHAO1 (**Supplementary Figure S9A**). In this work, we definitively observed a competitive inhibition mode (**Supplementary Figure S9B**), consistent with the orthosteric binding expected from the crystal structures.

We then measured inhibition of hHAO1 activity by the fragments (**Figure 4B**), showing that the active site fragment **1** had an IC_{50} of 420 μM whereas the remaining active site fragments, **2**, **4**, and **5**, demonstrated 10, 26, and 37% inhibition respectively at 1 mM. The loop site fragments **3** and **6** showed 2% and 12% inhibition respectively at 1 mM, with fragment **3** showing 19% inhibition at 10 mM.

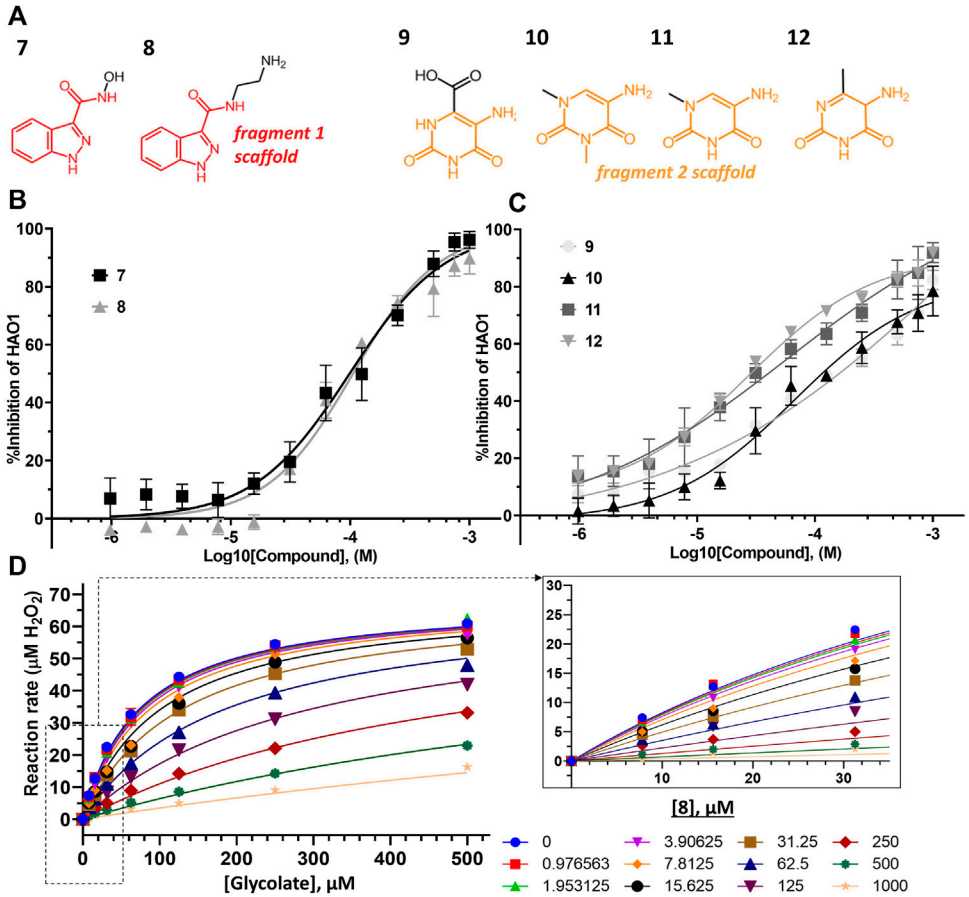

FIGURE 5 | Binding to and inhibition of hHAO1 by follow-up compounds from the active site. **(A)** Chemical structures of follow-up compounds derived from active site fragments. Fragment **1** scaffold is colored red, and fragment **2** scaffold is colored orange. **(B)** Concentration-response curve for inhibition of hHAO1 by compounds **7** and **8** measured in the Amplex Red activity assay at 30 μM glycolate. Error bars are standard deviation of three replicates. **(C)** Concentration-response curve for inhibition of hHAO1 by compounds **9–12** measured in the Amplex Red activity assay at 30 μM glycolate. Error bars are standard deviation of three replicates. **(D)** Least-squares nonlinear fit of hHAO1 reaction rate (total H_2O_2 produced after 15 min reaction, μM) against increasing glycolate concentrations (0–500 μM) in the presence of different concentrations of compound **8** (0–1 mM). Curves were fitted to the competitive inhibition model, the best fitting Enzyme kinetics–Inhibition equation, in GraphPad Prism. Inset: Close-up view of plot showing hHAO1 reaction rate (total H_2O_2 produced after 15 min reaction, μM) against increasing glycolate concentrations (0–35 μM) in the presence of different concentrations of compound **8** (0–1 mM).

The above-observed binding and inhibitor effects prompted us to perform one round of optimization to improve fragment potency. Of the different approaches described to optimize fragment hits (Joseph-McCarthy et al., 2014), we adopted the approach of fragment growing, in the absence of groups of nearby fragments suited to the alternative fragment linking or merging approaches.

Optimizing Active Site Fragments Into μM Potency Inhibitors

For fragments binding at the active site, we purchased 40 follow-up compounds from the Enamine Building Blocks commercial library, aiming to explore subtle changes to the two fragment scaffolds. We focused on ring additions at different positions of the fragment **1** scaffold and substitution of the cyclohexane (that showed no interaction with the protein) for the fragment **2** scaffold. Compounds were screened for inhibition of hHAO1 in the Amplex red assay at 1 mM concentration. Half-maximal inhibitory concentration (IC_{50}) and (Astex therapeutics lipophilic ligand efficiency score (LLE_{AT}; (Mortenson and Murray 2011)) values were determined for compounds showing good inhibition (chemical structures shown in **Figure 5A**).

Removal of the methyl group from the pyrazole and addition of a hydroxyl (compound **7**; IC_{50} 153 μM; LLE_{AT} 0.40 kcal/mol) or an amino-ethyl (compound **8**; IC_{50} 81 μM; LLE_{AT} 0.47 kcal/mol) to the carboxamide of fragment **1** provided a 5-fold increase in potency (**Figure 5B**; **Table 1**). Surprisingly, a huge increase in potency was observed relative to the fragment **2** scaffold by removing the cyclohexane and substituting the piperidine with methyl groups, yielding four compounds with IC_{50} < 100 μM and LLE_{AT} > 0.7 kcal/mol. Specifically, substitution of the piperidine with 6-carboxylate

TABLE 1 | Kinetic parameters for inhibition of hHAO1 by follow-up compounds 7–14.95% confidence intervals (CI) and best-fit values for IC_{50}, K_i and α were determined by fitting log [inhibitor] vs. response (%inhibition) curves. Best-fit values for IC_{50} are those reported in the text. Best-fit values for K_m and V_{max} were determined by individual fitting of Michaelis-Menten curves—[glycolate] vs. response (reaction rate, glycolate consumed)—in the presence and absence of 1 mM compound.

	95% CI IC_{50}, μM (Best-fit)	95% CI K_i, μM (Best-fit)	95% CI α (Best-fit)	K_m, μM, Best-fit		V_{max}, μM, Best-fit	
				None	1 mM	None	1 mM
Active site fragment **1** (indazole carboxamide)-derived compounds							
7	110.3–215.2 (152.9)	56.73–64.25 (60.37)	NA	64.62	811.2	62.16	47.76
8	57.1–117.1 (81.26)	37.72–44.32 (40.89)	NA	67.98	1,193	69.00	54.60
Active site fragment **2** (dioxo-pyrimidine)-derived compounds							
9	48.1–193.5 (93.35)	113.1–125.9 (119.4)	NA	63.65	572.3	57.40	56.25
10	39.5–92.0 (59.78)	157.4–177.2 (166.9)	NA	53.34	304.65	60.08	56.47
11	22.8–71.1 (39.77)	219.2–247.8 (233.0)	NA	48.89	270.1	55.07	55.85
12	19.9–38.0 (27.40)	141.4–155.9 (148.4)	NA	55.39	395.7	56.49	54.05
Gating loop fragment **3** (phenylpiperazine)-derived compounds							
13	27.4–71.4 (43.83)	59.07–82.92 (69.7)	7.84–27.32 (13.27)	61.73	279.1	67.02	27.28
14	100.5–255.7 (157.5)	83.06–118.7 (98.9)	9.41–59.28 (18.4)	70.70	349.7	73.49	43.12

(compound **9**; IC_{50} 93 μM; LLE_{AT} 0.71 kcal/mol), 1,3-dimethyl (compound **10**; IC_{50} 60 μM; LLE_{AT} 0.77 kcal/mol), 1-methyl (compound **11**; IC_{50} 40 μM; LLE_{AT} 0.88 kcal/mol), or 6-methyl (compound **12**; IC_{50} 27 μM; LLE_{AT} 0.89 kcal/mol) substituents result in a more than 10-fold increase in potency (**Figure 5C**; **Table 1**).

Next, we measured an array of compound concentrations (0–1 mM) versus glycolate concentrations (0–500 μM) to determine the inhibition mode of these improved compounds. As expected, all compounds derived from active site fragments demonstrate competitive inhibition mode with respect to glycolate, entirely consistent with their binding in the substrate-binding pocket (exemplified by **8**, **Figure 5D**; further data in **Supplementary Figure S10**).

Optimizing Gating Loop Site Fragments Into μM Potency Inhibitor

To generate analogs based on fragments at the gating loop site, we searched commercial catalogs through MolPort for compounds containing the scaffold of fragment **3** as a substructure, with the expectation that such compounds could improve affinity while maintaining binding at the gating loop pocket. Screening of these analogs using the Amplex Red activity assay, as described for the active site follow-up compounds, led to the identification of two promising hit compounds, **13** and **14**, with IC_{50} values of 44 μM and 158 μM and LLE_{AT} scores of 0.30 kcal/mol and 0.25 kcal/mol, respectively (**Figure 6A**).

We next investigated whether the inhibitory effect of compounds **13** and **14** was mediated by binding to the active site (akin to published inhibitors), or a non-orthosteric site (such as that revealed from the parent fragment's co-structure). Glycolate-titration experiments with compound **13** showed a concentration-dependent decrease in V_{max}, up to 2.8-fold reduction at 1 mM compound ($p < 0.0001$) and a concentration-dependent increase in K_m, up to 4-fold increase at 1 mM compound ($p < 0.0001$), collectively indicating mixed model inhibition with respect to glycolate by compound **13**, which is supported by fitting in GraphPad Prism (**Figure 6B**; **Table 1**). Similarly, glycolate-titration experiments with compound **14** showed a concentration-dependent reduction in V_{max}, up to 1.7-fold decrease at 1 mM compound ($p < 0.0001$) and a concentration-dependent increase in K_m, up to 4.9-fold increase at 1 mM compound ($p < 0.0001$), supporting mixed model inhibition, as observed when fitting in GraphPad Prism (**Figure 6C**; **Table 1**). Fitting of glycolate-titration curves for both compounds yield alpha (α) values (indicating the difference between binding to the enzyme alone (K_i) and binding to the enzyme-substrate complex (αK_i), see materials and methods for details) of 13 and 18 for compounds **13** and **14,** respectively, which indicates both compounds bind more readily in the absence of substrate (**Table 1**).

Therefore, our competition data indicate that compounds **13** and **14** can bind to either hHAO1-FMN or hHAO1-FMN-glycolate complex, with a preference for the holoenzyme ($\alpha > 1$), and in doing so reduce both substrate turnover (decreased V_{max}) and hHAO1 affinity for glycolate (increased K_m).

DISCUSSION

Inhibition of hHAO1 is a promising and recently validated approach for the treatment of primary hyperoxaluria. There is also potential to inhibit hHAO1 in the treatment of multifactorial kidney stone formation disorders as approximately 12% of the world population will suffer from kidney stone disease (urolithiasis) within their lifetime and 76% of these stones contain oxalate (Lowther, Holmes, and Yohannes 2017; Huang et al., 2020).

Currently, the only approved therapeutic modality for hHAO1 inhibition is RNAi. Existing small molecules in development include chemical series of pyrazole (Barawkar et al., 2012; Chen et al., 2012; Bourhis et al., 2009), triazole (Stenberg and Lindqvist 1997; Murray et al., 2008), or salicylate (Moya-Garzón

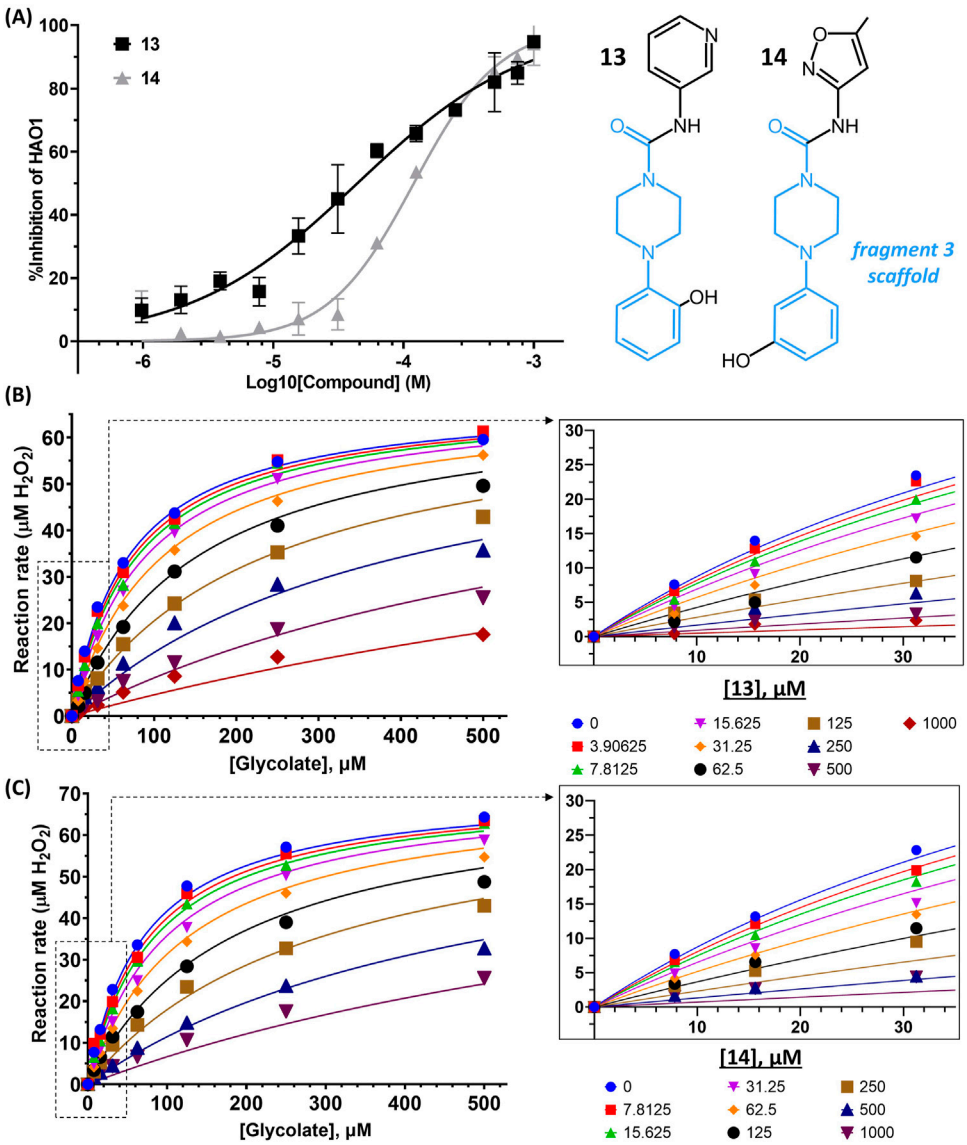

FIGURE 6 | Binding to and inhibition of hHAO1 by follow-up compounds from the gating loop site. **(A)** Concentration-response curve for inhibition of hHAO1 by compounds **13** and **14** measured in the Amplex Red activity assay at 30 μM glycolate. Error bars are standard deviation of three replicates. *Inset*: Chemical structures of compounds **13** and compound **14**, fragment **3** scaffold is in blue. **(B–C)** Least-squares nonlinear fit of hHAO1 reaction rate (total H_2O_2 produced after 15 min reaction, μM) against increasing glycolate concentrations (0–500 μM) in the presence of different concentrations of compound **13** (0–1 mM; B) or compound **14** (0–1 mM; C). Curves were fitted to mixed inhibition model, the best fitting Enzyme kinetics–Inhibition equation, in GraphPad Prism. Inset: Close-up view of plot showing HAO1 reaction rate (total H_2O_2 produced after 15 min reaction, μM) against increasing glycolate concentrations (0–35 μM) in the presence of different concentrations of compound **13** (0–1 mM; B) or compound **14** (0–1 mM; C).

et al., 2018) backbones and generally consist of a carboxylic acid like moiety mimicking the substrate carboxylic acid and one or more heterocyclic rings that pi stack with FMN (recently reviewed by (Moya-Garzon et al., 2021)).

Aside from the lack of diversity in these chemical series, their therapeutic use is limited by the metabolic instability, poor cell permeability, and cellular toxicity associated with carboxylic acid-containing drugs (Ballatore, Huryn, and Smith 2013), and consequently, no small-molecule inhibitor of hHAO1 has yet advanced to clinical trials in primary hyperoxaluria patients. Considering these limitations, we set out to identify new starting points for inhibitor development using fragment screening by X-ray crystallography. Our fragment screen identified two new active sites targeting scaffolds and a novel allosteric binding site with mid-micromolar affinity that hold promise for the development of selective and potent hHAO1 inhibitors.

Fragment **1** and its derivatives (**4**, **7**, **8**) are superficially similar to published pyrazole inhibitors in structure except that, instead

of a carboxylic acid, they contain a carboxamide (**1**), methyl-carboxamide (**4**), hydroxy-carboxamide (**7**), or aminoethyl-carboxamide (**8**) group as part of the polar head group and the hydrophobic moiety is a phenyl ring fused to the pyrazole. Exploration of similar rLCHAO inhibitors showed no activity upon similar modification of the pyrazole ring and a 5-fold reduction in potency with a carboxamide (Barawkar et al., 2012), which may explain why carboxamide derivatives of hHAO1 inhibitors have not previously been explored despite the potential improvements in metabolic stability, cellular toxicity and permeability relative to the current carboxylic acid-containing compounds (Ballatore, Huryn, and Smith 2013). This work, however, demonstrates carboxamide derivatives can serve as highly efficient starting points for hHAO1 inhibitor development.

Fragment **2** and its derivatives (**5**, **9–12**) are somewhat similar to published diketone scaffolds (Rooney et al., 1983; Stenberg and Lindqvist 1997) but piperidines rather than pyrroles. Fragments **2** and **5** validate the diketone N-substituted ring scaffold for inhibition of hHAO1. These results suggest that the published dioxo-pyrroles described as inhibitors of the plant (Stenberg and Lindqvist 1997), pig (Rooney et al., 1983), and rat (Rooney et al., 1983) HAO enzymes may also inhibit hHAO1 and could be used as starting points for therapeutic inhibitor development. It is interesting to note that the most potent compound of this set (**12**) had a 6-methyl substituent and potency was 3-fold lower with a carboxylic acid, the traditional HAO1 binding functional group, at this position (**9**). Further structural work will be needed to unravel the interactions made by these very small fragments to guide their optimization.

While these new compounds provide a much-needed increase in scaffold diversity of hHAO1 inhibitors, their orthosteric binding mode means that they are unlikely to be selective against hHAO2, which could be important to reduce toxicity associated with cross-reactivity (Mattu et al., 2016). Screening methods that are independent of enzymatic activity and known binding sites, such as X-ray crystallography, are useful in identifying less conserved pockets, to reduce the risk of poor target specificity often associated with active site inhibitors. Discovery of fragments **3** and **6**, which bind at the highly variable gating loop, validates this approach for hHAO1. Sequence alignment shows poor conservation of residues at this site between hHAO1 and hHAO2 (**Supplementary Figure S1**).

This gating loop pocket does not overlay with the hydrophobic portions of the described HAO inhibitors, but a small part of a recently published dual HAO1-LDH inhibitor does reach this pocket. This supports merging of a gating loop "selectivity" moiety to an active site "potency" moiety to generate the next generation of HAO1 inhibitors and suggests chemistry to direct groups from the active site to the gating loop. For example, the cyclopropyl group of fragment **3** could be joined to the nitrogen at position 1 of the central pyrazole of the described HAO1-LDH inhibitor and the extraneous substitutions on the central pyrazole removed (**Supplementary Figure S6**).

Collectively the two fragment-bound structures (**3**, **6**), combined with the enzyme kinetics of follow-up compounds (**13**, **14**), indicate a persistent, true allosteric site at the gating loop that is a novel target for developing hHAO1 inhibitors to treat primary hyperoxaluria. A more specific and thorough investigation optimizing compounds **13** and **14** would likely yield potent, selective lead candidates for the development of therapeutic hHAO1 inhibitors for primary hyperoxaluria, and as such these early compounds present considerable utility for developing molecules distinct in both chemical scaffold and mechanism of action from all previously known inhibitors.

DATA AVAILABILITY STATEMENT

The datasets presented in this study can be found in the Protein Data Bank (http://www.wwpdb.org). The accession numbers are 5qih, 5qib, 5qic, 7r4n, 7r4p, 7r4o, 6gmc.

AUTHOR CONTRIBUTIONS

WWY conceived the study. SRM performed experiments, analyzed data, prepared figures, and contributed to writing the manuscript. GAB, TK and TS contributed to data collection and analysis. FvD, PEB and WWY designed and supervised the experiments. All authors have contributed to the preparation of the manuscript.

FUNDING

The Structural Genomics Consortium, which the authors were part of, is a registered charity (Number 1097737) that receives funds from AbbVie, Bayer Pharma AG, Boehringer Ingelheim, Canada Foundation for Innovation, Eshelman Institute for Innovation, Genome Canada, Innovative Medicines Initiative (EU/EFPIA) (ULTRA-DD grant no. 115766), Janssen, Merck & Co., Novartis Pharma AG, Ontario Ministry of Economic Development and Innovation, Pfizer, São Paulo Research Foundation-FAPESP, Takeda, and Wellcome Trust (092809/Z/10/Z). SRM was supported by NDM Prize Studentship at the University of Oxford.

ACKNOWLEDGMENTS

We acknowledge Diamond Light Source for time on Beamline I04-1 and access to Lab 34 facilities under Proposal lb18145.

SUPPLEMENTARY MATERIAL

The Supplementary Material for this article can be found online at: https://www.frontiersin.org/articles/10.3389/fchem.2022.844598/full#supplementary-material

REFERENCES

Ballatore, C., Huryn, D. M., and Smith, A. B. (2013). Carboxylic Acid (Bio)Isosteres in Drug Design. *ChemMedChem* 8 (3), 385–395. doi:10.1002/cmdc.201200585

Barawkar, D. A., Bandyopadhyay, A., Deshpande, A., Koul, S., KandalkarPatil, S. P., Patil, P., et al. (2012). Discovery of Pyrazole Carboxylic Acids as Potent Inhibitors of Rat Long Chain L-2-Hydroxy Acid Oxidase. *Bioorg. Med. Chem. Lett.* 22 (13), 4341–4347. doi:10.1016/j.bmcl.2012.05.020

Bourhis, J.-M., Vignaud, C., Pietrancosta, N., Guéritte, F., Guénard, D., Lederer, F., et al. (2009). Structure of Human Glycolate Oxidase in Complex with the Inhibitor 4-Carboxy-5-[(4-Chlorophenyl)Sulfanyl]-1,2,3-Thiadiazole. *Acta Cryst. Sect. F* 65 (12), 1246–1253. doi:10.1107/S1744309109041670

Bradley, A. R., Echalier, A., Fairhead, M., Strain-Damerell, C., Brennan, P., Bullock, A. N., et al. (2017). The SGC beyond Structural Genomics: Redefining the Role of 3D Structures by Coupling Genomic Stratification with Fragment-Based Discovery. *Essays Biochem.* 61 (5), 495–503. doi:10.1042/EBC20170051

Chen, Z.-w., Vignaud, C., Jaafar, A., Lévy, B., Guéritte, F., Guénard, D., et al. (2012). High Resolution Crystal Structure of Rat Long Chain Hydroxy Acid Oxidase in Complex with the Inhibitor 4-Carboxy-5-[(4-Chlorophenyl)Sulfanyl]-1, 2, 3-Thiadiazole. Implications for Inhibitor Specificity and Drug Design. *Biochimie* 94 (5), 1172–1179. doi:10.1016/j.biochi.2012.02.003

Cochat, P., Deloraine, A., Rotily, M., Olive, F., Liponski, I., and Deries, N. (1995). "Epidemiology of Primary Hyperoxaluria Type 1," in *Nephrology Dialysis Transplantation* (Lyon, France: Nephrology, Dialysis, Transplantation: Official Publication of the European Dialysis and Transplant Association - European Renal Association), 10, 3–7. doi:10.1093/ndt/10.supp8.3

Cochat, P., Hulton, S.-A., Acquaviva, C., Danpure, C. J., Daudon, M., De Marchi, M., et al. (2012). "Primary Hyperoxaluria Type 1: Indications for Screening and Guidance for Diagnosis and Treatment," in *Nephrology Dialysis Transplantation* (Lyon, France: Official Publication of the European Dialysis and Transplant Association - European Renal Association), 27, 1729–1736. doi:10.1093/ndt/gfs078

Cox, O. B., Krojer, T., Collins, P., Monteiro, O., Talon, R., Bradley, A., et al. (2016). A Poised Fragment Library Enables Rapid Synthetic Expansion Yielding the First Reported Inhibitors of PHIP(2), an Atypical Bromodomain. *Chem. Sci.* 7 (3), 2322–2330. doi:10.1039/c5sc03115j

Danpure, C. J., and Jennings, P. R. (1986). Peroxisomal Alanine:Glyoxylate Aminotransferase Deficiency in Primary Hyperoxaluria Type I. *FEBS Lett.* 201 (1), 20–34. doi:10.1016/0014-5793(86)80563-4

Danpure, C. J. (2005). Primary Hyperoxaluria: From Gene Defects to Designer Drugs? *Nephrol. Dial. Transplant.* 20 (8), 1525–1529. doi:10.1093/ndt/gfh923

Ding, J., Gumpena, R., Boily, M.-O., Caron, A., Chong, O., Cox, J. H., et al. (2021). Dual Glycolate Oxidase/Lactate Dehydrogenase A Inhibitors for Primary Hyperoxaluria. *ACS Med. Chem. Lett.* 12 (7), 1116–1123. doi:10.1021/acsmedchemlett.1c00196

Dutta, C., Avitahl-Curtis, N., Pursell, N., Larsson Cohen, M., Holmes, B., Diwanji, R., et al. (2016). Inhibition of Glycolate Oxidase with Dicer-Substrate SiRNA Reduces Calcium Oxalate Deposition in a Mouse Model of Primary Hyperoxaluria Type 1. *Mol. Ther.* 24 (4), 770–778. doi:10.1038/mt.2016.4

Fox, B. G., and Blommel, P. G. (2009). Autoinduction of Protein Expression. *Curr. Protoc. Protein Sci.* 56. 523. doi:10.1002/0471140864.ps0523s56

Frishberg, Y., Deschênes, G., Groothoff, J. W., Hulton, S.-A., Magen, D., Harambat, J., et al. (2021). Phase 1/2 Study of Lumasiran for Treatment of Primary Hyperoxaluria Type 1. *Cjasn* 16 (7), 1025–1036. doi:10.2215/CJN.14730920

Frishberg, Y., Zeharia, A., Lyakhovetsky, R., Bargal, R., and Belostotsky, R. (2014). Mutations in *HAO1* encoding Glycolate Oxidase Cause Isolated Glycolic Aciduria. *J. Med. Genet.* 51 (8), 526–529. doi:10.1136/jmedgenet-2014-102529

Harambat, J., van Stralen, K. J., Espinosa, L., Groothoff, J. W., Hulton, S.-A., Cerkauskiene, R., et al. (2012). Characteristics and Outcomes of Children with Primary Oxalosis Requiring Renal Replacement Therapy. *Cjasn* 7 (3), 458–465. doi:10.2215/CJN.07430711

Hoffer, L., Voitovich, Y. V., Raux, B., Carrasco, K., Muller, C., Fedorov, A. Y., et al. (2018). Integrated Strategy for Lead Optimization Based on Fragment Growing: The Diversity-Oriented-Target-Focused-Synthesis Approach. *J. Med. Chem.* 61 (13), 5719–5732. doi:10.1021/acs.jmedchem.8b00653

Hopp, K., Cogal, A. G., Bergstralh, E. J., Seide, B. M., Olson, J. B., Meek, A. M., et al. (2015). Phenotype-Genotype Correlations and Estimated Carrier Frequencies of Primary Hyperoxaluria. *Jasn* 26 (10), 2559–2570. doi:10.1681/asn.2014070698

Huang, Y., Zhang, Y. H., Chi, Z. P., Huang, R., Huang, H., Liu, G., et al. (2020). The Handling of Oxalate in the Body and the Origin of Oxalate in Calcium Oxalate Stones. *Urol. Int.* 104 (3–4), 167–176. doi:10.1159/000504417

Jones, J. M., Morrell, J. C., and Gould, S. J. (2000). Identification and Characterization of HAOX1, HAOX2, and HAOX3, Three Human Peroxisomal 2-Hydroxy Acid Oxidases. *J. Biol. Chem.* 275 (17), 12590–12597. doi:10.1074/jbc.275.17.12590

Joseph-McCarthy, D., Campbell, A. J., Kern, G., and Moustakas, D. (2014). Fragment-Based Lead Discovery and Design. *J. Chem. Inf. Model.* 54, 693–704. American Chemical Society. doi:10.1021/ci400731w

Kopp, N., and Leumann, E. (1995). "Changing Pattern of Primary Hyperoxaluria in Switzerland," in *Nephrology, Dialysis, Transplantation* (Lyon, France: Official Publication of the European Dialysis and Transplant Association - European Renal Association), 10, 2224–2227. doi:10.1093/ndt/10.12.2224

Krojer, T., Talon, R., Pearce, N., Collins, P., Douangamath, A., Brandao-Neto, J., et al. (2017). The *XChemExplorer* graphical Workflow Tool for Routine or Large-Scale Protein-Ligand Structure Determination. *Acta Cryst. Sect. D Struct. Biol.* 73, 267–278. doi:10.1107/S2059798316020234

Lee, E. C. Y., McRiner, A. J., Georgiadis, K. E., Liu, J., Wang, Z., Ferguson, A. D., et al. (2021). Discovery of Novel, Potent Inhibitors of Hydroxy Acid Oxidase 1 (HAO1) Using DNA-Encoded Chemical Library Screening. *J. Med. Chem.* 64, 6730–6744. doi:10.1021/acs.jmedchem.0c02271

Li, X., Knight, J., Fargue, S., Buchalski, B., Guan, Z., Inscho, E. W., et al. (2016). Metabolism of 13C5-Hydroxyproline in Mouse Models of Primary Hyperoxaluria and its Inhibition by RNAi Therapeutics Targeting Liver Glycolate Oxidase and Hydroxyproline Dehydrogenase. *Biochim. Biophys. Acta (Bba) - Mol. Basis Dis.* 1862 (2), 233–239. doi:10.1016/j.bbadis.2015.12.001

Liebow, A., Li, X., Racie, T., Hettinger, J., Bettencourt, B. R., Najafian, N., et al. (2017). An Investigational RNAi Therapeutic Targeting Glycolate Oxidase Reduces Oxalate Production in Models of Primary Hyperoxaluria. *Jasn* 28 (2), 494–503. doi:10.1681/ASN.2016030338

Linsqvist, Y. (1989). Refined Structure of Spinach Glycolate Oxidase at 2 A Resolution. *J. Mol. Biol.* 209, 151–166. doi:10.1016/0022-2836(89)90178-2

Lowther, W. T., Holmes, R. P., and Yohannes, D. (2017). *Glycolate Oxidase Inhibitors and Methods of Use for the Treatment of Kidney Stones*. Available at: https://patentscope.wipo.int/search/en/detail.jsf?docId=WO2017100266.

Mackinnon, S., Bezerra, G. A., Krojer, T., Bradley, A. R., Talon, R., Brandao-Neto, J., et al. (2018). Human Hydroxyacid Oxidase (HAO1): A Target Enabling Package. *Zenodo*. doi:10.5281/zenodo.1342617

Martin-Higueras, C., Luis-Lima, S., and Salido, E. (2016). Glycolate Oxidase Is a Safe and Efficient Target for Substrate Reduction Therapy in a Mouse Model of Primary Hyperoxaluria Type I. *Mol. Ther.* 24 (4), 719–725. doi:10.1038/mt.2015.224

Mattu, S., Fornari, F., Quagliata, L., Perra, A., Angioni, M. M., Petrelli, A., et al. (2016). The Metabolic Gene HAO2 Is Downregulated in Hepatocellular Carcinoma and Predicts Metastasis and Poor Survival. *J. Hepatol.* 64 (4), 891–898. doi:10.1016/J.JHEP.2015.11.029

McGregor, T. L., Hunt, K. A., Yee, E., Mason, D., Nioi, P., Ticau, S., et al. (2020). Characterising a Healthy Adult with a Rare HAO1 Knockout to Support a Therapeutic Strategy for Primary Hyperoxaluria. *ELife* 9 (March), e54363. doi:10.7554/eLife.54363

Milliner, D. S., Harris, P. C., Sas, D. J., Cogal, A. G., and Lieske, J. C. (2017). Primary Hyperoxaluria Type I. In *Gene Reviews*. Editors M. P. Adam H. H. Ardinger, et al. (Seattle, WA: University of Washington, Seattle).

Mortenson, P. N., and Murray, C. W. (2011). Assessing the Lipophilicity of Fragments and Early Hits. *J. Comput. Aided Mol. Des.* 25 (7), 663–667. doi:10.1007/s10822-011-9435-z

Moya-Garzon, M. D., Gomez-Vidal, J. A., Alejo-Armijo, A., Altarejos, J., Rodriguez-Madoz, J. R., Fernandes, M. X., et al. (2021). Small Molecule-Based Enzyme Inhibitors in the Treatment of Primary Hyperoxalurias. *Jpm* 11, 74. doi:10.3390/jpm11020074

Moya-Garzón, M. D., Martín Higueras, C., Peñalver, P., Romera, M., Fernandes, M. X., Franco-Montalbán, F., et al. (2018). Salicylic Acid Derivatives Inhibit Oxalate Production in Mouse Hepatocytes with

Primary Hyperoxaluria Type 1. *J. Med. Chem.* 61 (16), 7144–7167. doi:10.1021/acs.jmedchem.8b00399

Murray, M. (2008). *Primary Hyperoxaluria and Kidney Stone Disease: Structural and Biochemical Analyses of Enzymes Involved in Glyoxylate Metabolism*. (NC): Wake Forest University. [PhD thesis] [Winston-Salem].

Murray, M. S., Holmes, R. P., and Lowther, W. T. (2008). Active Site and Loop 4 Movements within Human Glycolate Oxidase: Implications for Substrate Specificity and Drug Design. *Biochemistry* 47, 2439–2449. doi:10.1021/bi701710r

Narasimhan, V. M., Hunt, K. A., Mason, D., Baker, C. L., Karczewski, K. J., Barnes, M. R., et al. (2016). Health and Population Effects of Rare Gene Knockouts in Adult Humans with Related Parents. *Science* 352 (6284), 474–477. doi:10.1126/science.aac8624

Pearce, N. M., Krojer, T., Bradley, A. R., Collins, P., Nowak, R. P., Marsden, B. D., et al. (2017). A Multi-Crystal Method for Extracting Obscured Crystallographic States from Conventionally Uninterpretable Electron Density. *Nat. Commun.* 8, 15123. doi:10.1038/ncomms15123

Rooney, C. S., Randall, W. C., Streeter, K. B., Ziegler, C., Cragoe, E. J., Schwam, H., et al. (1983). Inhibitors of Glycolic Acid Oxidase. 4-Substituted 3-Hydroxy-1h-Pyrrole-2,5-Dione Derivatives. *J. Med. Chem.* 26 (5), 700–714. doi:10.1021/jm00359a015

Salido, E., PeyRodriguez, A. L. R., Rodriguez, R., and Lorenzo, V. (2012). Primary Hyperoxalurias: Disorders of Glyoxylate Detoxification. *Biochim. Biophys. Acta (Bba) - Mol. Basis Dis.* 1822 (9), 1453–1464. doi:10.1016/j.bbadis.2012.03.004

Scott, L. J., and Keam, S. J. (2021). Lumasiran: First Approval. *Drugs* 81, 277–282. doi:10.1007/s40265-020-01463-0

Stenberg, K., and Lindqvist, Y. (1997). Three-Dimensional Structures of Glycolate Oxidase with Bound Active-Site Inhibitors. *Protein Sci.* 6 (5), 1009–1015. doi:10.1002/pro.5560060506

Van Woerden, C. S., Groothoff, J. W., Wanders, R. J. A., Davin, J., and Wijburg, F. A. (2003). "Primary Hyperoxaluria Type 1 in The Netherlands: Prevalence and Outcome," in *Nephrology, Dialysis, Transplantation* (Lyon, France: Official Publication of the European Dialysis and Transplant Association - European Renal Association), 18, 273–279. doi:10.1093/ndt/18.2.273

Wang, M., Xu, M., Long, Y., Fargue, S., Southall, N., Hu, X., et al. (2016). High Throughput Cell-Based Assay for Identification of Glycolate Oxidase Inhibitors as a Potential Treatment for Primary Hyperoxaluria Type 1. *Sci. Rep.* 6 (1), 34060. doi:10.1038/srep34060

Wojdyr, M., Keegan, R., Winter, G., and Ashton, A. (2013). DIMPLE- a Pipeline for the Rapid Generation of Difference Maps from Protein Crystals with Putatively Bound Ligands. *Acta Cryst. Sect. A.* 69, A69–s299. doi:10.1107/S0108767313097419

Yue, W. W., Mackinnon, S., and Bezerra, G. A. (2019). Substrate Reduction Therapy for Inborn Errors of Metabolism. *Emerging Top. Life Sci.* 3 (February), 63. doi:10.1042/etls20180058

Zabaleta, N., Barberia, M., Martin-Higueras, C., Zapata-Linares, N., Betancor, I., Rodriguez, S., et al. (2018). CRISPR/Cas9-Mediated Glycolate Oxidase Disruption Is an Efficacious and Safe Treatment for Primary Hyperoxaluria Type I. *Nat. Commun.* 9, e7827. doi:10.1038/s41467-018-07827-1

Conflict of Interest: The authors declare that the research was conducted in the absence of any commercial or financial relationships that could be construed as a potential conflict of interest.

frontiers | Frontiers in Chemistry

REVIEW
published: 12 May 2022
doi: 10.3389/fchem.2022.886382

Deciphering the Structure and Formation of Amyloids in Neurodegenerative Diseases With Chemical Biology Tools

Isabelle Landrieu[1,2], *Elian Dupré*[1,2], *Davy Sinnaeve*[1,2], *Léa El Hajjar*[1,2] *and Caroline Smet-Nocca*[1,2]*

[1]University Lille, Inserm, CHU Lille, Institut Pasteur de Lille, U1167 - RID-AGE - Risk Factors and Molecular Determinants of Aging-Related Diseases, Lille, France, [2]CNRS EMR9002 Integrative Structural Biology, Lille, France

Protein aggregation into highly ordered, regularly repeated cross-β sheet structures called amyloid fibrils is closely associated to human disorders such as neurodegenerative diseases including Alzheimer's and Parkinson's diseases, or systemic diseases like type II diabetes. Yet, in some cases, such as the HET-s prion, amyloids have biological functions. High-resolution structures of amyloids fibrils from cryo-electron microscopy have very recently highlighted their ultrastructural organization and polymorphisms. However, the molecular mechanisms and the role of co-factors (posttranslational modifications, non-proteinaceous components and other proteins) acting on the fibril formation are still poorly understood. Whether amyloid fibrils play a toxic or protective role in the pathogenesis of neurodegenerative diseases remains to be elucidated. Furthermore, such aberrant protein-protein interactions challenge the search of small-molecule drugs or immunotherapy approaches targeting amyloid formation. In this review, we describe how chemical biology tools contribute to new insights on the mode of action of amyloidogenic proteins and peptides, defining their structural signature and aggregation pathways by capturing their molecular details and conformational heterogeneity. Challenging the imagination of scientists, this constantly expanding field provides crucial tools to unravel mechanistic detail of amyloid formation such as semisynthetic proteins and small-molecule sensors of conformational changes and/or aggregation. Protein engineering methods and bioorthogonal chemistry for the introduction of protein chemical modifications are additional fruitful strategies to tackle the challenge of understanding amyloid formation.

Keywords: amyloid fibril, aggregation, neurodegenerative diseases, protein semisynthesis, posttranslational modifications, native chemical ligation, fluorescent probes, nanobody

OPEN ACCESS

Edited by:
Matthew A. Coleman, Department of Radiation Oncology, School of Medicine, University of California, Davis, United States

Reviewed by:
Wai-Lung Ng, The Chinese University of Hong Kong, China
Son Tung Ngo, Ton Duc Thang University, Vietnam

***Correspondence:**
Caroline Smet-Nocca
caroline.smet-nocca@univ-lille.fr

Specialty section:
This article was submitted to Chemical Biology, a section of the journal Frontiers in Chemistry

Received: *28 February 2022*
Accepted: *20 April 2022*
Published: *12 May 2022*

Citation:
Landrieu I, Dupré E, Sinnaeve D, El Hajjar L and Smet-Nocca C (2022) Deciphering the Structure and Formation of Amyloids in Neurodegenerative Diseases With Chemical Biology Tools. Front. Chem. 10:886382. doi: 10.3389/fchem.2022.886382

1 INTRODUCTION

Amyloids correspond to amorphous deposits of insoluble proteinaceous materials that are found in a variety of body tissues and organs. Amyloidoses is a group of diseases associated with amyloid deposits, including localized amyloidoses such as many neurodegenerative disorders (NDs) or type-II diabetes mellitus, and systemic amyloidoses. Amyloidoses can be also defined as "protein misfolding diseases" since their molecular basis relies on misfolding as an early event in the

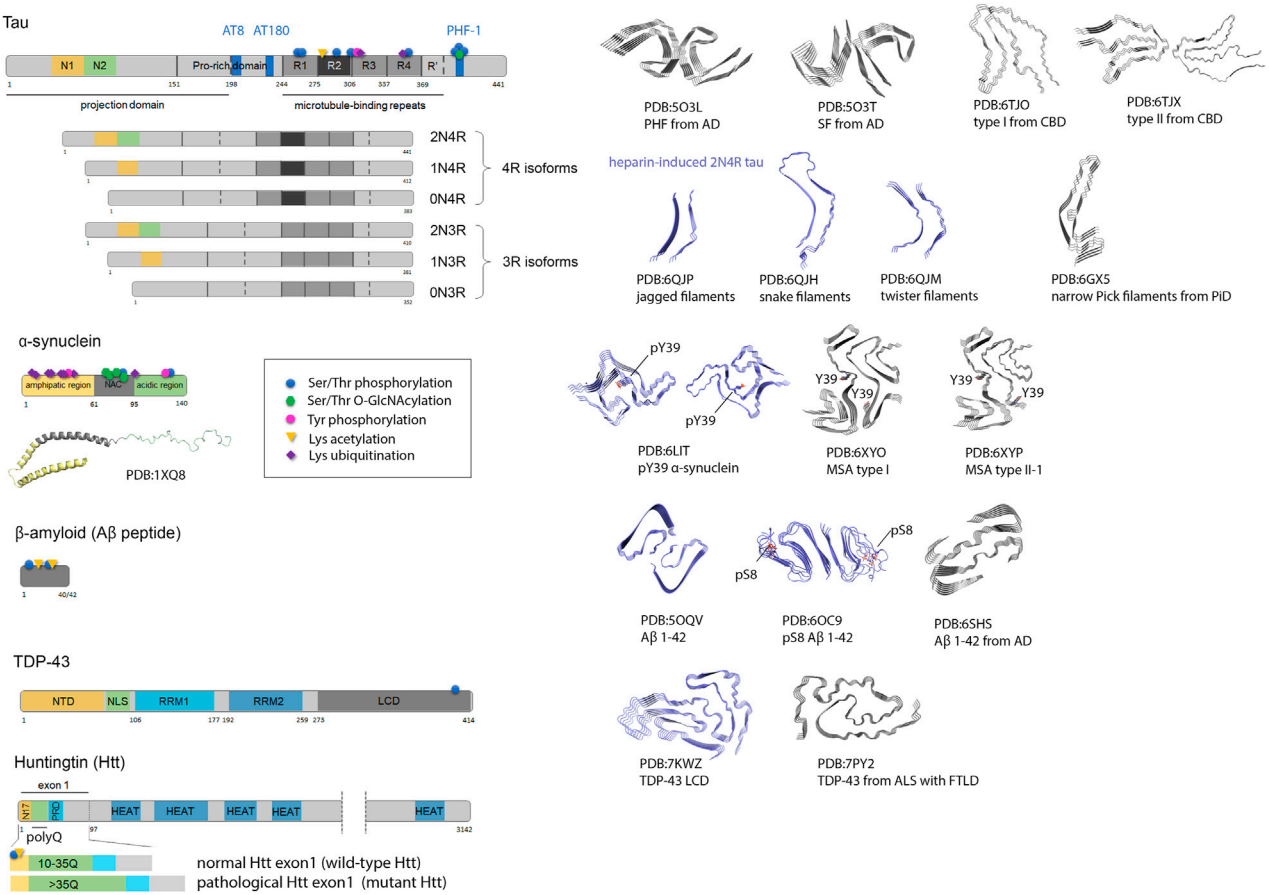

FIGURE 1 | Amyloid proteins involved in neurodegenerative diseases (tau, Aβ, α-synuclein, TDP-43 and Huntingtin), and their amyloid folds and polymorphs. Scheme of protein sequences highlighting domains, and eventually isoforms are presented (left). For tau protein, some prominent pathological phospho-epitopes (AT8, AT180, PHF-1) associated to tauopathies are indicated. N1, N2, N-terminal inserts; R1-R4, microtubule-binding repeats 1 to 4; NAC, non-amyloid-β component; NTD, N-terminal domain; NLS, nuclear localization signal; RRM, RNA Recognition Motifs; LCD, low complexity domain; N17, 17-residue N-terminal region; PRD, proline-rich domain; polyQ, polyglutamine; HEAT, HEAT repeats. The solution NMR structure of micelle-bound α-synuclein is depicted. Some PTM sites studied by chemical ligation and/or chemical mutagenesis are indicated. The cryo-EM structures of representative fibrils from individual brains (grey structures) and synthetic fibrils (blue structures) highlight structural discrepancies pointing to the role of trans-acting cofactors and PTMs of amyloid proteins in the amyloidogenic process. For a more comprehensive description of the multiple tau folds associated to diverse tauopathies and their classification, refer to (Shi et al., 2021). AD, Alzheimer's disease; CBD, corticobasal degeneration; PiD, Pick's disease; MSA, multiple system atrophy; ALS with FTLD, amyotrophic lateral sclerosis with frontotemporal lobar degeneration.

amyloid transformation (Benson et al., 2018; Benson et al., 2020). Indeed, the amyloid-forming protein converts into an abnormal, misfolded conformation from the same primary sequence that otherwise encodes either its native functional structure for globular proteins or its unfolded, dynamic conformational ensemble for intrinsically disordered proteins (IDPs) (Dobson, 2003; Knowles et al., 2014). Genetic alterations leading to protein misfolding may increase protein aggregation rate, modify mRNA splicing or impact the protein lifecycle. Moreover, changes in the oxidation state, posttranslational modification (PTM) patterns, protein interaction networks or environmental factors can trigger amyloid transformation without involvement of any mutation. Ultimately, protein misfolding results in a "loss-of-function" and/or a "gain-of-toxic function" (Winklhofer et al., 2008). However, amyloid formation cannot be strictly reduced to a defect of protein folding: defects in the cellular machinery of protein folding and quality control (mediated by molecular chaperones) or protein homeostasis (mediated by the proteasome and the lyzosomes) often associated to ageing are major players in the process. Cellular responses to external stimuli might in addition participate in the process by inducing incorrect protein trafficking, mislocalization, and aberrant interactions with aggregates or "seeds". Mislocalization can give rise to changes in the oxidation state, in the PTM patterns or levels, and in the protein interaction networks (Yan et al., 2013; Ke et al., 2020).

Natively folded proteins involved in amyloidosis are for instance transthyretin (TTR) associated to familial amyloidotic cardiomyopathy, superoxide dismutase-1 (SOD-1) and transactive response DNA binding protein 43 (TDP-43) associated to familial amyotrophic lateral sclerosis (fALS), Huntingtin (Htt) associated to Huntington's disease (HD), or the cellular form of prion protein PrP^{C} associated to prion diseases or transmissible spongiform encephalopathies (TSEs).

The latter are the only transmissible neurodegenerative diseases identified to date arising from proteinaceous infectious particles (i.e., without involvement of any nucleic acid) called prions (PrP^{Sc}) (Prusiner, 1982; Aguzzi and Calella, 2009). The IDP class includes the β-amyloid peptide (Aβ) as one of the sequential proteolysis products of amyloid precursor protein (APP) in Alzheimer's disease (AD), tau protein in AD and other tauopathies, α-synuclein in Parkinson's disease (PD), and islet amyloid polypeptide (IAPP) in type II diabetes (**Figure 1**). It should be noted that IDPs or alternatively long intrinsically disordered regions (IDRs), have generally important signaling and regulatory functions despite their disordered nature, acting as scaffolds for versatile interactions with multiple binding partners in cell signaling or to stabilize large structural components of the cells (Morris et al., 2011).

First histologically stained with Congo red, amyloids are widely detected with Thioflavin S (ThS) or Thioflavin T (ThT) fluorescent dyes that are used for both histological staining and the *in vitro* kinetics follow-up of amyloid assembly. In tissues, amyloids can be visualized under polarized light using the apple-green birefringent properties of the bound Congo red dye owing to its specific orientation in the regular arrangement of amyloid's proteinaceous component (Howie and Brewer, 2009). For clinical use, aggregated amyloid imaging involves the search of radioligands for positron emission tomography (PET) that enable the noninvasive detection of amyloids in the brain with either pan-amyloids or, recently developed, selective imaging agents for diagnosis purpose like Pittsburgh compound B (PiB) targeting Aβ (Shin et al., 2011; Mathis et al., 2017).

In 1950s, electron microscopy shed light into their fibrillary structure while X-ray diffraction showed a typical pattern of structures dominating by β-sheet conformations. The fibrillar structure of amyloids is constituted by the assembly of a given protein -or part of it-as a repetition unit in a cross β-sheet conformation running perpendicular to the fibril axis (**Figure 1**). At low resolution as investigated by electron or atomic force microscopy, or by spectroscopic methods such as Fourier transform infrared spectroscopy or circular dichroism, amyloids from multiple origins share structural and spectroscopic similarities.

The investigations of amyloid structures at high resolution has benefited from the development of biophysical approaches such as X-ray crystallography, solid-state nuclear magnetic resonance (ssNMR) or more recently, cryo-electron microscopy (cryo-EM). The latter enables now to distinguish between diseases with close clinical features but associated to distinct strains (Shi et al., 2021). However, despite the abundance of structural and kinetics studies of amyloid proteins, external stimuli or stress signals as well as the molecular mechanisms that drive a native functional conformation to protein misfolding from the same primary sequence are not yet fully understood. Moreover, prediction of amyloid folds is still an issue since amyloid assembly is not limited to intramolecular contacts (Anfinsen et al., 1961; Anfinsen, 1973; Jumper et al., 2021; Tunyasuvunakool et al., 2021). Therefore, structure predictions based on protein sequence or evolution-based approaches could not be properly applied to protein aggregation and pathological amyloid fibrils that also make use of intermolecular interactions and are not evolutionarily selected (Pinheiro et al., 2021).

In view of the causative roles that the amyloids have in a large number of diseases with yet unmet medical need, understanding their formation and structure is a priority. This is also a challenge due their solid-like state, polymorphic nature, the multi-causative aspect of amyloidosis, the various organs and tissues affected by the process and the complex mechanistic steps of their formation. New tools issued from chemical biology are much needed to address these challenges in research, and open the way to innovative therapies.

2 ASSEMBLY, PROPERTIES AND PROPAGATION OF AMYLOID FIBRILS IN NEURODEGENERATIVE DISEASES

2.1 Amyloid Structure and Formation

Amyloid fibrils are very stable protein assemblies at the thermodynamic (Buell et al., 2014) and mechanic (Knowles et al., 2007; Buehler and Cranford, 2010; Knowles and Buehler, 2011; Herling et al., 2015) levels due to the combination of both a tight packing of the polypeptide backbone into stacked β-sheets and intertwining of residue side chains. These cross-β structures result invariably in long, unbranched filaments. Hence, the amyloid core is stabilized by a wide array of non-covalent interactions and this packing by far exceeds the stability of the native 3D fold. However, hydrogen bonding interactions engaging the polypeptide main chain are prevalent explaining the structural similarity between amyloids despite the variety of protein sequences in sharp contrast with protein native state involving a great number of native contacts between side chains of key residues (Fandrich, 2002; Dobson, 2003). Despite this apparent simplicity, amyloid can take a large number of distinct folds illustrating their intricate structures and remarkable heterogeneity. Unexpectedly, an identical sequence can adopt several folds called polymorphs or strains, associated with different diseases, and even coexist in a single disease such as tau protein or Aβ42 in AD (Fitzpatrick et al., 2017; Yang et al., 2022).

Amyloid structures are only a single, yet peculiar, class of aggregates that can build up from a misfolded or denatured protein that stems either from an IDP or an initially folded protein for which secondary structures were reassigned. As every conformer, their formation depends on both thermodynamics (relative free energy) and kinetics parameters (interconversion rates) that confer stability (Baldwin et al., 2011; Buell et al., 2014). In addition, tight packing of the amyloid core is responsible for a lack of polypeptide chain accessibility to degradation (Novak et al., 1993) that confer to amyloids an increased lifetime (Makin et al., 2005). Amyloid formation mainly consists of three main stages defined as nucleation, growth and maturation. During the nucleation step, metastable species expose aggregation-prone sequences that self-associate into soluble oligomers or amorphous aggregates that serves as nuclei of the fibrillization process. Then, the fibrils rapidly grow during the elongation phase by an autocatalytic mechanism involving the addition of

new monomers to the nuclei or seeds that convert their conformation into the templated amyloid fold resulting in insoluble, ordered structures with fibril-like morphologies. Prefibrillar aggregates or seeds evolved into fibrils or eventually, may be involved in amplifying aggregation through a secondary nucleation mechanism that catalyzes fibril assembly at the seed surface or upon fibril fragmentation (Cohen et al., 2013; Meisl et al., 2014; Gaspar et al., 2017; Rodriguez Camargo et al., 2021). This process was described as secondary nucleation since it requires the formation of protofibrils or pre-fibrillar species to be effective. Finally, during the fibril maturation, the protofilaments formed during the growth phase associate through protein-protein interactions at the protofilament interfaces to form high-ordered fibrillar structures as seen by electron or atomic force microscopy. In cells, the maturation step may involve other proteinaceous components and PTMs including proteolysis leading ultimately to fibrillar deposits (Kimura et al., 1996; Braak et al., 2006; Aragão Gomes et al., 2021). The protofilaments can thus assemble into diverse interfaces leading to different morphologies or strains in the eye of the electron microscope. Some of them are periodic structures such as Paired Helical Filaments (PHFs) observed in AD by negative staining transmission electron microscopy (TEM) in which a pair of protofilaments assemble by twisting around each other with a helical turn period of about 80 nm (Kidd, 1963).

Very recently, cryo-EM, remarkably exploited by Goedert, Scheres and collaborators, provides structural details at near-atomic resolution on amyloid folds of tau protein either from patients with various tauopathies or made *in vitro* with heparin as aggregation inducer (Fitzpatrick et al., 2017; Falcon et al., 2018a; Falcon et al., 2018b; Zhang et al., 2019a; Falcon et al., 2019; Zhang et al., 2020) highlighting profound structural discrepancies. The same has been noted for fibrils of α-synuclein, wild-type or mutants, in synucleinopathies (Li et al., 2018a; Li et al., 2018b; Guerrero-Ferreira et al., 2018; Guerrero-Ferreira et al., 2020; Schweighauser et al., 2020) or TDP-43 in ALS/FTD (amyotrophic lateral sclerosis/frontotemporal dementia) (Arseni et al., 2021) and synthetic filaments. Each new fibril structure solved by cryo-EM from different diseases highlights the incredible plasticity of protein sequences of various origins to adopt multiple amyloid folds as well as the complexity of cofactors that shape the final amyloid structure and the misfolding pathway (Diaz-Espinoza, 2021). In the case of tau protein, the involvement of several protein isoforms in patients' fibrils (either by a combination of the 3R/4R isoforms, as in AD, or exclusively 3R, as in Pick's disease, or 4R isoforms, as in corticobasal degeneration) is in part responsible of distinct folds of tau in tauopathies. Interestingly, the amyloid folds of tau between distinct tauopathies are different, but individuals with the same disease share an identical fold. Actually, tau folds into either three or four layers when embedded in filaments, each categories being divided into distinct folds thereby suggesting a possible hierarchical classification of diseases based on tau amyloid folds (Shi et al., 2021).

Remarkably, in most instances, the region encompassed within the fibril core only represents part of the protein sequence while a large, if not the most part of the protein, retains a high degree of flexibility and accessibility, and projects from the fibril core. For example, in the case of tau protein, the ratio of residues involved in the fibril core can be as low as roughly 20% of the largest isoform (Fitzpatrick et al., 2017; Falcon et al., 2019; Zhang et al., 2020; Shi et al., 2021). The remaining of the sequence, i.e. the N- and C-terminal segments, forms a "fuzzy coat" around the amyloid core (Wegmann et al., 2013). First suggested by negative-staining and scanning TEM (Wischik et al., 1988), the structurally variable regions of tau fibrils largely escape further structural characterization by cryo-EM or ssNMR (Andronesi et al., 2008). They can still be addressed by ensemble-based methods such as solution-state NMR (Sillen et al., 2005; Bibow et al., 2011; Lippens et al., 2016) as well as fluorescence-based single-molecule approaches that enables dissecting low-populated, transient states that form during the amyloid assembly including oligomers or secondary nucleation processes (Kundel et al., 2018a; Kundel et al., 2018b; Kjaergaard et al., 2018; Rice et al., 2021; Yang et al., 2021). These structurally dynamic, disordered regions yet deserve particular attention as they can play a regulatory role in amyloid fibril formation especially through their abundant and diverse PTMs including truncations (Morris et al., 2015; Despres et al., 2017).

Cryo-EM has become prominent for the structural analysis of macromolecules from *postmortem* tissues at a near-atomic resolution (**Figure 1**). Cryo-EM structures point toward a role of cofactors and PTMs in fibril assembly and polymorphism (Li and Liu, 2021). Indeed, unresolved, non-proteinaceous densities (Falcon et al., 2019; Schweighauser et al., 2020; Zhang et al., 2020; Arseni et al., 2021; Shi et al., 2021), or (poly)ubiquitin chains (Arakhamia et al., 2020) were found in the vicinity of fibril surfaces made of tau, α-synuclein or TDP-43 proteins. Beyond their potential participation to the amyloidogenic transformation, these protein and non-protein entities highlight interfaces that could be targeted to prevent fibril assembly or disrupt existing fibrils. Even though atomic details were not observed for PTMs corresponding to the addition of small chemical groups such as Ser/Thr/Tyr phosphorylation, or Lys acetylation and methylation, these modifications are definitely present in fibrillar structures extracted from patient brains as detected by MS methods although heterogeneity or location outside the fibril core in adjacent flexible regions correspond to weaker densities or no density at all in cryo-EM high-resolution maps leaving open the role of these PTMs in fibrillogenesis, fibril packing and stabilization, and polymorph selection. Finally, the structure of the amyloid fibril as a final product provide no clue about the mechanism and kinetics as well as the intermediate structures that appears along the fibrillization process.

2.2 Features and Properties Related to Amyloids

Mature fibrillar assemblies, as histopathological hallmarks of amyloidoses, have long been considered as the causal agent of disease pathogenesis. In AD, a toxic "gain-of-function" is tightly related to the formation of amyloid structures that at least partly correlates with clinical manifestations when a certain amount of aggregates and/or certain brain areas were affected (Chung et al.,

2018). It has also become clear that small aggregates formed early during the fibrillization process, referred to as oligomers or prefibrillar species, would be the most toxic species and more damaging to neurons than fibrils (Caughey and Lansbury, 2003). Hence, it has been argued they are most probably best targets than fibrillar species from a therapeutic perspective. However, as metastable assemblies of heterogenous composition and structure, their molecular description with experimental methods are scarce. Atomic details of amyloid structures from combination of experimental models (ssNMR, X-ray, AFM, TEM) were complemented by molecular dynamics simulations. Simulations provide details at different aggregation stages of amyloid peptides such as Aβ40/42, tau, α-synuclein ranging from the monomeric to the oligomeric states and protofibrils up to amyloid fibrils (Nasica-Labouze et al., 2015; Ilie and Caflisch, 2019; Nguyen et al., 2021). For example, structures of low-populated intermediates of Aβ or IAPP were trapped in NMR or X-ray studies and observed in computational studies. Such models provide a molecular basis for pharmacological targeting of early, on-pathway aggregation species. While experimental models give time- and space-averaged properties, computational models offer a view of dominant states in the aggregation pathway by sampling various time and length scales and using different representations such as the all-atom, the coarse-grained and mesoscopic models. The major issues relate on the accuracy of the force field, the concentration of monomers, and the limited size of the simulated system. Moreover, the simulation time is several orders of magnitude less than the time of *in vitro* or *in vivo* fibrillar assembly that takes typically several hours up to several days. Besides the investigations of the early steps of aggregation and the mechanism of fibril elongation, interactions with cell membrane or metal ions, the role of PTM and complex coacervation (e.g., for tau protein) can also be explored with computational methods as discussed in comprehensive reviews (Nasica-Labouze et al., 2015; Ilie and Caflisch, 2019; Nguyen et al., 2021). Furthermore, a crosstalk between an amyloid conformation, or strain, and a naive amyloid-prone protein is a critical event in neurodegenerative diseases (Soto and Pritzkow, 2018). The ability of amyloid to convert normal protein conformers into new amyloid conformations is a process coined as seeding in which "seeds", an elusive term with respect to their composition and structure, act as templates of their self-copy. Hence, the main property of seeds is the imprinting of the misfolded conformation as a "conformational memory" that may be structurally propagated over several seeding generations (Frost et al., 2009; Nizynski et al., 2018). This is another aspect in favor of the irreversible cellular accumulation of amyloids once they have started forming. Moreover, the amyloid transformation of a given protein could also be triggered in a process named "cross-seeding" by heterologous seeds, i.e., seeds formed by a heterologous protein, be it from an unrelated protein, another isoform or a mutant form of the same protein. To implement innovative therapeutic routes in amyloid diseases, understanding the mechanisms of amyloid formation and emphasizing critical molecular species along the pathway are of the highest importance.

According to Braak staging, proteinaceous lesions of PD and AD progress through the brain in a spatiotemporal manner (Braak and Braak, 1991; Braak and Braak, 1995; Braak et al., 2004). They first start at defined, selectively vulnerable brain sites depending on the pathology, and gradually extend to neighboring neurons and distant brain structures through connected neurons. Overall, these pathologies progress silently over years before becoming symptomatic. Hence, it has been suggested that spreading of pathological amyloid species by cell-to-cell transmission is not confined to the sole prion proteins (Prusiner, 1982). By templating their own replication, many misfolded proteins including α-synuclein (Luk et al., 2012), β-amyloid (Ruiz-Riquelme et al., 2018), tau (Braak and Del Tredici, 2018) and huntingtin (Pearce and Kopito, 2018) behave like infectious prions by propagating seeds of various structures from a donor cell in a so-called "prion-like" spreading that results in the formation of amyloid aggregates in recipient cells (Mudher et al., 2017). However, the "prion-like" spreading hypothesis is still controversial and the spatiotemporal evolution of AD and PD that was elegantly demonstrated by Braak and colleagues is not a proof *per se* in favor of a prion-like spreading mechanism that physically involves seed release and capture from diseased to connected neurons. A model of selective neuron vulnerability has been proposed as an alternative to the "prion-like" spreading hypothesis arguing that neurons bearing aggregates or oligomers induce external stress on selected neuron populations that start producing aggregates in response to adverse stimuli (Walsh and Selkoe, 2016; Chung et al., 2018). The latter hypothesis does not preclude the "prion-like" spreading hypothesis, and both mechanisms may coexist.

Among the challenges attributed to amyloid diseases, the definition of the pathogenic species and how they can cross cellular membranes and spread from cell to cell is of crucial importance to be able to decipher disease progression and mechanisms, find specific and early diagnostic tools and devise efficient therapies (Colin et al., 2020). Linked to the prion-like propagation hypothesis, the concept of amyloid strains has evolved to explain distinct patterns of neuropathology and transmission through the central nervous system (CNS). The exact paths of cell-to-cell transmission of the pathogenic species seem not to be unique and might be dependent on the protein of interest. Nonetheless, this transmission is described as a non-cell-autonomous progressive spreading in many studied cases.

Finally, it was suggested that liquid-liquid phase separation (LLPS) that forms membraneless organelles by molecular reversible self-assembly, might be the missing link between protein misfolding, aggregation and pathogenesis associated to neurodegenerative disorders (Nedelsky and Taylor, 2019; Babinchak and Surewicz, 2020; Alberti and Hyman, 2021). Notably, many amyloidogenic proteins are prone to phase transition that can initiate protein misfolding and aggregation, and modulate their biological function as shown for tau (Ambadipudi et al., 2017; Zhang et al., 2017a; Hernández-Vega et al., 2017; Wegmann et al., 2018; Boyko et al., 2019; Majumdar et al., 2019; Kanaan et al., 2020; Singh et al., 2020; Rai et al., 2021), TDP-43 (Li et al., 2018c; Wang et al., 2018;

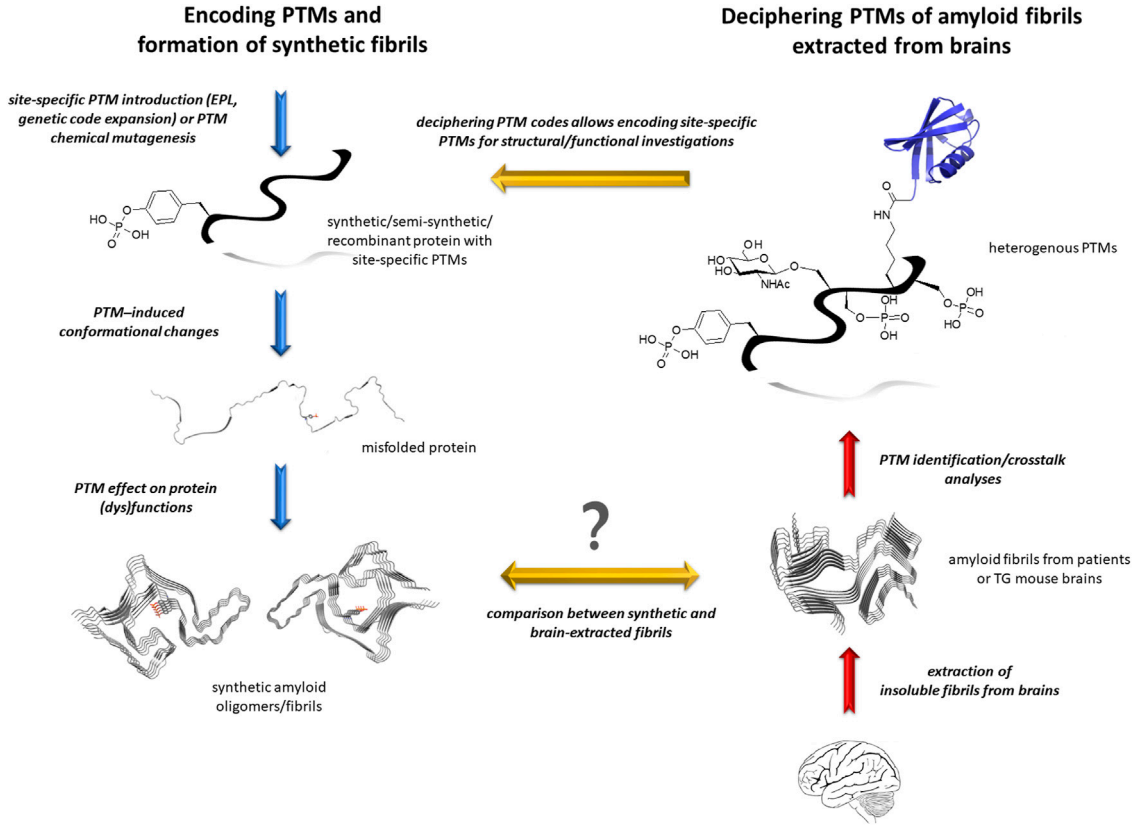

FIGURE 2 | Investigating the role of PTMs in amyloidogenesis by protein semisynthesis and/or chemical mutagenesis. Amyloid proteins are extracted from patient brains and purified as insoluble material, then the PTM patterns of amyloid fibrils are deciphered by complementary biophysical and biochemical tools (right panel). The precise role of site-specific PTMs is unraveled by encoding individual PTM or pathological epitope using chemical biology tools. This allows investigating the effect of these specific chemical modifications on protein conformation and function, on oligomer and amyloid assembly, stability and properties (left panel). The synthetic fibril morphology and cryo-EM atomic structures could thus be compared to *bona fide* fibrils from patient brains, here illustrated with pY39 α-synuclein synthetic fibrils (PDB ID: 6LIT) and α-synuclein fibrils from MSA (PDB ID: 6XYO), providing important information about the role of cofactors in amyloid aggregation.

Babinchak et al., 2019; Conicella et al., 2020; Watanabe et al., 2020; Dang et al., 2021; Grese et al., 2021; Hallegger et al., 2021; Pakravan et al., 2021), α-synuclein (Sawner et al., 2021), the amyloidogenic type II diabetes-associated IAPP (Pytowski et al., 2020) and the fused in sarcoma (FUS) protein (Patel et al., 2015; Monahan et al., 2017; Murthy et al., 2019; Ishiguro et al., 2021; Levone et al., 2021; Reber et al., 2021). Understanding the molecular mechanisms of aberrant phase separation should provide new strategies to control protein aggregation in neurodegeneration.

2.3 Modulators of Amyloid Aggregation

2.3.1 Trans Acting Factors of Protein Aggregation

The deposits and inclusions in neurodegenerative disorders such as NFTs, senile plaques, Lewy bodies. . . consist of several proteins and non-proteinaceous components (carbohydrates, nucleic acids, metals, lipids, lipid rafts and cholesterol) that could be linked to the amyloid polymorphisms observed in diseases (Kollmer et al., 2016; Stewart et al., 2016; Shahmoradian et al., 2019; Li and Liu, 2021). The proteome analysis of amyloid deposits has revealed hundreds of proteins (Drummond et al., 2017; Lutz and Peng, 2018). Some of them act as critical regulators in protein misfolding diseases exemplified by heat shock proteins (HSPs) and their co-chaperones, 14-3-3 proteins (Xu et al., 2013; Jia et al., 2014), S100B calcium-binding protein (Moreira et al., 2021), and the peptidyl-prolyl isomerases (PPIases) FKBPs and Pin1 (Hamdane et al., 2002; Landrieu et al., 2006a; Balastik et al., 2007; Lippens et al., 2007; Chambraud et al., 2010; Giustiniani et al., 2012; Giustiniani et al., 2014; Kamah et al., 2016; Chen et al., 2018; Wang et al., 2020a). Notably, Pin1 and 14-3-3 proteins interact with phosphorylated forms of tau making the link with amyloid PTMs (Lu et al., 1999; Zhou et al., 2000; Smet et al., 2004; Lim and Ping Lu, 2005; Smet et al., 2005; Pastorino et al., 2006; Landrieu et al., 2011; Kondo et al., 2017; Neves et al., 2021). A role of cofactors has been shed into light in the aggregation of tau protein to specifically address the challenges of forming amyloid fibrils from full-length tau *in vitro* (Fichou et al., 2018; Fichou et al., 2019) in contrast to Aβ or α-synuclein that readily form amyloid fibrils in a wider range of conditions. Glycosaminoglycans, lipid membranes and metal ions are key cofactors that were pointed out in the amyloidogenic process. They have been found to modulate aggregation rates and

are associated with amyloid deposits within the brain. Interactions of amyloidogenic species with cofactors may represent an orthogonal strategy of intervention to aggregation inhibitors in neurodegenerative disorders.

2.3.2 Posttranslational Modifications of Amyloid Proteins

The polymorphism of amyloid structures from the same protein reflects distinct environments leading ultimately to different diseases. In this respect, PTMs and non-amino acid components associated with the fibrils have focused particular attention (**Figure 2**). Arising from the most recent cryo-EM structures of human prion PrP, wild-type α-synuclein from multiple system atrophy (MSA), tau from corticobasal degeneration (CBD) - all of which were from brains of patients- and phospho-Tyr39 (pY39) α-synuclein from semisynthesis (Arakhamia et al., 2020; Wang et al., 2020b; Schweighauser et al., 2020; Zhang et al., 2020; Zhao et al., 2020), it has been proposed to categorize PTMs based on their location with respect to the fibril core (Li and Liu, 2021). PTMs in the interior of the core are likely involved in the initial step of fibril assembly while PTMs on the exterior may act rather in the polymorph selection either by driving the folding of protofilaments or stabilizing the protofilament interface. The role in fibril assembly of PTMs outside the core, within the "fuzzy coat", still remains poorly defined although they are known to regulate the protein functions, interactions and aggregation properties by modulating the rate of fibrillar assembly, toxicity and phase separation. Importantly, they remain accessible even within the amyloid fibril and may still be targeted by posttranslational modifying and proteolytic enzymes (Wegmann et al., 2013; Ulamec et al., 2020).

Hyperphosphorylation, a common feature of tau proteins in NFTs and inclusions from diverse tauopathies, is mainly found within the N- and C-terminal regions flanking the amyloid core (Morishima-Kawashima et al., 1995a; Hanger et al., 1998; Alonso et al., 2001; Hanger et al., 2007; Hanger et al., 2009; Šimić et al., 2016) that greatly inhibit the formation of filaments (Abraha et al., 2000; Lövestam et al., 2021). Tau also exhibits a large diversity of PTMs such as lysine ubiquitination, SUMOylation, acetylation and methylation (Morris et al., 2015; Wesseling et al., 2020). These modifications can be specifically linked to the disease stage and mediate the structural diversity of tau strains (Arakhamia et al., 2020). Interestingly, the seeding activity of the hyperphosphorylated, oligomeric tau species was found to be heterogeneous from one patient with pure, typical AD to another while enhanced seeding activity and worse clinical outcomes both correlate with specific PTM sites (Dujardin et al., 2020). Whereas phosphorylation of α-synuclein at serine 129 (pS129) is a dominant characteristic of PD inclusions such as Lewy bodies, its role in aggregation and toxicity of α-synuclein has not yet been clearly established (Anderson et al., 2006; Oueslati, 2016; Ghanem et al., 2022). TDP-43, the main component of intracellular ubiquitin inclusion bodies found as a hallmark of ALS-FTLD (Frontotemporal Lobar Degeneration), is hyperphosphorylated and polyubiquitinated whereas these PTMs were not detected in normal brain (Dong and Chen, 2018).

Commonly associated to phosphoproteins, the *O*-β-linked N-acetylglucosaminylation (*O*-GlcNAc) is another PTM of serine/threonine residues that corresponds to the addition of a single sugar moiety that is regulated in a dynamic fashion by the antagonist action of two enzymes, the *O*-GlcNAc transferase (OGT) and *O*-GlcNAc hydrolase (OGA) (Iyer and Hart, 2003). Protein *O*-GlcNAcylation is extremely sensitive to glucose uptake and metabolism that may be altered in aging brain. Additionally, the *O*-GlcNAc modification has been reported for neuronal proteins such as APP, tau and α-synuclein highlighting a potential role in neurodegenerative diseases (Lazarus et al., 2009; Ma et al., 2017). *O*-GlcNAcylation of amyloid-forming proteins has been shown to regulate aggregation (Yuzwa et al., 2014a) and to some extent, phosphorylation of tau (Liu et al., 2004; Gong et al., 2006; Liu et al., 2009; Smet-Nocca et al., 2011; Bourré et al., 2018; Cantrelle et al., 2021). The treatment of transgenic mice with Thiamet-G, an OGA inhibitor, results in increased brain *O*-GlcNAc levels, and alleviate tau pathology and associated neurodegeneration offering an alternative therapeutic strategy to kinase and aggregation inhibitors in tauopathies (Yuzwa et al., 2008; Yuzwa et al., 2012; Yuzwa et al., 2014b; Graham et al., 2014; Hastings et al., 2017; Lee et al., 2021).

2.3.3 Proteolysis

In addition to PTMs involving the covalent linkage of proteinaceous or small chemical entities, truncated forms of amyloid proteins are also frequently found associated to pathological transformation. The N-terminal region of Htt is the site of HD-associated pathogenic changes through an elongation of the CAG repeat of *htt* gene encoding an expanded polyglutamine repeat. The truncated N-terminal proteoforms are more toxic than full-length Htt and form intranuclear inclusions that disrupt synaptic and axonal functions (Sun et al., 2002). At the basis of the amyloid cascade hypothesis in AD, the Aβ peptide is the product of the sequential cleavage of the transmembrane APP protein by secretases that generates peptides of different length, the most common forms being Aβ40 and Aβ42. With a proportion significantly increased in AD brain, this latter form is the most neurotoxic and readily form oligomers and fibrils in a wide range of conditions (Nirmalraj et al., 2020; Yang et al., 2022). A large panel of tau fragments resulting from cleavage at N- or C-terminal regions or both are found in fibrillar structures, cerebrospinal and interstitial fluids, and plasma of patients with different tauopathies (Quinn et al., 2018; Boyarko and Hook, 2021). The predominant role of proteolysis in various neurodegenerative disorders deserves particular attention for characterizing the fragments, their toxicity related to aggregation and transcellular spreading, and their role in the selection of strain polymorphs. This approach could afford new biomarkers and disease-modifying therapies by modulating the fragment generation and associated toxicity (Rodriguez Camargo et al., 2021).

The wide range of disease-associated modifications represents several challenges: 1) discriminating between physiological and disease-associated changes, 2) characterizing PTMs in terms of

site-specific identification, quantification, and crosstalk between PTMs, and their relevance to disease, 3) characterizing PTM-induced conformational changes, 4) identifying enzymes responsible of the installation/removal of specific PTMs and defining the pathway of their (dys)regulation, 5) determining the functional role of specific PTMs in physiology and pathology, and 6) identifying and deciphering the role of amyloid interacting entities or cofactors (Kametani et al., 2020). The role of proteins, non-proteinaceous entities and PTMs in the aggregation process, toxicity and spreading of various species that form during the fibrillization course still deserves further investigations (**Figure 2**). They may have prominent implications in modulating nucleation, aggregation rate, selection of fibril polymorph, seeding capacity, and amyloid toxicity. Additionally, interactions of amyloid-prone proteins with cofactors and posttranslationally modifying enzymes could be valuable targets for therapeutic intervention (Dujardin et al., 2020).

3 DECIPHERING THE POSTTRANSLATIONAL MODIFICATION CODES OF AMYLOIDS: COMBINING PROTEIN ENGINEERING WITH THE CHEMICAL BIOLOGY'S TOOL KIT

As small chemical groups or proteinaceous components, PTMs is a dynamic way to modulate physicochemical properties and hence, the biological and pathological functions of proteins by rapidly and reversibly enlarging the proteome complexity. In this regard, PTMs regulate the aggregation propensity of amyloid proteins, the stability of oligomers and seeds, the propagation of seeds and other toxic species, demixing into liquid droplets, . . . all as crucial steps in amyloidogenesis. Defining a PTM signature may be relevant to track disease-associated changes, connect changes in PTM patterns to a loss or gain of function, and find new biomarkers and therapeutic targets in disease-modifying strategies. Deciphering the role of site-specific PTMs is of highest importance in this area but this knowledge needs to overcome the issue of multiple, heterogenous modifications found in a cellular environment or provided *in vitro* by enzymatic activities. Mutation of site-specific positions, e.g. into alanine, is commonly employed to reduce the number of PTM sites (Despres et al., 2017). Introducing amino acids mimicking the physiochemical properties of posttranslationally-modified residues, such as aspartate or glutamate for phospho-serine/threonine, or glutamine for acetyl-lysine, is an easy way to achieve homogenous levels of modification but is poor proxy of the corresponding PTM (Paleologou et al., 2008). The alternative modification of proteins by the enzymatic route provides heterogenous patterns due to multiple sites, PTM crosstalk and different stoichiometry that are invariably associated to sample complexity for modified proteins (Theillet et al., 2012). This feature has been extensively described by our group illustrating the exceptional complexity of PTMs and PTM crosstalk within tau protein, as well as their impact on tau conformation and physiopathological functions (Landrieu et al., 2006b; Amniai et al., 2009; Landrieu et al., 2010; Leroy et al., 2010; Landrieu et al., 2011; Kamah et al., 2014; Lippens et al., 2016; Despres et al., 2017; Gandhi et al., 2017; Bourré et al., 2018; Despres et al., 2019; Cantrelle et al., 2021).

Chemical biology on the other hand provides a wide range of tools to unravel the role of PTMs in the mechanism of amyloid aggregation and tackle the process of fibril assembly. This goes hand-in-hand with progresses in protein engineering. Specifically, the development of efficient expression vectors combined to bacterial strains and other heterologous systems for recombinant protein expression, together with the use of multiple purification tags allowed the production of milligram amounts of proteins (depending on expression systems) with a high degree of purity. Although this procedure can be routinely implemented for the preparation of proteins, it is limited to the 20 genetically-encoded amino acids, excluding in most instances the possibility of chemical modifications of amino acids including insertion of PTMs, probes, or the incorporation of unnatural or D-amino acids. However, solving inherent limitations of site-specific modification of recombinant proteins has benefited from the development of both protein synthesis by chemical ligation strategies (Dawson et al., 1994; Moon et al., 2021) and genetic code expansion through reassignment of sense and nonsense codons combined to engineered aminoacyl-tRNA synthetase/tRNA pairs (Wang et al., 2001). In this area, cell-free expression systems are efficiently developed for the incorporation of unnatural amino acids (UAAs) that are not genetically encoded (Gao et al., 2019) or manipulating isotopic labeling schemes (uniform labeling, selective labeling and site-specific labeling) for NMR structural analyses. By controlling the isotopic scheme of amino acids used in cell-free reactions, these approaches allow reducing isotopic scrambling. This strategy has been successfully applied for the NMR study of low-complexity regions of Htt exon1 combining cell-free expression using transcription-translation systems of *Escherichia coli* extracts and nonsense suppression for the site-specific isotopic labeling (Morató et al., 2020).

3.1 Understanding the Role of Specific Posttranslational Modifications in Amyloidogenesis Using Native Chemical Ligation

The combination of solid phase peptide synthesis (SPPS) with native chemical ligation (NCL) strategies provide the most efficient way to quantitatively introduce site-specific PTMs, and/or chemical/fluorescent labels or UAAs, into a protein of interest. Of note, amyloid-forming peptides/proteins, as exemplified by Aβ and IAAP, exhibit an intrinsic tendency to aggregation during SPPS and purification. Several strategies of chemical synthesis were implemented to prevent aggregation into β-sheet structures and improve solubility of difficult sequences (Butterfield et al., 2012), but these considerations are beyond the scope of this review. NCL, initially developed by Kent and co-workers, uses chemoselective reactions between the α-carboxyl

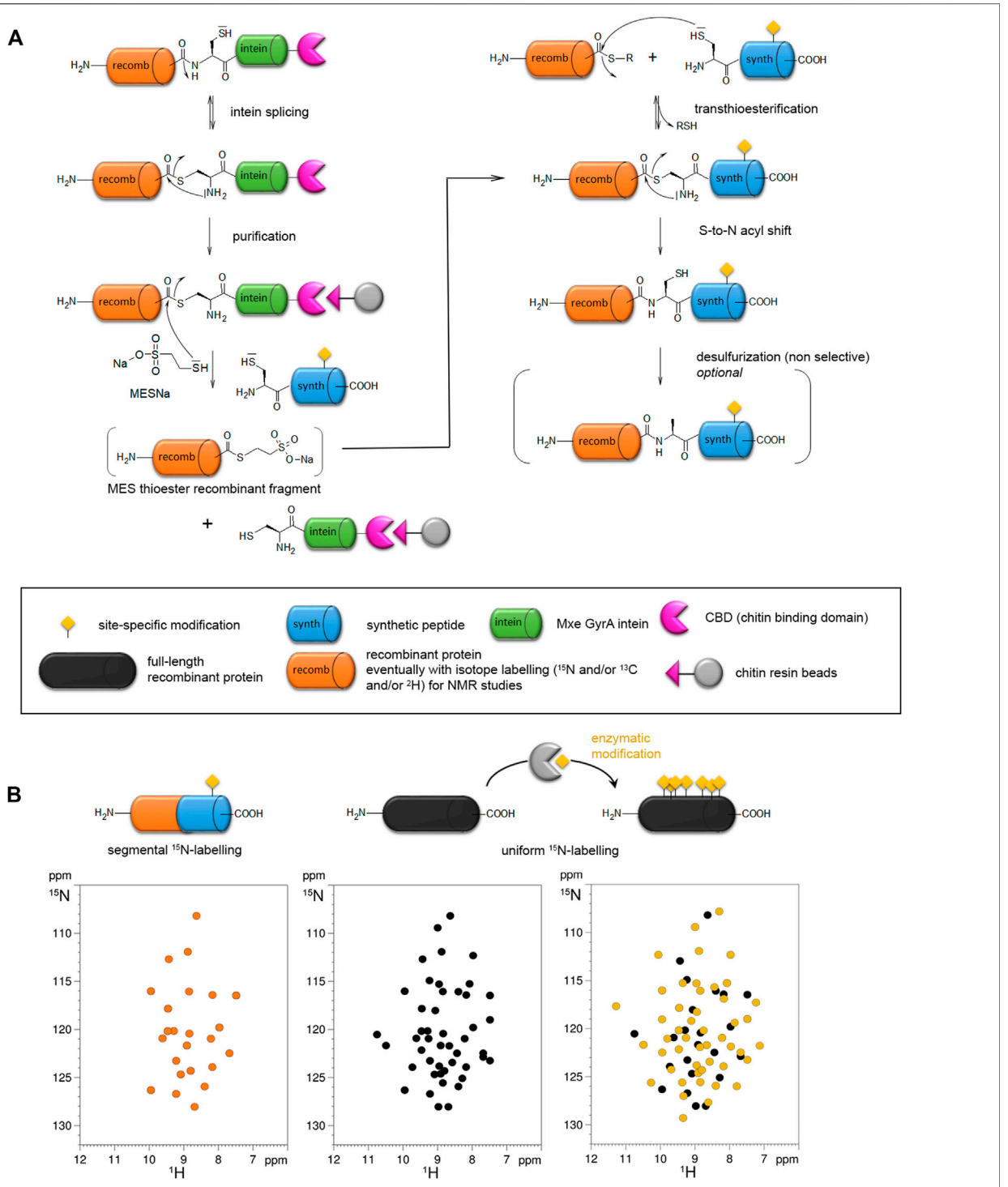

FIGURE 3 | Expressed protein ligation (EPL) strategy for site-specific modification of proteins **(A)** and segmental isotope labeling for NMR studies **(B)**. **(A)** The synthetic peptide (blue) incorporating a site-specific modification (yellow) is obtained by SPPS and ligated to a recombinant protein fragment (orange) expressed in a heterologous system which can eventually be isotopically labeled for NMR study. The recombinant protein can be expressed as intein fusion protein (intein in green) with a CBD tag (pink) for purification on chitin beads. The reaction with sodium 2-mercaptoethane sulfonate (MESNa) and a synthetic peptide with a N-terminal cysteine leads to a semisynthetic protein. **(B)** In the NMR ^{1}H-^{15}N HSQC spectrum, only the ^{15}N-labeled region of the protein is visible, therefore the synthetic region bearing the modification is invisible (orange spectrum). This strategy called segmental isotopic labeling allows a reduction of NMR signals in the spectrum relative to the full-length, uniformly labeled protein (black) without PTM (black spectrum) or with enzymatically installed PTMs (yellow spectrum). It is noteworthy that modifications of protein resonances observed locally for the modified residues and its neighbors in the primary sequence in the uniformly labeled protein cannot be observed in the semisynthetic protein with segmental labeling due to the absence of isotopic labeling in the region of PTM. However, this modification may have a long-range structural impact on residues of the ^{15}N-labeled fragment due to conformational proximity that can be detected through perturbations of signals in the isotopically labeled region.

and the α-amino groups of two unprotected peptides to form a native peptide bond (Muir and Kent, 1993; Dawson et al., 1994; Hackenberger and Schwarzer, 2008; Agouridas et al., 2019; Moon et al., 2022). This strategy allows introducing selective and quantitative modifications of amino acids without altering any usual peptide bond. However, the requirement of SPPS is limiting the length of affordable peptides to 50–60 residues, and multiple rounds of NCL can extend the polypeptide length at the expense of a significant reduction of the overall yield. To circumvent this issue, expressed protein ligation (EPL) implements the two-step reaction of NCL to generate semisynthetic proteins.

The first step of NCL consists of a transthioesterification, or reversible thiol/thioester reaction, by the nucleophilic attack of a N-terminal cysteine (through the side chain thiol function) of a synthetic peptide on the activated C-terminal thioester of another peptide. Both fragments will constitute the C-terminal and N-terminal parts of the full-length synthetic protein, respectively. The second step is a spontaneous and irreversible rearrangement called "S-to-N acyl shift" that restores a native peptide bond with a cysteine residue at the junction of both fragments (**Figure 3A**). Alternatively, EPL makes use of engineered mini-inteins as fusion to the expressed recombinant protein fragment of interest to introduce a C-terminal α-thioester. Inteins are self-processing domains involved in posttranslational protein splicing processes. The intramolecular rearrangement at the intein N-terminal cysteine generates the C-terminal α-thioester of the expressed fragment. The functionalized fragment can be next ligated to a synthetic fragment containing a N-terminal cysteine to generate a semisynthetic protein (**Figure 3A**). As the C-terminal fragment is obtained by SPPS, any modification (PTM, probe, other chemical modification of amino acid) can be easily inserted into a specific position of this region of the final semisynthetic protein. A synthetic N-terminal fragment bearing a thioester can also be ligated to an expressed C-terminal fragment. In this case, a N-terminal cleavable fusion tag, e. g. His_6-SUMO tag, is used to afford the N-terminal cysteine required for the subsequent ligation step (Chiki et al., 2021). The use of a SUMO tag offers the advantages of improving protein expression and solubility, and facilitates protein handling and purification. All these strategies may require final steps of refolding, oxidation of the ligation product, and eventually desulfurization of the cysteine residue at the ligation site to restore a native alanine residue. They are better suited to introduce modifications of the terminal regions of semisynthetic proteins. Introducing modifications in the central region requires two ligation steps with a three-segment strategy (or more) at the expense of the reaction yield. We refer the readers to references (Hackenberger and Schwarzer, 2008; Agouridas et al., 2019) for extensive, general considerations in addressing NCL/EPL including the choice of ligation site, protection/deprotection strategies, desulfurization reactions.

The NCL strategy has been successfully used to introduce UAAs bearing chemical modifications (Chuh et al., 2016), e.g. metabolically stable phosphonate and difluoro-phosphonate analogs of phosphorylated residues. It proved to be also useful for segmental isotopic labeling of large proteins for structural analyses by NMR spectroscopy (Vogl et al., 2021). In this field, EPL helped to partially overcome the size limitations inherent to solution-state NMR by alleviating the number of resonances and thus, spectral overlap (**Figure 3B**). Additionally, NMR offers an orthogonal viewpoint to the study of PTMs from an analytical, mechanistical, structural and functional perspective (Theillet et al., 2012). By providing homogenous PTM patterns and reducing the number of PTM sites, EPL can help characterizing PTM-driven conformational and functional changes, although with a limited knowledge on the local conformational impact due to the absence of isotopic labeling of the synthetic fragment containing site-specific PTM(s) (**Figure 3B**). The occasional use of isotopically labeled amino acid synthons for SPPS may partially overcome this limitation albeit with a significant cost increase. An alternative route to PTM incorporation is the chemoenzymatic semisynthesis employing *in vitro* enzymatic modification of an expressed fragment, or co-expression of the fragment with the modification enzyme in *E. coli*, preceding the ligation step (Pan et al., 2020; Chiki et al., 2021; Kolla et al., 2021; Pan et al., 2021). This approach is limited to either small or mutated fragments, or scarce PTMs (such as pTyr) to reduce the number of modification sites or alternatively, it requires an efficient purification method to isolate a homogenously modified fragment preferably before ligation.

As exemplified by the whole proteome, phosphorylation is an important PTM in neurodegenerative diseases through modifications of most, if not all, amyloid proteins (Tenreiro et al., 2014). Involved in the crosstalk with phosphorylation, *O*-GlcNAcylation has been extensively investigated by semisynthetic approaches since the low enzymatic activity of OGT *in vitro* still limits the purely enzymatic strategy (Schwagerus et al., 2016; Balana and Pratt, 2021). Among other PTMs commonly found in amyloid proteins, lysine modifications such as acetylation, methylation (poly) ubiquination and SUMOylation are also explored by EPL. Several chemical biology groups have thus addressed the role of site-specific PTMs of amyloid proteins by developing various strategies of chemical synthesis, EPL and chemoenzymatic semisynthesis to improve the efficiency and yield of the ligation reaction as well as traceless purification of the ligation product (Ansaloni et al., 2014; Reimann et al., 2015; Levine et al., 2019; Kolla et al., 2021). Because, the NCL/EPL strategy depends on protein sequence and length, and on the nature and site(s) of PTM, specific strategies are elaborated in a case-by-case basis, i.e. for a specific amyloid protein and PTM. In the following, some examples are given to illustrate both the NCL/EPL approach involved and the findings related to the amyloidogenic pathways.

3.1.1 α-synuclein

Either a three-fragment ligation or chemoenzymatic semisynthesis approach was employed to achieve tyrosine phosphorylation of α-synuclein at Y39 to evaluate its impact on aggregation properties and toxicity (Pan et al., 2021; Pan et al., 2020; Dikiy et al., 2016). Phosphorylation of Y39 was made possible by the chemoenzymatic strategy because the three

other Tyr residues of α-synuclein are all located in the C-terminus that was recombinantly expressed in bacteria while the N-terminal part was enzymatically phosphorylated before ligation. Furthermore, desulfurization following the ligation steps restores native residues at junction sites considering the absence of cysteine in the native sequence of α-synuclein. It is noteworthy that recombinant expression of all fragments further assembled by ligation allowed the uniform ^{15}N isotopic labeling of the site-specific pY39 α-synuclein for NMR studies (Vogl et al., 2021). It has been shown using these strategies that pY39 accelerates aggregation kinetics (Pan et al., 2020; Dikiy et al., 2016) and alters fibril morphology of α-synuclein with pY39 attracting the entire N-terminus within the fibril core through an array of electrostatic interactions giving rise to the largest fibril core (residues 1–100) ever seen for the α-synuclein amyloid fibrils (**Figure 2**) (Zhao et al., 2020). The homogenously phosphorylated α-synuclein at S129, one of the major pathological marks of Lewy bodies in PD, forms a different amyloid fold and has different propagation properties related to the wild-type protein, indicating the formation of a distinct strain associated to higher toxicity (Ma et al., 2016). Be it either localized at pY39 or pS129, single phosphorylation of α-synuclein provided by NCL highlights a capacity of site-specific phosphorylation to modulate the fold of the amyloid structure and pathological strain properties. In contrast, phosphorylation at Y125 does not alter the structure and morphology of the α-synuclein fibrils (Hejjaoui et al., 2012).

As α-synuclein has multiple *O*-GlcNAcylation sites, the site-specific *O*-GlcNAcylation provided by EPL underscored its inhibitory role in fibril assembly on either T72, T75, T81 or the three together, or S87, with the strongest effect observed for T75, all these sites being embedded within the fibril core (Marotta et al., 2015; Lewis et al., 2017; Li et al., 2018b; Zhang et al., 2019b; Levine et al., 2019; Tavassoly et al., 2021). Additionally, the combination of three T72/T75/T81 GlcNAc *O*-glycosylation reduces the aggregation of wild-type α-synuclein or aggregation-prone mutant (A53T) that causes early-onset, familial PD. *O*-GlcNAcylation alters the structure of aggregates in a site-specific manner, reduces the cytotoxicity of extracellular fibrils and impaired the calpain-mediated proteolysis of α-synuclein. Interestingly, the Pratt's group has highlighted that *O*-GlcNAc at T72 is unique in its aggregation inhibitory properties as compared to other single sugars including *O*-GalNAc suggesting an effect that extend beyond its mere bulky size and polar properties, owing likely to the chirality of specific asymmetric carbons that would require further investigations (Galesic et al., 2021).

Finally, the investigation of site-specific ubiquitination of α-synuclein involved a strategy of disulfide-directed ubiquitination, as implemented by Pratt and co-workers, requiring a lysine-to-cysteine point mutation for installation of ubiquitin through a disulfide bond instead of the native isopeptide bond. This strategy involved the recombinant production of a ubiquitin-intein fusion protein followed by reaction with cysteamine that simultaneously affords intein cleavage and thiol functionalization of ubiquitin C-terminus (**Figures 4A,B**). The subsequent thiol activation as a disulfide or a redox non-labile function by reaction with dibromoacetone provided ubiquitinated α-synuclein by reaction with a free thiol function positioned at diverse biologically relevant sites (K6, K10, K12, K21, K23, K32, K34, K46, and K96) (Meier et al., 2012; Abeywardana et al., 2013; Moon et al., 2020; Lewis et al., 2016). Whatever the ubiquitination or polyubiquitination site, an inhibition of α-synuclein aggregation was observed (Meier et al., 2012; Haj-Yahya et al., 2013). However, the disulfide bond is not chemically stable and other approaches were used to establish stable isopeptide linkage of ubiquitin. An alternative strategy formerly developed by Lashuel and co-workers although less flexible affords a native isopeptide linkage between K6 of α-synuclein and ubiquitin (**Figures 4A,C**). The synthesis of a thiol protected δ-mercaptolysine derivative is used in SPPS of a N-terminal fragment, then EPL with a recombinant C-terminal fragment provides the modified K6 within full-length α-synuclein. Subsequent NCL between the thiol function of δ-mercaptolysine and ubiquitin C-terminal thioester forms a native isopeptide bond between ubiquitin and the targeted lysine after subsequent desulfurization of the thiol handle of δ-mercaptolysine (Hejjaoui et al., 2011).

3.1.2 Aβ Peptide

Aβ peptides from AD brain contain a variety of peptide lengths and post-translationally modified forms with phosphorylation, isomerization, and pyroglutamate, that modulate aggregation and propagation properties, and toxicity. In AD, modifications of the N-terminus in several Aβ subtypes were shown to both accelerate fibrillation and stabilize fibril structures. Phosphorylation of S8 is a modification of Aβ featured in late-stage of AD in the dispersed, membrane- and plaque-associated fractions (Kumar et al., 2011; Rijal Upadhaya et al., 2014). Homogenous phosphorylation of S8 of Aβ(1–40) peptide, afforded by SPPS, induces a higher cross-seeding efficiency when compared to unmodified Aβ(1–40) and a modification of fibril structure shown by ssNMR that highlights a tight N-terminus association with the amyloid core (Hu et al., 2019). In contrast, selective enzymatic modification of S26 stabilizes oligomeric forms but inhibits aggregation. Hence, it has been proposed that an ordered N-terminal region may be favorable to pS8-Aβ(1–40) strain to propagate to multiple Aβ subtypes by exerting a dominant role in fibril morphology. Furthermore, ordered N-terminal conformations in Aβ fibril structures may be biologically relevant as illustrated by brain-extracted Aβ40 and Aβ42 fibril structures. In contrast, Y10 *O*-glycosylation of Aβ with a (Galβ1-3GalNAc) disaccharide or sialylated trisaccharide (NeuAcα2-3Galβ1-3GalNAc) was shown to destabilize the amyloid structure to form a new fibril polymorph with a less stable protofilament interface rendering fibrils more prone to degradation in agreement with short tyrosine *O*-glycosylated forms found in CSF of AD patients (Liu et al., 2021).

Recently, the O-GlcNAc glycosylation of small heat shock proteins (sHSPs) by EPL in the Pratt's group has extended targeting modulators of amyloid aggregation to site-specific PTMs of their cofactors. O-GlcNAc modification was found to selectively improve the anti-amyloid activity of HSP27 and other sHSPs in aggregation of both α-synuclein and Aβ(1–42), by

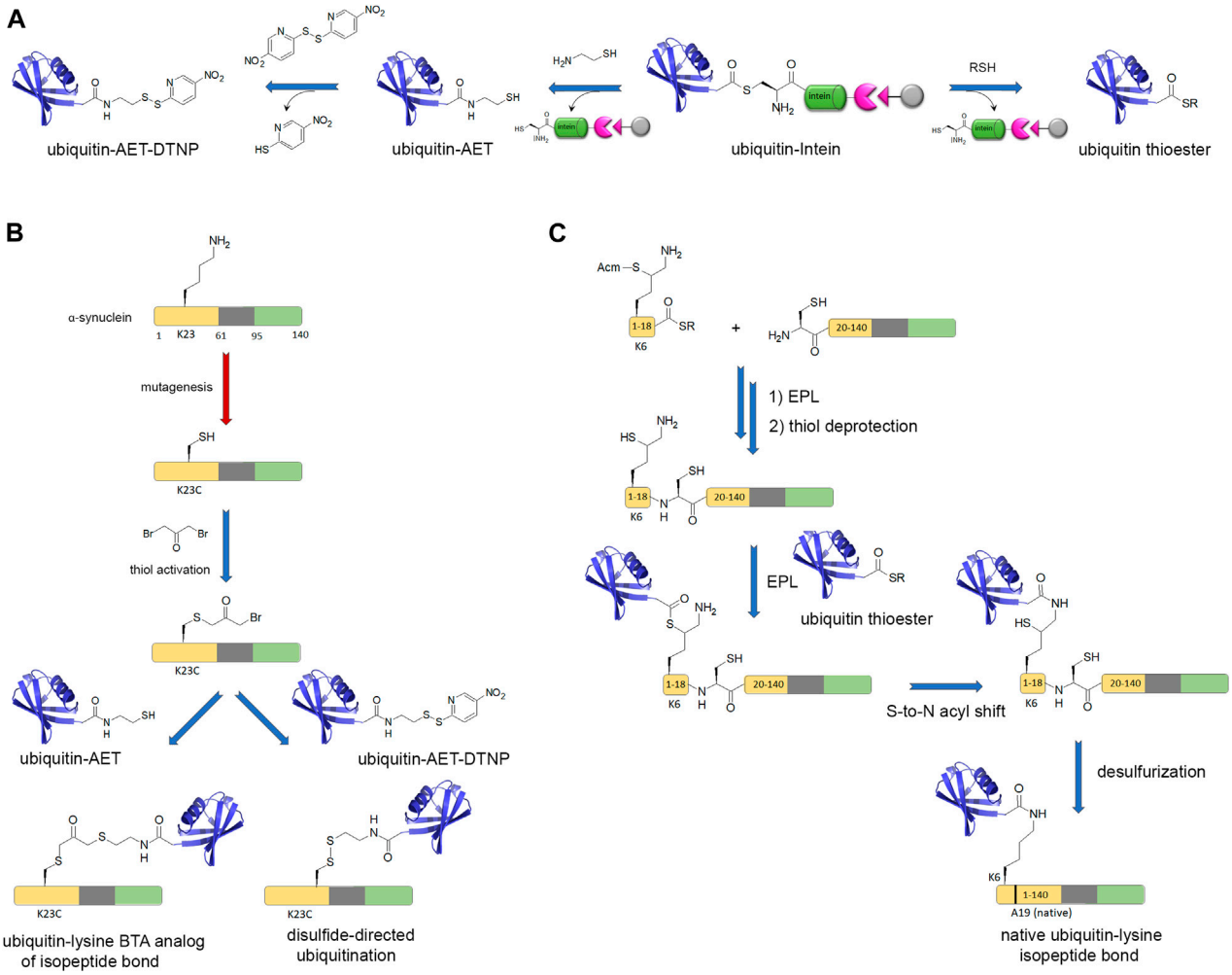

FIGURE 4 | Chemical biology strategies of protein ubiquitination. **(A)** Posttranslational chemical mutagenesis and EPL approaches involve both the preparation of a C-terminal activated ubiquitin from a ubiquitin-intein fusion protein that provides a reactive C-terminal thioester. **(B)** Posttranslational chemical mutagenesis exemplified for K23 ubiquitination of α-synuclein requires first the thiol activation of a cysteine residue obtained by site-directed mutagenesis at the PTM site. The activated thiol is further involved in a reaction with ubiquitin-aminoethanethiol (ubiquitin-AET) leading to a bis-thio-acetone (BTA) analog of the ubiquitin-lysine isopeptide bond (Lewis et al., 2016). Alternatively, a ubiquitin-AET activated by 2,2′-dithiobis(5-nitropyridine) (ubiquitin-AET-DTNP) can react with the cysteine thiol in a disulfide-directed ubiquitination (Moon et al., 2020). **(C)** The EPL strategy involves first, the synthesis of full-length α-synuclein by EPL of two fragments, a N-terminal peptide (fragment 1–18) bearing a protected δ-mercaptolysine at position K6 for further ubiquitin linkage and a C-terminal recombinantly expressed fragment with a N-terminal cysteine. After NCL and thiol deprotection of the δ-mercaptolysine, EPL with the recombinantly expressed ubiquitin with C-terminal thioester and subsequent desulfurization provide the full-length, native α-synuclein with a native ubiquitin-lysine isopeptide bond (Hejjaoui et al., 2011). Chemical reactions are indicated by blue arrows and enzymatic reactions by red arrows.

competing with intramolecular interactions. The subsequent conformational rearrangement upon HSP27 O-GlcNAcylation most likely favors the formation of larger multimers with increased activity (Balana et al., 2021). Besides highlighting a protective role of O-GlcNAc in amyloid aggregation, this work opens new avenues for orthogonal strategies to inhibit the formation of amyloid fibril by targeting their cofactors.

3.1.3 Tau Protein

The long sequence of tau protein combined to a high proportion of polar residues (Ser, Thr, Lys, Arg) and Pro in the proline-rich domain coincides with a large number of PTMs such as phosphorylation, acetylation, ubiquitination, SUMOylation, methylation and *O*-GlcNAcylation. Hyperphosphorylation was shown to have a dominant role in tau fibril formation and loss-of-function in MT stabilization (Alonso et al., 1994; Morishima-Kawashima et al., 1995b; Alonso et al., 2001; Tepper et al., 2014), but other PTMs may have important effects in modulating tau functions and amyloid assembly. Site-specific PTMs may exert antagonist roles as well with some phosphorylation sites promoting aggregation while others have an inhibitory effect (Schneider et al., 1999; Liu et al., 2007; Despres et al., 2017; Brotzakis et al., 2021). Tuning on and off specific phospho-epitopes was shown to modulate tau function on tubulin

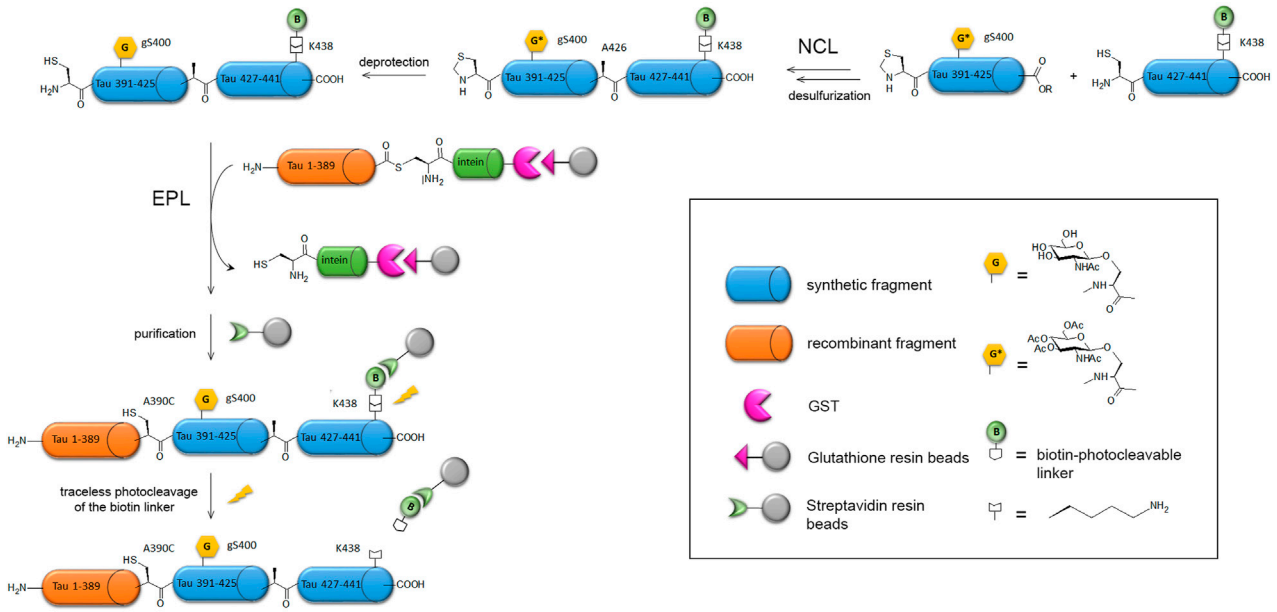

FIGURE 5 | EPL strategy applied to the semisynthesis of full-length tau-S400-O-GlcNAc protein (Schwagerus et al., 2016). The C-terminal synthetic fragment incorporating the S400-O-GlcNAc modification and a biotin selectively linked to K438 residue for purification is obtained by NCL of two synthetic peptides, followed by desulfurization to restore the native A426 at the ligation site and deprotection of the GlcNAc moiety. The resulting C-terminal S400-O-GlcNAc peptide is then ligated by EPL with the N-terminal fragment recombinantly expressed as intein-GST fusion purified on glutathione affinity chromatography. The ligation product is isolated from the unreacted recombinant fragment through streptavidin-biotin affinity chromatography and traceless released by photocleavage of the biotin linker. The final product is the full-length protein tau-S400-O-GlcNAc with a A390C mutation at the EPL ligation site that cannot be recovered by desulfurization due to the presence of two native cysteine in tau sequence.

polymerization or the Pin1-mediated regulation of tau dephosphorylation by PP2A (Amniai et al., 2009; Landrieu et al., 2011). The use of enzymes for introducing a limited pool of PTMs generally requires multiple mutations into an amino acid that cannot be modified as exemplified by the restriction of phosphorylation patterns to single phospho-epitopes, such as AT8 and PHF-1, for functional investigations (Amniai et al., 2009; Landrieu et al., 2011; Despres et al., 2017; Cantrelle et al., 2021). Alternatively, mimetics of PTM-amino acid may be inserted at single or multiple place mimicking a permanently modified state (Eidenmüller et al., 2001; Min et al., 2015). First attempts of full-length tau EPL semisynthesis were made by Hackenberger and co-workers, for the introduction of phosphorylation on S404 in the C-terminal region by ligation of a C-terminal phosphorylated peptide (from residue 390–441) to a N-terminal recombinantly expressed fragment (from residue 1–389) fused to intein (Broncel et al., 2012). Further improvement of the ligation strategy was required to afford the triple phosphorylation of PHF-1 epitope (pS396/pS400/pS404) or S400 O-GlcNAcylation owing to the length of the synthetic peptide (52 residues) (Reimann et al., 2015; Schwagerus et al., 2016). Hence, the synthesis of the C-terminal peptide involved NCL of two fragments followed by desulfurization, then EPL with the recombinant N-terminal fragment provides the full-length protein. A traceless purification strategy was also implemented through the use of a photocleavable biotin handle to purify the ligation product (**Figure 5**).

The presence of two native cysteine in tau primary sequence prevents from desulfurization of the EPL product. To circumvent this issue, the Lashuel's group has exploited the native cysteine residues (C291 and C322) in a three-fragment ligation strategy for the synthesis of the tau K18 fragment (residues 243–372) corresponding to the microtubule-binding repeats (MTBR) containing four repeat/inter-repeat sequences, a region overlapping the core of amyloid fibrils from diverse tauopathies. This approach involves the native cysteine at the NCL junction sites preventing any introduction of non-native cysteine. The total chemical synthesis of K18 allowed the installation of phosphorylation at single (pS356) or multiple sites (pS262/pS356 and pS258/pS262/pS356) known to modulate tau function in microtubule polymerization/binding and amyloid assembly (Schneider et al., 1999). The site-specific phosphorylation of K18 proved to inhibit its aggregation *in vitro*, its seeding property in biosensor cells, and its ability to promote microtubule polymerization (Haj - Yahya et al., 2020). The same strategy including first NCL of a C-terminal synthetic fragment was used in combination with an expressed N-terminal tau fragment (residues 2–245) for EPL allowing the semisynthesis of full-length tau after ligation of five fragments with either pY310, Ac-K280 or pS396/pS404 modification (Haj-Yahya and Lashuel, 2018). To obtain wild-type tau, two desulfurization steps were performed restoring native alanine at ligation sites before the incorporation of both fragments bearing native cysteine residues. The site-specific acetylation of K280 reproduces with

increased outcome the effect of K280Q acetylation mimicking mutant on tau aggregation by forming rather oligomers and short fibrils instead of the long filaments observed for unmodified tau consistently with the increased seeding efficiency and toxicity of this mutant in AD models of tau pathology (Min et al., 2010; Cohen et al., 2011; Gorsky et al., 2016).

PHF-tau isolated from AD brains is conjugated to ubiquitin at multiple lysine residues within the MTBR, such as monoubiquitination at K254, K257, K311 and K317, and K48-linked polyubiquitination at K254, K311 and K353. Hence, the chemoselective disulfide coupling reaction implemented for ubiquitination of α-synuclein was similarly employed for the site-specific monoubiquitination of the K18 tau fragment at K254, K311 or K353 in which both native cysteine were mutated into alanine to prevent unwanted conjugation of ubiquitin. In contrast to multiple enzyme-derived ubiquitination that prevents the formation of both prefibrillar oligomers and amyloid fibrils, the semisynthetic ubiquitinated tau conjugates form oligomers and filaments to different extent with ubiquitination at K311 position being the strongest inhibitor (Munari et al., 2020).

3.1.4 Huntingtin

Mutant Huntingtin as a primary cause of Huntington's disease is characterized by an abnormal expansion of polyglutamine (poly Q) tract at the N terminus which has been described as pathological when exceeding 40 glutamine repeats instead of the normal 9 to 35. The length of the expanded polyQ tract was suggested to be proportional to disease severity. The first 17 N-terminal residues of Htt act in modulating Htt structure, interactions and aggregation. Hence, polyQ expansion was shown to cause misfolding of the N-terminus and could play a key role in aggregation and toxicity. The polyQ expansion in mutant Htt exon1 causes conformational changes and increases phosphorylation at multiple sites across the entire protein (Jung et al., 2020). It was suggested that phosphorylation of Htt N-terminus could reverse the conformational rigidity related to polyQ expansion and improve the toxic properties. Phosphorylation of the N-terminal fragment of Htt at T3 homogeneously obtained by EPL, either in wild-type (23Q) or mutant Htt protein (43Q) was shown to stabilize the α-helical conformation of the N-terminal 17 amino acids and significantly inhibit aggregation while K6 acetylation reverses the inhibitory effect of pT3 without exhibiting any intrinsic inhibitory effect by itself (Ansaloni et al., 2014; Chiki et al., 2017). More recently, a new chemoenzymatic semisynthesis of Htt N-terminal fragment (1–170) that forms nuclear and cytoplasmic inclusions in cell and animal models of HD enables the introduction of phosphorylation in exon3 (Kolla et al., 2021). Phosphorylation of T107 was shown to have opposite roles on Htt(1–171)-43Q aggregation depending on the phosphorylation status of S116 highlighting the benefits of site-specific PTM installation through semisynthesis in deciphering the PTM code that regulates the aggregation properties of amyloidogenic proteins.

3.1.5 TDP-43

The semisynthesis of TDP-43 prion-like domain bearing a site-specific phosphorylation at S404 required the use of denaturing conditions to solubilize protein fragments expressed in bacterial expression systems. Indeed, the strategy of EPL through purification of full-length TDP-43 or prion-like domain as protein thioesters by the traditional fusion intein-CBD was unsuccessful to produce soluble TDP-43 variants in contrast to α-synuclein, Htt or tau proteins. Hence, the selected approach made use of a polyhistidine tag attached to a C-terminal cysteine residue which is submitted to S-cyanylated cysteine-promoted C-terminal hydrazinolysis to remove the tag. The tag removal then leaves a reactive C-terminal hydrazide that can be converted into a thioester for further NCL with the C-terminal pS404 fragment afforded by SPPS. Using this procedure, phosphorylation of S404 of TDP-43 prion-like domain was shown to accelerate the amyloid aggregation of the TDP-43 prion-like domain and worsen cytotoxicity (Li et al., 2020a).

Although the semisynthesis of post-translationally modified proteins has taken advantage of the NCL/EPL strategy, its major drawback is related to the need for a combined expertise in both peptide synthesis and chemical ligation reactions, and when applicable, the refolding of protein fragments of interest may be limiting. Expansion of the genetic code using amber stop codons and an orthogonal tRNA/tRNA synthase pair is an alternative strategy to introduce site-specific PTMs such as phosphoserine, acetyl-lysine, mono-/di-methyl-lysine, and UAAs (Wang et al., 2006; Tarrant and Cole, 2009; Park et al., 2011; Ge and Woo, 2021). However, this route has not been extensively applied so far to amyloid proteins. Finally, a more flexible method analogous to NCL implemented the sortase-mediated ligation (SML), or sortagging, which benefits from the transpeptidase activity of bacterial Sortase A (SrtA) enzymes that recognize with a high substrate specificity LPXT motifs and conjugate them to oligoglycine units through a native peptide bond (Dai et al., 2019; Li et al., 2020b). This versatile ligation approach demonstrates broad applications *in vivo* and *in vitro* for protein engineering, for instance by ligating a peptide substrate bearing PTMs, UAAs or other labeling probes (obtained from SPPS) into sortagging reactions. The directed evolution of SrtA to recognize the LMVGG sequence of Aβ (residues 34–38) enabled labeling of endogenous Aβ in human CSF for sensitive detection and conjugating a hydrophilic peptide to Aβ42 that blocks amyloid aggregation (Podracky et al., 2021). Dual-color fluorogenic aggregation sensors were introduced by SML to monitor protein co-aggregation in transthyretin amyloidosis by a thermal shift assay (Bai et al., 2021).

3.2 Posttranslational Chemical Mutagenesis

3.2.1 Reactions With Cysteine Thiol Function

The site-specific chemical installation of PTMs made use of the reactivity of cysteine thiol group and requires first the site-directed mutagenesis of the PTM site to introduce a non-native cysteine residue, and eventually replacing native cysteine(s) by serine or

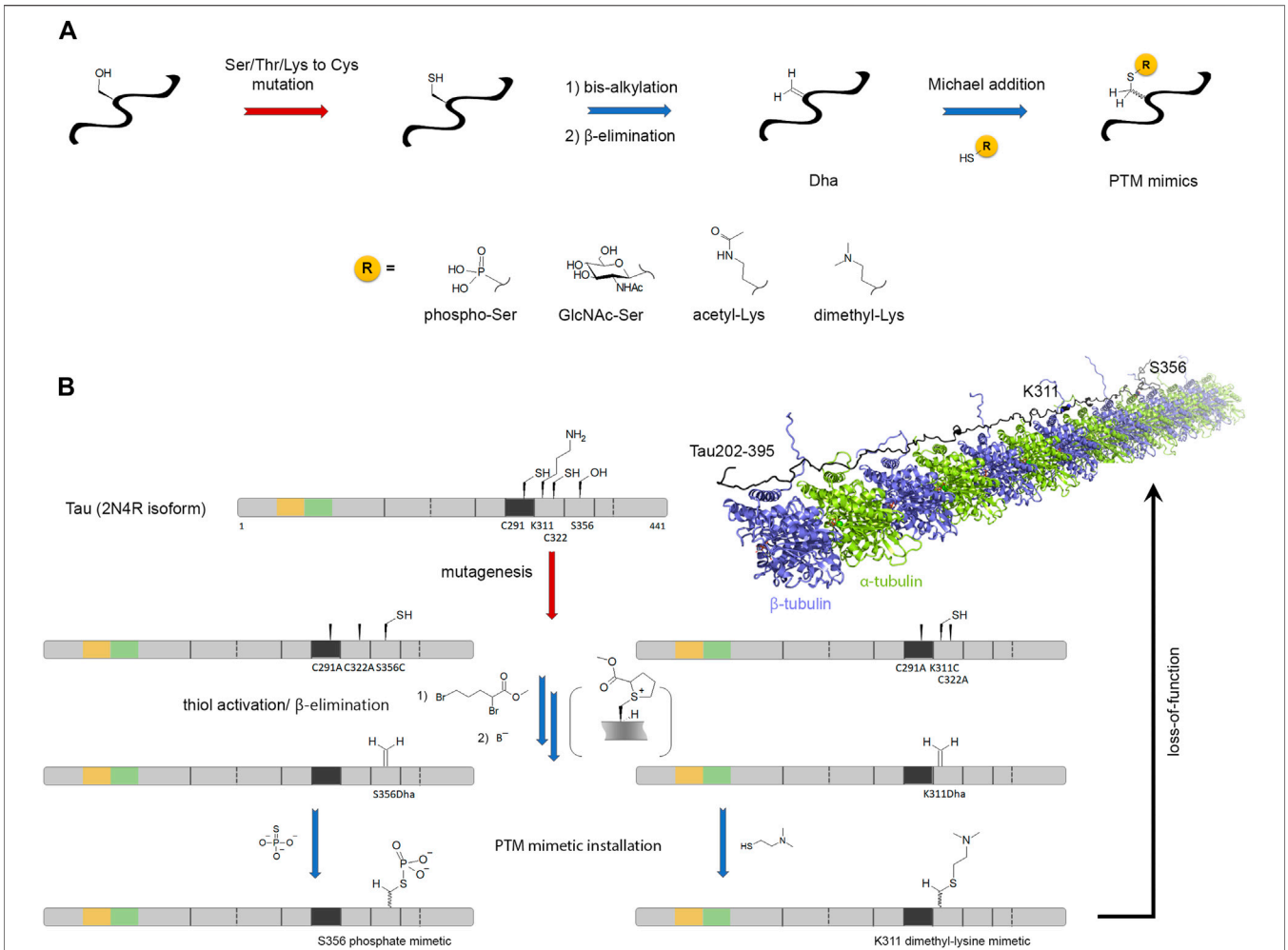

FIGURE 6 | Posttranslational chemical mutagenesis. **(A)** General scheme of the posttranslational chemical mutagenesis approach for incorporation of PTM mimics by Michael addition of PTM-thiol derivatives on dehydroalanine (Dha) alkene function. The latter is obtained from serine/threonine/lysine-to-cysteine mutation at the PTM site and β-elimination of the bis-alkylated thiol function of cysteine. Addition of thiophosphate, S-GlcNAc, N-acetylcysteamine and captamine generates mimetics of phosphorylation, O-GlcNAcylation, N-acetylation and N,N-dimethylation, respectively. The thio-ether bond formation leads to a racemization of amino acid Cα. **(B)** This approach is illustrated by S356 phosphorylation and K311 acetylation in tau protein for the investigation of the PTM effect on loss-of-function in microtubule polymerization (PDB ID: 7PQP) (Brotzakis et al., 2021; Lindstedt et al., 2021). Chemical reactions are indicated by blue arrows and enzymatic reactions by red arrows.

alanine residues. An acetyl-lysine analog can be introduced through Lys-to-Cys mutation at a specific site and subsequent thiol alkylation with methylthiocarbonylaziridine leading to a thioether bond bearing a terminal S-methyl thiocarbamate group as acetyl mimic (Huang et al., 2010). Other chemical approaches for the site-specific ubiquitination of proteins, comprise the formation of thioether bonds (Hemantha et al., 2014) or triazole moiety through Copper(I)-catalyzed azide-alkyne cycloaddition (CuAAC) (Rösner et al., 2015) as stable analogs of the ubiquitin isopeptide bond. Mono- and di-methylated (symmetric or asymmetric) arginine-containing proteins can be prepared by reaction of cysteine thiol with *α,β*-unsaturated amidines leading to the corresponding methylated arginine analogs (Le et al., 2013). The chemical installation of mono-, di- and tri-methyl-lysine analogs can be provided by thiol alkylation with the respective N-methylated (2-chloroethyl)-ammonium halide (Simon et al., 2007). However, none of these reactions were applied so far to amyloid proteins to our knowledge.

3.2.2 Versatile Chemistry of Dha/Dhb Precursors

Besides NCL, an increasing number of chemical methods has been developed to encode or decode PTMs in various proteins, as extensively described in excellent reviews (Chuh et al., 2016; Ge and Woo, 2021; Yang et al., 2018). A versatile approach is the chemical editing of amino acids into protein after their synthesis, thus independently of the ribosome or any enzymatic machinery. Dehydroalanine (Dha)/dehydrobutyrine (Dhb) are versatile chemical precursors to a range of PTMs including phosphorylation, glycosylation, methylation, acetylation,

lipidation, and their analogs (**Figure 6A**). Dha/Dhb precursors can be introduced chemically or genetically into proteins (Jones, 2020; Yang et al., 2019). These reactive Ser/Thr analogs allow following olefin addition chemistry introducing a wide variety of PTMs in a strategy named "posttranslational chemical mutagenesis" as well as UAAs or molecular probes for purification or detection purposes. A simple way to obtain Dha site-specifically is through β-elimination of the cysteine thiol function that requires 1) the site-directed mutagenesis of the PTM target site to install a cysteine precursor and 2) the Cys-to-Dha conversion through a bis-alkylation elimination reaction (**Figure 6A**) (Chalker et al., 2011). Although the Cys-to-Dha conversion was used to map cysteine accessibility in a globular protein (Bertoldo et al., 2017), all cysteines are equally reactive in IDPs and, whenever needed, native cysteines must be mutated. An alternative strategy is the genetic introduction of Dha precursors reactive to β-elimination, like phosphoserine, through genetic code expansion using amber codon suppression (Yang et al., 2016).

Subsequent to Dha formation, the installation of PTMs or PTM analogs is provided by Michael addition (**Figure 6A**). Thiol derivative precursors of PTMs are the most convenient way to introduce PTM but the formation of the thio-ether bond induces Cα racemization (and also at Cβ in the case of Dhb derivatives) which seems not to be an issue in most amyloid case studies. This strategy was employed to introduce PTMs in full-length tau protein like pseudo-phosphorylation at pS262, pS356, pS199 by reaction with thiophosphate (to generate a phosphocysteine) and lysine K311 acetylation (K311-Ac) and dimethylation (K311-diMe) by reaction with N-acetylcysteamine and captamine (to generate thio-ether mimetics of PTM-lysine), respectively (**Figure 6B**) (Brotzakis et al., 2021; Lindstedt et al., 2021). While K311-diMe and K311-Ac have little effect on the formation of microtubules, pseudo-phosphorylation of pS262 and pS356 in the MTBR as well as pS199 in the proline-rich region were shown to inhibit the polymerization activity of tau confirming the role of pS262/pS356 that was previously investigated by *in vitro* kinase phosphorylation and highlighting a novel functional role for pS199 that is located far outside the MTBR, in the proline-rich domain (PRD). This is not surprising however, since other AD-specific phosphorylation epitopes embedded in the PRD were shown to modulate microtubule assembly (Amniai et al., 2009). Alternative elegant and versatile strategies to create C-C (sp3-sp3) bonds instead of unnatural carbon-heteroatom bonds were described, albeit not applied so far to amyloid proteins. They made use of mild, carbon-centered free radical chemistry that are compatible with Dha precursor reactivity and aqueous conditions suitable for protein chemical reactions. Most importantly, free radicals are unreactive with most of functionalities found in biomolecules. The reaction of Dha with a wide range of free radical precursor halides generates a stabilized Cα free radical that is further quenched after formation of the C-C bond allowing the installation of side chain chemical diversity (unnatural, fluorinated, PTM or isotopically labeled amino acids) at a specific position with a high site- and regio-selectivity (creation of Cβ-Cγ bonds), albeit with Cα racemization (Wright et al., 2016; Aguilar Troyano et al., 2021).

3.3 Focus on the O-GlcNAc exception: the chemical biology toolbox for the installation, detection and enrichment of O-GlcNAcylated amyloid proteins

The O-GlcNAc modification of proteins, and more particularly amyloid proteins, has required special attention. As an addition of single sugar on Ser/Thr, this PTM is closely comparable to phosphorylation. In addition, the O-GlcNAcome tightly overlaps the phosphoproteome. Thus, protein O-GlcNAcylation has long been occulted due to its close interplay with phosphorylation and a lack of appropriate detection/analytical methods (Thompson et al., 2018). For example, the poor immunogenicity of this small, neutral sugar prevents from raising selective antibodies, and only a few site-specific O-GlcNAc antibodies are available (e.g. S400-O-GlcNAc tau-directed antibody from Vocadlo's lab (Yuzwa et al., 2011)). Another major limitation is related to the low sub-stoichiometry of the O-GlcNAc modification requiring the development of specific enrichment methods for O-GlcNAc profiling. Finally, the absence of consensus sequences emerging from the number of O-GlcNAc databases hamper the prediction of O-GlcNAc sites. Particularly intriguing is the mode of regulation of both OGT and OGA as the only two enzymes encoded in the human genome to implement the whole O-GlcNAc modifications of the O-GlcNAcome facing approximately 500 kinases. This suggests the recruitment of regulating sub-units for specific substrate targeting.

Biochemical and genetic manipulations of OGT and its substrates has provided several solutions to produce enzymatically O-GlcNAc modified proteins as exemplified by the co-expression of OGT and the protein of interest in *E. coli* given that bacteria do not have any equivalent of OGT protein but produce UDP-GlcNAc in sufficient amounts. This strategy was employed with tau (Yuzwa et al., 2011) and α-synuclein (Zhang et al., 2017b) to address the O-GlcNAc modification pattern of tau and the role of O-GlcNAc in tau and α-synuclein aggregation, respectively. The co-expression OGT/substrate can be optionally accompanied by 1) the co-expression of GlmM and GlmU enzymes that participate to the bacterial UDP-GlcNAc biosynthesis and therefore help protein O-GlcNAcylation by enhancing intracellular UDP-GlcNAc concentration (Gao et al., 2018), and 2) the treatment of bacterial cultures and extracts with PUGNAc, a potent glycosidase inhibitor, since endogenous NagZ glycosidase can hydrolyze O-GlcNAc in exogenous glycosylated proteins, hence reducing the O-GlcNAc modification level (Goodwin et al., 2013). This strategy together with the *in vitro* incorporation of O-GlcNAc through incubation of the protein substrate with UDP-GlcNAc and expressed OGT (from heterologous expression system) lead to heterogenous, and most importantly, low sub-stoichiometry modification in most cases. The lack of regulatory sub-units in artificial systems could in part explain the inefficiency of protein

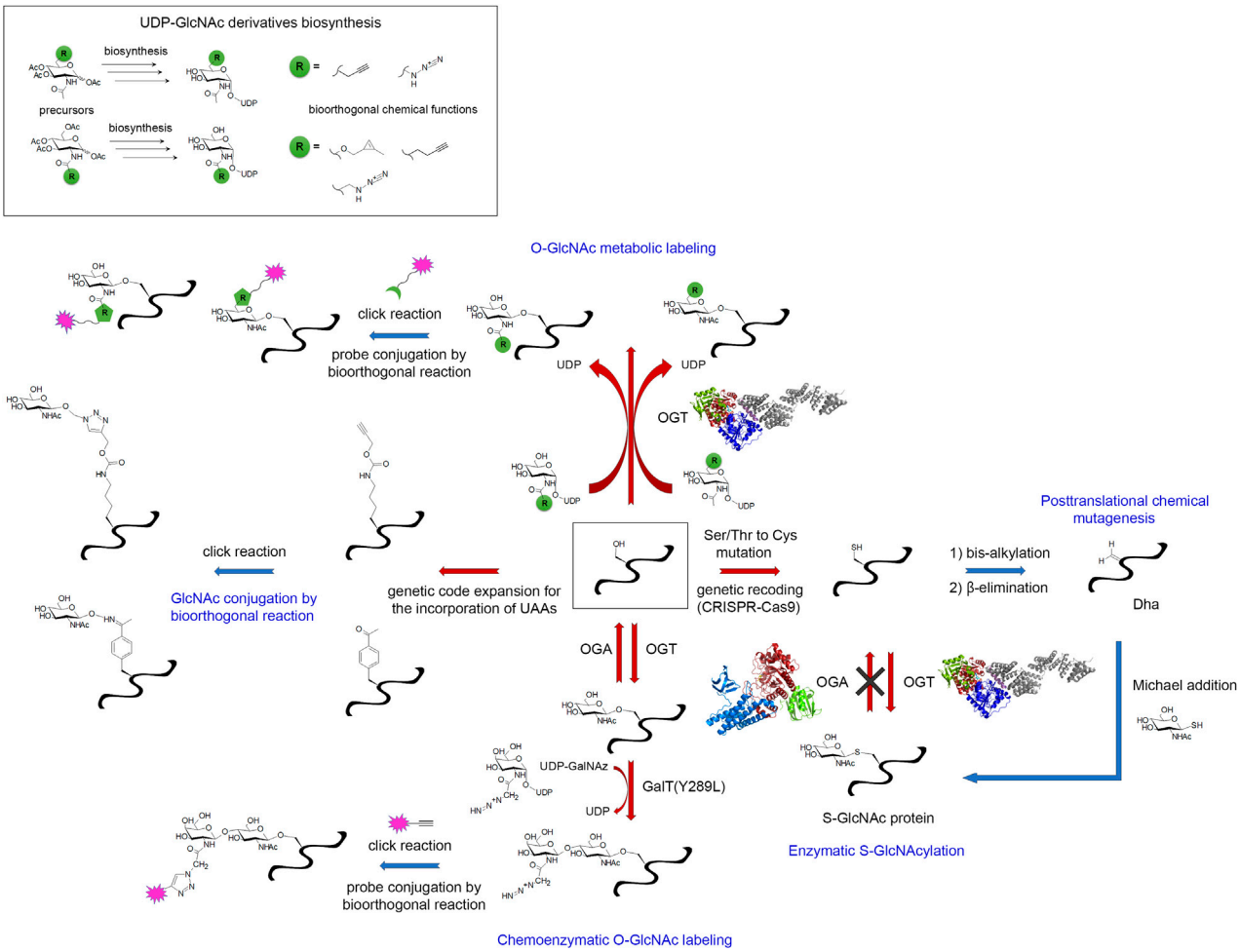

FIGURE 7 | Posttranslational chemical mutagenesis, genetic code expansion and chemo-enzymatic reactions for incorporation of O-GlcNAc mimics and derivatives for O-GlcNAc detection/purification. Chemical reactions are indicated by blue arrows and enzymatic reactions by red arrows. Some examples of the manifold approaches for the incorporation of S-GlcNAc and O-GlcNAc derivatives are given. An extensive review of O-GlcNAc installation and detection can be found in (Saha et al., 2021). Site-specific O-GlcNAc mimics can be incorporated directly on the cysteine thiol function after Ser/Thr into Cys site-directed mutagenesis or using the gene-editing tool CRISPR-Cas9. This allows for instance the enzymatic installation of S-GlcNAc mimics with OGT leading to a stable GlcNAc derivative since hydrolysis by OGA is not possible. Alternatively, the engineered cysteine residue may also be an intermediate to provide a bioorthogonal reactive dehydroalanine (Dha) derivative after thiol bis-alkylation and subsequent β-elimination. The Dha handle is amenable to a Michael addition with a GlcNAc-thiol derivative for installation of a S-GlcNAc derivative. A third approach involved the incorporation of unnatural amino acids (UAAs) bearing a reactive handle amenable to "click" chemistry, e.g., acetophenone or propargyl-lysine, using the amber codon suppression strategy of genetic code expansion for the site-specific O-GlcNAc modifications. Coupling of the O-GlcNAc moiety is performed by azide-alkyne [3 + 2] cycloaddition. For detection or enrichment of O-GlcNAcylated proteins, labeling of O-GlcNAc is performed as a first step either (i) by "metabolic labeling" through oligosaccharide engineering that introduces chemical handles (azide, alkyne,. . .) directly on the GlcNAc group for subsequent reaction (via the biosynthesis of UDP-GlcNAc derivatives, depicted in the box) or (ii) by "chemoenzymatic labeling" through an enzymatic reaction of the O-GlcNAc group with a mutant of β1,4-galactosyltransferase (GalT-Y289L) that forms a glycosidic bond with a galactose derivative (GalNAz). In both strategies, the second step is the subsequent conjugation of reactive probes (e.g., fluorescent probes, mass tag, biotin. . .) for downstream enrichment or detection. The latter processes through a reaction of "click" chemistry making use of azide bioorthogonal reactivity through the copper(I)-catalyzed (CuAAC) or strain-promoted azide-alkyne cycloaddition (SPAAC).

O-GlcNAcylation with recombinant OGT or bacterial co-expression systems.

The semisynthesis of α-synuclein incorporating a site-specific S-GlcNAcylation at S87C mutation site was used to probe the OGA activity on S-linked GlcNAc modification. Accordingly, the S-GlcNAc moiety was shown to be enzymatically stable upon OGA treatment. Moreover, it has the same effect than the O-linked counterpart in membrane binding of α-synuclein and inhibition of its fibrillar aggregation (De Leon et al., 2017). Following this approach, genetic methods implementing the CRISPR-Cas9 methodology for the site-specific Ser-to-Cys mutation of the glycosylation site has allowed incorporating S-GlcNAc derivatives with high level of protein modification in living cells (Gorelik et al., 2019) considering the ability of OGT

to process cysteine residues while OGA cannot hydrolyze the S-linked GlcNAc sugar, thereby increasing the stability of the modification in the cell (**Figure 7**) (De Leon et al., 2017). Then, engineering of a hexosamine thioligase inspired from the GH20 hexoaminidase enzymatic mechanism and utilizing 4-nitrophenyl N-acetyl-β-D-glucosaminide (pNP-GlcNAc) as glycosyl donor has improved the GlcNAc S-linkage to targeted sites after Ser-to-Cys mutation (Tegl et al., 2019). The enzymatic S-GlcNAcylation of tau at S400C was performed using this approach. In addition, efforts were made to produce GlcNAcylated proteins both *in vitro* and *in vivo* through "proximity-induced reactions" improving levels and detection of GlcNAcylated proteins (see paragraph 4.3) (Ge and Woo, 2021).

Interestingly, O-GlcNAc seems to have an overall protective effect in amyloid aggregation of various proteins involved in neurodegenerative diseases, in part owing to its interplay with phosphorylation. The phosphorylation/O-GlcNAcylation crosstalk in tau protein derived from the overall modulation of O-GlcNAcylation (OGA inhibitors, mouse starvation) and distinct transgenic mouse models suffers from contradictory outcomes (Yuzwa et al., 2008; Yuzwa et al., 2012; Graham et al., 2014; Hastings et al., 2017) while *in vitro* studies highlight only a limited direct interplay between both PTMs at the protein level (Bourré et al., 2018; Cantrelle et al., 2021). Phosphorylation of S129 of α-synuclein, a marker of typical PD aggregates, was shown to be sensitive to the O-GlcNAc modulation, either by genetic or pharmacological upregulation of O-GlcNAcylation, while pS129 reduction has been observed in the homogenously T72-O-GlcNAc modified semisynthetic protein upon phosphorylation by different kinases (Marotta et al., 2015; Lee et al., 2020). Unraveling the regulation of tau or α-synuclein (hyper)phosphorylation and pathophysiological functions by the O-GlcNAc glycosylation would deserve further investigations with the targeted protein O-GlcNAcylation approaches.

The investigations of the functional impact of amyloid PTMs and PTM dysregulation in cell and *in vivo* systems require the isolation, detection and analytical characterization of posttranslationally modified proteins which proved to be particularly difficult in the general case of O-GlcNAcylated proteins. Indeed, both detection and/or enrichment of O-GlcNAc proteins usually apply succinylated wheat germ agglutinin (sWGA) lectin or pan-O-GlcNAc monoclonal antibodies, RL2 and CTD110.6, that detect O-GlcNAc proteins in cytosolic and nuclear extracts (Saha et al., 2021). However, sWGA although relatively selective has a low affinity for the single O-GlcNAc sugar while pan-O-GlcNAc antibodies have a low affinity and a limited specificity, sometimes exhibiting cross-reactivity with terminal GlcNAc of branched N-glycans (Isono, 2011; Tashima and Stanley, 2014). Significant advances using chemical biology tools during the last decade has strongly expanded the detection of O-GlcNAcylated proteins as a long-standing demand, and helped deciphering the functional role of O-GlcNAcylation as extensively reviewed in (Saha et al., 2021). Bioorthogonal chemical reactions have been implemented to afford a wide range of tools and probes for the detection or enrichment of O-GlcNAcylated proteins from *in vivo* systems (**Figure 7**). In particular, the O-GlcNAc enrichment methods combined with mass spectrometry-based proteomics have led to important advances in the profiling of protein O-GlcNAcylation in systemic approaches. As a first step, the labeling of O-GlcNAc is performed either by metabolic oligosaccharide engineering that consists of introducing several types of reporter groups (ketone, azide, alkene, alkyne, isonitrile) as chemical handles for subsequent reaction or, alternatively, by enzymatically coupling a galactose derivative using the specific reaction of β1,4-galactosyltransferase (GalT). The former approach uses the manipulation of the UDP-GlcNAc metabolic pathway and the OGT plasticity to a variety of UDP-GlcNAc derivatives (e.g. peracetylated N-azidoacetylglucosamine) to directly incorporate chemical reactive group in the GlcNAc moiety of glycosylated proteins (Moon et al., 2022; Saha et al., 2021). The latter approach achieved better efficiency by using a mutant of GalT (GalT-Y289L) tolerant to UDP-GalNAc derivatives, such UDP-GalNAz containing an azide group, as a substrate donor for glycosidic linkage to GlcNAc (**Figure 7**) (Khidekel et al., 2003). The second step is the subsequent reaction with diverse reactive probes (e.g. fluorescent probes, mass tag, biotin. . .) for downstream enrichment or detection. An example is the use of azide bioorthogonal reactivity through the [3 + 2] cycloaddition with alkynes. The development of a copper(I)-catalyzed azide-alkyne cycloaddition (CuAAC), termed "click" chemistry, improved the conditions of the initial Huisgen reaction to proceed in physiological conditions compatible with biomolecule functionalities. However, as Cu(I) is toxic in cellular environment, activated alkynes, e.g. induced by ring strain such as cyclooctyne, has been implemented in a strategy compatible with cellular environments named strain-promoted azide-alkyne cycloaddition (SPAAC) (Agard et al., 2004). The conjugation of fluorescent probes and biotin through a click chemistry reaction allowed subsequent O-GlcNAcylated protein detection and isolation while mass tagging (e.g. with resolvable polyethylene glycol mass tags) provides a rapid insight into the distribution of O-GlcNAc proteoforms.

4 DETECTING AND CHARACTERIZING AMYLOIDS WITH CHEMICAL BIOLOGY TOOLS

4.1 Chemical Tools for Amyloid Detection and Structural Characterization

4.1.1 Small-Molecule Sensors of Amyloid Aggregation

Historical fluorescent probes for the detection of amyloids (e.g., ThS, ThT, ANS, Bis-ANS, Congo Red, Nile Red. . .) (**Figure 8A**) (Naiki et al., 1989; Biancalana and Koide, 2010; Krebs et al., 2005; Groenning, 2010; Amdursky et al., 2012) were recently complemented by a wide range of aggregation-induced emission (AIE) molecules (Tang et al., 2022; Tang et al., 2021) including hexaphenylsilole (HPS), tetraphenylethylene (TPE) and tetraphenylbutadiene that expand the detection of aggregates formed along the amyloidogenic pathway such as

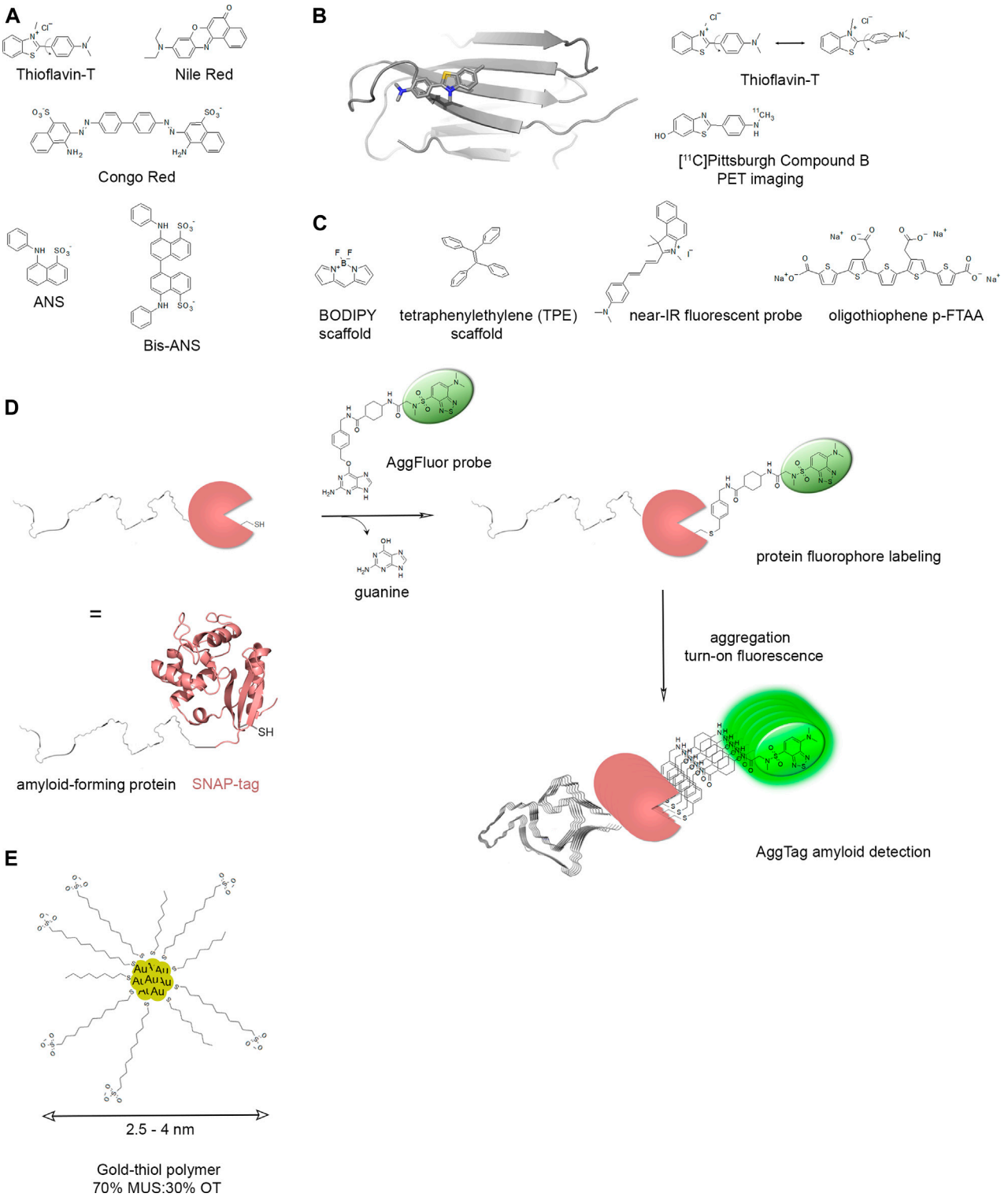

FIGURE 8 | Detection of amyloids by fluorescence labeling **(A–D)** or functionalized gold nanoparticles **(E)**. **(A)** Structures of extrinsic fluorescent probes used for amyloid detection. **(B)** Aggregation-induced emission (AIE) molecules exemplified by Thioflavin-T (ThT) emit a fluorescent signal upon binding into hydrophobic pockets of amyloid β-sheet structures due to restriction of intramolecular rotation (PDB ID: 3MYZ). The structure of [^{11}C]-Pittsburgh Compound B used for PET imaging is based on ThT structure. **(C)** Some examples of fluorescent molecules based on BODIPY or tetraphenylethylene (TPE) scaffolds are depicted as well as a near-infrared (near-IR) fluorescent probe and the oligothiophene p-FTAA (pentameric form of formyl thiophene acetic acid). **(D)** An example of fluorescent SNAP-tagging is depicted in a strategy called "AggTag" for amyloid detection. The engineering of a SNAP-tag amyloid protein allows coupling of an AggFluor probe through the selective reaction of a

(*Continued*)

FIGURE 8 | SNAP tag cysteine residue with O-benzylguanine derivatives. The subsequent aggregation of amyloid-forming proteins turns on fluorescence of the AggFluor probe. Various AggFluor probes has been designed to detect oligomers and amyloid fibrils, or amyloid fibrils selectively (Liu et al., 2018; Wolstenholme et al., 2020). **(E)** Functionalization of gold nanoparticles (gold-thiol polymer) with a mixture of 11-mercapto-1-undecanesulfonate: 1-octanethiol (MUS:OT) enables the selective detection of amyloid fibrils and polymorphism by cryo-EM imaging (Cendrowska et al., 2020).

oligomers that are poorly detected by ThT, Congo Red and their derivatives. AIE molecules usually possess twisted structures in solution limiting the fluorescence yield by non-radiative transition (Kumar et al., 2017; Aliyan et al., 2019). Restricted intramolecular motions upon binding to amyloid β-sheets alleviates this phenomenon due to electrostatic and/or hydrophobic interactions, structural complementarity and/or chemical reactions (**Figure 8B**). For instance, increased fluorescence signal of new AIE probes with the size increase of Aβ aggregates enables a sensitive detection of Aβ aggregation and inhibition (Gour et al., 2019). Development of AIE probes includes the coverage of a large wavelength spectrum from the visible to the near-infrared (NIR) (**Figure 8C**). NIR probes are more convenient for super-resolution imaging of amyloids in cells and tissues by increasing the spatiotemporal resolution and photostability while reducing tissue damages. Probes for excited state intramolecular proton transfer (ESIPT) or a series of boron dipyrromethene (BODIPY) derivatives were designed with AIE properties for the follow-up of amyloid aggregation (**Figure 8C**) (Hu et al., 2011; Liu et al., 2019). A fluorescent BODIPY-based binuclear Zn(II) complex was rationally designed as a molecular probe with phospho-selective binding properties for peptides presenting phosphorylated groups at the relative *i* and *i*+4 positions. This molecule allowed for a selective detection of NFTs of hyperphosphorylated tau proteins in AD brain as it discriminated between NFTs and SPs of Aβ peptides in histological imaging of hippocampus sections from AD patients (Ojida et al., 2009). The luminescent amyloid-binding conjugated poly- and oligothiophenes (LCPs and LCOs) is a class of amyloid dyes of fibrillar aggregates for emission fluorescence staining or imaging (**Figure 8C**) (Åslund et al., 2009; Brelstaff et al., 2015; Klingstedt et al., 2011). LCOs are uniquely capable to discriminate different molecular architectures. The aggregate-specific emission is achieved due to conformational restriction of the thiophene backbone upon interaction with specific protein aggregates. Using the LCOs fluorescence signature, fibril polymorphism can be monitored both *in vivo* and *in vitro*. LCOs will be useful to link protein conformational features with disease phenotypes for a variety of neurodegenerative proteinopathies (Magnusson et al., 2014). Another series of molecular rotor fluorophores named AggFluor derived from the chromophore core of green fluorescent proteins (GFPs) was rationally designed with a gradient of viscosity sensitivity over a wide range (**Figure 8D**). AggFluor probes were capable of differentiating between soluble oligomers and insoluble aggregates through distinct turn-on fluorescence. This method was extended to dual-color imaging of aggregation and its modulation thereof with small-molecule proteostasis regulators in living cells (Wolstenholme et al., 2020).

4.1.2 Functionalized Gold Nanoparticles

Probing of amyloids with gold nanoparticles or nanorods, or through immunogold labeling as gold nanoparticle conjugates to a specific antibody allowed mapping amyloid fibrils in tissue sections as well as identifying proteins and some of their molecular features. The presence of PTMs and cofactors, or the presence/accessibility of a particular sequence can be characterized in this manner (Fitzpatrick et al., 2017; Falcon et al., 2018b; Goedert et al., 1996; Al - Hilaly et al., 2020). However, these methods do not provide detailed information on the fibril morphology and polymorphism owing to either the bulkiness of the particle itself or to the distance between the particles and coated fibrils due to the size of the antibody and/or nanoparticle attachment linker. Functionalization of gold nanoparticles of 3 nm-diameter with negatively charged ligands (e.g. 11-mercapto-1-undecanesulfonate: 1-octanethiol mixture) enables to detect amyloid polymorphism over a variety of amyloid sequences under hydrated conditions by cryo-EM imaging (**Figure 8E**) (Cendrowska et al., 2020). The functionalized particles act as contrast agents to rapidly stain fibrillar structures. Fibrils are stained either at the fibril edges as exemplified with Aβ40 and tau R2 peptides, or on the whole fibril surface as for proteins tau and Htt exon 1 with a 43 polyQ segment, probably through interactions with the fibril fuzzy coat. This nanoparticle labeling facilitates the characterization of fibril morphology thereby revealing distinct polymorphs. Moreover, differential fibril decoration also reflects distinct morphologies. The functionalized gold nanoparticles have highlighted a higher homogeneity of periodicity length distribution for *in vivo* related to synthetic fibrils in agreement with cryo-EM structures.

4.1.3 Site-specific Introduction of Probes for the Study of Amyloids

Site-specific labeling of amyloid proteins allows to track conformation dynamics, interactions, modifications and seeding aspects by both *in vitro* approaches based on biophysical experiments and cell-based assays through microscopy imaging. Moreover, protein fluorescent labeling can be helpful in the screening of compounds for anti-aggregation or disaggregation activity by avoiding displacement of external fluorescent probes by competitive binding. The labels can be introduced with approaches similar to introduction of PTMs as detailed in paragraph 2 by incorporation of the labeled amino acid, or an amino acid amenable to bioorthogonal click chemistry (Arsić et al., 2022; Shimogawa and Petersson, 2021), by UAA mutagenesis, or based on suppression of stop codons. Another strategy of label incorporation is the conjugation of SPPS (peptide modified with a label) combined with NCL (see paragraph 2.1). In addition, the labels can be introduced using genetically

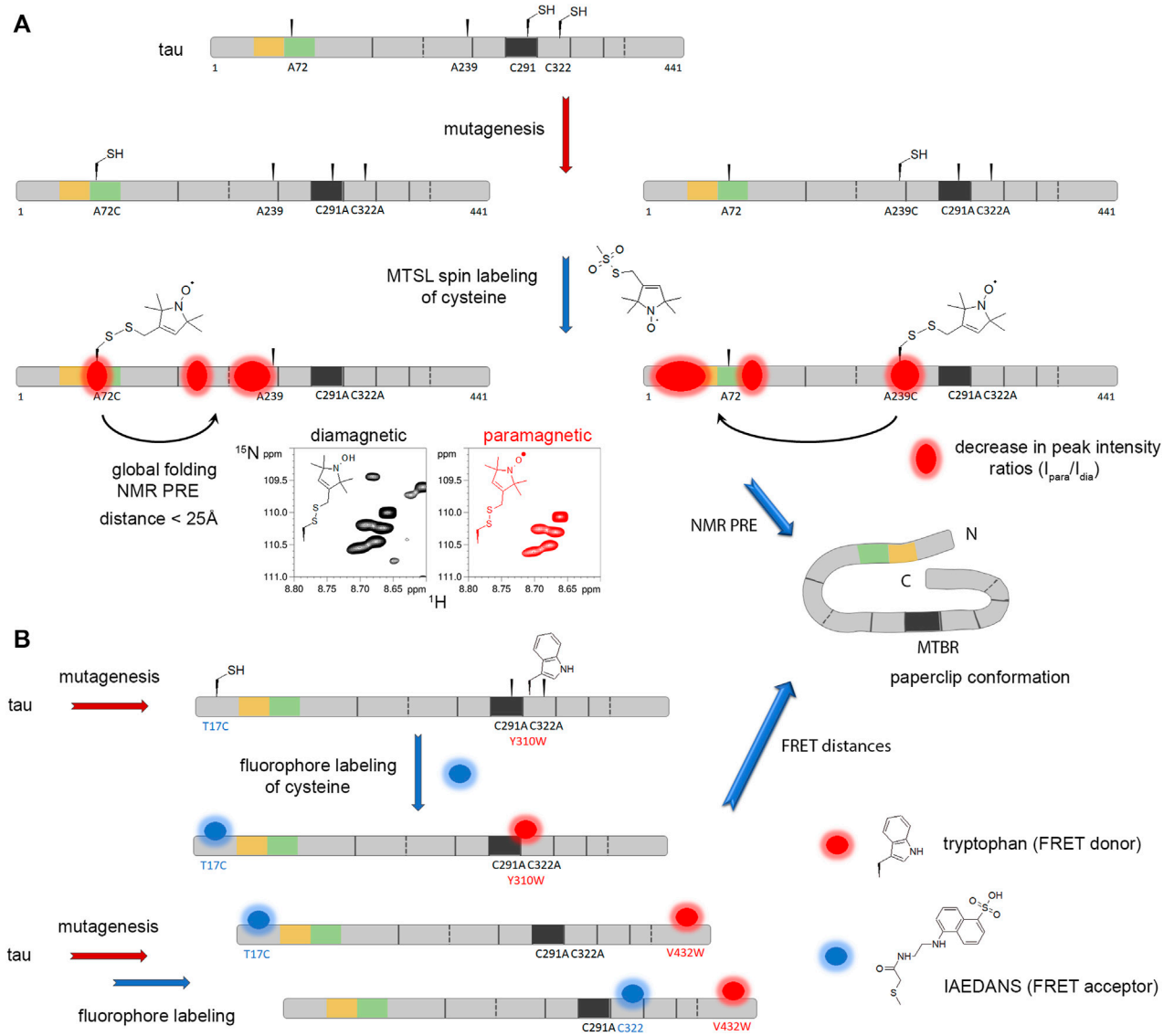

FIGURE 9 | Nitroxide spin labeling and FRET fluorescent pair labeling for distance measurements by NMR, EPR and FRET exemplified in tau protein. **(A)** Nitroxide spin labels such as MTSL (S-(1-oxyl-2,2,5,5-tetramethyl-2,5-dihydro-1H-pyrrol-3-yl)methyl methanesulfonothioate) can be introduced on thiol function(s) of engineered cysteine residues obtained by site-directed mutagenesis for NMR experiments. Single spin label is used in paramagnetic relaxation enhancement (PRE) experiments. Double spin labeling of two distinct cysteine residues is used for paramagnetic relaxation interference (PRI) experiments (not shown in the figure). The same labeling strategy with single or double paramagnetic probes can be used in EPR experiments (not shown in the figure). Single spin labels are introduced at different positions along the protein sequence as illustrated by A72C and A239C labeling. Proximal and long-range perturbations of NMR signals (distance >10 Å up to 25 Å) from the spin label is indicated by red areas (Bibow et al., 2011). The PRE phenomenon is characterized by a selected decrease of peak intensities in the ^{1}H-^{15}N HSQC experiment acquired on the ^{15}N-uniformly labeled protein and quantified by the I_{para}/I_{dia} ratio corresponding to the intensities measured in the paramagnetic specie (I_{para}) and the intensities measured in the diamagnetic specie (I_{dia}) in which the nitroxide is reduced by vitamin C. Such a spatial proximity to the probe of remote residues in the protein sequence suggests an overall folding of tau protein in its native monomeric form such as the paperclip-like conformation. **(B)** FRET measurement of distances requires both the mutagenesis of a hydrophobic amino acid into tryptophan as FRET donor probe (red spot) and coupling of IAEDANS as FRET acceptor probe (blue spot) to either a native (C322) or engineered cysteine (T17C) of tau protein. Different combinations of positions of FRET donor and acceptor probes allowed to define the paperclip conformation of native monomeric tau where both N- and C-termini are in close proximity of the central MTBR functional domain (Jeganathan et al., 2006; Jeganathan et al., 2012).

engineered reactive tags for N- or C- terminal labeling, such as SNAP-tag (Keppler et al., 2003) CLIP-tag (Gautier et al., 2008) and Halo-tag (Liu et al., 2018) that react with derivatives of O-benzylguanine bearing a chemical probe to label the protein via a benzyl linker (**Figure 8D**). SNAP and CLIP or Halo tags can be simultaneously and differentially labeled with fluorescent reporters in living cells (Gautier et al., 2008; Jung et al., 2019). Compared with fluorescent proteins as GFP or mCherry, these tags are small and can be modified with more stable and brighter fluorophores.

The easiest way to introduce a tag is probably by using Cys residues as attachment points for maleimide or iodoacetamide derivatives, or other thiol reactive species (Gunnoo and Madder, 2016). The Cys residues can be native protein residues, or introduced at a unique position by site-specific mutagenesis, with replacement of the natural Cys residues by an unreactive amino acid. This has been conveniently used for α-synuclein labeling with an environment-sensitive fluorescent reporter to probe binding to lipid membranes and fibrillization by discriminating between unstructured, membrane-bound and fibrillar states (Kucherak et al., 20182018). However, for the introduction of two different probes, a selective (de)protection of one of the two cysteine is required involving necessarily SPPS of a fragment at least of the protein of interest. Otherwise, a combination of different methods should be used. Cysteine conjugation was combined with amber codon suppression, transferase mediated N-terminal modification and NCL to produce α-synuclein variants bearing single or double site-specific fluorescent labels to probe conformational changes upon fibril formation and cellular uptake of fibrils (Haney et al., 2016; Haney et al., 2017).

Fluorescent probes differ whether investigating amyloidogenic processes *in vitro* or in living cells, and upon the fluorescence experiment employed being ensemble or single-molecule Förster resonance energy transfer (FRET), fluorescence polarization (FP), fluorescence correlated spectroscopy (FCS) or ESIPT. In any cases, careful considerations must be taken regarding the choice of labeling sites to avoid probe-induced perturbations of the protein conformation and fibrillization process even though small-molecule fluorophores are less invasive than their proteinaceous counterparts (e.g., GFP and its derivatives). Fluorophore are sensitive to change in their environments (e.g., exposure to the solvent, pH variation, ion concentration) as probed by FP and FCS. Introduction of two fluorophore labels gives access to FRET measurements based on distance-dependent fluorophore interactions. The distance between the fluorescent probes and dynamic fluctuation of these distances can be evaluated during fibril formation, upon interaction with small molecules (for example aggregation inhibitors) or due to a PTM. Single molecule FRET is of high interest when heterogeneity is considered, for example to characterize a population of oligomers. The use of fluorophore labels combined with microscopy imaging of live-cells is of importance to monitor cellular uptake, seeding and proteolysis.

The measurement of distance between FRET pairs in tau mutants carrying a tryptophan and a AEDANS-labeled cysteine, both residues being introduced by site-directed mutagenesis highlighted a paperclip-like conformation in native, soluble tau protein where both N- and C-termini fold over the MTBR (**Figure 9B**). Conformational changes of the paperclip preferential dynamic fold was observed upon phosphorylation and denaturation (Jeganathan et al., 2006; Jeganathan et al., 2012). The global fold was further confirmed by paramagnetic relaxation enhancement (PRE) NMR signals (see here below). The synthesis and FRET analysis of a site-specific, dual-labeled Htt exon1 indicated a progressive compaction of the protein upon increasing polyQ length in contrast to the pathological threshold length associated to HD (Warner et al., 2017).

Different conformational ensembles of α-synuclein were investigated inside cells using FRET pairs of fluorophores. FRET measurements allow to distinguish the unstructured α-synuclein and the α-helical conformation when α-synuclein is bound to the membrane, as both conformations are characterized by differences in the distance between both labels, the distance between the labeled amino-acid position being larger in the unstructured form (Fakhree et al., 2018). Introduction of labels can be coupled to introduction of modifications, using combination of the strategies here above briefly described using strategies addressed in paragraph 2. The semisynthesis of pY39 α-synuclein allowed to include a pair of FRET fluorescent labels using 1) coupling to cysteine and 2) UAA (propargyl-tyrosine, PpY) incorporation by amber codon suppression followed by click chemistry to reveal that phosphorylation of Y39 primarily acts on aggregation with only small interference with monomer conformation (Pan et al., 2020).

Processing of APP to generate the Aβ peptide was elegantly investigated in cells using a dual labeling scheme (van Husen et al., 2019). The APP C-terminal tail was labeled using a SNAP-tag while an UAA (trans-cyclooctene lysine) was introduced at a specific location in APP, corresponding to the Aβ peptide, by stop codon suppression. The side-chain of this UAA was next modified to attach a fluorescent dye (6-methyl-tetrazine-BODIPY-FL) by click chemistry reaction, while the unnatural residue was functionalized using TMR-Star. This double-labeling scheme allows to follow APP processing into a C-terminal fragment and Aβ peptide, and imaging the trafficking of the APP cleavage products in live cells.

Some *in vivo* experiments take advantage of the specific pH that characterizes some subcellular microenvironments to track the processing of amyloid proteins once they enter the cells. For example, CPX azide derivative was attached on α-synuclein using the UAA PpY functionalized by an azide-alkyne cycloaddition in a click chemistry approach. The labeled α-synuclein incorporated in fibrils was then tracked over time after it had entered neurons. Aggregates penetrating endosomes were highlighted by the green to red emission shift of CPX in that specific compartment (Jun et al., 2019).

Site-directed spin labeling, coupled to nuclear magnetic and/or electron paramagnetic resonance (EPR) measurements, are also of interest to study conformational fluctuations of amyloid proteins. A commonly employed paramagnetic label is the nitroxide moiety, which harbors an unpaired electron. This label is small and expected to cause no conformational perturbation of the functionalized protein. The paramagnetic effect of the electron is indirectly detected by NMR upon perturbation of the recorded signals due to enhanced transverse relaxation rate induced by proximity to the label (Clore et al., 2007). This effect has a r^{-6} dependence on the electron-proton distance (r) and thus allows the detection of long-range interactions in proteins (**Figure 9A**). To determine an ensemble of conformations consistent with PRE measurements, NMR signal intensity ratio (with/without nitroxide effect) can be converted into distance restraints.

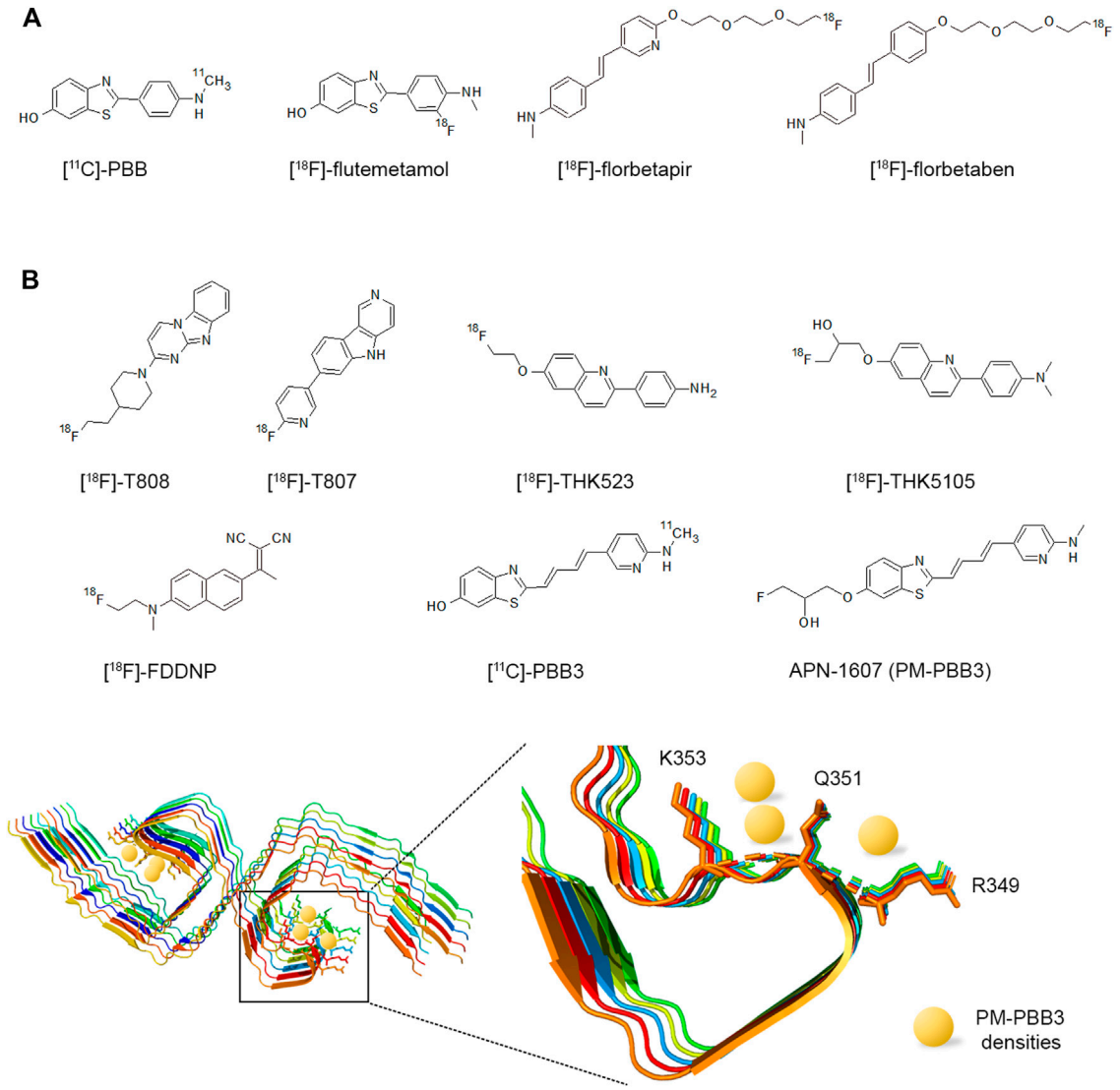

FIGURE 10 | Structures of PET radiotracers for amyloid imaging of Aβ deposits **(A)** or tau inclusions **(B)**. The cryo-EM structure of the PM-PBB3 (APN-1607) compound bound to PHF-tau amyloid structure shows selected interactions in the C-shaped cavities with R349, Q351 and K353 amino acids of the tau MTBR R4 repeats (PDB ID: 7NRV).

Direct measurements by EPR spectroscopy give information on the dynamics of the probe environment and is a convenient way to track oligomer formation (Zurlo et al., 2019). Double nitroxide labeling have interesting applications in both cases. Pulsed double electron–electron resonance (DEER) EPR on frozen samples can be used to derive a distribution of distances between the paramagnetic probes. For NMR applications, paramagnetic relaxation interference (PRI) in the presence of two nitroxide probes has been proposed to detect concerted conformational fluctuation in disordered proteins (Kurzbach et al., 2016). PRI being sensitive to correlated motions in the protein can help to detect a sparsely populated state in the ensemble, which nevertheless can be significant on the aggregation pathway. The Overhauser dynamic nuclear polarization (DNP) made use of site-specific nitroxide spin label attachment to monitor electron-spin interactions with water molecules and detect localized perturbations of hydration during tau protein aggregation related to the magnetic dipolar nature of interactions between the nitroxide unpaired electron and water protons that are mostly localized within 5Å. This allows discriminating hydration changes upon the formation of organized protein-protein interfaces associated to fibrils from non-specific protein-protein interactions (Pavlova et al., 2009).

Kinetics of α-synuclein aggregation was followed by continuous wave (CW) EPR using nitroxide spin-labeling to monitor oligomer formation/disappearance and how the aggregation pathway develops. The CW-EPR method uses the rotational diffusion time of the spin-labeled protein, visualized as EPR lineshapes, to cover the nanosecond to second time scales.

The label dynamics is influenced by the local structure and macromolecular interactions at proximity of the probe. The MTSL label ((1-oxyl-2,2,5,5-tetramethylpyrroline-3-methyl)-methanethiosulfonate) was attached on α-synuclein C56, introduced by site-specific mutagenesis. The monomer, oligomer and fibril concentrations were evaluated at different time points during kinetics experiment, based on mobility differences of the species (Zurlo et al., 2019). Pulsed EPR measurements of various amyloid fibrils were also performed to gain structural information (Bedrood et al., 2012; Siddiqua et al., 2012; Pornsuwan et al., 2013).

Interestingly, EPR is also amenable to *in vivo* experiments (Cattani et al., 2017). Intracellular CW-EPR combined to a systematic spin-labeling scan of micro-injected recombinant α-synuclein shows that the majority of α-synuclein remains in monomeric, intrinsically disordered state in the *Xenopus laevis* oocyte cells, even in the case of disease variants A30P or A53T that are correlated with PD familial forms. These latter variants show an increased rate of oligomerization and decreased membrane binding (Flagmeier et al., 2016). The spin label for this *in-cell* study is 3-maleimido-PROXYL, which is more stable in the reducing environment of the cell than MTSL.

PRE of NMR signals were used to obtain structural information on α-synuclein. Three MTSL nitroxide labels were attached to single cysteine mutants. Measurements showed that α-synuclein adopts in its native state an ensemble of conformations that is stabilized by long-range interactions. These interactions are characterized by contacts between the central and C-terminal domains that shield the aggregation-prone non-amyloid-β component (NAC) (Bertoncini et al., 2005a; Dedmon et al., 2005). PRE of NMR signals additionally show that the familial PD mutations, A30P and A53T, perturb the ensemble of α-synuclein conformations pointing toward a reduced shielding of the hydrophobic NAC region in the A30P and A53T mutants of α-synuclein (Bertoncini et al., 2005b).

PRE of NMR signals were also used to build tau conformational ensemble. The paramagnetic probe MTSL was attached on the native cysteine residues, or on five single-cysteine mutants located in the various tau domains (**Figure 9A**). The intricate network of transient long-range interactions confirms the "hairpin model" of tau dynamic conformation. Interactions of the spin-label with distinct area of the tau sequence indeed show that the C-terminal domain transiently interacts with both the PRD and the N-terminus. The conformational dynamics of tau wild-type or harboring the P301L familial FTDP mutation were additionally compared using a combination of PRE and PRI experiments (Kawasaki and Tate, 2020). PRI data demonstrate alteration of the short- and long-range correlated motions in P301L tau mutant, promoting transient exposure of the PHF6 motif that plays a role as nucleus of tau aggregation (Kawasaki and Tate, 2020).

4.1.4 Positron Emission Tomography Imaging Tracers

Brain imaging is a major area for which chemical biology has made a crucial contribution to support research on disease mechanisms in central nervous system proteinopathies and to deliver promising compounds for clinical use by providing tracers for *in vivo* imaging using positron emission tomography (PET) (Ni and Nitsch, 2022). This topic can be here only briefly covered given its scope. The challenge in this field is to provide specific and sensitive tracers reaching the brain, based on ^{18}F, ^{11}C or ^{3}H radio-compounds. Ideally, the tracers should allow early and differential detection of diagnostic biomarkers before the appearance of clinical symptoms to facilitate access to treatment ahead of the irreversible damages due to neuronal and synaptic connectivity loss.

Imaging of AD brain deposits started with the radio-compound [^{11}C]Pittsburgh compound B (Klunk et al., 2004) that derives from ThT to detect β-amyloid deposits by PET imaging (**Figure 8B**). Amyloid PET is based on β-sheet structure detection and compounds are mainly benzothiazole and benzoxazole derivatives. Among these tracers, three have already been approved for clinical use: florbetapir (Clark, 2011), flutemetamol (Curtis et al., 2015) and florbetaben (**Figure 10A**) (Sabri et al., 2015). Six binding sites on Aβ fibrils are proposed for the tracers, based on molecular modeling studies. Binding sites can be divided between core sites (buried in the fold with low solvent accessibility), and surface binding sites, the latter providing less specificity (Murugan et al., 2016). These *in silico* studies suggest that amyloid tracers of different structures could detect different Aβ fibrils.

Tau-specific ligands have also been developed for clinical use, and enable *in vivo* PET imaging of tau deposition (Leuzy et al., 2019; Saint-Aubert et al., 2017). Monitoring tau deposits is of interest for diagnosis as cortical retention of tau tracers better correlates with cognitive decline than Aβ deposits (Pontecorvo et al., 2017). These small molecules are however specific for the β-sheet structure adopted in tau fibers, and not to tau protein *per se*. This structure is found in other proteinopathies that might co-exist, which can complicate the image interpretation. Tau tracers should not only be able to cross the blood brain barrier, but additionally penetrate the intracellular compartment where tau fibrils also reside. Tau tracers belong to three major different chemical families, namely, pyridinyl-butadienyl-benzothiazole derivative (^{11}C-PBB3) derived from the same family as Pittsburgh compound B, benzimidazole-pyrimidine derivatives (^{18}F-T807/AV 1451, and ^{18}F-T808) as well as different arylquinoline derivatives (^{18}F-THK5105, ^{18}F-THK523, ^{18}F-THK5117, and ^{18}F-THK5351) (**Figure 10B**). These tracers bind to tau with affinities in the nanomolar-picomolar range. These first-generation tracers are however reported to bind to a number of off-targets such as monoamine oxidase-B in the basal ganglia (Lemoine et al., 2017). It leads to optimization of the tracer binding properties and delivered a second-generation of tracers with better specificity and a broader dynamic range. Based on *in vitro* binding assays, three different high affinity binding sites have been proposed in tau fibrils (**Figure 10B**). Computer-assisted docking of the tracers based on the cryo-EM structures of tau fibrils predict four different binding sites for the various tracers (Murugan et al., 2018; Kuang et al., 2020; Murugan et al., 2021).

The tau tracer AV-1451 (Johnson et al., 2016), also known as flortaucipir, specifically binds to tau fibril from AD and non-AD tauopathies (Lowe et al., 2016). The clinical validity of flortaucipir has been demonstrated as diagnostic biomarker and it is approved for imaging tauopathy in AD patients. A study based on PET

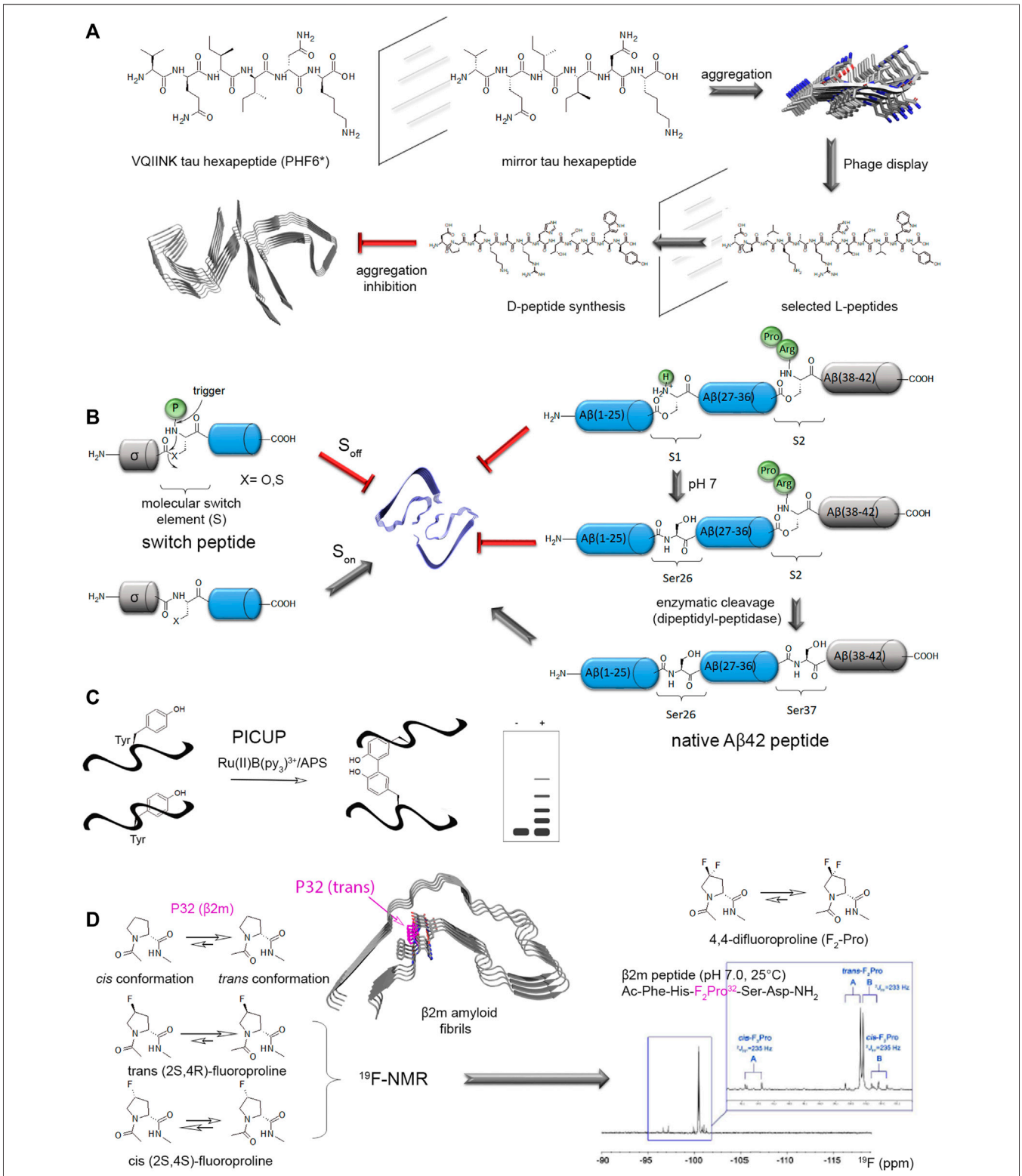

FIGURE 11 | Chemical biology tools for controlling and deciphering the amyloid aggregation pathways. **(A)** Fibrils made of the mirror PHF6* hexapeptide of tau consisting of D-enantiomeric amino acids was used in mirror image phage display to screen L-peptides that bind to mirror PHF6* fibrils. The mirror peptides of the selected L-peptides were synthesized and evaluated as inhibitors of full-length tau aggregation exhibiting protease stability and reduced immunogenicity (Dammers et al., 2016; Malhis et al., 2021). **(B)** The strategy of "click" peptides or "switch" peptides is used to control protein aggregation and decipher the molecular elements responsible of amyloid aggregation (left panel). A molecular switch element (S) is under control of a protecting group "P" (green dots) that prevent aggregation (S_{off}) and is

(*Continued*)

FIGURE 11 | cleaved by an appropriate trigger factor (pH, enzyme, reducing agents, light, . . .). Upon deprotection, the spontaneous O→N or S→N acyl shift within the molecular switch element restores the native peptide bond between both fragments at its N- and C-terminal sides. As a result, the structural induction unit σ (grey fragment) is linked through a native peptide bond to the remaining part of the protein (blue fragment). If the deprotection and subsequent acyl shift trigger the amyloid aggregation of the protein of interest (S_{on}), σ is identified as an aggregation hot spot as exemplified by the C-terminal region of Aβ42 peptide (right panel). In this case, a first molecular switch element (S1) at S26 under control of pH is removed without triggering any fibril formation. The enzymatic cleavage of the second switch element (S2) by the dipeptidyl-peptidase at S37 enables the fibrillization of native Aβ42 peptide supporting a role of the C-terminus in conformational changes and aggregation. **(C)** The photo-induced cross-linking of unmodified protein (PICUP) strategy is used to generate protein oligomers by light irradiation of a photocatalyst, the tris(bipyridyl) ruthenium(II), in presence of ammonium persulfate. Metastable oligomers that form transiently along the amyloid aggregation pathway, as shown by polyacrylamide gel electrophoresis under denaturing conditions, can thus be captured for further structural and functional investigations. **(D)** The use of fluoroproline derivatives, 4-cis-fluoro, 4-trans-fluoro or 4,4-difluoro-proline, in controlling amyloid protein conformational changes and aggregation rely on the alteration of the cis/trans conformational exchange rate and equilibrium of the peptidyl-prolyl bond with the 4-cis-fluoroproline the most favorable to the cis amide bond conformation. Furthermore, fluoroproline can be involved as probes in ^{19}F-NMR studies of conformational exchange in peptides and proteins as shown for a model peptide of β2m, Ac-FH(F_2-P^{32})SD-NH_2. The ^{19}F-NMR spectrum of the β2m peptide containing a 4,4-difluoroproline was reproduced from reference (Torbeev and Hilvert, 2013). The corresponding sequence is shown as sticks in the structure of β2m amyloid fibrils (PDB ID: 6GK3) with P32 (magenta) in trans conformation.

imaging with [^{18}F]AV-1451 confirms that tau pathology can propagate though a neuron-to-neuron transfer (Cope et al., 2018). The different types of tau deposits in the different diseases, highlighted at the atomic level by the cryo-EM structures (Lippens and Gigant, 2019), made it quite challenging to develop tau PET tracers. Given the heterogeneity in tau strains, tracers could be developed that recognize a sub-set of such strains. This strain heterogeneity, not only between pathologies but also between individual patients, is highly relevant because it is proposed to be linked to clinical heterogeneity in patients with typical AD (Dujardin et al., 2020). These *in vivo* diagnostics tool compounds will have huge impact on future assembly of better characterized cohorts and provide an adequate monitoring in clinical assays of the treatment effects.

4.2 Chemical Methods for Deciphering the Amyloid Aggregation Pathway

4.2.1 Keeping Amyloids Under Control With Chirality and Molecular Switches

Manipulating amino acid chirality into amyloid sequences has been implemented through SPPS to reveal amyloidogenic pathways and critical hot spots in amyloid assembly (Foley and Raskatov, 2021). In a strategy termed "chiral editing", D-amino acid (D-AA) enantiomers that are site-specifically introduced either at selected positions of interest or randomly by D-AA scanning proved to be useful tools to highlight mechanistic details of Aβ aggregation and toxicity, as well as key residues in this process. Mirror peptides of Aβ42 and Aβ40 that incorporate D-AA along the entire sequence were shown to accelerate Aβ fibrillization into nontoxic fibrils in a racemic mixture with L-Aβ peptide (Dutta et al., 2017). The chiral inactivation of Aβ generates distinct fibrillar structures likely through the formation of rippled instead of pleated cross-β sheets (Dutta et al., 2019a). D-Aβ42 oligomers were also shown to have a reduced, if any, cytotoxicity and cellular internalization (Dutta et al., 2019b). Stereoselective interactions with chiral components of the phospholipid membrane could be responsible for this differential effect. Overall, the advantage of D-AA and mirror peptides is that chiral mutations do not change the physicochemical properties of the peptides (side chain chemical groups, size, polarity, charge. . .). It was shown that D-peptides targeting the mirror VQIINK tau hexapeptide (PHF6*) fibrils inhibit full-length tau aggregation while exhibiting protease stability and reduced immunogenicity (**Figure 11A**) (Dammers et al., 2016; Malhis et al., 2021). Based on these properties, D-peptides may be useful as therapeutic and diagnostic agents in amyloid-related diseases (Abdulbagi et al., 2021).

It is well documented that some amyloid-forming sequences spontaneously undergo into conformational changes and aggregate during SPPS, purification and other processing steps. Keeping amyloids under control with molecular switches is an efficient strategy to decipher their mechanism of aggregation and toxicity by controlling the onset of aggregation at early stages of initiation/nucleation, and identifying aggregation hot spots in amyloid sequences (Butterfield et al., 2012). A molecular switch is defined as a reversible modification at a selected location within the peptide sequence that tunes on and off the amyloid aggregation properties. O→N (or S→N) acyl shift of isopeptide bonds in so-called "click peptides" or "switch peptides" are usual molecular switches that are under control of a protecting group (**Figure 11B**). The native peptide bond is restored by O→N or S→N intramolecular rearrangement once the protection is released. The introduction of O-acyl or S-acyl isopeptide bonds efficiently disrupt misfolding and oligomerization of amyloid-forming sequences. In some instances, the release of an inhibitory element elicits amyloid assembly. A panel of triggering factors (pH change, enzymatic reactions, reducing agents, photoreactions) can be used for this purpose allowing a rapid switch from the inert into aggregation-prone sequence as conveniently illustrated for small, synthetic Aβ, IAPP or PrP peptides (Taniguchi et al., 2009; Taniguchi et al., 2006; Bosques and Imperiali, 2003). This provided information into the fine molecular mechanisms of Aβ42 (dis) aggregation by decoupling aggregation-prone sequence from a nucleating or structural element to prevent aggregation or, reversely, by favoring disassembly of amyloid fibrils into a soluble conformation (**Figure 11B**) (Dos Santos et al., 2005; Mimna et al., 2007). These methods also found applications in the screening of anti-aggregation compounds (Sohma et al., 2011).

4.2.2 Stabilizing Oligomers by Photo-Induced Cross-Linking

Often poorly defined at the molecular level, oligomers are of variable size ranging from dimers to a few hundred monomers. Their molecular and structural characterization suffers from their unstable nature and heterogeneity, and must overcome methodological hurdles. Cross-linking has been used to stabilize Aβ dimers in several experimental setup (Bitan and Teplow, 2004) although covalently cross-linked Aβ dimers isolated from AD brains were found to be neurotoxic species of biological relevance (Vázquez de la Torre et al., 2018; Brinkmalm et al., 2019). Cross-linking applied to tau protein has shown conformational differences between inert and seed-competent monomer highlighting inaccessibility vs. exposure, respectively, of the hydrophobic, amyloid-prone PHF6 and PHF6* sequences (Mirbaha et al., 2018). The photo-induced cross-linking of unmodified proteins (PICUP) method by light irradiation of a tris(bipyridyl) ruthenium(II) photocatalyst was amenable to the study of amyloid proteins to capture intermediate, metastable oligomers for further purification, characterization and investigation of their seeding activity in inducing fibril formation (**Figure 11C**) (Bitan et al., 2001). The site-specific incorporation of photo-induced cross-linking probes such as trifluoromethyldiazirine derivative of phenylalanine into the sequence of Aβ peptide fragment stabilized "on-pathway" oligomeric species providing structural details about the very first pathological species involved in fibrillization onset (Smith et al., 2008).

4.2.3 Fluorine Labeling and ^{19}F NMR

^{19}F NMR offers an interesting opportunity to study fibril formation, as it provides residue-level quantitative information about structure and mechanism. Because the ^{19}F nucleus is highly sensitive to its chemical environment, it displays a very wide range of chemical shifts and chemical shift perturbations even for very subtle structural changes. Given also the complete absence of ^{19}F in biomolecules, no background signals are present, meaning conformational changes can be detected using simple 1D spectra. A wide repertoire of fluorine labelled amino acids exists, and can be incorporated in recombinant proteins or via chemical peptide synthesis (Salwiczek et al., 2012; Gimenez et al., 2021). ^{19}F NMR spectroscopy is able to detect signals from soluble proteins or small soluble aggregates, conversely to ThT that detects fibrils. Fluorotyrosine-labelled α-synuclein was used to monitor aggregation kinetics by acquisition of one-dimensional spectra (Li et al., 2009). These kinetics data were compared with a fluorescence-monitored time course, in the presence of ThT, in the same conditions. The time course of the ^{19}F NMR data was similar to the ThT-monitored aggregation kinetics. ^{19}F NMR allows the additional quantification of the fraction of monomers or small oligomers remaining in solution at all time-points during the kinetics. Tracking amyloid formation of IAPP using this technique shows that IAPP fibrillizes without formation of nonfibrillar intermediates, in contrast to the well-studied Aβ and α-synuclein proteins (Suzuki et al., 2012). Interestingly, aggregation can be monitored in this manner without addition of an external reporter, such as ThT. This is of importance when studying inhibitor compounds of the aggregation process. It was indeed shown that ThT strongly competes with a polyphenolic compound for binding sites on IAPP fibers. To investigate the conformational polymorphism of the prion oligomers, a 3-fluoro-phenylalanine reporter was introduced in the prion fragment PrP(90–231). ^{19}F-NMR spectroscopy was used to quantify the populations of oligomeric species on the path from the monomeric soluble PrP state to fiber formation. In addition, thermodynamic and kinetic parameters of the interconversion of the oligomeric species were extracted from the ^{19}F NMR data obtained by temperature or pressure scanning (Larda et al., 2013). ^{19}F NMR real-time measurements was also used to investigate the formation of small oligomers during the aggregation of Aβ1–40. Five distinct oligomers (estimated of 30–100 kDa) with unique spectral signatures, which allow to monitor each individually, were detected at distinct time points in the time-course of fibril formation (Suzuki et al., 2013). Their build-up and decay were evaluated in real-time during aggregation and transient species could be identified. Fluorine can also be used to subtly alter the conformational preference of individual amino acids, allowing their role in the aggregation process to be interrogated. A well-known example is fluorinated prolines, which, besides allowing ^{19}F NMR investigation (Sinnaeve et al., 2021), also modulates the proline *cis*/*trans* ratio and the interconversion rate (**Figure 11D**) (Verhoork et al., 2018). The human protein β2-microglobulin (β2m) aggregates as amyloid fibers in patients undergoing long-term hemodialysis. Isomerization of P32 from its native *cis* to a nonnative *trans* conformation was shown to cause β2m misfolding and aggregation using replacement of this crucial residue with 4-fluoroprolines by total chemical synthesis (99 residues) (**Figure 11D**). The β2m monomer was stabilized by incorporation of (2S,4S)-fluoroproline (or *cis*-fluoroproline), which favors the native *cis* amide bond while the monomer was destabilized by the (2S,4R)-fluoroproline (or *trans*-fluoroproline), which disfavors *cis* conformation (**Figure 11D**). 4,4-difluoroproline, which enhances the isomerization rate without modifying the *cis*/*trans* equilibrium relative to regular proline, increases the oligomerization rate. Altogether, these data demonstrate the major effect of P32 conformation on β2m aggregation (Torbeev and Hilvert, 2013). To study the role in the aggregation process of a kink within the R3 repeat of the tau protein, at residue S316, a peptide was used containing a S316P mutation (Jiji et al., 2016). In the peptide wherein (2S,4S)-fluoroproline at position 316 was introduced, the *cis* conformation is favored compared to regular prolines and the modified peptide aggregates twice as fast. In the peptide containing the stereoisomeric (2S,4R)-fluoroproline at position 316, the *trans* conformation is preferred and the modified peptide aggregates at a slower rate. The results clearly showed that favoring the cis conformer of L315-P316 peptide bond promotes aggregation of the R3-S316P peptide. The authors of this study propose that a *trans*-to-

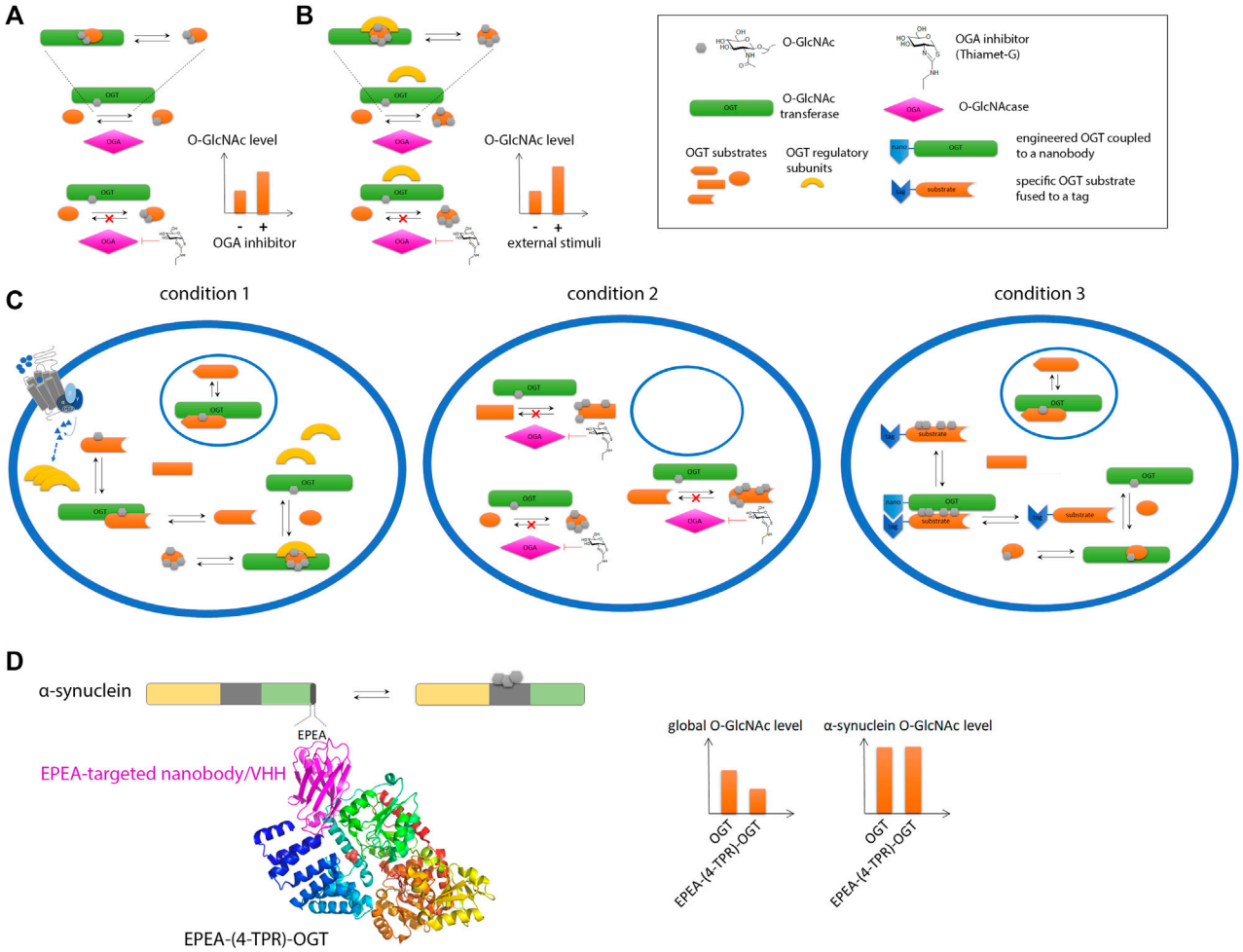

FIGURE 12 | Modulation of O-GlcNAc modification of proteins by proximity-induced protein glycosylation using nanobody-OGT protein engineering. **(A)** Schematic representation of the O-GlcNAc dynamics regulated by single OGT and OGA enzymes, and modulation of OGA activity by an OGA inhibitor such as Thiamet G contributing to overall increased O-GlcNAc levels. **(B)** As OGT is the unique O-GlcNAc transferase in human, it has been suggested that it may act with regulatory subunits that address OGT to specific substrates depending on external stimuli and increase protein-specific O-GlcNAc levels. Treatment with Thiamet-G by increasing overall O-GlcNAc levels may contribute to increase protein-specific O-GlcNAc level. **(C)** Modulation of protein O-GlcNAc levels in cell or animal models. Condition 1, external stimuli and signal transduction lead to the expression of protein-specific regulatory subunits of OGT that increase its activity on selected proteins; condition 2, overall increase of protein O-GlcNAc levels upon treatment with Thiamet-G; condition 3, selected increase of O-GlcNAcylation of a target substrate by a nanobody fused to OGT targeting a specific protein tag. **(D)** This latter method (C, condition 3) was further extended to O-GlcNAcylation of endogenous α-synuclein using a nanobody-OGT targeting α-synuclein EPEA C-terminal sequence (Ramirez et al., 2020). EPEA-(4-TPR)-OGT refers to a truncated form of OGT containing 4 tetratricopeptide repeats fused to a nanobody targeting the EPEA sequence of α-synuclein. The TPR truncation of OGT limits the overall increase of O-GlcNAc levels while OGT coupling to a nanobody targeting the EPEA sequence increases the selectivity for α-synuclein. This approach leads to a selective elevation of α-synuclein O-GlcNAc levels.

cis conformation shift in the peptide bond preceding P316 occurs during peptide aggregation, with the potential type I β-turn encompassing P316 being replaced by a type VI β-turn favored by the *cis* bound in the R3-S316P fibrils.

Taken together, these various examples illustrate that the introduction of fluorine can be very useful in deciphering key aspects of the aggregation process by directly reporting events at a residue scale. This allows tracking of conformational changes occurring on the path to fibril formation and documenting the conformational heterogeneity due to the formation of oligomeric species using ^{19}F NMR, but equally can be used to elucidate the role of individual residue conformations during aggregation.

4.3 Nanobody-Directed Detection and Modulation of Amyloid Proteins

Single domain antibody fragments, scFv (single chain variable fragments), and VHHs (heavy chain variable domain or single-domain antibodies or nanobodies) are interesting tools to probe protein aggregation (De Genst et al., 2012; Pain et al., 2015). These single domain antibodies have many interesting properties such as

their low molecular weight and their ease of production, which makes them perfect candidate for protein engineering (Holliger and Hudson, 2005; Deffar et al., 2009; Desmyter et al., 2015; Könning et al., 2017).

In vitro-based ligand selection, without the use of animal immunization, made it possible to identify antibody fragments with a conformational selectivity. Antibody fragments can thus be selected to target each species formed on the way of fibril formation, from the soluble monomer to the fibril structure. Their ease of expression and small size in particular allow them to be used efficiently in combination with NMR spectroscopy and X-ray crystallography. Single domain antibodies have been reported to specifically detect soluble oligomers of various amyloidogenic proteins (Emadi et al., 2009; Zhang et al., 2011; Butler et al., 2016). They can thus be used to address the biophysical properties/cytotoxicity relationship of the oligomers, which is a challenging task given their transient and heterogenous nature (Bitencourt et al., 2020). Antibody fragments are also helpful to decipher the underlying microscopic stages of the aggregation mechanism (De Genst et al., 2012; Pain et al., 2015). NUsc1, for an example of scFv, recognizes a unique conformational epitope displayed on oligomers of Aβ and preferentially select for oligomers larger than 50 kDa that are neurotoxic (Sebollela et al., 2017). NUsc1 discriminates oligomers over monomers or fibrils. Interestingly, rational design was used to obtain conformation-specific single domain antibodies able to detect Aβ oligomers (Aprile et al., 2020; Limbocker et al., 2020). These antibody fragments were designed to bind different epitopes covering the entire sequence of the target protein. This procedure enables the determination through *in vitro* assays of the regions exposed in the oligomers but not in the fibrillar deposits. VHHs that recognize α-synuclein fibers at different maturation stages have also been characterized and used to gain insight in fibril structures (Guilliams et al., 2013), thus helping in deciphering the fibril formation mechanisms. Even antibody fragments that bind the monomeric soluble forms of amyloidogenic proteins can be used to provide information on the aggregation process. For example, scFv antibody D10, which binds α-synuclein monomers in the C-terminal part, was instrumental in showing that this region of α-synuclein interferes in the aggregation process (Zhou et al., 2004). The nanobodies NbSyn2 and NbSyn87 have similarly been used to identify the role of different C-terminal regions of α-synuclein in aggregation (De Genst et al., 2010; El-Turk et al., 2016). Finally, a VHH targeting α-synuclein showed protection against α-synuclein toxicity in a cellular model. This study also showed that a proteasome targeting PEST motif enhanced this protective effect (Butler et al., 2016). The use of VHH in tauopathies is also considered: a VHH directed against the PHF6 motif of tau, a nucleation core, proved to be efficient against tau fibril formation in *in vitro* and cellular models, and showed efficacy in preventing tau seeding in a mouse model (Dupré et al., 2019; Danis et al., 2022).

Besides nanobodies directly targeting the amyloid-forming regions in proteins, other routes involved in the regulation of amyloidogenic properties such as functional modulation by PTMs may be addressed with nanobodies (El Turk et al., 2018). As a PTM involved in regulation of protein functions, the *O*-GlcNAc modification started to be scrutinized in the processes of amyloid formation (Ryan et al., 2019). To achieve this goal, global alteration of *O*-GlcNAc levels can be fulfilled with chemical inhibitors (Yuzwa et al., 2008; Yuzwa et al., 2012; Yuzwa et al., 2014b; Gloster et al., 2011; Dorfmueller et al., 2006; Macauley et al., 2005; Martin et al., 2018; Haltiwanger et al., 1998; Macauley and Vocadlo, 2010) (**Figures 12A–C**) or through manipulating gene expression of enzymes involved in the hexosamine biosynthesis pathway (HBP) (Wells et al., 2003) or directly the *O*-GlcNAc cycling enzymes, OGT and OGA (Akan et al., 2018; Wang et al., 2012; Shafi et al., 2000; O'Donnell et al., 2004; Olivier-Van Stichelen et al., 2017). Alternatively, approaches limiting an overall elevation of *O*-GlcNAc levels in cells are of great interest (Gorelik et al., 2019; Ramirez et al., 2020). Along these lines, nanobodies fused to OGT were engineered as proximity-directing agents in an innovative strategy for selectively increasing *O*-GlcNAc levels on a target protein in cells aiming at understanding the role of this key PTM (**Figure 12C**) (Ramirez et al., 2020). Truncation of the tetratricopeptide repeat (TPR) domain of OGT which is implicated in protein-protein interactions for substrate recognition and binding further achieved increased nanobody-directed selectivity for the target protein (Ramirez et al., 2020). First attempts were made with nanobodies targeting protein tags excluding the modification of endogenous proteins but providing increased levels of *O*-GlcNAcylation with similar O-GlcNAc profiles as OGT (**Figure 12C**). Moreover, this approach represents a versatile and economical way of increasing *O*-GlcNAc levels of a specific protein by preventing from screening nanobody libraries against the protein of interest. The use of a α-synuclein-targeted nanobody-OGT further proved its efficiency by selectively modifying endogenous α-synuclein in a cell model (**Figure 12D**). This approach could be further extended to *in vitro* systems to improve the efficiency of O-GlcNAc installation. A similar strategy for targeted protein deglycosylation in cells was described using nanobody-fused split OGA (Ge et al., 2021). As OGT TPR truncation reduces the overall elevation of protein O-GlcNAcylation, splitting of OGA minimize the overall effect of OGA overexpression on the O-GlcNAcome. Both nanobody-fused OGT and OGA are informative, complementary approaches to decipher O-GlcNAc-mediated functional regulation *in vivo* and in cells. Other strategies of proximity-induced O-GlcNAc modulation were evolved albeit not applied to amyloid proteins by now. They are based on designing recombined RNA aptamers that bind to both OGT and the protein of interest thereby inducing proximity for targeting OGT to specific proteins in cells (Zhu and Hart, 2020).

An extension of the antibody fragment properties in tracking amyloid formation could be *in vivo* diagnosis to track disease progression. VHHs are well considered in imaging the brain on multiple targets (Li et al., 2016), and coupling with the possibility to engineer them to cross the blood brain barrier could lead to a whole new series of molecule in diagnosis of brain pathologies. VHHs could well be the new trend in brain diagnostic tools, as many studies have shown their potency, as in amyloid plaques imaging (Li et al., 2016; Vandesquille et al., 2017; Pothin et al., 2020).

These different examples give a short glimpse at the power of antibody fragments targeting various forms of amyloid proteins. They can be useful research tools, easy to manipulate and engineer, to help in deciphering complex mechanisms down to a molecular basis. Coupled to the progresses in rational design, antibody fragments show additional promises for diagnosis and therapy (Gerdes et al., 2020; Messer and Butler, 2020) and could address the bottle-neck of crossing the blood brain barrier to reach amyloid deposits in the central nervous system.

5 CONCLUSION

The recent resolution of amyloid fibril structures from individual brains at near-atomic resolution by cryo-EM has brought into focus the complexity of amyloid folds and polymorphism associated to neurodegenerative diseases while leaving open many questions. The regulation of amyloid assembly and selection of polymorph by PTMs of amyloid proteins and their interacting cofactors still remains to be deciphered as they are only poorly described in the cryo-EM structures due to heterogeneity. Chemical biology is helping to delineate the intricate processes of amyloid fibril formation and propagation, and amyloid protein toxicity. The tool kit from chemical biology and protein engineering offers handling of site-specific, posttranslationally modified amyloid proteins by semisynthesis, genetic code expansion, posttranslational chemical mutagenesis, or combination thereof. It also provides specific tools for the detection and characterization of amyloid PTM codes including enrichment strategies. In conjunction with cryo-EM, it should afford new insights into the role of PTMs in the mechanism of amyloid aggregation and how they shape the amyloid fold. In this regard, this rapidly expanding field also provides new probes to control and unravel the mechanisms of amyloid formation and associated conformational changes as probed by spectroscopic and optical methods, and for the detection of amyloids *in vitro* and *in vivo* as crucial mechanistic and diagnosis tools.

AUTHOR CONTRIBUTIONS

CS-N wrote the initial version of the manuscript, made Figures. IL and DS contributed to the paragraph "Fluorine labeling and 19F NMR". IL contributed to the paragraphs "Site-specific introduction of probes for the study of amyloids" and "PET imaging tracers". IL, ED and CS-N contributed to the paragraph "Nanobody-directed detection and modulation of amyloid proteins". LE contributed insights into O-GlcNAc processing/labeling. CS-N and IL edited and revised the manuscript.

FUNDING

This study was supported by the LabEx (Laboratory of Excellence) DISTALZ (Development of Innovative Strategies for a Transdisciplinary approach to Alzheimer's disease ANR-11-LABX-01), by the French research agency ANR (projects ANR-18-CE44-0016 ToNIC and ANR-21-CE29-0024 MAGNETAU) and a grant from the Mizutani Foundation for Glycosciences (2018 Research Grant number 180122). Our laboratories are also supported by LiCEND (Lille Centre of Excellence in Neurodegenerative Disorders), Inserm, Métropole Européenne de Lille, University Lille and FEDER.

REFERENCES

Abdulbagi, M., Wang, L., Siddig, O., Di, B., and Li, B. (2021). D-amino Acids and D-Amino Acid-Containing Peptides: Potential Disease Biomarkers and Therapeutic Targets? *Biomolecules* 11, 1716. doi:10.3390/biom11111716

Abeywardana, T., Lin, Y. H., Rott, R., Engelender, S., and Pratt, M. R. (2013). Site-Specific Differences in Proteasome-dependent Degradation of Monoubiquitinated α-Synuclein. *Chem. Biol.* 20, 1207–1213. doi:10.1016/j.chembiol.2013.09.009

Abraha, A., Ghoshal, N., Gamblin, T. C., Cryns, V., Berry, R. W., Kuret, J., et al. (2000). C-terminal Inhibition of Tau Assembly *In Vitro* and in Alzheimer's Disease. *J. Cell Sci.* 113, 3737–3745. doi:10.1242/jcs.113.21.3737

Agard, N. J., Prescher, J. A., and Bertozzi, C. R. (2004). A Strain-Promoted [3 + 2] Azide–Alkyne Cycloaddition for Covalent Modification of Biomolecules in Living Systems. *J. Am. Chem. Soc.* 126, 15046–15047. doi:10.1021/ja044996f

Agouridas, V., El Mahdi, O., Diemer, V., Cargoët, M., Monbaliu, J.-C. M., and Melnyk, O. (2019). Native Chemical Ligation and Extended Methods: Mechanisms, Catalysis, Scope, and Limitations. *Chem. Rev.* 119, 7328–7443. doi:10.1021/acs.chemrev.8b00712

Aguilar Troyano, F. J., Merkens, K., Anwar, K., and Gómez-Suárez, A. (2021). Radical-Based Synthesis and Modification of Amino Acids. *Angew. Chem. Int. Ed.* 60, 1098–1115. doi:10.1002/anie.202010157

Aguzzi, A., and Calella, A. M. (2009). Prions: Protein Aggregation and Infectious Diseases. *Physiol. Rev.* 89, 1105–1152. doi:10.1152/physrev.00006.2009

Akan, I., Olivier-Van Stichelen, S., Bond, M. R., and Hanover, J. A. (2018). Nutrient-drivenO-GlcNAc in Proteostasis and Neurodegeneration. *J. Neurochem.* 144, 7–34. doi:10.1111/jnc.14242

Al-Hilaly, Y. K., Foster, B. E., Biasetti, L., Lutter, L., Pollack, S. J., Rickard, J. E., et al. (2020). Tau (297-391) Forms Filaments that Structurally Mimic the Core of Paired Helical Filaments in Alzheimer's Disease Brain. *FEBS Lett.* 594, 944–950. doi:10.1002/1873-3468.13675

Alberti, S., and Hyman, A. A. (2021). Biomolecular Condensates at the Nexus of Cellular Stress, Protein Aggregation Disease and Ageing. *Nat. Rev. Mol. Cell Biol.* 22, 196–213. doi:10.1038/s41580-020-00326-6

Aliyan, A., Cook, N. P., and Martí, A. A. (2019). Interrogating Amyloid Aggregates Using Fluorescent Probes. *Chem. Rev.* 119, 11819–11856. doi:10.1021/acs.chemrev.9b00404

Alonso, A. C., Zaidi, T., Grundke-Iqbal, I., and Iqbal, K. (1994). Role of Abnormally Phosphorylated Tau in the Breakdown of Microtubules in Alzheimer Disease. *Proc. Natl. Acad. Sci. U.S.A.* 91, 5562–5566. doi:10.1073/pnas.91.12.5562

Alonso, A. d. C., Zaidi, T., Novak, M., Grundke-Iqbal, I., and Iqbal, K. (2001). Hyperphosphorylation Induces Self-Assembly of τ into Tangles of Paired Helical Filaments/straight Filaments. *Proc. Natl. Acad. Sci. U.S.A.* 98, 6923–6928. doi:10.1073/pnas.121119298

Ambadipudi, S., Biernat, J., Riedel, D., Mandelkow, E., and Zweckstetter, M. (2017). Liquid-liquid Phase Separation of the Microtubule-Binding Repeats of the Alzheimer-Related Protein Tau. *Nat. Commun.* 8, 275. doi:10.1038/s41467-017-00480-0

Amdursky, N., Erez, Y., and Huppert, D. (2012). Molecular Rotors: What Lies behind the High Sensitivity of the Thioflavin-T Fluorescent Marker. *Acc. Chem. Res.* 45, 1548–1557. doi:10.1021/ar300053p

Amniai, L., Barbier, P., Sillen, A., Wieruszeski, J.-M., Peyrot, V., Lippens, G., et al. (2009). Alzheimer Disease Specific Phosphoepitopes of Tau Interfere with Assembly of Tubulin but Not Binding to Microtubules. *FASEB J.* 23, 1146–1152. doi:10.1096/fj.08-121590

Anderson, J. P., Walker, D. E., Goldstein, J. M., de Laat, R., Banducci, K., Caccavello, R. J., et al. (2006). Phosphorylation of Ser-129 Is the Dominant Pathological Modification of α-Synuclein in Familial and Sporadic Lewy Body Disease. *J. Biol. Chem.* 281, 29739–29752. doi:10.1074/jbc.M600933200

Andronesi, O. C., Bergen, M. v., Biernat, J., Seidel, K., Griesinger, C., Mandelkow, E., et al. (2008). Characterization of Alzheimer's-like Paired Helical Filaments from the Core Domain of Tau Protein Using Solid-State NMR Spectroscopy. *J. Am. Chem. Soc.* 130, 5922–5928. doi:10.1021/ja7100517

Anfinsen, C. B., Haber, E., Sela, M., and White, F. H. (1961). The Kinetics of Formation of Native Ribonuclease during Oxidation of the Reduced Polypeptide Chain. *Proc. Natl. Acad. Sci. U.S.A.* 47, 1309–1314. doi:10.1073/pnas.47.9.1309

Anfinsen, C. B. (1973). Principles that Govern the Folding of Protein Chains. *Science* 181, 223–230. doi:10.1126/science.181.4096.223

Ansaloni, A., Wang, Z.-M., Jeong, J. S., Ruggeri, F. S., Dietler, G., and Lashuel, H. A. (2014). One-Pot Semisynthesis of Exon 1 of the Huntingtin Protein: New Tools for Elucidating the Role of Posttranslational Modifications in the Pathogenesis of Huntington's Disease. *Angew. Chem. Int. Ed.* 53, 1928–1933. doi:10.1002/anie.201307510

Aprile, F. A., Sormanni, P., Podpolny, M., Chhangur, S., Needham, L.-M., Ruggeri, F. S., et al. (2020). Rational Design of a Conformation-specific Antibody for the Quantification of Aβ Oligomers. *Proc. Natl. Acad. Sci. U.S.A.* 117, 13509–13518. doi:10.1073/pnas.1919464117

Aragão Gomes, L., Uytterhoeven, V., Lopez-Sanmartin, D., Tomé, S. O., Tousseyn, T., Vandenberghe, R., et al. (2021). Maturation of Neuronal AD-Tau Pathology Involves Site-specific Phosphorylation of Cytoplasmic and Synaptic Tau Preceding Conformational Change and Fibril Formation. *Acta Neuropathol.* 141, 173–192. doi:10.1007/s00401-020-02251-6

Arakhamia, T., Lee, C. E., Carlomagno, Y., Kumar, M., Duong, D. M., Wesseling, H., et al. (2020). Posttranslational Modifications Mediate the Structural Diversity of Tauopathy Strains. *Cell* 180, 633–644. e12. doi:10.1016/j.cell.2020.01.027

Arseni, D., Hasegawa, M., Murzin, A. G., Kametani, F., Arai, M., Yoshida, M., et al. (2021). Structure of Pathological TDP-43 Filaments from ALS with FTLD. *Nature* 601, 139–143. doi:10.1038/s41586-021-04199-3

Arsić, A., Hagemann, C., Stajković, N., Schubert, T., and Nikić-Spiegel, I. (2022). Minimal Genetically Encoded Tags for Fluorescent Protein Labeling in Living Neurons. *Nat. Commun.* 13, 314. doi:10.1038/s41467-022-27956-y

Åslund, A., Sigurdson, C. J., Klingstedt, T., Grathwohl, S., Bolmont, T., Dickstein, D. L., et al. (2009). Novel Pentameric Thiophene Derivatives for *In Vitro* and *In Vivo* Optical Imaging of a Plethora of Protein Aggregates in Cerebral Amyloidoses. *ACS Chem. Biol.* 4, 673–684. doi:10.1021/cb900112v

Babinchak, W. M., Haider, R., Dumm, B. K., Sarkar, P., Surewicz, K., Choi, J.-K., et al. (2019). The Role of Liquid-Liquid Phase Separation in Aggregation of the TDP-43 Low-Complexity Domain. *J. Biol. Chem.* 294, 6306–6317. doi:10.1074/jbc.RA118.007222

Babinchak, W. M., and Surewicz, W. K. (2020). Liquid-Liquid Phase Separation and its Mechanistic Role in Pathological Protein Aggregation. *J. Mol. Biol.* 432, 1910–1925. doi:10.1016/j.jmb.2020.03.004

Bai, Y., Wan, W., Huang, Y., Jin, W., Lyu, H., Xia, Q., et al. (2021). Quantitative Interrogation of Protein Co-aggregation Using Multi-Color Fluorogenic Protein Aggregation Sensors. *Chem. Sci.* 12, 8468–8476. doi:10.1039/D1SC01122G

Balana, A. T., Levine, P. M., Craven, T. W., Mukherjee, S., Pedowitz, N. J., Moon, S. P., et al. (2021). O-GlcNAc Modification of Small Heat Shock Proteins Enhances Their Anti-amyloid Chaperone Activity. *Nat. Chem.* 13, 441–450. doi:10.1038/s41557-021-00648-8

Balana, A. T., and Pratt, M. R. (2021). Mechanistic Roles for Altered O-GlcNAcylation in Neurodegenerative Disorders. *Biochem. J.* 478, 2733–2758. doi:10.1042/BCJ20200609

Balastik, M., Lim, J., Pastorino, L., and Lu, K. P. (2007). Pin1 in Alzheimer's Disease: Multiple Substrates, One Regulatory Mechanism? *Biochimica Biophysica Acta (BBA) - Mol. Basis Dis.* 1772, 422–429. doi:10.1016/j.bbadis.2007.01.006

Baldwin, A. J., Knowles, T. P. J., Tartaglia, G. G., Fitzpatrick, A. W., Devlin, G. L., Shammas, S. L., et al. (2011). Metastability of Native Proteins and the Phenomenon of Amyloid Formation. *J. Am. Chem. Soc.* 133, 14160–14163. doi:10.1021/ja2017703

Bedrood, S., Li, Y., Isas, J. M., Hegde, B. G., Baxa, U., Haworth, I. S., et al. (2012). Fibril Structure of Human Islet Amyloid Polypeptide. *J. Biol. Chem.* 287, 5235–5241. doi:10.1074/jbc.M111.327817

Benson, M. D., Buxbaum, J. N., Eisenberg, D. S., Merlini, G., Saraiva, M. J. M., Sekijima, Y., et al. (2018). Amyloid Nomenclature 2018: Recommendations by the International Society of Amyloidosis (ISA) Nomenclature Committee. *Amyloid* 25, 215–219. doi:10.1080/13506129.2018.1549825

Benson, M. D., Buxbaum, J. N., Eisenberg, D. S., Merlini, G., Saraiva, M. J. M., Sekijima, Y., et al. (2020). Amyloid Nomenclature 2020: Update and Recommendations by the International Society of Amyloidosis (ISA) Nomenclature Committee. *Amyloid* 27, 217–222. doi:10.1080/13506129.2020.1835263

Bertoldo, J. B., Rodrigues, T., Dunsmore, L., Aprile, F. A., Marques, M. C., Rosado, L. A., et al. (2017). A Water-Bridged Cysteine-Cysteine Redox Regulation Mechanism in Bacterial Protein Tyrosine Phosphatases. *Chem* 3, 665–677. doi:10.1016/j.chempr.2017.07.009

Bertoncini, C. W., Fernandez, C. O., Griesinger, C., Jovin, T. M., and Zweckstetter, M. (2005). Familial Mutants of α-Synuclein with Increased Neurotoxicity Have a Destabilized Conformation. *J. Biol. Chem.* 280, 30649–30652. doi:10.1074/jbc.C500288200

Bertoncini, C. W., Jung, Y.-S., Fernandez, C. O., Hoyer, W., Griesinger, C., Jovin, T. M., et al. (2005). Release of Long-Range Tertiary Interactions Potentiates Aggregation of Natively Unstructured α-synuclein. *Proc. Natl. Acad. Sci. U.S.A.* 102, 1430–1435. doi:10.1073/pnas.0407146102

Biancalana, M., and Koide, S. (2010). Molecular Mechanism of Thioflavin-T Binding to Amyloid Fibrils. *Biochimica Biophysica Acta (BBA) - Proteins Proteomics* 1804, 1405–1412. doi:10.1016/j.bbapap.2010.04.001

Bibow, S., Mukrasch, M. D., Chinnathambi, S., Biernat, J., Griesinger, C., Mandelkow, E., et al. (2011). The Dynamic Structure of Filamentous Tau. *Angew. Chem. Int. Ed.* 50, 11520–11524. doi:10.1002/anie.201105493

Bitan, G., Lomakin, A., and Teplow, D. B. (2001). Amyloid β-Protein Oligomerization. *J. Biol. Chem.* 276, 35176–35184. doi:10.1074/jbc.M102223200

Bitan, G., and Teplow, D. B. (2004). Rapid Photochemical Cross-LinkingA New Tool for Studies of Metastable, Amyloidogenic Protein Assemblies. *Acc. Chem. Res.* 37, 357–364. doi:10.1021/ar000214l

Bitencourt, A. L. B., Campos, R. M., Cline, E. N., Klein, W. L., and Sebollela, A. (2020). Antibody Fragments as Tools for Elucidating Structure-Toxicity Relationships and for Diagnostic/Therapeutic Targeting of Neurotoxic Amyloid Oligomers. *IJMS* 21, 8920. doi:10.3390/ijms21238920

Bosques, C. J., and Imperiali, B. (2003). Photolytic Control of Peptide Self-Assembly. *J. Am. Chem. Soc.* 125, 7530–7531. doi:10.1021/ja035360b

Bourré, G., Cantrelle, F.-X., Kamah, A., Chambraud, B., Landrieu, I., and Smet-Nocca, C. (2018). Direct Crosstalk between O-GlcNAcylation and Phosphorylation of Tau Protein Investigated by NMR Spectroscopy. *Front. Endocrinol.* 9, 595. doi:10.3389/fendo.2018.00595

Boyarko, B., and Hook, V. (2021). Human Tau Isoforms and Proteolysis for Production of Toxic Tau Fragments in Neurodegeneration. *Front. Neurosci.* 15, 702788. doi:10.3389/fnins.2021.702788

Boyko, S., Qi, X., Chen, T.-H., Surewicz, K., and Surewicz, W. K. (2019). Liquid-liquid Phase Separation of Tau Protein: The Crucial Role of Electrostatic Interactions. *J. Biol. Chem.* 294, 11054–11059. doi:10.1074/jbc.AC119.009198

Braak, H., Alafuzoff, I., Arzberger, T., Kretzschmar, H., and Del Tredici, K. (2006). Staging of Alzheimer Disease-Associated Neurofibrillary Pathology Using Paraffin Sections and Immunocytochemistry. *Acta Neuropathol.* 112, 389–404. doi:10.1007/s00401-006-0127-z

Braak, H., and Braak, E. (1991). Neuropathological Stageing of Alzheimer-Related Changes. *Acta Neuropathol.* 82, 239–259. doi:10.1007/bf00308809

Braak, H., and Braak, E. (1995). Staging of Alzheimer's Disease-Related Neurofibrillary Changes. *Neurobiol. Aging* 16, 271–278. doi:10.1016/0197-4580(95)00021-6

Braak, H., and Del Tredici, K. (2018). Spreading of Tau Pathology in Sporadic Alzheimer's Disease along Cortico-Cortical Top-Down Connections. *Cereb. Cortex* 28, 3372–3384. doi:10.1093/cercor/bhy152

Braak, H., Ghebremedhin, E., Rüb, U., Bratzke, H., and Del Tredici, K. (2004). Stages in the Development of Parkinson's Disease-Related Pathology. *Cell Tissue Res.* 318, 121–134. doi:10.1007/s00441-004-0956-9

Brelstaff, J., Ossola, B., Neher, J. J., Klingstedt, T. s., Nilsson, K. P. R., Goedert, M., et al. (2015). The Fluorescent Pentameric Oligothiophene pFTAA Identifies Filamentous Tau in Live Neurons Cultured from Adult P301S Tau Mice. *Front. Neurosci.* 9, 9. doi:10.3389/fnins.2015.00184

Brinkmalm, G., Hong, W., Wang, Z., Liu, W., O'Malley, T. T., Sun, X., et al. (2019). Identification of Neurotoxic Cross-Linked Amyloid-β Dimers in the Alzheimer's Brain. *Brain* 142, 1441–1457. doi:10.1093/brain/awz066

Broncel, M., Krause, E., Schwarzer, D., and Hackenberger, C. P. R. (2012). The Alzheimer's Disease Related Tau Protein as a New Target for Chemical Protein Engineering. *Chem. Eur. J.* 18, 2488–2492. doi:10.1002/chem.201103032

Brotzakis, Z. F., Lindstedt, P. R., Taylor, R. J., Rinauro, D. J., Gallagher, N. C. T., Bernardes, G. J. L., et al. (2021). A Structural Ensemble of a Tau-Microtubule Complex Reveals Regulatory Tau Phosphorylation and Acetylation Mechanisms. *ACS Cent. Sci.* 7, 1986–1995. doi:10.1021/acscentsci.1c00585

Buehler, M. J., and Cranford, fnm. (2010). Materiomics: Biological Protein Materials, from Nano to Macro. *NSA*, 127. doi:10.2147/NSA.S9037

Buell, A. K., Dobson, C. M., and Knowles, T. P. J. (2014). The Physical Chemistry of the Amyloid Phenomenon: Thermodynamics and Kinetics of Filamentous Protein Aggregation. *Essays Biochem.* 56, 11–39. doi:10.1042/bse0560011

Butler, D. C., Joshi, S. N., Genst, E. D., Baghel, A. S., Dobson, C. M., and Messer, A. (2016). Bifunctional Anti-non-amyloid Component α-Synuclein Nanobodies Are Protective *In Situ*. *PLoS ONE* 11, e0165964. doi:10.1371/journal.pone.0165964

Butterfield, S., Hejjaoui, M., Fauvet, B., Awad, L., and Lashuel, H. A. (2012). Chemical Strategies for Controlling Protein Folding and Elucidating the Molecular Mechanisms of Amyloid Formation and Toxicity. *J. Mol. Biol.* 421, 204–236. doi:10.1016/j.jmb.2012.01.051

Cantrelle, F.-X., Loyens, A., Trivelli, X., Reimann, O., Despres, C., Gandhi, N. S., et al. (2021). Phosphorylation and O-GlcNAcylation of the PHF-1 Epitope of Tau Protein Induce Local Conformational Changes of the C-Terminus and Modulate Tau Self-Assembly into Fibrillar Aggregates. *Front. Mol. Neurosci.* 14, 661368. doi:10.3389/fnmol.2021.661368

Cattani, J., Subramaniam, V., and Drescher, M. (2017). Room-temperature In-Cell EPR Spectroscopy: Alpha-Synuclein Disease Variants Remain Intrinsically Disordered in the Cell. *Phys. Chem. Chem. Phys.* 19, 18147–18151. doi:10.1039/C7CP03432F

Caughey, B., and Lansbury, P. T. (2003). Protofibrils, Pores, Fibrils, and Neurodegeneration: Separating the Responsible Protein Aggregates from the Innocent Bystanders. *Annu. Rev. Neurosci.* 26, 267–298. doi:10.1146/annurev.neuro.26.010302.081142

Cendrowska, U., Silva, P. J., Ait-Bouziad, N., Müller, M., Guven, Z. P., Vieweg, S., et al. (2020). Unraveling the Complexity of Amyloid Polymorphism Using Gold Nanoparticles and Cryo-EM. *Proc. Natl. Acad. Sci. U.S.A.* 117, 6866–6874. doi:10.1073/pnas.1916176117

Chalker, J. M., Gunnoo, S. B., Boutureira, O., Gerstberger, S. C., Fernández-González, M., Bernardes, G. J. L., et al. (2011). Methods for Converting Cysteine to Dehydroalanine on Peptides and Proteins. *Chem. Sci.* 2, 1666. doi:10.1039/c1sc00185j

Chambraud, B., Sardin, E., Giustiniani, J., Dounane, O., Schumacher, M., Goedert, M., et al. (2010). A Role for FKBP52 in Tau Protein Function. *Proc. Natl. Acad. Sci. U.S.A.* 107, 2658–2663. doi:10.1073/pnas.0914957107

Chen, Y., Wu, Y.-r., Yang, H.-y., Li, X.-z., Jie, M.-m., Hu, C.-j., et al. (2018). Prolyl Isomerase Pin1: a Promoter of Cancer and a Target for Therapy. *Cell Death Dis.* 9, 883. doi:10.1038/s41419-018-0844-y

Chiki, A., DeGuire, S. M., Ruggeri, F. S., Sanfelice, D., Ansaloni, A., Wang, Z.-M., et al. (2017). Mutant Exon1 Huntingtin Aggregation Is Regulated by T3 Phosphorylation-Induced Structural Changes and Crosstalk between T3 Phosphorylation and Acetylation at K6. *Angew. Chem. Int. Ed.* 56, 5202–5207. doi:10.1002/anie.201611750

Chiki, A., Ricci, J., Hegde, R., Abriata, L. A., Reif, A., Boudeffa, D., et al. (2021). Site-Specific Phosphorylation of Huntingtin Exon 1 Recombinant Proteins Enabled by the Discovery of Novel Kinases. *ChemBioChem* 22, 217–231. doi:10.1002/cbic.202000508

Chuh, K. N., Batt, A. R., and Pratt, M. R. (2016). Chemical Methods for Encoding and Decoding of Posttranslational Modifications. *Cell Chem. Biol.* 23, 86–107. doi:10.1016/j.chembiol.2015.11.006

Chung, C. G., Lee, H., and Lee, S. B. (2018). Mechanisms of Protein Toxicity in Neurodegenerative Diseases. *Cell. Mol. Life Sci.* 75, 3159–3180. doi:10.1007/s00018-018-2854-4

Clark, C. M. (2011). Use of Florbetapir-PET for Imaging β-Amyloid Pathology. *JAMA* 305, 275. doi:10.1001/jama.2010.2008

Clore, G. M., Tang, C., and Iwahara, J. (2007). Elucidating Transient Macromolecular Interactions Using Paramagnetic Relaxation Enhancement. *Curr. Opin. Struct. Biol.* 17, 603–616. doi:10.1016/j.sbi.2007.08.013

Cohen, S. I. A., Linse, S., Luheshi, L. M., Hellstrand, E., White, D. A., Rajah, L., et al. (2013). Proliferation of Amyloid-B42 Aggregates Occurs through a Secondary Nucleation Mechanism. *Proc. Natl. Acad. Sci. U.S.A.* 110, 9758–9763. doi:10.1073/pnas.1218402110

Cohen, T. J., Guo, J. L., Hurtado, D. E., Kwong, L. K., Mills, I. P., Trojanowski, J. Q., et al. (2011). The Acetylation of Tau Inhibits its Function and Promotes Pathological Tau Aggregation. *Nat. Commun.* 2, 252. doi:10.1038/ncomms1255

Colin, M., Dujardin, S., Schraen-Maschke, S., Meno-Tetang, G., Duyckaerts, C., Courade, J.-P., et al. (2020). From the Prion-like Propagation Hypothesis to Therapeutic Strategies of Anti-tau Immunotherapy. *Acta Neuropathol.* 139, 3–25. doi:10.1007/s00401-019-02087-9

Conicella, A. E., Dignon, G. L., Zerze, G. H., Schmidt, H. B., D'Ordine, A. M., Kim, Y. C., et al. (2020). TDP-43 α-helical Structure Tunes Liquid-Liquid Phase Separation and Function. *Proc. Natl. Acad. Sci. U.S.A.* 117, 5883–5894. doi:10.1073/pnas.1912055117

Cope, T. E., Rittman, T., Borchert, R. J., Jones, P. S., Vatansever, D., Allinson, K., et al. (2018). Tau Burden and the Functional Connectome in Alzheimer's Disease and Progressive Supranuclear Palsy. *Brain* 141, 550–567. doi:10.1093/brain/awx347

Curtis, C., Gamez, J. E., Singh, U., Sadowsky, C. H., Villena, T., Sabbagh, M. N., et al. (2015). Phase 3 Trial of Flutemetamol Labeled with Radioactive Fluorine 18 Imaging and Neuritic Plaque Density. *JAMA Neurol.* 72, 287. doi:10.1001/jamaneurol.2014.4144

Dai, X., Böker, A., and Glebe, U. (2019). Broadening the Scope of Sortagging. *RSC Adv.* 9, 4700–4721. doi:10.1039/C8RA06705H

Dammers, C., Yolcu, D., Kukuk, L., Willbold, D., Pickhardt, M., Mandelkow, E., et al. (2016). Selection and Characterization of Tau Binding □-Enantiomeric Peptides with Potential for Therapy of Alzheimer Disease. *PLoS ONE* 11, e0167432. doi:10.1371/journal.pone.0167432

Dang, M., Lim, L., Kang, J., and Song, J. (2021). ATP Biphasically Modulates LLPS of TDP-43 PLD by Specifically Binding Arginine Residues. *Commun. Biol.* 4, 714. doi:10.1038/s42003-021-02247-2

Danis, C., Dupré, E., Zejneli, O., Caillierez, R., Arrial, A., Bégard, S., et al. (2022). Inhibition of Tau Seeding by Targeting Tau Nucleation Core within Neurons with a Single Domain Antibody Fragment. *Mol. Ther.* 30, 1484S1525001622000090–1499. doi:10.1016/j.ymthe.2022.01.009

Dawson, P. E., Muir, T. W., Clark-Lewis, I., and Kent, S. B. H. (1994). Synthesis of Proteins by Native Chemical Ligation. *Science* 266, 776–779. doi:10.1126/science.7973629

De Genst, E., and Dobson, C. M. (2012). "Nanobodies as Structural Probes of Protein Misfolding and Fibril Formation," in Single Domain Antibodies. *Methods in Molecular Biology*. Editors D Saerens and S Muyldermans (Totowa, NJ: Humana Press), 533–558. doi:10.1007/978-1-61779-968-6_34

De Genst, E. J., Guilliams, T., Wellens, J., O'Day, E. M., Waudby, C. A., Meehan, S., et al. (2010). Structure and Properties of a Complex of α-Synuclein and a Single-Domain Camelid Antibody. *J. Mol. Biol.* 402, 326–343. doi:10.1016/j.jmb.2010.07.001

De Leon, C. A., Levine, P. M., Craven, T. W., and Pratt, M. R. (2017). The Sulfur-Linked Analogue of O-GlcNAc (S-GlcNAc) Is an Enzymatically Stable and Reasonable Structural Surrogate for O-GlcNAc at the Peptide and Protein Levels. *Biochemistry* 56, 3507–3517. doi:10.1021/acs.biochem.7b00268

Dedmon, M. M., Lindorff-Larsen, K., Christodoulou, J., Vendruscolo, M., and Dobson, C. M. (2005). Mapping Long-Range Interactions in α-Synuclein Using

Spin-Label NMR and Ensemble Molecular Dynamics Simulations. *J. Am. Chem. Soc.* 127, 476–477. doi:10.1021/ja044834j

Deffar, K., Shi, H., Li, L., Wang, X., and Zhu, X. (2009). Nanobodies - the New Concept in Antibody Engineering. *Afr. J. Biotechnol.* 8.

Desmyter, A., Spinelli, S., Roussel, A., and Cambillau, C. (2015). Camelid Nanobodies: Killing Two Birds with One Stone. *Curr. Opin. Struct. Biol.* 32, 1–8. doi:10.1016/j.sbi.2015.01.001

Despres, C., Byrne, C., Qi, H., Cantrelle, F.-X., Huvent, I., Chambraud, B., et al. (2017). Identification of the Tau Phosphorylation Pattern that Drives its Aggregation. *Proc. Natl. Acad. Sci. U.S.A.* 114, 9080–9085. doi:10.1073/pnas.1708448114

Despres, C., Di, J., Cantrelle, F.-X., Li, Z., Huvent, I., Chambraud, B., et al. (2019). Major Differences between the Self-Assembly and Seeding Behavior of Heparin-Induced and *In Vitro* Phosphorylated Tau and Their Modulation by Potential Inhibitors. *ACS Chem. Biol.* 14, 1363–1379. doi:10.1021/acschembio.9b00325

Diaz-Espinoza, R. (2021). Recent High-Resolution Structures of Amyloids Involved in Neurodegenerative Diseases. *Front. Aging Neurosci.* 13, 782617. doi:10.3389/fnagi.2021.782617

Dikiy, I., Fauvet, B., Jovičić, A., Mahul-Mellier, A.-L., Desobry, C., El-Turk, F., et al. (2016). Semisynthetic and *In Vitro* Phosphorylation of Alpha-Synuclein at Y39 Promotes Functional Partly Helical Membrane-Bound States Resembling Those Induced by PD Mutations. *ACS Chem. Biol.* 11, 2428–2437. doi:10.1021/acschembio.6b00539

Dobson, C. M. (2003). Protein Folding and Misfolding. *Nature* 426, 884–890. doi:10.1038/nature02261

Dong, Y., and Chen, Y. (2018). The Role of Ubiquitinated TDP-43 in Amyotrophic Lateral Sclerosis. *NN* 5, 5. doi:10.20517/2347-8659.2017.47

Dorfmueller, H. C., Borodkin, V. S., Schimpl, M., Shepherd, S. M., Shpiro, N. A., and van Aalten, D. M. F. (2006). GlcNAcstatin: a Picomolar, Selective O-GlcNAcase Inhibitor that Modulates Intracellular O-GlcNAcylation Levels. *J. Am. Chem. Soc.* 128, 16484–16485. doi:10.1021/ja066743n

Dos Santos, S., Chandravarkar, A., Mandal, B., Mimna, R., Murat, K., Saucède, L., et al. (2005). Switch-Peptides: Controlling Self-Assembly of Amyloid β-Derived Peptides *In Vitro* by Consecutive Triggering of Acyl Migrations. *J. Am. Chem. Soc.* 127, 11888–11889. doi:10.1021/ja052083v

Drummond, E., Nayak, S., Faustin, A., Pires, G., Hickman, R. A., Askenazi, M., et al. (2017). Proteomic Differences in Amyloid Plaques in Rapidly Progressive and Sporadic Alzheimer's Disease. *Acta Neuropathol.* 133, 933–954. doi:10.1007/s00401-017-1691-0

Dujardin, S., Commins, C., Lathuiliere, A., Beerepoot, P., Fernandes, A. R., Kamath, T. V., et al. (2020). Tau Molecular Diversity Contributes to Clinical Heterogeneity in Alzheimer's Disease. *Nat. Med.* 26, 1256–1263. doi:10.1038/s41591-020-0938-9

Dupré, E., Danis, C., Arrial, A., Hanoulle, X., Homa, M., Cantrelle, F.-X., et al. (2019). Single Domain Antibody Fragments as New Tools for the Detection of Neuronal Tau Protein in Cells and in Mice Studies. *ACS Chem. Neurosci.* 10, 3997–4006. doi:10.1021/acschemneuro.9b00217

Dutta, S., Finn, T. S., Kuhn, A. J., Abrams, B., and Raskatov, J. A. (2019). Chirality Dependence of Amyloid β Cellular Uptake and a New Mechanistic Perspective. *ChemBioChem* 20, 1023–1026. doi:10.1002/cbic.201800708

Dutta, S., Foley, A. R., Kuhn, A. J., Abrams, B., Lee, H. W., and Raskatov, J. A. (2019). New Insights into Differential Aggregation of Enantiomerically Pure and Racemic Aβ40 Systems. *Peptide Sci.* 111, 111. doi:10.1002/pep2.24139

Dutta, S., Foley, A. R., Warner, C. J. A., Zhang, X., Rolandi, M., Abrams, B., et al. (2017). Suppression of Oligomer Formation and Formation of Non-Toxic Fibrils upon Addition of Mirror-Image Aβ42 to the Natural L -Enantiomer. *Angew. Chem. Int. Ed.* 56, 11506–11510. doi:10.1002/anie.201706279

Eidenmüller, J., Fath, T., Maas, T., Pool, M., Sontag, E., and Brandt, R. (2001). Phosphorylation-mimicking Glutamate Clusters in the Proline-Rich Region Are Sufficient to Simulate the Functional Deficiencies of Hyperphosphorylated Tau Protein. *Biochem. J.* 357, 759–767. doi:10.1042/bj3570759

El Turk, F., De Genst, E., Guilliams, T., Fauvet, B., Hejjaoui, M., Di Trani, J., et al. (2018). Exploring the Role of Post-translational Modifications in Regulating α-synuclein Interactions by Studying the Effects of Phosphorylation on Nanobody Binding. *Protein Sci.* 27, 1262–1274. doi:10.1002/pro.3412

El-Turk, F., Newby, F. N., De Genst, E., Guilliams, T., Sprules, T., Mittermaier, A., et al. (2016). Structural Effects of Two Camelid Nanobodies Directed to Distinct C-Terminal Epitopes on α-Synuclein. *Biochemistry* 55, 3116–3122. doi:10.1021/acs.biochem.6b00149

Emadi, S., Kasturirangan, S., Wang, M. S., Schulz, P., and Sierks, M. R. (2009). Detecting Morphologically Distinct Oligomeric Forms of α-Synuclein. *J. Biol. Chem.* 284, 11048–11058. doi:10.1074/jbc.M806559200

Fakhree, M. A. A., Nolten, I. S., Blum, C., and Claessens, M. M. A. E. (2018). Different Conformational Subensembles of the Intrinsically Disordered Protein α-Synuclein in Cells. *J. Phys. Chem. Lett.* 9, 1249–1253. doi:10.1021/acs.jpclett.8b00092

Falcon, B., Zhang, W., Murzin, A. G., Murshudov, G., Garringer, H. J., Vidal, R., et al. (2018). Structures of Filaments from Pick's Disease Reveal a Novel Tau Protein Fold. *Nature* 561, 137–140. doi:10.1038/s41586-018-0454-y

Falcon, B., Zhang, W., Schweighauser, M., Murzin, A. G., Vidal, R., Garringer, H. J., et al. (2018). Tau Filaments from Multiple Cases of Sporadic and Inherited Alzheimer's Disease Adopt a Common Fold. *Acta Neuropathol.* 136, 699–708. doi:10.1007/s00401-018-1914-z

Falcon, B., Zivanov, J., Zhang, W., Murzin, A. G., Garringer, H. J., Vidal, R., et al. (2019). Novel Tau Filament Fold in Chronic Traumatic Encephalopathy Encloses Hydrophobic Molecules. *Nature* 568, 420–423. doi:10.1038/s41586-019-1026-5

Fandrich, M. (2002). The Behaviour of Polyamino Acids Reveals an Inverse Side Chain Effect in Amyloid Structure Formation. *EMBO J.* 21, 5682–5690. doi:10.1093/emboj/cdf573

Fichou, Y., Lin, Y., Rauch, J. N., Vigers, M., Zeng, Z., Srivastava, M., et al. (2018). Cofactors Are Essential Constituents of Stable and Seeding-Active Tau Fibrils. *Proc. Natl. Acad. Sci. U.S.A.* 115, 13234–13239. doi:10.1073/pnas.1810058115

Fichou, Y., Oberholtzer, Z. R., Ngo, H., Cheng, C.-Y., Keller, T. J., Eschmann, N. A., et al. (2019). Tau-Cofactor Complexes as Building Blocks of Tau Fibrils. *Front. Neurosci.* 13, 1339. doi:10.3389/fnins.2019.01339

Fitzpatrick, A. W. P., Falcon, B., He, S., Murzin, A. G., Murshudov, G., Garringer, H. J., et al. (2017). Cryo-EM Structures of Tau Filaments from Alzheimer's Disease. *Nature* 547, 185–190. doi:10.1038/nature23002

Flagmeier, P., Meisl, G., Vendruscolo, M., Knowles, T. P. J., Dobson, C. M., Buell, A. K., et al. (2016). Mutations Associated with Familial Parkinson's Disease Alter the Initiation and Amplification Steps of α-synuclein Aggregation. *Proc. Natl. Acad. Sci. U.S.A.* 113, 10328–10333. doi:10.1073/pnas.1604645113

Foley, A. R., and Raskatov, J. A. (2021). Understanding and Controlling Amyloid Aggregation with Chirality. *Curr. Opin. Chem. Biol.* 64, 1–9. doi:10.1016/j.cbpa.2021.01.003

Frost, B., Ollesch, J., Wille, H., and Diamond, M. I. (2009). Conformational Diversity of Wild-type Tau Fibrils Specified by Templated Conformation Change. *J. Biol. Chem.* 284, 3546–3551. doi:10.1074/jbc.M805627200

Galesic, A., Rakshit, A., Cutolo, G., Pacheco, R. P., Balana, A. T., Moon, S. P., et al. (2021). Comparison of N-Acetyl-Glucosamine to Other Monosaccharides Reveals Structural Differences for the Inhibition of α-Synuclein Aggregation. *ACS Chem. Biol.* 16, 14–19. doi:10.1021/acschembio.0c00716

Gandhi, N. S., Kukic, P., Lippens, G., and Mancera, R. L. (2017). Molecular Dynamics Simulation of Tau Peptides for the Investigation of Conformational Changes Induced by Specific Phosphorylation Patterns. *Methods Mol. Biol.* 1523, 33–59. doi:10.1007/978-1-4939-6598-4_3

Gao, H., Shi, M., Wang, R., Wang, C., Shao, C., Gu, Y., et al. (2018). A Widely Compatible Expression System for the Production of Highly O-GlcNAcylated Recombinant Protein in *Escherichia coli*. *Glycobiology* 28, 949–957. doi:10.1093/glycob/cwy077

Gao, W., Cho, E., Liu, Y., and Lu, Y. (2019). Advances and Challenges in Cell-free Incorporation of Unnatural Amino Acids into Proteins. *Front. Pharmacol.* 10, 611. doi:10.3389/fphar.2019.00611

Gaspar, R., Meisl, G., Buell, A. K., Young, L., Kaminski, C. F., Knowles, T. P. J., et al. (2017). Secondary Nucleation of Monomers on Fibril Surface Dominatesα-Synuclein Aggregation and Provides Autocatalytic Amyloid Amplification. *Quart. Rev. Biophys.* 50, e6. doi:10.1017/S0033583516000172

Gautier, A., Juillerat, A., Heinis, C., Corrêa, I. R., Kindermann, M., Beaufils, F., et al. (2008). An Engineered Protein Tag for Multiprotein Labeling in Living Cells. *Chem. Biol.* 15, 128–136. doi:10.1016/j.chembiol.2008.01.007

Ge, Y., Ramirez, D. H., Yang, B., D'Souza, A. K., Aonbangkhen, C., Wong, S., et al. (2021). Target Protein Deglycosylation in Living Cells by a Nanobody-Fused Split O-GlcNAcase. *Nat. Chem. Biol.* 17, 593–600. doi:10.1038/s41589-021-00757-y

Ge, Y., and Woo, C. M. (2021). Writing and Erasing O-GlcNAc from Target Proteins in Cells. *Biochem. Soc. Trans.* 49, 2891–2901. doi:10.1042/BST20210865

Gerdes, C., Waal, N., Offner, T., Fornasiero, E. F., Wender, N., Verbarg, H., et al. (2020). A Nanobody-Based Fluorescent Reporter Reveals Human α-synuclein in the Cell Cytosol. *Nat. Commun.* 11, 2729. doi:10.1038/s41467-020-16575-0

Ghanem, S. S., Majbour, N. K., Vaikath, N. N., Ardah, M. T., Erskine, D., Jensen, N. M., et al. (2022). α-Synuclein Phosphorylation at Serine 129 Occurs after Initial Protein Deposition and Inhibits Seeded Fibril Formation and Toxicity. *Proc. Natl. Acad. Sci. U.S.A.* 119, e2109617119. doi:10.1073/pnas.2109617119

Gimenez, D., Phelan, A., Murphy, C. D., and Cobb, S. L. (2021). 19F NMR as a Tool in Chemical Biology. *Beilstein J. Org. Chem.* 17, 293–318. doi:10.3762/bjoc.17.28

Giustiniani, J., Chambraud, B., Sardin, E., Dounane, O., Guillemeau, K., Nakatani, H., et al. (2014). Immunophilin FKBP52 Induces Tau-P301l Filamentous Assembly *In Vitro* and Modulates its Activity in a Model of Tauopathy. *Proc. Natl. Acad. Sci. U.S.A.* 111, 4584–4589. doi:10.1073/pnas.1402645111

Giustiniani, J., Sineus, M., Sardin, E., Dounane, O., Panchal, M., Sazdovitch, V., et al. (2012). Decrease of the Immunophilin FKBP52 Accumulation in Human Brains of Alzheimer's Disease and FTDP-17. *Jad* 29, 471–483. doi:10.3233/JAD-2011-111895

Gloster, T. M., Zandberg, W. F., Heinonen, J. E., Shen, D. L., Deng, L., and Vocadlo, D. J. (2011). Hijacking a Biosynthetic Pathway Yields a Glycosyltransferase Inhibitor within Cells. *Nat. Chem. Biol.* 7, 174–181. doi:10.1038/nchembio.520

Goedert, M., Jakes, R., Spillantini, M. G., Hasegawa, M., Smith, M. J., and Crowther, R. A. (1996). Assembly of Microtubule-Associated Protein Tau into Alzheimer-like Filaments Induced by Sulphated Glycosaminoglycans. *Nature* 383, 550–553. doi:10.1038/383550a0

Gong, C.-X., Liu, F., Grundke-Iqbal, I., and Iqbal, K. (2006). Impaired Brain Glucose Metabolism Leads to Alzheimer Neurofibrillary Degeneration through a Decrease in Tau O-GlcNAcylation. *Jad* 9, 1–12. doi:10.3233/jad-2006-9101

Goodwin, O. Y., Thomasson, M. S., Lin, A. J., Sweeney, M. M., and Macnaughtan, M. A. (2013). *E. coli* Sabotages the *In Vivo* Production of O-Linked β-N-acetylglucosamine-modified Proteins. *J. Biotechnol.* 168, 315–323. doi:10.1016/j.jbiotec.2013.10.008

Gorelik, A., Bartual, S. G., Borodkin, V. S., Varghese, J., Ferenbach, A. T., and van Aalten, D. M. F. (2019). Genetic Recoding to Dissect the Roles of Site-specific Protein O-GlcNAcylation. *Nat. Struct. Mol. Biol.* 26, 1071–1077. doi:10.1038/s41594-019-0325-8

Gorsky, M. K., Burnouf, S., Dols, J., Mandelkow, E., and Partridge, L. (2016). Acetylation Mimic of Lysine 280 Exacerbates Human Tau Neurotoxicity *In Vivo*. *Sci. Rep.* 6, 22685. doi:10.1038/srep22685

Gour, N., Kshtriya, V., Gupta, S., Koshti, B., Singh, R., Patel, D., et al. (2019). Synthesis and Aggregation Studies of a Pyridothiazole-Based AIEE Probe and its Application in Sensing Amyloid Fibrillation. *ACS Appl. Bio Mat.* 2, 4442–4455. doi:10.1021/acsabm.9b00627

Graham, D. L., Gray, A. J., Joyce, J. A., Yu, D., O'Moore, J., Carlson, G. A., et al. (2014). Increased O-GlcNAcylation Reduces Pathological Tau without Affecting its Normal Phosphorylation in a Mouse Model of Tauopathy. *Neuropharmacology* 79, 307–313. doi:10.1016/j.neuropharm.2013.11.025

Grese, Z. R., Bastos, A. C., Mamede, L. D., French, R. L., Miller, T. M., and Ayala, Y. M. (2021). Specific RNA Interactions Promote TDP-43 Multivalent Phase Separation and Maintain Liquid Properties. *EMBO Rep.* 22, 22. doi:10.15252/embr.202153632

Groenning, M. (2010). Binding Mode of Thioflavin T and Other Molecular Probes in the Context of Amyloid Fibrils-Current Status. *J. Chem. Biol.* 3, 1–18. doi:10.1007/s12154-009-0027-5

Guerrero-Ferreira, R., Kovacik, L., Ni, D., and Stahlberg, H. (2020). New Insights on the Structure of Alpha-Synuclein Fibrils Using Cryo-Electron Microscopy. *Curr. Opin. Neurobiol.* 61, 89–95. doi:10.1016/j.conb.2020.01.014

Guerrero-Ferreira, R., Taylor, N. M., Mona, D., Ringler, P., Lauer, M. E., Riek, R., et al. (2018). Cryo-EM Structure of Alpha-Synuclein Fibrils. *eLife* 7, e36402. doi:10.7554/eLife.36402

Guilliams, T., El-Turk, F., Buell, A. K., O'Day, E. M., Aprile, F. A., Esbjörner, E. K., et al. (2013). Nanobodies Raised against Monomeric α-Synuclein Distinguish between Fibrils at Different Maturation Stages. *J. Mol. Biol.* 425, 2397–2411. doi:10.1016/j.jmb.2013.01.040

Gunnoo, S. B., and Madder, A. (2016). Chemical Protein Modification through Cysteine. *ChemBioChem* 17, 529–553. doi:10.1002/cbic.201500667

Hackenberger, C. P. R., and Schwarzer, D. (2008). Chemoselective Ligation and Modification Strategies for Peptides and Proteins. *Angew. Chem. Int. Ed.* 47, 10030–10074. doi:10.1002/anie.200801313

Haj-Yahya, M., Gopinath, P., Rajasekhar, K., Mirbaha, H., Diamond, M. I., and Lashuel, H. A. (2020). Site-Specific Hyperphosphorylation Inhibits, rather Than Promotes, Tau Fibrillization, Seeding Capacity, and its Microtubule Binding. *Angew. Chem. Int. Ed.* 59, 4059–4067. doi:10.1002/anie.201913001

Haj-Yahya, M., Fauvet, B., Herman-Bachinsky, Y., Hejjaoui, M., Bavikar, S. N., Karthikeyan, S. V., et al. (2013). Synthetic Polyubiquitinated α-Synuclein Reveals Important Insights into the Roles of the Ubiquitin Chain in Regulating its Pathophysiology. *Proc. Natl. Acad. Sci. U.S.A.* 110, 17726–17731. doi:10.1073/pnas.1315654110

Haj-Yahya, M., and Lashuel, H. A. (2018). Protein Semisynthesis Provides Access to Tau Disease-Associated Post-translational Modifications (PTMs) and Paves the Way to Deciphering the Tau PTM Code in Health and Diseased States. *J. Am. Chem. Soc.* 140, 6611–6621. doi:10.1021/jacs.8b02668

Hallegger, M., Chakrabarti, A. M., Lee, F. C. Y., Lee, B. L., Amalietti, A. G., Odeh, H. M., et al. (2021). TDP-43 Condensation Properties Specify its RNA-Binding and Regulatory Repertoire. *Cell* 184, 4680–4696. e22. doi:10.1016/j.cell.2021.07.018

Haltiwanger, R. S., Grove, K., and Philipsberg, G. A. (1998). Modulation of O-LinkedN-Acetylglucosamine Levels on Nuclear and Cytoplasmic Proteins *In Vivo* Using the PeptideO-GlcNAc-β-N-Acetylglucosaminidase InhibitorO-(2-Acetamido-2-Deoxy-Dglucopyranosylidene)amino-N-Phenylcarbamate. *J. Biol. Chem.* 273, 3611–3617. doi:10.1074/jbc.273.6.3611

Hamdane, M., Smet, C., Sambo, A.-V., Leroy, A., Wieruszeski, J.-M., Delobel, P., et al. (2002). Pin1 : A Therapeutic Target in Alzheimer Neurodegeneration. *Jmn* 19, 275–288. doi:10.1385/JMN:19:3:275

Haney, C. M., Cleveland, C. L., Wissner, R. F., Owei, L., Robustelli, J., Daniels, M. J., et al. (2017). Site-Specific Fluorescence Polarization for Studying the Disaggregation of α-Synuclein Fibrils by Small Molecules. *Biochemistry* 56, 683–691. doi:10.1021/acs.biochem.6b01060

Haney, C. M., Wissner, R. F., Warner, J. B., Wang, Y. J., Ferrie, J. J., J. Covell, D., et al. (2016). Comparison of Strategies for Non-perturbing Labeling of α-synuclein to Study Amyloidogenesis. *Org. Biomol. Chem.* 14, 1584–1592. doi:10.1039/C5OB02329G

Hanger, D. P., Betts, J. C., Loviny, T. L., Blackstock, W. P., and Anderton, B. H. (1998). New Phosphorylation Sites Identified in Hyperphosphorylated Tau (Paired Helical Filament-Tau) from Alzheimer's Disease Brain Using Nanoelectrospray Mass Spectrometry. *J. Neurochem.* 71, 2465–2476. doi:10.1046/j.1471-4159.1998.71062465.x

Hanger, D. P., Anderton, B. H., and Noble, W. (2009). Tau Phosphorylation: the Therapeutic Challenge for Neurodegenerative Disease. *Trends Mol. Med.* 15, 112–119. doi:10.1016/j.molmed.2009.01.003

Hanger, D. P., Byers, H. L., Wray, S., Leung, K.-Y., Saxton, M. J., Seereeram, A., et al. (2007). Novel Phosphorylation Sites in Tau from Alzheimer Brain Support a Role for Casein Kinase 1 in Disease Pathogenesis. *J. Biol. Chem.* 282, 23645–23654. doi:10.1074/jbc.M703269200

Hastings, N. B., Wang, X., Song, L., Butts, B. D., Grotz, D., Hargreaves, R., et al. (2017). Inhibition of O-GlcNAcase Leads to Elevation of O-GlcNAc Tau and Reduction of Tauopathy and Cerebrospinal Fluid Tau in rTg4510 Mice. *Mol. Neurodegener.* 12, 39. doi:10.1186/s13024-017-0181-0

Hejjaoui, M., Butterfield, S., Fauvet, B., Vercruysse, F., Cui, J., Dikiy, I., et al. (2012). Elucidating the Role of C-Terminal Post-Translational Modifications Using Protein Semisynthesis Strategies: α-Synuclein Phosphorylation at Tyrosine 125. *J. Am. Chem. Soc.* 134, 5196–5210. doi:10.1021/ja210866j

Hejjaoui, M., Haj-Yahya, M., Kumar, K. S. A., Brik, A., and Lashuel, H. A. (2011). Towards Elucidation of the Role of Ubiquitination in the Pathogenesis of Parkinson's Disease with Semisynthetic Ubiquitinated α-Synuclein. *Angew. Chem. Int. Ed.* 50, 405–409. doi:10.1002/anie.201005546

Hemantha, H. P., Bavikar, S. N., Herman-Bachinsky, Y., Haj-Yahya, N., Bondalapati, S., Ciechanover, A., et al. (2014). Nonenzymatic Polyubiquitination of Expressed Proteins. *J. Am. Chem. Soc.* 136, 2665–2673. doi:10.1021/ja412594d

Herling, T. W., Garcia, G. A., Michaels, T. C. T., Grentz, W., Dean, J., Shimanovich, U., et al. (2015). Force Generation by the Growth of Amyloid Aggregates. *Proc. Natl. Acad. Sci. U.S.A.* 112, 9524–9529. doi:10.1073/pnas.1417326112

Hernández-Vega, A., Braun, M., Scharrel, L., Jahnel, M., Wegmann, S., Hyman, B. T., et al. (2017). Local Nucleation of Microtubule Bundles through Tubulin Concentration into a Condensed Tau Phase. *Cell Rep.* 20, 2304–2312. doi:10.1016/j.celrep.2017.08.042

Holliger, P., and Hudson, P. J. (2005). Engineered Antibody Fragments and the Rise of Single Domains. *Nat. Biotechnol.* 23, 1126–1136. doi:10.1038/nbt1142

Howie, A. J., and Brewer, D. B. (2009). Optical Properties of Amyloid Stained by Congo Red: History and Mechanisms. *Micron* 40, 285–301. doi:10.1016/j.micron.2008.10.002

Hu, R., Li, S., Zeng, Y., Chen, J., Wang, S., Li, Y., et al. (2011). Understanding the Aggregation Induced Emission Enhancement for a Compound with Excited State Intramolecular Proton Transfer Character. *Phys. Chem. Chem. Phys.* 13, 2044–2051. doi:10.1039/C0CP01181A

Hu, Z.-W., Vugmeyster, L., Au, D. F., Ostrovsky, D., Sun, Y., and Qiang, W. (2019). Molecular Structure of an N-Terminal Phosphorylated β-amyloid Fibril. *Proc. Natl. Acad. Sci. U.S.A.* 116, 11253–11258. doi:10.1073/pnas.1818530116

Huang, R., Holbert, M. A., Tarrant, M. K., Curtet, S., Colquhoun, D. R., Dancy, B. M., et al. (2010). Site-Specific Introduction of an Acetyl-Lysine Mimic into Peptides and Proteins by Cysteine Alkylation. *J. Am. Chem. Soc.* 132, 9986–9987. doi:10.1021/ja103954u

Ilie, I. M., and Caflisch, A. (2019). Simulation Studies of Amyloidogenic Polypeptides and Their Aggregates. *Chem. Rev.* 119, 6956–6993. doi:10.1021/acs.chemrev.8b00731

Ishiguro, A., Lu, J., Ozawa, D., Nagai, Y., and Ishihama, A. (2021). ALS-linked FUS Mutations Dysregulate G-quadruplex-dependent Liquid-Liquid Phase Separation and Liquid-To-Solid Transition. *J. Biol. Chem.* 297, 101284. doi:10.1016/j.jbc.2021.101284

Isono, T. (2011). O-GlcNAc-specific Antibody CTD110.6 Cross-Reacts with N-GlcNAc2-Modified Proteins Induced under Glucose Deprivation. *PLoS ONE* 6, e18959. doi:10.1371/journal.pone.0018959

Iyer, S. P. N., and Hart, G. W. (2003). Dynamic Nuclear and Cytoplasmic Glycosylation: Enzymes of O-GlcNAc Cycling. *Biochemistry* 42, 2493–2499. doi:10.1021/bi020685a

Jeganathan, S., Chinnathambi, S., Mandelkow, E.-M., and Mandelkow, E. (2012). Conformations of Microtubule-Associated Protein Tau Mapped by Fluorescence Resonance Energy Transfer. *Methods Mol. Biol.* 849, 85–99. doi:10.1007/978-1-61779-551-0_7

Jeganathan, S., von Bergen, M., Brutlach, H., Steinhoff, H.-J., and Mandelkow, E. (2006). Global Hairpin Folding of Tau in Solution. *Biochemistry* 45, 2283–2293. doi:10.1021/bi0521543

Jia, B., Wu, Y., and Zhou, Y. (2014). 14-3-3 and Aggresome Formation: Implications in Neurodegenerative Diseases. *Prion* 8, 173–177. doi:10.4161/pri.28123

Jiji, A. C., Shine, A., and Vijayan, V. (2016). Direct Observation of Aggregation-Induced Backbone Conformational Changes in Tau Peptides. *Angew. Chem. Int. Ed.* 55, 11562–11566. doi:10.1002/anie.201606544

Johnson, K. A., Schultz, A., Betensky, R. A., Becker, J. A., Sepulcre, J., Rentz, D., et al. (2016). Tau Positron Emission Tomographic Imaging in Aging and Early Alzheimer Disease. *Ann. Neurol.* 79, 110–119. doi:10.1002/ana.24546

Jones, L. H. (2020). Dehydroamino Acid Chemical Biology: an Example of Functional Group Interconversion on Proteins. *RSC Chem. Biol.* 1, 298–304. doi:10.1039/D0CB00174K

Jumper, J., Evans, R., Pritzel, A., Green, T., Figurnov, M., Ronneberger, O., et al. (2021). Highly Accurate Protein Structure Prediction with AlphaFold. *Nature* 596, 583–589. doi:10.1038/s41586-021-03819-2

Jun, J. V., Haney, C. M., Karpowicz, R. J., Giannakoulias, S., Lee, V. M.-Y., Petersson, E. J., et al. (2019). A "Clickable" Photoconvertible Small Fluorescent Molecule as a Minimalist Probe for Tracking Individual Biomolecule Complexes. *J. Am. Chem. Soc.* 141, 1893–1897. doi:10.1021/jacs.8b13094

Jung, K. H., Kim, S. F., Liu, Y., and Zhang, X. (2019). A Fluorogenic AggTag Method Based on Halo- and SNAP-Tags to Simultaneously Detect Aggregation of Two Proteins in Live Cells. *ChemBioChem* 20, 1078–1087. doi:10.1002/cbic.201800782

Jung, T., Shin, B., Tamo, G., Kim, H., Vijayvargia, R., Leitner, A., et al. (2020). The Polyglutamine Expansion at the N-Terminal of Huntingtin Protein Modulates the Dynamic Configuration and Phosphorylation of the C-Terminal HEAT Domain. *Structure* 28, 1035–1050. e8. doi:10.1016/j.str.2020.06.008

Kamah, A., Cantrelle, F. X., Huvent, I., Giustiniani, J., Guillemeau, K., Byrne, C., et al. (2016). Isomerization and Oligomerization of Truncated and Mutated Tau Forms by FKBP52 Are Independent Processes. *J. Mol. Biol.* 428, 1080–1090. doi:10.1016/j.jmb.2016.02.015

Kamah, A., Huvent, I., Cantrelle, F.-X., Qi, H., Lippens, G., Landrieu, I., et al. (2014). Nuclear Magnetic Resonance Analysis of the Acetylation Pattern of the Neuronal Tau Protein. *Biochemistry* 53, 3020–3032. doi:10.1021/bi500006v

Kametani, F., Yoshida, M., Matsubara, T., Murayama, S., Saito, Y., Kawakami, I., et al. (2020). Comparison of Common and Disease-specific Post-translational Modifications of Pathological Tau Associated with a Wide Range of Tauopathies. *Front. Neurosci.* 14, 581936. doi:10.3389/fnins.2020.581936

Kanaan, N. M., Hamel, C., Grabinski, T., and Combs, B. (2020). Liquid-liquid Phase Separation Induces Pathogenic Tau Conformations *In Vitro*. *Nat. Commun.* 11, 2809. doi:10.1038/s41467-020-16580-3

Kawasaki, R., and Tate, S.-i. (2020). Impact of the Hereditary P301L Mutation on the Correlated Conformational Dynamics of Human Tau Protein Revealed by the Paramagnetic Relaxation Enhancement NMR Experiments. *IJMS* 21, 3920. doi:10.3390/ijms21113920

Ke, P. C., Zhou, R., Serpell, L. C., Riek, R., Knowles, T. P. J., Lashuel, H. A., et al. (2020). Half a Century of Amyloids: Past, Present and Future. *Chem. Soc. Rev.* 49, 5473–5509. doi:10.1039/C9CS00199A

Keppler, A., Gendreizig, S., Gronemeyer, T., Pick, H., Vogel, H., and Johnsson, K. (2003). A General Method for the Covalent Labeling of Fusion Proteins with Small Molecules *In Vivo*. *Nat. Biotechnol.* 21, 86–89. doi:10.1038/nbt765

Khidekel, N., Arndt, S., Lamarre-Vincent, N., Lippert, A., Poulin-Kerstien, K. G., Ramakrishnan, B., et al. (2003). A Chemoenzymatic Approach toward the Rapid and Sensitive Detection of O-GlcNAc Posttranslational Modifications. *J. Am. Chem. Soc.* 125, 16162–16163. doi:10.1021/ja038545r

Kidd, M. (1963). Paired Helical Filaments in Electron Microscopy of Alzheimer's Disease. *Nature* 197, 192–193. doi:10.1038/197192b0

Kimura, T., Ono, T., Takamatsu, J., Yamamoto, H., Ikegami, K., Kondo, A., et al. (1996). Sequential Changes of Tau-site-specific Phosphorylation during Development of Paired Helical Filaments. *Dement. Geriatr. Cogn. Disord.* 7, 177–181. doi:10.1159/000106875

Kjaergaard, M., Dear, A. J., Kundel, F., Qamar, S., Meisl, G., Knowles, T. P. J., et al. (2018). Oligomer Diversity during the Aggregation of the Repeat Region of Tau. *ACS Chem. Neurosci.* 9, 3060–3071. doi:10.1021/acschemneuro.8b00250

Klingstedt, T., Åslund, A., Simon, R. A., Johansson, L. B. G., Mason, J. J., Nyström, S., et al. (2011). Synthesis of a Library of Oligothiophenes and Their Utilization as Fluorescent Ligands for Spectral Assignment of Protein Aggregates. *Org. Biomol. Chem.* 9, 8356. doi:10.1039/c1ob05637a

Klunk, W. E., Engler, H., Nordberg, A., Wang, Y., Blomqvist, G., Holt, D. P., et al. (2004). Imaging Brain Amyloid in Alzheimer's Disease with Pittsburgh Compound-B. *Ann. Neurol.* 55, 306–319. doi:10.1002/ana.20009

Knowles, T. P., Fitzpatrick, A. W., Meehan, S., Mott, H. R., Vendruscolo, M., Dobson, C. M., et al. (2007). Role of Intermolecular Forces in Defining Material Properties of Protein Nanofibrils. *Science* 318, 1900–1903. doi:10.1126/science.1150057

Knowles, T. P. J., and Buehler, M. J. (2011). Nanomechanics of Functional and Pathological Amyloid Materials. *Nat. Nanotech* 6, 469–479. doi:10.1038/nnano.2011.102

Knowles, T. P. J., Vendruscolo, M., and Dobson, C. M. (2014). The Amyloid State and its Association with Protein Misfolding Diseases. *Nat. Rev. Mol. Cell Biol.* 15, 384–396. doi:10.1038/nrm3810

Kolla, R., Gopinath, P., Ricci, J., Reif, A., Rostami, I., and Lashuel, H. A. (2021). A New Chemoenzymatic Semisynthetic Approach Provides Insight into the Role of Phosphorylation beyond Exon1 of Huntingtin and Reveals N-Terminal Fragment Length-dependent Distinct Mechanisms of Aggregation. *J. Am. Chem. Soc.* 143, 9798–9812. doi:10.1021/jacs.1c03108

Kollmer, M., Meinhardt, K., Haupt, C., Liberta, F., Wulff, M., Linder, J., et al. (2016). Electron Tomography Reveals the Fibril Structure and Lipid Interactions in Amyloid Deposits. *Proc. Natl. Acad. Sci. U.S.A.* 113, 5604–5609. doi:10.1073/pnas.1523496113

Kondo, A., Albayram, O., Zhou, X. Z., and Lu, K. P. (2017). Pin1 Knockout Mice: A Model for the Study of Tau Pathology in Alzheimer's Disease. *Methods Mol. Biol.* 1523, 415–425. doi:10.1007/978-1-4939-6598-4_28

Könning, D., Zielonka, S., Grzeschik, J., Empting, M., Valldorf, B., Krah, S., et al. (2017). Camelid and Shark Single Domain Antibodies: Structural Features and Therapeutic Potential. *Curr. Opin. Struct. Biol.* 45, 10–16. doi:10.1016/j.sbi.2016.10.019

Krebs, M. R. H., Bromley, E. H. C., and Donald, A. M. (2005). The Binding of Thioflavin-T to Amyloid Fibrils: Localisation and Implications. *J. Struct. Biol.* 149, 30–37. doi:10.1016/j.jsb.2004.08.002

Kuang, G., Murugan, N. A., Zhou, Y., Nordberg, A., and Ågren, H. (2020). Computational Insight into the Binding Profile of the Second-Generation PET Tracer PI2620 with Tau Fibrils. *ACS Chem. Neurosci.* 11, 900–908. doi:10.1021/acschemneuro.9b00578

Kucherak, O. A., Shvadchak, V. V., Kyriukha, Y. A., and Yushchenko, D. A. (20182018). Synthesis of a Fluorescent Probe for Sensing Multiple Protein States. *Eur. J. Org. Chem.* 2018, 5155–5162. doi:10.1002/ejoc.201800524

Kumar, M., Hong, Y., Thorn, D. C., Ecroyd, H., and Carver, J. A. (2017). Monitoring Early-Stage Protein Aggregation by an Aggregation-Induced Emission Fluorogen. *Anal. Chem.* 89, 9322–9329. doi:10.1021/acs.analchem.7b02090

Kumar, S., Rezaei-Ghaleh, N., Terwel, D., Thal, D. R., Richard, M., Hoch, M., et al. (2011). Extracellular Phosphorylation of the Amyloid β-peptide Promotes Formation of Toxic Aggregates during the Pathogenesis of Alzheimer's Disease. *EMBO J.* 30, 2255–2265. doi:10.1038/emboj.2011.138

Kundel, F., De, S., Flagmeier, P., Horrocks, M. H., Kjaergaard, M., Shammas, S. L., et al. (2018). Hsp70 Inhibits the Nucleation and Elongation of Tau and Sequesters Tau Aggregates with High Affinity. *ACS Chem. Biol.* 13, 636–646. doi:10.1021/acschembio.7b01039

Kundel, F., Hong, L., Falcon, B., McEwan, W. A., Michaels, T. C. T., Meisl, G., et al. (2018). Measurement of Tau Filament Fragmentation Provides Insights into Prion-like Spreading. *ACS Chem. Neurosci.* 9, 1276–1282. doi:10.1021/acschemneuro.8b00094

Kurzbach, D., Vanas, A., Flamm, A. G., Tarnoczi, N., Kontaxis, G., Maltar-Strmečki, N., et al. (2016). Detection of Correlated Conformational Fluctuations in Intrinsically Disordered Proteins through Paramagnetic Relaxation Interference. *Phys. Chem. Chem. Phys.* 18, 5753–5758. doi:10.1039/C5CP04858C

Landrieu, I., Lacosse, L., Leroy, A., Wieruszeski, J.-M., Trivelli, X., Sillen, A., et al. (2006). NMR Analysis of a Tau Phosphorylation Pattern. *J. Am. Chem. Soc.* 128, 3575–3583. doi:10.1021/ja054656+

Landrieu, I., Leroy, A., Smet-Nocca, C., Huvent, I., Amniai, L., Hamdane, M., et al. (2010). NMR Spectroscopy of the Neuronal Tau Protein: Normal Function and Implication in Alzheimer's Disease. *Biochem. Soc. Trans.* 38, 1006–1011. doi:10.1042/BST0381006

Landrieu, I., Smet, C., Wieruszeski, J., Sambo, A., Wintjens, R., Buee, L., et al. (2006). Exploring the Molecular Function of PIN1 by Nuclear Magnetic Resonance. *Cpps* 7, 179–194. doi:10.2174/138920306777452303

Landrieu, I., Smet-Nocca, C., Amniai, L., Louis, J. V., Wieruszeski, J.-M., Goris, J., et al. (2011). Molecular Implication of PP2A and Pin1 in the Alzheimer's Disease Specific Hyperphosphorylation of Tau. *PLoS ONE* 6, e21521. doi:10.1371/journal.pone.0021521

Larda, S. T., Simonetti, K., Al-Abdul-Wahid, M. S., Sharpe, S., and Prosser, R. S. (2013). Dynamic Equilibria between Monomeric and Oligomeric Misfolded States of the Mammalian Prion Protein Measured by 19F NMR. *J. Am. Chem. Soc.* 135, 10533–10541. doi:10.1021/ja404584s

Lazarus, B. D., Love, D. C., and Hanover, J. A. (2009). O-GlcNAc Cycling: Implications for Neurodegenerative Disorders. *Int. J. Biochem. Cell Biol.* 41, 2134–2146. doi:10.1016/j.biocel.2009.03.008

Le, D. D., Cortesi, A. T., Myers, S. A., Burlingame, A. L., and Fujimori, D. G. (2013). Site-Specific and Regiospecific Installation of Methylarginine Analogues into Recombinant Histones and Insights into Effector Protein Binding. *J. Am. Chem. Soc.* 135, 2879–2882. doi:10.1021/ja3108214

Lee, B. E., Kim, H. Y., Kim, H.-J., Jeong, H., Kim, B.-G., Lee, H.-E., et al. (2020). O-GlcNAcylation Regulates Dopamine Neuron Function, Survival and Degeneration in Parkinson Disease. *Brain* 143, 3699–3716. doi:10.1093/brain/awaa320

Lee, B. E., Suh, P.-G., and Kim, J.-I. (2021). O-GlcNAcylation in Health and Neurodegenerative Diseases. *Exp. Mol. Med.* 53, 1674–1682. doi:10.1038/s12276-021-00709-5

Lemoine, L., Gillberg, P.-G., Svedberg, M., Stepanov, V., Jia, Z., Huang, J., et al. (2017). Comparative Binding Properties of the Tau PET Tracers THK5117, THK5351, PBB3, and T807 in Postmortem Alzheimer Brains. *Alz Res. Ther.* 9, 96. doi:10.1186/s13195-017-0325-z

Leroy, A., Landrieu, I., Huvent, I., Legrand, D., Codeville, B., Wieruszeski, J.-M., et al. (2010). Spectroscopic Studies of GSK3β Phosphorylation of the Neuronal Tau Protein and its Interaction with the N-Terminal Domain of Apolipoprotein E. *J. Biol. Chem.* 285, 33435–33444. doi:10.1074/jbc.M110.149419

Leuzy, A., Chiotis, K., Lemoine, L., Gillberg, P.-G., Almkvist, O., Rodriguez-Vieitez, E., et al. (2019). Tau PET Imaging in Neurodegenerative Tauopathies-Still a Challenge. *Mol. Psychiatry* 24, 1112–1134. doi:10.1038/s41380-018-0342-8

Levine, P. M., Galesic, A., Balana, A. T., Mahul-Mellier, A.-L., Navarro, M. X., De Leon, C. A., et al. (2019). α-Synuclein O-GlcNAcylation Alters Aggregation and Toxicity, Revealing Certain Residues as Potential Inhibitors of Parkinson's Disease. *Proc. Natl. Acad. Sci. U.S.A.* 116, 1511–1519. doi:10.1073/pnas.1808845116

Levone, B. R., Lenzken, S. C., Antonaci, M., Maiser, A., Rapp, A., Conte, F., et al. (2021). FUS-dependent Liquid-Liquid Phase Separation Is Important for DNA Repair Initiation. *J. Cell Biol.* 220, e202008030. doi:10.1083/jcb.202008030

Lewis, Y. E., Abeywardana, T., Lin, Y. H., Galesic, A., and Pratt, M. R. (2016). Synthesis of a Bis-Thio-Acetone (BTA) Analogue of the Lysine Isopeptide Bond and its Application to Investigate the Effects of Ubiquitination and SUMOylation on α-Synuclein Aggregation and Toxicity. *ACS Chem. Biol.* 11, 931–942. doi:10.1021/acschembio.5b01042

Lewis, Y. E., Galesic, A., Levine, P. M., De Leon, C. A., Lamiri, N., Brennan, C. K., et al. (2017). O-GlcNAcylation of α-Synuclein at Serine 87 Reduces Aggregation without Affecting Membrane Binding. *ACS Chem. Biol.* 12, 1020–1027. doi:10.1021/acschembio.7b00113

Li, B., Ge, P., Murray, K. A., Sheth, P., Zhang, M., Nair, G., et al. (2018). Cryo-EM of Full-Length α-synuclein Reveals Fibril Polymorphs with a Common Structural Kernel. *Nat. Commun.* 9, 3609. doi:10.1038/s41467-018-05971-2

Li, C., Lutz, E. A., Slade, K. M., Ruf, R. A. S., Wang, G.-F., and Pielak, G. J. (2009). 19F NMR Studies of α-Synuclein Conformation and Fibrillation. *Biochemistry* 48, 8578–8584. doi:10.1021/bi900872p

Li, D., and Liu, C. (2021). Hierarchical Chemical Determination of Amyloid Polymorphs in Neurodegenerative Disease. *Nat. Chem. Biol.* 17, 237–245. doi:10.1038/s41589-020-00708-z

Li, H.-R., Chiang, W.-C., Chou, P.-C., Wang, W.-J., and Huang, J.-r. (2018). TAR DNA-Binding Protein 43 (TDP-43) Liquid-Liquid Phase Separation Is Mediated by Just a Few Aromatic Residues. *J. Biol. Chem.* 293, 6090–6098. doi:10.1074/jbc.AC117.001037

Li, J., Zhang, Y., Soubias, O., Khago, D., Chao, F.-a., Li, Y., et al. (2020). Optimization of Sortase A Ligation for Flexible Engineering of Complex Protein Systems. *J. Biol. Chem.* 295, 2664–2675. doi:10.1074/jbc.RA119.012039

Li, Q.-Q., Liu, Y.-Q., Luo, Y.-Y., Chu, T.-T., Gao, N., Chen, P.-G., et al. (2020). Uncovering the Pathological Functions of Ser404 Phosphorylation by Semisynthesis of a Phosphorylated TDP-43 Prion-like Domain. *Chem. Commun.* 56, 5370–5373. doi:10.1039/D0CC01409E

Li, T., Vandesquille, M., Koukouli, F., Dudeffant, C., Youssef, I., Lenormand, P., et al. (2016). Camelid Single-Domain Antibodies: A Versatile Tool for *In Vivo* Imaging of Extracellular and Intracellular Brain Targets. *J. Control. Release* 243, 1–10. doi:10.1016/j.jconrel.2016.09.019

Li, Y., Zhao, C., Luo, F., Liu, Z., Gui, X., Luo, Z., et al. (2018). Amyloid Fibril Structure of α-synuclein Determined by Cryo-Electron Microscopy. *Cell Res.* 28, 897–903. doi:10.1038/s41422-018-0075-x

Lim, J., and Ping Lu, K. (2005). Pinning Down Phosphorylated Tau and Tauopathies. *Biochimica Biophysica Acta (BBA) - Mol. Basis Dis.* 1739, 311–322. doi:10.1016/j.bbadis.2004.10.003

Limbocker, R., Mannini, B., Cataldi, R., Chhangur, S., Wright, A. K., Kreiser, R. P., et al. (2020). Rationally Designed Antibodies as Research Tools to Study the Structure-Toxicity Relationship of Amyloid-β Oligomers. *IJMS* 21, 4542. doi:10.3390/ijms21124542

Lindstedt, P. R., Taylor, R. J., Bernardes, G. J. L., and Vendruscolo, M. (2021). Facile Installation of Post-translational Modifications on the Tau Protein via Chemical Mutagenesis. *ACS Chem. Neurosci.* 12, 557–561. doi:10.1021/acschemneuro.0c00761

Lippens, G., and Gigant, B. (2019). Elucidating Tau Function and Dysfunction in the Era of Cryo-EM. *J. Biol. Chem.* 294, 9316–9325. doi:10.1074/jbc.REV119.008031

Lippens, G., Landrieu, I., Smet, C., Huvent, I., Gandhi, N., Gigant, B., et al. (2016). NMR Meets Tau: Insights into its Function and Pathology. *Biomolecules* 6, 28. doi:10.3390/biom6020028

Lippens, G., Landrieu, I., and Smet, C. (2007). Molecular Mechanisms of the Phospho-dependent Prolyl Cis/trans Isomerase Pin1. *Febs J.* 274, 5211–5222. doi:10.1111/j.1742-4658.2007.06057.x

Liu, D., Wei, Q., Xia, W., He, C., Zhang, Q., Huang, L., et al. (2021). O-glycosylation Induces Amyloid-β to Form New Fibril Polymorphs Vulnerable for Degradation. *J. Am. Chem. Soc.* 143, 20216–20223. doi:10.1021/jacs.1c08607

Liu, F., Iqbal, K., Grundke-Iqbal, I., Hart, G. W., and Gong, C.-X. (2004). O-GlcNAcylation Regulates Phosphorylation of Tau: A Mechanism Involved in Alzheimer's Disease. *Proc. Natl. Acad. Sci. U.S.A.* 101, 10804–10809. doi:10.1073/pnas.0400348101

Liu, F., Li, B., Tung, E.-J., Grundke-Iqbal, I., Iqbal, K., and Gong, C.-X. (2007). Site-specific Effects of Tau Phosphorylation on its Microtubule Assembly Activity and Self-Aggregation. *Eur. J. Neurosci.* 26, 3429–3436. doi:10.1111/j.1460-9568.2007.05955.x

Liu, F., Shi, J., Tanimukai, H., Gu, J., Gu, J., Grundke-Iqbal, I., et al. (2009). Reduced O-GlcNAcylation Links Lower Brain Glucose Metabolism and Tau Pathology in Alzheimer's Disease. *Brain* 132, 1820–1832. doi:10.1093/brain/awp099

Liu, Y., Wolstenholme, C. H., Carter, G. C., Liu, H., Hu, H., Grainger, L. S., et al. (2018). Modulation of Fluorescent Protein Chromophores to Detect Protein Aggregation with Turn-On Fluorescence. *J. Am. Chem. Soc.* 140, 7381–7384. doi:10.1021/jacs.8b02176

Liu, Z., Jiang, Z., Yan, M., and Wang, X. (2019). Recent Progress of BODIPY Dyes with Aggregation-Induced Emission. *Front. Chem.* 7, 712. doi:10.3389/fchem.2019.00712

Lövestam, S., Koh, F. A., van Knippenberg, B., Kotecha, A., Murzin, A. G., Goedert, M., et al. (2021). Assembly of Recombinant Tau into Filaments Identical to Those of Alzheimer's Disease and Chronic Traumatic Encephalopathy. *Neuroscience*. doi:10.1101/2021.12.16.472950

Lowe, V. J., Curran, G., Fang, P., Liesinger, A. M., Josephs, K. A., Parisi, J. E., et al. (2016). An Autoradiographic Evaluation of AV-1451 Tau PET in Dementia. *acta neuropathol. Commun.* 4, 58. doi:10.1186/s40478-016-0315-6

Lu, P.-J., Wulf, G., Zhou, X. Z., Davies, P., and Lu, K. P. (1999). The Prolyl Isomerase Pin1 Restores the Function of Alzheimer-Associated Phosphorylated Tau Protein. *Nature* 399, 784–788. doi:10.1038/21650

Luk, K. C., Kehm, V., Carroll, J., Zhang, B., O'Brien, P., Trojanowski, J. Q., et al. (2012). Pathological α-Synuclein Transmission Initiates Parkinson-like Neurodegeneration in Nontransgenic Mice. *Science* 338, 949–953. doi:10.1126/science.1227157

Lutz, B., and Peng, J. (2018). Deep Profiling of the Aggregated Proteome in Alzheimer's Disease: From Pathology to Disease Mechanisms. *Proteomes* 6, 46. doi:10.3390/proteomes6040046

Ma, M.-R., Hu, Z.-W., Zhao, Y.-F., Chen, Y.-X., and Li, Y.-M. (2016). Phosphorylation Induces Distinct Alpha-Synuclein Strain Formation. *Sci. Rep.* 6, 37130. doi:10.1038/srep37130

Ma, X., Li, H., He, Y., and Hao, J. (2017). The Emerging Link between O-GlcNAcylation and Neurological Disorders. *Cell. Mol. Life Sci.* 74, 3667–3686. doi:10.1007/s00018-017-2542-9

Macauley, M. S., and Vocadlo, D. J. (2010). Increasing O-GlcNAc Levels: An Overview of Small-Molecule Inhibitors of O-GlcNAcase. *Biochimica Biophysica Acta (BBA) - General Subj.* 1800, 107–121. doi:10.1016/j.bbagen.2009.07.028

Macauley, M. S., Whitworth, G. E., Debowski, A. W., Chin, D., and Vocadlo, D. J. (2005). O-GlcNAcase Uses Substrate-Assisted Catalysis. *J. Biol. Chem.* 280, 25313–25322. doi:10.1074/jbc.M413819200

Magnusson, K., Simon, R., Sjölander, D., Sigurdson, C. J., Hammarström, P., and Nilsson, K. P. R. (2014). Multimodal Fluorescence Microscopy of Prion Strain Specific PrP Deposits Stained by Thiophene-Based Amyloid Ligands. *Prion* 8, 319–329. doi:10.4161/pri.29239

Majumdar, A., Dogra, P., Maity, S., and Mukhopadhyay, S. (2019). Liquid-Liquid Phase Separation Is Driven by Large-Scale Conformational Unwinding and Fluctuations of Intrinsically Disordered Protein Molecules. *J. Phys. Chem. Lett.* 10, 3929–3936. doi:10.1021/acs.jpclett.9b01731

Makin, O. S., Atkins, E., Sikorski, P., Johansson, J., and Serpell, L. C. (2005). Molecular Basis for Amyloid Fibril Formation and Stability. *Proc. Natl. Acad. Sci. U.S.A.* 102, 315–320. doi:10.1073/pnas.0406847102

Malhis, M., Kaniyappan, S., Aillaud, I., Chandupatla, R. R., Ramirez, L. M., Zweckstetter, M., et al. (2021). Potent Tau Aggregation Inhibitor D-Peptides Selected against Tau-Repeat 2 Using Mirror Image Phage Display. *ChemBioChem* 22, 3049–3059. doi:10.1002/cbic.202100287

Marotta, N. P., Lin, Y. H., Lewis, Y. E., Ambroso, M. R., Zaro, B. W., Roth, M. T., et al. (2015). O-GlcNAc Modification Blocks the Aggregation and Toxicity of the Protein α-synuclein Associated with Parkinson's Disease. *Nat. Chem.* 7, 913–920. doi:10.1038/nchem.2361

Martin, S. E. S., Tan, Z.-W., Itkonen, H. M., Duveau, D. Y., Paulo, J. A., Janetzko, J., et al. (2018). Structure-Based Evolution of Low Nanomolar O-GlcNAc Transferase Inhibitors. *J. Am. Chem. Soc.* 140, 13542–13545. doi:10.1021/jacs.8b07328

Mathis, C. A., Lopresti, B. J., Ikonomovic, M. D., and Klunk, W. E. (2017). Small-molecule PET Tracers for Imaging Proteinopathies. *Seminars Nucl. Med.* 47, 553–575. doi:10.1053/j.semnuclmed.2017.06.003

Meier, F., Abeywardana, T., Dhall, A., Marotta, N. P., Varkey, J., Langen, R., et al. (2012). Semisynthetic, Site-specific Ubiquitin Modification of α-Synuclein Reveals Differential Effects on Aggregation. *J. Am. Chem. Soc.* 134, 5468–5471. doi:10.1021/ja300094r

Meisl, G., Yang, X., Hellstrand, E., Frohm, B., Kirkegaard, J. B., Cohen, S. I. A., et al. (2014). Differences in Nucleation Behavior Underlie the Contrasting Aggregation Kinetics of the Aβ40 and Aβ42 Peptides. *Proc. Natl. Acad. Sci. U.S.A.* 111, 9384–9389. doi:10.1073/pnas.1401564111

Messer, A., and Butler, D. C. (2020). Optimizing Intracellular Antibodies (Intrabodies/nanobodies) to Treat Neurodegenerative Disorders. *Neurobiol. Dis.* 134, 104619. doi:10.1016/j.nbd.2019.104619

Mimna, R., Camus, M.-S., Schmid, A., Tuchscherer, G., Lashuel, H. A., and Mutter, M. (2007). Disruption of Amyloid-Derived Peptide Assemblies through the Controlled Induction of a β-Sheet to α-Helix Transformation: Application of the Switch Concept. *Angew. Chem. Int. Ed.* 46, 2681–2684. doi:10.1002/anie.200603681

Min, S.-W., Chen, X., Tracy, T. E., Li, Y., Zhou, Y., Wang, C., et al. (2015). Critical Role of Acetylation in Tau-Mediated Neurodegeneration and Cognitive Deficits. *Nat. Med.* 21, 1154–1162. doi:10.1038/nm.3951

Min, S.-W., Cho, S.-H., Zhou, Y., Schroeder, S., Haroutunian, V., Seeley, W. W., et al. (2010). Acetylation of Tau Inhibits its Degradation and Contributes to Tauopathy. *Neuron* 67, 953–966. doi:10.1016/j.neuron.2010.08.044

Mirbaha, H., Chen, D., Morazova, O. A., Ruff, K. M., Sharma, A. M., Liu, X., et al. (2018). Inert and Seed-Competent Tau Monomers Suggest Structural Origins of Aggregation. *eLife* 7, e36584. doi:10.7554/eLife.36584

Monahan, Z., Ryan, V. H., Janke, A. M., Burke, K. A., Rhoads, S. N., Zerze, G. H., et al. (2017). Phosphorylation of the FUS Low-complexity Domain Disrupts Phase Separation, Aggregation, and Toxicity. *EMBO J.* 36, 2951–2967. doi:10.15252/embj.201696394

Moon, S. P., Balana, A. T., Galesic, A., Rakshit, A., and Pratt, M. R. (2020). Ubiquitination Can Change the Structure of the α-Synuclein Amyloid Fiber in a Site Selective Fashion. *J. Org. Chem.* 85, 1548–1555. doi:10.1021/acs.joc.9b02641

Moon, S. P., Balana, A. T., and Pratt, M. R. (2021). Consequences of Post-translational Modifications on Amyloid Proteins as Revealed by Protein Semisynthesis. *Curr. Opin. Chem. Biol.* 64, 76–89. doi:10.1016/j.cbpa.2021.05.007

Moon, S. P., Javed, A., Hard, E. R., and Pratt, M. R. (2022). Methods for Studying Site-specific O-GlcNAc Modifications: Successes, Limitations, and Important Future Goals. *JACS Au* 2, 74–83. doi:10.1021/jacsau.1c00455

Morató, A., Elena-Real, C. A., Popovic, M., Fournet, A., Zhang, K., Allemand, F., et al. (2020). Robust Cell-free Expression of Sub-pathological and Pathological Huntingtin Exon-1 for NMR Studies. General Approaches for the Isotopic Labeling of Low-Complexity Proteins. *Biomolecules* 10, 1458. doi:10.3390/biom10101458

Moreira, G. G., Cantrelle, F.-X., Quezada, A., Carvalho, F. S., Cristóvão, J. S., Sengupta, U., et al. (2021). Dynamic Interactions and Ca2+-Binding Modulate the Holdase-type Chaperone Activity of S100B Preventing Tau Aggregation and Seeding. *Nat. Commun.* 12, 6292. doi:10.1038/s41467-021-26584-2

Morishima-Kawashima, M., Hasegawa, M., Takio, K., Suzuki, M., Yoshida, H., Titani, K., et al. (1995). Proline-directed and Non-proline-directed Phosphorylation of PHF-Tau. *J. Biol. Chem.* 270, 823–829. doi:10.1074/jbc.270.2.823

Morishima-Kawashima, M., Hasegawa, M., Takio, K., Suzuki, M., Yoshida, H., Watanabe, A., et al. (1995). Hyperphosphorylation of Tau in PHF. *Neurobiol. Aging* 16, 365–371. doi:10.1016/0197-4580(95)00027-c

Morris, M., Knudsen, G. M., Maeda, S., Trinidad, J. C., Ioanoviciu, A., Burlingame, A. L., et al. (2015). Tau Post-translational Modifications in Wild-type and Human Amyloid Precursor Protein Transgenic Mice. *Nat. Neurosci.* 18, 1183–1189. doi:10.1038/nn.4067

Morris, M., Maeda, S., Vossel, K., and Mucke, L. (2011). The Many Faces of Tau. *Neuron* 70, 410–426. doi:10.1016/j.neuron.2011.04.009

Mudher, A., Colin, M., Dujardin, S., Medina, M., Dewachter, I., Alavi Naini, S. M., et al. (2017). What Is the Evidence that Tau Pathology Spreads through Prion-like Propagation? *Acta Neuropathol. Commun.* 5, 99. doi:10.1186/s40478-017-0488-7

Muir, T. W., and Kent, S. B. H. (1993). The Chemical Synthesis of Proteins. *Curr. Opin. Biotechnol.* 4, 420–427. doi:10.1016/0958-1669(93)90007-J

Munari, F., Barracchia, C. G., Franchin, C., Parolini, F., Capaldi, S., Romeo, A., et al. (2020). Semisynthetic and Enzyme-Mediated Conjugate Preparations Illuminate the Ubiquitination-Dependent Aggregation of Tau Protein. *Angew. Chem. Int. Ed.* 59, 6607–6611. doi:10.1002/anie.201916756

Murthy, A. C., Dignon, G. L., Kan, Y., Zerze, G. H., Parekh, S. H., Mittal, J., et al. (2019). Molecular Interactions Underlying Liquid–liquid Phase Separation of the FUS Low-Complexity Domain. *Nat. Struct. Mol. Biol.* 26, 637–648. doi:10.1038/s41594-019-0250-x

Murugan, N. A., Halldin, C., Nordberg, A., Långström, B., and Ågren, H. (2016). The Culprit Is in the Cave: The Core Sites Explain the Binding Profiles of Amyloid-specific Tracers. *J. Phys. Chem. Lett.* 7, 3313–3321. doi:10.1021/acs.jpclett.6b01586

Murugan, N. A., Nordberg, A., and Ågren, H. (2021). Cryptic Sites in Tau Fibrils Explain the Preferential Binding of the AV-1451 PET Tracer toward Alzheimer's Tauopathy. *ACS Chem. Neurosci.* 12, 2437–2447. doi:10.1021/acschemneuro.0c00340

Murugan, N. A., Nordberg, A., and Ågren, H. (2018). Different Positron Emission Tomography Tau Tracers Bind to Multiple Binding Sites on the Tau Fibril: Insight from Computational Modeling. *ACS Chem. Neurosci.* 9, 1757–1767. doi:10.1021/acschemneuro.8b00093

Naiki, H., Higuchi, K., Hosokawa, M., and Takeda, T. (1989). Fluorometric Determination of Amyloid Fibrils *In Vitro* Using the Fluorescent Dye, Thioflavine T. *Anal. Biochem.* 177, 244–249. doi:10.1016/0003-2697(89)90046-8

Nasica-Labouze, J., Nguyen, P. H., Sterpone, F., Berthoumieu, O., Buchete, N.-V., Coté, S., et al. (2015). Amyloid β Protein and Alzheimer's Disease: When Computer Simulations Complement Experimental Studies. *Chem. Rev.* 115, 3518–3563. doi:10.1021/cr500638n

Nedelsky, N. B., and Taylor, J. P. (2019). Bridging Biophysics and Neurology: Aberrant Phase Transitions in Neurodegenerative Disease. *Nat. Rev. Neurol.* 15, 272–286. doi:10.1038/s41582-019-0157-5

Neves, J. F., Petrvalská, O., Bosica, F., Cantrelle, F. X., Merzougui, H., O'Mahony, G., et al. (2021). Phosphorylated Full-length Tau Interacts with 14-3-3 Proteins via Two Short Phosphorylated Sequences, Each Occupying a Binding Groove of 14-3-3 Dimer. *Febs J.* 288, 1918–1934. doi:10.1111/febs.15574

Nguyen, P. H., Ramamoorthy, A., Sahoo, B. R., Zheng, J., Faller, P., Straub, J. E., et al. (2021). Amyloid Oligomers: A Joint Experimental/Computational Perspective on Alzheimer's Disease, Parkinson's Disease, Type II Diabetes, and Amyotrophic Lateral Sclerosis. *Chem. Rev.* 121, 2545–2647. doi:10.1021/acs.chemrev.0c01122

Ni, R., and Nitsch, R. M. (2022). Recent Developments in Positron Emission Tomography Tracers for Proteinopathies Imaging in Dementia. *Front. Aging Neurosci.* 13, 751897. doi:10.3389/fnagi.2021.751897

Nirmalraj, P. N., List, J., Battacharya, S., Howe, G., Xu, L., Thompson, D., et al. (2020). Complete Aggregation Pathway of Amyloid β (1-40) and (1-42) Resolved on an Atomically Clean Interface. *Sci. Adv.* 6, eaaz6014. doi:10.1126/sciadv.aaz6014

Nizynski, B., Nieznanska, H., Dec, R., Boyko, S., Dzwolak, W., and Nieznanski, K. (2018). Amyloidogenic Cross-Seeding of Tau Protein: Transient Emergence of Structural Variants of Fibrils. *PLoS ONE* 13, e0201182. doi:10.1371/journal.pone.0201182

Novak, M., Kabat, J., and Wischik, C. M. (1993). Molecular Characterization of the Minimal Protease Resistant Tau Unit of the Alzheimer's Disease Paired Helical Filament. *EMBO J.* 12, 365–370. doi:10.1002/j.1460-2075.1993.tb05665.x

O'Donnell, N., Zachara, N. E., Hart, G. W., and Marth, J. D. (2004). Ogt-dependent X-Chromosome-Linked Protein Glycosylation Is a Requisite Modification in Somatic Cell Function and Embryo Viability. *Mol. Cell Biol.* 24, 1680–1690. doi:10.1128/mcb.24.4.1680-1690.2004

Ojida, A., Sakamoto, T., Inoue, M.-a., Fujishima, S.-h., Lippens, G., and Hamachi, I. (2009). Fluorescent BODIPY-Based Zn(II) Complex as a Molecular Probe for Selective Detection of Neurofibrillary Tangles in the Brains of Alzheimer's Disease Patients. *J. Am. Chem. Soc.* 131, 6543–6548. doi:10.1021/ja9008369

Olivier-Van Stichelen, S., Wang, P., Comly, M., Love, D. C., and Hanover, J. A. (2017). Nutrient-driven O-Linked N-Acetylglucosamine (O-GlcNAc) Cycling Impacts Neurodevelopmental Timing and Metabolism. *J. Biol. Chem.* 292, 6076–6085. doi:10.1074/jbc.M116.774042

Oueslati, A. (2016). Implication of Alpha-Synuclein Phosphorylation at S129 in Synucleinopathies: What Have We Learned in the Last Decade? *Jpd* 6, 39–51. doi:10.3233/JPD-160779

Pain, C., Dumont, J., and Dumoulin, M. (2015). Camelid Single-Domain Antibody Fragments: Uses and Prospects to Investigate Protein Misfolding and Aggregation, and to Treat Diseases Associated with These Phenomena. *Biochimie* 111, 82–106. doi:10.1016/j.biochi.2015.01.012

Pakravan, D., Michiels, E., Bratek-Skicki, A., De Decker, M., Van Lindt, J., Alsteens, D., et al. (2021). Liquid-Liquid Phase Separation Enhances TDP-43 LCD Aggregation but Delays Seeded Aggregation. *Biomolecules* 11, 548. doi:10.3390/biom11040548

Paleologou, K. E., Schmid, A. W., Rospigliosi, C. C., Kim, H.-Y., Lamberto, G. R., Fredenburg, R. A., et al. (2008). Phosphorylation at Ser-129 but Not the Phosphomimics S129E/D Inhibits the Fibrillation of α-Synuclein. *J. Biol. Chem.* 283, 16895–16905. doi:10.1074/jbc.M800747200

Pan, B., Park, J. H., Ramlall, T., Eliezer, D., Rhoades, E., and Petersson, E. J. (2021). Chemoenzymatic Semi-synthesis Enables Efficient Production of Isotopically Labeled α-Synuclein with Site-Specific Tyrosine Phosphorylation. *ChemBioChem* 22, 1440–1447. doi:10.1002/cbic.202000742

Pan, B., Rhoades, E., and Petersson, E. J. (2020). Chemoenzymatic Semisynthesis of Phosphorylated α-Synuclein Enables Identification of a Bidirectional Effect on Fibril Formation. *ACS Chem. Biol.* 15, 640–645. doi:10.1021/acschembio.9b01038

Park, H.-S., Hohn, M. J., Umehara, T., Guo, L.-T., Osborne, E. M., Benner, J., et al. (2011). Expanding the Genetic Code of *Escherichia coli* with Phosphoserine. *Science* 333, 1151–1154. doi:10.1126/science.1207203

Pastorino, L., Sun, A., Lu, P.-J., Zhou, X. Z., Balastik, M., Finn, G., et al. (2006). The Prolyl Isomerase Pin1 Regulates Amyloid Precursor Protein Processing and Amyloid-β Production. *Nature* 440, 528–534. doi:10.1038/nature04543

Patel, A., Lee, H. O., Jawerth, L., Maharana, S., Jahnel, M., Hein, M. Y., et al. (2015). A Liquid-To-Solid Phase Transition of the ALS Protein FUS Accelerated by Disease Mutation. *Cell* 162, 1066–1077. doi:10.1016/j.cell.2015.07.047

Pavlova, A., McCarney, E. R., Peterson, D. W., Dahlquist, F. W., Lew, J., and Han, S. (2009). Site-specific Dynamic Nuclear Polarization of Hydration Water as a

Generally Applicable Approach to Monitor Protein Aggregation. *Phys. Chem. Chem. Phys.* 11, 6833. doi:10.1039/b906101k

Pearce, M. M. P., and Kopito, R. R. (2018). Prion-Like Characteristics of Polyglutamine-Containing Proteins. *Cold Spring Harb. Perspect. Med.* 8, a024257. doi:10.1101/cshperspect.a024257

Pinheiro, F., Santos, J., and Ventura, S. (2021). AlphaFold and the Amyloid Landscape. *J. Mol. Biol.* 433, 167059. doi:10.1016/j.jmb.2021.167059

Podracky, C. J., An, C., DeSousa, A., Dorr, B. M., Walsh, D. M., and Liu, D. R. (2021). Laboratory Evolution of a Sortase Enzyme that Modifies Amyloid-β Protein. *Nat. Chem. Biol.* 17, 317–325. doi:10.1038/s41589-020-00706-1

Pontecorvo, M. J., Devous, M. D., Navitsky, M., Lu, M., Salloway, S., Schaerf, F. W., et al. (2017). Relationships between Flortaucipir PET Tau Binding and Amyloid Burden, Clinical Diagnosis, Age and Cognition. *Brain*, aww334. doi:10.1093/brain/aww334

Pornsuwan, S., Giller, K., Riedel, D., Becker, S., Griesinger, C., and Bennati, M. (2013). Long-Range Distances in Amyloid Fibrils of α-Synuclein from PELDOR Spectroscopy. *Angew. Chem. Int. Ed.* 52, 10290–10294. doi:10.1002/anie.201304747

Pothin, E., Lesuisse, D., and Lafaye, P. (2020). Brain Delivery of Single-Domain Antibodies: A Focus on VHH and VNAR. *Pharmaceutics* 12, 937. doi:10.3390/pharmaceutics12100937

Prusiner, S. B. (1982). Novel Proteinaceous Infectious Particles Cause Scrapie. *Science* 216, 136–144. doi:10.1126/science.6801762

Pytowski, L., Lee, C. F., Foley, A. C., Vaux, D. J., and Jean, L. (2020). Liquid-liquid Phase Separation of Type II Diabetes-Associated IAPP Initiates Hydrogelation and Aggregation. *Proc. Natl. Acad. Sci. U.S.A.* 117, 12050–12061. doi:10.1073/pnas.1916716117

Quinn, J. P., Corbett, N. J., Kellett, K. A. B., and Hooper, N. M. (2018). Tau Proteolysis in the Pathogenesis of Tauopathies: Neurotoxic Fragments and Novel Biomarkers. *Jad* 63, 13–33. doi:10.3233/JAD-170959

Rai, S. K., Savastano, A., Singh, P., Mukhopadhyay, S., and Zweckstetter, M. (2021). Liquid-liquid Phase Separation of Tau: From Molecular Biophysics to Physiology and Disease. *Protein Sci.* 30, 1294–1314. doi:10.1002/pro.4093

Ramirez, D. H., Aonbangkhen, C., Wu, H.-Y., Naftaly, J. A., Tang, S., O'Meara, T. R., et al. (2020). Engineering a Proximity-Directed O-GlcNAc Transferase for Selective Protein O-GlcNAcylation in Cells. *ACS Chem. Biol.* 15, 1059–1066. doi:10.1021/acschembio.0c00074

Reber, S., Jutzi, D., Lindsay, H., Devoy, A., Mechtersheimer, J., Levone, B. R., et al. (2021). The Phase Separation-dependent FUS Interactome Reveals Nuclear and Cytoplasmic Function of Liquid-Liquid Phase Separation. *Nucleic Acids Res.* 49, 7713–7731. doi:10.1093/nar/gkab582

Reimann, O., Smet-Nocca, C., and Hackenberger, C. P. R. (2015). Traceless Purification and Desulfurization of Tau Protein Ligation Products. *Angew. Chem. Int. Ed.* 54, 306–310. doi:10.1002/anie.201408674

Rice, L. J., Ecroyd, H., and van Oijen, A. M. (2021). Illuminating Amyloid Fibrils: Fluorescence-Based Single-Molecule Approaches. *Comput. Struct. Biotechnol. J.* 19, 4711–4724. doi:10.1016/j.csbj.2021.08.017

Rijal Upadhaya, A., Kosterin, I., Kumar, S., von Arnim, C. A. F., Yamaguchi, H., Fändrich, M., et al. (2014). Biochemical Stages of Amyloid-β Peptide Aggregation and Accumulation in the Human Brain and Their Association with Symptomatic and Pathologically Preclinical Alzheimer's Disease. *Brain* 137, 887–903. doi:10.1093/brain/awt362

Rodriguez Camargo, D. C., Sileikis, E., Chia, S., Axell, E., Bernfur, K., Cataldi, R. L., et al. (2021). Proliferation of Tau 304-380 Fragment Aggregates through Autocatalytic Secondary Nucleation. *ACS Chem. Neurosci.* 12, 4406–4415. doi:10.1021/acschemneuro.1c00454

Rösner, D., Schneider, T., Schneider, D., Scheffner, M., and Marx, A. (2015). Click Chemistry for Targeted Protein Ubiquitylation and Ubiquitin Chain Formation. *Nat. Protoc.* 10, 1594–1611. doi:10.1038/nprot.2015.106

Ruiz-Riquelme, A., Lau, H. H. C., Stuart, E., Goczi, A. N., Wang, Z., Schmitt-Ulms, G., et al. (2018). Prion-like Propagation of β-amyloid Aggregates in the Absence of APP Overexpression. *Acta Neuropathol. Commun.* 6, 26. doi:10.1186/s40478-018-0529-x

Ryan, P., Xu, M., Davey, A. K., Danon, J. J., Mellick, G. D., Kassiou, M., et al. (2019). O-GlcNAc Modification Protects against Protein Misfolding and Aggregation in Neurodegenerative Disease. *ACS Chem. Neurosci.* 10, 2209–2221. doi:10.1021/acschemneuro.9b00143

Sabri, O., Sabbagh, M. N., Seibyl, J., Barthel, H., Akatsu, H., Ouchi, Y., et al. (2015). Florbetaben PET Imaging to Detect Amyloid Beta Plaques in Alzheimer's Disease: Phase 3 Study. *Alzheimer's & Dement.* 11, 964–974. doi:10.1016/j.jalz.2015.02.004

Saha, A., Bello, D., and Fernández-Tejada, A. (2021). Advances in Chemical Probing of Protein O-GlcNAc Glycosylation: Structural Role and Molecular Mechanisms. *Chem. Soc. Rev.* 50, 10451–10485. doi:10.1039/D0CS01275K

Saint-Aubert, L., Lemoine, L., Chiotis, K., Leuzy, A., Rodriguez-Vieitez, E., and Nordberg, A. (2017). Tau PET Imaging: Present and Future Directions. *Mol. Neurodegener.* 12, 19. doi:10.1186/s13024-017-0162-3

Salwiczek, M., Nyakatura, E. K., Gerling, U. I. M., Ye, S., and Koksch, B. (2012). Fluorinated Amino Acids: Compatibility with Native Protein Structures and Effects on Protein-Protein Interactions. *Chem. Soc. Rev.* 41, 2135–2171. doi:10.1039/C1CS15241F

Sawner, A. S., Ray, S., Yadav, P., Mukherjee, S., Panigrahi, R., Poudyal, M., et al. (2021). Modulating α-Synuclein Liquid-Liquid Phase Separation. *Biochemistry* 60, 3676–3696. doi:10.1021/acs.biochem.1c00434

Schneider, A., Biernat, J., von Bergen, M., Mandelkow, E., and Mandelkow, E.-M. (1999). Phosphorylation that Detaches Tau Protein from Microtubules (Ser262, Ser214) Also Protects it against Aggregation into Alzheimer Paired Helical Filaments. *Biochemistry* 38, 3549–3558. doi:10.1021/bi981874p

Schwagerus, S., Reimann, O., Despres, C., Smet-Nocca, C., and Hackenberger, C. P. R. (2016). Semi-synthesis of a Tag-freeO-GlcNAcylated Tau Protein by Sequential Chemoselective Ligation. *J. Pept. Sci.* 22, 327–333. doi:10.1002/psc.2870

Schweighauser, M., Shi, Y., Tarutani, A., Kametani, F., Murzin, A. G., Ghetti, B., et al. (2020). Structures of α-synuclein Filaments from Multiple System Atrophy. *Nature* 585, 464–469. doi:10.1038/s41586-020-2317-6

Sebollela, A., Cline, E. N., Popova, I., Luo, K., Sun, X., Ahn, J., et al. (2017). A Human scFv Antibody that Targets and Neutralizes High Molecular Weight Pathogenic Amyloid-β Oligomers. *J. Neurochem.* 142, 934–947. doi:10.1111/jnc.14118

Shafi, R., Iyer, S. P. N., Ellies, L. G., O'Donnell, N., Marek, K. W., Chui, D., et al. (2000). The O-GlcNAc Transferase Gene Resides on the X Chromosome and Is Essential for Embryonic Stem Cell Viability and Mouse Ontogeny. *Proc. Natl. Acad. Sci. U.S.A.* 97, 5735–5739. doi:10.1073/pnas.100471497

Shahmoradian, S. H., Lewis, A. J., Genoud, C., Hench, J., Moors, T. E., Navarro, P. P., et al. (2019). Lewy Pathology in Parkinson's Disease Consists of Crowded Organelles and Lipid Membranes. *Nat. Neurosci.* 22, 1099–1109. doi:10.1038/s41593-019-0423-2

Shi, Y., Zhang, W., Yang, Y., Murzin, A. G., Falcon, B., Kotecha, A., et al. (2021). Structure-based Classification of Tauopathies. *Nature* 598, 359–363. doi:10.1038/s41586-021-03911-7

Shimogawa, M., and Petersson, E. J. (2021). New Strategies for Fluorescently Labeling Proteins in the Study of Amyloids. *Curr. Opin. Chem. Biol.* 64, 57–66. doi:10.1016/j.cbpa.2021.04.011

Shin, J., Kepe, V., Barrio, J. R., and Small, G. W. (2011). The Merits of FDDNP-PET Imaging in Alzheimer's Disease. *JAD* 26, 135–145. doi:10.3233/JAD-2011-0008

Siddiqua, A., Luo, Y., Meyer, V., Swanson, M. A., Yu, X., Wei, G., et al. (2012). Conformational Basis for Asymmetric Seeding Barrier in Filaments of Three- and Four-Repeat Tau. *J. Am. Chem. Soc.* 134, 10271–10278. doi:10.1021/ja303498q

Sillen, A., Leroy, A., Wieruszeski, J.-M., Loyens, A., Beauvillain, J.-C., Buée, L., et al. (2005). Regions of Tau Implicated in the Paired Helical Fragment Core as Defined by NMR. *Chembiochem* 6, 1849–1856. doi:10.1002/cbic.200400452

Šimić, G., Babić Leko, M., Wray, S., Harrington, C., Delalle, I., Jovanov-Milošević, N., et al. (2016). Tau Protein Hyperphosphorylation and Aggregation in Alzheimer's Disease and Other Tauopathies, and Possible Neuroprotective Strategies. *Biomolecules* 6, 6. doi:10.3390/biom6010006

Simon, M. D., Chu, F., Racki, L. R., de la Cruz, C. C., Burlingame, A. L., Panning, B., et al. (2007). The Site-specific Installation of Methyl-Lysine Analogs into Recombinant Histones. *Cell* 128, 1003–1012. doi:10.1016/j.cell.2006.12.041

Singh, V., Xu, L., Boyko, S., Surewicz, K., and Surewicz, W. K. (2020). Zinc Promotes Liquid-Liquid Phase Separation of Tau Protein. *J. Biol. Chem.* 295, 5850–5856. doi:10.1074/jbc.AC120.013166

Sinnaeve, D., Ben Bouzayene, A., Ottoy, E., Hofman, G.-J., Erdmann, E., Linclau, B., et al. (2021). Fluorine NMR Study of Proline-Rich Sequences Using Fluoroprolines. *Magn. Reson.* 2, 795–813. doi:10.5194/mr-2-795-2021

Smet, C., Sambo, A.-V., Wieruszeski, J.-M., Leroy, A., Landrieu, I., Buée, L., et al. (2004). The Peptidyl Prolyl Cis/trans-Isomerase Pin1 Recognizes the Phospho-Thr212-Pro213 Site on Tau. *Biochemistry* 43, 2032–2040. doi:10.1021/bi035479x

Smet, C., Wieruszeski, J.-M., Buée, L., Landrieu, I., and Lippens, G. (2005). Regulation of Pin1 Peptidyl-Prolylcis/transisomerase Activity by its WW Binding Module on a Multi-Phosphorylated Peptide of Tau Protein. *FEBS Lett.* 579, 4159–4164. doi:10.1016/j.febslet.2005.06.048

Smet-Nocca, C., Broncel, M., Wieruszeski, J.-M., Tokarski, C., Hanoulle, X., Leroy, A., et al. (2011). Identification of O-GlcNAc Sites within Peptides of the Tau Protein and Their Impact on Phosphorylation. *Mol. Biosyst.* 7, 1420–1429. doi:10.1039/c0mb00337a

Smith, D. P., Anderson, J., Plante, J., Ashcroft, A. E., Radford, S. E., Wilson, A. J., et al. (2008). Trifluoromethyldiazirine: an Effective Photo-Induced Cross-Linking Probe for Exploring Amyloid Formation. *Chem. Commun.*, 5728. doi:10.1039/b813504e

Sohma, Y., Hirayama, Y., Taniguchi, A., Mukai, H., and Kiso, Y. (2011). 'Click Peptide' Using Production of Monomer Aβ from the O-Acyl Isopeptide: Application to Assay System of Aggregation Inhibitors and Cellular Cytotoxicity. *Bioorg. Med. Chem.* 19, 1729–1733. doi:10.1016/j.bmc.2011.01.021

Soto, C., and Pritzkow, S. (2018). Protein Misfolding, Aggregation, and Conformational Strains in Neurodegenerative Diseases. *Nat. Neurosci.* 21, 1332–1340. doi:10.1038/s41593-018-0235-9

Stewart, K. L., Hughes, E., Yates, E. A., Akien, G. R., Huang, T.-Y., Lima, M. A., et al. (2016). Atomic Details of the Interactions of Glycosaminoglycans with Amyloid-β Fibrils. *J. Am. Chem. Soc.* 138, 8328–8331. doi:10.1021/jacs.6b02816

Sun, B., Fan, W., Balciunas, A., Cooper, J. K., Bitan, G., Steavenson, S., et al. (2002). Polyglutamine Repeat Length-dependent Proteolysis of Huntingtin. *Neurobiol. Dis.* 11, 111–122. doi:10.1006/nbdi.2002.0539

Suzuki, Y., Brender, J. R., Hartman, K., Ramamoorthy, A., and Marsh, E. N. G. (2012). Alternative Pathways of Human Islet Amyloid Polypeptide Aggregation Distinguished by 19F Nuclear Magnetic Resonance-Detected Kinetics of Monomer Consumption. *Biochemistry* 51, 8154–8162. doi:10.1021/bi3012548

Suzuki, Y., Brender, J. R., Soper, M. T., Krishnamoorthy, J., Zhou, Y., Ruotolo, B. T., et al. (2013). Resolution of Oligomeric Species during the Aggregation of Aβ1-40 Using 19F NMR. *Biochemistry* 52, 1903–1912. doi:10.1021/bi400027y

Tang, S., Wang, W., and Zhang, X. (2021). Direct Visualization and Profiling of Protein Misfolding and Aggregation in Live Cells. *Curr. Opin. Chem. Biol.* 64, 116–123. doi:10.1016/j.cbpa.2021.05.008

Tang, Y., Zhang, D., Zhang, Y., Liu, Y., Cai, L., Plaster, E., et al. (2022). Fundamentals and Exploration of Aggregation-Induced Emission Molecules for Amyloid Protein Aggregation. *J. Mater Chem. B* 10, 2208–2295. doi:10.1039/D1TB01942B

Taniguchi, A., Sohma, Y., Hirayama, Y., Mukai, H., Kimura, T., Hayashi, Y., et al. (2009). "Click Peptide": pH-Triggered *In Situ* Production and Aggregation of Monomer Aβ1-42. *ChemBioChem* 10, 710–715. doi:10.1002/cbic.200800765

Taniguchi, A., Sohma, Y., Kimura, M., Okada, T., Ikeda, K., Hayashi, Y., et al. (2006). "Click Peptide" Based on the "O-Acyl Isopeptide Method": Control of Aβ1–42 Production from a Photo-Triggered Aβ1–42 Analogue. *J. Am. Chem. Soc.* 128, 696–697. doi:10.1021/ja057100v

Tarrant, M. K., and Cole, P. A. (2009). The Chemical Biology of Protein Phosphorylation. *Annu. Rev. Biochem.* 78, 797–825. doi:10.1146/annurev.biochem.78.070907.103047

Tashima, Y., and Stanley, P. (2014). Antibodies that Detect O-Linked β-d-N-Acetylglucosamine on the Extracellular Domain of Cell Surface Glycoproteins. *J. Biol. Chem.* 289, 11132–11142. doi:10.1074/jbc.M113.492512

Tavassoly, O., Yue, J., and Vocadlo, D. J. (2021). Pharmacological Inhibition and Knockdown of O-GlcNAcase Reduces Cellular Internalization of α-synuclein Preformed Fibrils. *FEBS J.* 288, 452–470. doi:10.1111/febs.15349

Tegl, G., Hanson, J., Chen, H. M., Kwan, D. H., Santana, A. G., and Withers, S. G. (2019). Facile Formation of β-thioGlcNAc Linkages to Thiol-Containing Sugars, Peptides, and Proteins Using a Mutant GH20 Hexosaminidase. *Angew. Chem. Int. Ed.* 58, 1632–1637. doi:10.1002/anie.201809928

Tenreiro, S., Eckermann, K., and Outeiro, T. F. (2014). Protein Phosphorylation in Neurodegeneration: Friend or Foe? *Front. Mol. Neurosci.* 7, 7. doi:10.3389/fnmol.2014.00042

Tepper, K., Biernat, J., Kumar, S., Wegmann, S., Timm, T., Hübschmann, S., et al. (2014). Oligomer Formation of Tau Protein Hyperphosphorylated in Cells. *J. Biol. Chem.* 289, 34389–34407. doi:10.1074/jbc.M114.611368

Theillet, F.-X., Smet-Nocca, C., Liokatis, S., Thongwichian, R., Kosten, J., Yoon, M.-K., et al. (2012). Cell Signaling, Post-translational Protein Modifications and NMR Spectroscopy. *J. Biomol. NMR* 54, 217–236. doi:10.1007/s10858-012-9674-x

Thompson, J. W., Griffin, M. E., and Hsieh-Wilson, L. C. (2018). Methods for the Detection, Study, and Dynamic Profiling of O-GlcNAc Glycosylation. *Methods Enzym.* 2018, 101–135. doi:10.1016/bs.mie.2017.06.009

Torbeev, V. Y., and Hilvert, D. (2013). Both the Cis - Trans Equilibrium and Isomerization Dynamics of a Single Proline Amide Modulate β2-microglobulin Amyloid Assembly. *Proc. Natl. Acad. Sci. U.S.A.* 110, 20051–20056. doi:10.1073/pnas.1310414110

Tunyasuvunakool, K., Adler, J., Wu, Z., Green, T., Zielinski, M., Žídek, A., et al. (2021). Highly Accurate Protein Structure Prediction for the Human Proteome. *Nature* 596, 590–596. doi:10.1038/s41586-021-03828-1

Ulamec, S. M., Brockwell, D. J., and Radford, S. E. (2020). Looking beyond the Core: The Role of Flanking Regions in the Aggregation of Amyloidogenic Peptides and Proteins. *Front. Neurosci.* 14, 611285. doi:10.3389/fnins.2020.611285

van Husen, L. S., Schedin-Weiss, S., Trung, M. N., Kazmi, M. A., Winblad, B., Sakmar, T. P., et al. (2019). Dual Bioorthogonal Labeling of the Amyloid-β Protein Precursor Facilitates Simultaneous Visualization of the Protein and its Cleavage Products. *JAD* 72, 537–548. doi:10.3233/JAD-190898

Vandesquille, M., Li, T., Po, C., Ganneau, C., Lenormand, P., Dudeffant, C., et al. (2017). Chemically-defined Camelid Antibody Bioconjugate for the Magnetic Resonance Imaging of Alzheimer's Disease. *MAbs* 9, 1016–1027. doi:10.1080/19420862.2017.1342914

Vázquez de la Torre, A., Gay, M., Vilaprinyó-Pascual, S., Mazzucato, R., Serra-Batiste, M., Vilaseca, M., et al. (2018). Direct Evidence of the Presence of Cross-Linked Aβ Dimers in the Brains of Alzheimer's Disease Patients. *Anal. Chem.* 90, 4552–4560. doi:10.1021/acs.analchem.7b04936

Verhoork, S. J. M., Killoran, P. M., and Coxon, C. R. (2018). Fluorinated Prolines as Conformational Tools and Reporters for Peptide and Protein Chemistry. *Biochemistry* 57, 6132–6143. doi:10.1021/acs.biochem.8b00787

Vogl, D. P., Conibear, A. C., and Becker, C. F. W. (2021). Segmental and Site-specific Isotope Labelling Strategies for Structural Analysis of Posttranslationally Modified Proteins. *RSC Chem. Biol.* 2, 1441–1461. doi:10.1039/D1CB00045D

Walsh, D. M., and Selkoe, D. J. (2016). A Critical Appraisal of the Pathogenic Protein Spread Hypothesis of Neurodegeneration. *Nat. Rev. Neurosci.* 17, 251–260. doi:10.1038/nrn.2016.13

Wang, A., Conicella, A. E., Schmidt, H. B., Martin, E. W., Rhoads, S. N., Reeb, A. N., et al. (2018). A Single N-terminal Phosphomimic Disrupts TDP-43 Polymerization, Phase Separation, and RNA Splicing. *EMBO J.* 37. doi:10.15252/embj.201797452

Wang, L.-Q., Zhao, K., Yuan, H.-Y., Wang, Q., Guan, Z., Tao, J., et al. (2020). Cryo-EM Structure of an Amyloid Fibril Formed by Full-Length Human Prion Protein. *Nat. Struct. Mol. Biol.* 27, 598–602. doi:10.1038/s41594-020-0441-5

Wang, L., Brock, A., Herberich, B., and Schultz, P. G. (2001). Expanding the Genetic Code of *Escherichia coli*. *Science* 292, 498–500. doi:10.1126/science.1060077

Wang, L., Xie, J., and Schultz, P. G. (2006). EXPANDING THE GENETIC CODE. *Annu. Rev. Biophys. Biomol. Struct.* 35, 225–249. doi:10.1146/annurev.biophys.35.101105.121507

Wang, L., Zhou, Y., Chen, D., and Lee, T. H. (2020). Peptidyl-Prolyl Cis/Trans Isomerase Pin1 and Alzheimer's Disease. *Front. Cell Dev. Biol.* 8, 355. doi:10.3389/fcell.2020.00355

Wang, P., Lazarus, B. D., Forsythe, M. E., Love, D. C., Krause, M. W., and Hanover, J. A. (2012). O-GlcNAc Cycling Mutants Modulate Proteotoxicity in *Caenorhabditis elegans* Models of Human Neurodegenerative Diseases. *Proc. Natl. Acad. Sci. U.S.A.* 109, 17669–17674. doi:10.1073/pnas.1205748109

Warner, J. B., Ruff, K. M., Tan, P. S., Lemke, E. A., Pappu, R. V., and Lashuel, H. A. (2017). Monomeric Huntingtin Exon 1 Has Similar Overall Structural Features for Wild-type and Pathological Polyglutamine Lengths. *J. Am. Chem. Soc.* 139, 14456–14469. doi:10.1021/jacs.7b06659

Watanabe, S., Inami, H., Oiwa, K., Murata, Y., Sakai, S., Komine, O., et al. (2020). Aggresome Formation and Liquid-Liquid Phase Separation Independently

Induce Cytoplasmic Aggregation of TAR DNA-Binding Protein 43. *Cell Death Dis.* 11, 909. doi:10.1038/s41419-020-03116-2

Wegmann, S., Eftekharzadeh, B., Tepper, K., Zoltowska, K. M., Bennett, R. E., Dujardin, S., et al. (2018). Tau Protein Liquid-Liquid Phase Separation Can Initiate Tau Aggregation. *EMBO J.* 37. doi:10.15252/embj.201798049

Wegmann, S., Medalsy, I. D., Mandelkow, E., and Müller, D. J. (2013). The Fuzzy Coat of Pathological Human Tau Fibrils Is a Two-Layered Polyelectrolyte Brush. *Proc. Natl. Acad. Sci. U.S.A.* 110, E313–E321. doi:10.1073/pnas.1212100110

Wells, L., Vosseller, K., and Hart, G. W. (2003). A Role for N -acetylglucosamine as a Nutrient Sensor and Mediator of Insulin Resistance. *Cell. Mol. Life Sci. (CMLS)* 60, 222–228. doi:10.1007/s000180300017

Wesseling, H., Mair, W., Kumar, M., Schlaffner, C. N., Tang, S., Beerepoot, P., et al. (2020). Tau PTM Profiles Identify Patient Heterogeneity and Stages of Alzheimer's Disease. *Cell* 183, 1699–1713. e13. doi:10.1016/j.cell.2020.10.029

Winklhofer, K. F., Tatzelt, J., and Haass, C. (2008). The Two Faces of Protein Misfolding: Gain- and Loss-Of-Function in Neurodegenerative Diseases. *EMBO J.* 27, 336–349. doi:10.1038/sj.emboj.7601930

Wischik, C. M., Novak, M., Edwards, P. C., Klug, A., Tichelaar, W., and Crowther, R. A. (1988). Structural Characterization of the Core of the Paired Helical Filament of Alzheimer Disease. *Proc. Natl. Acad. Sci. U.S.A.* 85, 4884–4888. doi:10.1073/pnas.85.13.4884

Wolstenholme, C. H., Hu, H., Ye, S., Funk, B. E., Jain, D., Hsiung, C.-H., et al. (2020). AggFluor: Fluorogenic Toolbox Enables Direct Visualization of the Multi-step Protein Aggregation Process in Live Cells. *J. Am. Chem. Soc.* 142, 17515–17523. doi:10.1021/jacs.0c07245

Wright, T. H., Bower, B. J., Chalker, J. M., Bernardes, G. J. L., Wiewiora, R., Ng, W.-L., et al. (2016). Posttranslational Mutagenesis: A Chemical Strategy for Exploring Protein Side-Chain Diversity. *Science* 354, aag1465. doi:10.1126/science.aag1465

Xu, Z., Graham, K., Foote, M., Liang, F., Rizkallah, R., Hurt, M., et al. (2013). 14-3-3 Targets Chaperone-Associated Misfolded Proteins to Aggresomes. *J. Cell Sci.*, 126102. doi:10.1242/jcs.126102

Yan, M. H., Wang, X., and Zhu, X. (2013). Mitochondrial Defects and Oxidative Stress in Alzheimer Disease and Parkinson Disease. *Free Radic. Biol. Med.* 62, 90–101. doi:10.1016/j.freeradbiomed.2012.11.014

Yang, A., Cho, K., and Park, H.-S. (2018). Chemical Biology Approaches for Studying Posttranslational Modifications. *RNA Biol.* 15, 427–440. doi:10.1080/15476286.2017.1360468

Yang, A., Ha, S., Ahn, J., Kim, R., Kim, S., Lee, Y., et al. (2016). A Chemical Biology Route to Site-specific Authentic Protein Modifications. *Science* 354, 623–626. doi:10.1126/science.aah4428

Yang, B., Wang, N., Schnier, P. D., Zheng, F., Zhu, H., Polizzi, N. F., et al. (2019). Genetically Introducing Biochemically Reactive Amino Acids Dehydroalanine and Dehydrobutyrine in Proteins. *J. Am. Chem. Soc.* 141, 7698–7703. doi:10.1021/jacs.9b02611

Yang, J., Perrett, S., and Wu, S. (2021). Single Molecule Characterization of Amyloid Oligomers. *Molecules* 26, 948. doi:10.3390/molecules26040948

Yang, Y., Arseni, D., Zhang, W., Huang, M., Lövestam, S., Schweighauser, M., et al. (2022). Cryo-EM Structures of Amyloid-β 42 Filaments from Human Brains. *Science* 375, 167–172. doi:10.1126/science.abm7285

Yuzwa, S. A., Cheung, A. H., Okon, M., McIntosh, L. P., and Vocadlo, D. J. (2014). O-GlcNAc Modification of Tau Directly Inhibits its Aggregation without Perturbing the Conformational Properties of Tau Monomers. *J. Mol. Biol.* 426, 1736–1752. doi:10.1016/j.jmb.2014.01.004

Yuzwa, S. A., Macauley, M. S., Heinonen, J. E., Shan, X., Dennis, R. J., He, Y., et al. (2008). A Potent Mechanism-Inspired O-GlcNAcase Inhibitor that Blocks Phosphorylation of Tau *In Vivo*. *Nat. Chem. Biol.* 4, 483–490. doi:10.1038/nchembio.96

Yuzwa, S. A., Shan, X., Jones, B. A., Zhao, G., Woodward, M. L., Li, X., et al. (2014). Pharmacological Inhibition of O-GlcNAcase (OGA) Prevents Cognitive Decline and Amyloid Plaque Formation in Bigenic Tau/APP Mutant Mice. *Mol. Neurodegener.* 9, 42. doi:10.1186/1750-1326-9-42

Yuzwa, S. A., Shan, X., Macauley, M. S., Clark, T., Skorobogatko, Y., Vosseller, K., et al. (2012). Increasing O-GlcNAc Slows Neurodegeneration and Stabilizes Tau against Aggregation. *Nat. Chem. Biol.* 8, 393–399. doi:10.1038/nchembio.797

Yuzwa, S. A., Yadav, A. K., Skorobogatko, Y., Clark, T., Vosseller, K., and Vocadlo, D. J. (2011). Mapping O-GlcNAc Modification Sites on Tau and Generation of a Site-specific O-GlcNAc Tau Antibody. *Amino Acids* 40, 857–868. doi:10.1007/s00726-010-0705-1

Zhang, J., Lei, H., Chen, Y., Ma, Y.-T., Jiang, F., Tan, J., et al. (2017). Enzymatic O-GlcNAcylation of α-synuclein Reduces Aggregation and Increases SDS-Resistant Soluble Oligomers. *Neurosci. Lett.* 655, 90–94. doi:10.1016/j.neulet.2017.06.034

Zhang, J., Li, X., and Li, J.-D. (2019). The Roles of Post-translational Modifications on α-Synuclein in the Pathogenesis of Parkinson's Diseases. *Front. Neurosci.* 13, 381. doi:10.3389/fnins.2019.00381

Zhang, W., Falcon, B., Murzin, A. G., Fan, J., Crowther, R. A., Goedert, M., et al. (2019). Heparin-induced Tau Filaments Are Polymorphic and Differ from Those in Alzheimer's and Pick's Diseases. *Elife* 8, e43584. doi:10.7554/eLife.43584

Zhang, W., Tarutani, A., Newell, K. L., Murzin, A. G., Matsubara, T., Falcon, B., et al. (2020). Novel Tau Filament Fold in Corticobasal Degeneration. *Nature* 580, 283–287. doi:10.1038/s41586-020-2043-0

Zhang, X., Lin, Y., Eschmann, N. A., Zhou, H., Rauch, J. N., Hernandez, I., et al. (2017). RNA Stores Tau Reversibly in Complex Coacervates. *PLoS Biol.* 15, e2002183. doi:10.1371/journal.pbio.2002183

Zhang, X., Sun, X.-x., Xue, D., Liu, D.-g., Hu, X.-y., Zhao, M., et al. (2011). Conformation-dependent scFv Antibodies Specifically Recognize the Oligomers Assembled from Various Amyloids and Show Colocalization of Amyloid Fibrils with Oligomers in Patients with Amyloidoses. *Biochimica Biophysica Acta (BBA) - Proteins Proteomics* 1814, 1703–1712. doi:10.1016/j.bbapap.2011.09.005

Zhao, K., Lim, Y.-J., Liu, Z., Long, H., Sun, Y., Hu, J.-J., et al. (2020). Parkinson's Disease-Related Phosphorylation at Tyr39 Rearranges α-synuclein Amyloid Fibril Structure Revealed by Cryo-EM. *Proc. Natl. Acad. Sci. U.S.A.* 117, 20305–20315. doi:10.1073/pnas.1922741117

Zhou, C., Emadi, S., Sierks, M. R., and Messer, A. (2004). A Human Single-Chain Fv Intrabody Blocks Aberrant Cellular Effects of Overexpressed α-synuclein. *Mol. Ther.* 10, 1023–1031. doi:10.1016/j.ymthe.2004.08.019

Zhou, X. Z., Kops, O., Werner, A., Lu, P.-J., Shen, M., Stoller, G., et al. (2000). Pin1-dependent Prolyl Isomerization Regulates Dephosphorylation of Cdc25C and Tau Proteins. *Mol. Cell* 6, 873–883. doi:10.1016/s1097-2765(05)00083-3

Zhu, Y., and Hart, G. W. (2020). Targeting the O-GlcNAc Transferase to Specific Proteins Using RNA Aptamers. *FASEB J.* 34, 1. doi:10.1096/fasebj.2020.34.s1.02729

Zurlo, E., Gorroño Bikandi, I., Meeuwenoord, N. J., Filippov, D. V., and Huber, M. (2019). Tracking Amyloid Oligomerization with Monomer Resolution Using a 13-amino Acid Peptide with a Backbone-Fixed Spin Label. *Phys. Chem. Chem. Phys.* 21, 25187–25195. doi:10.1039/C9CP01060B

Conflict of Interest: The authors declare that the research was conducted in the absence of any commercial or financial relationships that could be construed as a potential conflict of interest.

Publisher's Note: All claims expressed in this article are solely those of the authors and do not necessarily represent those of their affiliated organizations, or those of the publisher, the editors and the reviewers. Any product that may be evaluated in this article, or claim that may be made by its manufacturer, is not guaranteed or endorsed by the publisher.

frontiers | Frontiers in Chemistry

ORIGINAL RESEARCH
published: 26 May 2022
doi: 10.3389/fchem.2022.896386

Novel Stilbene-Nitroxyl Hybrid Compounds Display Discrete Modulation of Amyloid Beta Toxicity and Structure

*Silvia Hilt[1†], Ruiwu Liu[1†], Izumi Maezawa[2], Tatu Rojalin[3], Hnin H. Aung[4,5], Madhu Budamagunta[1], Ryan Slez[1], Qizhi Gong[6], Randy P. Carney[3] and John C. Voss[1,7]**

[1]Department of Biochemistry and Molecular Medicine, University of California, Davis, Davis, CA, United States, [2]M.I.N.D. Institute and Department of Pathology and Laboratory Medicine, University of California, Davis, Davis, CA, United States, [3]Department of Biomedical Engineering, University of California, Davis, Davis, CA, United States, [4]Division of Cardiovascular Medicine, Department of Internal Medicine, School of Medicine, University of California, Davis, Davis, CA, United States, [5]Research Division, California Air Resource Board, Sacramento, CA, United States, [6]Department of Cell Biology and Human Anatomy, School of Medicine, University of California, Davis, Davis, CA, United States, [7]Paramag Biosciences Inc., Davis, CA, United States

OPEN ACCESS

Edited by:
Matthew A. Coleman,
University of California, Davis,
United States

Reviewed by:
Praveen Nekkar Rao,
University of Waterloo, Canada
Caroline Smet-Nocca,
Université de Lille, France

***Correspondence:**
John C. Voss
jcvoss@ucdavis.edu

[†]These authors share first authorship

Specialty section:
This article was submitted to Chemical Biology, a section of the journal Frontiers in Chemistry

Received: 15 March 2022
Accepted: 21 April 2022
Published: 26 May 2022

Citation:
Hilt S, Liu R, Maezawa I, Rojalin T, Aung HH, Budamagunta M, Slez R, Gong Q, Carney RP and Voss JC (2022) Novel Stilbene-Nitroxyl Hybrid Compounds Display Discrete Modulation of Amyloid Beta Toxicity and Structure. Front. Chem. 10:896386. doi: 10.3389/fchem.2022.896386

Several neurodegenerative diseases are driven by misfolded proteins that assemble into soluble aggregates. These "toxic oligomers" have been associated with a plethora of cellular dysfunction and dysregulation, however the structural features underlying their toxicity are poorly understood. A major impediment to answering this question relates to the heterogeneous nature of the oligomers, both in terms of structural disorder and oligomer size. This not only complicates elucidating the molecular etiology of these disorders, but also the druggability of these targets as well. We have synthesized a class of bifunctional stilbenes to modulate both the conformational toxicity within amyloid beta oligomers (AβO) and the oxidative stress elicited by AβO. Using a neuronal culture model, we demonstrate this bifunctional approach has the potential to counter the molecular pathogenesis of Alzheimer's disease in a powerful, synergistic manner. Examination of AβO structure by various biophysical tools shows that each stilbene candidate uniquely alters AβO conformation and toxicity, providing insight towards the future development of structural correctors for AβO. Correlations of AβO structural modulation and bioactivity displayed by each provides insights for future testing *in vivo*. The multi-target activity of these hybrid molecules represents a highly advantageous feature for disease modification in Alzheimer's, which displays a complex, multifactorial etiology. Importantly, these novel small molecules intervene with intraneuronal AβO, a necessary feature to counter the cycle of dysregulation, oxidative stress and inflammation triggered during the earliest stages of disease progression.

Keywords: protein misfolding, protein aggregation, oxidative stress, EPR (electron paramagnetic resonance), circular dichroism (CD), amyloid beta peptide (Aβ), Alzheimer's disease

1 INTRODUCTION

The amyloid beta peptide (Aβ) plays central role in the etiology of Alzheimer's Disease (AD), representing the earliest and most validated marker for the disease (Selkoe and Hardy, 2016; Sperling et al., 2020). Despite decades of study, a poor understanding of the conformational/thermodynamic states of the soluble oligomeric Aβ peptide (AβO) continues to confound efforts to design interventions targeting this species. In recent years, clinical trials have focused on lowering extracellular Aβ by immunotherapy (Usman et al., 2021). The results from most studies have missed their defined endpoints, raising the question as to whether lowering extracellular Aβ alone is sufficient to alter disease progression. In addition, complications associated with targeting extracellular Aβ deposits immunotherapy are common, such as inadvertently generating AβO from deposits [e.g., "the dust raising effect" (Liu et al., 2012)].

AβOs are distinguished from the Aβ monomers or fibrillar deposits by their neurotoxicity (Gong et al., 2003; Haass and Selkoe, 2007; Guerrero-Muñoz et al., 2014) and association to pathology in AD brains and animal models (Kayed et al., 2003; Selkoe and Hardy, 2016). For example, cell culture studies blocking Aβ oligomerization show protection from toxicity while compounds that promote fibril formation can be protective (Necula et al., 2007; Bieschke et al., 2011; Dutta et al., 2017). Other studies have established that AβOs trigger a variety of downstream effects resulting in cognitive deficits and neuronal destruction (Shankar et al., 2008; Almeida et al., 2009; Cottart et al., 2010; Rege et al., 2014; Currais et al., 2016; Selkoe and Hardy, 2016). This includes measurements in animal and cell culture models demonstrating that AβO drives Tau phosphorylation and aggregation (Brouillette et al., 2012; Bloom, 2014; Dunning et al., 2016; Park et al., 2018).

The self-association of Aβ occurs through a complex interplay of different oligomeric sizes and peptide conformations, whose dynamic equilibrium is sensitive to the peptide concentration, length, modification and local environment (Cline et al., 2018). For example, smaller species have been identified as causing synaptic dysfunction, whereas larger oligomers are associated with overall neurotoxicity (Figueiredo et al., 2013). Thus, identifying a single pathogenic species *via* a defined size and conformational state common to the various intra- and extracellular milieus is unlikely. While it is not possible for synthetic AβO preps to fully recapitulate the heterogeneity and post-translational modifications of Aβ assemblies found *in vivo*, a multitude of studies suggest that preparations of mid-sized oligomers (>50 kDa) correlate strongest along various pathways of neurotoxicity and cellular dysregulation (Cline et al., 2018; Shea et al., 2019). These oligomers are structurally disordered, react with the conformational antibody A11, ranging in size from the dodecamer up to 150 kDa. The pathogenic conformation of the peptides within these assemblies is still unknown, although pathogenic conformations have been proposed including the β-sheet edge (Yoshiike et al., 2008), exposure of hydrophobic patches (Ladiwala et al., 2012), alpha-sheet secondary structure (Shea et al., 2019), or alternative states of the hairpin region of the peptide that correlate to a "toxic" turn (Murakami, 2014; Silverman et al., 2018).

AβOs in brain tissue are found in both extracellular and intracellular compartments (Oakley et al., 2006; Oddo et al., 2006; Pensalfini et al., 2014). While disease diagnosis relies on extracellular amyloid, the pool of intracellular Aβ may play a greater role in the initiation of AD (Takahashi et al., 2017). Intraneuronal Aβ precedes both intracellular NFT and extracellular amyloid deposits (Knobloch et al., 2007; Pensalfini et al., 2014) and has profound effects on neuronal health (Takahashi et al., 2017). There is also accumulating evidence that suggests that intraneuronal Aβ42 is a major risk factor for neuronal loss and a trigger for the Aβ cascade of pathological events (Kienlen-Campard et al., 2002). Because intraneuronal Aβ precedes extracellular amyloid deposits and pTau filament formation, small molecules with access to the brain and cell interior may have a superior potential to intervene at the earliest stages of AD. Small molecules also offer flexibility in the ability to engage more than one type of misfolded protein, which may be key as increasing evidence indicates a direct influence among the various misfolded proteins (Aβ, Tau, α-Syn, TDP-43) associated with neurodegenerative proteinopathies (Colom-Cadena et al., 2013; Limanaqi et al., 2020).

The multifactorial nature of AD is commonly recognized, implying the involvement of several neurobiological targets in the initiation and development of this neurodegenerative disease. This challenge may in part be related to the complexity and dynamic nature of the AβO, leading to a multitude of reported mechanisms for its cytotoxicity (Kayed and Lasagna-Reeves, 2012). One important mechanism involves the elevation of reactive oxygen species (ROS), as oxidative damage can be considered the earliest known biochemical marker in the AD brain (Gong et al., 2003). AβO triggers oxidative stress in neurons, whereas oxidative stress increases Aβ production and/or clearance (Jo et al., 2010; Sultana and Butterfield, 2010). This process propagates a circular cascade of increased Aβ and ROS production (Swerdlow et al., 2014), which can also trigger microglial activation and Tau phosphorylation and misfolding (Maccioni et al., 2010; Rudenko et al., 2019).

Stilbenes such as resveratrol have shown therapeutic potential in models for AD and other neurodegenerative diseases (Rege et al., 2014; Ahmed et al., 2017; Drygalski et al., 2018). For example, resveratrol promotes Aβ clearance (Marambaud et al., 2005; Moussa et al., 2017), alters Aβ structure and aggregation properties (Ladiwala et al., 2010; Ge et al., 2012; Fu et al., 2014), and attenuates inflammation and oxidative stress in models for dementia and neurodegenerative disease (Sarubbo et al., 2017; Wang et al., 2018). Support for clinical evaluation of resveratrol in AD treatment has been shown in Alzheimer's mouse models (Karuppagounder et al., 2009; Capiralla et al., 2012; Ma et al., 2014). We have developed a new series of small molecules that alter both the conformational toxicity of AβO and provide potent, long-lived antioxidant activity. The molecules are constructed to contain a stilbene scaffold for AβO engagement and a nitroxide spin label for antioxidant activity. We have designated these bifunctional molecules as paramagnetic amyloid ligands (PALs). Here we show five chemically distinct

PAL molecules for their effect on AβO structure and assembly, as well as their ability to protect against AβO toxicity and oxidative stress.

2 MATERIALS AND METHODS

2.1 Materials

Amyloid beta (Aβ) peptide (1–40) was purchased from EZBiolab Inc., Carmel, IN, United States. $A\beta^{TOAC26}$ was synthesized by Prof. Lorigan and co-workers at Miami University (Petrlova et al., 2012). Hoechst Blue 3342 nuclear stain and oligomer A11 polyclonal antibody were purchased from Thermo Fisher, Waltham, MA, United States. CellROX (Deep Red; λex/λem 640/665 nm) was purchased from Life Technologies, Carlsbad, CA, United States. Opti-Minimal Essential Medium (OPTIMEM) was purchased from Invitrogen/Life Technologies, United States. PBS pH 7.4 (-Calcium Chloride, -Magnesium Chloride), Opti-MEM® I Reduced Serum Medium (no phenol red), DMEM (Dulbecco's modified Eagle's medium +4.5 g/L Glucose, L-Glutamine and 110 mg/L Sodium Pyruvate) and Fetal Bovine Serum (FBS) were purchased from Gibco (Carlsbad, CA, United States). 35 mm Glass Bottom Dishes (No. 1.5) purchased from MatTek. Trypan Blue Solution (0.4%) was purchased from Sigma-Aldrich. Resveratrol 3,4′-diacetate, 3-hydroxymethyl-(1-oxy-2,2,5,5 -tetramethylpyrroline, 3-(2′-Iodoacetamido)-2,2,5,5-tetramethyl-1-pyrrolidinyl-1-oxyl, (1-oxyl-2,2,5,5,-tetramethyl-Δ3-pyrroline)formaldehyde, 2,2,5,5-tetramethyl-3-pyrrolin-1-oxyl-3-carboxylic acid, free radical, were purchased from Toronto Research Chemicals, Toronto, Canada. Acetonitrile was purchased from Thermo Fisher Scientific (Houston, TX, United States). All other chemical reagents and solvents were purchased from Aldrich (Milwaukee, WI, United States).

2.2 Synthesis of Spin-Labeled Paramagnetic Amyloid Ligands

2.2.1 Synthesis of PMT-301

The synthetic scheme of PMT-301 is shown in **Supplementary Figure S1**. In brief, resveratrol 3,4′-diacetate (8.3 mg, 0.0266 mmol), 3-hydroxymethyl-(1-oxy-2,2,5,5 -tetramethylpyrroline) (5 mg, 0.0294 mmol), triphenylphosphine (PPh_3, 8.0 mg, 0.0305 mmol), and anhydrous tetrahydrofuran (THF, 0.2 ml) were combined into a 1.5 ml microcentrifuge tube. The reaction tube was then lowered into a 42-kHz sonication bath (Cole-Parmer) and sonicated for 2 min. While sonicating, diisopropyl azodicarboxylate (DIAD, 6.6 µl, 0.0335 mmol) was added to the reaction mixture. The reaction mixture was sonicated for 25 min. The reaction mixture was then added to a KOH solution (20 µl, 10% aqueous solution) and stirred for 30 min at room temperature. The solution was neutralized with 0.05% trifluroacetic acid (TFA) in acetonitrile and then submitted for purification with preparative reversed-phase high performance liquid chromatography (HPLC) using a C18 column (Vydac, 10 µm, 2.2 cm i.d. × 25 cm) and gradient of 25%–100% B over 34 min at a flow rate of 5 ml/min (solvent A, H_2O/0.05% TFA; B, acetonitrile/0.05% TFA). The eluant was collected and lyophilized to give powder PMT-301. The chemical identity was confirmed with Orbitrap ESI-MS, with a calculated mass for $C_{23}H_{26}NO_4$ of 380.19, and observed mass of 381.20 [M+1] and 382.20 [M+2].

2.2.2 Synthesis of PMT-302

The synthetic scheme of PMT-302 is shown in **Supplementary Figure S2**. Cs_2CO_3 (20 mg, 0.0624 mmol) was added to a solution of resveratrol 3,4′-diacetate (13 mg, 0.0416 mmol) in anhydrous dimethylformamide (DMF, 1 ml) and the reaction mixture was stirred at room temperature for 45 min, 3-(2′-Iodoacetamido)-2,2,5,5-tetramethyl-1-pyrrolidinyl-1-oxyl (13.5 mg, 0.0415 mmol) was then added to the solution and the resulting mixture was stirred at room temperature overnight. The reaction mixture was added to KOH solution (20 µl, 10% aqueous solution) and then stirred for 30 min at room temperature. The solution was neutralized with acetic acid and then purified by HPLC using the above-mentioned conditions. The eluent was lyophilized to give powder PMT-302. The chemical identity was confirmed with Orbitrap ESI-MS, with a calculated mass for $C_{24}H_{29}N_2O_5$ of 425.21, and observed mass of 426.22 [M+1] and 427.22 [M+2].

2.2.3 Synthesis of PMT-303

The synthetic scheme of PMT-303 is shown in **Supplementary Figure S3**. 2,2,5,5-Tetramethyl-3-pyrrolin-1-oxyl-3-carboxylic acid anhydride free radical was first prepared by adding *N,N′*-dicyclohexylcarbodiimide (DCC, 56 mg, 0.271 mmol) to a solution of 2,2,5,5- tetramethyl-3-pyrrolin-1-oxyl-3-carboxylic acid, free radical (100 mg, 0.542 mmol) in anhydrous dichloromethane (3 ml). The mixture was stirred at room temperature for 1 h. The precipitate was filtered out and the clear solution was concentrated and dried over vacuum to give the SL-anhydride. To a solution of resveratrol (25.3 mg, 0.11 mmol) in 1 ml anhydrous dimethyl sulfoxide (DMSO) in a round-bottomed flask, sodium hydride (11 mg, 60% dispersion in mineral oil) was added. The resulting mixture was stirred at room temperature for 20 min, followed by the addition of SL-anhydride (38.5 mg, 0.11 mmol). The reaction solution was stirred at room temperature for 2 h. The reaction was quenched with water (100 µl), then 5 ml of cold water (with 0.1% acetic acid) was added to the solution. The solid was separated by centrifuge, redissolved in 80% acetonitrile in water (with 0.05% TFA) and purified by HPLC as described above. The chemical identity was confirmed with Orbitrap ESI-MS, with a calculated mass for $C_{23}H_{24}NO_5$ of 394.16, and observed mass of 395.18 [M+1] and 396.18 [M+2].

2.2.4 Synthesis of PMT-401

The synthetic scheme of PMT-401 is shown in **Supplementary Figure S4**. Stannous chloride (4.74 g, 25 mmol) was added to a solution of (*E*)-4-(4-nitrostyryl) phenol (1.2 g, 5 mmol) in ethanol (40 ml) followed by the addition of concentrated hydrochloric acid (2.0 ml). The solution was refluxed for 3 h and then cooled down to room temperature stirring overnight. Dark brown precipitate was collected by filtration and washed with small amount of ethanol to give (*E*)-4-(4-aminostyryl) phenol as HCl salt, light brown powder,

850 mg, yield 68.4%. Orbitrap ESI-MS for $C_{14}H_{13}NO$ 211.10, Found 212.10 [M+1]. To a mixture of (*E*)-4-(4-aminostyryl) phenol HCl salt (495.4 mg, 2.0 mmol), paraformaldehyde (600 mg, 20 mmol) and sodium cyanoborohydride (378 mg, 6.0 mmol), acetic acid (20 ml) was added. The resulting mixture was heated until the solution became clear and stirred at room temperature overnight. 200 ml of water was added to the reaction solution. Sodium carbonate was added to adjust the pH to 8–9. After extraction with dichloromethane (3 ml × 40 ml), the combined dichloromethane layer was washed with water and brine, and dried over anhydrous Na_2SO_4. The liquid was collected by filtration and concentrated *via* rotovap to give (*E*)-4-(4-(dimethylamino) styryl)phenol as a light grey solid, 144 mg, yield 30%. Orbitrap ESI-MS for $C_{16}H_{17}NO$ 239.13, Found 240.14 [M+1]. To an 1.5 ml eppendorf tube was added (*E*)-4-(4-(dimethylamino) styryl)phenol (7.7 mg, 0.032 mmol), 3-hydroxymethyl-(1-oxy-2,2,5,5 -tetramethylpyrroline) (6.0 mg, 0.0352 mmol), triphenylphosphine (PPh_3, 9.7 mg, 0.0368 mmol), and anhydrous tetrahydrofuran (THF, 0.3 ml). The reaction tube was then lowered into a 42-kHz sonication bath (Cole-Parmer) and sonicated for 2 min. While sonicating, diisopropyl azodicarboxylate (DIAD, 7.9 μl, 0.04 mmol) was added to the reaction mixture. The reaction mixture was sonicated for 15 min, repeated three times, total 45 min. The reaction mixture was diluted with 2 ml of 50% acetonitrile/water (0.05% TFA) and then submitted for HPLC purification as described above. The eluent was collected and lyophilized to yield PMT-401 as dark brown powder. Orbitrap ESI-MS for $C_{25}H_{31}N_2O_2$ 391.24, found 392.25 [M+1].

2.2.5 Synthesis of PMT-402

The synthetic scheme of PMT-402 is shown in **Supplementary Figure S5**. PMT-402 was synthesized from (*E*)-4-(4-aminostyryl) phenol. Its HCl salt (200 mg) was suspended in ethanol (25 ml) and then K_2CO_3 aqueous solution was added until pH 9. Water (25 ml) was added to the suspension and mixed. After centrifuge, the solid was collected by filtration and washed with water, 70% ethanol in water and dried over vacuum to give (*E*)-4-(4-aminostyryl)phenol as brownish solid. A suspension of (*E*)-4-(4-aminostyryl)phenol (7.6 mg, 0.0357 mmol), (1-oxyl-2,2,5,5,-tetramethyl-Δ3-pyrroline)f ormaldehyde (6 mg, 0.0357 mmol) and p-toluenesulfonic acid (1 mg, 0.0058 mmol) in mixture of ethanol (1.5 ml) and anhydrous THF (0.8 ml) was sonicated for 5 min until the solution became clear and stirred at room temperature for additional 15 min. After the resulting solution was cooled down with ice-water bath, $NaBH_4$ (27 mg, 0.714 mmol) was added. After the mixture was stirred at room temperature overnight, water (20 ml) was added, followed by addition of acetic acid to adjust the pH to 6. The precipitate was collected after centrifuge and redissolved in 80% acetonitrile in water (with 0.05% TFA) for HPLC purification as described above. The eluent was collected and lyophilized to yield PMT-402 as brownish powder. The chemical identity was confirmed with Orbitrap ESI-MS. Calcd. for $C_{23}H_{27}N_2O_2$: 363.21, found: 364.22 [M+1], 365.22 [M+2].

For experimental use, PALs were used from stock solutions (1 mM or 4 mM) of the agent in DMSO.

2.3 Preparation of Aqueous Amyloid Beta

Aqueous Aβ for A11-positive oligomer generation was prepared using modifications to the protocol reported by Chunhui et al. (2018). Aβ powder was dissolved to a concentration of 2.5 mg/ml in hexa-fluoro-isopropanol (HFIP), rotated overnight and stored in 0.4 ml aliquots at −80°C. An aqueous solution was then made by combining the HFIP stock to a 2 ml microfuge tube and then, while stirring, adding 1 ml of 0.1 M $NaHCO_3$, pH 9.6. HFIP was then removed by with nitrogen gas flow over the stirred solution until the volume reaches ~0.9 ml. The sample volume was QS to 1.0 ml with 0.1 M $NaHCO_3$, pH 9.6. The sample was then centrifuged at 15,000 rpm in a microfuge for 10 min to remove large amorphous aggregates as described previously (Altman et al., 2015). The supernatant was collected and the removal of large aggregates verified by circular dichroism as the broadening of the negative 200 nm band (Fezoui and Teplow, 2002; Hopping et al., 2014). The final concentration of Aβ after removal of large amorphous aggregates was ~0.9 mg/ml (estimated from absorbance at 280 nm).

For EPR measurements, $Aβ_{(1–40)}$ containing the TOAC spin label at position 26 ($Aβ^{26TOAC}$) was dissolved in HFIP at 2.5 mg/ml and combined with the native peptide (2.5 mg/ml in HFIP) at a 4:1 ratio (native:TOAC-labeled). An aqueous solution of the mixture was then obtained as described above.

Samples of oligomeric Aβ (AβO) were then made by combining the 0.9 mg/ml sample of Aβ (in 0.1 M $NaHCO_3$) at a 1:1 ratio with 100 mM Tris Borate (pH 7.4). After 60 min of incubation, samples were diluted to their experimental concentration with 50 mM Tris-Borate (pH 7.4) and used within 3 hours.

Aβ protofibrils were made by combining the 0.9 mg/ml sample of Aβ (in 0.1 M $NaHCO_3$) at a 1:1 ratio with 100 mM Tris Borate (pH 7.0), 300 mM NaF and stirring the sample for 24-h with a 4 mm magnetic stir bar. Samples were then diluted to their experimental concentration with 50 mM Tris Borate (pH 7.0), 150 mM NaF. Beta-sheet content of protofibrils was verified by circular dichroism.

2.4 Cell Culture Model Over-Expressing Intracellular Amyloid Beta

MC65 cells are a neuronal cell line showing intracellular accumulation of Aβ (Jin et al., 2004; Maezawa et al., 2006; Hong et al., 2007; Maezawa et al., 2008). The MC65 cells are derived from a human neuroblastoma line with conditional expression of the carboxyl-terminal 99 residues of the amyloid-β precursor protein (APP-C99) under the negative regulation of the suppressor tetracycline (TC) in the culture medium. Expression of APPC99 is induced by removing TC from cell culture medium. Proteolysis of APP-C99 by the cellular γ and β secretases generates Aβ. Intracellular Aβ is known to start to accumulate as early as 4 h after TC removal with maximal

levels at 24 h. Cell death in 3 days after removal of TC was shown to be due to the intracellular accumulation of AβO rather than to the small amounts of secreted Aβ (Maezawa et al., 2006).

The cytotoxicity was determined using MTT assay in the presence of TC, the results of which were comparable with data obtained using counts of viable cells based on trypan blue exclusion and the live/dead assay. Cells were treated with either DMSO or the indicated concentration of PAL at the same time as TC removal, with a uniform level of DMSO (0.05%) in all assay cultures. Data are expressed as mean percentage viability of 3×10^4 cells/well counted from $n = 3$ cultures, with parallel +TC cultures of equal numbers of cells set at 100% viability.

2.5 Detection of Intracellular Oxidative Stress Signal by Confocal Microscopy

Treated and control MC65 cell cultures were gently washed with untreated culture medium and incubated for 30 min with the ROS detection reagent CellROX, a fluorogenic probe that when oxidized develops a red fluorescent signal seen around the nuclei of cells experiencing oxidative stress. At 20 min, the cells were treated for the remaining 10 min with Hoechst Blue 3342 nuclear stain, gently washed for 15 min ×3 with untreated culture medium and imaged immediately. The images of CellROX staining were collected on an Olympus Fluoview 3000 confocal laser scanning microscope. Each individual field was imaged using an 40× objective. Single plane confocal scans of the cultured neuronal cell areas were taken *via* sequential scanning mode using diode excitation lasers of 653 nm for CellROX Deep Red ($\lambda_{ex}/\lambda_{em}$ = 640/665 nm).

Intensity comparison of CellROX emission was calculated by transforming images to 8-bit gray scale and fluorescence intensity was analyzed with Image J, FIJI for MAC OS X, using the particle analysis function (Schneider et al., 2012). Triplicate measurements of the mean fluorescence intensity were done in three randomly selected areas of each of the cell culture fields, with background correction. Statistical significance between groups was determined by ordinary one-way ANOVA test using GraphPad Prism version 7.0c for MAC OS X (GraphPad Software, La Jolla California United States), where the p value from the ANOVA is reported as a result of the Brown-Forsythe test and considered significant if $p < 0.05$ for each treatment group. All data was expressed as the mean ±SEM.

2.6 A11 ELISA Assay

For ELISA measurements, peptide was passively bound to a 96-well Greiner FLUOTRAC™ 600 high binding microplate by adding 60 µl of 0.2 mg/ml aqueous Aβ solution per plate well, followed by 200 µl of freshly made 0.1 M $NaHCO_3$, pH 9.6. Each assay was performed using quadruplicate wells for each sample treatment. The plates were then incubated overnight at 4°C. Wells were then treated with 300 µl blocking solution [50 mM Tris buffer (pH 7.4) containing 100 g/L dried milk] for 1-h, then washed twice with the same solution. Each well was then incubated with 300 µl of 40 µM PAL (or vehicle control) in wash buffer [50 mM Tris buffer (pH 7.4) containing 50 g/L dried milk] for 1-h, and then washed 3X with wash buffer. Wells were then treated with 300 µl of primary antibody in the presence of the PAL or vehicle control (A11 antibody diluted 1:1,200 in wash buffer containing 40 µM PAL) and incubated for 2-h. Wells were then washed 3× with wash buffer and incubated with HRP-conjugated secondary antibody (GAR antibody diluted 1:1,200 in wash buffer). Wells were then washed ×3 with wash buffer and the HRP activity quantified by luminescence by adding 150 µl of each SuperSignal (Thermo) chemiluminescent HRP substrate reagent to each well.

2.7 Electron Paramagnetic Resonance Spectroscopy

EPR measurements were carried out in a JEOL TE-100 X-band spectrometer fitted with a loop-gap resonator as described previously (Shea et al., 2019) (JEOL United States, Peabody, MA). PALs (or vehicle control) were added to the spin-labeled AβO (80 µM) at a final concentration of 40 µM 30 min prior to EPR measurements, carried out on ~5 µl of sample loaded into a sealed quartz capillary tube. The spectra were obtained by averaging two 2-min scans with a sweep width of 100 G at a microwave power of 4 mW and modulation amplitude optimized to the natural line width of the attached spin probe. All the spectra were recorded at room temperature.

2.8 Circular Dichroism Measurements

For Circular dichroism spectroscopy (CD) measurements, aqueous AβO was diluted with 50 mM Tris-Borate, pH 7.4 to a concentration of ~0.15 mg/ml with measurements made within 2-h. Aβ protofibrils was diluted with 50 mM Tris-Borate, 150 mM NaF, pH 7.0 to a concentration of ~0.15 mg/ml. PALs were added from a 4 mM stock in acetonitrile to a final concentration of 40 µM. CD measurements were performed on a Jasco J-715 spectropolarimeter equipped with a Peltier temperature control (Quantum Northwest) set to 25°C. For spectral acquisition, samples were placed in a 1 mm quartz cuvette and CD spectra were collected by signal averaging three scans in the region 190–260 nm using a scan speed of 20 nm/min, bandwidth of 1 nm and response time of 4 s. Prior to analysis, all spectra were baseline-subtracted from the appropriate background buffer containing either the PAL alone or the solvent vehicle (the background signals were generally indistinguishable). The percent of secondary structure was estimated by deconvolution using the BeStSel CD analysis program (Micsonai et al., 2015), which can be accessed online at http://bestsel.elte.hu.

2.9 Nanoparticle Tracking Analysis

For Nanoparticle Tracking Analysis (NTA) measurements, aqueous Aβ was diluted 1:1 with 100 mM Tris-Borate, pH 7.4 to a concentration of ~0.1 mg/ML with measurements made within 2-h. NTA was performed using a NanoSight model LM10 (Malvern Panalytical Ltd., United Kingdom), equipped with a violet (405 nm) laser and sCMOS camera. A daily calibration and data consistency confirmation was carried out using analytical standard quality polystyrene beads (Thermo

Fisher Scientific, MA, United States) of sizes 70, 100, and 200 nm, and silica beads (nanoComposix, CA, United States) of sizes 80, 200, and 400 nm before the actual analyte measurements. Consequently, the samples of interest were measured by optimizing the concentration on the typical NanoSight LM10 range (~10^8–10^9 particles per milliliter). Thus, typically dilutions between 1–15 k fold were applied. Filtered ultrapure Milli-Q water (resistivity = 18.2 MW cm^{-1}) was used between each sample to thoroughly flush the NTA lines to confirm that the background was completely free of remnant particles before running a new sample. A 1 ml of sample was loaded into a syringe and fit into an automated syringe pump (Harvard Bioscience, MA, United States) for injection. In order to achieve rigorous and representative sampling, at minimum nine consecutive 30 s videos of each sample in flow conditions with at least 200 particle tracks present per video were recorded at camera level 12. The data was analyzed using NanoSight NTA 3.1 software with the detection threshold set to 5 and screen gain 10 to track the statistically relevant number of particles, simultaneously minimizing the distorting background artifacts.

2.10 Thioflavin T Assay

Three microliters of aqueous Aβ (~0.9 mg/ml in $NaHCO_3$) were added to the wells of a black, Nunc MicroWell, 384-well nonbinding optical bottom microplate (cat # P9241-30EA) containing 50 µl of PBS. Samples were treated with PALs (18 µM) or vehicle control. Prior to each assay, a fresh 1 mM ThT (Sigma Aldrich, product # T3516) was prepared in cold DI water and filtered through a 0.22 µm syringe filter. Assays were initiated with 1 µl of ThT. ThT fluorescence was measured at room temperature, using a TECAN Infinite 200Pro plate reader, through the bottom of the plate, with of 440 nm and emission of 486 nm. The fluorescence intensity of a free ThT solution (20 µM) in PBS was used for background subtraction of the control sample and the background of ThT + PAL was subtracted from samples containing Aβ.

2.11 Nile Red Assay

Three microliters of aqueous Aβ (~0.9 mg/ml in $NaHCO_3$) were added to the wells of a black, Nunc MicroWell, 384-well nonbinding optical bottom microplate (cat # P9241-30EA) containing 50 µl of PBS. Samples were treated with PALs (18 µM) or vehicle control. Prior to each assay, a fresh solution 1 mM Nile Red (Sigma Aldrich, product # 19123) was prepared in DMSO and centrifuged at 10,000 RPM to remove any aggregates. Assays were initiated with 1 µl of Nile Red. Nile Red fluorescence at $t = 5$ h was measured at room temperature, using a TECAN Infinite 200Pro plate reader, through the bottom of the plate, with of 558 nm and emission of 635 nm. The fluorescence intensity of a free Nile Red solution (20 µM) in PBS was used for background subtraction of the control sample and the background of Nile Red + PAL was subtracted from samples containing Aβ.

2.12 Cytokine Measurements

2.12.1 Human TGRL Isolation

The protocol for obtaining human TGRL (Protocol No. 447043) was approved by the Human Subjects Review Committee/IRB at the University of California Davis and informed consents were obtained from all study subjects. Healthy adult human volunteers consumed a moderately high-fat meal containing at least 40% fat, and postprandial (3.5 h) blood was collected by standard venipuncture (Vacutainer K2EDTA tubes; BD, Franklin Lakes, NJ). We recruited five to six human donors/week, pooled the plasma, and isolated TGRLs. The average pooled TGRL concentration was ~700–800 mg/dl. We used 150 mg/dl concentration to treat endothelial cells in our study. For experiments, we pooled TGRL isolated from donors. Through extensive experience, we have found the data were very consistent using this method of collection and pooling of TGRLs (Aung et al., 2013; Aung et al., 2014; Aung et al., 2016). Whole blood samples were then centrifuged at 3,000 rpm for 15 min at 4°C, and the plasma fraction was collected. Sodium azide was added to the plasma as a preservative. TGRL were isolated from human plasma at a density of less than 1.0063 g/ml following an 18 h centrifugation at 40,000 rpm in a SW41 Ti swinging bucket rotor (Beckman Coulter, Sunnyvale, CA, United States) held at 14°C within a Beckman L8-70M (Beckman) ultracentrifuge. The top fraction TGRL was collected and dialyzed in Spectrapor membrane tubing (MWCO 3,500; Spectrum Medical Industries, Los Angeles, CA, United States) at 4°C overnight against a saline solution containing 0.01% EDTA. Total triglyceride content of samples was determined using the serum triglyceride determination kit (Sigma Aldrich cat # TR0100). The kit converts triglycerides to free fatty acids and glycerol. Glycerol is assayed enzymatically.

2.12.2 Cell Culture and Lipid Treatments

Human brain microvascular endothelial cells (HBMECs) were obtained from Angio-Proteome (Boston, MA, United States) and cultured in EGM™-2MV BulletKit™ containing 5% serum (CC-3202, Lonza, Walkersville MD) in a 37°C incubator with a humidified 5% CO_2 and 95% air environment. Medium was changed every other day until 90% confluency and cells were used at passage 6. One hour prior to experiments, cell culture medium was changed to fresh medium. Cells were exposed for 3 h to the following conditions: control of media containing DMSO at a final concentration of 0.01% (control) and TGRL hydrolyzed with lipoprotein lipase (L2254, Sigma, St. Louis, MO, United States) [referred to as TGRL lipolysis product, TGRL (150 mg/dl = 1.5 mg/ml) + lipoprotein lipase (LpL; 2 U/mL)]. The final concentration of TGRL lipolysis products were diluted in media and pre-incubated for 30 min at 37°C prior to application. After the incubation with media or TGRL lipolysis products, cells were washed with cold PBS and harvested by scraping them in ice cold PBS.

To test the suppression of compounds on TGRL lipolysis products-induced gene expression, cells were pre-incubated with each individual compound of interest indicated for 30 min and followed by co-incubated with TGRL lipolysis for 3 h. These compounds are Tempo, Mito-Tempo, PMT-301, PMT-302, PMT-303, PMT-401, and PMT-402. The final concentration of each compound is 1 µM. After the incubation, the cells were washed with cold PBS and mRNA expression of ATF3, E-selectin, IL-8, IL-6, and COX-2 were analyzed.

2.12.3 mRNA Expression by Quantitative RT-PCR

Total RNA was extracted from cells in each of treatment group [control or TGRL lipolysis products (TL) or TL + individual compound of PAL] in 6-well plate (3 well per sample, n = 3/group) using RNeasy Mini Kit (Qiagen, Valencia, CA, United States) including the DNA digestion step as described by the manufacturer. Sample quality was assessed using Nanodrop ND-1000 Spectrophotometer (Thermo Fisher Scientific, Wilmington, DE, United States). An aliquot equivalent to 5 µg of total RNA extracted from each sample was reverse-transcribed to obtain cDNA in a final volume of 21 µl consisting of buffer, random hexamers, DTT, dNTPs, and SuperScript® III First-Strand Synthesis System (Invitrogen). qRT-PCR with SYBR as fluorescent reporter was used to quantify the gene expression. Specific human primers were designed with Primer Express 1.0 software (Applied Biosystems) using the gene sequences (**Supplementary Table S1**) obtained from previously published Affymetrix Probeset IDs (Aung et al., 2014). Reactions were carried out in 384-well optical plates containing 25 ng RNA in each well. The quantity of applied RNA was normalized by simultaneously amplifying cDNA samples with glyceraldehyde-3-phosphate dehydrogenase (GAPDH)-specific primers. The transcript levels were measured by real-time RT-PCR using the ABI ViiA™7 Real-Time PCR system (PE Applied Biosystems, Foster City, CA, United States). The PCR amplification parameters were: initial denaturation step at 95°C for 10 min followed by 40 cycles, each at 95°C for 15 s (melting) and 60°C for 1 min (annealing and extension). A comparative threshold cycle (Ct) method was used to calculate relative changes in gene transcription determined from real-time quantitative PCR experiments [Applied Biosystems user bulletin no. 2 (P/N4303859)] (Livak and Schmittgen, 2001). The threshold cycle, Ct, which correlates inversely with the target mRNA levels, was measured as the cycle number at which the SYBR Green emission increases above a preset threshold level. The specific mRNA transcripts were expressed as fold difference in the transcription of the specific mRNAs in RNA samples from the TL or TL + individual compound of PAL (Tempo or Mito-Tempo or PMT-401or PMT-402 or PMT-101 or PMT-301 or PMT-302 or PMT-303)-treated cells compared with those from the control-treated cells.

3.12.4 Statistical Analysis

Data for changes in gene expression obtained by qRT-PCR were analyzed by GraphPad PRISM software (San Diego, CA). An unpaired student's t test was used for comparisons between treatments. Differences with $p \leq 0.05$ were considered significant. Results are expressed as MEAN ± SEM.

3 RESULTS

3.1 Differential Potency of Stilbene Paramagnetic Amyloid Ligands

The structures of the stilbene-based PALs are shown in **Figure 1**. Importantly, these results demonstrate the utility of the MC65 model in measuring intracellular AD pathology such as oxidative stress (Hilt et al., 2018), Ca^{2+}-dysregulation (Copenhaver et al., 2011), activation of inflammatory pathways (Currais et al., 2016) as well as autophagy and pTau formation (Mputhia et al., 2019). In the MC65 model, expression of the progenitor of the Aβ peptide (C99) is repressed in the presence of tetracycline (+TC). Upon removal of tetracycline (−TC), induction of C99/AβO decreases the cell viability by ~90%. The ability of the stilbene PALs to protect against Aβ-induced cytotoxicity was assessed using the MC65 neuronal culture model, where the inducible expression of the C99 fragment of APP results in cell death within 72 h (Petrlova et al., 2012; Currais et al., 2016). Each of the stilbene PALs provides protection against cell death in the MC65 assay (**Figure 2**). However, the potency of the PAL candidates varies, with PMT-402 more than 50-times more potent than PMT-302. PMT-401 was the only PAL that could not restore viability to 100%. The poor performance of PMT-401 at higher concentrations is likely related to its poor solubility.

3.2 Stilbene Paramagnetic Amyloid Ligands Reduce Binding of the Conformation-Specific Antibody A11

The identification by Glabe and co-workers (Kayed et al., 2003) of an antibody that recognizes the pathogenic state of disparate proteins involved in neurodegeneration provides a tool for probing modulation of the AβO away from its "toxic" conformation (Necula et al., 2007). To evaluate the effect of the stilbene PAL agents on A11 recognition, we measured A11 binding to immobilized AβO with and without PAL treatment. As shown in **Figure 3**, treating immobilized AβO with a stoichiometric amount of the PAL agent reduces the average A11 capture by ~50%. PMT-402 appears most effective in reducing the amount of A11 recognition in this assay.

3.3 Paramagnetic Amyloid Ligands Combat Aβ-dependent Oxidative Stress

We have previously demonstrated the highly potent antioxidant capacity of the nitroxyl-based PALs (Hilt et al., 2018). To confirm this property in the stilbene PALs, the CellROX dye in MC65 cells was imaged for levels of reactive oxygen (ROS) species. **Figure 4** illustrates the antioxidant activity of the PMT-301 PAL. Shown are confocal microscopy images of the ROS-sensitive CellROX dye (red) in live MC65 neurons. Oxidative stress is absent when expression of the progenitor of the Aβ peptide (C99) is repressed (+TC, top row). Induction of C99/Aβ production (−TC) generates high ROS levels (middle row). In contrast, as shown in the bottom row, ROS levels in −TC cells are highly (~60%) attenuated by PMT-301 treatment (see **Supplementary Figure S6**).

Oxidative-stress and inflammation are closely connected in neurodegenerative disorders (Bonda et al., 2010; Liu et al., 2017), so the PAL antioxidant activity is expected to also attenuate markers of inflammation. In order to access whether the PALs elicit anti-inflammatory activity independent of the AβO-driven oxidative stress, we also looked at whether any of the stilbene PALs carry anti-inflammatory activity in the human brain endothelial cell (HBMEC) model (Aung et al., 2014). In this model, TGRL

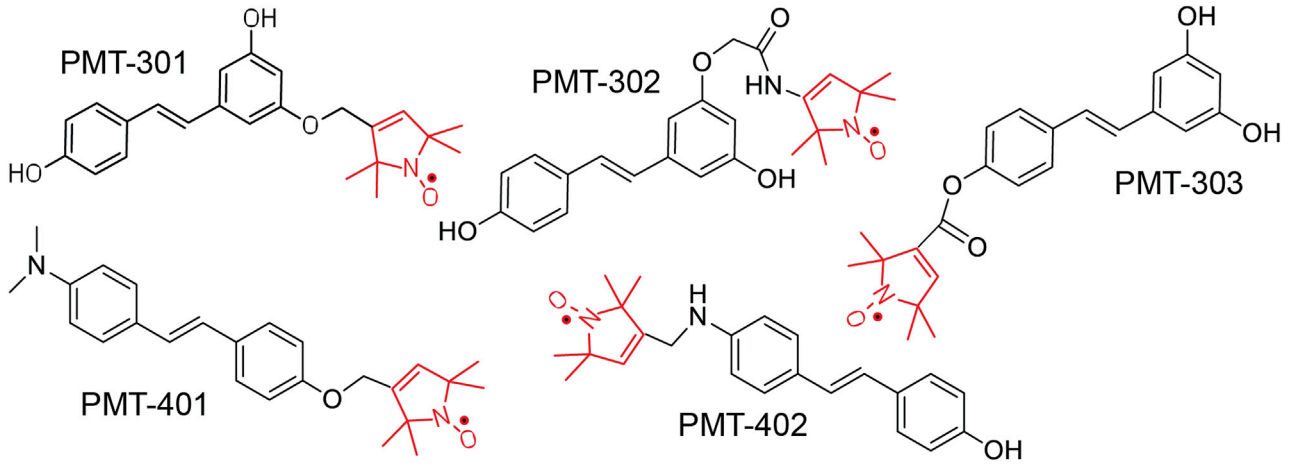

FIGURE 1 | Structure of Paramagnetic Amyloid Ligand (PAL) candidates. The stilbene core binds to oligomeric Aβ, inhibiting oligomer growth and toxicity. The spin label moiety (red) contains the nitroxide that functions as a catalytic antioxidant.

lipolysis products (TL) are used to upregulate stress-responsive transcription factor ATF3, COX-2, and proinflammatory genes (IL-6, IL-8 and E-selectin) using microarray data analysis (Aung et al., 2014) and RNA Seq analysis (Nyunt et al., 2019). TL substantially increases stress-responsive transcription factor ATF3, COX-2, and proinflammatory genes (IL-6, IL-8 and E-selectin). We previously showed that TL causes lipotoxic injury to HBMECs and this lipotoxicity occurs through stimulation of mitochondrial metabolism resulting in overproduction of superoxide radical ($O_2\bullet^-$) (Aung et al., 2016). Moreover, TL increased mitochondrial $O_2\bullet^-$ generation, ATF3-mediated inflammatory, and apoptotic responses in *in vitro* HBMECs culture (Nyunt et al., 2019). Here we analyzed the biological activity of the stilbene PALs plus two common nitroxide agents (Tempo and Mito-Tempo) on TL-induced gene expression. As a group, only PMT-401 provides broad anti-inflammatory activity as measured by gene expression. As shown in **Supplementary Figure S7**, PMT-401 significantly suppressed TL-induced ATF3, E-selectin, IL-6, IL8, and COX-2 gene expression. Additionally, COX-2 expression was suppressed by PMT-302 and PMT-303 ($p = 0.07$). Because PMT-401 is distinguished in part by its greater hydrophobicity (CLogP of 4.5, vs. CLogP values of 2.9–4.0 for the other PAL compounds), the effectiveness of nitroxide antioxidants to attenuate inflammation in the TL-activated HMMEC model may rely on the compound's ability to partition into a lipophilic environment. Consistent with this notion is the lack of anti-inflammatory activity found with Tempo and Mito-Tempo treatment, and in fact increased TL-induced ATF3, E-selectin, IL-6, IL8 and COX-2 gene expression. Thus, the simple addition of a hydrophilic nitroxide is insufficient to attenuate inflammation in this model.

3.4 Target Engagement and Conformational Adaptation

In order to investigate how the stilbene PALs affect AβO conformation, CD spectroscopy was carried out to probe for secondary structure changes in the PAL-treated peptide. The untreated early AβO generates a low amplitude CD spectrum indicative of its unstructured state (Shea et al., 2019; Clements et al., 1996) (**Figure 5**, black trace). After 24 h, the AβO sample undergoes a substantial increase in the pleated beta-sheet content as it converts into soluble protofibrils (Walsh et al., 1999; Kayed et al., 2009) (**Figure 5**, inset). While each of the stilbene PALs induce significant changes to the CD spectrum of AβO, the stilbene PALs do not order the early AβO into an α-helical or β-strand state. This finding is consistent with previous CD measurements of stilbene effects on AβO (Ladiwala et al., 2010; Feng et al., 2009). Nevertheless, each of the five PALs drive a significant change in the AβO CD spectrum, with PMT-301, PMT-302, PMT-303 and PMT-402 generating strong negative bands at 198 nm, characteristic of PP-II structure (Adzhubei et al., 2013). This response is similar to a fluorene-based PAL (Altman et al., 2015). In contrast, PMT-401 does not induce the PPII-like spectral change. Results from the fitting of the CD spectra by the BeStSel algorithm (Micsonai et al., 2015) to estimate fractions of secondary structure are given in **Table 1**. In each of the early AβO samples, the low structure folds (random coil/loop, 3_{10}- and π-helices, PP-II helix) constitute the major population before and after PAL treatment. Of the compounds that produce a PPII-like spectrum, only a marginal increase in α-helical structure is seen, accompanied by a slight decrease in the β-strand population. The effect of PMT-401 on AβO is distinguished by helical content and decreased beta content compared to the other PALs. Interestingly, PMT-401 (which displays the lowest potency in cell protection) generates a very unique CD spectrum for AβO in an aqueous solution, although a similar 204 nm minima has been reported following treatment of AβO with 10% trifluoroethanol or 50% acetonitrile (Fezoui and Teplow, 2002; Bartolini et al., 2007).

Finally, we also looked to see the effect of PAL addition to protofibrillar oligomers formed after 24-h incubation (**Figure 5**, inset). These species have much lower toxicity and lack recognition by the conformational antibody A11 (Kayed et al., 2009; Bieschke et al., 2011). Consistent with

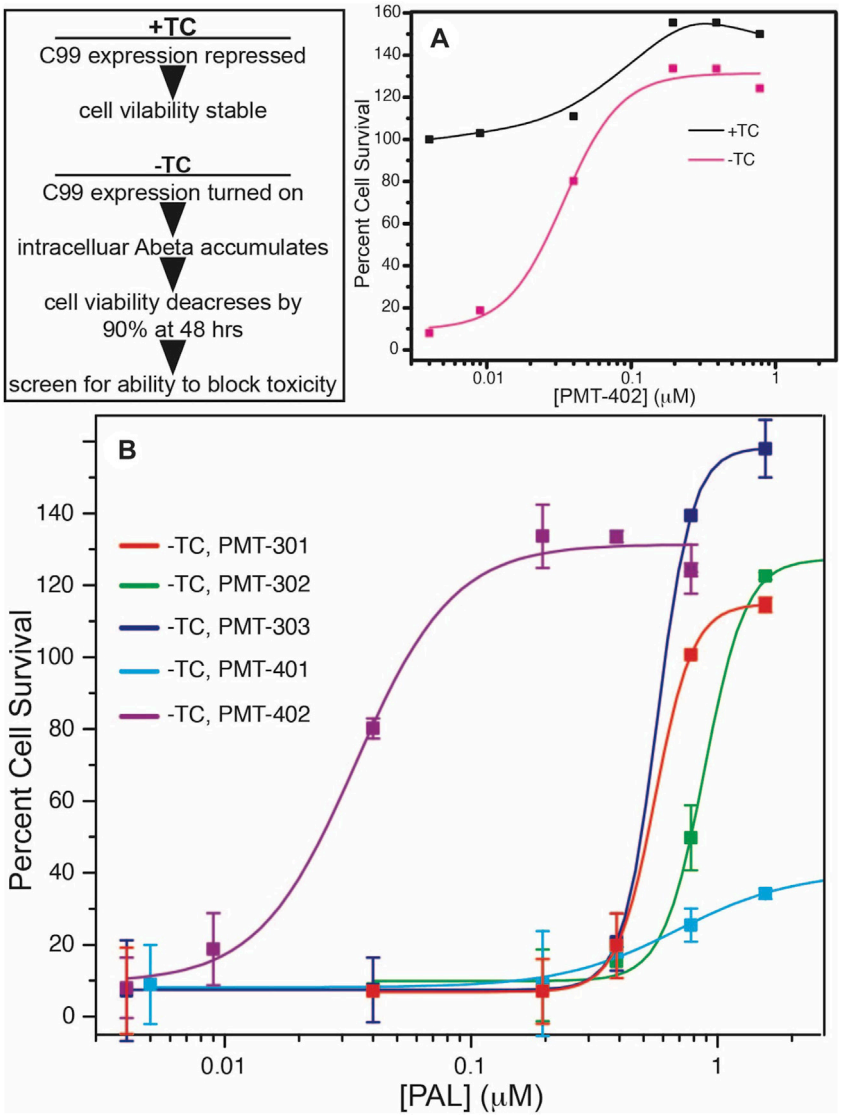

FIGURE 2 | Neuronal protection activity of the stilbene PAL agents in the MC65 model. Removal or tetracycline from the MC65 culture media results in C99 expression and amyloid beta cytotoxicity **(A). (B)** shows rescue of cytotoxicity with PAL titration. Error bars are the SEM from the assay of three separate cultures.

previous findings (Walsh et al., 1999; Bartolini et al., 2007; Corsale et al., 2012; Roychaudhuri et al., 2014), the CD spectrum of the protofibril Aβ sample displays a high percentage of β-strand. In this more ordered species, the CD spectra of each PAL-treated preparation is similar to the untreated control, although each of the PALs enhance the conversion of the disordered components into β-strand by 7%–10% (**Table 1**).

3.5 Alteration of Amyloid Beta Oligomers Dye Binding

We also measured the effect of the stilbene PALs on modulating the interaction of dyes with AβO over time, whose fluorescence is influenced by its association with proteins and their aggregates. The fluorescence of the Nile Red (NR) dye is indicative for its degree of solvation, where its quantum yield increases within more hydrophobic environments (Singh et al., 2013). The NR fluorescence intensity in the presence of AβO with and without PAL treatment is shown in **Figure 6A**. Each of the stilbene PALs, except for PMT-302, increases the solvent exposure of NR. We also looked at the fluorescence intensity of Thioflavin T (ThT), which is greatly amplified upon its intercalation within β-sheet structure. ThT fluorescence therefore provides a fundamental marker for Aβ assembly along the amyloidogenic pathway (Hellstrand et al., 2010). To evaluate the ability of the stilbene PALs to inhibit AβO conversion into a protofibril species, ThT fluorescence in the presence of AβO was measured with and without PAL treatment. **Figure 6B** shows the ThT signal following 24-h of incubation. These results, in combination

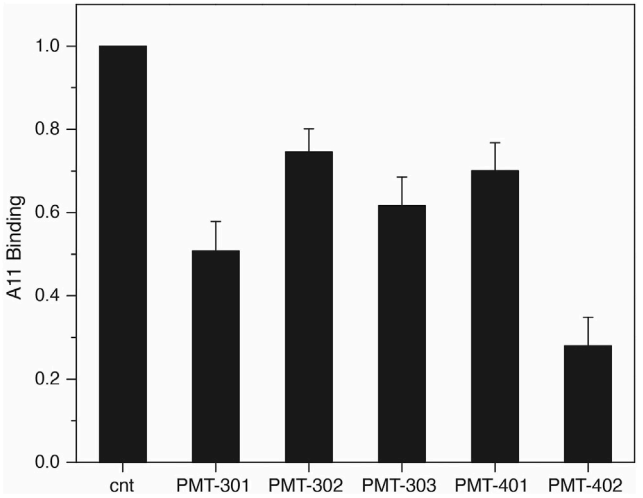

FIGURE 3 | Decrease in A11 antibody recognition of AβO following PAL treatment. the A11 antibody. Shown is the oxidized luminol signal (normalized to the untreated control) as reported by the HRP-secondary antibody. Quadruplicate samples were measured in each assay. Results are the average of three independent assays with error reported as SEM.

with the NR findings, suggest PMT-303 is highly efficient in both AβO conformational adaption and inhibition of β-sheet formation.

3.6 Effect of Paramagnetic Amyloid Ligands on Amyloid Beta Oligomers Structure

Although the CD results do not indicate conversion into a well-defined state of secondary structure, electron paramagnetic resonance (EPR) spectroscopy of AβO's reveals, that with the exception of PMT-401, the stilbene PALs trigger a major reorganization of the peptide's central region. In these experiments, Ser26 of Aβ was substituted with TOAC, an amino acid spin label. The TOAC nitroxide provides a sensitive indicator of both the local within the peptide and its proximity to other spin labels within the assembly (Petrlova et al., 2012; Altman et al., 2015). Thus, although CD spectroscopy reveals a lack of secondary structural order in the AβOs, the central turn region provides a constricted environment at position 26, and represents a common region for peptide-peptide interaction. The level of spin-coupling in the sample was attenuated by preparing AβOs consisting of 75% native Aβ and 25% of the TOAC-substituted Aβ ($AβO^{TOAC}$). The EPR spectra of the PAL-treated $AβO^{TOAC}$ are shown in **Figure 7**. The black trace in panel A shows the broad spectrum of the TOAC label within AβO, reflecting a local region of order and a close proximity to other TOAC labels. This indicates the central hairpin turn region facilitates self-interaction within the oligomer. In contrast, the EPR spectrum of the PMT301 PAL alone displays a narrow line shape owing to the rapid rotational motion of the free small molecule in solution (panel A, inset). Upon addition of PMT301 to $AβO^{TOAC}$, a composite spectrum is obtained (red trace in panel A). The effect of the PAL agent on the isolated $AβO^{TOAC}$ signal can be observed by subtracting the spectrum of free PMT301 from the composite $AβO^{TOAC}$ + PMT301 spectrum to produce the resulting PAL-modified $AβO^{TOAC}$ spectrum (green trace in panel A). Thus, by comparing the black trace to the green trace we are comparing the AβO central region dynamics before and after PMT301 treatment. The altered state of the TOAC can also be confirmed by comparing the experimental composite spectrum (red trace) to the calculated sum of the two samples alone (blue trace in panel A). For example, if the PAL had no effect on AβO dynamics, the red and the blue traces would be identical. Panels B and C show the comparative effects of each PAL on $AβO^{TOAC}$. Here, the untreated $AβO^{TOAC}$ spectrum (black trace) is compared to the sample after the PAL-alone component was subtracted. Thus, comparing each sample to the untreated AβO (black trace) reveals the degree of alteration each PAL has on the oligomer's central region. These results show that PMT301, PMT303 and PMT402 are most effective in increasing the dynamics at position 26 of Aβ. This is a significant finding, as PALs provide the highest potency in protection against AβO toxicity. In contrast the PMT302 treated AβO spectrum (panel B, green trace) looks similar to control AβO (panel B, black trace). Remarkably, the compound with the lowest potency (PMT401), is not only incapable of increasing the local dynamics of the turn region but displays spin-spin interaction with the TOAC label. This is evident from the resulting inverted amplitude line shape following subtraction of the free PMT401 component from the composite AβO (panel C, red trace). This indicates PMT401 binds and maintains AβO in a stable conformation with its nitroxyl moiety close (<1 nm) to the vicinity of TOAC26.

The effect of the stilbene PALs on the protofibril $AβO^{TOAC}$ was also explored (**Figures 7D–F**). Panels D-F show the results of similar measurements on the protofibril AβO (fAβO) sample. A comparison of AβO to fAβO is shown in the inset of panel D. fAβO displays a broader EPR spectrum than AβO (including a discernable strongly immobilized component), reflecting the increased order and spin coupling found in the protofibril sample (Petrlova et al., 2012). The PALs have a similar, though smaller effect on fAβO. Thus, although CD reveals that PALs are unable to reverse the beta structure in the protofibril species, with the exception of PMT401, they do affect the packing geometry about the central region of the peptide.

3.7 Nanoparticle Tracking Analysis Measurements of Amyloid Beta Oligomers Treated With Each Stilbene PAL Candidate

We examined AβO preparations by Nanoparticle Tracking Analysis (NTA). NTA utilizes the properties of both light scattering and Brownian motion in order to obtain the nanoparticle size distribution of samples in liquid suspension. Briefly, 9–18 videos of 30 s duration per each sample were acquired, with a frame rate of 30 frames per second. The NTA software is optimized to first identify and subsequently track each particle on a frame-by-frame basis. The velocity of particle movement is used to calculate particle size by employing the

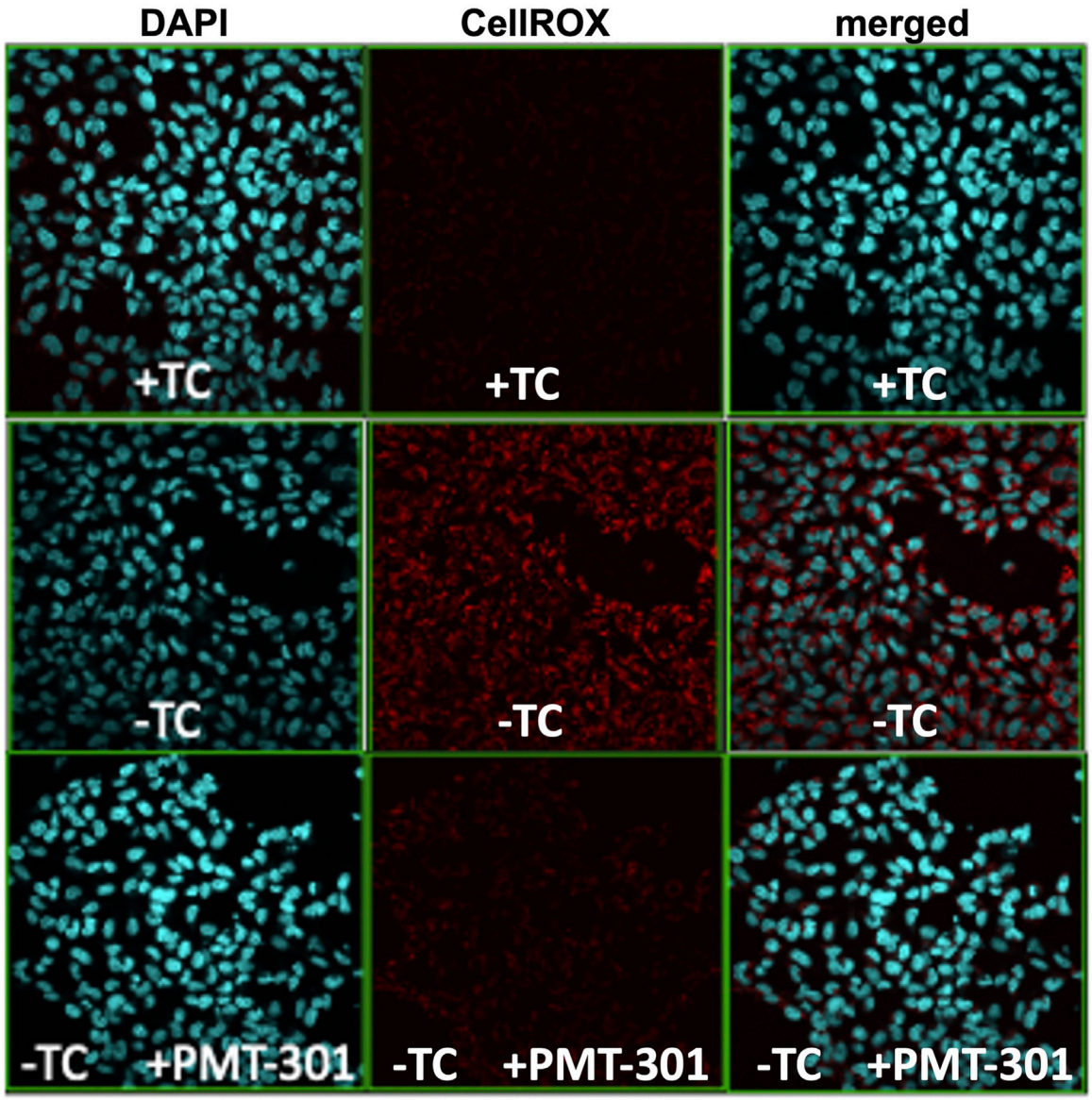

FIGURE 4 | Confocal imaging of the CellRox dye to measure the PAL reduction of oxidative stress. Induction of C99/Ab (–TC) results in ROS production (red punctae in second row, center panel). PMT-301 reduces oxidative stress levels in MC65 cells (third row, center panel) to levels comparative to +TC protected state.

two-dimensional Stokes-Einstein equation. Given the relatively low refractive index of protein/peptide species, the smallest detectable size using the NTA system is roughly in the order of 70 nm. Since volume of the sample chamber is known and the NTA is essentially a single-nanoparticle detection system whereby each detected particle in the field of view over the duration of the recorded videos is calculated, the instrument also yields concentration data as particles per milliliter (part/ml). Thus, the data consists of particle concentration on the ordinate (y, part/ml) as the function of detected particle size on the abscissa (x, nm). The AβO prep is expected to generate a broad range of sizes (Hepler et al., 2006; Corsale et al., 2012), ranging from oligomers of 50–200 kD to much larger amylospheroid and protofibrils, which do not migrate through size exclusion. For these measurements, stoichiometric amounts of PALs were added to preformed AβOs. The NTA results shown in **Figure 8A** indicate that the PAL compounds do not dramatically change the observed particle size, however each PAL generates a distinct distribution. There is a moderate correlation between the width of the major distribution peak to neuronal protection, with a narrower distribution favoring better protection. For example, the full-width at half maximal value (FWHM) of the distributions to potency of neuronal protection, with two of the more potent PALs (PMT-303 and PMT-402) having FWHM values ~45% lower than the other agents (**Table 2**). A major advantage of the NTA measurements is

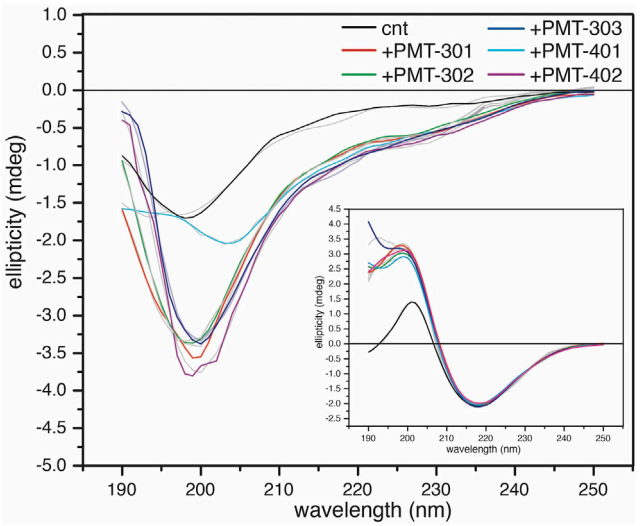

FIGURE 5 | CD spectra of AβOs treated with a stoichiometric amount of PAL agent. CD spectra of 1-h AβO treated with 40 μM PAL. The control (black) was treated with an equal volume of vehicle. The inset shows the high β-sheet structure fibrillar oligomers show little structural response to the PAL agents. BeStSel fits of the spectra are given in light gray lines.

their ability to quantify the particle concentration. As shown in **Table 2**, each of the PALs increases the population (relative to the untreated control) of oligomers into the NTA observable regime. Thus, a depletion of the smaller more toxic oligomers may constitute a part of the PALs' protective mechanism.

The NTA size distribution data is essentially spectral data whereby different peaks point out the predominant particle sizes in the measured solution. However, it is rather tedious to distinguish the prevalent sizes the different AβO + stilbene PAL combinations yield by only visually inspecting the size distribution charts. Therefore, we implemented a principal component analysis (PCA) in order to unveil whether there were certain trends in the observed particle sizes and if these trends potentially correlate with other measurements of PAL-induced structural adaptation. Briefly, PCA is a dimensionality reduction technique for multivariate data sets to simultaneously capture as much variability as possible and conserve the pertinent information responsible for the major sources of variability (Abdi and Williams, 2010). Analysis of the NTA results reveals that 86.5% of the total variance is captured using two principal components (PC1 and PC2). **Figure 8B** displays the 2-dimensional PC score plot that highlights the magnitude of variance and groupings within the NTA size distribution

TABLE 1 | Results from the fitting of the CD spectra by the BeStSel algorithm to estimate fractions of secondary structure in Aβ samples.

Species	AβO						Protofibril Aβ					
	cnt	301	302	303	401	402	Cnt	301	302	303	401	402
α	0	4.5	2.6	2.8	7.2	2.8	1.9	0	0	0	0	0
β	40.9	34.6	38.6	35.2	30.4	35.0	50.3	57.0	57.2	60.6	57.1	57.3
Turn	14.4	15.6	14.7	15.0	15.7	15.4	10.6	9.6	10.3	11.3	10.7	10.7
Other	44.7	45.3	44.2	47.0	47.1	46.7	37.2	33.4	32.5	28.1	32.1	32.1

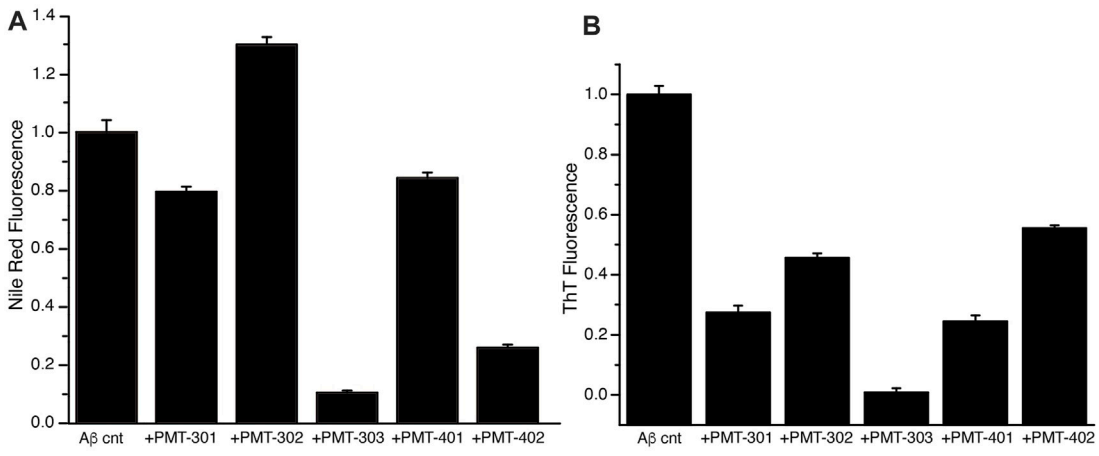

FIGURE 6 | PAL effect on AβO-associated dyes. **(A)** Nile Red fluorescence intensity with or without designated PAL addition after 5-h incubation. **(B)** ThT fluorescence intensity at t = 24 h was measured for Aβ alone or Aβ + PAL compounds. All samples were run in triplicates.

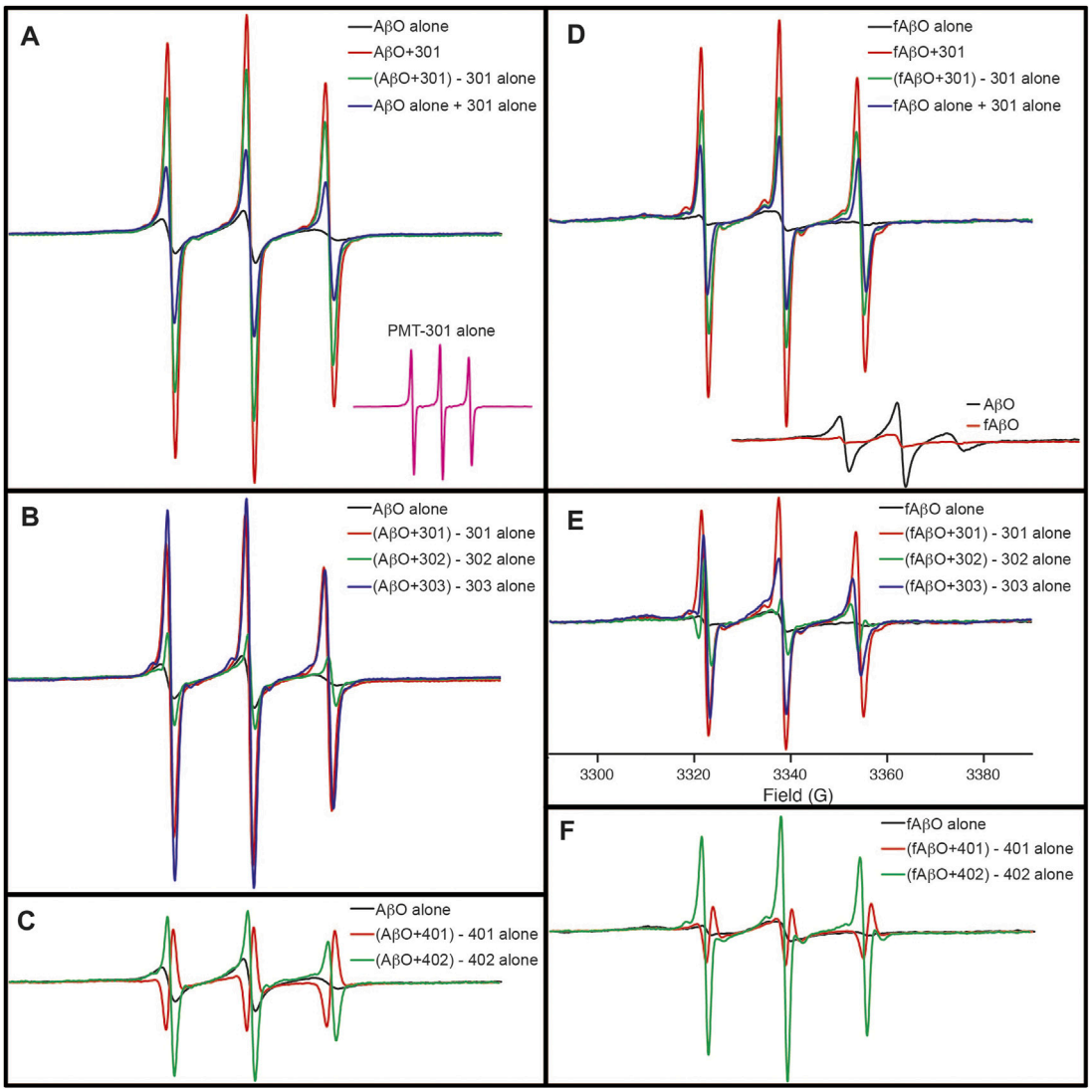

FIGURE 7 | EPR spectra showing the how PALs alter the order within AβO. Shown are X-band EPR spectra of $AβO^{TOAC}$ with and without PAL treatment. The black trace in panel **(A)** shows the broad spectrum of the TOAC label within AβO, reflecting a local region of order and a close proximity to other TOAC labels. In contrast, the EPR spectrum of the PMT301 PAL alone displays a narrow line shape owing to the rapid rotational motion of the free small molecule in solution [**(A)**, inset]. Upon addition of PMT301 to AβO, a composite spectrum is obtained [red trace in **(A)**]. The effect of the PAL agent on the isolated AβO signal can be observed by subtracting the spectrum of free PMT301 from the composite AβO + PMT301 spectrum to produce the resulting PAL-modified AβO spectrum [green trace in **(A)**]. The increased amplitude of the green spectrum in panel A reflects a decrease in the TOAC spin label order following PMT301 treatment. The conformational effect of PMT301 is also evident when comparing the experimental composite spectrum (red trace) to the calculated sum of the two samples alone [blue trace in panel **(A)**]. **(B,C)** show the comparative effects of each PAL on AβO. In **(B,C)** the untreated AβO spectrum (black trace) is compared to the sample after subtraction of the PAL-alone (free PAL) component. **(D–F)** show the results of similar measurements on the protofibril AβO (fAβO) sample. A comparison of AβO to fAβO is shown in the inset of **(D)**. fAβO displays a broader EPR spectrum than AβO, reflecting the increased order and spin coupling found in the protofibril sample. Notably, subtraction of the free PMT401 component from the composite AβO and fAβO spectra results in spectra with inverted amplitudes [red traces in **(C,F)**]. This finding reveals evidence of spin coupling between the PMT401 nitroxyl moiety and the TOAC label on Aβ (i.e., the PMT401 contribution is substantially broadened in both the composite AβO + 401 spectrum and fAβO + 401 spectrum. Except for the inset spectra in **(A,D)**, spectral intensities represent stoichiometric amounts of $AβO^{TOAC}$ and PAL agent (both at 80 μM). The spectral amplitudes of each panel are normalized to the same amount of $AβO^{TOAC}$, and all spectra were collected over 100 G [field sweep axis displayed in **(E)**].

data. One single marker in the 2D score plot represents an average of 3 independent size distribution measurements by NTA. Thus, for instance the AβO only group comprises the data from 18 independent NTA measurements. Collectively both PC1 and PC2 loading spectra produce peaks that encapsulate the majority of variance within the NTA size distribution data.

Intriguingly, each stilbene PAL group is clearly distinguished from the AβO alone group (red markers), except the AβO + PMT-401 (green markers) group. This feature indicates that each stilbene PAL treatment influences the AβO size distribution to some extent, although PMT-401 treatment produces very similar size distribution profile with the AβO

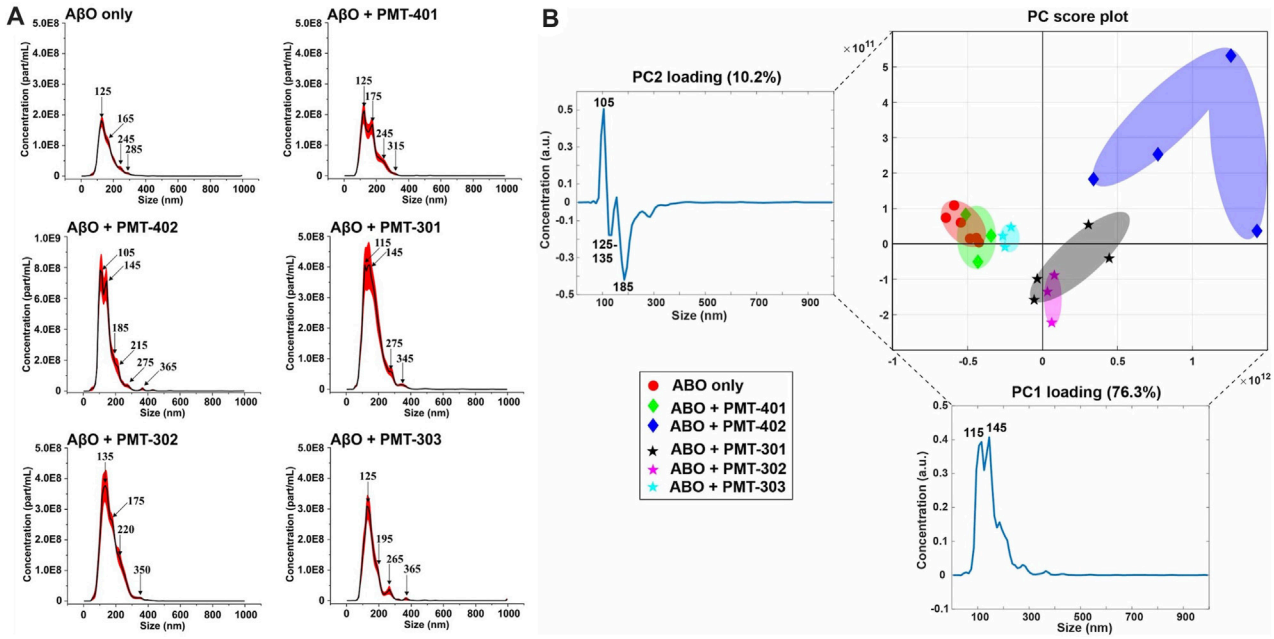

FIGURE 8 | NTA measurements of AβO treated with each stilbene PAL candidate. **(A)** Nanoparticle Tracking Analysis (NTA) scattering profiles of AβO preparations with and without PAL treatment. The black curves represent the average particle size vs. concentration distribution recorded and analyzed from 9–18 × 30 s videos and the red curves display the corresponding ±1 standard deviations. **(B)** A principal component analysis (PCA) on the NTA size distribution data for different combinations of AβO and stilbene PALs. The 2-dimensional PC score plot displays the separation of the tested groups: AβO alone (red circles) from a total of 1.23×10^5 particles detected and analyzed and on average 6.86×10^3 particles per video detected and analyzed); AβO + PMT-401 (green diamonds) from a total of 3.56×10^4 particles and on average 3.95×10^3 particles; AβO + PMT-402 (blue diamonds) from a total of 6.26×10^4 particles and on average 5.22×10^3 particles; AβO + PMT-301 (black stars) from a total of 1.35×10^5 particles and on average 7.51×10^3 particles; AβO + PMT-302 (magenta stars) from a total of 7.19×10^4 particles and on average 7.98×10^3 particles; AβO + PMT303 (cyan stars) from a total of 4.40×10^4 particles and on average 4.89×10^3 particles. The PC1 loading explains 76.3% of the total variation in the examined data set whereas PC2 loading corresponds to 10.2% of the total variation. Two prominent peaks can be distinguished in PC1 loading spectrum at 115 and 145 nm, and respectively PC2 reveals three predominant peaks at 105 nm, 125–135 nm, and 185 nm. In the PC score plot (upper right), the shaded areas serve as visual guides to discern the different groups.

TABLE 2 | Calculated particle parameters from NTA analysis of AβO samples.

Specimen	Average size (nm)	Mode size (nm)	Conc (part/ml)	195–595 nm fraction (%)	FWHM
ABO Only	159.2 ± 1.5	127.9 ± 3.3	$1.59 \pm 10^9 \pm 3.70 \pm 10^7$	20.3	76.58
ABO + PMT-401	161.8 ± 1.9	124.1 ± 6.3	$2.07 \pm 10^9 \pm 9.12 \pm 10^8$	23.7	90.44
ABO + PMT-402	145.9 ± 2.2	116.7 ± 3.7	$3.40 \pm 10^9 \pm 1.10 \pm 10^8$	28.7	71.32
ABO + PMT-301	164.9 ± 1.3	129.7 ± 4.7	$4.84 \pm 10^9 \pm 1.47 \pm 10^8$	26.0	104.39
ABO + PMT-302	166.0 ± 2.5	134.5 ± 2.9	$4.23 \pm 10^9 \pm 1.74 \pm 10^8$	28.4	98.64
ABO + PMT-303	155.6 ± 3.8	133.8 ± 5.5	$2.56 \pm 10^9 \pm 6.82 \pm 10^7$	17.0	68.63

alone group (the red and green groups highly overlapping). This result aligns with our other measurements showing the comparably poor characteristics of PMT-401 in AβO modulation. Furthermore, AβO treated with PMT-402 (blue markers) is the most discernible group from the others, which is also consistent with our other analyses. The 301–303 candidates not only differentiate from untreated AβO, but also from each other, with a slight overlapping of the AβO + PMT-301 (black markers) and AβO + PMT-302 (magenta markers) groups. The AβO + PMT-303 group (cyan markers) is noticeably tight compared to the others reflecting a significantly low internal variation.

As the PC1 and PC2 loading spectra are investigated, PMT-301, PMT-302 and PMT-402 have mostly positive score values along the PC1 axis of the score plot, corresponding to their intensities at 115 and 145 nm. Therefore, it is evident that these PALs produce more AβOs of approximate diameter of 115 and 145 nm than Aβ-alone, PMT-401, and PMT-303. Moreover, the PMT-402 group has markedly positive scores along the PC2 axis, and the corresponding PC2 loading spectrum possesses a prominent positive peak at 105 nm. This is indicative of PMT-402 also generating a subpopulation of 105 nm particulates. On the other hand, the majority of PMT-301 and PMT-302 measurements have negative score values along the PC2 axis,

and the PC2 loading spectrum displays two negative peaks at 125–135 and 185 nm region. Taken together, PMT-301 and PMT-302 yield more particles of these sizes more than the other stilbenes.

4 DISCUSSION

In aqueous solution, Aβ forms a large size and conformational distribution that is highly influenced by its method of preparation (Teplow, 2006). Soluble Aβ can assume multiple states, with various oligomeric states implicated in different aspects of AD pathogenesis (Lesné et al., 2006; Amar et al., 2017; De et al., 2019). However, the correlation of a specific oligomeric size to a specific cellular target is difficult to establish, as very large assemblies can be overlooked in sieving methods and the dynamic nature of AβO makes its state highly sensitive to reagent and matrix influences (Hepler et al., 2006; Hubin et al., 2014). A general consensus across studies points to intermediate-sized (>50 kDa), A11-positive oligomers inducing the broadest range of neuronal toxicity and dysfunction (Vandersteen et al., 2012; Cline et al., 2018). We therefore employed a simple prep that produces A11-positive, neurotoxic oligomers, and can likewise reproducibly transition into a soluble protofibril species. These oligomers retain a significant amount of conformational heterogeneity and ~40% beta sheet content (Sandberg et al., 2010; Vandersteen et al., 2012; Roy et al., 2017).

Our previous reports on a fluorene-based PAL compound demonstrated its high potency is related to the localization of nitroxide antioxidant activity within the cell, interrupting the cycle of ROS-enhanced AβO cytotoxicity and accumulation (Petrlova et al., 2012; Altman et al., 2015; Hilt et al., 2018). The high antioxidant potency of the nitroxide can be attributed its ability to cycle through alternate redox states, mimicking the antioxidant defense of superoxide dismutase (SOD) (Hideg and Kálai, 2007; Mandal et al., 2007). In cells, the redox cycle for a nitroxide begins with the reduction of the N-O state to the N-OH state, which can be re-oxidized to N-O by ROS. Likewise, hydroxyl and peroxyl radicals can oxidize the N-O state to the nitrone (N=O), which is then available to remove superoxide and regenerate the N-O state. Subsequent reduction (e.g., by GSH) to N-OH allows for a single nitroxide to perform several rounds of scavenging. Importantly the N-oxyl (nitroxyl) is not oxidative to other biomolecules (lipids, proteins, DNA). Consistent with previous studies of a fluorene-based PAL, the synergistic activity of stilbene PALs provides a potency 10–500 times greater than other anti-amyloid small molecules such as SEN1269 (Scopes et al., 2012) and resveratrol (Marambaud et al., 2005).

The antioxidant activity of the PALs is exemplified by the strong attenuation of the CellROX signal in MC65 cells induced for C99 expression. This potency is significant for two reasons: 1) brain bioavailability is a challenge for nearly all agents targeting amyloid-like proteins, and 2) it facilitates a targeted mechanism for countering oxidative stress, which is important as high antioxidant doses can become prooxidants, down-regulate endogenous antioxidant pathways and interfere with beneficial ROS/RNS-dependent signaling (Bouayed and Bohn, 2010).

Because each of the stilbene PAL agents contain a similar nitroxyl moiety, their effects on AβO conformation and assembly can point to structures that are superior in AβO engagement and/or remodeling. However, caveats remain, such as differences in the availability of free compound to the cell interior (e.g., differences in permeation, off-target protein binding). In terms of bioactivity and various metrics of AβO engagement, the aminostilbene PMT-402 displays the highest potency. In contrast, the aminostilbene PMT-401 shows the lowest potency. Although care was taken to maximize compound dispersion in all assays, the markedly lower solubility of PMT-401 could lower its effective concentration in our measurements.

Recognition of oligomer species by the A11 antibody provides a basis for identifying conformational toxicity, as it reacts against a diverse set of protein aggregates known to trigger neurodegeneration (Kayed et al., 2003). As described previously (Necula et al., 2007), attenuation of A11 binding can help identify compounds that convert AβO towards a less toxic conformation. Each of the 5 stilbene PALs significantly reduce A11 binding to AβO. The results suggest PMT-402 is most potent in this regard, however the variability inherent to the assay precludes ranking the other PAL agents according to potency. The reduction in binding may reflect an allosteric transition of the peptide away from its A11-positive conformation, although PAL occupation of the A11 epitope is also possible.

The CD spectrum of the aqueous AβO sample prior to its 1-h incubation displays a relatively flat, low amplitude signal (not shown) that increase in β-sheet content with time (Clements et al., 1996; Shea et al., 2019). This characteristic signal has been attributed to the peptide in the extended α-sheet, a conformation predicted to populate "toxic" soluble oligomers that ultimately mature into amyloid fibrils (Hayward and Milner-White, 2008; Babin et al., 2011; Hopping et al., 2014; Shea et al., 2019). After 1-h of incubation, the CD spectrum of the Aβ oligomers used in this study indicates the major fraction of secondary structure falls within the "disordered" portion of the spectra, however non-random conformations such as the extended poly-proline-II (PPII)-like helix also contribute intensities in this regime (i.e., a band with defined minimum in the 195–200 nm) (Gokce et al., 2005; Sandberg et al., 2010; Nisbet et al., 2013).

Deconvolution of the CD spectra for secondary structure composition indicates that PAL treatment of AβO with PALs in general results in a slight reduction in β-strand and corresponding increase in the helical component, with the major spectral change occurring within the regime classified as "other." The most significant effect is, with the exception of PMT-401, is the generation of a polyproline II (PPII)-like spectral intensity (Adzhubei et al., 2013). A similar result has been observed when treating AβO with a fluorene-based PAL (Altman et al., 2015), or examining the peptide at low temperature (Danielsson et al., 2005). Both the α-sheet and PP-II configurations display exposed backbone carbonyls, which have been postulated to drive protein-protein interactions (Fernández and Crespo, 2008; Hayward and Milner-White, 2008; Theillet et al., 2013; Adzhubei et al., 2017), readily convert to β-strand (Blanch et al., 2000; Hayward and Milner-White,

2008; Adzhubei et al., 2017), and have been proposed to illicit "toxic" conformations (Blanch et al., 2000; Shea et al., 2019). With respect to these populations within AβO, the CD results are consistent with a decrease in the fraction of α-sheet structure for the bioactive PALs.

We also examined the effect of the stilbene PALs on the CD spectrum of protofibril oligomers formed after 24-h incubation. These species display significantly more order with a high fraction of β-sheet secondary structure (Kayed et al., 2009). A far less dramatic alteration of the CD spectrum is observed with PAL treatment of protofibrils, although each of the compounds increase β-sheet content and decrease disordered content. With protofibrils showing low cytotoxicity, the absence of their disruption by the stilbene PALs can be viewed as a favorable property.

With respect to dye binding, compared to ThT, changes in NR fluorescence intensity appear to provide a better predictive value for the potency in the MC65 assay. In contrast to the CD measurements PMT-402 is not distinguished in either dye assay. Each of the PAL agents provide a strong inhibition of b-sheet formation as determined by ThT. However, the NR assay reports a differential effect with PMT-302, with the compound producing increased NR solvent exposure. Thus, the ability of PALs to occlude hydrophobic patches within AβO may provide a useful metric in identifying candidates to protect against AβO toxicity.

As shown in previous studies (Petrlova et al., 2012; Altman et al., 2015), EPR analyses of both $A\beta O^{TOAC}$ and protofibril $A\beta O^{TOAC}$ demonstrate that the TOAC spin label at position 26 reflects a moderate degree of order within the oligomer. Although the TOAC label is diluted with the oligomer to minimize spin-spin interaction, dipolar interactions between labels in close (~1.5 nm) proximity also contribute to the spectral broadening. Thus, we cannot attribute increased motional freedom as the only source behind the PAL-induced effects onto the $A\beta O^{TOAC}$ and protofibrils (Petrlova et al., 2012; Altman et al., 2015). In any event, both an increase in the spin label correlation time and decreased dipolar coupling are indicative of oligomer remodeling. PMT-301 and PMT-303 induce the largest effects on the EPR spectrum of $A\beta O^{TOAC}$, while PMT-402 had the greatest effect in the protofibril $A\beta^{TOAC}$ sample. Interestingly, PMT-401 showed no ability to alter the structure around the TOAC spin label. Therefore, EPR spectral changes reported by the TOAC label at position 26 may also be predictive for active candidates in the MC65 assay. Furthermore, the subtraction of the free PAL component from the PMT-401 treated $A\beta O^{TOAC}$ results in a negative spectral line. This can be explained if the PMT-401 contribution to the composite sample is broadened *via* dipolar coupling. Thus, PMT-401 may uniquely position its nitroxyl moiety in close proximity position 26 of the $A\beta O^{TOAC}$ sample. Finally, the EPR results again identified PMT-302 and PMT-401 as the least consequential PALs, showing a general agreement among the bioactivity, CD and dye binding results.

While the explicit molecular level mechanisms on how the stilbene PALs give rise to specimens of different sizes remain to be solved, the NTA-PCA analysis reveals some noteworthy aspects. First, PMT-401 (least effective in bioactivity) most resembles the untreated AβO; and PMT-402 (most effective in bioactivity) is the most distinguished in the PCA plot. Also, the FWHM feature of the distribution curve is somewhat predictive (**Table 2**), with PMT-402 and PMT-303 showing the lowest values (the high FWHM value of PMT-301 – intermediate bioactivity–suggests this metric may not serve as predictive in all cases). Second, with the exception of PMT-401, all the stilbene PAL modulators yield unique size distribution profiles that are markedly different from the AβO-alone sample and across each other as well. Therefore, the neural cell protective nature of the potent stilbene PALs may at least partially be explained by their capability to either 1) dislodge very large AβOs and protofibrils (>200 nm) into smaller particulates (105–145 nm), 2) assemble smaller toxic AβO (oligomers of 50–200 kD) into larger entities (105–145 nm), or 3) stabilize the existing less-toxic AβOs in the approximate size range of 105–145 nm. We cautiously hypothesize that whichever is the mechanism, the ultimate benefit is to generate AβOs of suitable size that are more easily dispatched from the cells. However, these hypotheses warrant for further targeted studies that were out of the scope of this study.

The amyloid-independent anti-inflammatory activity on HBMECs challenged by TGRL lipolysis products (TL) provides insights as to whether the antioxidant activity of the stilbene PALs can reduce inflammation on a more general basis. Only PMT-401 significantly suppressed TL-induced expression of all measured cytokines as well as COX-2 gene expression. Because PMT-401 is significantly more hydrophobic than the other PALs, effective downregulation of inflammation in the HBMEC model requires is likely dependent on the agent's partition into lipophilic domains. The other PALs did not suppress cytokine gene expression, however PMT-302 and PMT-303 did significantly suppress TL-induced COX-2 expression.

The fact that the secondary structure of the PAL-treated AβO remains largely disordered implies that shifting the equilibrium away from the toxic conformer may only require the modulation of a discrete structural feature within the ensemble. As the clinical quantification of AD risk *via* early biomarkers becomes a reality, small molecules are practical for continuous treatment to maintain a favorable balance of Aβ species (with respect to toxicity cellular clearance) in patients. This concept is similar to the administration of statins in cardiovascular health. In this regard, describing the interaction of our distinct PAL agents as a function of conformational toxicity will aid future development of small molecule structural correctors.

Developing small molecules with bifunctionality provides meaningful advantages as potential clinical applications are considered. Because *in vivo* safety and efficacy testing (e.g., tolerance, pharmacokinetics, pharmacodynamics) are carried out for single agents, there is a growing interest in developing compounds to address more than one target (Corson et al., 2008; Bachurin et al., 2017; Ramsay et al., 2018). The bi-functional approach provides synergistic action on two pathogenetic hallmarks of the disease resulting in considerable enhancement of the overall pharmacological effect and may provide both cognition-stimulating and disease-modifying actions.

DATA AVAILABILITY STATEMENT

The original contributions presented in the study are included in the article/**Supplementary Material**, further inquiries can be directed to the corresponding author.

ETHICS STATEMENT

The studies involving human participants were reviewed and approved by Human Subjects Review Committee/IRB at the University of California, Davis.

AUTHOR CONTRIBUTIONS

JV directed the study (lead on collection, interpretation, writing). SH collected bioactivity data and edited paper, RS collected dye binding data, MB collected EPR data, TR collected and analyzed NTA data, RC supervised NTA experiments and edited paper, HA collected and analyzed cytokine data, QG helped with confocal data, IM collected cell protection data, RL designed and synthesized the PAL compounds and wrote the chemistry portion of the paper.

FUNDING

This work was supported by a STAIR Award from the University of California, Davis to JV, and in part with funding from the National Institutes of Health (grant P30 AG010129 to JV). SH was supported by the NIH Post-doctoral Neuroscience of Cognitive Aging Training Program (NoCA-T32).

ACKNOWLEDGMENTS

HA acknowledges support from the Packer Wizard Foundation. The authors would like to thank the Combinatorial Chemistry and Chemical Biology Shared Resource at University of California, Davis for its assistance with the synthesis of PAL compounds.

SUPPLEMENTARY MATERIAL

The Supplementary Material for this article can be found online at: https://www.frontiersin.org/articles/10.3389/fchem.2022.896386/full#supplementary-material

REFERENCES

Abdi, H., and Williams, L. J. (2010). Principal Component Analysis. *WIREs Comp. Stat.* 2 (4), 433–459. doi:10.1002/wics.101

Adzhubei, A. A., Anashkina, A. A., and Makarov, A. A. (2017). Left-handed Polyproline-II Helix Revisited: Proteins Causing Proteopathies. *J. Biomol. Struct. Dyn.* 35 (12), 2701–2713. doi:10.1080/07391102.2016.1229220

Adzhubei, A. A., Sternberg, M. J. E., and Makarov, A. A. (2013). Polyproline-II Helix in Proteins: Structure and Function. *J. Mol. Biol.* 425 (12), 2100–2132. doi:10.1016/j.jmb.2013.03.018

Ahmed, T., Javed, S., Javed, S., Tariq, A., Šamec, D., Tejada, S., et al. (2017). Resveratrol and Alzheimer's Disease: Mechanistic Insights. *Mol. Neurobiol.* 54 (4), 2622–2635. doi:10.1007/s12035-016-9839-9

Almeida, L., Vaz-da-Silva, M., Falcão, A., Soares, E., Costa, R., Loureiro, A. I., et al. (2009). Pharmacokinetic and Safety Profile of Trans-resveratrol in a Rising Multiple-Dose Study in Healthy Volunteers. *Mol. Nutr. Food Res.* 53 (Suppl. 1), S7–S15. doi:10.1002/mnfr.200800177

Altman, R., Ly, S., Hilt, S., Petrlova, J., Maezawa, I., Kálai, T., et al. (2015). Protective Spin-Labeled Fluorenes Maintain Amyloid Beta Peptide in Small Oligomers and Limit Transitions in Secondary Structure. *Biochimica Biophysica Acta (BBA) - Proteins Proteomics* 1854 (12), 1860–1870. doi:10.1016/j.bbapap.2015.09.002

Amar, F., Sherman, M. A., Rush, T., Larson, M., Boyle, G., Chang, L., et al. (2017). The Amyloid-β Oligomer Aβ*56 Induces Specific Alterations in Neuronal Signaling that Lead to Tau Phosphorylation and Aggregation. *Sci. Signal.* 10 (478), eaal2021. doi:10.1126/scisignal.aal2021

Aung, H. H., Altman, R., Nyunt, T., Kim, J., Nuthikattu, S., Budamagunta, M., et al. (2016). Lipotoxic Brain Microvascular Injury Is Mediated by Activating Transcription Factor 3-dependent Inflammatory and Oxidative Stress Pathways. *J. Lipid Res.* 57 (6), 955–968. doi:10.1194/jlr.M061853

Aung, H. H., Lame, M. W., Gohil, K., An, C.-I., Wilson, D. W., and Rutledge, J. C. (2013). Induction of ATF3 Gene Network by Triglyceride-Rich Lipoprotein Lipolysis Products Increases Vascular Apoptosis and Inflammation. *Arterioscler. Thromb. Vasc. Biol.* 33 (9), 2088–2096. doi:10.1161/ATVBAHA.113.301375

Aung, H. H., Tsoukalas, A., Rutledge, J. C., and Tagkopoulos, I. (2014). A Systems Biology Analysis of Brain Microvascular Endothelial Cell Lipotoxicity. *BMC Syst. Biol.* 8, 80. doi:10.1186/1752-0509-8-80

Babin, V., Roland, C., and Sagui, C. (2011). The α-sheet: A Missing-In-Action Secondary Structure? *Proteins* 79 (3), 937–946. doi:10.1002/prot.22935

Bachurin, S. O., Shevtsova, E. F., Makhaeva, G. F., Grigoriev, V. V., Boltneva, N. P., Kovaleva, N. V., et al. (2017). Novel Conjugates of Aminoadamantanes with Carbazole Derivatives as Potential Multitarget Agents for AD Treatment. *Sci. Rep.* 7, 45627. doi:10.1038/srep45627

Bartolini, M., Bertucci, C., Bolognesi, M. L., Cavalli, A., Melchiorre, C., and Andrisano, V. (2007). Insight into the Kinetic of Amyloid β (1-42) Peptide Self-Aggregation: Elucidation of Inhibitors' Mechanism of Action. *ChemBioChem* 8 (17), 2152–2161. doi:10.1002/cbic.200700427

Bieschke, J., Herbst, M., Wiglenda, T., Friedrich, R. P., Boeddrich, A., Schiele, F., et al. (2011). Small-molecule Conversion of Toxic Oligomers to Nontoxic β-sheet-rich Amyloid Fibrils. *Nat. Chem. Biol.* 8 (1), 93–101. doi:10.1038/nchembio.719

Blanch, E. W., Morozova-Roche, L. A., Cochran, D. A. E., Doig, A. J., Hecht, L., and Barron, L. D. (2000). Is Polyproline II Helix the Killer Conformation? a Raman Optical Activity Study of the Amyloidogenic Prefibrillar Intermediate of Human Lysozyme 1 1Edited by A. R. Fersht. *J. Mol. Biol.* 301 (2), 553–563. doi:10.1006/jmbi.2000.3981

Bloom, G. S. (2014). Amyloid-β and Tau. *JAMA Neurol.* 71 (4), 505–508. doi:10.1001/jamaneurol.2013.5847

Bonda, D. J., Wang, X., Perry, G., Nunomura, A., Tabaton, M., Zhu, X., et al. (2010). Oxidative Stress in Alzheimer Disease: a Possibility for Prevention. *Neuropharmacology* 59 (4-5), 290–294. doi:10.1016/j.neuropharm.2010.04.005

Bouayed, J., and Bohn, T. (2010). Exogenous Antioxidants-Double-Edged Swords in Cellular Redox State: Health Beneficial Effects at Physiologic Doses versus Deleterious Effects at High Doses. *Oxidative Med. Cell. Longev.* 3 (4), 228–237. doi:10.4161/oxim.3.4.12858

Brouillette, J., Caillierez, R., Zommer, N., Alves-Pires, C., Benilova, I., Blum, D., et al. (2012). Neurotoxicity and Memory Deficits Induced by Soluble Low-Molecular-Weight Amyloid- 1-42 Oligomers Are Revealed *In Vivo* by Using a Novel Animal Model. *J. Neurosci.* 32 (23), 7852–7861. doi:10.1523/JNEUROSCI.5901-11.2012

Capiralla, H., Vingtdeux, V., Zhao, H., Sankowski, R., Al-Abed, Y., Davies, P., et al. (2012). Resveratrol Mitigates Lipopolysaccharide- and Aβ-Mediated Microglial Inflammation by Inhibiting the TLR4/NF-Kb/STAT Signaling Cascade. *J. Neurochem.* 120 (3), 461–472. doi:10.1111/j.1471-4159.2011.07594.x

Chunhui, H., Dilin, X., Ke, Z., Jieyi, S., Sicheng, Y., Dapeng, W., et al. (2018). A11-positive β-amyloid Oligomer Preparation and Assessment Using Dot Blotting Analysis. *J. Vis. Exp.* 135. doi:10.3791/57592

Clements, A., Allsop, D., Walsh, D. M., and Williams, C. H. (1996). Aggregation and Metal-Binding Properties of Mutant Forms of the Amyloid Aβ Peptide of Alzheimer's Disease. *J. Neurochem.* 66 (2), 740–747. doi:10.1046/j.1471-4159.1996.66020740.x

Cline, E. N., Bicca, M. A., Viola, K. L., and Klein, W. L. (2018). The Amyloid-β Oligomer Hypothesis: Beginning of the Third Decade. *Jad* 64 (s1), S567–S610. doi:10.3233/JAD-179941

Colom-Cadena, M., Gelpi, E., Charif, S., Belbin, O., Blesa, R., Martí, M. J., et al. (2013). Confluence of α-Synuclein, Tau, and β-Amyloid Pathologies in Dementia with Lewy Bodies. *J. Neuropathol. Exp. Neurol.* 72 (12), 1203–1212. doi:10.1097/NEN.0000000000000018

Copenhaver, P. F., Anekonda, T. S., Musashe, D., Robinson, K. M., Ramaker, J. M., Swanson, T. L., et al. (2011). A Translational Continuum of Model Systems for Evaluating Treatment Strategies in Alzheimer's Disease: Isradipine as a Candidate Drug. *Dis. Model Mech.* 4 (5), 634–648. doi:10.1242/dmm.006841

Corsale, C., Carrotta, R., Mangione, M. R., Vilasi, S., Provenzano, A., Cavallaro, G., et al. (2012). Entrapment of Aβ1–40peptide in Unstructured Aggregates. *J. Phys. Condens. Matter* 24 (24), 244103. doi:10.1088/0953-8984/24/24/244103

Corson, T. W., Aberle, N., and Crews, C. M. (2008). Design and Applications of Bifunctional Small Molecules: Why Two Heads Are Better Than One. *ACS Chem. Biol.* 3 (11), 677–692. doi:10.1021/cb8001792

Cottart, C.-H., Nivet-Antoine, V., Laguillier-Morizot, C., and Beaudeux, J.-L. (2010). Resveratrol Bioavailability and Toxicity in Humans. *Mol. Nutr. Food Res.* 54 (1), 7–16. doi:10.1002/mnfr.200900437

Currais, A., Quehenberger, O., Armando, A. M., Daugherty, D., Maher, P., and Schubert, D. (2016). Amyloid Proteotoxicity Initiates an Inflammatory Response Blocked by Cannabinoids. *NPJ Aging Mech. Dis.* 2, 16012. doi:10.1038/npjamd.2016.12

Danielsson, J., Jarvet, J., Damberg, P., and Gräslund, A. (2005). The Alzheimer β-peptide Shows Temperature-dependent Transitions between Left-Handed 31-helix, β-strand and Random Coil Secondary Structures. *FEBS J.* 272 (15), 3938–3949. doi:10.1111/j.1742-4658.2005.04812.x

De, S., Wirthensohn, D. C., Flagmeier, P., Hughes, C., Aprile, F. A., Ruggeri, F. S., et al. (2019). Different Soluble Aggregates of Aβ42 Can Give Rise to Cellular Toxicity through Different Mechanisms. *Nat. Commun.* 10 (1), 1541. doi:10.1038/s41467-019-09477-3

Drygalski, K., Fereniec, E., Koryciński, K., Chomentowski, A., Kiełczewska, A., Odrzygóźdź, C., et al. (2018). Resveratrol and Alzheimer's Disease. From Molecular Pathophysiology to Clinical Trials. *Exp. Gerontol.* 113, 36–47. doi:10.1016/j.exger.2018.09.019

Dunning, C. J., McGauran, G., Willén, K., Gouras, G. K., O'Connell, D. J., and Linse, S. (2016). Direct High Affinity Interaction between Aβ42 and GSK3α Stimulates Hyperphosphorylation of Tau. A New Molecular Link in Alzheimer's Disease? *ACS Chem. Neurosci.* 7 (2), 161–170. doi:10.1021/acschemneuro.5b00262

Dutta, S., Foley, A. R., Warner, C. J. A., Zhang, X., Rolandi, M., Abrams, B., et al. (2017). Suppression of Oligomer Formation and Formation of Non-toxic Fibrils upon Addition of Mirror-Image Aβ42 to the Natural L-Enantiomer. *Angew. Chem. Int. Ed.* 56 (38), 11506–11510. doi:10.1002/anie.201706279

Feng, Y., Wang, X.-p., Yang, S.-g., Wang, Y.-j., Zhang, X., Du, X.-t., et al. (2009). Resveratrol Inhibits Beta-Amyloid Oligomeric Cytotoxicity but Does Not Prevent Oligomer Formation. *Neurotoxicology* 30 (6), 986–995. doi:10.1016/j.neuro.2009.08.013

Fernández, A., and Crespo, A. (2008). Protein Wrapping: a Molecular Marker for Association, Aggregation and Drug Design. *Chem. Soc. Rev.* 37 (11), 2373–2382. doi:10.1039/b804150b

Fezoui, Y., and Teplow, D. B. (2002). Kinetic Studies of Amyloid β-Protein Fibril Assembly. *J. Biol. Chem.* 277 (40), 36948–36954. doi:10.1074/jbc.M204168200

Figueiredo, C. P., Clarke, J. R., Ledo, J. H., Ribeiro, F. C., Costa, C. V., Melo, H. M., et al. (2013). Memantine Rescues Transient Cognitive Impairment Caused by High-Molecular-Weight A Oligomers but Not the Persistent Impairment Induced by Low-Molecular-Weight Oligomers. *J. Neurosci.* 33 (23), 9626–9634. doi:10.1523/JNEUROSCI.0482-13.2013

Fu, Z., Aucoin, D., Ahmed, M., Ziliox, M., Van Nostrand, W. E., and Smith, S. O. (2014). Capping of Aβ42 Oligomers by Small Molecule Inhibitors. *Biochemistry* 53 (50), 7893–7903. doi:10.1021/bi500910b

Ge, J.-F., Qiao, J.-P., Qi, C.-C., Wang, C.-W., and Zhou, J.-N. (2012). The Binding of Resveratrol to Monomer and Fibril Amyloid Beta. *Neurochem. Int.* 61 (7), 1192–1201. doi:10.1016/j.neuint.2012.08.012

Gokce, I., Woody, R. W., Anderluh, G., and Lakey, J. H. (2005). Single Peptide Bonds Exhibit Poly(pro)II ("random Coil") Circular Dichroism Spectra. *J. Am. Chem. Soc.* 127 (27), 9700–9701. doi:10.1021/ja052632x

Gong, Y., Chang, L., Viola, K. L., Lacor, P. N., Lambert, M. P., Finch, C. E., et al. (2003). Alzheimer's Disease-Affected Brain: Presence of Oligomeric Aβ Ligands (ADDLs) Suggests a Molecular Basis for Reversible Memory Loss. *Proc. Natl. Acad. Sci. U.S.A.* 100 (18), 10417–10422. doi:10.1073/pnas.1834302100

Guerrero-Muñoz, M. J., Castillo-Carranza, D. L., and Kayed, R. (2014). Therapeutic Approaches against Common Structural Features of Toxic Oligomers Shared by Multiple Amyloidogenic Proteins. *Biochem. Pharmacol.* 88 (4), 468–478. doi:10.1016/j.bcp.2013.12.023

Haass, C., and Selkoe, D. J. (2007). Soluble Protein Oligomers in Neurodegeneration: Lessons from the Alzheimer's Amyloid β-peptide. *Nat. Rev. Mol. Cell Biol.* 8 (2), 101–112. doi:10.1038/nrm2101

Hayward, S., and Milner-White, E. J. (2008). The Geometry of α-sheet: Implications for its Possible Function as Amyloid Precursor in Proteins. *Proteins* 71 (1), 415–425. doi:10.1002/prot.21717

Hellstrand, E., Boland, B., Walsh, D. M., and Linse, S. (2010). Amyloid β-Protein Aggregation Produces Highly Reproducible Kinetic Data and Occurs by a Two-phase Process. *ACS Chem. Neurosci.* 1, 13–18. doi:10.1021/cn900015v

Hepler, R. W., Grimm, K. M., Nahas, D. D., Breese, R., Dodson, E. C., Acton, P., et al. (2006). Solution State Characterization of Amyloid β-Derived Diffusible Ligands. *Biochemistry* 45 (51), 15157–15167. doi:10.1021/bi061850f

Hideg, K., and Kálai, T. (2007). Novel Antioxidants in Anthracycline Cardiotoxicity. *Cardiovasc Toxicol.* 7 (2), 160–164. doi:10.1007/s12012-007-0019-z

Hilt, S., Altman, R., Kálai, T., Maezawa, I., Gong, Q., Wachsmann-Hogiu, S., et al. (2018). A Bifunctional Anti-amyloid Blocks Oxidative Stress and the Accumulation of Intraneuronal Amyloid-Beta. *Molecules* 23 (8), 2010. doi:10.3390/molecules23082010

Hong, H.-S., Maezawa, I., Yao, N., Xu, B., Diaz-Avalos, R., Rana, S., et al. (2007). Combining the Rapid MTT Formazan Exocytosis Assay and the MC65 Protection Assay Led to the Discovery of Carbazole Analogs as Small Molecule Inhibitors of Aβ Oligomer-Induced Cytotoxicity. *Brain Res.* 1130 (1), 223–234. doi:10.1016/j.brainres.2006.10.093

Hopping, G., Kellock, J., Barnwal, R. P., Law, P., Bryers, J., Varani, G., et al. (2014). Designed α-sheet Peptides Inhibit Amyloid Formation by Targeting Toxic Oligomers. *Elife* 3, e01681. doi:10.7554/eLife.01681

Hubin, E., van Nuland, N. A. J., Broersen, K., and Pauwels, K. (2014). Transient Dynamics of Aβ Contribute to Toxicity in Alzheimer's Disease. *Cell. Mol. Life Sci.* 71 (18), 3507–3521. doi:10.1007/s00018-014-1634-z

Jin, L.-W., Maezawa, I., Vincent, I., Bird, T., and Bird, T. (2004). Intracellular Accumulation of Amyloidogenic Fragments of Amyloid-β Precursor Protein in Neurons with Niemann-Pick Type C Defects Is Associated with Endosomal Abnormalities. *Am. J. Pathology* 164 (3), 975–985. doi:10.1016/s0002-9440(10)63185-9

Jo, D.-G., Arumugam, T. V., Woo, H.-N., Park, J.-S., Tang, S.-C., Mughal, M., et al. (2010). Evidence that γ-secretase Mediates Oxidative Stress-Induced β-secretase Expression in Alzheimer's Disease. *Neurobiol. Aging* 31 (6), 917–925. doi:10.1016/j.neurobiolaging.2008.07.003

Karuppagounder, S. S., Pinto, J. T., Xu, H., Chen, H.-L., Beal, M. F., and Gibson, G. E. (2009). Dietary Supplementation with Resveratrol Reduces Plaque Pathology in a Transgenic Model of Alzheimer's Disease. *Neurochem. Int.* 54 (2), 111–118. doi:10.1016/j.neuint.2008.10.008

Kayed, R., Head, E., Thompson, J. L., McIntire, T. M., Milton, S. C., Cotman, C. W., et al. (2003). Common Structure of Soluble Amyloid Oligomers Implies Common Mechanism of Pathogenesis. *Science* 300 (5618), 486–489. doi:10.1126/science.1079469

Kayed, R., and Lasagna-Reeves, C. A. (2012). Molecular Mechanisms of Amyloid Oligomers Toxicity. *J. Alzheimers Dis.* 33 (Suppl. 1), S67–S78. doi:10.3233/JAD-2012-129001

Kayed, R., Pensalfini, A., Margol, L., Sokolov, Y., Sarsoza, F., Head, E., et al. (2009). Annular Protofibrils Are a Structurally and Functionally Distinct Type of Amyloid Oligomer. *J. Biol. Chem.* 284 (7), 4230–4237. doi:10.1074/jbc.M808591200

Kienlen-Campard, P., Miolet, S., Tasiaux, B., and Octave, J.-N. (2002). Intracellular Amyloid-B1-42, but Not Extracellular Soluble Amyloid-β Peptides, Induces Neuronal Apoptosis. *J. Biol. Chem.* 277 (18), 15666–15670. doi:10.1074/jbc.M200887200

Knobloch, M., Konietzko, U., Krebs, D. C., and Nitsch, R. M. (2007). Intracellular Aβ and Cognitive Deficits Precede β-amyloid Deposition in Transgenic arcAβ Mice. *Neurobiol. Aging* 28 (9), 1297–1306. doi:10.1016/j.neurobiolaging.2006.06.019

Ladiwala, A. R. A., Lin, J. C., Bale, S. S., Marcelino-Cruz, A. M., Bhattacharya, M., Dordick, J. S., et al. (2010). Resveratrol Selectively Remodels Soluble Oligomers and Fibrils of Amyloid Aβ into Off-Pathway Conformers. *J. Biol. Chem.* 285 (31), 24228–24237. doi:10.1074/jbc.M110.133108

Ladiwala, A. R. A., Litt, J., Kane, R. S., Aucoin, D. S., Smith, S. O., Ranjan, S., et al. (2012). Conformational Differences between Two Amyloid β Oligomers of Similar Size and Dissimilar Toxicity. *J. Biol. Chem.* 287 (29), 24765–24773. doi:10.1074/jbc.M111.329763

Lesné, S., Koh, M. T., Kotilinek, L., Kayed, R., Glabe, C. G., Yang, A., et al. (2006). A Specific Amyloid-β Protein Assembly in the Brain Impairs Memory. *Nature* 440 (7082), 352–357. doi:10.1038/nature04533

Limanaqi, F., Biagioni, F., Gambardella, S., Familiari, P., Frati, A., and Fornai, F. (2020). Promiscuous Roles of Autophagy and Proteasome in Neurodegenerative Proteinopathies. *Int. J. Mol. Sci.* 21 (8), 3028. doi:10.3390/ijms21083028

Liu, Y.-H., Giunta, B., Zhou, H.-D., Tan, J., and Wang, Y.-J. (2012). Immunotherapy for Alzheimer Disease-The Challenge of Adverse Effects. *Nat. Rev. Neurol.* 8 (8), 465–469. doi:10.1038/nrneurol.2012.118

Liu, Z., Zhou, T., Ziegler, A. C., Dimitrion, P., and Zuo, L. (2017). Oxidative Stress in Neurodegenerative Diseases: From Molecular Mechanisms to Clinical Applications. *Oxidative Med. Cell. Longev.* 2017, 1–11. doi:10.1155/2017/2525967

Livak, K. J., and Schmittgen, T. D. (2001). Analysis of Relative Gene Expression Data Using Real-Time Quantitative PCR and the 2−ΔΔCT Method. *Methods* 25 (4), 402–408. doi:10.1006/meth.2001.1262

Ma, T., Tan, M.-S., Yu, J.-T., and Tan, L. (2014). Resveratrol as a Therapeutic Agent for Alzheimer's Disease. *BioMed Res. Int.* 2014, 1–13. doi:10.1155/2014/350516

Maccioni, R. B., Farías, G., Morales, I., and Navarrete, L. (2010). The Revitalized Tau Hypothesis on Alzheimer's Disease. *Archives Med. Res.* 41 (3), 226–231. doi:10.1016/j.arcmed.2010.03.007

Maezawa, I., Hong, H. S., Liu, R., Wu, C. Y., Cheng, R. H., Kung, M. P., et al. (2008). Congo Red and Thioflavin-T Analogs Detect Abeta Oligomers. *J. Neurochem.* 104 (2), 457–468. doi:10.1111/j.1471-4159.2007.04972.x

Maezawa, I., Hong, H.-S., Wu, H.-C., Battina, S. K., Rana, S., Iwamoto, T., et al. (2006). A Novel Tricyclic Pyrone Compound Ameliorates Cell Death Associated with Intracellular Amyloid-Beta Oligomeric Complexes. *J. Neurochem.* 98 (1), 57–67. doi:10.1111/j.1471-4159.2006.03862.x

Mandal, R., Kutala, V. K., Khan, M., Mohan, I. K., Varadharaj, S., Sridhar, A., et al. (2007). N-hydroxy-pyrroline Modification of Verapamil Exhibits Antioxidant Protection of the Heart against Ischemia/reperfusion-Induced Cardiac Dysfunction without Compromising its Calcium Antagonistic Activity. *J. Pharmacol. Exp. Ther.* 323 (1), 119–127. doi:10.1124/jpet.107.127167

Marambaud, P., Zhao, H., and Davies, P. (2005). Resveratrol Promotes Clearance of Alzheimer's Disease Amyloid-β Peptides. *J. Biol. Chem.* 280 (45), 37377–37382. doi:10.1074/jbc.M508246200

Micsonai, A., Wien, F., Kernya, L., Lee, Y.-H., Goto, Y., Réfrégiers, M., et al. (2015). Accurate Secondary Structure Prediction and Fold Recognition for Circular Dichroism Spectroscopy. *Proc. Natl. Acad. Sci. U.S.A.* 112 (24), E3095–E3103. doi:10.1073/pnas.1500851112

Moussa, C., Hebron, M., Huang, X., Ahn, J., Rissman, R. A., Aisen, P. S., et al. (2017). Resveratrol Regulates Neuro-Inflammation and Induces Adaptive Immunity in Alzheimer's Disease. *J. Neuroinflammation* 14 (1), 1. doi:10.1186/s12974-016-0779-0

Mputhia, Z., Hone, E., Tripathi, T., Sargeant, T., Martins, R., and Bharadwaj, P. (2019). Autophagy Modulation as a Treatment of Amyloid Diseases. *Molecules* 24 (18), 3372. doi:10.3390/molecules24183372

Murakami, K. (2014). Conformation-specific Antibodies to Target Amyloid β Oligomers and Their Application to Immunotherapy for Alzheimer's Disease. *Biosci. Biotechnol. Biochem.* 78 (8), 1293–1305. doi:10.1080/09168451.2014.940275

Necula, M., Kayed, R., Milton, S., and Glabe, C. G. (2007). Small Molecule Inhibitors of Aggregation Indicate that Amyloid β Oligomerization and Fibrillization Pathways Are Independent and Distinct. *J. Biol. Chem.* 282 (14), 10311–10324. doi:10.1074/jbc.M608207200

Nisbet, R. M., Nuttall, S. D., Robert, R., Caine, J. M., Dolezal, O., Hattarki, M., et al. (2013). Structural Studies of the Tethered N-Terminus of the Alzheimer's Disease Amyloid-β Peptide. *Proteins* 81 (10), 1748–1758. doi:10.1002/prot.24312

Nyunt, T., Britton, M., Wanichthanarak, K., Budamagunta, M., Voss, J. C., Wilson, D. W., et al. (2019). Mitochondrial Oxidative Stress-Induced Transcript Variants of ATF3 Mediate Lipotoxic Brain Microvascular Injury. *Free Radic. Biol. Med.* 143, 25–46. doi:10.1016/j.freeradbiomed.2019.07.024

Oakley, H., Cole, S. L., Logan, S., Maus, E., Shao, P., Craft, J., et al. (2006). Intraneuronal Beta-Amyloid Aggregates, Neurodegeneration, and Neuron Loss in Transgenic Mice with Five Familial Alzheimer's Disease Mutations: Potential Factors in Amyloid Plaque Formation. *J. Neurosci.* 26 (40), 10129–10140. doi:10.1523/JNEUROSCI.1202-06.2006

Oddo, S., Caccamo, A., Smith, I. F., Green, K. N., and LaFerla, F. M. (2006). A Dynamic Relationship between Intracellular and Extracellular Pools of Aβ. *Am. J. Pathology* 168 (1), 184–194. doi:10.2353/ajpath.2006.050593

Park, J., Wetzel, I., Marriott, I., Dréau, D., D'Avanzo, C., Kim, D. Y., et al. (2018). A 3D Human Triculture System Modeling Neurodegeneration and Neuroinflammation in Alzheimer's Disease. *Nat. Neurosci.* 21 (7), 941–951. doi:10.1038/s41593-018-0175-4

Pensalfini, A., Albay, R., 3rd, Rasool, S., Wu, J. W., Hatami, A., Arai, H., et al. (2014). Intracellular Amyloid and the Neuronal Origin of Alzheimer Neuritic Plaques. *Neurobiol. Dis.* 71, 53–61. doi:10.1016/j.nbd.2014.07.011

Petrlova, J., Kálai, T., Maezawa, I., Altman, R., Harishchandra, G., Hong, H.-S., et al. (2012). The Influence of Spin-Labeled Fluorene Compounds on the Assembly and Toxicity of the Aβ Peptide. *PLoS One* 7 (4), e35443. doi:10.1371/journal.pone.0035443

Ramsay, R. R., Popovic-Nikolic, M. R., Nikolic, K., Uliassi, E., and Bolognesi, M. L. (2018). A Perspective on Multi-Target Drug Discovery and Design for Complex Diseases. *Clin. Transl. Med.* 7 (1), 3. doi:10.1186/s40169-017-0181-2

Rege, S. D., Geetha, T., Griffin, G. D., Broderick, T. L., and Babu, J. R. (2014). Neuroprotective Effects of Resveratrol in Alzheimer Disease Pathology. *Front. Aging Neurosci.* 6, 218. doi:10.3389/fnagi.2014.00218

Roy, A., Chandra, K., Dolui, S., and Maiti, N. C. (2017). Envisaging the Structural Elevation in the Early Event of Oligomerization of Disordered Amyloid β Peptide. *ACS Omega* 2 (8), 4316–4327. doi:10.1021/acsomega.7b00522

Roychaudhuri, R., Lomakin, A., Bernstein, S., Zheng, X., Condron, M. M., Benedek, G. B., et al. (2014). Gly25-Ser26 Amyloid β-Protein Structural Isomorphs Produce Distinct Aβ42 Conformational Dynamics and Assembly Characteristics. *J. Mol. Biol.* 426 (13), 2422–2441. doi:10.1016/j.jmb.2014.04.004

Rudenko, L. K., Wallrabe, H., Periasamy, A., Siller, K. H., Svindrych, Z., Seward, M. E., et al. (2019). Intraneuronal Tau Misfolding Induced by Extracellular Amyloid-β Oligomers. *J. Alzheimers Dis.* 71 (4), 1125–1138. doi:10.3233/JAD-190226

Sandberg, A., Luheshi, L. M., Söllvander, S., Pereira de Barros, T., Macao, B., Knowles, T. P. J., et al. (2010). Stabilization of Neurotoxic Alzheimer Amyloid-β Oligomers by Protein Engineering. *Proc. Natl. Acad. Sci. U.S.A.* 107 (35), 15595–15600. doi:10.1073/pnas.1001740107

Sarubbo, F., Moranta, D., Asensio, V. J., Miralles, A., and Esteban, S. (2017). Effects of Resveratrol and Other Polyphenols on the Most Common Brain Age-Related Diseases. *Curr. Med. Chem.* 24 (38), 4245–4266. doi:10.2174/0929867324666170724102743

Schneider, C. A., Rasband, W. S., and Eliceiri, K. W. (2012). NIH Image to ImageJ: 25 Years of Image Analysis. *Nat. Methods* 9 (7), 671–675. doi:10.1038/nmeth.2089

Scopes, D., O'Hare, E., Jeggo, R., Whyment, A., Spanswick, D., Kim, E.-M., et al. (2012). Aβ Oligomer Toxicity Inhibitor Protects Memory in Models of Synaptic Toxicity. *Br. J. Pharmacol.* 167 (2), 383–392. doi:10.1111/j.1476-5381.2012.01973.x

Selkoe, D. J., and Hardy, J. (2016). The Amyloid Hypothesis of Alzheimer's Disease at 25 Years. *EMBO Mol. Med.* 8 (6), 595–608. doi:10.15252/emmm.201606210

Shankar, G. M., Li, S., Mehta, T. H., Garcia-Munoz, A., Shepardson, N. E., Smith, I., et al. (2008). Amyloid-β Protein Dimers Isolated Directly from Alzheimer's Brains Impair Synaptic Plasticity and Memory. *Nat. Med.* 14 (8), 837–842. doi:10.1038/nm1782

Shea, D., Hsu, C.-C., Bi, T. M., Paranjapye, N., Childers, M. C., Cochran, J., et al. (2019). α-Sheet Secondary Structure in Amyloid β-peptide Drives Aggregation and Toxicity in Alzheimer's Disease. *Proc. Natl. Acad. Sci. U.S.A.* 116 (18), 8895–8900. doi:10.1073/pnas.1820585116

Silverman, J. M., Gibbs, E., Peng, X., Martens, K. M., Balducci, C., Wang, J., et al. (2018). A Rational Structured Epitope Defines a Distinct Subclass of Toxic Amyloid-Beta Oligomers. *ACS Chem. Neurosci.* 9 (7), 1591–1606. doi:10.1021/acschemneuro.7b00469

Singh, P. K., Kotia, V., Ghosh, D., Mohite, G. M., Kumar, A., and Maji, S. K. (2013). Curcumin Modulates α-Synuclein Aggregation and Toxicity. *ACS Chem. Neurosci.* 4 (3), 393–407. doi:10.1021/cn3001203

Sperling, R. A., Donohue, M. C., Raman, R., Sun, C.-K., Yaari, R., Holdridge, K., et al. (2020). Association of Factors with Elevated Amyloid Burden in Clinically Normal Older Individuals. *JAMA Neurol.* 77, 735. doi:10.1001/jamaneurol.2020.0387

Sultana, R., and Butterfield, D. A. (2010). Role of Oxidative Stress in the Progression of Alzheimer's Disease. *J. Alzheimers Dis.* 19 (1), 341–353. doi:10.3233/JAD-2010-1222

Swerdlow, R. H., Burns, J. M., and Khan, S. M. (2014). The Alzheimer's Disease Mitochondrial Cascade Hypothesis: Progress and Perspectives. *Biochimica Biophysica Acta (BBA) - Mol. Basis Dis.* 1842 (8), 1219–1231. doi:10.1016/j.bbadis.2013.09.010

Takahashi, R. H., Nagao, T., and Gouras, G. K. (2017). Plaque Formation and the Intraneuronal Accumulation of β-amyloid in Alzheimer's Disease. *Pathol. Int.* 67 (4), 185–193. doi:10.1111/pin.12520

Teplow, D. B. (2006). Preparation of Amyloid β-Protein for Structural and Functional Studies. *Methods Enzymol.* 413, 20–33. doi:10.1016/S0076-6879(06)13002-5

Theillet, F.-X., Kalmar, L., Tompa, P., Han, K.-H., Selenko, P., Dunker, A. K., et al. (2013). The Alphabet of Intrinsic Disorder. *Intrinsically Disord. Proteins* 1 (1), e24360. doi:10.4161/idp.24360

Usman, M. B., Bhardwaj, S., Roychoudhury, S., Kumar, D., Alexiou, A., Kumar, P., et al. (2021). Immunotherapy for Alzheimer's Disease: Current Scenario and Future Perspectives. *J. Prev. Alz Dis.* 8 (4), 1–18. doi:10.14283/jpad.2021.52

Vandersteen, A., Hubin, E., Sarroukh, R., De Baets, G., Schymkowitz, J., Rousseau, F., et al. (2012). A Comparative Analysis of the Aggregation Behavior of Amyloid-β Peptide Variants. *FEBS Lett.* 586 (23), 4088–4093. doi:10.1016/j.febslet.2012.10.022

Walsh, D. M., Hartley, D. M., Kusumoto, Y., Fezoui, Y., Condron, M. M., Lomakin, A., et al. (1999). Amyloid β-Protein Fibrillogenesis. *J. Biol. Chem.* 274 (36), 25945–25952. doi:10.1074/jbc.274.36.25945

Wang, H., Jiang, T., Li, W., Gao, N., and Zhang, T. (2018). Resveratrol Attenuates Oxidative Damage through Activating Mitophagy in an *In Vitro* Model of Alzheimer's Disease. *Toxicol. Lett.* 282, 100–108. doi:10.1016/j.toxlet.2017.10.021

Yoshiike, Y., Minai, R., Matsuo, Y., Chen, Y.-R., Kimura, T., and Takashima, A. (2008). Amyloid Oligomer Conformation in a Group of Natively Folded Proteins. *PLoS One* 3 (9), e3235. doi:10.1371/journal.pone.0003235

Conflict of Interest: Author JV was employed by Paramag Biosciences Inc., which retains a license to commercialize the PAL compounds.

The remaining authors declare that the research was conducted in the absence of any commercial or financial relationships that could be construed as a potential conflict of interest.

The handling editor MC declared a shared affiliation with the authors at the time of review.

Publisher's Note: All claims expressed in this article are solely those of the authors and do not necessarily represent those of their affiliated organizations, or those of the publisher, the editors and the reviewers. Any product that may be evaluated in this article, or claim that may be made by its manufacturer, is not guaranteed or endorsed by the publisher.

frontiers | Frontiers in Chemistry

REVIEW
published: 26 May 2022
doi: 10.3389/fchem.2022.880128

Recent Chemical and Chemoenzymatic Strategies to Complex-Type *N*-Glycans

Xiaoya Zhao[1†], Yan Huang[1†], Siai Zhou[1], Jiaming Ao[1], Hui Cai[1], Katsunori Tanaka[2,3,4], Yukishige Ito[2,5], Akihiro Ishiwata[2]* and Feiqing Ding[1]**

[1]School of Pharmaceutical Sciences (Shenzhen), Sun Yat-sen University, Shenzhen, China, [2]RIKEN Cluster for Pioneering Research, Saitama, Japan, [3]School of Materials and Chemical Technology, Tokyo Institute of Technology, Tokyo, Japan, [4]Alexander Butlerov Institute of Chemistry, Kazan Federal University, Kazan, Russian Federation, [5]Graduate School of Science, Osaka University, Osaka, Japan

Glycosylation is one of the major forms of protein post-translational modification. *N*-glycans attached to proteins by covalent bonds play an indispensable role in intercellular interaction and immune function. In human bodies, most of the cell surface glycoproteins and secreted glycopeptides are modified with complex-type *N*-glycans. Thus, for analytical or medicinal purposes, efficient and universal methods to provide homogeneous complex-type *N*-glycans have been an urgent need. Despite the extremely complicated structures, tremendous progress in the synthesis of *N*-glycans has been achieved. On one hand, chemical strategies are shown to be effective to prepare core oligosaccharides of *N*-glycans by focusing on stereoselective glycosylations such as β-mannosylation and α-sialylation, as well as the methodology of the *N*-glycan assembly. On the other hand, chemoenzymatic strategies have also become increasingly powerful in recent years. This review attempts to highlight the very recent advancements in chemical and chemoenzymatic strategies for eukaryotic complex-type *N*-glycans.

Keywords: *N*-glycans, β-mannosylation, α-sialylation, chemical assembly, chemo-enzymatic strategies

OPEN ACCESS

Edited by:
Matthew A. Coleman, University of California, Davis, United States

Reviewed by:
Madhusudhan Reddy Gadi, Georgia State University, United States
Decai Xiong, Peking University, China

****Correspondence:***
Hui Cai
caihui5@mail.sysu.edu.cn
Akihiro Ishiwata
aishiwa@riken.jp
Feiqing Ding
dingfq3@mail.sysu.edu.cn

†These authors have contributed equally to this work

Specialty section:
This article was submitted to Chemical Biology, a section of the journal Frontiers in Chemistry

Received: *21 February 2022*
Accepted: *12 April 2022*
Published: *26 May 2022*

Citation:
Zhao X, Huang Y, Zhou S, Ao J, Cai H, Tanaka K, Ito Y, Ishiwata A and Ding F (2022) Recent Chemical and Chemoenzymatic Strategies to Complex-Type N-Glycans. Front. Chem. 10:880128. doi: 10.3389/fchem.2022.880128

INTRODUCTION

Glycosylation is one of the major post-translational modifications of protein, playing an important role in protein folding, transport, and localization (Varki et al., 2015). It affects protein secretion and stability and participates in cell adhesion and signal transduction. *N*-glycosylation is the most common protein modification, and the attached glycans called *N*-glycans are linked to the asparagine residues in the consensus amino acid sequence (Asn-X-Thr/Ser, X ≠ Pro) at the reducing terminal *N*-acetyl-glucosamine (GlcNAc). According to the differences in non-reducing terminal residues, three subtypes can further be derived, high-mannose type, hybrid type, and complex type. Typical structures are shown in **Figure 1A**. For medical use, the sialylated complex-type glycans are seen quite often as found in secretory and cell surface glycoproteins. The principal modification can directly improve the *in vivo* stability and physiological activity of glycoproteins, including extending half-life, participating in intermolecular recognition, and enhancing drug targeting compared to the unmodified ones (Reily et al., 2019; Shirakawa et al., 2021b).

In recent years, a variety of glycoproteins have been approved for the treatment and diagnosis of human diseases, such as erythropoietin (EPO), granulocyte colony-stimulating factor (GCSF), β-interferon, certain cancer biomarkers, and monoclonal antibodies for public health purposes as

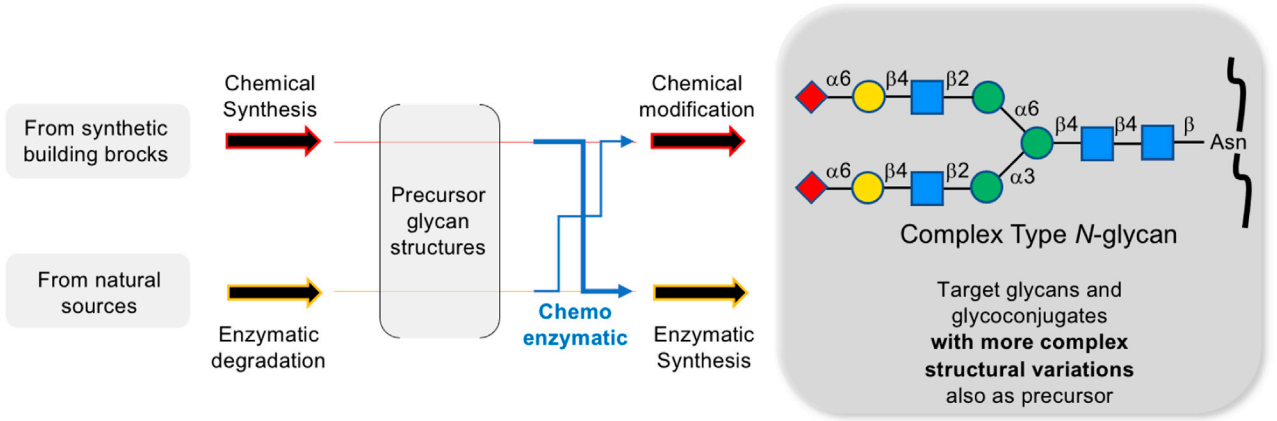

GRAPHICAL ABSTRACT |

similar biological products (SBPs) with acceptable levels of quality, safety and efficacy (Buettner et al., 2018). Large-scale production has been realized through glycoprotein expression by yeast, plant, insect, and Chinese hamster ovary (CHO) cells, but structures are quite different from those of glycans on human proteins (**Figure 1B**).

At present, many *N*-linked glycoproteins are produced through biosynthesis of recombinant protein in cell expression systems of insects, plants, yeast, and mammals, in which the required sets of glycosyl transfer systems including enzymes for the preassemble of dolichol pyrophosphate-linked tetradecasaccharide, oligosaccharyltransferase, ER and Golgi glycosidases, UDP glucose glucosyltransferase, and Golgi glycosyltransferases as well as many lectins, have already existed. However, the available proteins obtained by this method are mostly asialo form with lacking other modifications such as fucosylation to *N*-glycan and afford heterogeneous products due to the uncompleted biosynthesis to be a desired *N*-glycan structures (**Figure 2**) (Vinikangas et al., 2021). Since the heterogeneity of medicinal *N*-glycans affects clinical application, the preparation of humanized and homogeneous glycoforms is important for both research and therapeutic purposes. Meanwhile, isolation from natural resources requires rather complicated protocols with rather difficult purifications and is inadequate for researchers to study diverse structures, especially unnatural forms of *N*-glycans.

Isolation of *N*-glycans from natural resources remains one of the most common ways to acquire a large amount of *N*-glycan production (**Figure 3**). Asn-linked oligosaccharides containing biantennary complex-type *N*-glycans from egg yolk immunoglobulin after hydrazinolysis had been reported (Matsuura et al., 1993). The ammonia-catalyzed release method of ovalbumin and soy protein was reported recently without side reactions and degradation of core *N*-glycan structures (Yang et al., 2020). Sialylglycopeptide (SGP) was also found in hen's egg yolk and digested by PNGase, one of the most highly specific glycosidases extensively used in enzymatic isolation (Seko et al., 1997). Chemical modification of SGP to various other glycoproteins has been developed by Kajihara's group, which achieved semi-synthesis of poly-LacNAc containing complex-type biantennary oligosaccharide (Maki et al., 2017) and was recently applied to triantennary erythropoietin (EPO) *N*-glycan (Maki et al., 2020).

CHEMICAL AND CHEMOENZYMATIC STRATEGIES TOWARD EUKARYOTIC COMPLEX-TYPE *N*-GLYCANS

Chemical Assembly of Complex-Type *N*-Glycans

As shown in the introduction briefly, the extreme complexity of *N*-glycan structures, especially in terms of the regioselectivity and stereoselectivity control, strongly induces the current situation with no universal methods and strategies for chemical synthesis of *N*-glycan, although there have been widely studied all over the world. One of the issues for the chemical synthesis of *N*-glycan is stereoselective glycosylations including β-D-mannosylation in the core structure of all types of *N*-glycans, and α-sialylation at the non-reducing terminal end of the complex and the hybrid-type *N*-glycans.

The earliest glycosylation reaction dates back to the late 19th century. An example of simple phenolic glycosides synthesis, glycosylation between glycosyl chloride/bromide and nucleophilic potassium phenoxide, was first reported by Michael in 1879 (Michael and Norton, 1879). A great deal of work has been done since then in the development of glycosylation methods and dozens of novel glycosyl donors have been reported in succession, such as halide donors, semi-aldehyde glycosyl donors, trichloroacetimidate donors (TCAI, Schmidt donors), thioglycoside donors, glycal donors, glycosyl phosphate donors, and *o*-acetoxy benzoate glycosyl donors (Koenigs and Knorr, 1901; Danishefsky and Bilodeau, 1996; Garcia and Gin, 2000; Schmidt et al., 1986; Fügedi et al., 1987; Plante et al., 2001). With the emergence of these glycosyl donors, a variety of activation systems have also been developed to

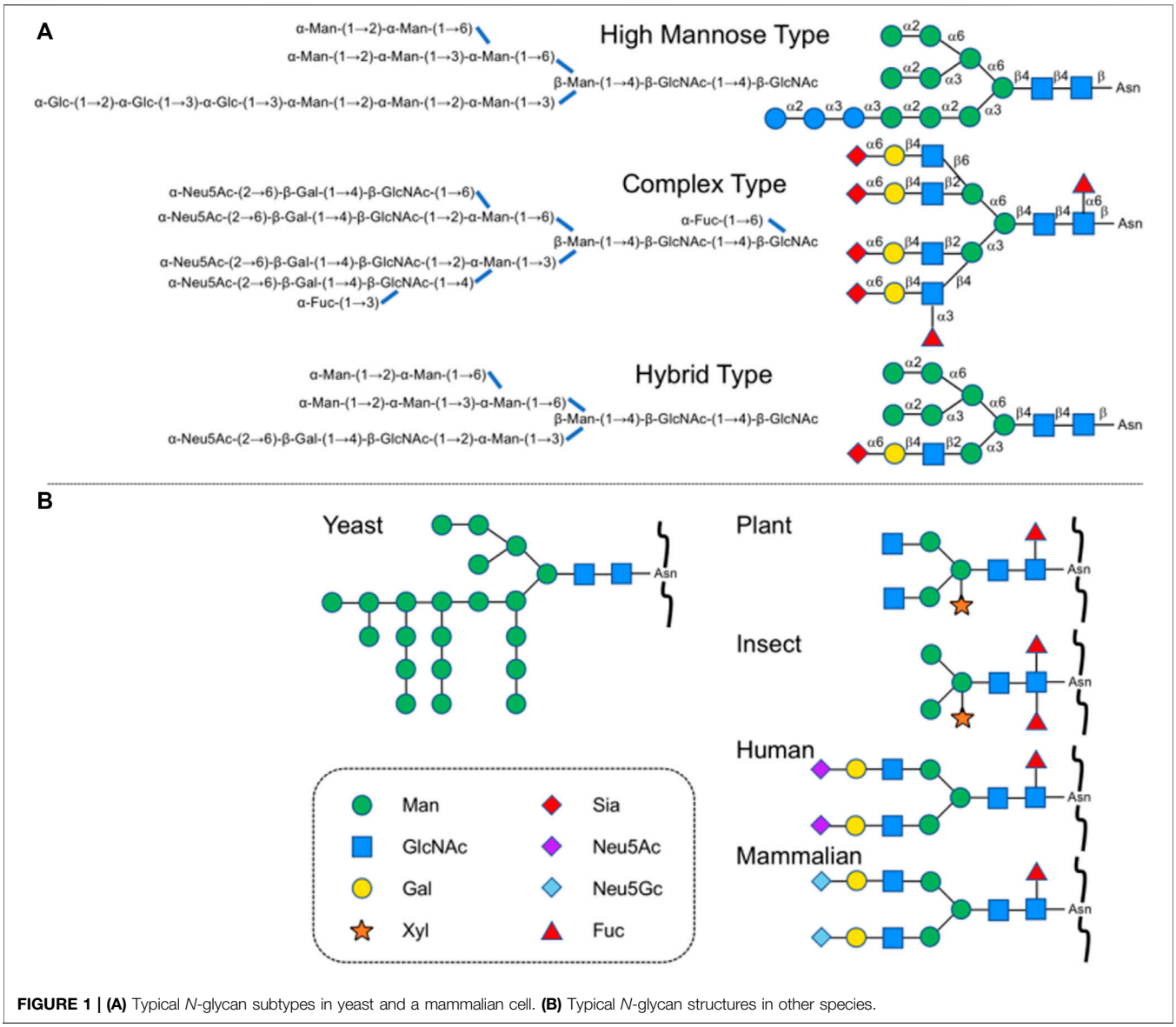

FIGURE 1 | (A) Typical *N*-glycan subtypes in yeast and a mammalian cell. **(B)** Typical *N*-glycan structures in other species.

optimize the yield and selectivity, which are still playing important roles in the synthesis of various glycans. Among the commonly use donors such as halide donors, Schmidt's donors, and thioglycosides, it is worth mentioning that, sulfides groups of thioglycosides can act as anomeric protecting groups, and sometimes orthogonal activated leaving groups as well, which give a unique value to thioglycosides, especially in the application to a liquid-phase one-pot synthesis of glycans.

The stereoselective construction of β-D-mannosidic bonds has always been a hot topic as one of the most difficult issues in glycochemistry (Tsutsui et al., 2020; Ding et al., 2018; Zhong et al., 2021). Stereo electronic effects such as the anomeric effect and C (2)-OH axial substitution of mannose is both beneficial to the formation of α-configuration products. For the construction of the core structure of *N*-glycan, a variety of effective methods has been reported. To sum up, there are three main chemical strategies so far for the construction of β-D-mannosidic bonds to synthesize complex-type *N*-glycans, including the β-glycosylation-inversion strategy (Matsuo et al., 1999), intramolecular aglycon delivery (IAD) (Barresi and Hindsgaul, 1991), and 4,6-*O*-benzylidene protecting strategy (Crich's mannosylation) (Crich and Sun, 1996) (**Figure 4**). Because of the efficiency of the simple intermolecular reaction, and the predominant β-selectivity of Crich's mannosylation (for a recent example of β-glycosylation-double inversion strategy, see Ishii et al., 2018) (for an example of an improved IAD, see Ishiwata et al., 2008), 4,6-*O*-benzylidene-protected glycosyl donors were trends to be selected, although the other methods also afford β-D-mannose in the acceptable stereoselectivity. Furthermore, some efforts have also been made to optimize this strategy (For example, the gold(I)-catalyzed glycosylation reaction with glycosyl ortho-alkynyl benzoates as donors, see: Zhu and Yu, 2015).

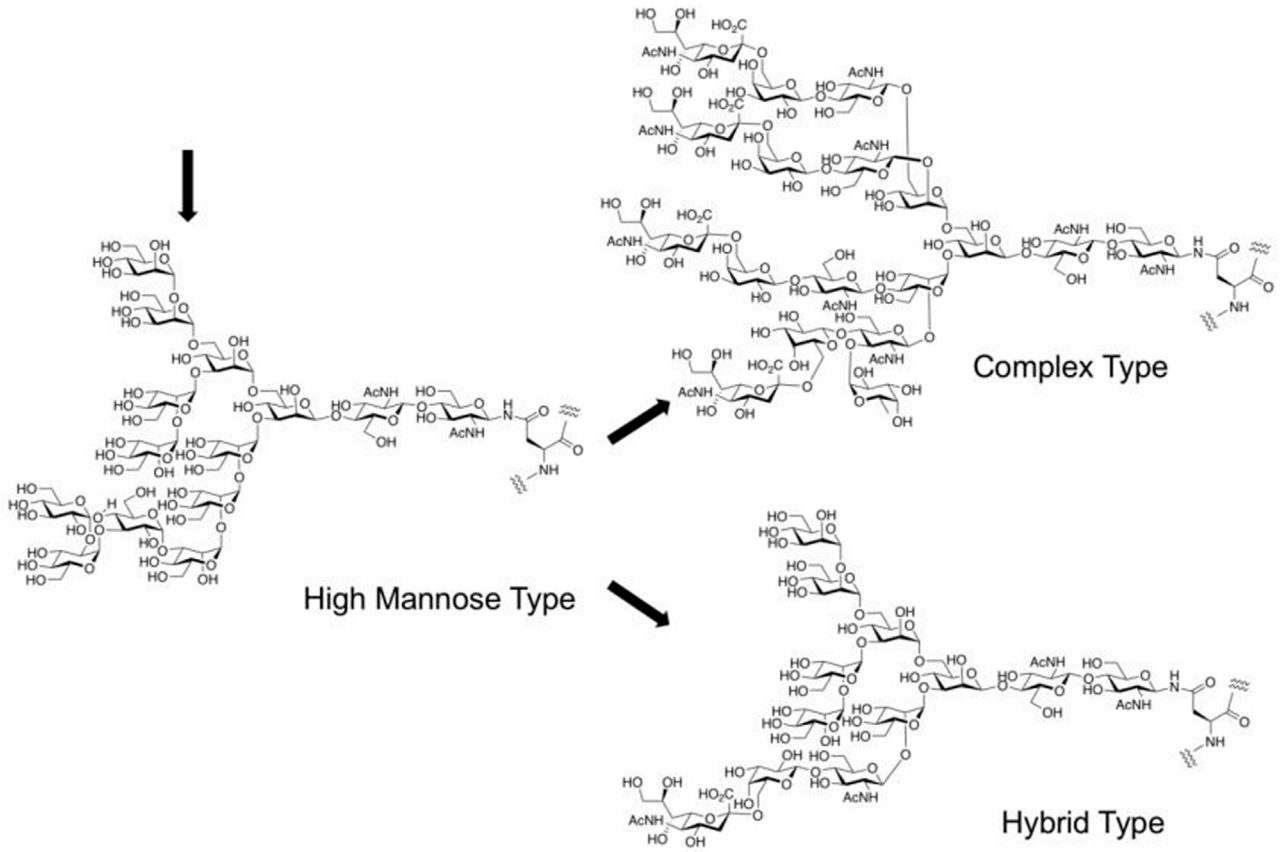

FIGURE 2 | Biosynthesis of *N*-glycan in a cell expression system.

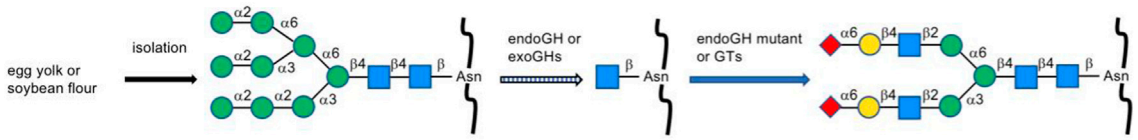

FIGURE 3 | Isolation of *N*-glycans from natural resources.

The non-reducing terminal modification of *N*-glycans with sialic acids has a great impact on the physiological and pathological function of glycoproteins. Sialic acids on proteins of mammalian cell surface can be divided into *N*-acetylneuraminic acid (Neu5Ac) and *N*-glycolylneuraminic acid (Neu5Gc), which link to 3 or 6 positions of D-galactopyranose residue of *N*-glycan through α-glycosidic linkages (Shirakawa et al., 2021a). The stereoselective formation of sialo side possessing a 3-deoxy-keto-pyranoside structure is extremely difficult since natural sialo side in *N*-glycan is in equatorial glycoside form, which can't be controlled by both anomeric effect and neighboring group participation when missing stereo-directing hydroxy group at 3-position of sialic acid. Scientists have applied chemical sialylation by effective stereoselective methodology including the effect of solvent (Kanie et al., 1988), the introduction of auxiliary at C3-position, functionality at C5-*N* and C1-*O* positions (for a recent review, see Vibhute et al., 2021), C4-*O*-,C5-*N*-oxazoline (Tanaka et al., 2020) and C1-*O*-,5-*N*-macrocyclic constrain (Komura et al., 2019) to the synthesis of the non-reducing terminal structure of *N*-glycan as well as cell surface glycolipid and polysialic acid structures. Ando's group designed bicyclic sialyl donors tethered by macrocycle formation between C1 and C5 to realize selectively α-sialylation in 2019, through constrained oxocarbenium ions, which could be applied to a wide range of substrates from simple aglycone to glycosyl acceptors, giving high yields and complete stereo control (Komura et al., 2019). In the recent example for *N*-glycan structure, 1-*O*-picolinyl-5-azido thiosialosides have been used as α-selective glycosyl donors followed by using a "latent-

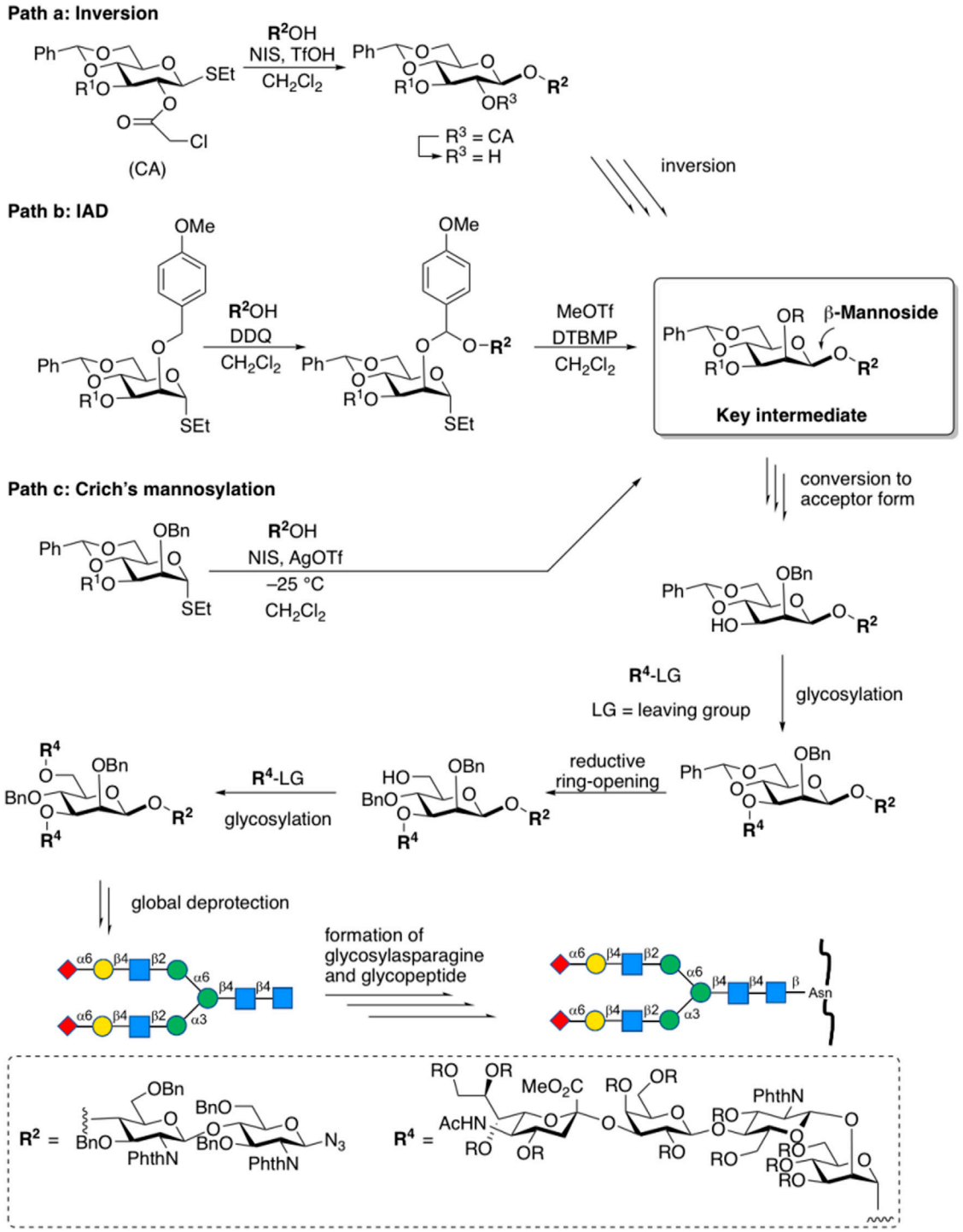

FIGURE 4 | Chemical strategies for the construction of β-d-mannosidic bonds in complex-type *N*-glycans.

active" protocol such as MPEP (*o*-(*p*-methoxyphenyl ethynyl) phenyl) glycosylation strategies for further elongation of reducing side residues (Chen et al., 2019).

The assembly strategy of glycans, in other words, by using existing glycosylation methods to construct complex-type glycan structures is another important part of glycochemistry. In 2009, Danishefsky et al. adopted a linear strategy to synthesize the I-type antenna sialylated *N*-glycans and coupled core heptasaccharide with mannose and fucose units (Wang et al., 2009), and Sun et al. recently reported the

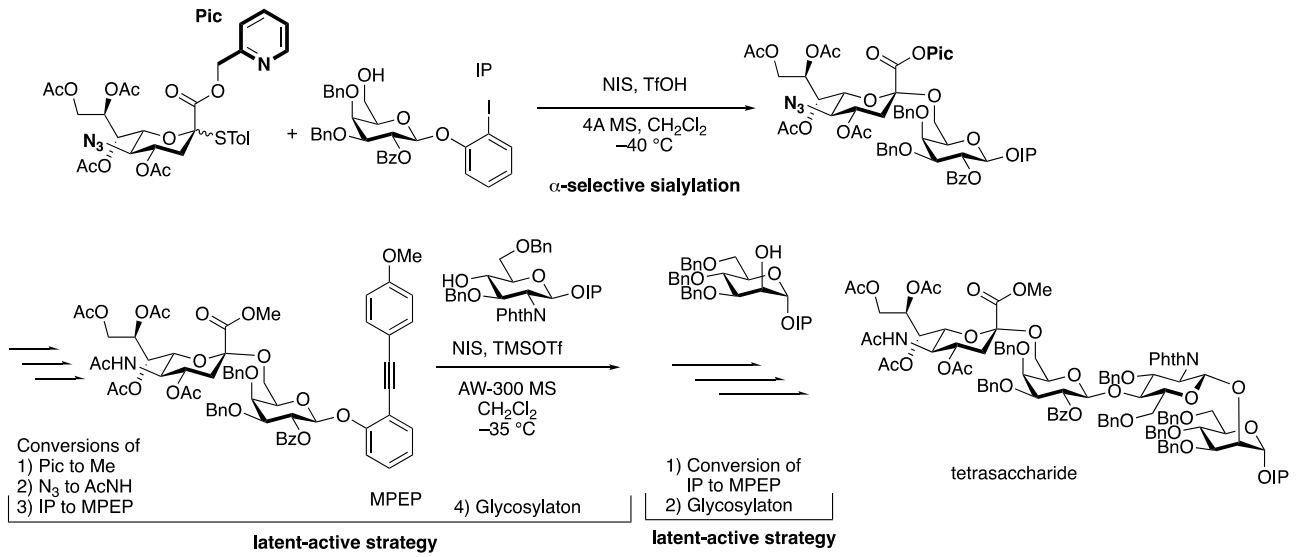

FIGURE 5 | α-Sialylation for α-2,6-linkage to galactose residue followed by latent-active strategies toward the synthesis of tetrasaccharide branch (type-I) in complex-type *N*-glycan.

linear strategy in fewer steps with higher selectivity (Chen et al., 2019) (**Figure 5**). On the other hand, Wang et al. developed a three-component one-pot synthetic strategy to assembly the core hyperbranched hexasaccharide of *N*-glycans linked to chloroviruses ATCV-1 using thioglycosides as building blocks, specifically attaching two xylose donors and a rhamnose donor to a trisaccharide, with regio- and stereo-selectivity (Wang Y. S. et al., 2019). Most recently, a convergent strategy was applied to synthesize the representative glycoform in homogeneous human E-cadherin *N*-linked glycopeptides containing a core tri- or tetra-saccharide and biantennary moiety, which attached the antennas to *N*-glycan by coupling glycosyl fluoride or thioglycoside donors with core oligosaccharide, and showed stereoselectivity controls (Zeng et al., 2020).

In 2019, the microfluidic systems combined with convergent synthetic routes had been applied to produce complex-type *N*-glycans (Manabe, 2019). In this strategy, glycosylated fragments are reproducibly obtained under strict control of reaction conditions by using microflow

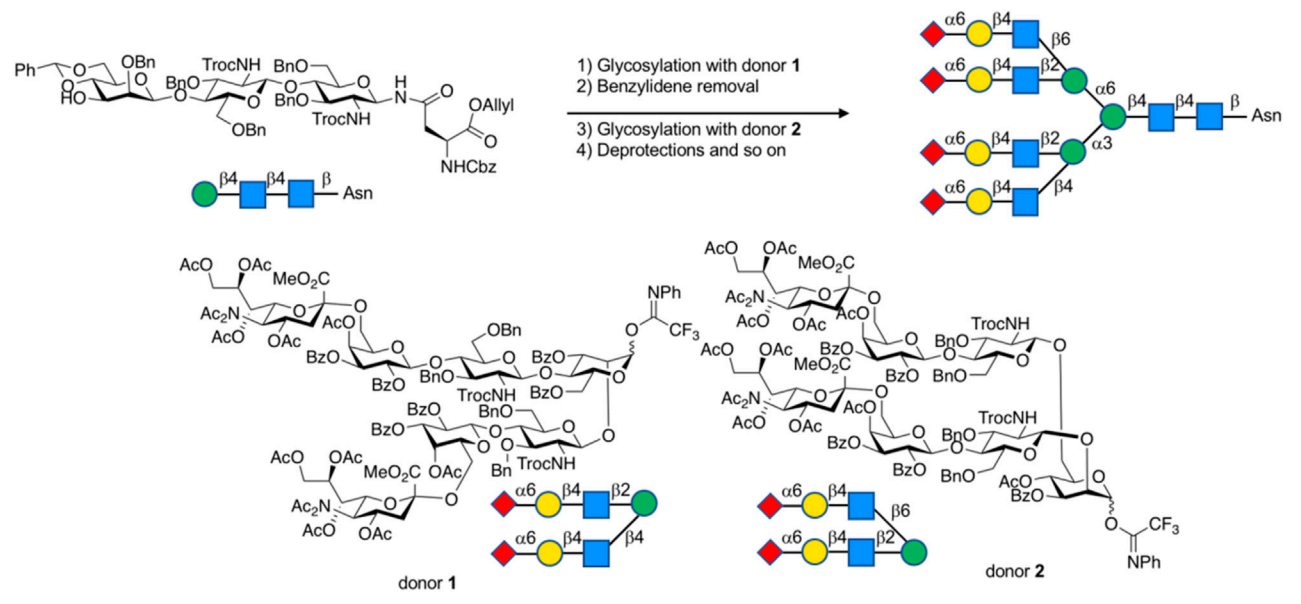

FIGURE 6 | Microfluidic assembly of complex-type *N*-glycans.

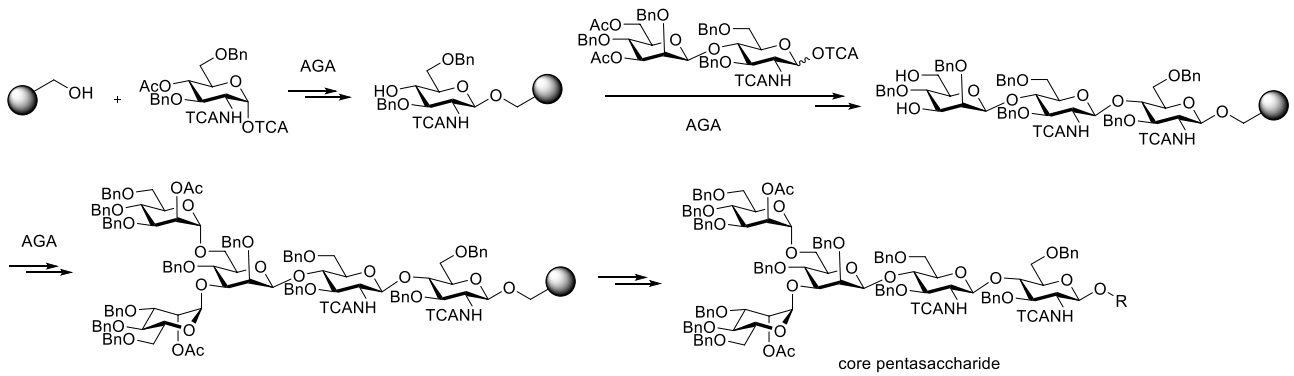

FIGURE 7 | Automated glycan assembly of core pentasaccharide present in complex-type *N*-glycans.

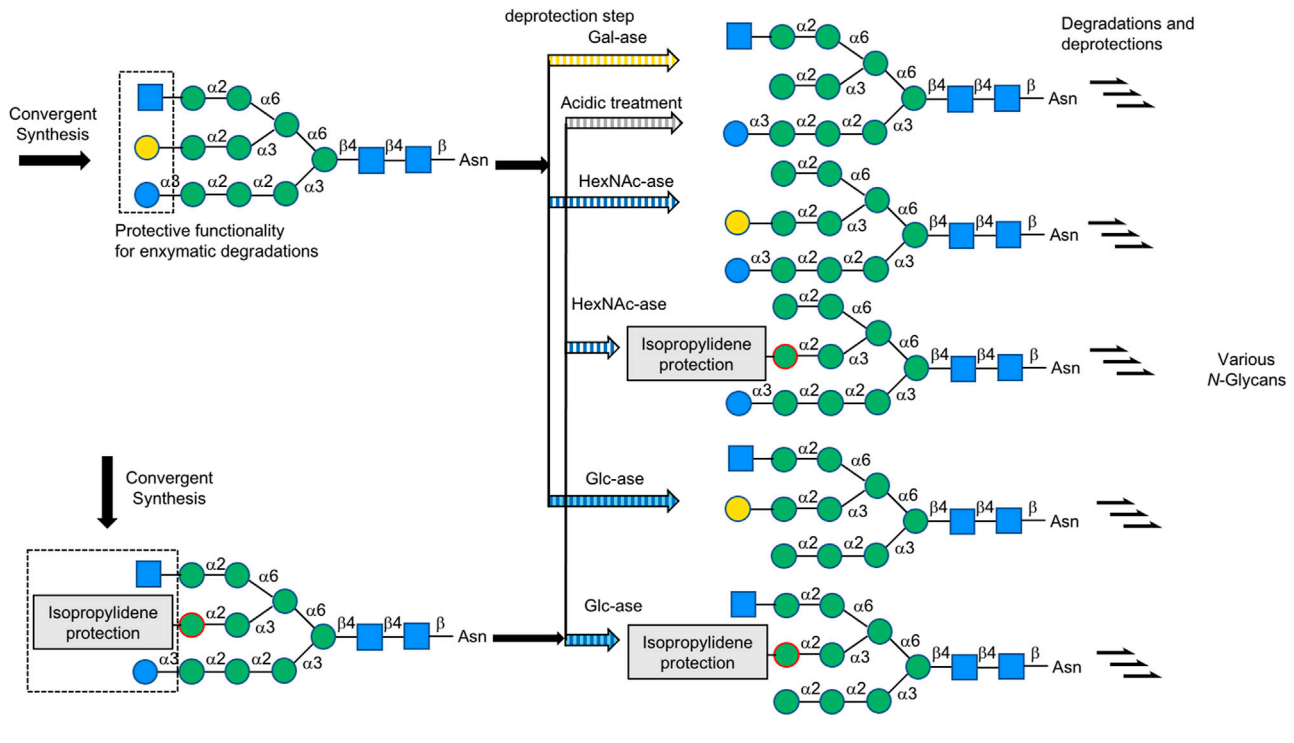

FIGURE 8 | Top to down strategy for complex-type *N*-glycans.

systems, followed by the assembly of fragments into desired oligosaccharide backbone structures through convergent synthetic routes. Overall, the synthesis of *N*-glycans could be accomplished in relatively short steps. The key to this strategy is how to achieve a satisfactory level of efficiency in glycosylation among less reactive large fragments. It shows that amide groups (NHAc) form intermolecular hydrogen bonds to reduce the reactivity. The glycosylation reactivity could be markedly improved by protecting them as imides (NAc_2) (Demchenko and Boons, 1998). A relatively high yield of the desired product can be achieved by using ether solvent for coordination stabilization of the oxocarbenium ion intermediate even in poorly reactive glycosylation. In addition, this strategy has successfully improved the stereoselectivity by carefully altering protection strategies. The strategy was applied to the synthesis of H antigen trisaccharide (Manabe, 2020) as well as 3- and 6-α-sialylated tetraantennary *N*-glycans for H1N1 neuraminidase recognition (Manabe, 2021) very recently (**Figure 6**).

The automated solid-phase strategy first reported in 2001 (Sabbavarapu Seeberger et al., 2001) has been applied to the *N*-glycan core structures (Le Mai Hoanget al., 2019) (**Figure 7**). As with the automated synthesis of peptides or nucleic acids, glycosyl acceptors are linked to resins via a connecting arm,

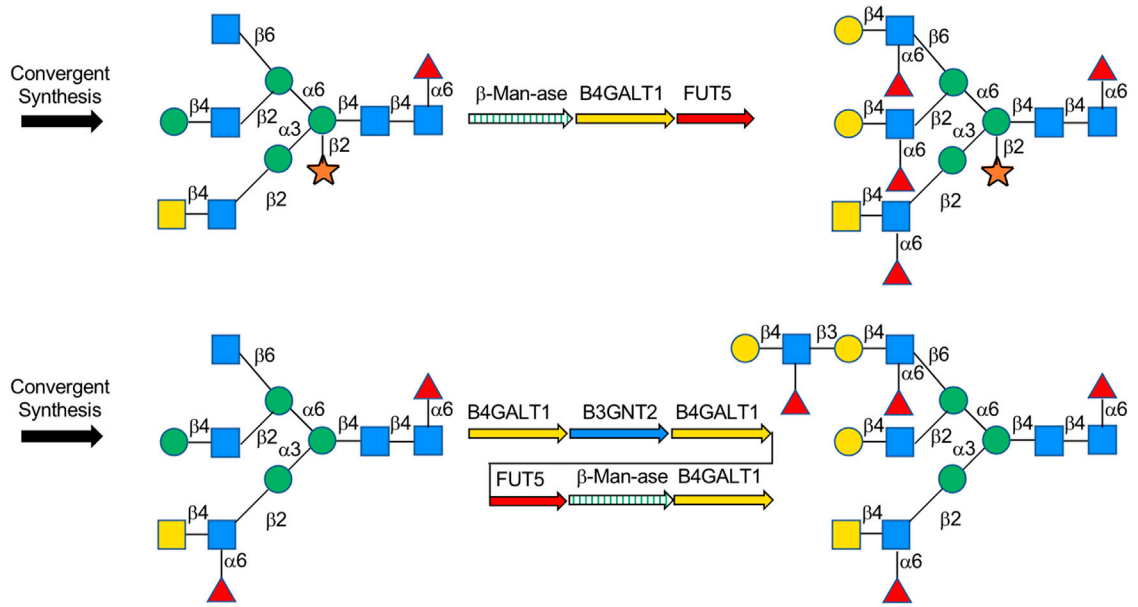

FIGURE 9 | Chemoenzymatic synthesis of complex-type *N*-glycans.

which is called a linker. Each desired linkage is completed by adding a glycosyl donor, and then the temporary protecting group has to be removed. The procedure is repeated and the solid support serves to keep the growing chain in a form that can be removed from the reaction mixture by filtration. The linker is disconnected upon completion of the synthesis. Finally, the fully assembled product is cut from the resin after purifying by simple filtration. Since donors in each step have overdosed, acceptors supported on resins could be completely glycosylated as far as possible, which leads to high overall efficiency in theory. Using this automated glycan assembly (AGA) strategy, the automatic synthesis has been applied to the chemical synthesis of core pentasaccharide of *N*-glycans, arabinomannan polysaccharides (Pardo-Vargas et al., 2019), chitooligosaccharides (Tyrikos-Ergas et al., 2021), galactofuranoses (Sabbavarapu and Seeberger, 2021) and starch and glycogen polysaccharides (Zhu et al., 2021).

Chemoenzymatic Strategies

Chemists have begun exploring the combination of biocatalytic and modern chemical methods to provide complex carbohydrates in a more efficient way since the 1990s. For example, Unverzagt reported the synthesis of a sialylated biantennary *N*-glycan in 2002 (Unverzagtet al., 2002). Such a chemoenzymatic approach not only shows the flexibility of chemical methods but also the high stereoselectivity and regioselectivity of enzymatic reactions. In general, there are two types of chemoenzymatic methods based on the sequence of reaction events. One starts from the chemical synthesis to generate substrate analogs for enzymatic extension, and the other is to apply enzymatic synthesis first before chemical diversification takes place. In the early stage, many studies focused on the chemoenzymatic synthesis of simple symmetrical *N*-glycans (recent review, see Chao et al., 2020; Li and Wang, 2018).

Top-Down Strategy From Synthetic Large Glycan (One Large Precursor) Using Glycosidases

In 2013, Ito's group first reported a "top-down" chemoenzymatic strategy to construct a high-mannose type *N*-glycan library from a designed precursor, a tetradecasaccharide modified with Glc, Gal, and GlcNAc terminal sugar residues, followed by trimming this precursor into a variety of high-mannose type glycans by glycosidases. For instance, D-glucose moiety was removed by glucosidase II and D-galactose by β-galactosidase, while *N*-acetyl-D-glucosamine was removed by β-HexNAc'ase (Koizumi et al., 2013) (**Figure 8**). They then developed the second generation precursor in 2016, substituted acetal protecting group directly on Mannose residue instead of Gal protection in that branch, due to the difficulty of galactosidase digestion (Fujikawa et al., 2016). So far, this strategy has been employed in the synthesis of high-mannose type *N*-glycans. Wang et al. also applied a top-down strategy starting from Soybean flour $Man_9GlcNAc_2Asn$ and Hen egg yolk sialylglycopeptide (SGP) to high-mannose and complex-type *N*-glycans (Wang Y. S. et al., 2019).

Elongation and Branching Strategy From Synthetic Small Glycan Using Glycosyltransferases

A lot of explorations have been done by Boons on the chemoenzymatic synthesis of complex-type *N*-glycans. In his previous explorations, Boons developed a common glycan precursor first by using modern chemical methods, followed

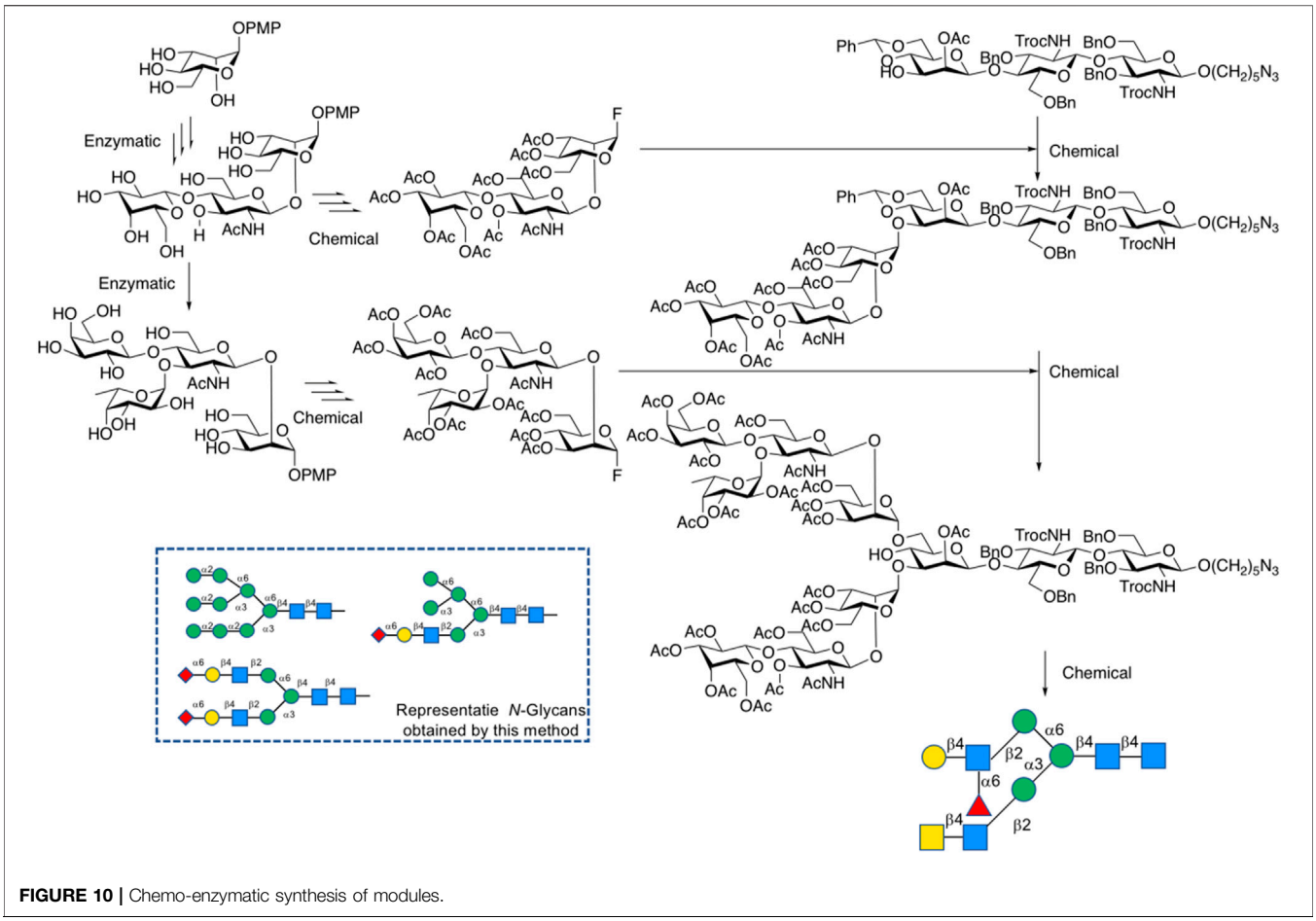

FIGURE 10 | Chemo-enzymatic synthesis of modules.

FIGURE 11 | Asymmetric glycan common-substrate (AGCS).

by the enzymatic extension of elongation and branching of *N*-glycans. For example, in 2013, a general strategy for chemoenzymatic synthesis of asymmetrically branched *N*-glycans was reported, and 14 tri-antennary *N*-glycans were obtained. In this strategy, the precursor decasaccharide was prepared from the core pentasaccharide that at potential branching positions was modified by orthogonal protecting groups and then modified branch-specifically by glycosyltransferases (Wang et al., 2013). Recently, Boons' group synthesized *N*-glycan heptasaccharide precursors of the Parasite *Schistosoma mansoni* by chemical glycosylation method, achieved xylose modification by β-1,2-xylosyltransferase XYLT, and transferred to multi-antennary glycans enzymatically via β-Man-ase, B4GalT1 and FUT5 (Srivastava et al., 2021) (**Figure 9**). Weiss et al. also applied the synthesis of the rare biantennary *N*-glycans with Gal-β1,4-linked bisecting GlcNAc motif found in IgG by using a chemical modular approach to assemble the core bisected *N*-glycans followed by simple enzymatic antenna modifications with β1,4-galactosyltransferase (Weiss et al., 2020). A previous application of this strategy was also shown in order to obtain various *N*-glycan structures including Neu5Ac/Gc and core-fucoses. It features the initial convergent chemical

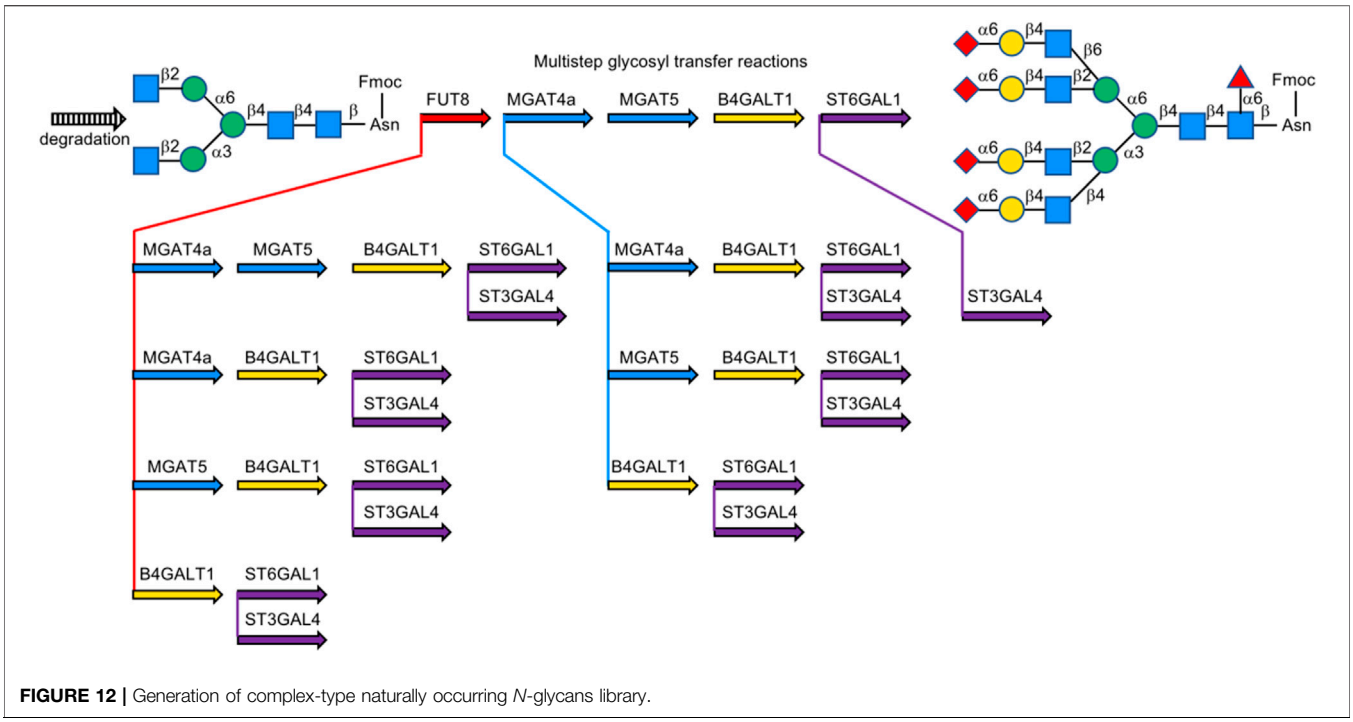

FIGURE 12 | Generation of complex-type naturally occurring *N*-glycans library.

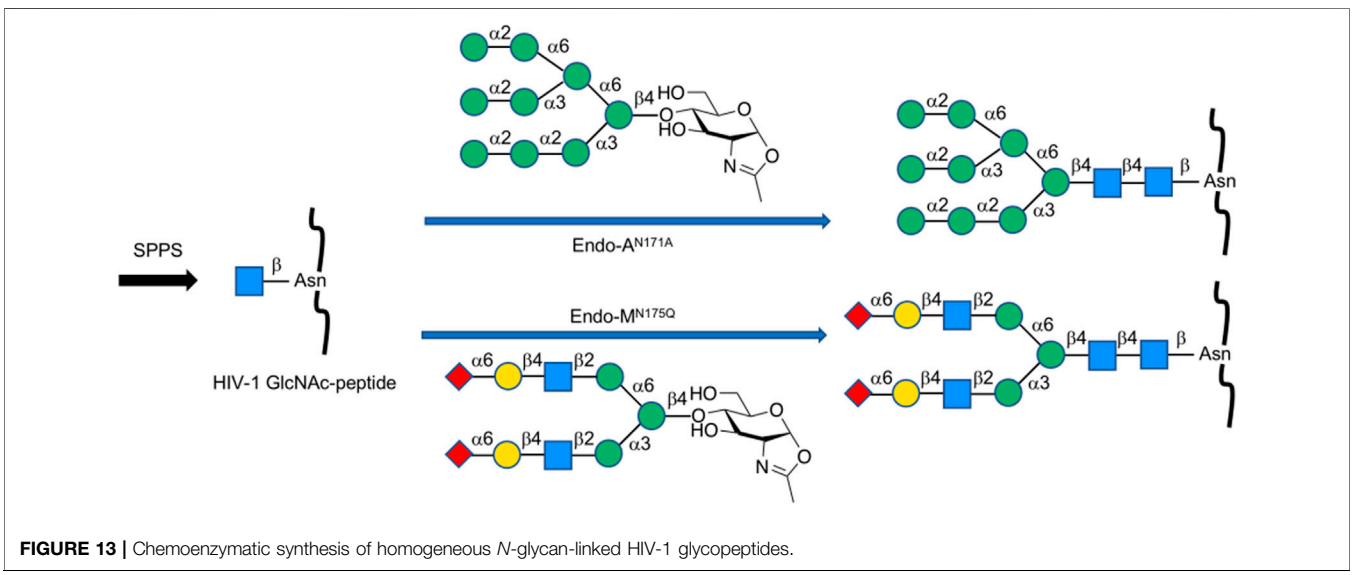

FIGURE 13 | Chemoenzymatic synthesis of homogeneous *N*-glycan-linked HIV-1 glycopeptides.

assembly of core oligosaccharide precursors and following enzymatic extension catalyzed by an alternative combination of four robust glycosyltransferases, PmST1m, Hpα1,3FT, B4GALT1, and Pd2,6ST, to yield a library of complex-type *N*-glycans. (Li et al., 2015).

Shivatare et al. prepared *N*-glycans of hybrid, high-mannose, and complex types for microarray and binding analysis of HIV antibodies first by chemical glycosylation to obtain building blocks, followed by a modular chemoenzymatic strategy to add antennas using various glycosyltransferases including β-1,4-galactosyltransferases, α-2,3/2,6-sialyltransferases and α-1,3/1,2-fucosyltransferases (Shivatare et al., 2016) (**Figure 10**).

Pawar et al. constructed *N*-glycan libraries by synthesizing oligosaccharide building blocks chemically in Asymmetric Glycan as Common-substrate Strategy (AGCS), followed by introducing fucose and sialic motifs to core structures via glycosyltransferases FUT, α-2,3-STGal, or α-2,6-STGal (Pawar et al., 2020) (**Figure 11**).

Cummings et al. enzymatically generated a multi-antennary oligosaccharide library containing 32 complex-type *N*-glycans from a natural source, in which recombinant glycosyltransferases (B4GALT1, ST3GAL4, ST6GAL1, MGAT, and FUT8) were used

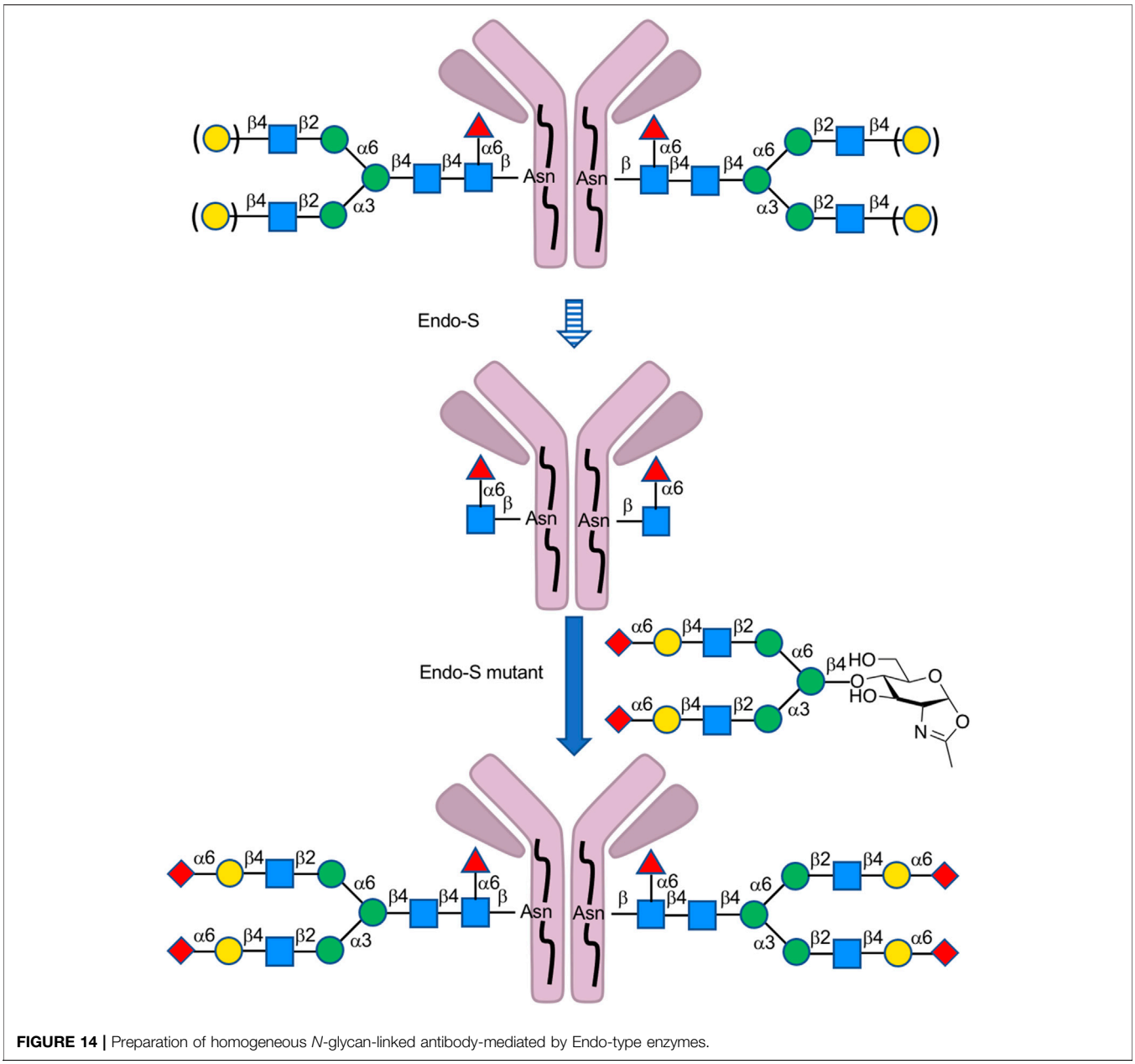

FIGURE 14 | Preparation of homogeneous *N*-glycan-linked antibody-mediated by Endo-type enzymes.

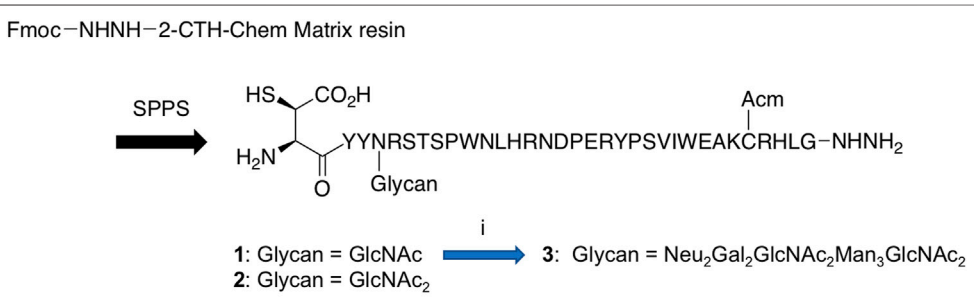

FIGURE 15 | Preparation of IL-17A glycopeptides.

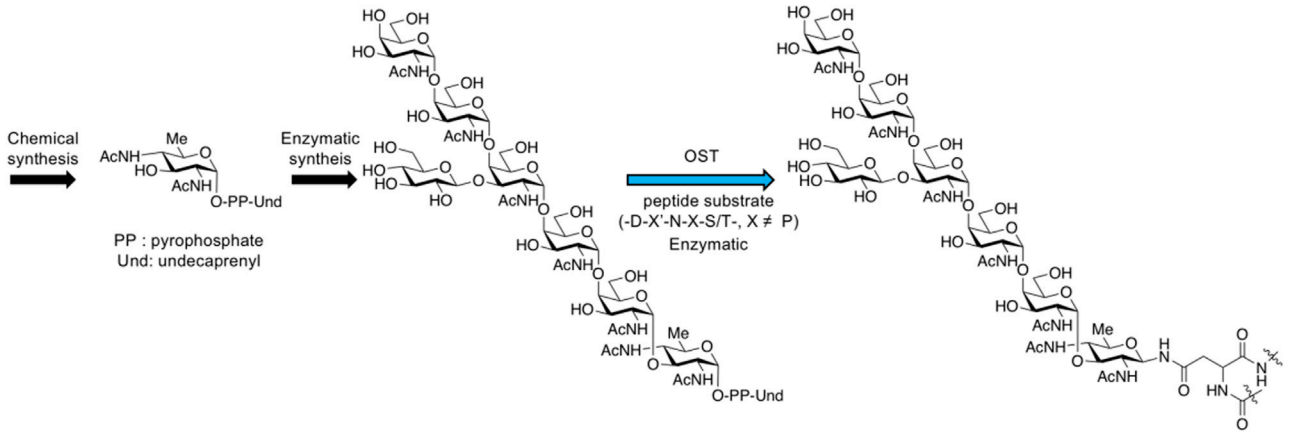

FIGURE 16 | *N*-glycan synthesis through bacterial biosynthesis including oligosaccharyltransferase reaction.

to expand synthesis from a precursor. Desired sialylated, fucosylated, and mannosylated terminal modifications and branching were realized on a biantennary GlcNAc-terminated structure (Gao et al., 2019) (**Figure 12**).

Strategy Using Endo-Type Enzymes and Mutants

Endo-β-*N*-acetylglucosaminidases, known as endo-type enzymes of wild types and mutants, are often used in the synthesis of *N*-linked glycopeptides, which perform activities of deglycosylation by breaking between GlcNAcs in *N*-linked chitobiosemoiety, and transglycosylation to GlcNAc-linked peptides. These enzymes are found in a wide range of species, such as Endo-A from *Arthrobacter*, Endo-M from *Mucor hiemalis,* and Endo-S from *Streptococcus pyogenes*. Since endo-α-*N*-acetylglucosaminidases are only specific to *O*-glycans, endo-β-*N*-acetylglucosaminidases (ENGases) are considered the main endo-type to prepare homogeneous *N*-linked glycoprotein. For the transfer of oligosaccharides back to the cleaved structure, the mutants mostly use glycan oxazolines as donor substrates and have stereoselective control on substrates. Recently, Wang et al. applied this procedure to synthesize HIV-1 glycopeptides through the preparation of GlcNAc-peptide precursor by using solid-phase peptide synthesis (SPPS) and followed by the connection of *N*-glycan to the precursor using the *N*-glycan oxazoline donor via endo-glycosidase (Endo-A or Endo-M) mutant catalysis (Zong et al., 2020) (**Figure 13**). They also reported recombinant Endo-S and mutants that proceeded deglycosylation to convert structurally heterogeneous sugar chains to GlcNAc-IgG acceptor and remodeling to homogeneously *N*-glycosylated Fc fragments on rituximab (Wang L.-X. et al., 2019) (**Figure 14**). Dong et al. introduced *N*-linked oligosaccharides including GlcNAc or $GlcNAc_2$ by chemical glycosylation with asparagine residue on peptide precursor as well as complex-type sialyl *N*-glycan by transfer using Endo-M mutant onto IL-17A peptide (Li H. et al., 2021) (**Figure 15**). It is notable as another previous example of this strategy that the chemo-enzymatic synthesis of *N*-glycopeptide structural motif of haptoglobin glycopeptides had been achieved by a total chemical synthesis of the highly branched oligosaccharide oxazoline donors through fragment couplings and an alternative wild-type Endo A-catalyzed transglycosylation of the oxazolines in the presence of bisecting GlcNAc to GlcNAc-introduced haptoglobin glycopeptide fragment (Yang et al., 2018). Interestingly, wild-type Endo A could be also applicable to the preparation of an *N*-linked glycoprotein that contains M6P-terminated glycans catalysis for the treatment of lysosomal storage disorders (LSDs) (Priyanka, et al., 2016).

OST Strategy

Oligosaccharyltransferases (OST) usually exist in prokaryotes (bacteria and archaea) and eukaryotes in the form of complex, playing a key role in *N*-glycosylation, with the catalysis of transferring oligosaccharide chains onto protein substrates. Single subunit OST was found in the bacterial pathway of glycoprotein biosynthesis, such as PglB from *Campylobacter jejuni* (Wacker et al., 2002; Deshpande et al., 2008; Lizak et al., 2011; Jinnelov et al., 2017; Poljak et al., 2017; Mohanty et al., 2020; Schjoldager et al., 2020) and TbSTT3A from *Trypanosoma brucei* for *N*-glycan (Wilson et al., 2021). The archaeal pathway also includes the single subunit OST such as AglB (Meyer and Albers, 2014; recent review, see Eichler, 2020), whose X-ray structure from *Archaeoglobusfulgidus* has been reported very recently (Taguchi et al., 2021). The most studied PglB can transfer the highly conserved heptasaccharide composed of $GalNAc_5Glc_1Bac_1$ (Bac: bacillosamine, 2,4-acetamide-2.4.6-trideoxy-D-glucose) to proteins in the periplasm of *C. jejuni*. Chemical and enzymatic synthesis of *N*-glycans and glycopeptide synthesis using OST have been already reported (Glover et al., 2005; Amin et al., 2007; Lee et al., 2009; Lukose et al., 2015; Ishiwata et al., 2015) (**Figure 16**).

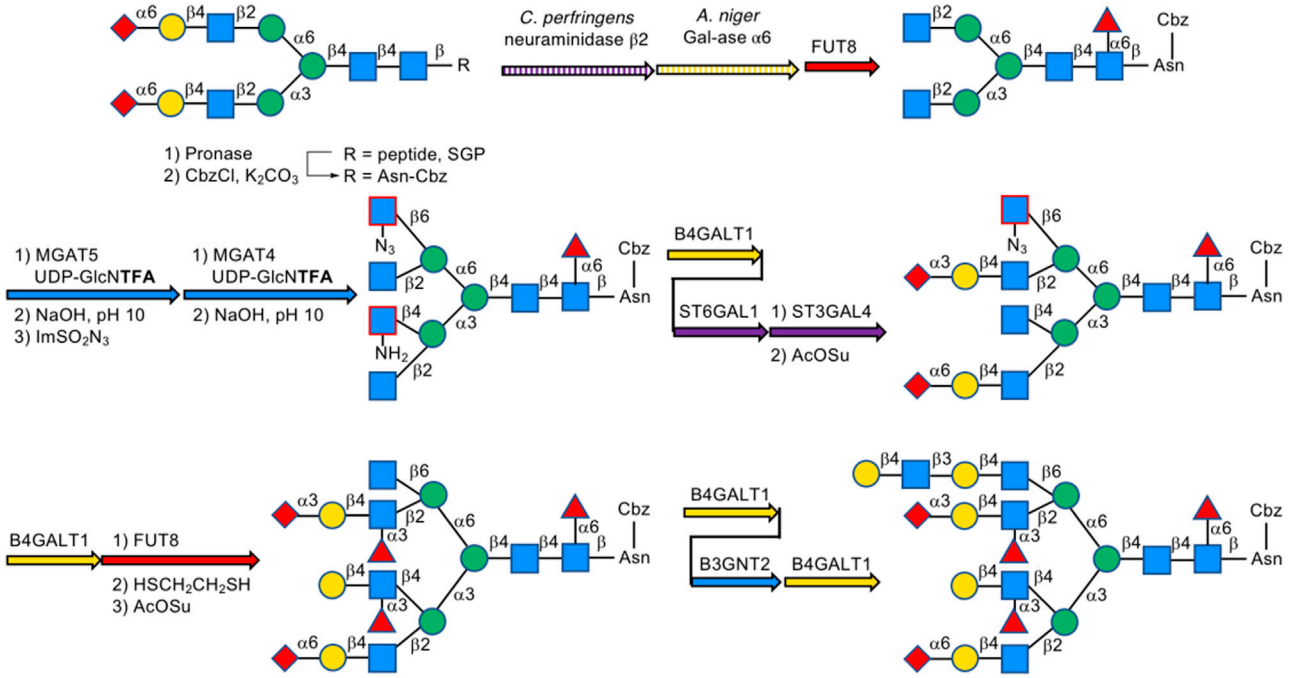

FIGURE 17 | Stop and Go strategy for multi-antennary *N*-glycans; For MGAT4/5&B3GNT2, B4GALT1, FUT8, and ST3/6GAL1/4, UDP-GlcNAc, UDP-Gal, GDP-Fuc, and CMP-Neu5Ac were used as the donor, respectively, unless otherwise noted.

In humans, mutations of gene encoding OST complex may cause some diseases, like congenital disorders of glycosylation (CDGs) (Ganetzky et al., 2017), making OST an important enzyme for human glycosyl transfer to maintain normal physiological functions, but there are no examples for using mammalian OST complex to produce the good quantity of *N*-glycoprotein effectively (Kay et al., 2019).

Enzymatic and Chemoenzymatic Strategy From Natural Resources (such as SGP) Using Glycosidases With/Without Glycosyltransferases

Chemical synthesis of precursors for enzymatic modification is still not efficient enough because it often requires many steps including cumbersome protection/deprotection, resulting in product loss, and hindering the preparation of various types of asymmetric *N*-glycans. Researchers have discovered starting materials from natural sources, such as sialylglycopeptide (SGP), and have greatly optimized the isolation method for gram quantities of homogeneous SGP from commercially available egg yolk powder. Hamilton et al. generated a library containing complex-type asymmetric and multi-antennary *N*-glycans for microarray analysis, by deglycosylation of biosynthetic precursor glycoproteins and lipid-linked oligosaccharides from natural sources (yeast- and bacteria-derived precursors) and structurally remodeling by GnTI, GnTII, and GnTIV as well as the following early mammalian glycosylation pathway (Hamilton et al., 2017). Wang et al. reported chemoenzymatic strategy on natural *N*-glycans from soybean flour and SGP from egg yolks and trimmed enzymatically by α-mannosidases to generate high-mannose glycan library also for microarray analysis (Toonstra et al., 2018).

In 2019, Boons et al. described a biomimetic strategy called Stop and Go strategy, in which SGP can be converted through degradations and glycosyl transfer reactions including the introduction of nonreactive chemically modified residue and its chemical modifications to activate form from unreactive one and further enzymatic steps into multi-antennary *N*-glycans that at each arm can be uniquely extended by glycosyltransferases to obtain highly complex asymmetrically branched *N*-glycans. By using this strategy, Boons has successfully accomplished the chemoenzymatic synthesis of several complex-type *N*-glycans found in human pathological tissues, like bi-antennary *N*-glycans observed on ovarian cancer cell lines as well as tetra-antennary *N*-glycans observed on human cytolytic T lymphocytes (Liu et al., 2019) (**Figure 17**).

In 2021, Wang et al. prepared the complex-type asialo-nonasaccharide of SARS-Cov-2 Spike Receptor-Binding Domain (RBD) using Boon's reported enzymatically trimming approach on SGP in 2017, after enzymolysis of neuraminidase and pronase to remove Neu5Ac and peptide, followed by transferring into glycosyl amine under Kochetkov amination condition and coupling with an acid group of RBD peptide fragment (Ye et al., 2021).

CONCLUDING REMARKS

Most of the human cell surface and secreted proteins are modified by complex-type *N*-glycans, which not only affect the structure and function of proteins but also participate in the signal transduction of tumor cells. In the field of biomedical applications, complex-type *N*-glycans and their glycoconjugates show broad prospects, such as anti-tumor kits and vaccines. However, unlike other important biopolymers such as DNA/RNA and proteins, the biosynthesis of glycans is neither driven by templates nor genetically encoded. This biosynthetic nature of *N*-glycan as a secondary metabolite leads directly to the micro-heterogeneity of the naturally obtained glycans, which means that it is difficult to obtain enough homogeneous complex-type *N*-glycans by means of separation and isolation. In order to learn more about the properties of *N*-linked glycopeptides and use them in the production of peptide vaccines, it is necessary to develop a universal and efficient method to prepare homogeneous *N*-glycans in addition to further optimization of purification methods from natural sources. Over the past few decades, researchers have made lots of efforts for the chemical and chemoenzymatic strategies for well-defined *N*-glycans. Though great progress has been made, there are still problems and difficulties to be solved urgently, which requires researchers to explore continuously in this field as the recent examples are shown here. Further improving efficiency and simplifying procedures are quite significant.

AUTHOR CONTRIBUTIONS

XZ, YH, AI, and FD wrote sections of the manuscript. All authors contributed to manuscript revision, read, and approved the submitted version.

FUNDING

This work was supported partly by the Fundamental Research Funds for the Central Universities (No. 31610011 to FD), the province natural science fund of Guangdong (No. 42030015 to FD; No. 2022A1515011109 to HC), the Sun Yat-sen University Startup fund (No.18841224 to FD) for financial support, and the grant-in-Aid for Specially Promoted Research (No. 16H06290 to YI and AI) and Scientific Research (no. 18K05345 and 19H00929 to AI) from the Japan Society for the Promotion of Science.

REFERENCES

Amin, M. N., Ishiwata, A., and Ito, Y. (2007). Synthesis of N-Linked Glycan Derived from Gram-Negative Bacterium, Campylobacter Jejuni. *Tetrahedron* 63, 8181–8198. doi:10.1016/j.tet.2007.05.126

Barresi, F., and Hindsgaul, O. (1991). Synthesis of .beta.-mannopyranosides by Intramolecular Aglycon Delivery. *J. Am. Chem. Soc.* 113, 9376–9377. doi:10.1021/ja00024a057

Buettner, M. J., Shah, S. R., Saeui, C. T., Ariss, R., and Yarema, K. J. (2018). Improving Immunotherapy through Glycodesign. *Front. Immunol.* 9, 2485. doi:10.3389/fimmu.2018.02485

Chao, Q., Ding, Y., Chen, Z.-H., Xiang, M.-H., Wang, N., and Gao, X.-D. (2020). Recent Progress in Chemo-Enzymatic Methods for the Synthesis of *N*-Glycans. *Front. Chem.* 8, 513. doi:10.3389/fchem.2020.00513

Chen, J., Hansen, T., Zhang, Q. J., Liu, D. Y., Sun, Y., Yan, H., et al. (2019). 1-Picolinyl-5-azido Thiosialosides: Versatile Donors for the Stereoselective Construction of Sialyl Linkages. *Angew. Chem. Int. Ed.* 58, 17000–17008. doi:10.1002/anie.201909177

Crich, D., and Sun, S. (1996). Formation of β-Mannopyranosides of Primary Alcohols Using the Sulfoxide Method. *J. Org. Chem.* 61, 4506–4507. doi:10.1021/jo9606517

Danishefsky, S. J., and Bilodeau, M. T. (1996). Glycals in Organic Synthesis: The Evolution of Comprehensive Strategies for the Assembly of Oligosaccharides and Glycoconjugates of Biological Consequence. *Angew. Chem. Int. Ed. Engl.* 35, 1380–1419. doi:10.1002/anie.199613801

Demchenko, A. V., and Boons, G.-J. (1998). A Novel and Versatile Glycosyl Donor for the Preparation of Glycosides of *N*-Acetylneuraminic Acid. *Tetrahedron Lett.* 39, 3065–3068. doi:10.1016/s0040-4039(98)00359-1

Deshpande, N., Wilkins, M. R., Packer, N., and Nevalainen, H. (2008). Protein Glycosylation Pathways in *Filamentous Fungi*. *Glycobiology* 18, 626–637. doi:10.1271/bbb.7008010.1093/glycob/cwn044

Ding, F., Ishiwata, A., and Ito, Y. (2018). Stereodivergent Mannosylation Using 2-O-(ortho-Tosylamido)benzyl Group. *Org. Lett.* 20, 4833–4837. doi:10.1021/acs.orglett.8b01979

Eichler, J. (2020). N-glycosylation in Archaea-New Roles for an Ancient Posttranslational Modification. *Mol. Microbiol.* 114, 735–741. doi:10.1111/mmi.14569

Fugedi, P., Garegg, P. J., Lunn, H., and Norberg, T. (1987). Thioglycosides as Glycosylating Agents in Oligosaccharide Synthesis. *Glycoconjugate J.* 4, 97–108. doi:10.1007/BF01049447

Fujikawa, K., Seko, A., Takeda, Y., and Ito, Y. (2016). Approaches toward High-mannose-type Glycan Libraries. *Chem. Rec.* 16, 35–46. doi:10.1002/tcr.201500222

Ganetzky, R., Reynoso, F. J., and He, M. (2017). Congenital Disorders of Glycosylation. Biomarkers in Inborn Errors of Metabolism. *Chapter* 15, 343–360. doi:10.1016/B978-0-12-802896-4.00014-6, ,

Gao, C., Hanes, M. S., Byrd-Leotis, L. A., Wei, M., Jia, N., Kardish, R. J., et al. (2019). Unique Binding Specificities of Proteins toward Isomeric Asparagine-Linked Glycans. *Cel Chem. Biol.* 26, 535–547. doi:10.1016/j.chembiol.2019.01.002

Garcia, B. A., and Gin, D. Y. (2000). Dehydrative Glycosylation with Activated Diphenyl Sulfonium Reagents. Scope, Mode of C(1)-Hemiacetal Activation, and Detection of Reactive Glycosyl Intermediates. *J. Am. Chem. Soc.* 122, 4269–4279. doi:10.1021/ja993595a

Glover, K. J., Weerapana, E., and Imperiali, B. (2005). *In Vitro* assembly of the Undecaprenylpyrophosphate-Linked Heptasaccharide for Prokaryotic *N*-Linked Glycosylation. *Proc. Natl. Acad. Sci. U.S.A.* 102, 14255–14259. doi:10.1073/pnas.0507311102

Hamilton, B. S., Wilson, J. D., Shumakovich, M. A., Fisher, A. C., Brooks, J. C., Pontes, A., et al. (2017). A Library of Chemically Defined Human N-Glycans Synthesized from Microbial Oligosaccharide Precursors. *Sci. Rep.* 7 (1), 15907. doi:10.1038/s41598-017-15891-8

Ishii, N., Ogiwara, K., Sano, K., Kumada, J., Yamamoto, K., Matsuzaki, Y., et al. (2018). Specificity of Donor Structures for Endo -β-N -Acetylglucosaminidase-Catalyzed Transglycosylation Reactions. *ChemBioChem* 19, 136–141. doi:10.1002/cbic.201700506

Ishiwata, A., Munemura, Y., and Ito, Y. (2008). NAP Ether Mediated Intramolecular Aglycon Delivery: A Unified Strategy for 1,2-*Cis*-Glycosylation. *Eur. J. Org. Chem.* 2008, 4250–4263. doi:10.1002/ejoc.200800249

Ishiwata, A., Taguchi, Y., Lee, Y. J., Watanabe, T., KohdaIto, D. Y., and Ito, Y. (2015). N-glycosylation with Synthetic Undecaprenyl Pyrophosphate-Linked Oligosaccharide to Oligopeptides by PglB Oligosaccharyltransferase fromCampylobacter Jejuni. *ChemBioChem* 16, 731–737. doi:10.1002/cbic.201402658

Jinnelov, A., Ali, L., Tinti, M., Güther, M. L. S., and Ferguson, M. A. J. (2017). Single-subunit Oligosaccharyltransferases of *Trypanosoma Brucei* Display Different and Predictable Peptide Acceptor Specificities. *J. Biol. Chem.* 292, 20328–20341. doi:10.1074/jbc.M117.810945

Kanie, O., Kiso, M., and Hasegawa, A. (1988). Glycosylation Using Methylthioglycosides ofN-Acetylneuraminic Acid and Dimethyl(Methylthio) Sulfonium Triflate. *J. Carbohydr. Chem.* 7, 501–506. doi:10.1080/07328308808058938

Kay, E., Cuccui, J., and Wren, B. W. (2019). Recent Advances in the Production of Recombinant Glycoconjugate Vaccines. *npj Vaccin.* 4, 16. doi:10.1038/s41541-019-0110-z

Koenigs, W., and Knorr, E. (1901). Ueber einige Derivate des Traubenzuckers und der Galactose. *Ber. Dtsch. Chem. Ges.* 34, 957–981. doi:10.1002/cber.190103401162

Koizumi, A., Matsuo, I., Takatani, M., Seko, A., Hachisu, M., Takeda, Y., et al. (2013). Top-Down Chemoenzymatic Approach to a High-mannose-type Glycan Library: Synthesis of a Common Precursor and its Enzymatic Trimming. *Angew. Chem. Int. Ed.* 52, 7426–7431. doi:10.1002/anie.201301613

Komura, N., Kato, K., Udagawa, T., Asano, S., Tanaka, H.-N., Imamura, A., et al. (2019). Constrained Sialic Acid Donors Enable Selective Synthesis of α-glycosides. *Science* 364, 677–680. doi:10.1126/science.aaw4866

Le Mai Hoang, K., Pardo-Vargas, A., Zhu, Y., Yu, Y., Loria, M., Delbianco, M., et al. (2019). Traceless Photolabile Linker Expedites the Chemical Synthesis of Complex Oligosaccharides by Automated Glycan Assembly. *J. Am. Chem. Soc.* 141, 9079–9086. doi:10.1021/jacs.9b03769

Lee, Y. J., Ishiwata, A., and Ito, Y. (2009). Synthesis of Undecaprenyl Pyrophosphate-Linked Glycans as Donor Substrates for Bacterial Protein N-Glycosylation. *Tetrahedron* 65, 6310–6319. doi:10.1016/j.tet.2009.06.032

Li, C., and Wang, L.-X. (2018). Chemoenzymatic Methods for the Synthesis of Glycoproteins. *Chem. Rev.* 118 (17), 8359–8413. doi:10.1021/acs.chemrev.8b00238

Li, H., Zhang, J., An, C., and Dong, S. (2021). Probing *N*-Glycan Functions in Human Interleukin-17A Based on Chemically Synthesized Homogeneous Glycoforms. *J. Am. Chem. Soc.* 143, 2846–2856. doi:10.1021/jacs.0c12448

Li, L., Liu, Y., Ma, C., Qu, J., Calderon, A. D., Wu, B., et al. (2015). Efficient Chemoenzymatic Synthesis of an N-Glycan Isomer Library. *Chem. Sci.* 6 (10), 5652–5661. doi:10.1039/C5SC02025E

Liu, L., Prudden, A. R., Capicciotti, C. J., Bosman, G. P., Yang, J.-Y., Chapla, D. G., et al. (2019). Streamlining the Chemoenzymatic Synthesis of Complex *N*-Glycans by a Stop and Go Strategy. *Nat. Chem* 11, 161–169. doi:10.1038/s41557-018-0188-3

Lizak, C., Gerber, S., Numao, S., Aebi, M., and Locher, K. P. (2011). X-ray Structure of a Bacterial Oligosaccharyltransferase. *Nature* 474, 350–355. doi:10.1038/nature10151

Lukose, V., Whitworth, G., Guan, Z., and Imperiali, B. (2015). Chemoenzymatic Assembly of Bacterial Glycoconjugates for Site-specific Orthogonal Labeling. *J. Am. Chem. Soc.* 137, 12446–12449. doi:10.1021/jacs.5b07146

Maki, Y., Mima, T., Okamoto, R., Izumi, M., and Kajihara, Y. (2017). Semisynthesis of Complex-type Biantennary Oligosaccharides Containing Lactosamine Repeating Units from a Biantennary Oligosaccharide Isolated from a Natural Source. *J. Org. Chem.* 83, 443–451. doi:10.1021/acs.joc.7b02485

Maki, Y., Okamoto, R., Izumi, M., and Kajihara, Y. (2020). Chemical Synthesis of an Erythropoietin Glycoform Having a Triantennary N-Glycan: Significant Change of Biological Activity of Glycoprotein by Addition of a Small Molecular Weight Trisaccharide. *J. Am. Chem. Soc.* 142, 20671–20679. doi:10.1021/jacs.0c08719

Manabe, Y. (2019). Efficient Syntheses of Complex-type N-Glycans Using Microflow Systems and Convergent Synthetic Routes. *Tigg* 31, E99–E108. doi:10.4052/tigg.1768.1E

Matsuo, I., Isomura, M., and Ajisaka, K. (1999). Synthesis of an Asparagine-Linked Core Pentasaccharide by Means of Simultaneous Inversion Reactions. *J. Carbohydr. Chem.* 18, 841–850. doi:10.1080/07328309908544039

Matsuura, F., Ohta, M., Murakami, K., and Matsuki, Y. (1993). Structures of Asparagine Linked Oligosaccharides of Immunoglobulins (IgY) Isolated from Egg-Yolk of Japanese Quail. *Glycoconjugate J.* 10, 202–213. doi:10.1007/BF00702201

Meyer, B. H., and Albers, S. V. (2014). AglB, Catalyzing the Oligosaccharyl Transferase Step of the archaealN-glycosylation Process, Is Essential in the Thermoacidophilic crenarchaeonSulfolobus Acidocaldarius. *Microbiologyopen* 3, 531–543. doi:10.1002/mbo3.185

Michael, A., and Norton, L. (1879). On the Action of Iodine Monochloride Upon Aromatic Amines. *J. Am. Chem. Soc.* 1 (11), 484–485. doi:10.1021/ja02151a603

Mohanty, S., P Chaudhary, B., and Zoetewey, D. (2020). Structural Insight into the Mechanism of *N*-Linked Glycosylation by Oligosaccharyltransferase. *Biomolecules* 10, 624. doi:10.3390/biom10040624

Nashida, J., Nishi, N., Takahashi, Y., Hayashi, C., Igarashi, M., Takahashi, D., et al. (2018). Systematic and Stereoselective Total Synthesis of Mannosylerythritol Lipids and Evaluation of Their Antibacterial Activity. *J. Org. Chem.* 83, 7281–7289. doi:10.1021/acs.joc.8b00032

Pardo-Vargas, A., Bharate, P., Delbianco, M., and Seeberger, P. H. (2019). Automated Glycan Assembly of Arabinomannan Oligosaccharides from *Mycobacterium tuberculosis*. *Beilstein J. Org. Chem.* 15, 2936–2940. doi:10.3762/bjoc.15.288

Pawar, S., Hsu, L., Narendar Reddy, T., Ravinder, M., Ren, C.-T., Lin, Y.-W., et al. (2020). Synthesis of Asymmetric *N*-Glycans as Common Core Substrates for Structural Diversification through Selective Enzymatic Glycosylation. *ACS Chem. Biol.* 15, 2382–2394. doi:10.1021/acschembio.0c00359

Plante, O. J., Palmacci, E. R., Andrade, R. B., and Seeberger, P. H. (2001). Oligosaccharide Synthesis with Glycosyl Phosphate and Dithiophosphate Triesters as Glycosylating Agents. *J. Am. Chem. Soc.* 123, 9545–9554. doi:10.1021/ja016227r

Plante, O. J., Palmacci, E. R., and Seeberger, P. H. (2001). Automated Solid-phase Synthesis of Oligosaccharides. *Science* 291, 1523–1527. doi:10.1126/science.1057324

Poljak, K., Breitling, J., Gauss, R., Rugarabamu, G., Pellanda, M., and Aebi, M. (2017). Analysis of Substrate Specificity of Trypanosoma Brucei Oligosaccharyltransferases (OSTs) by Functional Expression of Domain-Swapped Chimeras in Yeast. *J. Biol. Chem.* 292, 20342–20352. doi:10.1074/jbc.M117.811133

Priyanka, P., Parsons, T. B., Miller, A., Platt, F. M., and Fairbanks, A. J. (2016). Chemoenzymatic Synthesis of a Phosphorylated Glycoprotein. *Angew. Chem. Int. Ed.* 55, 5058–5061. doi:10.1002/anie.201600817

Reily, C., Stewart, T. J., RenfrowNovak, M. B. J., and Novak, J. (2019). Glycosylation in Health and Disease. *Nat. Rev. Nephrol.* 15, 346–366. doi:10.1038/s41581-019-0129-4

Sabbavarapu, N. M., and Seeberger, P. H. (2021). Automated Glycan Assembly of Oligogalactofuranosides Reveals the Influence of Protecting Groups on Oligosaccharide Stability. *J. Org. Chem.* 86, 7280–7287. doi:10.1021/acs.joc.1c00505

Schjoldager, K. T., Narimatsu, Y., Joshi, H. J., and Clausen, H.(2020). Global View of Human Protein Glycosylation Pathways and functionsNew Methods for the Synthesis of Glycosides and Oligosaccharides—Are There Alternatives to the Koenigs-Knorr Method? *Nat. Rev. Mol. Cel. Biol.Angew. Chem. Int. Ed. Engl.* 2125, 729212–749235. doi:10.1038/s41580-020-00294-x

Schmidt, R. R. (1986). New Methods for the Synthesis of Glycosides and Oligosaccharides—Are There Alternatives to the Koenigs-Knorr Method? *Chem. Int. Ed. Engl.* 25, 212–235. doi:10.1002/anie.198602121

Seko, A., Koketsu, M., Nishizono, M., Enoki, Y., Ibrahim, H. R., Juneja, L. R., et al. (1997). Occurrence of a Sialylglycopeptide and Free Sialylglycans in Hen's Egg Yolk. *Biochim. Biophys. Acta (Bba) - Gen. Subjects* 1335, 23–32. doi:10.1016/s0304-4165(96)00118-3

Shirakawa, A., Manabe, Y., and Fukase, K. (2021b). Recent Advances in the Chemical Biology of *N*-Glycans. *Molecules* 26, 1040. doi:10.3390/molecules26041040

Shirakawa, A., Manabe, Y., Marchetti, R., Yano, K., Masui, S., Silipo, A., et al. (2021a). Chemical Synthesis of Sialyl N -Glycans and Analysis of Their Recognition by Neuraminidase. *Angew. Chem. Int. Ed.* 60, 24686–24693. doi:10.1002/anie.202111035

Shivatare, S. S., Chang, S.-H., Tsai, T.-I., Tseng, S. Y., Shivatare, V. S., Lin, Y.-S., et al. (2016). Modular Synthesis of *N*-Glycans and Arrays for the Hetero-Ligand Binding Analysis of HIV Antibodies. *Nat. Chem* 8, 338–346. doi:10.1038/nchem.2463

Srivastava, A. D., Unione, L., Bunyatov, M., Gagarinov, I. A., Delgado, S., Abrescia, N. G. A., et al. (2021). Chemoenzymatic Synthesis of Complex N -Glycans of the

Parasite S. Mansoni to Examine the Importance of Epitope Presentation on DC-SIGN Recognition. *Angew. Chem. Intl Edit* 60, 19287–19296. doi:10.1002/anie.202105647

Taguchi, Y., Yamasaki, T., Ishikawa, M., Kawasaki, Y., Yukimura, R., Mitani, M., et al. (2021). The Structure of an Archaeal Oligosaccharyltransferase Provides Insight into the Strict Exclusion of Proline from the *N*-Glycosylation Sequon. *Commun. Biol.* 4, 941. doi:10.1038/s42003-021-02473-8

Tanaka, M., Sato, K., Yoshida, R., Nishi, N., Oyamada, R., Inaba, K., et al. (2020). Diastereoselective Desymmetric 1,2-*Cis*-Glycosylation of Meso-Diols via Chirality Transfer from a Glycosyl Donor. *Nat. Commun.* 11, 2431. doi:10.1038/s41467-020-16365-8

Toonstra, C., Wu, L., Li, C., Wang, D., and Wang, L.-X. (2018). Top-Down Chemoenzymatic Approach to Synthesizing Diverse High-Mannose N-Glycans and Related Neoglycoproteins for Carbohydrate Microarray Analysis. *Bioconjug. Chem.* 29, 1911–1921. doi:10.1021/acs.bioconjchem.8b00145

Tsutsui, M., Sianturi, J., Masui, S., Tokunaga, K., Manabe, Y., and Fukase, K. (2020). Efficient Synthesis of Antigenic Trisaccharides ContainingN-Acetylglucosamine: Protection of NHAc as NAc2. *Eur. J. Org. Chem.* 2020, 1802–1810. doi:10.1002/ejoc.201901809

Tyrikos-Ergas, T., Bordoni, V., Fittolani, G., Chaube, M. A., Grafmüller, A., Seeberger, P. H., et al. (2021). Systematic Structural Characterization of Chitooligosaccharides Enabled by Automated Glycan Assembly. *Chem. Eur. J.* 27, 2321–2325. doi:10.1002/chem.202005228

Unverzagt, C., André, S., Seifert, J., Kojima, S., Fink, C., Srikrishna, G., et al. (2002). Structure−Activity Profiles of Complex Biantennary Glycans with Core Fucosylation and With/without Additional α2,3/α2,6 Sialylation: Synthesis of Neoglycoproteins and Their Properties in Lectin Assays, Cell Binding, and Organ Uptake. *J. Med. Chem.* 45, 478–491. doi:10.1021/jm0110237

Varki, A., Cummings, R. D., Esko, J. D., Freeze, H. H., Stanley, P., Bertozzi, C. R., et al. (2015). *Essentials of Glycobiology*. NY: Cold spring harbor.

Vibhute, A. M., Komura, N., Tanaka, H. N., Imamura, A., and Ando, H. (2021). Advanced Chemical Methods for Stereoselective Sialylation and Their Applications in Sialoglycan Syntheses. *Chem. Rec.* 21, 3194–3223. doi:10.1002/tcr.202100080

Viinikangas, T., Khosrowabadi, E., and Kellokumpu, S. (2021). *N*-glycan Biosynthesis: Basic Principles and Factors Affecting its Outcome. *Exp. Suppl.* 112, 237–257. doi:10.1007/978-3-030-76912-3_7

Wacker, M., Linton, D., Hitchen, P. G., Nita-Lazar, M., Haslam, S. M., North, S. J., et al. (2002). N-linked Glycosylation in Campylobacter Jejuni and its Functional Transfer into *E. coli*. *Science* 298, 1790–1793. doi:10.1126/science.298.5599.1790

Wang, L.-X., Tong, X., and Li, T. (2019). Transglycosylation of Endoglycosidase Endo-S and Endo-S Mutants for a One-Pot Antibody Glycosylation Remodeling. US20190002945A1

Wang, P., Zhu, J., Yuan, Y., and Danishefsky, S. J. (2009). Total Synthesis of the 2,6-Sialylated Immunoglobulin G Glycopeptide Fragment in Homogeneous Form. *J. Am. Chem. Soc.* 131, 16669–16671. doi:10.1021/ja907136d

Wang, Y. S., Wu, Y., Xiong, D. C., and Ye, X. S. (2019). Total Synthesis of a Hyperbranched N -Linked Hexasaccharide Attached to ATCV-1 Major Capsid Protein without Precedent. *Chin. J. Chem.* 37, 42–48. doi:10.1002/cjoc.201800533

Wang, Z., Chinoy, Z. S., Ambre, S. G., Peng, W., McBride, R., de Vries, R. P., et al. (2013). A General Strategy for the Chemoenzymatic Synthesis of Asymmetrically Branched N -Glycans. *Science* 341, 379–383. doi:10.1126/science.1236231

Weiss, M., Ott, D., Karagiannis, T., Weishaupt, M., Niemietz, M., Eller, S., et al. (2020). Efficient Chemoenzymatic Synthesis of N-Glycans with a β1,4-Galactosylated Bisecting GlcNAc Motif. *Chembiochem* 21, 3212–3215. doi:10.1002/cbic.202000268

Wilson, M. P., Garanto, A., Pinto e Vairo, F., Ng, B. G., Ranatunga, W. K., Ventouratou, M., et al. (2021). Active Site Variants in STT3A Cause a Dominant Type I Congenital Disorder of Glycosylation with Neuromusculoskeletal Findings. *Am. J. Hum. Genet.* 108, 2130–2144. doi:10.1016/j.ajhg.2021.09.012

Yang, M., Wei, M., Wang, C., Lu, Y., Jin, W., Gao, X., et al. (2020). Separation and Preparation of N-Glycans Based on Ammonia-Catalyzed Release Method. *Glycoconj. J.* 37, 165–174. doi:10.1007/s10719-020-09909-z

Yang, W., Ramadan, S., Orwenyo, J., Kakeshpour, T., Diaz, T., Eken, Y., et al. (2018). Chemoenzymatic Synthesis of Glycopeptides Bearing Rare N-Glycan Sequences with or without Bisecting GlcNAc. *Chem. Sci.* 9, 8194–8206. doi:10.1039/c8sc02457j

Ye, F., Zhao, J., Xu, P., Liu, X., Yu, J., Shangguan, W., et al. (2021). Synthetic Homogeneous Glycoforms of the SARS-CoV-2 Spike Receptor-Binding Domain Reveals Different Binding Profiles of Monoclonal Antibodies. *Angew. Chem. Int. Ed.* 60, 12904–12910. doi:10.1002/anie.202100543

Zeng, C., Sun, B., Cao, X., Zhu, H., Oluwadahunsi, O. M., Liu, D., et al. (2020). Chemical Synthesis of Homogeneous Human E-Cadherin N-Linked Glycopeptides: Stereoselective Convergent Glycosylation and Chemoselective Solid-phase Aspartylation. *Org. Lett.* 22, 8349–8353. doi:10.1021/acs.orglett.0c02971

Zhong, X., Zhou, S., Ao, J., Guo, A., Xiao, Q., Huang, Y., et al. (2021). Zinc(II) Iodide-Directed β-Mannosylation: Reaction Selectivity, Mode, and Application. *J. Org. Chem.* 86, 16901–16915. doi:10.1021/acs.joc.1c02091

Zhu, Y., Delbianco, M., and Seeberger, P. H. (2021). Automated Assembly of Starch and Glycogen Polysaccharides. *J. Am. Chem. Soc.* 143, 9758–9768. doi:10.1021/jacs.1c02188

Zhu, Y., and Yu, B. (2015). Highly Stereoselective β-Mannopyranosylation via the 1-α-Glycosyloxy-isochromenylium-4-Gold(I) Intermediates. *Chem. Eur. J.* 21, 8771–8780. doi:10.1002/chem.201500648

Zong, G., Li, C., and Wang, L.-X. (2020). Chemoenzymatic Synthesis of HIV-1 Glycopeptide Antigens. *Methods Mol. Biol.* 2103, 249–262. doi:10.1007/978-1-0716-0227-0_17

Conflict of Interest: The authors declare that the research was conducted in the absence of any commercial or financial relationships that could be construed as a potential conflict of interest.

Publisher's Note: All claims expressed in this article are solely those of the authors and do not necessarily represent those of their affiliated organizations, or those of the publisher, the editors, and the reviewers. Any product that may be evaluated in this article, or claim that may be made by its manufacturer, is not guaranteed or endorsed by the publisher.

frontiers | Frontiers in Chemistry

ORIGINAL RESEARCH
published: 09 June 2022
doi: 10.3389/fchem.2022.911201

Bioactive Bibenzyl Enantiomers From the Tubers of *Bletilla striata*

Mei Zhou[1,2†], *Sai Jiang*[1,3†], *Changfen Chen*[1], *Jinyu Li*[1,2], *Huayong Lou*[1,2], *Mengyun Wang*[3], *Gezhou Liu*[1], *Hanfei Liu*[1,2], *Ting Liu*[4*] and *Weidong Pan*[1,2*]

[1]School of Basic Medical Sciences/State Key Laboratory of Functions and Applications of Medicinal Plants, Guizhou Medical University, Guiyang, China, [2]The Key Laboratory of Chemistry for Natural Products of Guizhou Province and Chinese Academy of Sciences, Guiyang, China, [3]TCM and Ethnomedicine Innovation and Development International Laboratory, School of Pharmacy, Innovative Materia Medica Research Institute, Hunan University of Chinese Medicine, Changsha, China, [4]Guizhou Provincial Key Laboratory of Pharmaceutics, Guizhou Medical University, Guiyang, China

Six new bibenzyls (three pairs of enantiomers), bletstrins D–F (1–3), were isolated from the ethyl acetate-soluble (EtOAc) extract of tubers of *Bletilla striata* (Thunb.) Rchb f. Their structures, including absolute configurations, were determined by 1D/2D NMR spectroscopy, optical rotation value, and experimental electronic circular dichroism (ECD) data analyses, respectively. Compounds 1–3 possess a hydroxyl-substituted chiral center on the aliphatic bibenzyl bridge, which represented the first examples of natural bibenzyl enantiomers from the genus of *Bletilla*. The antibacterial, antitumor necrosis factor (anti-TNF-α), and neuroprotective effects of the isolates have been evaluated. Compounds 3a and 3b were effective against three Gram-positive bacteria with minimum inhibitory concentrations (MICs) of 52–105 μg/ml. Compounds 2a and 2b exhibited significant inhibitory effects on TNF-α-mediated cytotoxicity in L929 cells with IC_{50} values of 25.7 ± 2.3 μM and 21.7 ± 1.7 μM, respectively. Subsequently, the possible anti-TNF-α mechanism of 2 was investigated by molecular docking simulation. Furthermore, the neuroprotective activities were tested on the H_2O_2-induced PC12 cell injury model, and compounds 2b, 3a, and 3b (10 μM) could obviously protect the cells with the cell viabilities of 57.86 ± 2.08%, 64.82 ± 2.84%, and 64.11 ± 2.52%, respectively.

Keywords: ***Bletilla striata*, bibenzyl enantiomers, antibacterial, anti-TNF-α activity, neuroprotection**

OPEN ACCESS

Edited by:
Matthew A. Coleman, University of California, Davis, United States

Reviewed by:
Jungui Dai, Chinese Academy of Medical Sciences and Peking Union Medical College, China
Rufeng Wang, Shanghai University of Traditional Chinese Medicine, China

***Correspondence:**
Ting Liu
liuting@gmc.edu.cn
Weidong Pan
wdpan@163.com

[†]*These authors have contributed equally to this work*

Specialty section:
This article was submitted to Chemical Biology, a section of the journal Frontiers in Chemistry

Received: *02 April 2022*
Accepted: *02 May 2022*
Published: *09 June 2022*

Citation:
Zhou M, Jiang S, Chen C, Li J, Lou H, Wang M, Liu G, Liu H, Liu T and Pan W (2022) Bioactive Bibenzyl Enantiomers From the Tubers of Bletilla striata. Front. Chem. 10:911201. doi: 10.3389/fchem.2022.911201

INTRODUCTION

The tubers of *Bletilla striata* (Thunb.) Rchb. f, named "Bai Ji", is a traditional Chinese medicine, which are used for the treatment of several health disorders, including gastrointestinal disorders, ulcers, lung disorders, chapped skin, and traumatic bleeding (He et al., 2017; Zhang et al., 2019; Liao et al., 2019; Wang et al., 2020; Hou et al., 2021; Wang et al., 2021; Jiang et al., 2021; Xu et al., 2021). As an Orchidaceae plant, it can biosynthesize many secondary stilbenes, such as bibenzyls, phenanthrenes, dihydrophenanthrenes, biphenanthrenes, dihydrophenanthrofurans, and phenanthrenequinones (Sun et al., 2016; Jiang et al., 2019a; Zhu et al., 2021). Some of these compounds showed a wide range of biological activities like antibacterial, anti-inflammatory, neuroprotective, anticancer, and antiviral effects (Qian et al., 2015; Wang and Meng, 2015; Xu et al., 2019; Jiang et al., 2020; Jiang et al., 2021). In our previous work, more than 40 stilbenes including 13 new compounds were isolated from the tubers of *B. striata* and just tested for their antibacterial effects (Jiang et al., 2019a, Jiang et al., 2019b).

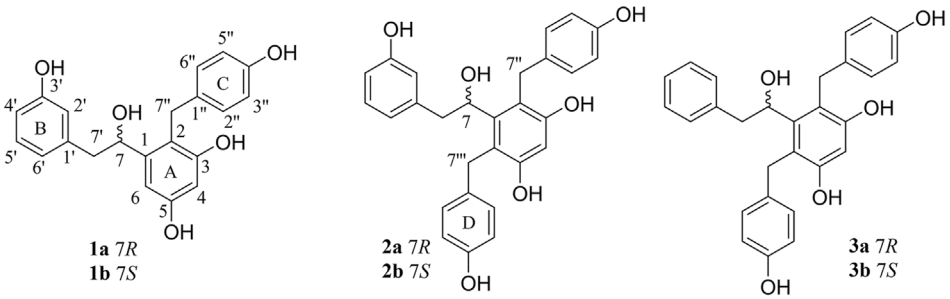

FIGURE 1 | Isolated compounds 1–3 from the tubers of *B. striata*.

Some literature studies showed that some compounds isolated from the tubers of *B. striata* presented obvious anti-neuroinflammatory activities (Sun et al., 2021), indicating that *B. striata* might be a promising source of neuroprotection lead compounds. The aim of this study was to obtain further chemical and biological properties of *B. striata*, which might provide deeper insights into the plant as a promising Chinese medicine. As a result, six new bibenzyls (three pairs of enantiomers), bletstrins D-F (1–3), were isolated (**Figure 1**). The isolation and identification of these undescribed compounds and their absolute configurations were elucidated in this study. Moreover, all the compounds were tested for their antibacterial, anti-TNF-α, and neuroprotective activities. The molecular docking experiment was further conducted to reveal the potential mechanism of anti-TNF-α activity.

MATERIALS AND METHODS

General Experimental Procedures

Optical rotations were measured on a Rudolph Autopol IV-T polarimeter equipped. The UV spectra were measured on an HP 8543E spectrometer. IR spectra were obtained on a Nicolet iS10 and an ICAN 9 FT-IR spectrometer with KBr pellets. ECD spectra were recorded with an Applied Photophysics Chirascan instrument. ^{1}D and ^{2}D NMR spectra were recorded on a Varian Inova 400 Hz NMR instrument or a Bruker Avance NEO 600 MHz spectrometer with tetramethylsilane (TMS) as the internal standard. The high-resolution electrospray ionization mass spectra (HRESIMS) were obtained on a Thermo Q-Exactive Focus mass spectrometer. All the solvents used were of analytical grade (Jiangsu Hanbang Science and Technology Co., Ltd.). Silica gel (300–400 mesh, Qingdao Haiyang Chemical Co., Ltd.), CHP20/P120 MCI gel (75–150 μm, Mitsubishi Chemical Industries, Ltd.), and Sephadex LH-20 (25–100 μm, Amersham Biosciences, Sweden) were used for column chromatography (CC). Semi-preparative HPLC was performed on a Waters-600 machine with a W2489 UV detector, column: ODS (5 μm, 10 × 250 mm, Waters Co., Ltd, United States). Chiral HPLC was performed on a Waters-600 machine with a W2489 UV detector equipped with a CHIRALPAK IA column (4.6 i. d. × 250 mm, S-5 μm, Daicel Chiral Technologies Co., Ltd., Japan). GF-254 (Qingdao Haiyang Chemical Co., Ltd.) was used for TLC.

Plant Material

The tubers of *B. striata* were collected from Anlong County of Guizhou Province, People's Republic of China, in March 2017, and authenticated by Prof. Ming-kai Wu (Institute of Modern Chinese Medicinal Materials, Guizhou Academy of Agricultural Sciences, Guizhou). A voucher specimen (No. 20170312003) was deposited at the State Key Laboratory of Functions and Applications of Medicinal Plants, Guizhou Medical University, People's Republic of China.

Extraction and Isolation

The dried tubers of *B. striata* (9.8 kg) were extracted with 95% ethyl alcohol (EtOH) under reflux four times to produce the crude extract. The residue was suspended in water and subsequently separated with EtOAc to yield an EtOAc-soluble fraction (386.1 g). The extract was purified on a silica gel column and eluted with a gradient $CHCl_3$-CH_3OH solvent system (100: 1→0:1) to give 11 fractions (Frs. 1–11). Frs. 5 (25.2 g) was separated by MCI CC eluted with H_2O-CH_3OH (from 60:0 to 0:100) to yield nine subfractions (Frs. 5.1–5.9). Frs. 5.5 (1.3 g) was further separated on a silica gel column and eluted with petroleum ether (PE)-EtOAc (10:1 to 1:1) to give five subfractions (Frs. 5.5.1–5.5.5). Frs. 5.5.4 (113.2 mg) was purified by semi-preparative HPLC (CH_3OH-H_2O, 56:44, flow rate 2.0 ml/min) to afford three subfractions (16.8 mg, t_R = 19.61 min). Frs. 5.5.5 (238.6 mg) was purified by semi-preparative HPLC (CH_3OH-H_2O, 56:44, flow rate 2.0 ml/min) to afford three subfractions (5.4 mg, t_R = 31.63 min). Frs. 5.6 (756.3 mg) was subjected to being chromatographed on a silica gel column and eluted with PE-EtOAc (10:1 to 1:1) to give three subfractions (Frs. 5.6.1–5.6.3). Frs. 5.6.3 (86.4 mg) was purified by semi-preparative HPLC (CH_3OH-H_2O, 55:45, flow rate 2.0 ml/min) to afford 1 subfraction (7.6 mg, t_R = 24.52 min). Compounds 1–3 were further purified by chiral HPLC, using CH_3OH-H_2O (50:50) as the mobile phase, to yield 1a (2.2 mg), 1b (2.8 mg), 2a (1.60 mg), 2b (1.85 mg), 3a (6.38 mg), and 3b (5.58 mg).

Bletstrin D (1) racemic mixture. Yellowish amorphous powder; UV (MeOH) λ_{max} (log ε) 280 (3.49) nm; IR (KBr):

TABLE 1 | ^{1}H and ^{13}C NMR data of compounds 1–3.

	1[a]		2[b]		3[c]	
No.	**δ_C**	**δ_H (*J* in Hz)**	**δ_C**	**δ_H (*J* in Hz)**	**δ_C**	**δ_H (*J* in Hz)**
1	146.7		144.0		144.0	
2	114.4		117.9		117.7	
3	155.7		155.3		155.4	
4	100.9	6.23, d (2.4)	103.0	6.43, s	102.7	6.45, s
5	156.1		156.9		156.9	
6	104.0	6.49, d (2.4)	118.8		118.8	
7	70.0	4.76, dd (10.8 and 6.0)	73.6	5.17, dd (8.8 and 4.8)	73.7	5.15, dd (9.2 and 4.4)
1′	141.2		142.4		140.9	
2′	116.3	6.58, m	117.4	6.41, m	130.5	6.72, m
3′	156.9		157.9		128.9	7.11, m
4′	112.7	6.55, m	113.7	6.53, m	126.8	7.08, m
5′	128.7	6.99, t (7.8)	129.9	6.94, m	128.9	7.11, m
6′	120.0	6.46, m	121.8	6.21, m	130.5	6.76, m
7′	45.3	2.47, d (6.0)	44.3	2.70, dd (13.6 and 8.8) 2.34, dd (13.6 and 4.8)	44.3	2.77, dd (13.6 and 9.2) 2.35, dd (13.6 and 4.4)
1″	131.8		134.3		134.3	
2″, 6″	128.9	6.89, d (8.4)	130.1	6.94, m	130.1	6.94, m
3″, 5″	114.8	6.60, d (8.4)	115.6	6.66, d (8.4)	115.6	6.67, m
4″	155.0		155.5		155.5	
7″	28.8	3.76, d (15.6) 3.68, d (15.6)	30.8	3.83, d (16.0) 3.69, d (16.0)	30.8	3.78, s
1‴			135.2		135.2	
2‴, 6‴			130.1	6.94, m	130.1	6.94, m
3‴, 5‴			115.9	6.66, d (8.4)	115.9	6.67, m
4‴			156.0		156.1	
7‴			31.6	4.56, d (16.0) 4.18, d (16.0)	31.7	4.57, d (15.6) 4.20, d (15.6)
1⁗						
2⁗, 6⁗						
3⁗, 5⁗						
4⁗						
7⁗						
3-OH		9.07, s				
5-OH		8.96, s				
7-OH		4.85, d (4.2)				
3′-OH		9.03, s or 9.16, s				
4″-OH		9.16, s or 9.03, s				

[a] *^{1}H (600 MHz) and ^{13}C (150 MHz) NMR, data on DMSO-d_6.*
[b] *^{1}H (400 MHz) and ^{13}C (100 MHz) NMR, data on methanol-d_4.*
[c] *^{1}H (400 MHz) and ^{13}C (100 MHz) NMR, data on methanol-d_4.*

ν_{max} = 3,374, 1,611, 1,513, 1,225, 1,145, 986, and 693 cm^{-1}; ^{1}H and ^{13}C NMR data (see **Table 1**; HRESIMS *m/z* 351.1241 $[M - H]^-$ (calcd. for $C_{21}H_{19}O_5$, 351.1232).

(7*R*)-bletstrin D (1a). $[\alpha]_D^{22}$ +18.3 (*c* 0.04, MeOH); ECD (MeOH) λ_{max} ($\Delta\varepsilon$) 206 (+2.97), 219 (−0.74), and 236 (+1.03) nm.

(7*S*)-bletstrin D (1b). $[\alpha]_D^{22}$ −2.1 (*c* 0.05, MeOH); ECD (MeOH) λ_{max} ($\Delta\varepsilon$) 206 (−2.24), 217 (+0.50), and 236 (−0.68) nm.

Bletstrin E (2) racemic mixture. Yellowish amorphous powder; UV (MeOH) λ_{max} (log ε) 280 (2.93) nm; IR (KBr): ν_{max} = 3,381, 1,595, 1,510, 1,457, 1,236, and 1,172 cm^{-1}; ^{1}H and ^{13}C NMR data (see **Table 1**); HRESIMS *m/z* 457.1664 $[M - H]^-$ (calcd. for $C_{28}H_{25}O_6$, 457.1651).

(7*R*)-bletstrin E (2a). $[\alpha]_D^{22}$ +12.5 (*c* 0.05, MeOH); ECD (MeOH) λ_{max} ($\Delta\varepsilon$) 202 (+6.49), 217 (−1.51), and 230 (+1.13) nm.

(7*S*)-bletstrin E (2b). $[\alpha]_D^{22}$ −4.5 (*c* 0.06, MeOH); ECD (MeOH) λ_{max} ($\Delta\varepsilon$) 201 (−3.97), 218 (+1.28), and 230 (−0.51) nm.

Bletstrin F (3) racemic mixture. Yellowish amorphous powder; UV (MeOH) λ_{max} (log ε) 285 (3.23) nm; IR (KBr): ν_{max} = 3,379, 1,599, 1,510, 1,238, 1,170, 1,083, and 702 cm^{-1}; ^{1}H and ^{13}C NMR data (see **Table 1**); HRESIMS *m/z* 443.1852 $[M + H]^+$ (calcd. for $C_{28}H_{27}O_5$, 443.1858).

(7*R*)-bletstrin F (3a). $[\alpha]_D^{22}$ +28.7 (*c* 0.05, MeOH); ECD (MeOH) λ_{max} ($\Delta\varepsilon$) 203 (+4.11), 219 (−1.07), and 231 (+1.35) nm.

(7*S*)-bletstrin F (3b). $[\alpha]_D^{22}$ −10.1 (*c* 0.05, MeOH); ECD (MeOH) λ_{max} ($\Delta\varepsilon$) 204 (−2.24), 219 (+1.38), and 231 (−0.54) nm.

Antibacterial Activity Assays

Antimicrobial activities of compounds 1–3 against Gram-positive bacteria (Methicillin-resistant *S. aureus* ATCC 43300, *S. aureus* ATCC 6538, and *Bacillus subtilis* ATCC 6051) and Gram-negative bacteria (*Escherichia coli* ATCC 11775) were performed using a microbroth dilution method in a 96-well

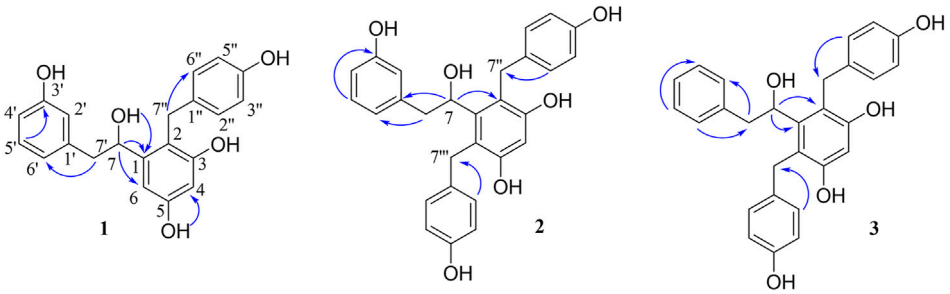

FIGURE 2 | Key HMBC correlations of compounds 1–3.

microtiter plate (Jiang, et al., 2019a). Bacteria were seeded at 1×10^6 cells per well (200 μL) in a 96-well plate containing Mueller-Hinton broth with different concentrations (from 1 to 420 μg/ml; 2-fold increments) of each test compound. Oxacillin, which was obtained from J&K Chemicals (Beijing, China), was used as a positive control.

Anti-TNF-α Activity Assay

L929 cells (Procell, Wuhan, China) were cultured in RPMI 1640 (Gibco, United States) supplemented with 10% fetal calf serum (Procell, Wuhan, China) at 37°C in a humidified atmosphere of 5% CO_2. Exponentially growing L929 cells were harvested and seeded in 96-well multiplates at a density of 1.5×10^5 cells/mL. After incubation for 24 h at 37°C, samples (0.01, 0.1, 10, 20, 40, 80, and 200 μM), TNF-α (GlpBio, Shanghai, China) (7.5 ng/ml), and actinomycin D (GlpBio, Shanghai, China) (0.5 μg/ml) were added. After 12 h incubation at 37°C, 100 μL of 3-(4,5-dimethylthiazol-2-yl)-5-2 -(4-sulfophenyl)-2H-tetrazolium (MTS) (Promega, United States) (0.5 mg/ml) was added to each well and incubated for an additional 2 h. The optical density (OD) of the formazan solution was measured using a microplate reader at 490 nm. UCB-9260 (GlpBio, Shanghai, China) was used as a positive control.

Neuroprotective Activity Assay

PC12 cells were cultured in Ham's F12K (Gibco, United States) with 10% fetal calf serum at 37°C in a humidified atmosphere of 5% CO_2. The cells were seeded in 96-well multiplates at a density of 1.5×10^5 cells/mL. After overnight incubation at 37°C with 5% CO_2, 10 μM test samples and H_2O_2 (final concentration of 450 μM) were added into the wells and incubated for another 12 h. The cell survival rate was measured by 3-(4,5-dimethylthiazol-2-yl)-2,5-diphenyltetrazolium bromide (MTT) (Gibco, United States) assay (Chu et al., 2019).

RESULTS AND DISCUSSION

Compound 1 was obtained as a yellowish amorphous powder. HRESIMS analysis established the molecular formula of 1 as $C_{21}H_{20}O_5$ (*m/z* 351.1241 [M - H]$^-$, calcd. 351.1232). The UV spectrum suggested the presence of aromatic ring functional groups. The ^{1}H NMR spectrum of 1 revealed signals for one 1,3-disubstituted phenyl group [δ_H 6,99 (1H, t, J = 7.8 Hz), 6.58 (1H, m), 6.55 (1H, m), and 6.46 (1H, m)]; one 4-hydroxybenzyl moiety [δ_H 6.89 (2H, d, J = 8.4 Hz), 6.60 (2H, d, J = 8.4 Hz), 3.76 (1H, d, J = 15.6 Hz), and 3.68 (1H, d, J = 15.6 Hz)]; one 1,2,3,5-tetrasubstituted aromatic moiety [δ_H 6.49 (1H, d, J = 2.4 Hz) and 6.23 (1H, d, J = 2.4 Hz)]; one methylene group [δ_H 2.47 (2H, d, J = 6.0 Hz)]; one oxymethine group [δ_H 4.22 (1H, dd, J = 10.8, 6.0 Hz)]; and four hydroxy groups [δ_H 9.16 (1H, s), 9.07 (1H, s), 8.96 (1H, s), and 4.85 (1H, d, J = 4.2 Hz)]. The ^{13}C NMR spectrum of 1 showed 21 signals, four of them were oxygen-bearing aromatic carbons (δ_C 156.9, 156.1, 155.7, and 155.0), and one of them was oxygen-bearing methylene group (δ_C 70.0). The 1D-NMR data of **1** were similar to those of bletstrin A (Jiang et al., 2019b), except for the existence of an extra hydroxy group linked to the C-3′ position. This conclusion was supported by the molecular weight and the HMBC (**Figure 2**) correlations of H-5′ (δ_H 6.99) and H-2′ (δ_H 6.58) to C-3′ (δ_C 156.9). Thus, the planar structure of **1** was established.

However, compound 1 was not optically pure but racemic according to its optical rotation data (Shao et al., 2019). We then separated optically pure compounds 1a and 1b from one by chiral HPLC. Compounds 1a and 1b exhibited opposite cotton effects at 206, 219, and 236 nm and further confirmed their racemic relationship. By comparison of the experimental ECD curves and data from the literature (Jiang et al., 2019b), the absolute configurations of 1a and 1b were determined as 7*R* and 7*S*, respectively. Finally, the structures of bletstrin D (1a and 1b) were defined. All the spectroscopic data of compound 1 are shown in **Supplementary Figures S1–8** in **Supplementary Material S1**.

Compound 2 was obtained as a yellowish amorphous powder. Its molecular formula of $C_{28}H_{26}O_6$ was determined by the (-)-HRESIMS ion peak at *m/z* 457.1644 [M - H]$^-$ (calcd. 457.1651). The comparison of the ^{1}D NMR data (**Table 1**) of 2 with those of 1 suggested that their structures were similar, except for the existence of an extra benzene moiety in 2. The ^{1}H NMR data of compound 2 showed an extra AA′BB' system benzene moiety at δ_H 6.94 (2H, m, H-2‴, 6‴), 6.66 (2H, d, J = 8.4 Hz, H-3‴, 5‴), 4.56 (1H, d, J = 16.0 Hz), and 4.18 (1H, d, J = 16.0 Hz) in the A ring. The ^{13}C NMR spectrum of compound 2 showed seven extra signals at δ_C 135.2 (C-1‴), 130.1 (C-2‴), 115.6 (C-3‴), 155.5 (C-4‴), 115.6 (C-5‴), 130.1 (C-6‴), and 31.6 (C-7‴). Furthermore, the HMBC (**Figure 2**) correlations from H-

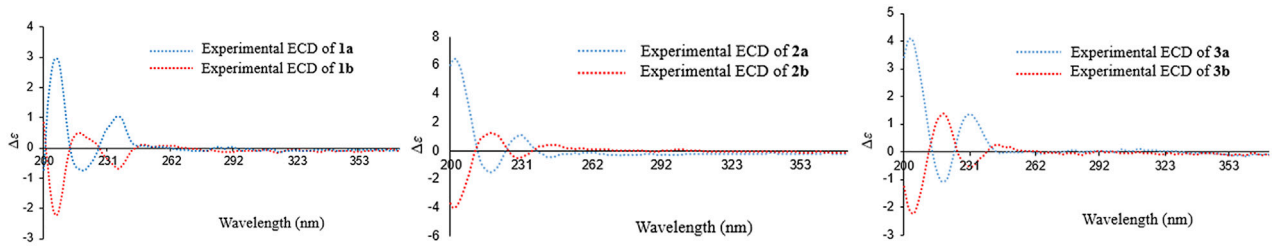

FIGURE 3 | Experimental ECD curves of compounds 1–3.

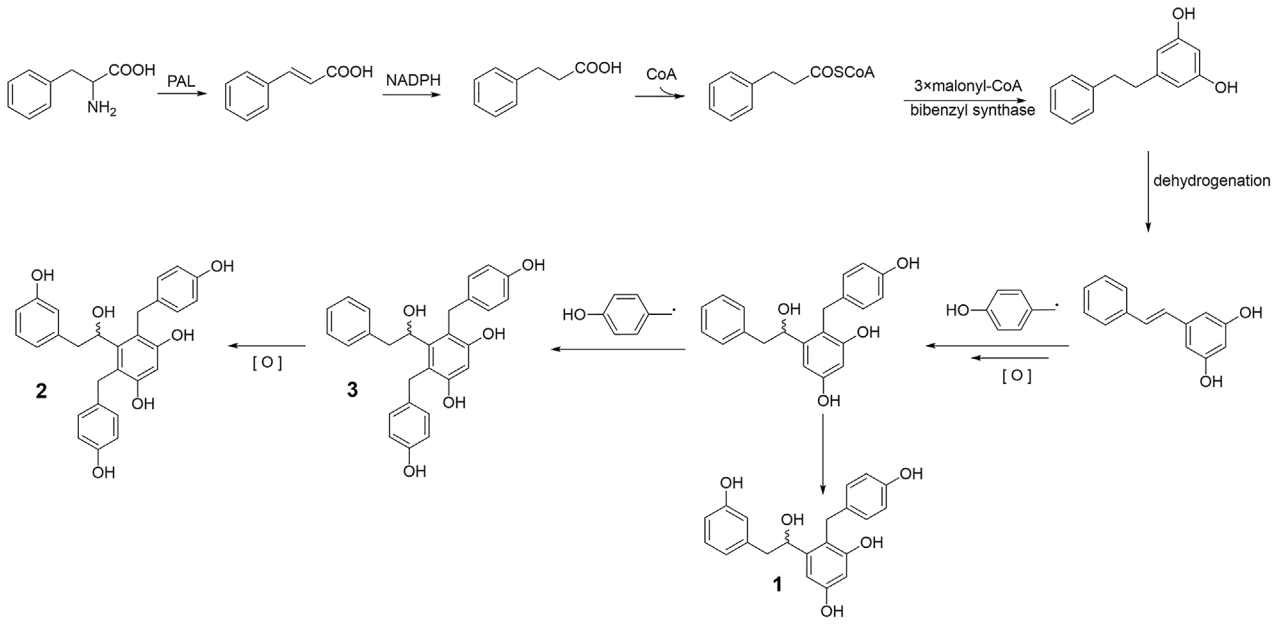

FIGURE 4 | Plausible biogenetic pathway of compounds 1–3.

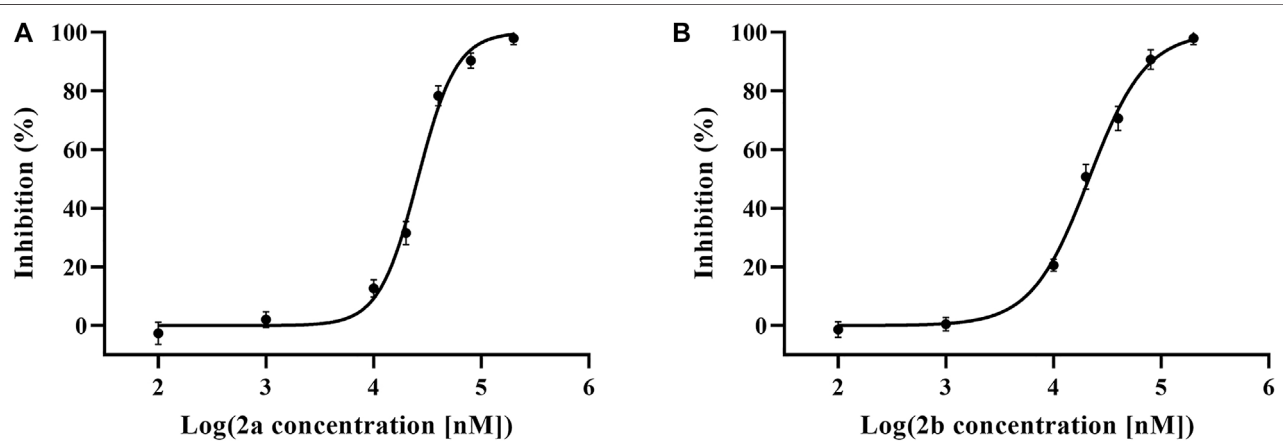

FIGURE 5 | L929 assay of compound 2 **(A,B)** in the presence of different concentrations (n = 3).

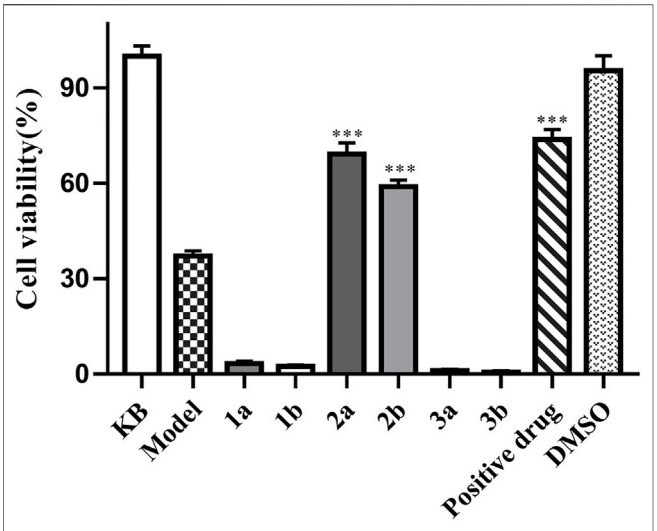

FIGURE 6 | Anti-TNF-α activities of compounds 1–3. L929 cells were cultured in the presence of isolated compounds and were measured by the MTS assay (n = 3). Data are expressed as mean ± S D. ***p < 0.001 vs. the model group.

7‴ (δ_H 4.56) to C-2‴, C‴, C-1, C-5, and C-6 suggested that the benzyl group was connected to C-6. Thus, the planar structure of 2 was defined and named as bletstrin E. Compound 2 was also a racemic mixture. Resolution by chromatography analysis is afforded to 2a and 2b. The absolute configurations of 2a and 2b were determined as 7*R* and 7*S* by comparing with the experimental ECD spectra of 1a and 1b. Finally, the structures of bletstrin E (2a and 2b) were defined. All the spectroscopic data on compound 2 are shown in **Supplementary Figures S8–16** in **Supplementary Material S1**.

Compound 3, a yellowish amorphous powder, was given the molecular formula of $C_{28}H_{26}O_5$ by (+)-HRESIMS ion peak at *m/z* 443.1852 $[M + H]^+$ (calcd. 443.1858). A comparison of the molecular formula of 3 with that of 2 inferred that it lacks an oxygen atom. By detailed analysis of the 1D NMR data (**Table 1**) of 3, it was suggested that its structure was similar to that of **2**, except for missing a hydroxy group at position C-3′. The location was supported by the downfield chemical shift of C-3′ at δ_C 128.9 ($\Delta\delta_C$ −29.0), as well as the HMBC (**Figure 2**) correlations of H-3′, 5′ (δ_H 7.11) with C-1′ (δ_C 140.9). Compound 3 was a racemate according to its optical rotation data. The pair of optically pure enantiomers (3a and 3b) was separated using chiral chromatography analysis. The absolute configurations of 3a and 3b were determined as 7*R* and 7*S* by comparing with the experimental ECD (**Figure 3**) spectra of 1a and 1b. Finally, the structures of bletstrin F (3a and 3b) were defined. All the spectroscopic data on compound 3 are shown in **Supplementary Figures S17–24** in **Supplementary Material S1**.

Bletstrins D–F (1–3) are all new bibenzyl derivatives possessing a rare hydroxyl substituted chiral center on the aliphatic bibenzyl bridge structure. In the field of a biosynthetic pathway, the establishment of the new structures may consist of a series of modifications from simple model blocks (Sun et al., 2021). As shown in **Figure 4**, bibenzyls are biosynthesized from dihydro-m-coumaroyl-CoA (Jiang et al., 2019). Subsequently, the target compounds 1, 2, and 3 were formed by dehydrogenation, oxidation, and the coupling of one or two benzyl groups.

Compounds 1–3 were tested on antibacterial activities against three common Gram-positive bacterial strains (Methicillin-resistant *Staphylococcus aureus* ATCC 43300, *S. aureus* ATCC 6538, and *Bacillus subtilis* ATCC 6051) and one Gram-negative bacterial strain (*Escherichia coli* ATCC 11775). The results revealed that compounds 3a and 3b were effective against three Gram-positive bacteria with MICs of 52–105 μg/ml (**Supplementary Table S1** in

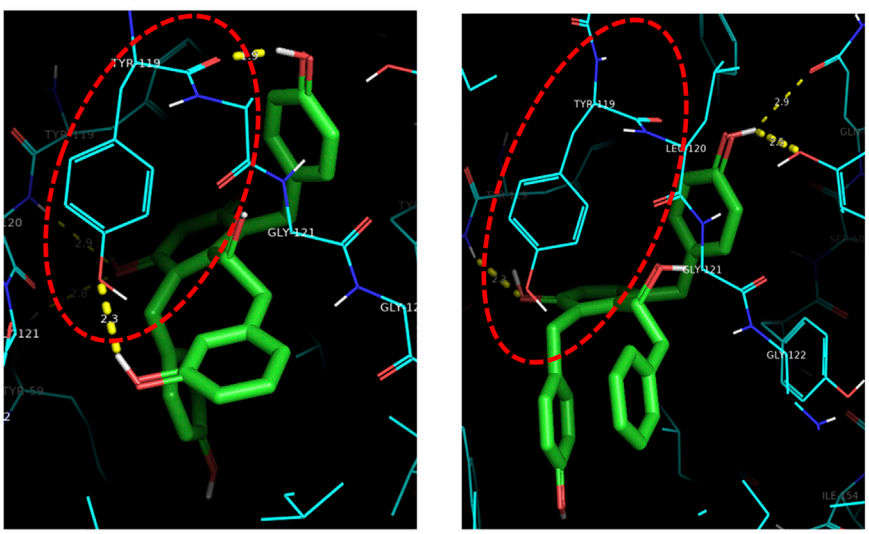

FIGURE 7 | Three-dimensional molecular docking model of compounds 2 and 3. Detail of the compound-binding pocket within the TNF homotrimer, with key residues involved in binding highlighted.

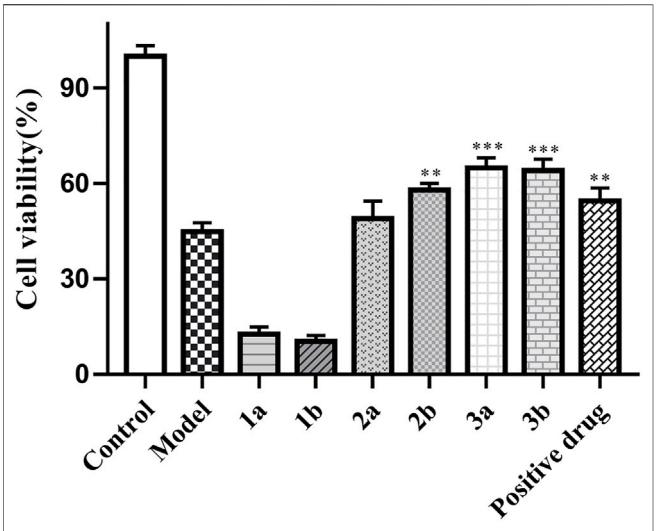

FIGURE 8 | Neuroprotective activities of compounds 1–3. PC12 cells were in the presence of isolated compounds at a concentration of 10 μM with the H_2O_2-induced injury model. Their cell viabilities were measured by the MTT assay (n = 3). Data are expressed as mean ± S D. ***p < 0.001 vs. the model group.

Supplementary Material S1). Furthermore, compounds 2a and 2b exhibited obvious anti-TNF-α bioactivity in TNF-α-mediated-cytotoxicity assay with IC_{50} values of 25.7 ± 2.3 μM and 21.7 ± 1.7 μM, respectively (**Figure 5**); these values are of the same order of magnitude to the published literature (He et al., 2005; Alexiou et al., 2014; Melagraki et al., 2017). The cell viability of 69.17 ± 2.42% and 58.89 ± 2.08% at 20 μM, compared to the model group (37.08 ± 1.68%), while that of the positive control UCB-9260 was 73.70 ± 3.12% (**Figure 6**). TNF-α is a proinflammatory cytokine that plays a key role in most of the inflammatory processes (Jacobi et al., 2006), and these results suggested that compounds 2a and 2b may have obvious anti-inflammatory activity. In the anti-TNF-α activity test, compound 2, which possesses one more hydroxy group than compound 3 at C-4′, showed significantly different activities (P < 0.001). The possible anti-TNF-α mechanisms of 2 and 3 were investigated by molecular docking simulation (**Figure 7**). From the docking mode of two compounds with TNF-α protein (PDB ID: 6OOY), it can be seen that compound 2 with hydroxy group at C-4′ can form two stable hydrogen bonds with 6OOY tyrosine at position 119 (tyrosine; Tyr), which could not be found in the docking model of 3 and 6OOY. In the published study on the crystal structure of 6OOY, it was also demonstrated that the ligand binds to the protein at position 119 of the B chain (O'Connell et al., 2019). This docking simulation revealed that compound 2 might form hydrogen bonds with amino acids at position 119 of the B chain of TNF-α, which can inhibit its activity by stabilizing the asymmetric trimer structure of TNF-α.

Moreover, *in vitro* assays, compounds 2b, 3a, and 3b (10 μM) exhibited excellent neuroprotective activities against H_2O_2-induced PC12 cell damage with the cell viabilities of 57.86 ± 2.08%, 64.82 ± 2.84%, and 64.11 ± 2.52%, respectively, while that of the positive control (±) α-Tocopherol was 54.51 ± 2.87% (**Figure 8**).

CONCLUSION

Six new bibenzyls (three pairs of enantiomers, 1a–3b) were isolated from the tubers of *B. striata*. The absolute configurations of compounds 1–3 were assigned by comparison of the optical rotation value combined with their experimental ECD data. All the compounds were evaluated for their antibacterial activities, but only compound 3 showed inhibitory activities against the three Gram-positive bacteria. This result preliminarily inferred that the orientation of hydroxyl at C-7 may not affect the antibacterial activities. Furthermore, the anti-TNF-α activity was influenced by the hydroxyl at C-4′ and the benzyl at C-6 by comparing the effects of 1, 2, and 3. Moreover, the absolute configurations may also not affect their neuroprotective activities, but the benzyl group at C-6 may affect their activity. In fact, this is the first example of natural bibenzyl enantiomers (a hydroxyl-substituted chiral center on the aliphatic bibenzyl bridge) from the genus of *Bletilla*. Furthermore, the anti-TNF-α and neuroprotective effects of bibenzyls from *B. striata* are also the first reported. In addition, some simple bibenzyls (not containing extra benzyl groups) from *Stemona* and *Dendrobium* species also showed neuroprotective activities against 6-hydroxydopamine-induced neurotoxicity in human neuroblastoma SH-SY5Y cells (Lee et al., 2006; Song et al., 2010). In summary, according to the structure and activity relationship (SAR), the hydroxyl on the aliphatic chain and/or benzyl groups, as well as the absolute configurations, may affect the bioactivities of bibenzyls.

DATA AVAILABILITY STATEMENT

The original contributions presented in the study are included in the article/**Supplementary Material**; further inquiries can be directed to the corresponding authors.

AUTHOR CONTRIBUTIONS

WP and TL conceived and designed the experiment. MZ and CC were responsible for compound isolation and writing. JS was responsible for structure identification. HL, MW, and GL completed the biological activity test. JL and HL reviewed the manuscript. All authors have read and agreed to the final manuscript.

FUNDING

This work was financially supported by the National Nature Science Foundation of China (Nos. U1812403-3-2, 81660580, and 32100322) and the Science and Technology Department of Guizhou Province (Nos. QKHZC(2019)2753, QKHZC(2020) 4Y067, QKHRC(2016)4037, and QKHPTRC(2021)5619).

SUPPLEMENTARY MATERIAL

The Supplementary Material for this article can be found online at: https://www.frontiersin.org/articles/10.3389/fchem.2022.911201/full#supplementary-material

REFERENCES

Alexiou, P., Papakyriakou, A., Ntougkos, E., Papaneophytou, C. P., Liepouri, F., Mettou, A., et al. (2014). Rationally Designed Less Toxic SPD-304 Analogs and Preliminary Evaluation of Their TNF Inhibitory Effects. *Arch. Pharm. Chem. Life Sci.* 347, 798–805. doi:10.1002/ardp.201400198

Chu, Q., Chen, M., Song, D., Li, X., Yang, Y., Zheng, Z., et al. (2019). Apios Americana Medik Flowers Polysaccharide (AFP-2) Attenuates H2O2 Induced Neurotoxicity in PC12 Cells. *Int. J. Biol. Macromol.* 123, 1115–1124. doi:10.1016/j.ijbiomac.2018.11.078

He, M. M., Smith, A. S., Oslob, J. D., Flanagan, W. M., Braisted, A. C., Whitty, A., et al. (2005). Small-Molecule Inhibition of TNF-α. *Science* 310, 1022–1025. doi:10.101126/science.111630410.1126/science.1116304

He, X., Wang, X., Fang, J., Zhao, Z., Huang, L., Guo, H., et al. (2017). Bletilla Striata: Medicinal Uses, Phytochemistry and Pharmacological Activities. *J. Ethnopharmacol.* 195, 20–38. doi:10.1016/j.jep.2016.11.026

Hou, X.-Y., Cao, Y., Wu, B.-L., Chen, B., Li, F., Wang, F., et al. (2021). New 2-isobutylmalates from the Tubers of *Bletilla Striata* and Their Potential Anti-pulmonary Fibrosis Activities. *Phytochem. Lett.* 46, 95–99. doi:10.1016/j.phytol.2021.09.009

Jacobi, A., Mahler, V., Schuler, G., and Hertl, M. (2006). Treatment of Inflammatory Dermatoses by Tumour Necrosis Factor Antagonists. *J. Eur. Acad. Dermatol Venerol.* 20 (10), 1171–1187. doi:10.1111/j.1468-3083.2006.01733.x

Jiang, S., Chen, C.-F., Ma, X.-P., Wang, M.-Y., Wang, W., Xia, Y., et al. (2019a). Antibacterial Stilbenes from the Tubers of *Bletilla Striata*. *Fitoterapia* 138, 104350. doi:10.1016/j.fitote.2019.104350

Jiang, S., Wan, K., Lou, H.-Y., Yi, P., Zhang, N., Zhou, M., et al. (2019b). Antibacterial Bibenzyl Derivatives from the Tubers of Bletilla Striata. *Phytochemistry* 162, 216–223. doi:10.1016/j.phytochem.2019.03.2210.1016/j.phytochem.2019.03.022

Jiang, S., Wang, M., Jiang, L., Xie, Q., Yuan, H., Yang, Y., et al. (2021). The Medicinal Uses of the Genus *Bletilla* in Traditional Chinese Medicine: A Phytochemical and Pharmacological Review. *J. Ethnopharmacol.* 280, 114263. doi:10.1016/j.jep.2021.114263

Jiang, S., Wang, M. Y., Yuan, H. W., Xie, Q., Liu, Y., Jian, Y. Q., et al. (2020). Medicinal Plant of *Bletilla Striata:* A Review of its Chemical Constituents, Pharmacological Activities, and Quality Control. *World J. Tradit. Chin. Med.* 6, 393–407. doi:10.4103/wjtcm.wjtcm5820

Lee, K. Y., Sung, S. H., and Kim, Y. C. (2006). Neuroprotective Bibenzyl Glycosides of *Stemona Tuberosa* Roots. *J. Nat. Prod.* 69, 679–681. doi:10.1021/np0504154

Liao, Z., Zeng, R., Hu, L., Maffucci, K. G., and Qu, Y. (2019). Polysaccharides from Tubers of *Bletilla Striata*: Physicochemical Characterization, Formulation of Buccoadhesive Wafers and Preliminary Study on Treating Oral Ulcer. *Int. J. Biol. Macromol.* 122, 1035–1045. doi:10.1016/j.ijbiomac.2018.09.050

Melagraki, G., Ntougkos, E., Rinotas, V., Papaneophytou, C., Leonis, G., Mavromoustakos, T., et al. (2017). Cheminformatics-aided Discovery of Small-Molecule Protein-Protein Interaction (PPI) Dual Inhibitors of Tumor Necrosis Factor (TNF) and Receptor Activator of NF-κB Ligand (RANKL). *PLoS Comput. Biol.* 13, e1005372. doi:10.1371/journal.pcbi.1005372

O'Connell, J., Porter, J., Kroeplien, B., Norman, T., Rapecki, S., Davis, R., et al. (2019). Small Molecules that Inhibit TNF Signalling by Stabilising an Asymmetric Form of the Trimer. *Nat. Commun.* 10, 5795–5805. doi:10.1038/s41467-019-1316-110.1038/s41467-019-13616-1

Qian, C.-D., Jiang, F.-S., Yu, H.-S., Shen, Y., Fu, Y.-H., Cheng, D.-Q., et al. (2015). Antibacterial Biphenanthrenes from the Fibrous Roots of *Bletilla Striata*. *J. Nat. Prod.* 78, 939–943. doi:10.1021/np501012n

Shao, S.-Y., Wang, C., Han, S.-W., Sun, M.-H., and Li, S. (2019). Phenanthrenequinone Enantiomers with Cytotoxic Activities from the Tubers of *Pleione Bulbocodioides*. *Org. Biomol. Chem.* 17, 567–572. doi:10.1039/C8OB02850H

Song, J.-X., Shaw, P.-C., Sze, C.-W., Tong, Y., Yao, X.-S., Ng, T.-B., et al. (2010). Chrysotoxine, a Novel Bibenzyl Compound, Inhibits 6-hydroxydopamine Induced Apoptosis in SH-SY5Y Cells via Mitochondria Protection and NF-κB Modulation. *Neurochem. Int.* 57, 676–689. doi:10.1016/j.neuint.2010.08.007

Sun, A., Liu, J., Pang, S., Lin, J., and Xu, R. (2016). Two Novel Phenanthraquinones with Anti-cancer Activity Isolated from Bletilla Striata. *Bioorg. Med. Chem. Lett.* 26, 2375–2379. doi:10.1016/j.bmcl.2016.01.076

Sun, M.-H., Ma, X.-J., Shao, S.-Y., Han, S.-W., Jiang, J.-W., Zhang, J.-J., et al. (2021). Phenanthrene, 9,10-dihydrophenanthrene and Bibenzyl Enantiomers from *Bletilla Striata* with Their Antineuroinflammatory and Cytotoxic Activities. *Phytochemistry* 182, 112609. doi:10.1016/j.phytochem.202011260910.1016/j.phytochem.2020.112609

Wang, B., Zhang, H., Chen, L., Mi, Z., Xu, Y., Zhao, G., et al. (2020). Extraction, Purification, and Determination of the Gastroprotective Activity of Glucomannan from *Bletilla Striata*. *Carbohydr. Polym.* 246, 116620. doi:10.1016/j.carbpol.202011662010.1016/j.carbpol.2020.116620

Wang, W., and Meng, H. (2015). Cytotoxic, Anti-inflammatory and Hemostatic Spirostane-Steroidal Saponins from the Ethanol Extract of the Roots of *Bletilla Striata*. *Fitoterapia* 101, 12–18. doi:10.16/j.fitote.2014.11.00510.1016/j.fitote.2014.11.005

Wang, X., Xing, M., Zhang, Z., Deng, L., Han, Y., Wang, C., et al. (2021). Using UPLC-QTOF/MS and Multivariate Analysis to Explore the Mechanism of *Bletilla Striata* Improving PM2.5-induced Lung Impairment. *Anal. Biochem.* 631, 114310. doi:10.1016/j.ab.2021.114310

Xu, D., Pan, Y., and Chen, J. (2019). Chemical Constituents, Pharmacologic Properties, and Clinical Applications of Bletilla Striata. *Front. Pharmacol.* 10, 1168–1186. doi:10.3389/fphar.2019.01168

Xu, J., Chen, Z., Liu, P., Wei, Y., Zhang, M., Huang, X., et al. (2021). Structural Characterization of a Pure Polysaccharide from Bletilla Striata Tubers and its Protective Effect against H2O2-Induced Injury Fibroblast Cells. *Int. J. Biol. Macromol.* 193, 2281–2289. doi:10.16/j.biomac.2021.11.06010.1016/j.ijbiomac.2021.11.060

Zhang, C., Gao, F., Gan, S., He, Y., Chen, Z., Liu, X., et al. (2019). Chemical Characterization and Gastroprotective Effect of an Isolated Polysaccharide Fraction from *Bletilla Striata* against Ethanol-Induced Acute Gastric Ulcer. *Food Chem. Toxicol.* 131, 110539. doi:10.1016/j.fct.2019.0504710.1016/j.fct.2019.05.047

Zhu, H., Dai, O., Zhou, F., Yang, L., Liu, F., Liu, Y., et al. (2021). Discovery of Bletillain, an Unusual Benzyl Polymer with Significant Autophagy-Inducing Effects in A549 Lung Cancer Cells through the Akt/GSK-3β/β-Catenin Signaling Pathway. *Bioorg. Chem.* 117, 105449. doi:10.1016/j.bioorg.2021.105449

Conflict of Interest: The authors declare that the research was conducted in the absence of any commercial or financial relationships that could be construed as a potential conflict of interest.

frontiers | Frontiers in Chemistry

REVIEW
published: 22 June 2022
doi: 10.3389/fchem.2022.879609

Rhodopsins: An Excitingly Versatile Protein Species for Research, Development and Creative Engineering

Willem J. de Grip[1,2]* *and Srividya Ganapathy*[3]*†

[1]Leiden Institute of Chemistry, Department of Biophysical Organic Chemistry, Leiden University, Leiden, Netherlands, [2]Radboud Institute for Molecular Life Sciences, Radboud University Medical Center, Nijmegen, Netherlands, [3]Department of Imaging Physics, Delft University of Technology, Netherlands

The first member and eponym of the rhodopsin family was identified in the 1930s as the visual pigment of the rod photoreceptor cell in the animal retina. It was found to be a membrane protein, owing its photosensitivity to the presence of a covalently bound chromophoric group. This group, derived from vitamin A, was appropriately dubbed retinal. In the 1970s a microbial counterpart of this species was discovered in an archaeon, being a membrane protein also harbouring retinal as a chromophore, and named bacteriorhodopsin. Since their discovery a photogenic panorama unfolded, where up to date new members and subspecies with a variety of light-driven functionality have been added to this family. The animal branch, meanwhile categorized as type-2 rhodopsins, turned out to form a large subclass in the superfamily of G protein-coupled receptors and are essential to multiple elements of light-dependent animal sensory physiology. The microbial branch, the type-1 rhodopsins, largely function as light-driven ion pumps or channels, but also contain sensory-active and enzyme-sustaining subspecies. In this review we will follow the development of this exciting membrane protein panorama in a representative number of highlights and will present a prospect of their extraordinary future potential.

Keywords: membrane protein, photoreceptor, retinal protein, visual pigments, optogenetics, ion pumps, microbial, eukaryotic

OPEN ACCESS

Edited by:
Matthew A. Coleman, University of California, United States

Reviewed by:
Keiichi Inoue, The University of Tokyo, Japan
Paul Park, Case Western Reserve University, United States

***Correspondence:**
Willem J. de Grip
w.j.de.grip@lic.leidenuniv.nl
Srividya Ganapathy
srganapathy@health.ucsd.edu

†Present address:
Srividya Ganapathy, Department of Pediatrics and Cellular and Molecular Medicine, UCSD School of Medicine, San Diego, CA, United States

Specialty section:
This article was submitted to Chemical Biology, a section of the journal Frontiers in Chemistry

Received: *19 February 2022*
Accepted: *16 May 2022*
Published: *22 June 2022*

Citation:
de Grip WJ and Ganapathy S (2022) Rhodopsins: An Excitingly Versatile Protein Species for Research, Development and Creative Engineering. Front. Chem. 10:879609. doi: 10.3389/fchem.2022.879609

Abbreviations: AFM, Atomic force microscopy; AR3, Archaerhodopsin-3; BR, Bacteriorhodopsin; C1C2, chimera between channelrhodopsin-1 and -2; Cryo-EM, Cryo-electron microscopy; CTAB, Cetyltrimethylammonium bromide; DDM, Dodecylmaltoside; DFT, Density functional theory; DPC, Dodecylphosphocholine; EPR, Electroparamagnetic resonance; FTIR, Fourier-transform infra-red; GR, *Gloeobacter violaceus* rhodopsin; LDAO, Lauryldimethylaminoxide; MSP, Membrane scaffold protein; NG, Nonylglucoside; OG, octylglucoside; PAR, Photosynthetically active region; PM, plasma membrane; RGR, RPE-retinal G protein-coupled receptor; RPE, Retinal Pigment Epithelium; SMA, Styrene-maleic-acid-copolymer; TR, Thermophilic rhodopsin; TR-WAXS, Time-resolved wide-angle X-ray scattering; XFEL, X-ray free electron laser.

INTRODUCTION

The first member and eponym of the rhodopsin family was identified in the 1930s as the visual pigment of the rod photoreceptor cell in the animal retina (Tansley, 1931; Wald, 1935). It turned out to be a membrane protein, owing its photosensitivity to the presence of a covalently bound chromophoric group. This photosensitive group, derived from vitamin A, was appropriately coined retinene, later officially renamed as retinal (Wald, 1935; Morton and Goodwin, 1944; Morton and Pitt, 1957). The visual pigments harboured a special conformer of this polyene compound, in casu the 11-*cis* configuration (Hubbard and Wald, 1952; Hubbard et al., 1971) (**Figure 1**). Upon photo-activation the chromophore was converted into the all-*trans* configuration, which triggered a sequel of conformational changes in the protein, leading to its active state (Wald, 1953; Morton and Pitt, 1957; Dartnall, 1962a). Eventually the chromophore was released as all-*trans* retinal (Dartnall, 1962c; Wald, 1968; Hubbard et al., 1971; Bridges, 1972). Surprisingly, in the 1970s a microbial counterpart of this protein was discovered in the archaeon *Halobacterium salinarum* (at the time referred to as *Halobacterium halobium*), which also harboured retinal as a chromophore, and was named bacteriorhodopsin (Oesterhelt and Stoeckenius, 1971). This membrane protein, however, contained the all-*trans* configuration, which upon photo-activation was converted into the 13-*cis* configuration (Smith et al., 1985; Oesterhelt, 1998). The resulting active state of the protein in this case thermally decayed in a sequel of steps whereby the chromophore eventually was thermally re-isomerized into the all-*trans* configuration returning to the original starting state (Oesterhelt, 1998; Lanyi, 2004).

Since their discovery a photogenic panorama unfolded, where up to date new members and subspecies with a variety of light-driven functionality have been added to these families. The animal branch, categorized as type-2 rhodopsins, turned out to form part of the major subclass in the superfamily of G protein-coupled receptors (Bennett et al., 1982; Kühn, 1984; Crescitelli, 1991; Hargrave and McDowell, 1992). Currently they have diversified into at least eleven groups (Opn1–Opn9, R-group, Cn-group) most of which are essential to multiple elements of light-dependent animal sensory physiology. Depending on the animal species, they can be located in multiple tissues next to the eye (Terakita, 2005; Davies et al., 2015). Meanwhile, the microbial branch was named as type-1 rhodopsins, which largely function as light-driven ion pumps or channels, but also contain sensory-active and enzyme-sustaining subspecies (Oesterhelt, 1998; Spudich et al., 2000; Ernst et al., 2014; Leung and Montell, 2017; Nagata and Inoue, 2022). The most recent addition to the microbial rhodopsins is the heliorhodopsin family, which is remarkably different from the type-1 family in their inverted orientation in the membrane, with the N-terminal now residing in the intracellular compartment (Pushkarev et al., 2018; Shihoya et al., 2019; Kovalev et al., 2020b; Rozenberg et al., 2021; Chazan

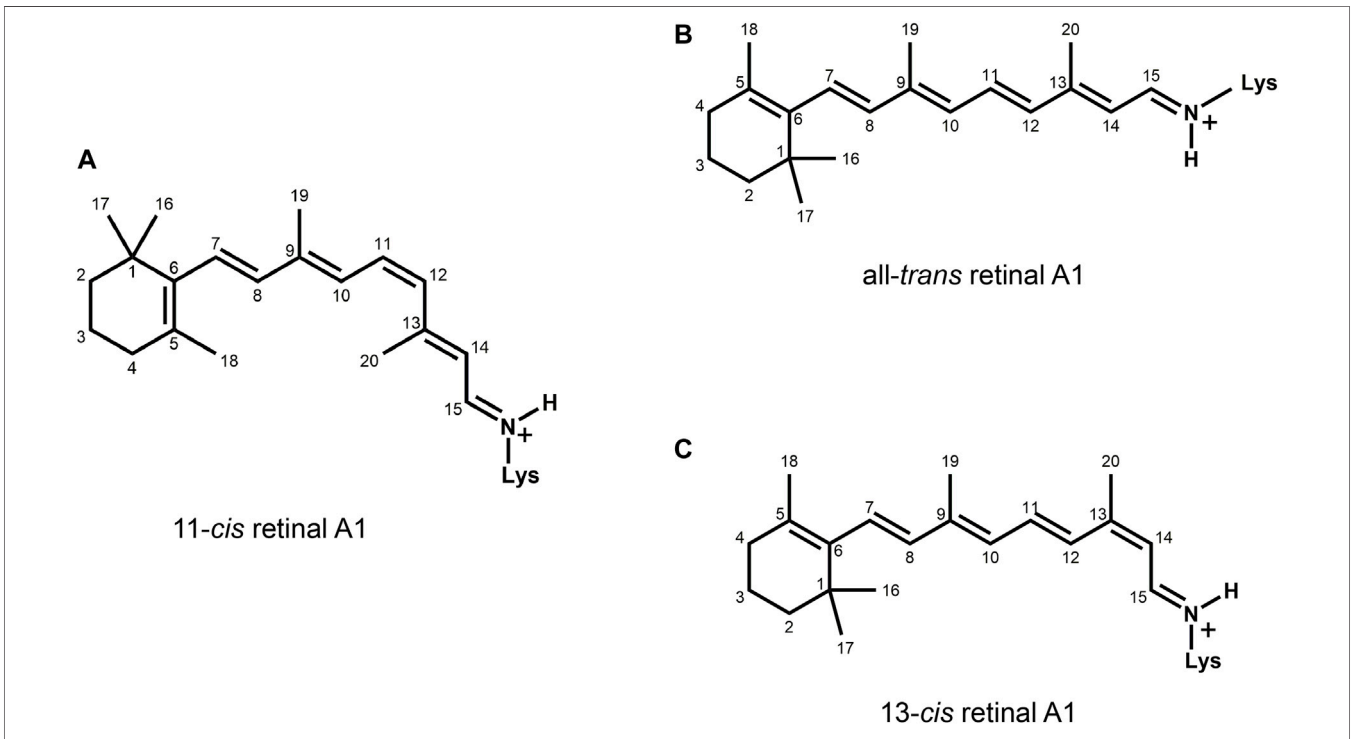

FIGURE 1 | Chemical structures of the most common chromophore configurations in the rhodopsin families. The type-2 pigments contain an 11-*cis*, 15-*anti* retinylidene Schiff base of retinal A1 **(A)** in the "dark state" (or "ground state" in photophysical terminology), which is photo-excited into the all-*trans* configuration. The Type-1 pigments contain the all-*trans* configuration **(B)** in the "dark state." This is photo-excited into the 13-*cis*, 15-*anti* configuration **(C)**, which thermally relaxes and re-isomerizes, returning to the ground state. The ring-polyene chain orientation is different for type-2 (6-s-*cis*) and type-1 (6-s-*trans*) rhodopsins.

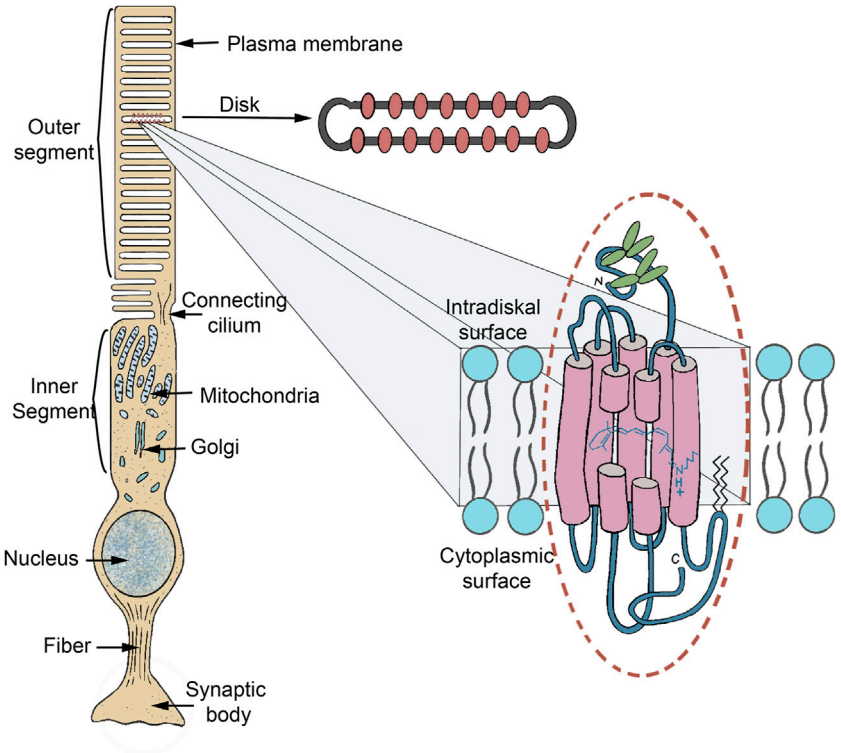

FIGURE 2 | Schematic of a vertebrate rod photoreceptor cell (scotopic vision), zooming in on the location of the rod visual pigment rhodopsin. The rod outer segment (ROS), a ciliary outgrowth, is densely filled with isolated flattened vesicles (discs) which contain rhodopsin as the major (ca 90% w/w) membrane protein. The vertebrate visual pigments are therefore also designated as "ciliary rhodopsins." Other disc membrane proteins are involved in signal propagation, stabilization of the disc shape and communication with the plasma membrane (PM). The phospholipids in the disc membrane have an exceptionally high content (ca 40%) of highly unsaturated fatty acids (22:6∞3) (Daemen, 1973). The discs are continuously generated at the base of the ROS as invaginations of the PM, then are nipped off and move upwards. After 7–10 days they reach the top of the ROS, which is pinched off in a circadian rhythm and degraded in the adjacent retinal pigment epithelium (RPE) (Young, 1976). The vertebrate cone photoreceptor (photopic vision) is organized in a similar fashion, except that the "discs" remain continuous with the PM as invaginations and are not pinched off. The organization of invertebrate visual photoreceptors is roughly similar, but the photoreceptive membranes are organized as numerous microvilli in rhabdomeric structures (Warrant and Mclintyre, 1993) and their rhodopsins are also designated as rhabdomeric visual pigments. Only the classical visual pigments (Opn1, Opn2 and R-gene families) are organized in these specialized cellular outgrowths. All other type-2 and all type-1 pigments are targeted to the PM or an eyespot and form only a small part (up to several percent) of that membrane protein population.

et al., 2022). The physiological function of this new family has not become very clear as of yet.

In this review we follow the historical development of this exciting membrane protein panorama in a representative number of highlights and present a prospect of their extraordinary future potential. We broadly outline their functional diversity and physiological relevance, as a comprehensive description is outside the scope of this review. A large number of excellent reviews on the rhodopsin families have been published, many of which we have referred to where appropriate, along with the most relevant early and recent papers. We refrain from presenting many molecular details, and therefore we refer to the following more recent reviews (DeGrip and Rothschild, 2000; Hofmann, 2000; Spudich et al., 2000; Hofmann et al., 2009; Yizhar et al., 2011; Palczewski and Orban, 2013; Ernst et al., 2014; Imamoto and Shichida, 2014; Inoue et al., 2014; Deisseroth, 2015; Hofmann and Palczewski, 2015; Brown and Ernst, 2017; Bando et al., 2019; El Khatib and Atamian, 2019; Dowling, 2020; Kandori, 2020; Kwon et al., 2020; Baillie et al., 2021; Moraes et al., 2021; Rozenberg et al., 2021; Bondar, 2022; Broser, 2022; Brown, 2022; Khelashvili and Menon, 2022; Nagata and Inoue, 2022).

This review presents a historical perspective and is therefore organized according to the landmark discoveries or progress in the field. In the following sections, we first discuss milestone studies and the common elements of the type-2 and type-1 rhodopsins, followed by individual subsections presenting typical elements for the type-2 and type-1 family, respectively. For the interested reader, we have compiled additional relevant citations in tables accompanying every section.

DISCOVERY

The discovery and identification of rhodopsins was governed by their spectral properties. Since they all absorb photons in the visible spectrum, careful visual observations were the cornerstone for these early studies.

Type-2 Family

Rhodopsin, the founding father of the type-2 family was first identified as the visual pigment of the rod photoreceptor cell. In the 19th century, groundbreaking research on vision by Müller, Boll and Kühne led to the visual perception, that light capture occurred in the distal part of the human retina (**Figure 2**), in particular the outer segments of the photoreceptor cells (Müller, 1855; Boll, 1877; Ewald and Kühne, 1878). The typical red color of this tissue disappeared upon illumination, which was termed "bleaching," and could to some extent be regenerated upon subsequent dark adaptation of the isolated eyecup. As of the 1930s it became apparent that a membrane-bound protein in the rod photoreceptor cell was responsible for the red color (Tansley, 1931; Bliss, 1948; Wald, 1953). This protein was named rhodopsin, after the ancient Greek words ροδεοσ (rhodeos, rose-coloured) and οψισ (opsis, which appropriately can be translated as sight or eyes). It was found to owe its spectral properties to a covalently bound cofactor, eventually named retinal (Wald, 1935, 1953, 1968; Hubbard et al., 1971). Subsequently, it was discovered that the cone photoreceptors in the vertebrate retina harboured closely related visual pigments (Morton and Pitt, 1957; Dartnall, 1962c; Mustafi et al., 2009). Thereafter, it became known that the invertebrate retina applied structurally very similar, but photochemically slightly differently operating visual pigments (Hara et al., 1967; Suzuki et al., 1993; Gärtner, 2000). Similar "bi-stable" pigments in fact are also active in the vertebrate retina, like the well-known melanopsins (Provencio et al., 1998; Kumbalasiri and Provencio, 2005). Another highlight was the growing insight that the visual pigments form part of the superfamily of G protein-coupled receptors (Kühn, 1984; Hargrave and McDowell, 1992; Palczewski and Orban, 2013). As a matter of fact, rhodopsin is the cornerstone of the major subfamily in this widespread receptor family.

Type-1 Family

In the early 1970s, fascinated by the dark-purple colonies of the salt lake thriving archaeon *Halobacterium salinarum*, Oesterhelt reported the surprising discovery that an intrinsic membrane protein was dominating purple patches in the cellular membrane of this archaeon and also harboured retinal as the chromophoric cofactor (Oesterhelt and Stoeckenius, 1971; Oesterhelt and Hess, 1973). At that time archaea were considered a subfamily of bacteria, and Oesterhelt coined the name bacteriorhodopsin (BR). Surprisingly, it was discovered that bacteriorhodopsin functions as a light-driven outward-directed proton pump, creating a proton-motive force enabling the cellular ATP-synthase complex to supply the cell with metabolic energy in the form of ATP (Oesterhelt et al., 1991). While bacteriorhodopsin is the dominant photoreceptor in *Halobacterium salinarum*, this archaeon eventually turned out to harbour several related photosensitive proteins, both with ion transport and sensory functions (Oesterhelt, 1998). Since the 1990s this field exploded, with more strains, including eukaryotic organisms like algae and fungi, and other functionalities being revealed every year (Béjà et al., 2000; Spudich et al., 2000; Brown, 2004; Rozenberg et al., 2021; Broser, 2022; Nagata and Inoue, 2022). More recently even viral rhodopsins have been discovered (Philosof and Béjà, 2013; Bratanov et al., 2019; Zabelskii et al., 2020). The overall structure and photochemistry of these pigments are very similar, and they are now considered to be a primary factor in marine phototrophy and solar energy conversion (Kirchman and Hanson, 2013; Gómez-Consarnau et al., 2019).

SPECTRAL AND STRUCTURAL PROPERTIES, AND SOLUBILIZATION

The spectral properties of all rhodopsins were discovered by visual observation, thanks to their absorbance of photons in the visible spectrum (350–750 nm). Accurate recording of their absorbance spectra was complicated in the spectrophotometers available at that time, due to the intense scattering of light by the rhodopsin containing membrane fragments isolated from host cells. Strong chemical reagents or alkaline conditions could dissolve these fragments, but with concomitant denaturation of the proteins and loss of their native spectral properties (bleaching). In the 1950s synthetic surface-active agents, termed detergents, became available, that were able to solubilize these membrane proteins in smaller mixed detergent-lipid-protein micelles, which strongly reduced light scattering (Hallett et al., 1991). Strong detergents like SDS still led to denaturation and release of retinal, but milder detergents were developed to avoid rapid partial unfolding at lab temperature or below. Accurate recording of absorbance spectra could then be established in detergent solutions. If some scattering still remained, or other visible light material interfered, difference spectroscopy was established by recording spectra before and after illumination in the presence of hydroxylamine and taking a difference spectrum. Hydroxylamine captures the released retinal as retinaloxime, which absorbs outside the main absorbance band of most rhodopsins (Wald and Brown, 1953; Hubbard et al., 1971; Kropf, 1975). This usually provides an accurate profile of the main absorbance band or at least the absorbance maximum. (**Figure 3**). A more recent and elegant approach is to insert a membrane protein into small nanodiscs (Civjan et al., 2003; Borch and Hamann, 2009; Ritchie et al., 2009) (**Figure 4**). This also strongly reduces light scattering and has the important advantage of embedding the protein in the more stabilizing lipid bilayer environment (Banerjee et al., 2008; Tsukamoto et al., 2011; Zhou and Cross, 2013; Ganapathy et al., 2020). Nanodiscs can be generated using either lipoproteins and membrane scaffold protein derivatives (MSPs) or small synthetic polymers of the amphipol or styrene-maleic acid copolymer family (SMAs) (Knowles et al., 2009; Popot et al., 2011; Hoi et al., 2021). For MSPs usually a brief detergent solubilization step is still required, while SMAs can extract the protein directly from the membrane, but have a smaller pH-profile (Shirzad-Wasei et al., 2015; Dörr et al., 2016; Kopf et al., 2020; Ueta et al., 2020).

The spectral profile of rhodopsins in the visible and near-UV region is very similar (**Figure 3**). It consists of the most red-

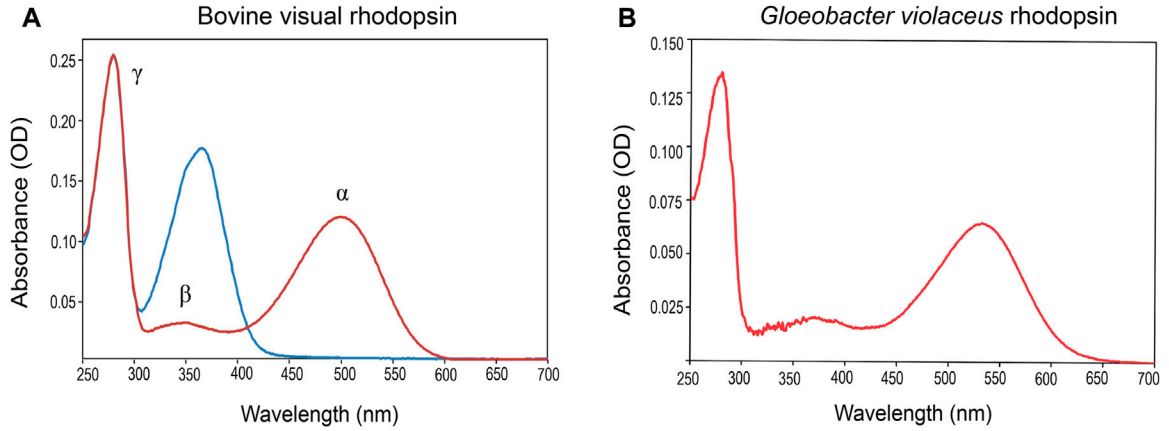

FIGURE 3 | Typical dark state absorbance spectra (red curves) of a purified type-2 **(A)** and type-1 **(B)** pigment. Both spectra exhibit a major peak (α-band) and a small satellite (β-band), both originating in the chromophore, and a γ-band near 280 nm, mainly originating in protein residues. The α-band derives from the whole conjugated polyene system (S0-S1) (cf. **Figure 1**), while the β-band derives from a smaller segment, and its intensity also depends on the torsion in the polyene chain. Upon short illumination of the monostable type-2 pigment **(A)** in the presence of hydroxylamine, the liberated retinal is converted into retinaloxime (blue curve). The Meta state of bistable type-2 pigments, also reacts with hydroxylamine generating retinaloxime, but usually quite slowly. Short illumination of type-1 pigments **(B)** in the presence of hydroxylamine hardly affects the photocycle and the return to the ground state. However, upon prolonged illumination hydroxylamine will slowly attack photo-intermediates, mainly M and N, releasing retinaloxime.

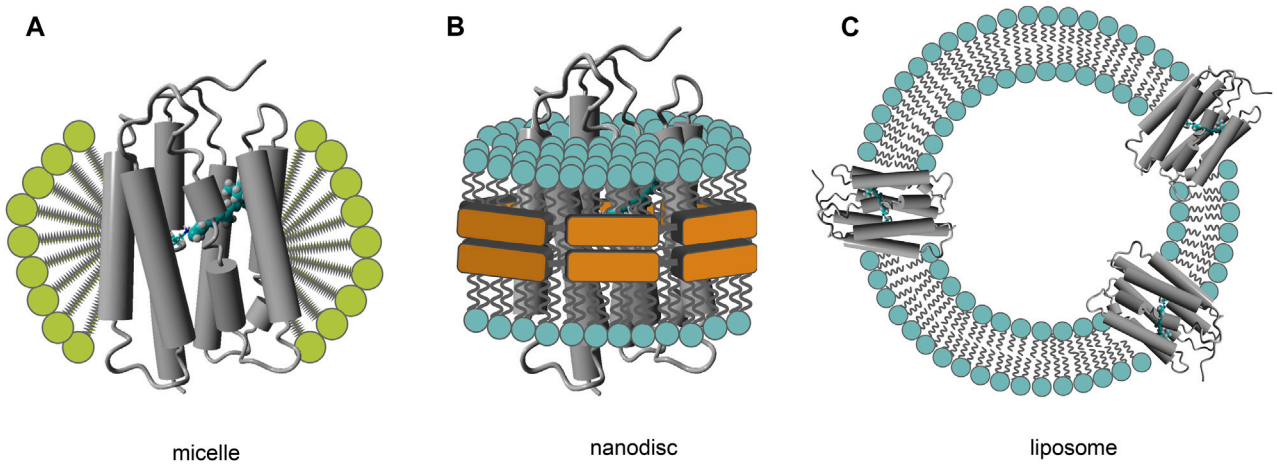

FIGURE 4 | Membrane mimics for purified membrane proteins. Schematics of the micellar **(A)**, nanodisc **(B)** and vesicular (**C**; proteoliposome) organization are displayed. Note that the relative dimensions are not to scale: diameters vary from 10–50 nm for the micelles and nanodiscs, and from 100 nm up to 10 μm for the liposomes. Several amphipatic components functioning as bilayer-stabilizing agents in the nanodiscs have been generated (MSP derivatives from lipoproteins, synthetic amphipols and SMAs, respectively), and are still under further development. Purification of the protein in a detergent environment generates the classical micellar state **(A)**. Because the thermal stability of membrane proteins in the micelles is generally reduced, often (phospho)lipids are added (bicelles). Alternatively, membrane proteins can be transferred into the bilayer membrane of a nanodisc **(B)** or liposome **(C)**. Membrane proteins can be directly (amphipol or SMA nanodiscs) or under very brief detergent exposure (MSP nanodiscs) transferred from the native membrane into nanodiscs, and the classical purification techniques can be applied upon the resulting nanodisc population. Liposomes offer a broader selection for the lipid population, and are used in vectorial transport studies and in AFM, FTIR and solid-state NMR spectroscopy. However, they are less suitable in optical spectroscopy because of their larger dimension, resulting in strong light scattering.

shifted main absorbance band or α-band, a smaller β-band, both originating in the bound retinal, and the γ-band near 280 nm, that largely originates in the aromatic residues of the protein part termed "opsin." In all rhodopsins retinal is covalently linked to a lysine residue in the seventh transmembrane segment (TM7) via a Schiff base (**Figure 1**) which is mostly protonated. The α-band is strongly red-shifted from the absorbance band of free retinal (maximum around 380 nm). This unusual polar grouping in the middle of a membrane protein is stabilized by the negatively charged "counterion complex," containing one, two or occasionally three protein residues (mostly Glu/Asp, sometimes Lys or in anion pumps a Cl^- ion) in a H-bonded network with nearby residues and bound water molecules (Lanyi, 2004; Ernst et al., 2014; Gerwert et al., 2014; Nomura et al., 2018).

Thus, the excitation energy in this retinylidene moiety is strongly reduced, compared to free retinal, which results in a red-shift of the absorbance profile. The magnitude of the red-shift strongly depends on the structure of the H-bonded network and counterion complex involving variable electrostatic interactions with the protonated Schiff base and to a lesser extent on the properties of protein residues in the opsin binding pocket (Lesca et al., 2018; Nikolaev et al., 2020; Shen et al., 2021; Shtyrov et al., 2021; Church et al., 2022a). By modifying these elements Nature created the spectacular broad variance in the spectral profile of rhodopsins, allowing them to cover the entire visible region.

The three-dimensional (3-D) structure of rhodopsins has been extensively investigated by classical electron diffraction on 2-D crystals and X-ray crystallography on large 3-D crystals, by solid-state NMR spectroscopy on membrane fragments and more recently by X-ray free electron lasers (XFEL) on small crystals (Schertler and Hargrave, 1995; Palczewski, 2012; Ladizhansky, 2017; Smith, 2021). Cryo-electron microscopy (Cryo-EM) has been traditionally performed on micellar solutions, but has also evolved to include nanodiscs (Maeda et al., 1991; Bertazolli-Filho et al., 2001; Hasegawa et al., 2018; Zhao et al., 2019; Zhang M. et al., 2021). Only solid-state NMR can be directly applied to membrane suspensions, but overall, there is quite good agreement between the various approaches. The overall structure is quite similar for all rhodopsin families, with the main scaffold consisting of seven closely packed transmembrane α-helices, which creates a tightly fitting binding pocket lined by a lysine residue to covalently bind retinal (**Figure 2**). The protein N- and C-terminal stretch reside at the extracellular and intracellular side of the membrane, respectively, except for the heliorhodopsin family where this sidedness is reverted (Pushkarev et al., 2018). However, the packing of the α-helices, the size of the loops connecting the α-helices and of the N-terminal and C-terminal stretches outside the membrane differ significantly between the type-1 and type-2 families.

Type-2 Family

Most type-2 rhodopsins, and in particular cone visual pigments and invertebrate pigments are very sensitive to at least partial denaturation upon solubilization in detergent solution (Bliss, 1948; Kropf, 1982; Okano et al., 1989). While commercial detergents like Triton X-100, CTAB, LDAO and Emulphogene BC-720 could dissolve the vertebrate rod pigment rhodopsin into mixed micelles with none or only very slow loss of spectral properties at room temperature, for most other pigments only the very mild agent digitonin could be applied (Tansley, 1931; Knudsen and Hubbell, 1978; Okano et al., 1989; Hofmann and Palczewski, 2015). This natural compound, a steroidal glycone extracted from *Digitalis purpurea*, however has the disadvantage that its commercial preparations were quite expensive and did vary in composition and aqueous solubility (Bridges, 1977). Major progress was attained in the 1970s upon development of the alkylsaccharide detergents 1-O-n-β-D-octylglucoside (octylglucoside, OG), nonylglucoside (NG) and dodecylmaltoside (DDM) (Stubbs et al., 1976; DeGrip and Bovee-Geurts, 1979). DDM in particular turned out to maintain thermal stability and spectral and photochemical properties of rhodopsin almost as well as digitonin (DeGrip, 1982; VanAken et al., 1986). Additionally, DDM is well accessible and affordable through organic synthesis, and has therefore become the most popular detergent in the membrane protein field. Also, in case a protein purified in DDM needs to be reconstituted in a lipid bilayer for certain applications (nanodisc or proteoliposome, **Figure 4**), DDM can be easily extracted via cyclodextrin inclusion (DeGrip et al., 1998). More recently, a large number of novel detergents based upon the structural principle of DDM have been developed, some of which provide better thermal stability or better crystallization conditions for selected membrane proteins than DDM, but all requiring more complex synthesis (Hussain et al., 2016; Nguyen et al., 2018; Ehsan et al., 2020; Urner et al., 2020).

The absorbance band profiles of type-2 rhodopsins are quite similar (**Figure 3**), but the position of the α-band varies strongly for the visual pigments. The vertebrate rod photoreceptor pigment rhodopsin has quite a broad range in its absorbance maximum (Rh1 subset, 440–520 nm), with fresh-water animals slightly red-shifted and marine animals blue-shifted depending on the depth of their habitat (Locket, 1977; Luk et al., 2016; Musilova et al., 2019). Vertebrate cone pigments cover the entire visible spectrum, and can be divided into four subsets, the long-wavelength (LWS, absorbance maximum range 520–640 nm), green (Rh2, 460–530 nm), blue (SWS2, 400–470 nm), and UV (SWS1, 350–450 nm) sensitive pigments (Crescitelli, 1991; Yokoyama and Yokoyama, 2000; Imamoto and Shichida, 2014). This classification is not only based upon spectral sensitivity, but also upon sequence similarity (Nathans, 1987; Hunt and Collin, 2014; Jacobs, 2018; El Khatib and Atamian, 2019). Invertebrate visual pigments are more scattered over the visible region and can range from 340 nm up to 600 nm (Gärtner, 2000; Katz and Minke, 2009; Tsukamoto and Terakita, 2010). Non-visual animal rhodopsins are scattered over the 340–550 nm region (Leung and Montell, 2017; Pérez J. H. et al., 2019; Moraes et al., 2021).

The spectral properties of the type-2 rhodopsins depend on the 11-*cis* configuration of the retinylidene chromophore. Next to the standard retinal (retinal A1, **Figure 1**), several natural modifications occur (analogs). In fresh-water and coastal vertebrates 11-*cis* 3-dehydroretinal (retinal A2) has been observed (**Figure 5**) (Bridges, 1972; Yoshizawa, 1984; Imai et al., 1999). The longer conjugated chain red-shifts the absorbance maximum by 20–40 nm in rod pigments and up to 70 nm in cone pigments, as compared to retinal A1, to compensate for the lower blue light intensity in their habitat (Dartnall, 1962c; Hubbard et al., 1971). These "A2-rhodopsins" are also referred to as porphyropsins. In insects and some other invertebrates, 11-*cis* 3-hydroxy- and 4-hydroxyretinals have been detected (**Figure 5**) (Vogt and Kirschfeld, 1984; Matsui et al., 1988; Seki and Vogt, 1998). These modifications blue-shift the absorbance maximum by 20–40 nm, as compared to retinal A1 (Sekharan et al., 2011).

While such natural modifications are exploited to modulate the spectral position of a rhodopsin, the most effective approaches to shift the absorbance spectrum of the rhodopsin chromophore away from that of free retinal (380 nm) are

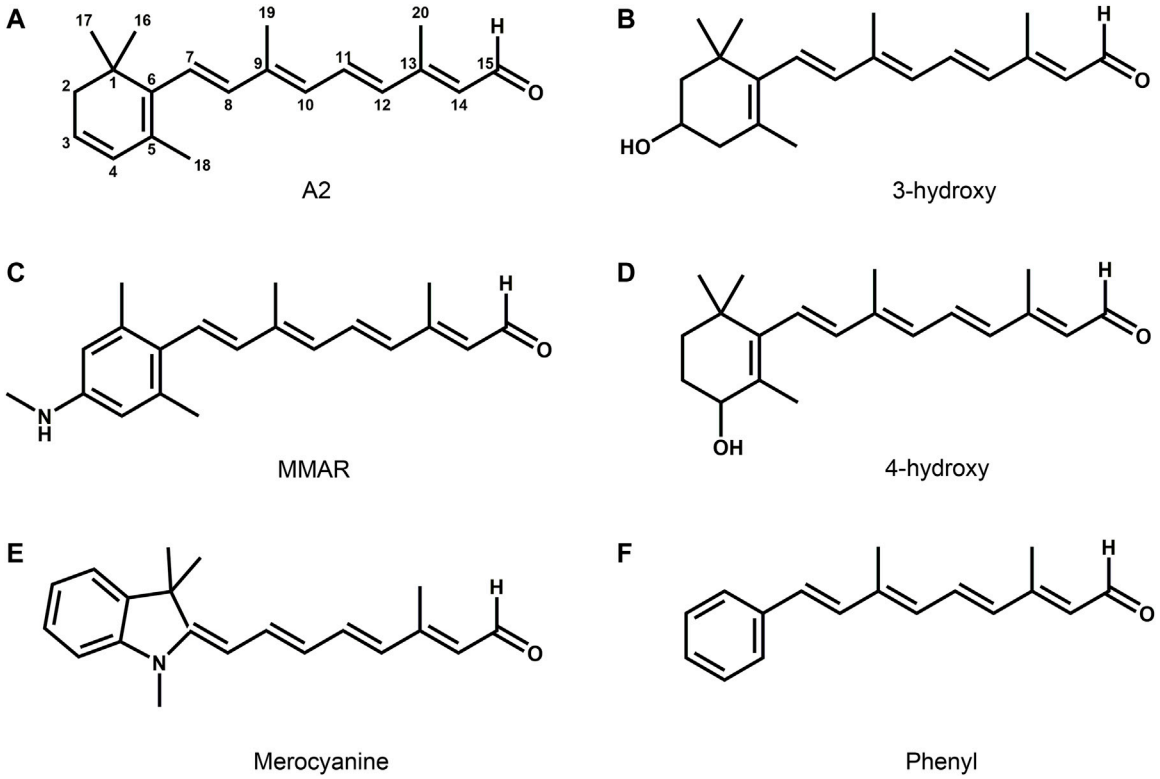

FIGURE 5 | Some uncommon retinal analogs occurring as natural chromophores or in engineered pigment analogs. 3, 4-didehydroretinal (retinal A2, **(A)**) red-shifts the rhodopsin spectrum relative to A1, and is mostly found in fish and amphibian visual pigments. 3-hydroxy- **(B)** and 4-hydroxy- **(D)** retinal A1 induce a blue-shift relative to A1 and are found in the visual pigments of insects and deep-sea shrimps, respectively. Phenylretinal **(F)**, MMAR **(C)** and the merocyanine derivative **(E)** are synthetic analogs, that, respectively, induce a blue-shift **(F)** and the largest red-shifts, observed so far (**(C,E)**; see text). All these analogs bind to the lysine residue in the native opsin binding pocket with a protonated Schiff base.

protonation of the Schiff base and mutation of selected opsin residues lining the retinal binding pocket. For instance, only the Schiff base in UV absorbing rhodopsins, which absorb in the 350–380 nm region, is not protonated, while in all other classes it is protonated (Kusnetzow et al., 2004; Imamoto and Shichida, 2014). The large variation in the spectral properties in the latter classes is mainly due to the combined inductive effect of opsin binding pocket residues, in combination with H-bonding networks involving water molecules. On top of that, some vertebrate LWS visual pigments have developed a unique mutation (Glu197->His) creating a chloride binding site that effectuates a further 20–30 nm red-shift (Wang et al., 1993).

With respect to structural biology, bovine rod rhodopsin was a forerunner among all animal intrinsic membrane proteins, presenting the first detailed 3-D structure via X-ray crystallography in 2000, with many more to follow (Palczewski et al., 2000; Li et al., 2004; Okada et al., 2004). The seven transmembrane α-helical scaffold surrounding an accessible cofactor binding pocket proved to be the general motif for the entire G protein-coupled receptor family (**Figure 6**) (Sanchez-Reyes et al., 2017). This feat has stimulated advances in many other research fields, including drug design in the pharmaceutical sciences, study of protein structure-function correlations, and membrane protein-lipid interactions, both from experimental, theoretical and *in-silico* standpoints. Several natural factors concurred to enable this important step forward. First of all, rod rhodopsin is one of the few intrinsic membrane proteins that is available in relatively large quantities in domesticated animals, the most used being cattle (up to 1 mg of rhodopsin per eye), bullfrogs (up to 100 μg per eye) and chick (up to 100 μg LWS cone pigment per eye) (DeGrip et al., 1980; Toba and Hanawa, 1985; Yoshizawa and Kuwata, 1991). After enucleation and proper dark adaptation of the eyes, intact rod or cone outer segments (ROS or COS) can be easily isolated in a dark room under dim red light (>650 nm) that will not activate and bleach the pigment (**Figure 3**). Further, in dark-adapted ROS, rhodopsin makes up about 85% of the total protein content (DeGrip et al., 1980). Eventually, dark-adapted bovine retinae even became commercially available (Hormel Co., Austin, Minnesota, United States). Finally, bovine rod rhodopsin was found to be relatively resistant to destabilization by detergents as compared to most other visual pigments, allowing extensive purification. Likewise, it proved to be sufficiently stable in less mild but more crystal-production-favoring small detergents like OG and

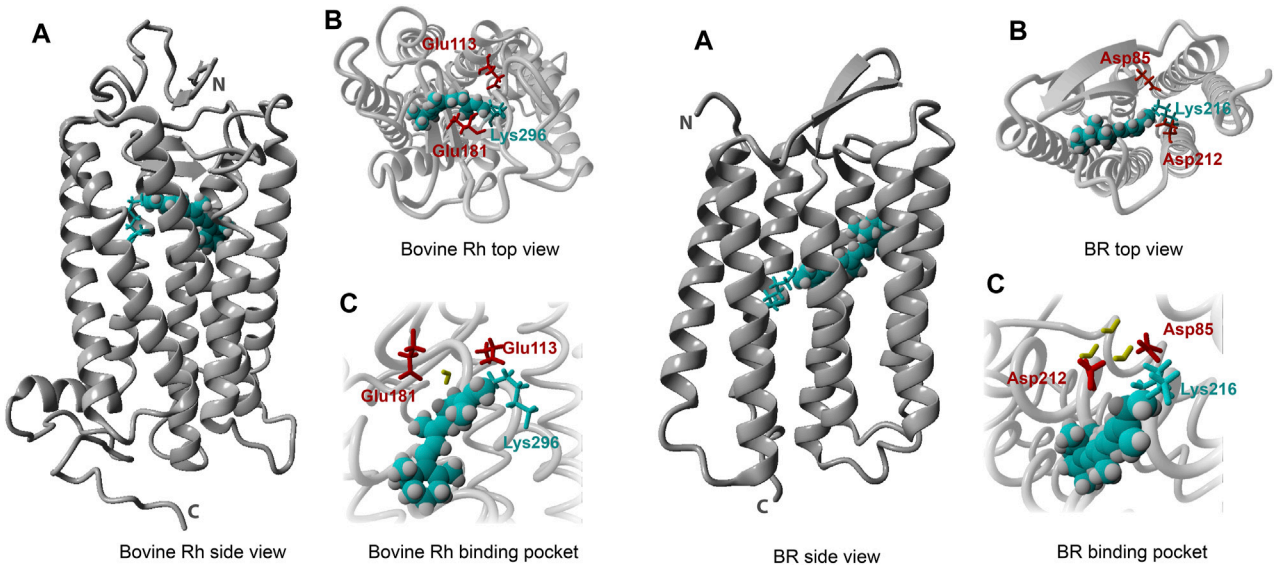

FIGURE 6 | Comparison of structural features of the type-2 and type-1 pigment archetypes bovine rod rhodopsin (left section) and bacteriorhodopsin (right section), respectively. Full crystal structures are presented in **(A)** and **(A)** (pdb 1U19 and 5ZIN), a top view is shown in **(B)** and **(B)** and a binding pocket exposure in **(C)** and **(C)**, respectively. The retinylidene chromophore (cyan) is represented as space-filling spheres, and the retinal binding lysine residue (cyan) is presented as sticks. The two protein residues displayed (red) contribute to the counterion complex stabilizing the pronated Schiff base. The two crystal structures share the seven α-helical transmembrane segment bundle, but the packing of the helices, the location and assembly of the binding pocket and the structure of the chromophore are clearly different.

NG to facilitate crystallization trials (Palczewski et al., 2000; Park et al., 2008).

The bovine rhodopsin amino acid sequence was established thanks to heroic protein sequencing efforts (Abdulaev et al., 1982; Hargrave et al., 1983). Over time, sequence information became available more easily via genome mining and c-DNA-sequencing. Thus, it came out that most invertebrate visual pigments are similar in size to the vertebrate pigments (36–42 kD), but mollusc pigments are significantly larger (46–55 kD), because of the presence of a much longer C-terminal (Ovchinnikov et al., 1988b; Gärtner, 2000). This additional stretch is unique in having an insertion of up to eleven copies of a peculiar pentapeptide sequence (Pro-Pro-Gln-Gly-Tyr), which probably helps in immobilization of the protein in the microvillar membrane (Ryba et al., 1993; Gärtner, 2000). Longer C-terminal stretches are also found in non-visual rhodopsins. For instance, the VA-opsin and melanopsin family also show this feature, except that the pentapeptide insertion does not occur. Here the extra sequence probably has a function in complex regulation of signal processing and desensitization (Valdez-Lopez et al., 2020; Contreras et al., 2021). Some VA-opsins and melanopsins are even produced in two or more splicing isoforms, with longer and shorter C-terminals (Davies et al., 2010).

While squid provides fair quantities of visual pigment, the first complete 3-D crystal structures only became available since 2008, both because of the much lower stability of the pigments in detergent solution and since crystallization could only be achieved after proteolytic removal of most of the long C-terminal (Murakami and Kouyama, 2008; Shimamura et al., 2008). The overall fold of the seven-transmembrane α-helical scaffold is quite similar to bovine rhodopsin, but the structure of the long C-terminal could not be determined, of course. The position of the retinal chromophore is slightly different, since the Glu residue functioning as the direct counterion for the protonated Schiff base is displaced from the site in the vertebrate pigments (Terakita et al., 2004). The first crystal structure of an arthropod rhodopsin (jumping spider) was only recently published in 2019, and again shows the familiar seven α-helical fold with overall high similarity with the squid structure (Varma et al., 2019). So far, crystal structures of non-visual rhodopsins have not been reported.

The crystal unit cell of bovine rod rhodopsin contains a dimer, but its interaction pattern is very different from the natural one (Fotiadis et al., 2006; Palczewski, 2006). In fact, rhodopsin is equally active as a monomer, and the organization in the ROS disc membranes is still debated (monomer, dimer, longer stretches?) (Fotiadis et al., 2004; Chabre and LeMaire, 2005; Mishra et al., 2016; Zhang et al., 2016; Feldman et al., 2019; Zhao et al., 2019). Invertebrate visual rhodopsins are probably rigidly immobilized in their native membrane, which allows to discern the polarization plane of the incoming light (Gärtner, 2000; Stavenga et al., 2000).

The crystal structures are essential to resolve the protein fold of the rhodopsins and have confirmed several conjectures of the binding pocket. Biochemical, vibrational (resonance Raman and FTIR spectroscopy) and solid-state NMR studies already produced very strong evidence that it indeed harboured the 11-*cis* configuration of retinal (Groenendijk et al., 1980; Mathies et al., 1987; Lugtenburg et al., 1988; DeGrip and

TABLE 1 | Selected additional citations for the section "Spectral and structural properties and solubilization".

Type-1 pigments

Optical spectroscopy: Rousso et al. (1998); Kanehara et al. (2017); Asido et al. (2021)

Vibrational spectroscopy: Garczarek and Gerwert, (2006); Lórenz-Fonfría and Kandori, (2009); Kraack et al. (2011); Verhoefen et al. (2011); Lórenz-Fonfría et al. (2015a); Ito et al. (2018); Watari et al. (2019); Lórenz-Fonfría et al. (2021)

NMR/EPR spectroscopy: Smith et al. (1989); Shi et al. (2009); Mao et al. (2014); Planchard et al. (2014); Shigeta et al. (2017); Mao et al. (2019); Naito et al. (2019); Friedrich et al. (2020)

Crystallography/EM: Havelka et al. (1995); Kimura et al. (1997); Belrhali et al. (1999); Subramaniam et al. (1999); Royant et al. (2001); Vogeley et al. (2004); Luecke et al. (2008); Wada et al. (2011); Kato et al. (2012); Wang et al. (2012); Frank et al. (2014); Kato et al. (2015); Nango et al. (2016); Tsukamoto et al. (2016); Broecker et al. (2017); Hasegawa et al. (2018); Ghanbarpour et al. (2019); Kovalev et al. (2019); Li et al. (2019); Morizumi et al. (2019); Shihoya et al. (2019); Yun et al. (2019); Besaw et al. (2020); Hayashi et al. (2020); Kovalev et al. (2020a); Lu et al. (2020); Bada Juarez et al. (2021); Higuchi et al. (2021); Li et al. (2021); Suzuki et al. (2022); Zhang et al. (2022)

Atomic force microscopy: Müller et al. (2002); Klyszejko et al. (2008); Yu et al. (2017); Heath et al. (2021)

Computational: Hayashi et al. (2001); Fujimoto et al. (2007); Melaccio et al. (2016); Karasuyama et al. (2018); Tsujimura and Ishikita, (2020); Fujimoto, (2021); Shen et al. (2021)

Reviews: Béjà et al. (2000); Caffrey, (2003); Engel and Gaub, (2008); Bamann et al. (2014); Grote et al. (2014); Neutze et al. (2015); Engelhard et al. (2018); Bibow, (2019); Kwon et al. (2020); Kawasaki et al. (2021)

Solubilization: Yu et al. (2000); Bayburt et al. (2006); Yeh et al. (2018); Ueta et al. (2020)

Other: Tribet et al. (1996)

Type-2 pigments

Optical spectroscopy: Seki et al. (1998); Salcedo et al. (1999); Schafer and Farrens, (2015); Katayama et al. (2019)

Vibrational spectroscopy: Rothschild et al. (1980); Kochendoerfer et al. (1999)

NMR/EPR spectroscopy: Creemers et al. (1999); Carravetta et al. (2004)

Crystallography/EM: Sardet et al. (1976); Davies et al. (1996); Davies et al. (2001); Krebs et al. (2003); Standfuss et al. (2007); Stenkamp, (2008); Hildebrand et al. (2009); Blankenship et al. (2015); García-Nafría and Tate, (2020); Zhang et al. (2021a)

Computational: Nikolaev et al. (2018); Patel et al. (2018)

Reviews: Neitz and Neitz, (1998); Spudich et al. (2000); Sakmar et al. (2002); McDermott, (2009); Smith, (2010); Bickelmann et al. (2015); Guo, (2020)

Solubilization: Kropf, (1982); Sadaf et al. (2015); Frauenfeld et al. (2016); Lee et al. (2020); Grime et al. (2021)

Rothschild, 2000; Mathies and Lugtenburg, 2000). Surely enough, this configuration best fitted the non-protein electronic density in the binding pocket. The same is true for the covalent binding of retinal to a lysine residue, for which the above-mentioned techniques also already provided a wealth of evidence (Bownds, 1967; DeGrip et al., 1973; Creemers et al., 1999; Mathies and Lugtenburg, 2000). However, to firmly establish protonation of the Schiff base the resolution of the crystal structures is not high enough. Instead, the evidence produced by vibrational and NMR spectroscopy is very convincing and in fact was later underpinned by quantum-chemical computation (Palings et al., 1987; Herzfeld and Lansing, 2002; Gascón et al., 2005; Tastan et al., 2014).

Type-1 Family

The sensitivity to detergent action also varies strongly between microbial rhodopsins. For instance, while bacteriorhodopsin (BR) is quite stable in OG, Triton X-100 and dodecylphosphocholine (DPC) even as a monomer, the rhodopsin proton pump from the cyanobacterium *Gloeobacter violaceus* (GR) strongly prefers DDM and is very unstable in DPC (Dencher and Heyn, 1978; Brouillette et al., 1989; Ganapathy et al., 2020). In general, OG and DDM are the preferred agents for solubilization of type-1 rhodopsins.

The spectral range of type-1 rhodopsins (360–690 nm) is comparable to that of type-2. There is less evidence for a clear relation to activity or habitat, an exception being the proton pump proteorhodopsin, which exhibits a blue-shift in deeper marine environments (Béjà et al., 2001; Bielawski et al., 2004). In a major distinction from type-2, microbial rhodopsins invariably exploit retinal A1 in the all-*trans* configuration as the basis for their light absorbance. Here, as well, a plethora of experimental evidence has demonstrated retinal binding to a lysine residue via a protonated Schiff base (Haupts et al., 1999).

Advanced angular electron diffraction studies on 2-D BR crystals in membrane patches already afforded a first glimpse into the organization of the helical transmembrane segments of type-1 rhodopsins (Henderson and Unwin, 1975; Mitra et al., 1993; Grigorieff et al., 1996; Heymann et al., 1997; Mitsuoka et al., 1999). The first 3-D crystal structures were reported for BR from 1997 onwards, and at a very high resolution slightly before that of bovine rhodopsin (Luecke et al., 1999; Pebay-Peyroula et al., 2000). This progress was aided by its high stability in detergent solutions and the relatively simple isolation from its native source. Bacteriorhodopsin is organized in large singular patches in the cellular membrane of *Halobacterium salinarum*, which can visually be observed and separated from other membrane fragments quite easily (Oesterhelt and Stoeckenius, 1971). In addition, type-1 rhodopsins complete a full photocycle (see below) and after photo-activation do not release the retinal, but thermally return to the ground state. This obviates the complexity of using dark rooms and shielding all experimental manipulations from room light exposure. Meanwhile, quite a number of crystal structures have been resolved for various classes of type-1 rhodopsins (**Table 1**). The most recent high resolution 3-D structures actually capitalized on the fantastic progress in cryo-EM (Hirschi et al., 2021; Kishi et al., 2022).

The available type-1 3-D structures show high similarity in protein fold and retinal pocket location. The basic seven α-helical transmembrane organization is comparable to that of type-2 (**Figure 6**), but for type-1 the helical packing is

somewhat different and more compact. The loop segments connecting the helices are generally shorter and the retinal pocket is positioned differently to accommodate the longer all-*trans* chromophore instead of the curved 11-*cis* one (**Figures 1**, **6**). Aspects of the binding pocket (retinal isomer and binding to a lysine residue via a Schiff base) again were in line with a wealth of evidence generated by biochemical and spectroscopic techniques (Lanyi, 2004). A recent XFEL study of the bacteriorhodopsin photocycle achieved a very high structural (ca 1.5 Å) and temporal (femtosecond) resolution and produced evidence for protonation of the Schiff base (Nogly et al., 2018). Also in the type-1 case the evidence generated by biophysical techniques like vibrational, EPR and NMR spectroscopy and by quantum-chemical computation is most convincing (Ernst et al., 2014; Brown and Ernst, 2017; Ryazantsev et al., 2019; Nagata and Inoue, 2022).

A conspicuous feature of most type-1 rhodopsins is that they organize in homo-oligomers, whether observed in the native membrane or in host cells. The most common arrangement for bacterial and archaeal rhodopsins are trimers or pentamers, though occasionally hexamers do occur as well (Hussain et al., 2015; Shibata et al., 2018; Kao et al., 2019). Circular dichroism spectroscopy provides evidence for exciton coupling between the chromophores (Cassim, 1992; Fujimoto and Inoue, 2020; Fujimoto, 2021). For eukaryotic type-1 rhodopsins, homo-dimeric as well as hetero-dimeric complexes are observed (Mukherjee et al., 2019; Govorunova et al., 2021; Broser, 2022). Isolated type-1 monomers are also functionally active, indicating that the oligomeric assembly probably affords optimal packing and mutual stabilization, and/or the opportunity to modulate monomer activity by inter-subunit interplay (Iizuka et al., 2019).

A novel feature was discovered in the enzyme-rhodopsins i.e. an additional transmembrane segment at the N-terminal (TM8), which functions as a connector with the cognate soluble enzyme domain and seems to be essential for modulating its activity (Ikuta et al., 2020; Tsunoda et al., 2021).

Interestingly, several thermostable microbial rhodopsins have been discovered. The crystal structure of the highly thermophilic rhodopsin (TR) from *Thermus thermophilus* was resolved to be very similar to that of the much less thermally stable xanthorhodopsin (XR) from *Salinibacter ruber*, including the binding crevice for the carotenoid antenna (Tsukamoto et al., 2016). Likewise, the crystal structure of the thermostable rhodopsin proton-pump from *Rubrobacter xylanophilus* (RxR) is very similar to that of bacteriorhodopsin (Hayashi et al., 2020). An unusually widely stable proton pump (pH, detergent, temperature), named Tara76 rhodopsin, was isolated from uncultured bacteria (Shim et al., 2021). Such data shed new light on the design options to increase thermal and environmental stability without a significant sacrifice in dynamics and activity (Hayashi et al., 2020).

Additional selected references relevant for this section have been compiled in **Table 1**.

FUNCTIONAL DIVERSITY, PHYLOGENY

It was relatively simple in the old days. On one hand, we knew of animal rhodopsins, being G protein-coupled receptors, very nicely developed and evolved into a set of proteins allowing photopic vision (color discrimination) and a single class for extremely sensitive scotopic vision (black-and-white). On the other hand, another class of retinal-proteins had evolved in archaea to exploit solar energy for active transport of protons and chloride ions. However, with the awakening of the genome era, this view became totally obsolete. While the notion that the type-1 and type-2 families probably do not have a common ancestor and have little overlap in physiological function was consistent, over time many new members were discovered and their classification revised (Porter et al., 2012; Yee et al., 2013; Zabelskii et al., 2021). In hindsight, it was to be expected that ahead of the large carotenoid and chlorophyll dependent protein complexes in the photosynthetic reaction centers, Nature would have taken advantage of the abundance of solar energy making maximal use of this fantastic toolbox of retinal-proteins, that are relatively simply to bioproduce and adapt.

It is likely that many products of this toolbox are yet to be discovered, but already the genetic and functional diversity is so vast and complex, that we provide a very general overview below and mostly refer to selected reviews.

Type-2 Family

The animal rhodopsins have meanwhile been classified in at least nine gene families (Opn1–Opn9) and two separate sets with some members still awaiting further assignment (**Table 2**). Physiological function and tissue distribution show incredible diversity (Janssen et al., 2003; Leung and Montell, 2017; Liebert et al., 2021; Moraes et al., 2021; Calligaro et al., 2022). The classical visual pigments come within Opn1 (cone pigments) and Opn2 (rod pigments). Pigments discovered later in the vertebrate retina, such as melanopsin, VA-opsin or neuropsin, peropsin (RRH) and RGR fall under Opn4, unclassified and Opn5, respectively (**Table 2**). The common thread still is primary signal transduction via at least one of the available G-protein species (Gt, Go, Gi, Gq, and Gs), with cross-activation, modulation or desensitization via a variety of other mediators. However, RGR and its mollusc counterpart retinochrome are exceptional in this context, since they act as photo-isomerases, binding all-*trans* retinal in the dark state, and releasing 11-*cis* retinal after photo-activation as a supply for regeneration of visual opsins (Hara et al., 1967; Pepe and Cugnoli, 1992; Zhang et al., 2019; Choi et al., 2021; Vöcking et al., 2021). Another remarkable subset are Opn5L, peropsin and Opn7 members, which also bind all-*trans* retinal in the dark state, but that seems to be the active state binding the G protein. Upon illumination they generate the 11-*cis* chromophore, which represents the resting state that in the case of Opn5L members may even thermally revert to the active state (Nagata et al., 2018; Yamashita, 2020; Karapinar et al., 2021; Sakai et al., 2022). An even more surprising observation is that some type-2 pigments may be involved

TABLE 2 | Current classification of type-2 rhodopsins.

Gene family or group	Main components[b]	Spectral range[a]	Location	Mono/bi-stable[a]	Special facts	Selected literature
Opn1	Vertebrate cone pigments	350–610 nm	Retina	Mono		Nathans, (1987); Imamoto and Shichida, (2014); Hofmann and Palczewski, (2015); Borgia et al. (2018); Jacobs, (2018); El Khatib and Atamian, (2019); Astakhova et al. (2021)
Opn2	Vertebrate Rod pigments	440–520 nm	Retina, Brain	Mono	Includes exorhodopsin	Ebrey and Koutalos, (2001); Rohrer et al. (2003); Warrant and Locket, (2004); Tarttelin et al. (2011); Davies et al. (2012); Liu et al. (2019); Ortega and Jastrzebska, (2019)
Opn3	Encephalopsins Panopsins TMT-opsins	Blue-green	Multiple tissues, Extra-ocular	Bi		Blackshaw and Snyder, (1999); Halford et al. (2001); Moutsaki et al. (2003); Leung and Montell, (2017); Lan et al. (2020); Olinski et al. (2020); Xu et al. (2020); Davies et al. (2012); Davies et al. (2021); Liebert et al. (2021)
Opn4	Melanopsins	450–500 nm	Multiple tissues	Bi	Long C-terminals	Provencio et al. (1998); Provencio et al. (2000); Panda et al. (2002); Kumbalasiri and Provencio, (2005); Panda et al. (2005); Giesbers et al. (2008); Davies et al. (2010); Shirzad-Wasei and DeGrip, (2016); Duda et al. (2020); Valdez-Lopez et al. (2020); Contreras et al. (2021)
Opn5[c]	Neuropsins Peropsins RGR's	UV-blue	Multiple tissues	Bi	11-*cis* - > all-*trans* Photoactivation All-*trans* -> 11-*cis*	Jiang et al. (1993); Sun et al. (1997); Tarttelin et al. (2003); Yamashita et al. (2010); Yamashita et al. (2014); Nagata et al. (2018); Sato et al. (2018b); Zhang et al. (2019); Yamashita, (2020); Choi et al. (2021); Liu et al. (2021); Calligaro et al. (2022); Fujiyabu et al. (2022)
Opn6		UV-blue	Multiple tissues	Mono and Bi	Zebrafish Monotrenes	Davies et al. (2015)
Opn7		UV-blue	Multiple tissues	Bi and Mono	Zebrafish All-*trans* -> 11-*cis*	Davies et al. (2015); Karapinar et al. (2021)
Opn8		UV-blue	Multiple tissues	Bi	Not in mammals	Davies et al. (2015)
Opn9		?	Multiple tissues	?	Zebrafish, long extra-cellular loop	Davies et al. (2015)
R (habdomeric) opsins	Molluscs Arthropods	340–600 nm	Mainly ocular	Bi	Molluscs, long C-terminal	Wald, (1953); Hara et al. (1967); Hillman et al. (1983); Vogt and Kirschfeld, (1984); Gärtner, (2000); Stavenga et al. (2000); Furutani et al. (2005); Porter et al. (2012); Nagata et al. (2018); Leung et al. (2020); Nagata and Inoue, (2022)
Cn(iderian) opsins	Jellyfish	?	Multiple tissues	?		Musio et al. (2001); Plachetzki et al. (2012); Porter et al. (2012); Feuda et al. (2014); Davies et al. (2015); Gerrard et al. (2018); Hayashi et al. (2020)
Separate gene groups	VA-opsins Parapinopsins Parietopsins Pinopsins Xenopsins Go-rhodopsins	Blue-green	Multiple tissues	Mostly Bi	Parietopsins mainly in pineal gland Xenopsins and Go-rhodopsins in invertebrates	Okano et al. (1994); Blackshaw and Snyder, (1997); Kojima et al. (1997); Soni and Foster, (1997); Nakamura et al. (1999); Spudich et al. (2000); Foster and Hankins, (2002); Su et al. (2006); Davies et al. (2010); Tsukamoto and Terakita, (2010); Passananeck et al. (2011); Sakai et al. (2012); Koyanagi et al. (2014); Davies et al. (2015); Leung and Montell, (2017); Sato et al. (2018a); Pérez et al. (2019b); Rawlinson et al. (2019); Döring et al. (2020); Eickelbeck et al. (2020); Copits et al. (2021); Rodgers et al. (2021)

[a]*Spectral range and mono/bistability not always exclusive within a group and very limited known for Opn6-Opn9 and Cn-opsins.*

[b]*Cone pigments are mainly involved in color (photopic) vision, rod pigments in (scotopic) dim-light vision. In mammals melanopsins are important for pupillary contraction and circadian regulation. Retinochromes (R-opsins) and peropsins and RGRs (Opn5) have photoisomerase activity (all-trans → 11-cis).*

[c]*The Opn5L group (Sato et al., 2018b; Yamashita, 2020) may have been classified wrongly, since they clade within the Opn6-9 framework.*

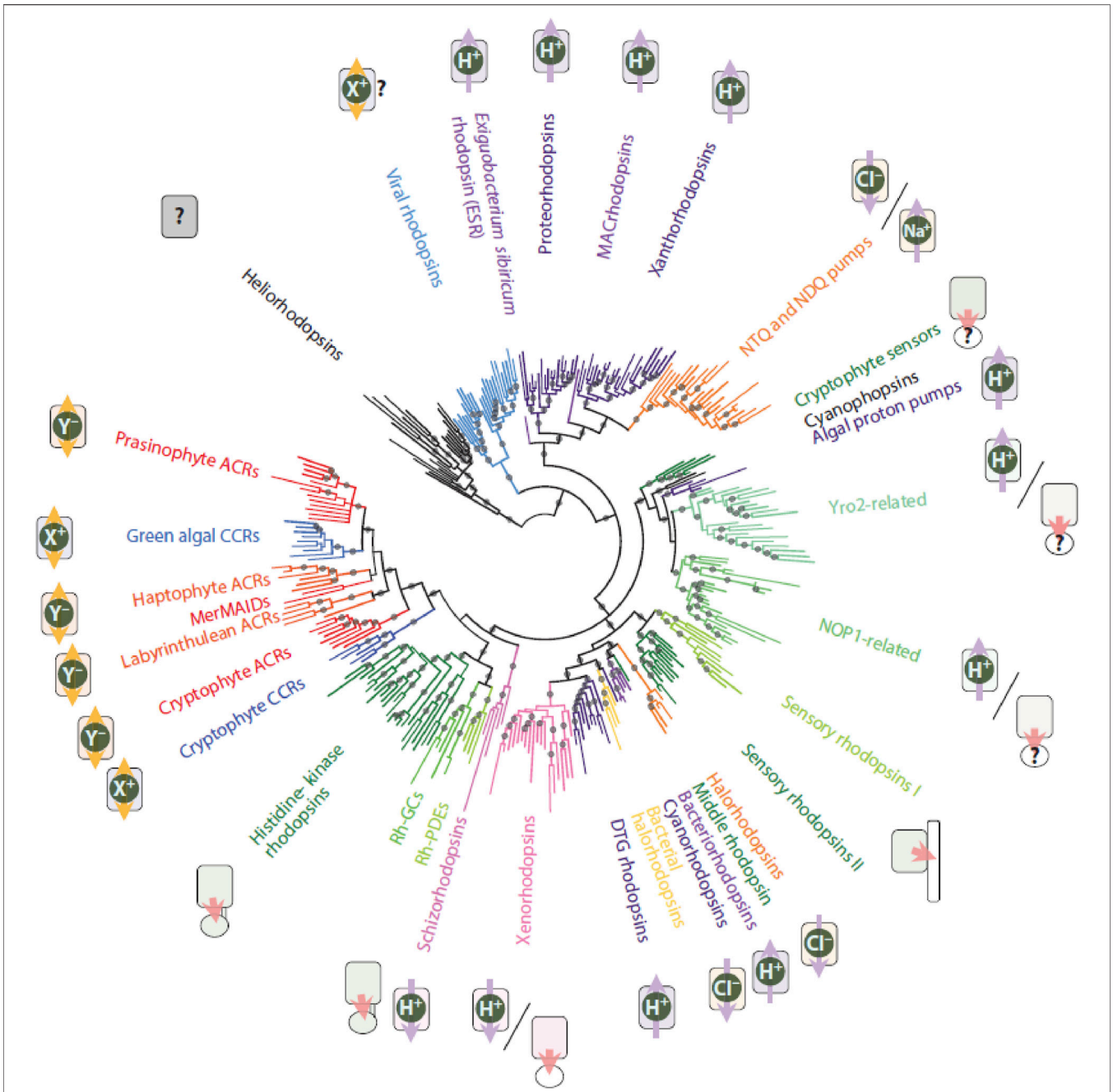

FIGURE 7 | Global phylogeny of type-1 pigments illustrating their formidable diversification. The figure was modified with consent from Rozenberg et al., 2021. We refer to the original paper for the construction of the tree and for all abbreviations. Purple arrows represent active outward (away from center) and inward ion transport, respectively. Orange arrows represent ion channels. Pink arrows represent enzyme-rhodopsins (fused enzyme domains) and sensory rhodopsins (detachable transducers). For further details of the various classes we refer to recent literature (Hasemi et al., 2016; Govorunova et al., 2016; id-, 2022; Nakajima et al., 2018; Oppermann et al., 2019; Kovalev et al., 2020a; Rozenberg et al., 2021).

in recognizing temperature differences or mechanical changes, or function as chemosensors or tumorigenic elements, possibly even without requiring their retinal cofactor (Shen et al., 2011; Park et al., 2013; Baker et al., 2015; Pérez-Cerezales et al., 2015; Leung et al., 2020; Xu et al., 2020; Córdova et al., 2021; Moraes et al., 2021).

Type-1 Family

Type-1 rhodopsins have been identified in archaea and eubacteria, including cyanobacteria, as well as in unicellular eukaryotes (algae, fungi, yeast) and more recently also in choanoflagellates and viruses (Lamarche et al., 2017; Bratanov et al., 2019; Zabelskii et al., 2020; Rozenberg et al., 2021;

Govorunova et al., 2022b; Nagata and Inoue, 2022). Most of these pigments function as light-driven ion transporters or ion channels (**Figure 7**). The newly discovered xenorhodopsins and schizorhodopsins are exceptional as they perform inward-directed proton transport (Inoue et al., 2018; Inoue et al., 2020; Weissbecker et al., 2021; Brown, 2022). However, some type-1 rhodopsins display a photosensory function (sensory rhodopsins) and signal via a cognate transducer protein, which is totally different functionally and structurally from the animal G-proteins (Bogomolni and Spudich, 1991; Krah et al., 1994; Deininger et al., 1995). Overall, type-1 pigments are the dominant contributors to marine phototrophy (Casey et al., 2017; Larkum et al., 2018; Gómez-Consarnau et al., 2019). In addition, eukaryotic type-1 rhodopsins have been discovered which are intracellularly fused to an enzymatic domain and mediate light-driven enzyme activation (guanylyl cyclase, phosphodiesterase) or inhibition (guanylyl cyclase, based upon histidine kinase activity) (Avelar et al., 2014; Lamarche et al., 2017; Luck et al., 2019; Mukherjee et al., 2019; Tsunoda et al., 2021; Broser, 2022; Tian et al., 2022). These pigments have been termed as enzyme-rhodopsins.

The overall structure and photochemistry of all type-1 rhodopsins present a very similar pattern, though the sequence identity can be as low as 12%, and the kinetics of the photocycle can vary up to at least thousand-fold. The most recent addition, the heliorhodopsins, are not very different in their protein fold from e.g. BR in spite of a very low sequence identity (<10%) (Shihoya et al., 2019). Considering their inverted insertion into the membrane, very long photocycle and so far unknown functionality, they probably are better classified separately as type-3 rhodopsins (Tanaka et al., 2020; Chazan et al., 2022).

HETEROLOGOUS EXPRESSION AND PURIFICATION

The congruent broad heterogeneity in the rhodopsin superfamily offers a fascinating spectrum for mechanistic studies as well as biomimetic adaptation and application. However, mechanistic studies still require large quantities of relatively pure material (at least several mg). With the exception of some visual pigments and archaeal rhodopsins, such quantities are not available from native sources. Besides, purifying minor quantities of rhodopsins out of a large excess of cellular membrane proteins turned out to be a "hell of a job" (Dartnall, 1962b; Hubbard et al., 1971). Furthermore, in-depth mechanistic studies and biomimetic applications need the ability to make modifications biosynthetically at the protein residue level, and synthetically at the chromophore level. And even when *in silico* molecular dynamics and quantum chemical computation would have reached the time-scale of protein conformational changes (femtoseconds to seconds range) and the native accuracy, then still experimental verification is in order. Experimentally modifying rhodopsins in the native organism was completely out of hand at the time, except for some limited success with bacteriorhodopsin mutants in *Halobacterium salinarum* which still did not solve the quantity requirement (Krebs et al., 1993). Hence, the search for suitable heterologous expression hosts started in the 1980s, and over time it became obvious that the eukaryotic rhodopsins required quite a different perspective.

With the start of the genome era, recombinant DNA technology (genome mining, DNA and c-DNA sequence information and comparison, DNA sequence modification) became accessible and have now become common experimental tools (Khorana, 1979; Khorana et al., 1987). Likewise, total synthesis of retinal isomers and a plethora of derivatives has improved significantly (Dawadi and Lugtenburg, 2010; Liu and Liu, 2011; Álvarez et al., 2014; El-Tahawy et al., 2020).

Type-2 Family

Type-2 rhodopsins can undergo a variety of posttranslational modifications (disulfide-bridge formation, N- and O-glycosylation, methylation, acetylation, myristylation, palmitoylation, phosphorylation), most of which are not properly executed by the bacterial or archaeal biosynthetic machinery (**Table 3**). Expression of bovine rhodopsin in bacteria and even yeast did not yield promising results (Mollaaghababa et al., 1996; Abdulaev and Ridge, 2000). Hence, for optimal heterologous expression a eukaryotic cell type had to be selected as a host. Attempts have been made to express type-2 pigments and related receptors in the eye of whole organisms (mouse, Xenopus) and in *Caenorhabditis elegans* using viral vectors or transgenic animals, but this gave relatively low yields or even led to retinal degeneration (Zhang et al., 2005; Salom et al., 2008; Cao et al., 2012; Salom et al., 2012). Eventually, the best results with sufficient posttranslational modification and targeting to the plasma membrane were obtained in some mammalian cell lines using plasmid transfection (COS, HEK, Neuroblastoma cell lines), in insect cell lines using baculoviral infection (Spodoptera Sf9 and Sf12 and Trichoplusia "High-Five") and in Xenopus oocytes (Oprian et al., 1987; Janssen et al., 1988; Khorana et al., 1988; Karnik et al., 1993; Kazmi et al., 1996). The highest expression levels of functional pigments, with addition of 11-*cis* retinal during culture or after isolation of the cells, were obtained in suspension culture of insect cells or specially adapted HEK293 cells, with yields up to 130 nmol/L, equivalent to ca 5 mg bovine rhodopsin per liter (Klaassen and DeGrip, 2000; Reeves et al., 2002). Even then the pigment accounts for maximally 5 percent of the total cellular membrane protein, and further purification is inevitable. Eventually, gene manipulation lent a helping hand and it has now become common practice to add a small sequence tag to the pigment c-DNA, encoding a short peptide sequence to easily identify and purify the expressed pigment. Two approaches have become the most popular in the type-2 rhodopsin field. One exploited the availability of a monoclonal antibody against the C-terminal octapeptide of bovine rhodopsin (Molday, 1989). This allows for highly selective immuno-affinity purification using a suitable detergent like DDM for solubilization (Ridge et al., 1995). By adding to or replacing the native C-terminal with this octapeptide, the resulting tagged protein can be comfortably isolated. The second approach involved extending the C-terminal with six to ten histidine residues (His6-tag to

TABLE 3 | Selected additional citations for the section "Heterelogous expression and purification".

Type-1 pigments
Optical spectroscopy: Chen and Gouaux, (1996); Kwon et al. (2019)
Posttranslational: Hildebrandt et al. (1991); Müller, (1992); Lang-Hinrichs et al. (1994); Feng et al. (2013)
Review: LinCereghino and Cregg, (2000); Lichty et al. (2005); Hasegawa et al. (2020)
Other: Schey et al. (1992)
Type-2 pigments
Optical spectroscopy: Oprian et al. (1991); Kojima et al. (1995); Radlwimmer and Yokoyama, (1997); Ma et al. (2001); Melyan et al. (2005); Qiu et al. (2005); Giesbers et al. (2008); Shirzad-Wasei et al. (2013); Kahremany et al. (2019)
Vibrational spectroscopy: Katayama et al. (2012); Katayama et al. (2017)
Posttranslational: Hargrave, (1977); Karnik et al. (1988); Ovchinnikov et al. (1988a); Janssen et al. (1991); O'Tousa, (1992); Fujita et al. (1994); Kaushal et al. (1994); Morello and Bouvier, (1996); Nakagawa et al. (1997); Zhang et al. (1997); Katanosaka et al. (1998); Gibson et al. (1999); Hwa et al. (1999); Ridge and Abdulaev, (2000); Maeda et al. (2003); Park et al. (2009); Tam and Moritz, (2009); Salom et al. (2019)
Expression: Schey et al. (1992); Harada et al. (1994); Townson et al. (1998); Reeves et al. (2002); Peirson et al. (2004); Panda et al. (2005)
Review: Hargrave, (1982)

His10-tag), which upon solubilization with a suitable detergent allows metal affinity purification over a matrix containing immobilized Ni^{2+} or Co^{2+} complexes (Janknecht et al., 1991; Janssen et al., 1995). Both approaches are very effective with hardly any perturbation of expression level and functionality of the pigment (Reeves et al., 1999; Bosman et al., 2003). Nevertheless, if necessary, a short target peptide sequence for a selective proteolytic enzyme can be introduced in front of the purification tag to remove it after purification (Sarramegna et al., 2006). Most Opn1 and Opn2 pigments can be satisfactorily purified by either procedure (Vissers and DeGrip, 1996; Shirzad-Wasei and DeGrip, 2016; Katayama et al., 2017; Katayama et al., 2019). Some pigments from the other subsets have been difficult to solubilize or are too unstable in detergent solution to survive purification. The alternative option then is to transfer the protein into the stabilizing lipid environment of nanodiscs (**Figure 4**), which requires hardly any detergent (amphipol or SMA-type) or very brief exposure to a suitable mild detergent (MSP-type). Exploiting the sequence tag on the incorporated protein, the protein-nanodisc unit is then easily purified again by affinity chromatography (Shirzad-Wasei et al., 2015; Cai et al., 2017; Ganapathy et al., 2020).

The opportunity to modify, bio-generate and purify type-2 pigments in sufficient quantities has given a tremendous boost to all mechanistic and functional studies. Analysis of the native proteins or binding pocket mutants, often in combination with ^{2}H-, ^{13}C- or F-labeling and/or chemical modification of retinal and/or with ^{15}N- and/or ^{13}C-labeling of protein residues or inserting modified amino acids, has provided a wealth of data, underpinning, extending and refining the information obtained from crystal structures (see next sections). Groundbreaking details of dark state structures have been excavated by biochemical (e.g. limited proteolysis, selective chemical modification, selective deuteration, atomic force microscopy, cryo-EM) and biophysical studies (e.g. FTIR and resonance Raman spectroscopy, solid-state NMR spectroscopy, EPR spectroscopy) (**Table 3**). This also fueled a large body of theoretical and *in-silico* efforts (molecular dynamics, quantum-chemical calculation and modeling) (Ryazantsev et al., 2019; Pedraza-González et al., 2020; Fujimoto, 2021; Mroginski et al., 2021; Church et al., 2022b). As a result of all these exertions, it has already been possible to construct a highly detailed picture of the dark state of bovine rhodopsin.

Type-1 Family

For the archaeal and bacterial type-1 rhodopsins, a heterologous expression host was more easily identified. *Escherichia coli* strains had already been developed for uncomplicated suspension culture, high productivity, low proteolytic activity and easy transformation. Plasmids with inducible promoters became available, and were further engineered with specific features, like producing the necessary enzymatic machinery to generate all-*trans* retinal from its precursor β-carotene (Kim et al., 2008). Nevertheless, in most cases just supplementing the cell culture with all-*trans* retinal together with inducing opsin expression or even after membrane isolation was sufficient to produce the full equivalent of the corresponding rhodopsin (Spudich et al., 2000; Ganapathy et al., 2015). In this way yields up to 20 mg/L have been reported (Ganapathy et al., 2015; Song et al., 2020). For some archaeal pigments, this straightforward approach only gave low yields and had to be adapted e.g. for bacteriorhodopsin itself (Bratanov et al., 2015; Tu et al., 2018). On the other hand, heterologous expression was more problematic for the eukaryotic type-1 rhodopsins, again because of their more complex posttranslational modification profile. Channelrhodopsins are commonly produced in yeast (*Pichia pistoris*), but successful production of eukaryotic type-1 pigments in insect and mammalian cell lines, *Caenorhabditis elegans* and Xenopus oocytes is also reported (Nagel et al., 2003; Bruun et al., 2015; Govorunova et al., 2017). An interesting new approach is using the trypanosome *Leishmania tarentolae* for over-expression (Volkov et al., 2017). For optogenetic applications (see below), functional production and targeting in a mammalian context is imperative, and often requires insertion of trafficking or targeting signals and/or sequence optimization to mammalian genetic code preferences.

The C-terminal His-tag has become the most popular option for purification of archaeal and eubacterial rhodopsins. For eukaryotic type-1 rhodopsins, several tags are used, including the His-tag, although the latter may sometimes interfere with particular electrophysiological or enzymatic analyses

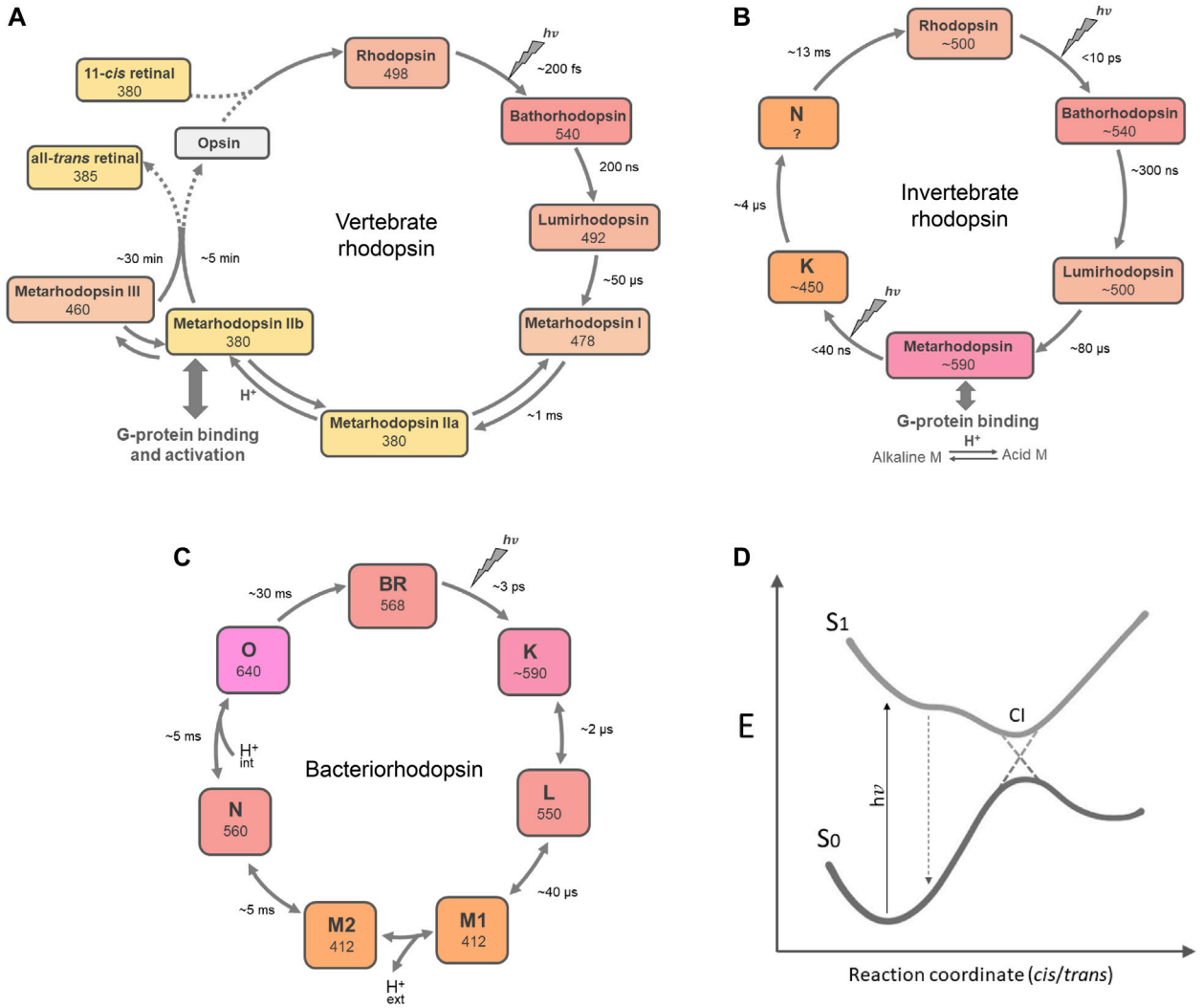

FIGURE 8 | Global presentation of the predominant photochemical pathways in the rhodopsin families. **(A)** Bovine rod rhodopsin as the archetype of the monostable type-2 pigments, **(B)** squid/fly visual pigment chimera, typical for the bistable type-2 pigments, and **(C)** bacteriorhodopsin (BR) as a prototype for the type-1 pigments. The "dark state" 11-*cis*, 15-*anti* chromophore configuration in type-2 pigments is photo-excited into all-*trans*. The all-*trans* chromophore configuration in type-1 pigments is photo-excited into 13-*cis*, 15-*anti*, which thermally relaxes, eventually returning to the ground state. The early photo-intermediates still contain a protonated Schiff base and relax thermally to deprotonated Meta II or M states. In proton pumps like BR this is accompanied by opening up proton pathways in the protein, while in most type-2 pigments binding of a G protein is initiated. At this stage, the pathways divert, as further explained in the text. Of course, here are exceptions: some type-2 pigments contain all-*trans* in the "dark state," which is photoexcited into 11-*cis*, either to change activity or to release 11-*cis* retinal for regeneration of visual opsins (**Table 2**). Some type-1 pigments can also photo-generate 9-*cis* or 11-*cis* states with deviating photocycles and/or functions. **(D)** Simplified schematic of a conical intersection where the excited chromophore at the S1 energy surface can cross over to the S0 energy surface of the photoproduct. The S1 surface can contain thermal transitions, and in type-1 pigments the kinetics to reach and cross-over at the conical intersection also depend on the pKa of the direct counterion to the Schiff base (Chang et al., 2022).

(Govorunova et al., 2021; Rozenberg et al., 2021; Tsunoda et al., 2021; Govorunova et al., 2022b).

Thanks to the powerful combination of the recombinant DNA toolbox with heterologous expression and purification making sufficient protein material available, an astounding repertoire of structural and functional data has also become available for the type-1 rhodopsins (**Table 3**). As a result, bacteriorhodopsin has become the best studied and fathomed membrane protein, with unprecedented insight into its structure and function (Ernst et al., 2014; Larkum et al., 2018; Nogly et al., 2018; Weinert et al., 2019). Next to that, the type-1 community has delivered prospects for a wealth of biotechnological and biomimical applications, far beyond any prognosis (see below).

PHOTOCHEMICAL PROPERTIES

The initial rapid steps after photoactivation of type-1 and type-2 rhodopsins are quite comparable (**Figure 8**). Ultrafast photoisomerization of the chromophore leads to the first

TABLE 4 | Selected additional citations for the section "Photochemical properties".

Type-1 pigments

Optical spectroscopy: Butt, (1990); Ogonah et al. (1991); Chizhov et al. (1996); Inoue et al. (2004); Rupenyan et al. (2008); (2009); Inoue et al. (2011); Bayraktar et al. (2012); Ogren et al. (2015); Tahara et al. (2015); Iyer et al. (2016); Hontani et al. (2017a); Hontani et al. (2017b); Smitienko et al. (2017); Inoue et al. (2018); Chang et al. (2019); Kao et al. (2019); Luck et al. (2019); Tahara et al. (2019b); Hontani et al. (2020); Smitienko et al. (2021); Sugimoto et al. (2021); Chang et al. (2022)

Vibrational spectroscopy: Rothschild et al. (1981); Rothschild and Marrero, (1982); Rothschild et al. (1984); Marrero and Rothschild, (1987); Rödig et al. (1999); McCamant et al. (2005); Amsden et al. (2007); Neumann et al. (2008); Schäfer et al. (2009); Sasaki et al. (2011); Sudo et al. (2011); Saint Clair et al. (2012a); Johnson et al. (2014); Liebel et al. (2014); Kuhne et al. (2015); Lórenz-Fonfría et al. (2015b); Schnedermann et al. (2016); Yi et al. (2017); Roy et al. (2018); Kataoka et al. (2019); Kuhne et al. (2019); Kaufmann et al. (2020); Fischer et al. (2021); Polito et al. (2021)

NMR/EPR spectroscopy: Hu et al. (1998); Ding et al. (2018)

Crystallography/EM: Schobert et al. (2002); Frank et al. (2014); Furuse et al. (2015); Kato et al. (2015a); Wickstrand et al. (2015); Hosaka et al. (2016); Ikuta et al. (2020); Kojima et al. (2020c); Kovalev et al. (2020a); Bada Juarez et al. (2021); Hirschi et al. (2021); Li et al. (2021); Axford et al. (2022); Kishi et al. (2022); Poddar et al. (2022)

Computational: Schapiro and Ruhman, (2014); Feng and Mertz, (2015); Yalouz et al. (2021)

Review: Wand et al. (2013); Kandori et al. (2018); Buhrke and Hildebrandt, (2020)

Type-2 pigments

Optical spectroscopy: Yoshizawa and Wald, (1967); Regan et al. (1978); Shichida, (1986); Imamoto et al. (1989); Lewis et al. (1990); Gärtner et al. (1991); Davidson et al. (1994); Imai et al. (1995); Imamoto et al. (1996); DeLange et al. (1997); Jäger et al. (1997); Lewis et al. (1997); Vought et al. (1999); Kusnetzow et al. (2001); Furutani et al. (2003); Sato et al. (2011); Tarttelin et al. (2011); Gulati et al. (2017); Van Eps et al. (2017); Nagata et al. (2019); Chawla et al. (2021); Sakai et al. (2022)

Vibrational spectroscopy: Rothschild et al. (1976); Rothschild et al. (1983); DeGrip et al. (1985); Pande et al. (1987); DeGrip et al. (1988); Bagley et al. (1989); Masuda et al. (1993); Rath et al. (1993); Hashimoto et al. (1996); Rath et al. (1998); DeLange et al. (1999); Ritter et al. (2004); Yan et al. (2004); Ye et al. (2010); Nonaka et al. (2020); Hanai et al. (2021)

NMR/EPR spectroscopy: Smith et al. (1992); Verhoeven et al. (2001); Struts et al. (2007); Altenbach et al. (2008); Eilers et al. (2012); Brinkmann et al. (2018)

Crystallography/EM: Ruprecht et al. (2004); Schertler, (2005); Nakamichi and Okada, (2006); Scheerer et al. (2008); Choe et al. (2011); Murakami and Kouyama, (2011); (2015); Panneels et al. (2015); Tsai et al. (2019)

Atomic force microscopy: Kawamura et al. (2013)

Computational: Schreiber et al. (2006); Bhattacharya et al. (2008); Tavanti and Tozzini, (2014); Feng et al. (2015); Ren et al. (2016); Tomobe et al. (2017); Demoulin et al. (2021)

Review: Zundel, (1988); Yoshizawa and Kandori, (1991); Farrens, (2010); Smith, (2010); Polli et al. (2015); Vlasov et al. (2020)

Other: Angel et al. (2009); Bayburt et al. (2011)

stable photoproduct within ps. This conversion is extremely efficient with quantum yields between 0.6 and 0.7 for type-2 pigments and varying between 0.3 and 0.7 for type-1 pigments and very low energy loss through fluorescence (Gozem et al., 2017). Often, this red-shifted photoproduct then thermally relaxes via spectrally distinguishable photo-intermediates within ms to a blue-shifted M(eta) intermediate, where the chromophore-binding Schiff base has become deprotonated through transfer of the proton to the direct counterion (Nakagawa et al., 1999; Hofmann, 2000; Tsukamoto and Terakita, 2010; Ernst et al., 2014; Govorunova et al., 2017). This explains the large blue-shift. In some type-1 pigments, a deprotonated M state is not formed, however a protonated L-like equivalent is observed (Spudich et al., 2014; Govorunova et al., 2017; Engelhard et al., 2018). The M or its L-like equivalent intermediate is the active state of the pigment, where the conformational changes in the protein evoke the subsequent cognate activity (grouping with cognate G protein or transducer, opening up an ion channel or vectorial ion pathway, regulating the enzymatic domain, etc.) (**Table 4**). At the M or L-like stage the type-2 and type-1 pathways take completely different directions.

Type-2 Family

For the type-2 rhodopsins ultrarapid spectroscopy data are limited, and mainly available for Opn1, Opn2, and R-type pigments (Shichida et al., 1978; Shichida, 1990; Schoenlein et al., 1991; Vought et al., 2000; Imamoto and Shichida, 2014; Schnedermann et al., 2018). Generally speaking, two schemes have been identified: Monostable pigments eventually release all-*trans* retinal (all Opn1 and Opn2 rhodopsins, **Figure 8A**) following which the opsins require supplementation with retinal re-isomerized elsewhere to regenerate the original "dark" state. Bistable pigments (most other type-2 pigments investigated, **Table 2**) progress until a stable M-intermediate is reached (all-*trans* chromophore), that requires photo-isomerization to return to the original "dark" state (11-*cis* chromophore) (**Figure 8B**) (Hillman et al., 1983; Gärtner, 2000; Stavenga et al., 2000).

The photochemical profile of the monostable bovine rod rhodopsin has been explored in great detail. The native pigment and a variety of isotopically labeled and/or mutant pigments have been investigated by femtosecond optical spectroscopy and vibrational and NMR spectroscopy. These studies have revealed intimate details on the kinetics, conformational changes in the chromophore and surrounding H-bonded networks with constrained water molecules, protein-chromophore interplay and Schiff base (de)protonation (**Table 4**). Overall protein conformational changes have been elucidated by fluorescence, ESR and NMR spectroscopy and TR-WAXS (DeGrip et al., 1999; Kusnetzow et al., 2006; Alexiev and Farrens, 2014; Malmerberg et al., 2015; Van Eps et al., 2017; Smith, 2021). Crystal structures have been resolved for all photo-intermediates and present a broad structural basis (**Table 4**). The power of theoretical and quantum-chemical calculations has grown immensely, laying a strong foundation for electronic and energetic elements of the process, in

particular (Schapiro et al., 2011; Gozem et al., 2017; Schnedermann et al., 2018; Agathangelou et al., 2021; Nikolaev et al., 2021).

A very effective combination of selectively labeled chromophore with femtosecond spectroscopy and advanced quantum chemical computation resolved many remaining issues in the photoisomerization process of bovine rhodopsin (Schnedermann et al., 2018). The global picture has arisen that after photo-excitation of the chromophore into the Franck-Condon state it rapidly relaxes along a barrierless trajectory on the potential surface to a minimal energy conical intersection (**Figure 8D**). Here, productive resonance of the electronic wave packet at the excited state potential surface with torsional and HOOP vibrational modes in the twisted C10-C13 segment of the 11-*cis* chromophore, can prime very effective cross-over to a ground state energy surface, generating a hot all-*trans*oid state (photorhodopsin) within tens of fs (Johnson et al., 2015). This relaxes thermally in about 200 fs into the photoproduct bathorhodopsin, which contains a still highly twisted all-*trans* chromophore, but is stable below 130 K (Yoshizawa and Wald, 1963). In free retinal, photoexcitation results in formation of several isomers (predominantly all-*trans*, 13-*cis*, 9-*cis*, and 11-*cis*), but in rhodopsins this conversion is remarkably selective from 11-*cis* to all-*trans.* This is clearly facilitated by the constraints of the binding site and the twist in the C10-C13 segment of the chromophore (Bismuth et al., 2007; Weingart, 2007; Schnedermann et al., 2018).

At room temperature, the ca 35 kcal of excitation energy stored in bathorhodopsin (Cooper, 1979) drives further relaxation via several intermediates until the metarhodopsin IIa-IIb equilibrium is reached within ms. This relaxation process subtly rearranges chromophore, protein residues and H-bonded networks up to the metarhodopsin stage, where the Schiff base transfers its proton, the counterion and another Glu at the intracellular side of the protein become protonated and an interhelical activity switch reshuffles helical segments to open up binding residues for the G-protein (Hofmann, 2000; Vogel et al., 2007; Vogel et al., 2008; Pope et al., 2020). The chromophore is subsequently slowly released via hydrolysis of the Schiff base to generate the nearly inactive apoprotein opsin (Wald, 1953; Rothschild et al., 1987; Jastrzebska et al., 2011). *In vivo* the active state is rapidly inactivated through phosphorylation and arrestin binding, however, which blocks activation of the G protein (Ranganathan and Stevens, 1995).

The photochemical profile of other monostable pigments (human rod rhodopsin, several cone pigments) has been investigated to much less depth, but is quite comparable to the bovine rod pigment (Barry and Mathies, 1987; Kusnetzow et al., 2001; Hofmann and Palczewski, 2015; Kazmin et al., 2015). However, the kinetics differ somewhat. For instance, the investigated cone pigments show more rapid kinetics in most steps (Imai et al., 1997; Vissers et al., 1998; Chen et al., 2012; Sato et al., 2012). Ultra-violet absorbing cone pigments may be more complex, as photoisomerization is accompanied by protonation of the Schiff base (Kusnetzow et al., 2004; Mooney et al., 2012).

The photochemical profile of bistable pigments, investigated thus far (squid, octopus and some insect pigments), follow a scheme similar to the monostable pigments up through formation of the M-intermediate and with comparable kinetics (**Figure 8B**) (Gärtner, 2000; Stavenga et al., 2000; Vought et al., 2000; Murakami and Kouyama, 2015). It is reported that in cephalopods the M-intermediate in fact forms a pH-dependent equilibrium between a protonated (acid M) and a deprotonated state (alkaline M). This involves the Schiff base of the chromophore, and the alkaline M is strongly blue-shifted (Liang et al., 1994; Vought et al., 2000). Photo-reisomerization of the M state to the original "dark" state is again quite efficient with a quantum yield around 0.4 (Stavenga et al., 2000).

Type-1 Family

The "dark" state of type-1 pigments contains a chromophore with the all-*trans,* 15-*syn* configuration (**Figure 1**). Rapid spectroscopy has been performed on quite a number of type-1 pigments, and the global scheme is quite similar to that of bacteriorhodopsin (**Figure 8C**). However, the kinetics of the slower steps (M and subsequent ones) and thereby the overall cycle time can vary considerably from ms up to minutes (Rozenberg et al., 2021; Tsunoda et al., 2021; Broser, 2022; Nagata and Inoue, 2022).

Out of all rhodopsins the photochemistry of BR is understood in most detail (Wickstrand et al., 2015; Nango et al., 2016). Femtosecond XFEL crystallography has even revealed very early responses to photoexcitation of the chromophore (Nogly et al., 2018). The adjacent protein residues and water molecules already react to the charge delocalization in the excited chromophore before the isomerization is initiated (Tahara et al., 2019a). During the isomerization process more of the protein environment becomes involved while the chromophore rapidly relaxes along a 2-state trajectory on the excited state potential surface to a conical intersection, where it effectively crosses in ca 500 fs over to a ground state energy surface into a "hot" transient hybrid state (J) and then relaxes thermally in about 3 ps into the photoproduct K, which contains a still significantly twisted 13-*cis*, 15-*anti* chromophore, but is stable below 150 K (Lanyi, 2004). Here, a major driving force is the elongation of the C13-C14 bond in the excited state in combination with electrostatic re-arrangement and weakening of the hydrated H-bonded network in the Schiff base region. At room temperature, the ca 15 kcal of excitation energy stored in K (this can be higher in sensory rhodopsins) (Birge et al., 1991; Govorunova et al., 2017; Rozenberg et al., 2021) drives further relaxation via the spectrally distinguishable L intermediate until the M states are reached in ca 50 μs. This relaxation process again subtly re-arranges chromophore, protein helices and H-bonded networks up to the M states, where the Schiff base transfers its proton via a water molecule to the counterion and the hydrated H-bonded network opens up a proton gateway to the extracellular membrane surface. The M-states thermally decay via several intermediates in tens of ms to the BR ground state, during which the Schiff base is reprotonated via proton transfer from residue Asp96, a proton is taken up from the intracellular surface and the chromophore is re-isomerized to the all-*trans*, 15-*syn* configuration. In fact, all-*trans* is the most stable configuration for free retinal (Ganapathy and Liu, 1992). Nevertheless, in some archaeal rhodopsins including BR the chromophore slowly enters an all-*trans*, 15-

anti ↔ *13-cis*, 15-*syn* equilibrium when stored in the dark (dark adaptation). The latter chromophore is photo-excited in the light and via a separate non-productive photocycle rerouted to the ground state BR (Smith et al., 1989; Oesterhelt et al., 1991). In channelrhodopsins the opposite phenomenon is observed, where prolonged illumination reduces the activity, since an equilibrium between pigments with an all-*trans,* 15-*anti* and a 13-*cis*, 15-*syn* chromophore configuration is generated (light-adaptation with partial desensitization) (Bruun et al., 2015; Kuhne et al., 2019; Rozenberg et al., 2021; Govorunova et al., 2022b).

Using serial synchrotron crystallography, the slower conformational changes from 5 to ca 40 ms were recorded in the BR photocycle and involve small α-helical rearrangements, chromophore re-isomerization and proton uptake, ending in formation of the ground state (Weinert et al., 2019). A very recent study using advanced high-resolution atomic force spectroscopy at the single-molecule level investigated the BR photocycle after M formation (Perrino et al., 2021). It was concluded that a cytoplasmic gate for proton uptake opens up at about 3 ms after photo-excitation lasting for about 14 ms. Surprisingly, this same study observes a "black-out period" of tens of ms before a recycled ground state can be photo-reactivated. This uncovers a very interesting new phenomenon reminiscent of comparable nonresponsive states in animal voltage-regulated channels (Armstrong, 1992). Meanwhile, XFEL studies have also been performed on other ion pumps and channels. A femtosecond XFEL study of the sodium-pumping rhodopsin from *Krokinobacter eikastus* (KR2) again observed photo-isomerization of the chromophore to start in the femtosecond range and completed within 2 ps (Skopintsev et al., 2020). Changes in the local structure of the binding site and early conformational changes in the protein backbone are observed in the early nanosecond range. Further subtle rearrangements result in Schiff base deprotonation in μs and in the early ms range a gate opens up and transient binding of a Na^+ ion in the vicinity of the Schiff base is observed with release within 20 ms. A femtosecond XFEL study of the chloride pump from the flavobacterium *Nonlabens marinus* follows the conformational adaptations between 1 and 100 ps after photo-excitation (Yun et al., 2021). It shows the final rearrangements of the chromophore to the 13-*cis* configuration within 50 ps, together with the dynamics of the hydrated H-bonded network and deformations in the local α-helical elements. Following chromophore isomerization the chloride ion first dissociates from the protonated Schiff base and then starts to diffuse away. Additional molecular details of the interactions and trajectory of the chloride ion are provided by recent ps up to ms studies using time-resolved serial crystallography in combination with spectral and theoretical analysis (Hosaka et al., 2022; Mous et al., 2022). An XFEL study of the channelrhodopsin chimera C1C2, that photochemically behaves like ChR1, investigated the photo-induced conformational changes from 1 μs to 4 ms (Oda et al., 2021). Photo-isomerization induces a kink in the chromophore structure, triggering shifts in the retinal binding lysine residue and TM7, starting at around 1 μs and increasing during formation of the M-state up to 4 ms. This induces small lateral shifts of the chromophore and in TM7 and TM3 at around 50 μs. It is postulated that these rearrangements forebode the subsequent opening of the gates in the cation channel pore, although these were not observed in the crystal. The XFEL and serial crystallography studies beautifully illustrate the powerful but subtle design and the broad potential of the photo-driven nanomachinery. Less detailed studies basically show a similar pattern (**Table 4**). Subtle differences in early kinetics and conformational adaptation in chromophore and adjacent protein elements following photo-excitation are observed in the ultrarapid studies. A cautious interpretation could be that the structure of the hydrated H-bonding network in the complex counterion is an important roadmap for the light-triggered protein activity, which also depends on the pKa of the direct counterion (Hontani et al., 2017b; Oda et al., 2021; Chang et al., 2022).

In this context it should be realized that crystal structures have their limitations (García-Nafría and Tate, 2020; Guo, 2020). Detergent exposure may affect elements of the protein structure, and the crystal will certainly constrain larger conformational alterations in the protein, which may occur in the slower phase of the photocycle (Weinert et al., 2019; Oda et al., 2021; Govorunova et al., 2022b). Hence, it would be preferable to study the slower photocycle phases with experimental approaches that can handle membrane-bound systems as shown in **Figure 4**, like time-resolved AFM, cryo-EM and vibrational spectroscopy.

The general scheme for the photocycle of BR (**Figure 8C**) also holds for other type-1 pigments, though the kinetics after M formation can vary significantly (Wand et al., 2013; Tahara et al., 2015; Han et al., 2020; Smitienko et al., 2021). The decay is much slower for sensory rhodopsins, enzyme-rhodopsins and heliorhodopsins, possibly since longer interaction with their cognate partner is required for regulated signal transduction. In fact, some sensory rhodopsins and enzyme-rhodopsins exhibit a bistable photocycle (Kawanabe et al., 2007; Broser et al., 2020) and proton transfer to the counterion may not occur (Bergo et al., 2006).

BIOENGINEERING

This section samples the impressive expansion in the field of rhodopsins bioengineered by creative exploitation of their design principles. Often, similar strategies are utilized for both type-1 and type-2 pigments, and therefore they are clustered together in the following subsections.

Shifts in Spectral And/or Functional Properties

Chromophore

Very early on in the 1960s, it was realized that the beautiful design and versatility of rhodopsins could be studied and exploited by modifying the chromophore and changing the spectral properties (Blatz et al., 1969; Kropf et al., 1973). Since protein modeling was not really established at that time, this led to a surge of trial-and-error synthetic efforts to test a large number of retinal analogs on

TABLE 5 | Selected additional citations for the section "Bioengineering".

Subsection	
Chromophore	
	Type-1 pigments: Balogh-Nair and Nakanishi, (1982); Muradin-Szweykowska et al. (1984); López et al. (2005); Sineshchekov et al. (2012); AzimiHashemi et al. (2014); Ganapathy et al. (2015); Mei et al. (2018); Ganapathy et al. (2019); Hontani et al. (2019); Munro et al. (2019); Chuon et al. (2021)
	Type-2 pigments: Arnaboldi et al. (1979); Mollevanger et al. (1987); Friedman et al. (1989); Bhattacharya et al. (1992b); Feng et al. (1997); Huang et al. (1997); DeLange et al. (1998a); Iwasa et al. (1998); Lugtenburg et al. (1999); Verdegem et al. (1999); Wada et al. (2000); Spooner et al. (2004); Wang et al. (2004); Hirano et al. (2006); Verhoeven et al. (2006); DeGrip et al. (2007); Concistrè et al. (2008); Aguilà et al. (2009); Bovee-Geurts et al. (2009); DeGrip et al. (2011); Srinivasan et al. (2014); Alexander et al. (2017); Bovee-Geurts et al. (2017); Buda et al. (2017)
Protein	
	Type-1 pigments
	Spectral properties: Alexiev et al. (2000); Béjà et al. (2001); Hayashi et al. (2001); Shimono et al. (2001); Bielawski et al. (2004); Mori et al. (2013); Ozaki et al. (2014); Ganapathy et al. (2015); Agathangelou et al. (2018); Oda et al. (2018); Singh et al. (2018); Ganapathy et al. (2019); Inoue et al. (2019); Kuhne et al. (2019); Kojima et al. (2020d); Nakajima et al. (2021); Tsujimura et al. (2021); Shim et al. (2022)
	Vibrational spectroscopy: Sonar et al. (1995); Amsden et al. (2007); Ikeda et al. (2007); Yi et al. (2016); Tomida et al. (2020)
	NMR/EPR spectroscopy: Steinhoff et al. (1995); Griffiths et al. (2000); Herzfeld and Lansing, (2002); Maly et al. (2008); Shi et al. (2009); Wang et al. (2013); Becker-Baldus et al. (2015); Brown and Ladizhansky, (2015); Shigeta et al. (2017); Azadi-Chegeni et al. (2018); Kaur et al. (2019); Lavington and Watts, (2020); Kawamura et al. (2021); Tomida et al. (2021)
	Crystallography/EM: Volkov et al. (2017)
	Other: Khorana et al. (1987); Steward and Chamberlin, (1998)
	Type-2 pigments
	Spectral properties: Nakayama and Khorana, (1991); Chan et al. (1992); Asenjo et al. (1994); Yokoyama, (1995); Hope et al. (1997); Dunham and Farrens, (1999); Kochendoerfer et al. (1999); Hunt et al. (2001); Alexiev et al. (2003); Piechnick et al. (2012); Devine et al. (2013); McKee et al. (2021)
	Vibrational spectroscopy: Haris et al. (1992); Lin et al. (1992); DeLange et al. (1998b); Lin et al. (1998); Ye et al. (2009); Rothschild, (2016)
	NMR/EPR spectroscopy: Smith et al. (1996); Creemers et al. (1999); Creemers et al. (2002); Eilers et al. (2002); Hubbell et al. (2003); Werner et al. (2007); Altenbach et al. (2008); Hornak et al. (2010)
	Computational: Nielsen, (2009); Collette et al. (2018); Peters et al. (2020)
	Other: Yokoyama, (2000)
Conversion: Berndt et al. (2014); Vogt et al. (2015); Inoue et al. (2016)	
Optogenetics	
	Type-1 pigments: Tsunoda et al. (2006); Airan et al. (2009); Erbguth et al. (2012); Sudo et al. (2013); Wietek et al. (2015); Alfonsa et al. (2016); Berglund et al. (2016); Berndt et al. (2016); Kulkarni and Miller, (2017); Brown et al. (2018); Pediani et al. (2018); Piatkevitch et al. (2018); Xu et al. (2018); Alabugin, (2019); del Carmen MarÍN et al. (2019a); Marshel et al. (2019); Jun and Cardin, (2020); Milosevic et al. (2020); Baillie et al. (2021); Hayashi et al. (2021); Kathe et al. (2021); Nakao et al. (2021); Panzer et al. (2021); Zhou et al. (2021); Govorunova et al. (2022a); Guo et al. (2022); Li et al. (2022); Nakao et al. (2022); Shim et al. (2022); Yaguchi et al. (2022)
	Type-2 pigments: De Silva et al. (2017); Patriarchi et al. (2018); Berry et al. (2019); Owen et al. (2019); Copits et al. (2021); Hickey et al. (2021); Banskota et al. (2022)
Cell factories: Charvolin et al. (2009); Kim et al. (2012); Schlinkmann and Plückthun, (2013); Pinhassi et al. (2016); Lips et al. (2018); Pérez et al. (2019a); Konno et al. (2021); Polito et al. (2021); Zhang et al. (2021); Fujiyabu et al. (2022)	

their ability to incorporate into the binding site and to modulate spectral and/or functional properties (Balogh-Nair and Nakanishi, 1982; Derguini and Nakanishi, 1986; Liu and Asato, 1990; Crouch et al., 2002). Initially, this was mainly performed on bovine rod rhodopsin and bacteriorhodopsin, which were easily isolated in sufficient quantities. In this way both bathochromic and hypsochromic spectral shifts up to ca 80 nm could be realized, frequently with retardation of photo-kinetics or total loss of function. For instance, using "locked" retinals (blocking functional photo-transformations) it was confirmed that the photo-isomerization process was essential for the functionality and that the ring-polyene chain connection was 6-s-*cis* in type-2 rhodopsins and 6-s-*trans* in type-1 pigments (**Figure 1**) (Crouch et al., 1984; Fukada et al., 1984; Harbinson et al., 1985; van der Steen et al., 1986; DeGrip et al., 1990; Bhattacharya et al., 1992a; Ganapathy et al., 2015). Also, the remarkable observation was made with bovine opsin, that next to the 11-*cis* and 9-*cis* retinal, also the 7-*cis*, 7, 9-di*cis*, and 7, 9, 13-tri*cis* retinal isomers could form a functional pigment, inducing a 40–50 nm blue-shift but reducing thermostability (DeGrip et al., 1976; Liu et al., 1984). In general, it turned out that the bovine opsin binding pocket could better accommodate more voluminous modifications than the bacterio-opsin pocket, suggesting a more constrained character for the latter one. This was later validated in 3-D structures, but other type-1 pigments or photo-intermediates can be less selective (Popp et al., 1993; Inoue et al., 2012; Mori et al., 2013). New analogs are still frequently generated, in particular because recombinant production of mutated opsins modifies the binding pocket constraints. In addition, protein modeling has become more straightforward and for optogenetics larger spectral shifts and other functionalities like higher photosensitivity or higher fluorescence yields are in demand (see below).

Protein Joins In

Once recombinant DNA technology allowed the production of functional opsins in heterologous hosts, one could use this technology to adapt the intrinsic potential of opsins to one's need and design. Combining synthetic retinal design with

recombinant DNA opsin modification opened up a marvelous toolbox to investigate the structure and functional mechanism of rhodopsins as well as to probe new functionalities and applications. This trend is evolving more and more rapidly. Initially, binding site residues were modified to probe their contribution to the packing, stabilization and spectral tuning of the chromophore (Khorana et al., 1987; Sakmar et al., 1989; Nathans, 1992; Sakmar and Fahmy, 1995; Giesbers et al., 2007). A salient example is the accumulating evidence for type-1 pigments, that three positions around the retinal chromophore, corresponding to L93, P186 and Ala215 in BR, function as natural spectral-tuning modules that systematically shift the absorbance spectrum of the chromophore without affecting molecular function (**Table 5**). This further inspired detailed analysis with modified and/or labeled retinals (^{13}C, ^{2}H, F) and protein residues (^{13}C, ^{15}N, F, azido, spin labels) using fluorescence, vibrational, EPR and NMR spectroscopy (**Table 5**). This profited from as well as steered development of sophisticated theoretical and *in-silico* procedures, like DFT, QM/MM and molecular dynamics (Altun et al., 2008; Collette et al., 2018; Del Carmen Marín et al., 2019b; Dokukina et al., 2019; Pieri et al., 2019; Shao et al., 2020; Nikolaev et al., 2021; Scholz and Neugebauer, 2021; Shen et al., 2021; Pedraza-González et al., 2022). All these elements have already profoundly deepened our insight into the structure and mechanism of bovine rod rhodopsin and bacteriorhodopsin, the frontrunners of type-2 and -1, respectively. However, more members are following up. Some recent conspicuous examples are mentioned in the next section.

Conversion

The manipulations described in the previous subsection frequently revealed surprising conversions in activity profile, exemplifying the versatile design principle of the rhodopsins (Kaneko et al., 2017). An interesting example is presented by the *Nonlabens marinus* inward chloride pump NMR-3 and the *Krokinobacter eikastus* sodium exporter KR2 (Hosaka et al., 2016; Yun et al., 2020). With only 35% sequence identity, the crystal structures are remarkably similar, but the gating residues for Cl^- and Na^+ are located at the opposite site of the membrane (Kato et al., 2015a; Hosaka et al., 2016; Kovalev et al., 2019; Yun et al., 2020). Another example is the huge mutagenesis effort that converted a thermophilic rhodopsin into the best thermally stable rhodopsin available to date, while retaining pump activity (Yasuda et al., 2022). On the other hand, selective mutations in the opsin could convert BR into an inward chloride pump, the sodium pump KR2 into a selective light-driven cation channel, the proton pumps Archaerhodopsin-3 (AR3) and *Coccomyxa subellipsoidea* rhodopsin (CsR) into light-driven proton channels, and the proton pump GR from *Gloeobacter violaceus* into a fluorescent chloride sensor (Sasaki et al., 1995; Brown et al., 1996; Inoue et al., 2015; 2016; Fudim et al., 2019; Vogt et al., 2019; Tutol et al., 2021). Alternatively, a cyanobacterial chloride pump could be converted into a proton pump (Hasemi et al., 2016; Kikukawa, 2021). Novel retinal A1 and A2 analogs with an elongated polyene chain (10 instead of 9 carbons) still could incorporate into the binding pocket of the ReaChR channelrhodopsin inducing red-shifts up to ca 30 nm (Okitsu et al., 2020). However, when tested upon AR3, one A2 analog induced a 41 nm blue-shift and again converted it into a light-driven proton channel (Takayama et al., 2018). Another novel retinal analog (MMAR, **Figure 5**.) smoothly incorporated into the binding pocket of the proton pump Green Proteorhodopsin (GPR), inducing a 47 nm red-shift, but when combined with a Phe →Ser mutation near the binding pocket, an unprecedented 200 nm red-shift was observed (Ganapathy et al., 2017). This retinal analog not only maintains some pump activity under near-infrared illumination (700–900 nm region; NIR), but also induces strong fluorescence emission in the NIR, probably emitted in the first picoseconds after excitation (Hontani et al., 2018; Mei et al., 2018; 2020). Proton-pumping rhodopsins in several eubacteria (XR, GR and TR) harbor a carotenoid derivative (salinixanthin) close enough to act as an antenna and transfer electronic excitation to the retinal (Balashov et al., 2010; Imasheva et al., 2011; Misra et al., 2019; Jana et al., 2020). This combination significantly broadens the spectral sensitivity of the rhodopsins for blue wavelengths, and the carotenoid binding option can also be introduced into other pigments (Anashkin et al., 2018). Attempts have also been made to generate chimeric pigments with combined functionality. The earliest example was a BR mutant containing loops of rod rhodopsin being able to weakly activate the G protein (Geiser et al., 2006). This concept in BR was further developed (Sasaki et al., 2014; Kaneko et al., 2017; Yoshida et al., 2017) and also found wider application in other rhodopsins (Kaneko et al., 2017). Chimeras could be produced between type-1 and type-2 pigments, often with shared properties and variable potential for G protein activation (Kojima et al., 1996; Geiser et al., 2006; Airan et al., 2009; Nakatsuma et al., 2011; Sasaki et al., 2014; Bedbrook et al., 2017a; Kaneko et al., 2017; Hickey et al., 2021). A remarkable example is that the C1C2 chimera could be crystallized and a high-resolution crystal structure obtained long before its "parent" channelrhodopsins ChR1 and ChR2, (Kato et al., 2012). In a sequel, new chimeric channelrhodopsins with better performance were generated using structure-guided recombination (Bedbrook et al., 2017a). The chimeric concept has also resulted in type-2 recombinants with variable success (Kojima et al., 1996; Giesbers et al., 2007; Hickey et al., 2021).

These selected examples, along with some more references collected in **Table 5**, already give an impression of the fabulous potential and prospects of the rhodopsin clan. The most impressive flux, however, is noticeable in the optogenetics field.

Optogenetics

Neuronal activity and circuitry are of the essence for multicellular life. Much effort is dedicated to studying activity regulation and circuitry in complex tissues like the brain. This used to be a highly challenging electrophysiological operation, requiring invasive electrodes and precise surgical location. Once it was realized, that rhodopsins could be properly expressed in animal tissues with genetic targeting to specific neurons using selective promoters, it became possible to monitor and regulate neuronal activity by light using endogenously expressed rhodopsins (Boyden et al., 2005). This led to an explosion of

research activity in a new field, coined optogenetics (Deisseroth, 2010, 2015; Rost et al., 2017; Kandori, 2020; Friedman, 2021). Initially, only type-1 rhodopsins were considered, since ion fluxes can directly modulate neuronal activity. Also, all-*trans* retinal is intrinsically available in animal cells and type-1 pigments complete a full photocycle.

In a first breakthrough, a cation-selective channelrhodopsin originally identified in *Chlamydomonas reinhardtii* termed ChR2 (Nagel et al., 2003) was exploited. ChR2 was shown to elicit action potentials in cultured neurons upon illumination (Boyden et al., 2005; Cardin et al., 2010; Klapoetke et al., 2014; Berndt et al., 2016; Deisseroth and Hegemann, 2017). This domain rapidly expanded into ion pumps, which can activate or silence neuronal activity (Chow et al., 2010). Simultaneously, pigments were modified to change spectral range, increase current output, alter photo- and response kinetics, improve membrane targeting, etc. (Lin et al., 2013; Kushibiki et al., 2014; Kato et al., 2015b; Brinks et al., 2016; Govorunova et al., 2017; Cho et al., 2019; Krol et al., 2019; Kojima et al., 2020b; Gong et al., 2020). Eventually, enzyme-rhodopsins as well as bistable type-2 pigments also entered the field, being able to modulate cellular metabolic processes up to gene expression (Mukherjee et al., 2019; Karapinar et al., 2021; Mahn et al., 2021; Rodgers et al., 2021; Tsunoda et al., 2021; Vierock et al., 2021). Bistable type-1 and -2 pigments allow further control, since their activity is triggered by illumination, but ends near the M(eta) stage, which can be photoreversed by illumination in another spectral range (Sheves and Friedman, 1986; Koyanagi and Terakita, 2014; Mederos et al., 2019; Eickelbeck et al., 2020).

A second breakthrough came with the discovery that the intensity of the fluorescence emission of the proton pumps GPR and AR3, be it quite weak, is modulated by the membrane potential (Kralj et al., 2011; Saint Clair et al., 2012b; Kralj et al., 2012). This triggered another burst of research dedicated to improve the voltage sensing of these pumps (minimizing pump activity, shifting spectral range, improving quantum yield, voltage sensing potential, temporal resolution, etc.) by a range of technologies like directed and scanning mutagenesis, multidimensional directed evolution, library screening and machine learning (McIsaac et al., 2014; Engqvist et al., 2015; McIsaac et al., 2015; Abdelfattah et al., 2016; Karasuyama et al., 2018; Kojima et al., 2020a). This was initially mostly performed on AR3, generating a whole family of mutants with different response characteristics (Quasar1 to 3, pa-Quasar3, Novarch, Archon1 and 2, Arch-EEN, Quasar6, Somarchon to name a few) (Piatkevich et al., 2019; Chien et al., 2021). The fluorescence of these voltage sensors most likely originates in late-stage photo-intermediates (Maclaurin et al., 2013). The introduced mutations may even result in a complex bistable photo-equilibrium between a fluorescent and a non-fluorescent state (Mei et al., 2021; Penzkofer et al., 2021). Meanwhile a host of additional voltage sensors have been developed. Next to optimized rhodopsins and chimeric rhodopsin fusions, fusion proteins of light-sensitive opsin cores with other fluorophores, often GFP derivatives or synthetic dyes, and of other voltage sensors with fluorescent rhodopsins have become popular (Bando et al., 2019; Kannan et al., 2019; Lee et al., 2019; Berglund et al., 2020; Zhang X. M. et al., 2021).

Further control has been sought by combining optogenetics with classical electrophysiology (electro-optogenetics) or combining voltage sensors and neuronal activators and/or silencers both based on rhodopsins (all-optical electrophysiology) (Hochbaum et al., 2014; Afshar Saber et al., 2018; Sridharan et al., 2022). In the latter case, it is important to separate the spectral sensitivities to allow selective control and avoid optical cross-talk. In addition, much effort has been put into shifting the spectral range of the optogenetic tools and sensors as far as possible into the NIR, since NIR radiation penetrates much further into the mammalian brain (up to cm compared to several mm for e.g. blue-green light) (Larkum et al., 2018; Govorunova et al., 2020; Broser, 2022). For this purpose, mutagenesis of far-red absorbing rhodopsins like Crimson and CrimsonSA would be a good starting point (Oda et al., 2018). Another option is the novel channelrhodopsin ChRmine, which has quite unusual properties, including a trimeric structure similar to BR (Marshel et al., 2019; Kishi et al., 2022). A very fascinating example is NeoR, a subunit in the heterodimeric rhodopsin-cyclase from the fungus *Rhizoclosmatium globosum*. NeoR is quite exceptional, as it harbors three carboxyl residues near the chromophore and has an absorbance maximum at 690 nm with strong fluorescence emission at 707 nm (Broser, 2022). Other gateways could include special optical technologies or local NIR-converting nanoparticles and two-photon spectroscopy, which are more complicated (Sneskov et al., 2013; Chen, 2019; Matarèse et al., 2019; Yu et al., 2019; Adesnik and Abdeladim, 2021; Lehtinen et al., 2022), or designing special retinal analogs. The latter was quite successful, shifting absorbance maxima up to ca 750 nm with fluorescent emission around 800 nm using merocyanine analogs or MMAR (**Figure 5**) (Derguini et al., 1983; Hoischen et al., 1997; Liu and Asato, 2003; Herwig et al., 2017; Hontani et al., 2018; Mei et al., 2020). The strong red-shift in these analog chromophores, as well as in the A1 chromophore in NeoR is contributed to extensive delocalization of the positive charge from the protonated Schiff base over the polyene element (**Figures 1**, **5**) (Liu and Asato, 2003; Lutnaes et al., 2004; Ganapathy et al., 2019; Broser, 2022). This will strongly reduce the energy gap between the ground and first excited state. Incorporation of retinal A2 into NeoR-opsin already effectuates a further 69 nm red-shift (Broser et al., 2020). Hence, it would be very interesting to investigate whether the combination of NeoR-opsin or mutants with bathochromic analogs like MMAR would even further red-shift the absorbance band and increase the gap with the emission band. Optogenetic application, however, requires invasive administration of the retinal analog and may need transient depletion of the endogenous A1.

So far, the field of optogenetics has progressed spectacularly, from neuron and brain slice cultures, up to intact animals including insects, *C. elegans*, mice and macaques (Bi et al., 2006; Flytzanis et al., 2014; Inagaki et al., 2014; AzimiHashemi et al., 2019; Babl et al., 2019; Piatkevich et al., 2019; Gong et al., 2020; Wagner et al., 2021; Wright et al., 2021) and is being extended to human disease models (Wright et al., 2017; Williams et al., 2019; Córdova et al., 2021; Fougère et al.,

2021; Lindner et al., 2021). Future prospects will be touched upon in the next section.

Cell Factories

While rhodopsins drive important physiological processes in prokaryotes and eukaryotes, and can contribute significantly to the energy requirement of their hosts, implementing this into biotechnological resources like cell factories has not yet developed very far (Walter et al., 2010). *E. coli* can profit from expression of a rhodopsin proton pump (Martinez et al., 2007; Choi et al., 2014; Na et al., 2015; Wang et al., 2015; Kim et al., 2017; Song et al., 2020). However, the extent to which this can for instance support production of useful consumables or commodity chemicals needs to be established. Cyanobacteria like *Synechocystis* sp. PCC6803 and *Synechococcus* already exploit chlorophyll-based oxidative photosynthesis to gather solar energy and are under intense investigation as cellular factories (Wijffels et al., 2013; Angermayr et al., 2015; Du et al., 2018; Knoot et al., 2018; Carpine et al., 2020). They do not have an endogenous opsin, but do produce all-*trans* retinal and can serve as a heterologous host for expression of rhodopsin proton pumps (Chen et al., 2016b; Chen et al., 2017; Chen et al., 2019a). Expression of these pumps was considered as a potential extra energy source, but the contribution of these pumps towards cellular energy production appeared to be limited (Chen et al., 2019b). This may be due to the metabolic constraint of proton fluxes, and/or to the chlorophylls and carotenoids absorbing much of the incoming radiation up to ca 650 nm (the PAR region). Attempts to express the GPR F234S mutant in combination with the retinal analog MMAR were successful in generating a proton pump absorbing in the 700–800 nm range, outside the PAR region. However, this still did not generate sufficient additional energy due to the lower pump activity of this mutant and failed to sustain bacterial growth under NIR illumination (Chen et al., 2018).

PROSPECTS

A major asset of the rhodopsin family is the impressive versatility of the design principle: a relatively simple photosensitive ligand, constrained to allow selective photoisomerization with a high quantum yield, triggering subtle but effective conformational changes in the protein opening up specific binding sites or ion transport pathways.

Genome mining will undoubtedly discover new type-1 and type-2 or related variants, especially considering the still vast reservoir of unexplored microbial and invertebrate life forms. For instance, the apparent non-photic activity of (rhod)opsins in certain physiological conditions (thermo-, mechano- or chemo-sensing) may add a new chapter to this family saga (Leung and Montell, 2017; Katana et al., 2019; Baden et al., 2020; Fleming et al., 2020; Hasegawa et al., 2020; Mei et al., 2020; Zabelskii et al., 2021; Feuda et al., 2022). Next to that, insight into the effect of pathological mutations will become an ever more important asset in medical diagnostics and potential treatment. This has already been widely explored in the case of rod rhodopsin and retina-degenerative diseases, (Athanasiou et al., 2018). Expression and functional and structural characterization of new (rhod)opsins or mutants still involves an elaborate effort, but this may be considerably mitigated soon.

The phenomenal progress in *artificial intelligence and machine learning* already culminated in the design of software packages like RoseTTAFold and Alphafold, that are quite successful in predicting the protein fold from the primary sequence (Humphreys et al., 2021; Jumper et al., 2021). Considering the respectable number of crystal structures for type-1 pigments and G protein-coupled receptors already obtained, this *in silico* approach will be of invaluable help to close in on the 3-D structures of rhodopsin sequences identified to date, as well as those yet to be identified. A similar track is conceivable for the assessment of spectral and functional properties. Experimental analyses, in combination with *in-silico* techniques like DFT, machine learning and quantum-chemical computing already made big strides in establishing the contribution of individual opsin residues and water molecules to the spectral tuning of rhodopsins (Kato et al., 2015; Bedbrook et al., 2017b; Karasuyama et al., 2018; Bedbrook et al., 2019; Nikolaev et al., 2020; Inoue et al., 2021; Yang et al., 2022). However, this approach always requires 3-D information. It would be very desirable to build in additional functionalities, e.g. to predict an approximate absorbance maximum, into the sequence-to-structure software packages. This could then be easily expanded towards predicting the effect of mutations and the fit and effects of retinal derivatives or even more distant chromophores. Suggestions for functionality (specific pump or channel, enzymatic domains, thermal stability) probably could also be in reach, though mechanistic details (photoisomerization process, quantum yield of isomerization or fluorescence emission, early conformational changes) may be aiming too high.

Such developments will be a goldmine for *optogenetics*. Rapid prediction of spectral and functional properties and optimal targeting of desired mutants would be very valuable. Likewise, assessment of new constructs like chimeric pigments, fused monomers, oligomeric assemblies, enzyme activating pigments, new signaling partners and the like can be set up *in silico* and will require much less experimental justification (Sasaki et al., 2014; Abdelfattah et al., 2020). This would undoubtedly be accompanied by further physiological expansion of optogenetic tools. A wider spectral range of neuronal activity modulators and voltage sensors together with improved optics will increase the scope for (all)-optical electrophysiological characterization of neural circuitry, also lending insight into neuronal function (and dysfunction) in the brain (Villette et al., 2019; Guimarães Backhaus et al., 2021; Sharma et al., 2021; Zou et al., 2021; Prakash et al., 2022; Sridharan et al., 2022; Tan et al., 2022). Other important medical targets may also arise using optogenetics to correct physiological defects and address pathological conditions, where first steps have already been taken (Braun et al., 1995; Deubner et al., 2019; Shen et al., 2020; Acharya et al., 2021; Cokic et al., 2021; Kathe et al., 2021; Gilhooley et al., 2022; Sun et al., 2022).

Several concepts to utilize rhodopsins in *bioelectronic and biomimic nanotechnology* have already been attempted, but did not yet really come to maturation (Khodonov et al., 2000; Kuang et al., 2014; Hirschi et al., 2019; Aprahamian, 2020; Shim et al.,

2021). With the rapidly growing insight in the structural and mechanistic potential of the rhodopsin pigments, this is expected to change at short notice. So far, electro-optical phenomena have been investigated in 2D crystals, lipid films and other matrices (Oesterhelt et al., 1991; Miyasaka et al., 1992; Hong, 1994; Wagner et al., 2013; Zhao et al., 2015; Ji et al., 2017; Gruber et al., 2022). With help of the above mentioned software packages, the design of specific constructs with high performance and stability under the system's conditions will be facilitated.

This would also be the case for application in *cell factories*. The most interesting and rewarding application in this respect is the notion of "synergistic photosynthesis," the combination of chlorophyll-based oxidative photosynthesis with retinal-based phototrophy, using high-performance rhodopsin proton pumps absorbing in the NIR (Chen et al., 2016a; Chen et al., 2019b). This will also require adaptation of proton regulation in the host cell or introduction of special cellular organelles containing the pump and an ATP-synthase. In eukaryotic cells like algae or fungi, targeting of a proton pump to mitochondria to increase ATP levels for production of commodity chemicals under selected conditions can be further developed (Hoffmann et al., 1994; Hara et al., 2013; Tkatch et al., 2017; Imai et al., 2019; Berry and Wojtovich, 2020). In general, designing highly active ion pumps absorbing in the 700–800 nm region, i.e. outside the PAR region, is essential for productive "synergistic photosynthesis." Again, artificial intelligence can be a decisive factor here.

EPILOGUE

In roughly 10 years, the rhodopsin field has reached a century's worth of experimental investigation. In this review, we have mainly touched upon the surface of the phenomenal development in this field, somewhat like molecular force microscopy. In the coming 10 years we expect its expansion to continue and to eventually require an at least ten-volume book series for full documentation. By that time, we will hopefully have a better understanding of how a selection of twenty amino acids can lead a membrane protein domain of 300–400 amino acids surrounding a small chromophoric group to such mechanistic versatility.

AUTHOR CONTRIBUTIONS

WdeG conceptualized and wrote the first draft of the manuscript. SG elaborated on sections of the manuscript and prepared the figures. Both authors contributed to manuscript revision, read, and approved the submitted version.

ACKNOWLEDGMENTS

WdeG acknowledges the many Master's and PhD students, postdocs, visiting researchers and collaborating colleagues for their contribution to the work in his research labs. Special thanks go to Petra Bovee-Geurts and Jenny van Oostrum (Radboudumc) for their long-term technical assistance and to Ken Rothschild (Boston University), Johan Lugtenburg and Huub de Groot (Leiden University) and Giel Bosman (Radboudumc) for a lasting amalgamation of science and friendship. The writing of this review was financially supported by Leiden University, Delft University and Radboudumc.

REFERENCES

Abdelfattah, A. S., Farhi, S. L., Zhao, Y., Brinks, D., Zou, P., Ruangkittisakul, A., et al. (2016). A Bright and Fast Red Fluorescent Protein Voltage Indicator that Reports Neuronal Activity in Organotypic Brain Slices. *J. Neurosci.* 36, 2458–2472. doi:10.1523/jneurosci.3484-15.2016

Abdelfattah, A. S., Valenti, R., Zheng, J., Wong, A., Chuong, A. S., Hasseman, J. P., et al. (2020). A General Approach to Engineer Positive-Going eFRET Voltage Indicators. *Nat. Commun.* 11, 3444–34413448. doi:10.1038/s41467-020-17322-1

Abdulaev, N. G., Artamonov, I. D., Bogachuk, A. S., Feigina, M. Y., Kostina, M. B., Kudelin, A. B., et al. (1982). Structure of Light-Activated Proteins - Visual Rhodopsin. *Biochem. Int.* 5, 693–703.

Abdulaev, N. G., and Ridge, K. D. (2000). Heterologous Expression of Bovine Opsin in *Pichia pastoris*. *Meth. Enzymol.* 315, 3–11. doi:10.1016/s0076-6879(00)15831-8

Acharya, A. R., Vandekerckhove, B., Larsen, L. E., Delbeke, J., Wadman, W. J., Vonck, K., et al. (2021). *In Vivo* blue Light Illumination for Optogenetic Inhibition: Effect on Local Temperature and Excitability of the Rat hippocampus. *J. Neural Eng.* 18, 066038–066031. doi:10.1088/1741-2552/ac3ef4

Adesnik, H., and Abdeladim, L. (2021). Probing Neural Codes with Two-Photon Holographic Optogenetics. *Nat. Neurosci.* 24, 1356–1366. doi:10.1038/s41593-021-00902-9

Afshar Saber, W., Gasparoli, F. M., Dirks, M. G., Gunn-Moore, F. J., and Antkowiak, M. (2018). All-Optical Assay to Study Biological Neural Networks. *Front. Neurosci.* 12, 451–451412. doi:10.3389/fnins.2018.00451

Agathangelou, D., Orozco-Gonzalez, Y., Del Carmen Marín, M., Roy, P. P., Brazard, J., Kandori, H., et al. (2018). Effect of Point Mutations on the Ultrafast Photo-Isomerization of *Anabaena* Sensory Rhodopsin. *Faraday Discuss.* in the press. doi:10.1039/c7fd00200a

Agathangelou, D., Roy, P. P., Del Carmen Marín, M., Ferré, N., Olivucci, M., Buckup, T., et al. (2021). Sub-picosecond C=C Bond Photo-Isomerization: Evidence for the Role of Excited State Mixing. *Comptes Rendus Phys.* 22, 1–28. doi:10.5802/crphys.41

Aguilà, M., Toledo, D., Morillo, M., Dominguez, M., Vaz, B., Álvarez, R., et al. (2009). Structural Coupling of 11-*Cis*-7-Methyl-Retinal and Amino Acids at the Ligand Binding Pocket of Rhodopsin. *Photochem. Photobiol.* 85, 485–493. doi:10.1111/j.1751-1097.2009.00535.x

Airan, R. D., Thompson, K. R., Fenno, L. E., Bernstein, H., and Deisseroth, K. (2009). Temporally Precise *In Vivo* Control of Intracellular Signalling. *Nature* 458, 1025–1029. doi:10.1038/nature07926

Alabugin, A. (2019). Near-IR Photochemistry for Biology: Exploiting the Optical Window of Tissue. *Photochem. Photobiol.* 95, 722–732. doi:10.1111/php.13068

Alexander, N. S., Katayama, K., Sun, W. Y., Salom, D., Gulati, S., Zhang, J. Y., et al. (2017). Complex Binding Pathways Determine the Regeneration of Mammalian Green Cone Opsin with a Locked Retinal Analogue. *J. Biol. Chem.* 292, 10983–10997. doi:10.1074/jbc.m117.780478

Alexiev, U., and Farrens, D. L. (2014). Fluorescence Spectroscopy of Rhodopsins: Insights and Approaches. *Biochimica Biophysica Acta-Bioenergetics* 1837, 694–709. doi:10.1016/j.bbabio.2013.10.008

Alexiev, U., Mollaaghababa, R., Khorana, H. G., and Heyn, M. P. (2000). Evidence for Long Range Allosteric Interactions between the Extracellular and Cytoplasmic Parts of Bacteriorhodopsin from the Mutant R82A and its

Second Site Revertant R82A/G231C. *J. Biol. Chem.* 275, 13431–13440. doi:10.1074/jbc.275.18.13431

Alexiev, U., Rimke, I., and Pöhlmann, T. (2003). Elucidation of the Nature of the Conformational Changes of the EF-Interhelical Loop in Bacteriorhodopsin and of the Helix VIII on the Cytoplasmic Surface of Bovine Rhodopsin: A Time-Resolved Fluorescence Depolarization Study. *J. Mol. Biol.* 328, 705–719. doi:10.1016/s0022-2836(03)00326-7

Alfonsa, H., Lakey, J. H., Lightowlers, R. N., and Trevelyan, A. J. (2016). Cl-out Is a Novel Cooperative Optogenetic Tool for Extruding Chloride from Neurons. *Nat. Commun.* 7, 13495–13499. doi:10.1038/ncomms13495

Altenbach, C. A., Kusnetzow, A. K., Ernst, O. P., Hofmann, K. P., and Hubbell, W. L. (2008). High-resolution Distance Mapping in Rhodopsin Reveals the Pattern of Helix Movement Due to Activation. *Proc. Natl. Acad. Sci. U. S. A.* 105, 7439–7444. doi:10.1073/pnas.0802515105

Altun, A., Yokoyama, S., and Morokuma, K. (2008). Spectral Tuning in Visual Pigments: An ONIOM(QM : MM) Study on Bovine Rhodopsin and its Mutants. *J. Phys. Chem. B* 112, 6814–6827. doi:10.1021/jp709730b

Álvarez, R., Vaz, B., Gronemeyer, H., and De Lera, A. R. (2014). Functions, Therapeutic Applications, and Synthesis of Retinoids and Carotenoids. *Chem. Rev.* 114, 1–125. doi:10.1021/cr400126u

Amsden, J. J., Kralj, J. M., Chieffo, L. R., Wang, X. H., Erramilli, S., Spudich, E. N., et al. (2007). Subpicosecond Protein Backbone Changes Detected during the Green-Absorbing Proteorhodopsin Primary Photoreaction. *J. Phys. Chem. B* 111, 11824–11831. doi:10.1021/jp073490r

Anashkin, V. A., Bertsova, Y. V., Mamedov, A. M., Mamedov, M. D., Arutyunyan, A. M., Baykov, A. A., et al. (2018). Engineering a Carotenoid-Binding Site in *Dokdonia* Sp PRO95 Na^+-Translocating Rhodopsin by a Single Amino Acid Substitution. *Photosynth. Res.* 136, 161–169. doi:10.1007/s11120-017-0453-0

Angel, T. E., Gupta, S., Jastrzebska, B., Palczewski, K., and Chance, M. R. (2009). Structural Waters Define a Functional Channel Mediating Activation of the GPCR, Rhodopsin. *Proc. Natl. Acad. Sci. U. S. A.* 106, 14367–14372. doi:10.1073/pnas.0901074106

Angermayr, S. A., Rovira, A. G., and Hellingwerf, K. J. (2015). Metabolic Engineering of Cyanobacteria for the Synthesis of Commodity Products. *Trends Biotechnol.* 33, 352–361. doi:10.1016/j.tibtech.2015.03.009

Aprahamian, I. (2020). The Future of Molecular Machines. *Acs Central Sci.* 6, 347–358. doi:10.1021/acscentsci.0c00064

Armstrong, C. M. (1992). Voltage-dependent Ion Channels and Their Gating. *Physiol. Rev.* 72, S5–S13. doi:10.1152/physrev.1992.72.suppl_4.s5

Arnaboldi, M., Motto, M. G., Tsujimoto, K., Balogh-Nair, V., and Nakanishi, K. (1979). Hydroretinals and Hydrorhodopsins. *J. Am. Chem. Soc.* 101, 7082–7084. doi:10.1021/ja00517a059

Asenjo, A. B., Rim, J., and Oprian, D. D. (1994). Molecular Determinants of Human Red/green Color Discrimination. *Neuron* 12, 1131–1138. doi:10.1016/0896-6273(94)90320-4

Asido, M., Kar, R. K., Kriebel, C. N., Braun, M., Glaubitz, C., Schapiro, I., et al. (2021). Transient Near-UV Absorption of the Light-Driven Sodium Pump Krokinobacter Eikastus Rhodopsin 2: A Spectroscopic Marker for Retinal Configuration. *J. Phys. Chem. Lett.* 12, 6284–6291. doi:10.1021/acs.jpclett.1c01436

Astakhova, L. A., Novoselov, A. D., Ermolaeva, M. E., Firsov, M. L., and Rotov, A. Y. (2021). Phototransduction in Anuran Green Rods: Origins of Extra-sensitivity. *Int. J. Mol. Sci.* 22, 13400. doi:10.3390/ijms222413400

Athanasiou, D., Aguila, M., Bellingham, J., Li, W. W., Mcculley, C., Reeves, P. J., et al. (2018). The Molecular and Cellular Basis of Rhodopsin Retinitis Pigmentosa Reveals Potential Strategies for Therapy. *Prog. Retin. Eye Res.* 62, 1–23. doi:10.1016/j.preteyeres.2017.10.002

Avelar, G. M., Schumacher, R. I., Zaini, P. A., Leonard, G., Richards, T. A., and Gomes, S. L. (2014). A Rhodopsin-Guanylyl Cyclase Gene Fusion Functions in Visual Perception in a Fungus. *Curr. Biol.* 24, 1234–1240. doi:10.1016/j.cub.2014.04.009

Axford, D., Judge, P. J., Bada Juarez, J. F., Kwan, T. O. C., Birch, J., Vinals, J., et al. (2022). Two States of a Light-Sensitive Membrane Protein Captured at Room Temperature Using Thin-Film Sample Mounts. *Acta Crystallogr. Sect. D. Struct. Biol.* 78, 52–58. doi:10.1107/s2059798321011220

Azadi-Chegeni, F., Schiphorst, C., and Pandit, A. (2018). *In Vivo* NMR as a Tool for Probing Molecular Structure and Dynamics in Intact *Chlamydomonas Reinhardtii* Cells. *Photosynth. Res.* 135, 227–237. doi:10.1007/s11120-017-0412-9

Azimihashemi, N., Bergs, A. C. F., Schüler, C., Scheiwe, A. R., Costa, W. S., Bach, M., et al. (2019). Rhodopsin-based Voltage Imaging Tools for Use in Muscles and Neurons of *Caenorhabditis elegans*. *Proc. Natl. Acad. Sci. U. S. A.* 116, 17051–17060. doi:10.1073/pnas.1902443116

Azimihashemi, N., Erbguth, K., Vogt, A., Riemensperger, T., Rauch, E., Woodmansee, D., et al. (2014). Synthetic Retinal Analogues Modify the Spectral and Kinetic Characteristics of Microbial Rhodopsin Optogenetic Tools. *Nat. Commun.* 5, 5810. doi:10.1038/ncomms6810

Babl, S. S., Rummell, B. P., and Sigurdsson, T. (2019). The Spatial Extent of Optogenetic Silencing in Transgenic Mice Expressing Channelrhodopsin in Inhibitory Interneurons. *Cell. Rep.* 29, 1381–1395. doi:10.1016/j.celrep.2019.09.049

Bada Juarez, J. F., Judge, P. J., Adam, S., Axford, D., Vinals, J., Birch, J., et al. (2021). Structures of the Archaerhodopsin-3 Transporter Reveal that Disordering of Internal Water Networks Underpins Receptor Sensitization. *Nat. Commun.* 12, 629. doi:10.1038/s41467-020-20596-0

Baden, T., Euler, T., and Berens, P. (2020). Understanding the Retinal Basis of Vision across Species. *Nat. Rev. Neurosci.* 21, 5–20. doi:10.1038/s41583-019-0242-1

Bagley, K. A., Eisenstein, L., Ebrey, T. G., and Tsuda, M. (1989). A Comparative Study of the Infrared Difference Spectra for octopus and Bovine Rhodopsins and Their Bathorhodopsin Photointermediates. *Biochemistry-USA* 28, 3366–3373. doi:10.1021/bi00434a036

Baillie, J. S., Stoyek, M. R., and Quinn, T. A. (2021). Seeing the Light: The Use of Zebrafish for Optogenetic Studies of the Heart. *Front. physiology* 12, 748570. doi:10.3389/fphys.2021.748570

Baker, G. E., De Grip, W. J., Turton, M., Wagner, H.-J., Foster, R. G., and Douglas, R. H. (2015). Light Sensitivity in a Vertebrate Mechanoreceptor? *J. Exp. Biol.* 218, 2826–2829. doi:10.1242/jeb.125203

Balashov, S. P., Imasheva, E. S., Choi, A. R., Jung, K.-H., Liaaen-Jensen, S., and Lanyi, J. K. (2010). Reconstitution of *Gloeobacter* Rhodopsin with Echinenone: Role of the 4-keto Group. *Biochemistry* 49, 9792–9799. doi:10.1021/bi1014166

Balogh-Nair, V., and Nakanishi, K. (1982). Synthetic Analogs of Retinal, Bacteriorhodopsin and Bovine Rhodopsin. *Meth. Enzymol.* 88, 496–506. doi:10.1016/0076-6879(82)88067-1

Bamann, C., Bamberg, E., Wachtveitl, J., and Glaubitz, C. (2014). Proteorhodopsin. *Biochimica Biophysica Acta-Bioenergetics* 1837, 614–625. doi:10.1016/j.bbabio.2013.09.010

Bando, Y., Grimm, C., Cornejo, V. H., and Yuste, R. (2019). Genetic Voltage Indicators. *BMC Biol.* 17, 71–7112. doi:10.1186/s12915-019-0682-0

Banerjee, S., Huber, T., and Sakmar, T. P. (2008). Rapid Incorporation of Functional Rhodopsin into Nanoscale Apolipoprotein Bound Bilayer (NABB) Particles. *J. Mol. Biol.* 377, 1067–1081. doi:10.1016/j.jmb.2008.01.066

Banskota, S., Raguram, A., Suh, S., Du, S. W., Davis, J. R., Choi, E. H., et al. (2022). Engineered Virus-like Particles for Efficient Invivo Delivery of Therapeutic Proteins. *Cell.* 185. doi:10.1016/j.cell.2021.12.021

Barry, B., and Mathies, R. A. (1987). Raman Microscope Studies on the Primary Photochemistry of Vertebrate Visual Pigments with Absorption Maxima from 430 to 502 Nm. *Biochemistry* 26, 59–64. doi:10.1021/bi00375a009

Bayburt, T. H., Grinkova, Y. V., and Sligar, S. G. (2006). Assembly of Single Bacteriorhodopsin Trimers in Bilayer Nanodiscs. *Archives Biochem. Biophysics* 450, 215–222. doi:10.1016/j.abb.2006.03.013

Bayburt, T. H., Vishnivetskiy, S. A., Mclean, M. A., Morizumi, T., Huang, C.-C., Tesmer, J. J. G., et al. (2011). Monomeric Rhodopsin Is Sufficient for Normal Rhodopsin Kinase (GRK1) Phosphorylation and Arrestin-1 Binding. *J. Biol. Chem.* 286, 1420–1428. doi:10.1074/jbc.m110.151043

Bayraktar, H., Fields, A. P., Kralj, J. M., Spudich, J. L., Rothschild, K. J., and Cohen, A. E. (2012). Ultrasensitive Measurements of Microbial Rhodopsin Photocycles Using Photochromic FRET. *Photochem. Photobiol.* 88, 90–97. doi:10.1111/j.1751-1097.2011.01011.x

Becker-Baldus, J., Bamann, C., Saxena, K., Gustmann, H., Brown, L. J., Brown, R. C. D., et al. (2015). Enlightening the Photoactive Site of Channelrhodopsin-2 by DNP-Enhanced Solid-State NMR Spectroscopy. *Proc. Natl. Acad. Sci. U. S. A.* 112, 9896–9901. doi:10.1073/pnas.1507713112

Bedbrook, C. N., Rice, A. J., Yang, K. K., Ding, X. Z., Chen, S. Y., Leproust, E. M., et al. (2017a). Structure-guided SCHEMA Recombination Generates Diverse

Chimeric Channelrhodopsins. *Proc. Natl. Acad. Sci. U. S. A.* 114, E2624–E2633. doi:10.1073/pnas.1700269114

Bedbrook, C. N., Yang, K. K., Rice, A. J., Gradinaru, V., and Arnold, F. H. (2017b). Machine Learning to Design Integral Membrane Channelrhodopsins for Efficient Eukaryotic Expression and Plasma Membrane Localization. *Plos Comput. Biol.* 13, 1005786. doi:10.1371/journal.pcbi.1005786

Bedbrook, C. N., Yang, K. K., Robinson, J. E., Mackey, E. D., Gradinaru, V., and Arnold, F. H. (2019). Machine Learning-Guided Channelrhodopsin Engineering Enables Minimally Invasive Optogenetics. *Nat. Methods* 16, 1176–1184. doi:10.1038/s41592-019-0583-8

Béjà, O., Aravind, L., Koonin, E. V., Suzuki, M. T., Hadd, A., Nguyen, L. P., et al. (2000). Bacterial Rhodopsin: Evidence for a New Type of Phototrophy in the Sea. *Science* 289, 1902–1906. doi:10.1126/science.289.5486.1902

Béjà, O., Spudich, E. N., Spudich, J. L., Leclerc, M., and Delong, E. F. (2001). Proteorhodopsin Phototrophy in the Ocean. *Nature* 411, 786–789. doi:10.1038/35081051

Belrhali, H., Nollert, P., Royant, A., Menzel, C., Rosenbusch, J. P., Landau, E. M., et al. (1999). Protein, Lipid and Water Organization in Bacteriorhodopsin Crystals: A Molecular View of the Purple Membrane at 1.9 Angstrom Resolution. *Struct. Fold. Des.* 7, 909–917. doi:10.1016/s0969-2126(99)80118-x

Bennett, N., Michel-Villaz, M., and Kühn, H. (1982). Light-induced Interaction between Rhodopsin and the GTP-Binding Protein: Metarhodopsin-II Is the Major Photoproduct Involved. *Eur. J. Biochem.* 127, 97–103. doi:10.1111/j.1432-1033.1982.tb06842.x

Berglund, K., Clissold, K., Li, H. F. E., Wen, L., Park, S. Y., Gleixner, J., et al. (2016). Luminopsins Integrate Opto- and Chemogenetics by Using Physical and Biological Light Sources for Opsin Activation. *Proc. Natl. Acad. Sci. U. S. A.* 113, E358–E367. doi:10.1073/pnas.1510899113

Berglund, K., Fernandez, A. M., Gutekunst, C. a. N., Hochgeschwender, U., and Gross, R. E. (2020). Step-function Luminopsins for Bimodal Prolonged Neuromodulation. *J. Neurosci. Res.* 98, 422–436. doi:10.1002/jnr.24424

Bergo, V. B., Ntefidou, M., Trivedi, V. D., Amsden, J. J., Kralj, J. M., Rothschild, K. J., et al. (2006). Conformational Changes in the Photocycle of Anabaena Sensory Rhodopsin - *Absence Of the Schiff Base Counterion Protonation Signal*. *J. Biol. Chem.* 281, 15208–15214. doi:10.1074/jbc.m600033200

Berndt, A., Lee, S. Y., Ramakrishnan, C., and Deisseroth, K. (2014). Structure-Guided Transformation of Channelrhodopsin into a Light-Activated Chloride Channel. *Science* 344, 420–424. doi:10.1126/science.1252367

Berndt, A., Lee, S. Y., Wietek, J., Ramakrishnan, C., Steinberg, E. E., Rashid, A. J., et al. (2016). Structural Foundations of Optogenetics: Determinants of Channelrhodopsin Ion Selectivity. *Proc. Natl. Acad. Sci. U. S. A.* 113, 822–829. doi:10.1073/pnas.1523341113

Berry, B. J., and Wojtovich, A. P. (2020). Mitochondrial Light Switches: Optogenetic Approaches to Control Metabolism. *FEBS J.* 287, 4544–4556. doi:10.1111/febs.15424

Berry, M. H., Holt, A., Salari, A., Veit, J., Visel, M., Levitz, J., et al. (2019). Restoration of High-Sensitivity and Adapting Vision with a Cone Opsin. *Nat. Commun.* 10, 1221. doi:10.1038/s41467-019-09124-x

Bertazolli-Filho, R., Ghosh, S., Huang, W. H., Wollmann, G., and Coca-Prados, M. (2001). Molecular Evidence that Human Ocular Ciliary Epithelium Expresses Components Involved in Phototransduction. *Biochem. Biophysical Res. Commun.* 284, 317–325. doi:10.1006/bbrc.2001.4970

Besaw, J. E., Ou, W. L., Morizumi, T., Eger, B. T., Sanchez Vasquez, J. D., Chu, J. H. Y., et al. (2020). The Crystal Structures of a Chloride-Pumping Microbial Rhodopsin and its Proton-Pumping Mutant Illuminate Proton Transfer Determinants. *J. Biol. Chem.* 295, 14793–14804. doi:10.1074/jbc.ra120.014118

Bhattacharya, S., Hall, S. E., and Vaidehi, N. (2008). Agonist-induced Conformational Changes in Bovine Rhodopsin: Insight into Activation of G-Protein-Coupled Receptors. *J. Mol. Biol.* 382, 539–555. doi:10.1016/j.jmb.2008.06.084

Bhattacharya, S. S., Marti, T., Otto, H., Heyn, M. P., and Khorana, H. G. (1992a). A Bacteriorhodopsin Analog Reconstituted with a Nonisomerizable 13-trans Retinal Derivative Displays Light Insensitivity. *J. Biol. Chem.* 267, 6757–6762. doi:10.1016/s0021-9258(19)50490-2

Bhattacharya, S. S., Ridge, K. D., Knox, B. E., and Khorana, H. G. (1992b). Light-stable Rhodopsin. 1. A Rhodopsin Analog Reconstituted with a Nonisomerizable 11-cis Retinal Derivative. *J. Biol. Chem.* 267, 6763–6769. doi:10.1016/s0021-9258(19)50491-4

Bi, A. D., Cui, J. J., Ma, Y.-P., Olshevskaya, E. V., Pu, M. L., Dizhoor, A. M., et al. (2006). Ectopic Expression of a Microbial-type Rhodopsin Restores Visual Responses in Mice with Photoreceptor Degeneration. *Neuron* 50, 23–33. doi:10.1016/j.neuron.2006.02.026

Bibow, S. (2019). Opportunities and Challenges of Backbone, Sidechain, and RDC Experiments to Study Membrane Protein Dynamics in a Detergent-free Lipid Environment Using Solution State NMR. *Front. Mol. Biosci.* 6, 103. doi:10.3389/fmolb.2019.00103

Bickelmann, C., Morrow, J. M., Du, J., Schott, R. K., Van Hazel, I., Lim, S., et al. (2015). The Molecular Origin and Evolution of Dim-Light Vision in Mammals. *Evolution* 69, 2995–3003. doi:10.1111/evo.12794

Bielawski, J. P., Dunn, K. A., Sabehi, G., and Béjà, O. (2004). Darwinian Adaptation of Proteorhodopsin to Different Light Intensities in the Marine Environment. *Proc. Natl. Acad. Sci. U. S. A.* 101, 14824–14829. doi:10.1073/pnas.0403999101

Birge, R. R., Cooper, T. M., Lawrence, A. F., Masthay, M. B., Zhang, C.-F., and Zidovetzki, R. (1991). Revised Assignment of Energy Storage in the Primary Photochemical Event in Bacteriorhodopsin. *J. Am. Chem. Soc.* 113, 4327–4328. doi:10.1021/ja00011a043

Bismuth, O., Friedman, N., Sheves, M., and Ruhman, S. (2007). Photochemical Dynamics of All-Trans Retinal Protonated Schiff-Base in Solution: Excitation Wavelength Dependence. *Chem. Phys.* 341, 267–275. doi:10.1016/j.chemphys.2007.06.052

Blackshaw, S., and Snyder, S. H. (1999). Encephalopsin: A Novel Mammalian Extraretinal Opsin Discretely Localized in the Brain. *J. Neurosci.* 19, 3681–3690. doi:10.1523/jneurosci.19-10-03681.1999

Blackshaw, S., and Snyder, S. H. (1997). Parapinopsin, a Novel Catfish Opsin Localized to the Parapineal Organ, Defines a New Gene Family. *J. Neurosci.* 17, 8083–8092. doi:10.1523/jneurosci.17-21-08083.1997

Blankenship, E., Vahedi-Faridi, A., and Lodowski, D. T. (2015). The High-Resolution Structure of Activated Opsin Reveals a Conserved Solvent Network in the Transmembrane Region Essential for Activation. *Structure* 23, 2358–2364. doi:10.1016/j.str.2015.09.015

Blatz, P. E., Lin, M., Balasubramaniyan, P., Balasubramaniyan, V., and Dewhurst, P. B. (1969). A New Series of Synthetic Visual Pigments from Cattle Opsin and Homologs of Retinal. *J. Am. Chem. Soc.* 91, 5930–5931. doi:10.1021/ja01049a069

Bliss, A. F. (1948). The Absorption Spectra of Visual Purple of the Squid and its Bleaching Products. *J. Biol. Chem.* 176, 563–569. doi:10.1016/s0021-9258(19)52673-4

Bogomolni, R. A., and Spudich, J. L. (1991). Archaebacterial Rhodopsins: Sensory and Energy Transducing Membrane Proteins. *Mod. Cell. Biol.* 10, 233–255.

Boll, F. (1877). Zur Anatomie und Physiologie der Retina. *Arch. Anat. Physiol.* 2, 175–286. doi:10.1007/BF02962033

Bondar, A.-N. (2022). Mechanisms of Long-Distance Allosteric Couplings in Proton-Binding Membrane Transporters. *Adv. protein Chem. Struct. Biol.* 128, 199–239. doi:10.1016/bs.apcsb.2021.09.002

Borch, J., and Hamann, T. (2009). The Nanodisc: A Novel Tool for Membrane Protein Studies. *Biol. Chem.* 390, 805–814. doi:10.1515/BC.2009.091

Borgia, A., Borgia, M. B., Bugge, K., Kissling, V. M., Heidarsson, P. O., Fernandes, C. B., et al. (2018). Extreme Disorder in an Ultrahigh-Affinity Protein Complex. *Nature* 555, 61–66. doi:10.1038/nature25762

Bosman, G. J. C. G. M., Vanoostrum, J., Breikers, G., Bovee-Geurts, P. H. M., Klaassen, C. H. W., and DeGrip, W. J. (2003). Functional Expression of His-Tagged Rhodopsin in Sf9 Insect Cells. *Meth. Mol. Biol.* 228, 73–86. doi:10.1385/1-59259-400-X:73

Bovee-Geurts, P. H. M., Fernández Fernández, I., Liu, R. S. H., Mathies, R. A., Lugtenburg, J., and DeGrip, W. J. (2009). Fluoro Derivatives of Retinal Illuminate the Decisive Role of the C_{12}-H Element in Photoisomerization and Rhodopsin Activation. *J. Am. Chem. Soc.* 131, 17933–17942. doi:10.1021/ja907577p

Bovee-Geurts, P. H. M., Lugtenburg, J., and DeGrip, W. J. (2017). Coupled HOOP Signature Correlates with Quantum Yield of Isorhodopsin and Analog Pigments. *Biochimica Biophysica Acta-Bioenergetics* 1858, 118–125. doi:10.1016/j.bbabio.2016.11.003

Bownds, M. D. (1967). Site of Attachment of Retinal in Rhodopsin. *Nature* 216, 1178–1181. doi:10.1038/2161178a0

Boyden, E. S., Zhang, F., Bamberg, E., Nagel, G., and Deisseroth, K. (2005). Millisecond-timescale, Genetically Targeted Optical Control of Neural Activity. *Nat. Neurosci.* 8, 1263–1268. doi:10.1038/nn1525

Bratanov, D., Balandin, T., Round, E., Shevchenko, V., Gushchin, I., Polovinkin, V., et al. (2015). An Approach to Heterologous Expression of Membrane Proteins. The Case of Bacteriorhodopsin. *PLoS ONE* 10, e0128390. doi:10.1371/journal.pone.0128390

Bratanov, D., Kovalev, K., Machtens, J.-P., Astashkin, R., Chizhov, I., Soloviov, D., et al. (2019). Unique Structure and Function of Viral Rhodopsins. *Nat. Commun.* 10, 4939. doi:10.1038/s41467-019-12718-0

Braun, R. D., Linsenmeier, R. A., and Goldstick, T. K. (1995). Oxygen Consumption in the Inner and Outer Retina of the Cat. *Investig. Ophthalmol. Vis. Sci.* 36, 542–554.

Bridges, C. D. B. (1977). Method for Preparing Stable Digitonin Solutions for Visual Pigment Extraction. *Vis. Res.* 17, 301–302. doi:10.1016/0042-6989(77)90095-5

Bridges, C. D. B. (1972). "The Rhodopsin-Porphyropsin Visual System," in *Photochemistry of Vision*. Editor H. J. A. Dartnall (Berlin: Springer-Verlag), 417–480. doi:10.1007/978-3-642-65066-6_11

Brinkmann, A., Sternberg, U., Bovee-Geurts, P. H. M., Fernández Fernández, I., Lugtenburg, J., Kentgens, A. P. M., et al. (2018). Insight into the Chromophore of Rhodopsin and its Meta-II Photointermediate by ^{19}F Solid-State NMR and Chemical Shift Tensor Calculations. *Phys. Chem. Chem. Phys.* 20, 30174–30188. doi:10.1039/c8cp05886e

Brinks, D., Adam, Y., Kheifets, S., and Cohen, A. E. (2016). Painting with Rainbows: Patterning Light in Space, Time, and Wavelength for Multiphoton Optogenetic Sensing and Control. *Accounts Chem. Res.* 49, 2518–2526. doi:10.1021/acs.accounts.6b00415

Broecker, J., Eger, B. T., and Ernst, O. P. (2017). Crystallogenesis of Membrane Proteins Mediated by Polymer-Bounded Lipid Nanodiscs. *Structure* 25, 384–392. doi:10.1016/j.str.2016.12.004

Broser, M. (2022). Far-Red Absorbing Rhodopsins, Insights from Heterodimeric Rhodopsin-Cyclases. *Front. Mol. Biosci.* 8, 806922. doi:10.3389/fmolb.2021.806922

Broser, M., Spreen, A., Konold, P. E., Peter, E., Adam, S., Borin, V., et al. (2020). NeoR, a Near-Infrared Absorbing Rhodopsin. *Nat. Commun.* 11, 5682. doi:10.1038/s41467-020-19375-8

Brouillette, C. G., Mcmichens, R. B., Stern, L. J., and Khorana, H. G. (1989). Structure and Thermal-Stability of Monomeric Bacteriorhodopsin in Mixed Phospholipid Detergent Micelles. *Proteins-Structure Funct. Genet.* 5, 38–46. doi:10.1002/prot.340050106

Brown, J., Behnam, R., Coddington, L., Tervo, D. G. R., Martin, K., Proskurin, M., et al. (2018). Expanding the Optogenetics Toolkit by Topological Inversion of Rhodopsins. *Cell.* 175, 1131–1140. doi:10.1016/j.cell.2018.09.026

Brown, L. S., and Ernst, O. P. (2017). Recent Advances in Biophysical Studies of Rhodopsins - Oligomerization, Folding, and Structure. *Biochimica Biophysica Acta-Proteins Proteomics* 1865, 1512–1521. doi:10.1016/j.bbapap.2017.08.007

Brown, L. S. (2004). Fungal Rhodopsins and Opsin-Related Proteins: Eukaryotic Homologues of Bacteriorhodopsin with Unknown Functions. *Photochem. Photobiological Sci.* 3, 555–565. doi:10.1039/b315527g

Brown, L. S., and Ladizhansky, V. (2015). Membrane Proteins in Their Native Habitat as Seen by Solid-State NMR Spectroscopy. *Protein Sci.* 24, 1333–1346. doi:10.1002/pro.2700

Brown, L. S. (2022). Light-driven Proton Transfers and Proton Transport by Microbial Rhodopsins - A Biophysical Perspective. *Biochimica Biophysica Acta-Biomembranes* 1864, 183867. doi:10.1016/j.bbamem.2022.183867

Brown, L. S., Needleman, R., and Lanyi, J. K. (1996). Interaction of Proton and Chloride Transfer Pathways in Recombinant Bacteriorhodopsin with Chloride Transport Activity: Implications for the Chloride Translocation Mechanism. *Biochemistry* 35, 16048–16054. doi:10.1021/bi9622938

Bruun, S., Stoeppler, D., Keidel, A., Kuhlmann, U., Luck, M., Diehl, A., et al. (2015). Light-dark Adaptation of Channelrhodopsin Involves Photoconversion between the All-*Trans* and 13-*cis* Retinal Isomers. *Biochemistry* 54, 5389–5400. doi:10.1021/acs.biochem.5b00597

Buda, F., Keijer, T., Ganapathy, S., and De Grip, W. J. (2017). A Quantum-Mechanical Study of the Binding Pocket of Proteorhodopsin: Absorption and Vibrational Spectra Modulated by Analogue Chromophores. *Photochem. Photobiol.* 93, 1399–1406. doi:10.1111/php.12800

Buhrke, D., and Hildebrandt, P. (2020). Probing Structure and Reaction Dynamics of Proteins Using Time-Resolved Resonance Raman Spectroscopy. *Chem. Rev.* 120, 3577–3630. doi:10.1021/acs.chemrev.9b00429

Butt, H.-J. (1990). Quantum Efficiency of Native and Mutant Bacteriorhodopsin Obtained from Blue Light Induced Relaxation Experiments. *Eur. Biophys. J.* 19, 31–39. doi:10.1007/bf00223571

Caffrey, M. (2003). Membrane Protein Crystallization. *J. Struct. Biol.* 142, 108–132. doi:10.1016/s1047-8477(03)00043-1

Cai, Y. Y., Liu, Y. T., Culhane, K. J., Devree, B. T., Yang, Y., Sunahara, R. K., et al. (2017). Purification of Family B G Protein-Coupled Receptors Using Nanodiscs: Application to Human Glucagon-like Peptide-1 Receptor. *PLoS ONE* 12, 0179568. doi:10.1371/journal.pone.0179568

Calligaro, H., Dkhissi-Benyahya, O., and Panda, S. (2022). Ocular and Extraocular Roles of Neuropsin in Vertebrates. *Trends Neurosci.* 1776, 1–12. doi:10.1016/j.tins.2021.11.008

Cao, P. X., Sun, W., Kramp, K., Zheng, M., Salom, D., Jastrzebska, B., et al. (2012). Light-sensitive Coupling of Rhodopsin and Melanopsin to $G_{i/o}$ and G_q Signal Transduction in *Caenorhabditis elegans*. *FASEB J.* 26, 480–491. doi:10.1096/fj.11-197798

Cardin, J. A., Carlén, M., Meletis, K., Knoblich, U., Zhang, F., Deisseroth, K., et al. (2010). Targeted Optogenetic Stimulation and Recording of Neurons *In Vivo* Using Cell-type-specific Expression of Channelrhodopsin-2. *Nat. Protoc.* 5, 247–254. doi:10.1038/nprot.2009.228

Carpine, R., Olivieri, G., Hellingwerf, K. J., Pollio, A., and Marzocchella, A. (2020). Industrial Production of Poly-Beta-Hydroxybutyrate from CO2: Can Cyanobacteria Meet This Challenge? *Processes* 8, 323–321323.

Carravetta, M., Zhao, X., Johannessen, O. G., Lai, W. C., Verhoeven, M. A., Bovee-Geurts, P. H. M., et al. (2004). Protein-induced Bonding Perturbation of the Rhodopsin Chromophore Detected by Double-Quantum Solid-State NMR. *J. Am. Chem. Soc.* 126, 3948–3953. doi:10.1021/ja039390q

Casey, J. R., Ferrón, S., and Karl, D. M. (2017). Light-Enhanced Microbial Organic Carbon Yield. *Front. Microbiol.* 8, 2157. doi:10.3389/fmicb.2017.02157

Cassim, J. Y. (1992). Unique Biphasic Band Shape of the Visible Circular Dichroism of Bacteriorhodopsin in Purple Membrane. Excitons, Multiple Transitions or Protein Heterogeneity? *Biophys. J.* 63, 1432–1442. doi:10.1016/s0006-3495(92)81701-0

Chabre, M., and Lemaire, M. (2005). Monomeric G-Protein-Coupled Receptor as a Functional Unit. *Biochemistry* 44, 9395–9403. doi:10.1021/bi050720o

Chan, T., Lee, M., and Sakmar, T. P. (1992). Introduction of Hydroxyl-Bearing Amino Acids Causes Bathochromic Spectral Shifts in Rhodopsin - Amino Acid Substitutions Responsible for Red-Green Color Pigment Spectral Tuning. *J. Biol. Chem.* 267, 9478–9480. doi:10.1016/s0021-9258(19)50115-6

Chang, C.-F., Kuramochi, H., Singh, M., Abe-Yoshizumi, R., Tsukuda, T., Kandori, H., et al. (2022). A Unified View on Varied Ultrafast Dynamics of the Primary Process in Microbial Rhodopsins. *Angew. Chem. Int. Ed.* 61, e202111930. doi:10.1002/anie.202111930

Chang, C. F., Kuramochi, H., Singh, M., Abe-Yoshizumi, R., Tsukuda, T., Kandori, H., et al. (2019). Acid-base Equilibrium of the Chromophore Counterion Results in Distinct Photoisomerization Reactivity in the Primary Event of Proteorhodopsin. *Phys. Chem. Chem. Phys.* 21, 25728–25734. doi:10.1039/c9cp04991f

Charvolin, D., Perez, J.-B., Rouvière, F., Giusti, F., Bazzacco, P., Abdine, A., et al. (2009). The Use of Amphipols as Universal Molecular Adapters to Immobilize Membrane Proteins onto Solid Supports. *Proc. Natl. Acad. Sci. U. S. A.* 106, 405–410. doi:10.1073/pnas.0807132106

Chawla, U., Perera, S. M. D. C., Fried, S. D. E., Eitel, A. R., Mertz, B., Weerasinghe, N., et al. (2021). Activation of the G-Protein-Coupled Receptor Rhodopsin by Water. *Angew. Chemie-International Ed.* 60, 2288–2295. doi:10.1002/anie.202003342

Chazan, A., Rozenberg, A., Mannen, K., Nagata, T., Tahan, R., Yaish, S., et al. (2022). Diverse Heliorhodopsins Detected via Functional Metagenomics in Freshwater *Actinobacteria, Chloroflexi* and *Archaea*. *Environ. Microbiol.* 2022, 15890. doi:10.1111/1462-2920.15890

Chen, G.-Q., and Gouaux, J. E. (1996). Overexpression of Bacterio-Opsin in *Escherichia coli* as a Water-Soluble Fusion to Maltose Binding Protein: Efficient Regeneration of the Fusion Protein and Selective Cleavage with Trypsin. *Protein Sci.* 5, 456–467. doi:10.1002/pro.5560050307

Chen, M.-H., Kuemmel, C., Birge, R. R., and Knox, B. E. (2012). Rapid Release of Retinal from a Cone Visual Pigment Following Photoactivation. *Biochemistry* 51, 4117–4125. doi:10.1021/bi201522h

Chen, Q., Arents, J. C., Schuurmans, J. M., Ganapathy, S., De Grip, W. J., Cheregi, O., et al. (2019b). Combining Retinal-Based and Chlorophyll-Based (Oxygenic) Photosynthesis: Proteorhodopsin Expression Increases Growth Rate and Fitness of a ΔPSI Strain of *Synechocystis* Sp. PCC6803. *Metab. Eng.* 52, 68–76. doi:10.1016/j.ymben.2018.11.002

Chen, Q., Arents, J., Ganapathy, S., DeGrip, W. J., and Hellingwerf, K. J. (2017). Functional Expression of *Gloeobacter* Rhodopsin in *Synechocystis* Sp PCC6803. *Photochem. Photobiol.* 93, 772–781. doi:10.1111/php.12745

Chen, Q., Arents, J., Schuurmans, J. M., Ganapathy, S., De Grip, W. J., Cheregi, O., et al. (2019a). Functional Expression of *Gloeobacter* Rhodopsin in PSI-Less *Synechocystis* Sp. PCC6803. *Front. Bioeng. Biotechnol.* 7, 67. doi:10.3389/fbioe.2019.00067

Chen, Q., Montesarchio, D., and Hellingwerf, K. J. (2016a). "'Direct Conversion': Artificial Photosynthesis with Cyanobacteria," in *Artificial Photosynthesis*. Editor R. Bruno, 43–61. doi:10.1016/bs.abr.2016.03.001

Chen, Q., Van Der Steen, J. B., Arents, J. C., Hartog, A. F., Ganapathy, S., De Grip, W. J., et al. (2018). Deletion of *Sll1541* in *Synechocystis* Sp Strain PCC 6803 Allows Formation of a Far-Red-Shifted *Holo*-Proteorhodopsin *In Vivo*. *Appl. Environ. Microbiol.* 84, e024351–0241714. doi:10.1128/AEM.02435-17

Chen, Q., Van Der Steen, J. B., Dekker, H. L., Ganapathy, S., De Grip, W. J., and Hellingwerf, K. J. (2016b). Expression of *Holo*-Proteorhodopsin in *Synechocystis* Sp PCC 6803. *Metab. Eng.* 35, 83–94. doi:10.1016/j.ymben.2016.02.001

Chen, S. (2019). Optical Modulation Goes Deep in the Brain. *Science* 365, 456–457. doi:10.1126/science.aay4350

Chien, M.-P., Brinks, D., Testa-Silva, G., Tian, H., Brooks, F. P. I., Adam, Y., et al. (2021). Photoactivated Voltage Imaging in Tissue with an Archaerhodopsin-Derived Reporter. *Sci. Adv.* 7, eabe3216. doi:10.1126/sciadv.abe3216

Chizhov, I., Chernavskii, D. S., Engelhard, M., Mueller, K.-H., Zubov, B. V., and Hess, B. (1996). Spectrally Silent Transitions in the Bacteriorhodopsin Photocycle. *Biophysical J.* 71, 2329–2345. doi:10.1016/s0006-3495(96)79475-4

Cho, Y. K., Park, D., Yang, A. M., Chen, F., Chuong, A. S., Klapoetke, N. C., et al. (2019). Multidimensional Screening Yields Channelrhodopsin Variants Having Improved Photocurrent and Order-Of-Magnitude Reductions in Calcium and Proton Currents. *J. Biol. Chem.* 294, 3806–3821. doi:10.1074/jbc.ra118.006996

Choe, H.-W., Kim, Y. J., Park, J. H., Morizumi, T., Pai, E. F., Krauß, N., et al. (2011). Crystal Structure of Metarhodopsin II. *Nature* 471, 651–655. doi:10.1038/nature09789

Choi, A. R., Shi, L. C., Brown, L. S., and Jung, K.-H. (2014). Cyanobacterial Light-Driven Proton Pump, *Gloeobacter* Rhodopsin: Complementarity between Rhodopsin-Based Energy Production and Photosynthesis. *PLoS ONE* 9, e110643. doi:10.1371/journal.pone.0110643

Choi, E. H., Daruwalla, A., Suh, S., Leinonen, H., and Palczewski, K. (2021). Retinoids in the Visual Cycle: Role of the Retinal G Protein-Coupled Receptor. *J. Lipid Res.* 62, 1000–1040. doi:10.1194/jlr.tr120000850

Chow, B. Y., Han, X., Dobry, A. S., Qian, X. F., Chuong, A. S., Li, M. J., et al. (2010). High-performance Genetically Targetable Optical Neural Silencing by Light-Driven Proton Pumps. *Nature* 463, 98–102. doi:10.1038/nature08652

Chuon, K., Kim, S. Y., Meas, S., Shim, J.-G., Cho, S.-G., Kang, K.-W., et al. (2021). Assembly of Natively Synthesized Dual Chromophores into Functional Actinorhodopsin. *Front. Microbiol.* 12, 652328. doi:10.3389/fmicb.2021.652328

Church, J. R., Amoyal, G. S., Borin, V. A., Adam, S., Olsen, J. M. H., and Schapiro, I. (2022). Deciphering the Spectral Tuning Mechanism in Proteorhodopsin: The Dominant Role of Electrostatics Instead of Chromophore Geometry. *Chem. - A Eur. J.* 28, e202200139. doi:10.1002/chem.202200139

Church, J. R., Haugaard Olsen, J. M., and Schapiro, I. (2022b). The Impact of Retinal Configuration on the Protein-Chromophore Interactions in Bistable Jumping Spider Rhodopsin-1. *Molecules* 27, 71. doi:10.3390/molecules27010071

Civjan, N. R., Bayburt, T. H., Schuler, M. A., and Sligar, S. G. (2003). Direct Solubilization of Heterologously Expressed Membrane Proteins by Incorporation into Nanoscale Lipid Bilayers. *BioTechniques* 35, 556–563. doi:10.2144/03353rr02

Cokic, M., Bruegmann, T., Sasse, P., and Malan, D. (2021). Optogenetic Stimulation of G_i Signaling Enables Instantaneous Modulation of Cardiomyocyte Pacemaking. *Front. physiology* 12, 768495. doi:10.3389/fphys.2021.768495

Collette, F., Renger, T., Müh, F., and Schmidt Am Busch, M. (2018). Red/Green Color Tuning of Visual Rhodopsins: Electrostatic Theory Provides a Quantitative Explanation. *J. Phys. Chem. B* 122, 4828–4837. doi:10.1021/acs.jpcb.8b02702

Concistrè, M., Gansmüller, A., Mclean, N., Johannessen, O. G., Marín-Montesinos, I., Bovee-Geurts, P. H. M., et al. (2008). Double-quantum ^{13}C Nuclear Magnetic Resonance of Bathorhodopsin, the First Photointermediate in Mammalian Vision. *J. Am. Chem. Soc.* 130, 10490–10491. doi:10.1021/ja803801u

Contreras, E., Nobleman, A. P., Robinson, P. R., and Schmidt, T. M. (2021). Melanopsin Phototransduction: beyond Canonical Cascades. *J. Exp. Biol.* 224, 224–221214. doi:10.1242/jeb.226522

Cooper, A. (1979). Energetics of Rhodopsin and Isorhodopsin. *FEBS Lett.* 100, 382–384. doi:10.1016/0014-5793(79)80375-0

Copits, B. A., Gowrishankar, R., O'neill, P. R., Li, J.-N., Girven, K. S., Yoo, J. J., et al. (2021). A Photoswitchable GPCR-Based Opsin for Presynaptic Inhibition. *Neuron* 109, 1791–1809. doi:10.1016/j.neuron.2021.04.026

Córdova, C., Lozano, C., Rodríguez, B., Marchant, I., Zúñiga, R., Ochova, P., et al. (2021). Optogenetic Control of Cancer Cell Survival in ChR2-Transfected HeLa Cells. *Int. J. Exp. pathology* 102, 242. doi:10.1111/iep.12426

Creemers, A. F. L., Kiihne, S. R., Bovee-Geurts, P. H. M., DeGrip, W. J., Lugtenburg, J., and De Groot, H. J. M. (2002). ^{1}H and ^{13}C MAS NMR Evidence for Pronounced Ligand-Protein Interactions Involving the Ionone Ring of the Retinylidene Chromophore in Rhodopsin. *Proc. Nat. Acad. Sci. U. S. A.* 99, 9101–9106. doi:10.1073/pnas.112677599

Creemers, A. F. L., Klaassen, C. H. W., Bovee-Geurts, P. H. M., Kelle, R., Kragl, U., Raap, J., et al. (1999). ^{15}N Solid State NMR Evidence for a Compex Schiff Base Counterion in the Visual G Protein-Coupled Receptor Rhodopsin. *Biochemistry-USA* 38, 7195–7199. doi:10.1021/bi9830157

Crescitelli, F. (1991). The Natural History of Visual Pigments: 1990. *Prog. Retin. Res.* 11, 1–32. doi:10.1111/j.1749-6632.1958.tb39548.x

Crouch, R. K., Kefalov, V. J., Gärtner, W., and Cornwall, M. C. (2002). Use of Retinal Analogues for the Study of Visual Pigment Function. *Meth. Enzymol.* 343, 29–48. doi:10.1016/s0076-6879(02)43126-6

Crouch, R. K., Nodes, B. R., Perlman, J. I., Pepperberg, D. R., Akita, H., and Nakanishi, K. (1984). Cycloheptatrienylidene Analog of 11-*cis* Retinal. Formation of Pigment in Photoreceptor Membranes. *Investig. Ophthalmol. Vis. Sci.* 25, 419–428.

Daemen, F. J. M. (1973). Vertebrate Rod Outer Segment Membranes. *Biochimica Biophysica Acta* 300, 255–288. doi:10.1016/0304-4157(73)90006-3

Dartnall, H. J. A. (1962a). "The Chemical Structure and Photochemistry of the Visual Pigments," in *The Visual Process*. Editor H. Davson. 1 ed (New York, U.S.A. Academic Press), 427–471.

Dartnall, H. J. A. (1962b). "The Identity and Distribution of Visual Pigments in the Animal Kingdom," in *The Visual Process*. Editor H. Davson (New York, U.S.A. Academic Press), 367–426.

Dartnall, H. J. A. (1962c). "The Properties of Visual Pigments in Photoreceptors," in *The Visual Process*. Editor H. Davson. 1 ed (New York, U.S.A. Academic Press), 473–533.

Davidson, F. F., Loewen, P. C., and Khorana, H. G. (1994). Structure and Function in Rhodopsin: Replacement by Alanine of Cysteine Residues 110 and 187, Components of a Conserved Disulfide Bond in Rhodopsin, Affects the Light-Activated Metarhodopsin II State. *Proc. Nat. Acad. Sci. U. S. A.* 91, 4029–4033. doi:10.1073/pnas.91.9.4029

Davies, A., Gowen, B. E., Krebs, A. M., Schertler, G. F. X., and Saibil, H. R. (2001). Three-dimensional Structure of an Invertebrate Rhodopsin and Basis for Ordered Alignment in the Photoreceptor Membrane. *J. Mol. Biol.* 314, 455–463. doi:10.1006/jmbi.2001.5167

Davies, A., Schertler, G. F. X., Gowen, B. E., and Saibil, H. R. (1996). Projection Structure of an Invertebrate Rhodopsin. *J. Struct. Biol.* 117, 36–44. doi:10.1006/jsbi.1996.0067

Davies, W. I. L., Collin, S. P., and Hunt, D. M. (2012). Molecular Ecology and Adaptation of Visual Photopigments in Craniates. *Mol. Ecol.* 21, 3121–3158. doi:10.1111/j.1365-294x.2012.05617.x

Davies, W. I. L., Hankins, M. W., and Foster, R. G. (2010). Vertebrate Ancient Opsin and Melanopsin: Divergent Irradiance Detectors. *Photochem. Photobiological Sci.* 9, 1444–1457. doi:10.1039/c0pp00203h

Davies, W. I. L., Sghari, S., Upton, B. A., Nord, C., Hahn, M., Ahlgren, U., et al. (2021). Distinct Opsin 3 (Opn3) Expression in the Developing Nervous System during Mammalian Embryogenesis. *eNeuro* 8, 0141–0121. doi:10.1523/eneuro.0141-21.2021

Davies, W. I. L., Tamai, T. K., Zheng, L., Fu, J. K., Rihel, J., Foster, R. G., et al. (2015). An Extended Family of Novel Vertebrate Photopigments Is Widely Expressed and Displays a Diversity of Function. *Genome Res.* 25, 1666–1679. doi:10.1101/gr.189886.115

Dawadi, P. B. S., and Lugtenburg, J. (2010). Synthesis and Use of Stable Isotope Enriched Retinals in the Field of Vitamin A. *Molecules* 15, 1825–1872. doi:10.3390/molecules15031825

De Silva, S. R., Barnard, A. R., Hughes, S., Tam, S. K. E., Martin, C., Singh, M. S., et al. (2017). Long-term Restoration of Visual Function in End-Stage Retinal Degeneration Using Subretinal Human Melanopsin Gene Therapy. *Proc. Natl. Acad. Sci. U. S. A.* 114, 11211–11216. doi:10.1073/pnas.1701589114

DeGrip, W. J., Bonting, S. L., and Daemen, F. J. M. (1973). The Binding Site of Retinaldehyde in Cattle Rhodopsin. *Biochimica Biophysica Acta* 303, 189–193. doi:10.1016/0005-2795(73)90162-1

DeGrip, W. J., and Bovee-Geurts, P. H. M. (1979). Synthesis and Properties of Alkylglucosides with Mild Detergent Action: Improved Synthesis and Purification of β-1-octyl, -nonyl- and -Decyl-Glucose. Synthesis of β-1-undecylglucose and β-1-dodecylmaltose. *Chem. Phys. Lipids* 23, 321–335. doi:10.1016/0009-3084(79)90010-0

DeGrip, W. J., Bovee-Geurts, P. H. M., Van Der Hoef, I., and Lugtenburg, J. (2007). 7, 8-Dihydro-Retinals Outperform the Native Retinals in Conferring Photosensitivity to Visual Opsin. *jacs* 129, 13265–13269. doi:10.1021/ja074937c

DeGrip, W. J., Bovee-Geurts, P. H. M., Wang, Y.-J., Verhoeven, M. A., and Lugtenburg, J. (2011). Cyclopropyl and Isopropyl Derivatives of 11-*cis* and 9-*cis* Retinals at C-9 and C-13: Subtle Steric Differences with Major Effects on Ligand Efficacy in Rhodopsin. *J. Nat. Prod.* 74, 383–390. doi:10.1021/np100744v

DeGrip, W. J., Daemen, F. J. M., and Bonting, S. L. (1980). Isolation and Purification of Bovine Rhodopsin. *Meth. Enzymol.* 67, 301–320. doi:10.1016/s0076-6879(80)67038-4

DeGrip, W. J., DeLange, F., Klaassen, C. H. W., Verdegem, P. J. E., Wallace-Williams, S. E., Creemers, A. F. L., et al. (1999). "Photoactivation of Rhodopsin: Interplay between Protein and Chromophore," in *Rhodopsins and Phototransduction*. Editor J. A. Goode (Chichester, UK: John Wiley & Sons), 102–118.

DeGrip, W. J., Gillespie, J., and Rothschild, K. J. (1985). Carboxyl Group Involvement in the Meta I and Meta II Stages in Rhodopsin Bleaching. A Fourier Transform Infra-red Spectroscopic Study. *Biochim. Biophys. Acta* 809, 97–106. doi:10.1016/0005-2728(85)90172-0

DeGrip, W. J., Gray, D., Gillespie, J., Bovee-Geurts, P. H. M., Vandenberg, E. M. M., Lugtenburg, J., et al. (1988). Photoexcitation of Rhodopsin: Conformation Changes in the Chromophore, Protein and Associated Lipid, as Determined by FTIR Difference Spectroscopy. *Photochem. Photobiol.* 48, 497–504. doi:10.1111/j.1751-1097.1988.tb02852.x

DeGrip, W. J., Liu, R. S. H., Ramamurthy, V., and Asato, A. E. (1976). Rhodopsin Analogues from Highly Hindered 7-*cis* Isomers of Retinal. *Nature* 262, 416–418. doi:10.1038/262416a0

DeGrip, W. J., and Rothschild, K. J. (2000). "Structure and Mechanism of Vertebrate Visual Pigments," in *Molecular Mechanisms in Visual Transduction*. Editors D. G. Stavenga, W. J. DeGrip, and E. N. PughJr. (Amsterdam, Netherlands: Elsevier Science Pub.), 1–54. doi:10.1016/s1383-8121(00)80004-4

DeGrip, W. J. (1982). Thermal Stability of Rhodopsin and Opsin in Some Novel Detergents. *Meth. Enzymol.* 81, 256–265. doi:10.1016/s0076-6879(82)81040-9

DeGrip, W. J., VanOostrum, J., and Bovee-Geurts, P. H. M. (1998). Selective Detergent-Extraction from Mixed Detergent/lipid/protein Micelles, Using Cyclodextrin Inclusion Compounds: A Novel Generic Approach for the Preparation of Proteoliposomes. *Biochem. J.* 330, 667–674. doi:10.1042/bj3300667

DeGrip, W. J., VanOostrum, J., Bovee-Geurts, P. H. M., Van Der Steen, R., Van Amsterdam, L. J. P., Groesbeek, M., et al. (1990). 10, 20-Methanorhodopsins: (7*E*, 9*E*, 13*E*)-10, 20-methanorhodopsin and (7*E*, 9*Z*, 13*Z*)-10, 20-methanorhodopsin - 11-*Cis*-Locked Rhodopsin Analog Pigments with Unusual Thermal and Photo-Stability. *Eur. J. Biochem.* 191, 211–220. doi:10.1111/j.1432-1033.1990.tb19112.x

Deininger, W., Kröger, P., Hegemann, U., Lottspeich, F., and Hegemann, P. (1995). Chlamyrhodopsin Represents a New Type of Sensory Photoreceptor. *EMBO J.* 14, 5849–5858. doi:10.1002/j.1460-2075.1995.tb00273.x

Deisseroth, K. (2010). Controlling the Brain with Light. *Sci. Am.* 303, 48–55. doi:10.1038/scientificamerican1110-48

Deisseroth, K., and Hegemann, P. (2017). The Form and Function of Channelrhodopsin. *Science* 357, eaan5544. doi:10.1126/science.aan5544

Deisseroth, K. (2015). Optogenetics: 10 Years of Microbial Opsins in Neuroscience. *Nat. Neurosci.* 18, 1213–1225. doi:10.1038/nn.4091

Del Carmen Marín, M., Agathangelou, D., Orozco-Gonzalez, Y., Valentini, A., Kato, Y., Abe-Yoshizumi, R., et al. (2019a). Fluorescence Enhancement of a Microbial Rhodopsin via Electronic Reprogramming. *J. Am. Chem. Soc.* 141, 262–271. doi:10.1021/jacs.8b09311

Del Carmen Marín, M., De Vico, L., Dong, S. J. S., Gagliardi, L., Truhlar, D. G., and Olivucci, M. (2019b). Assessment of MC-PDFT Excitation Energies for a Set of QM/MM Models of Rhodopsins. *J. Chem. Theory Comput.* 15, 1915–1923. doi:10.1021/acs.jctc.8b01069

DeLange, F., Bovee-Geurts, P. H. M., Pistorius, A. M. A., Rothschild, K. J., and DeGrip, W. J. (1999). Probing Intramolecular Orientations in Rhodopsin and Metarhodopsin II by Polarized Infrared Difference Spectroscopy. *Biochemistry-USA* 38, 13200–13209. doi:10.1021/bi9909501

DeLange, F., Bovee-Geurts, P. H. M., Vanoostrum, J., Portier, M. D., Verdegem, P. J. E., Lugtenburg, J., et al. (1998a). An Additional Methyl Group at the 10-position of Retinal Dramatically Slows Down the Kinetics of the Rhodopsin Photocascade. *Biochemistry-USA* 37, 1411–1420. doi:10.1021/bi972397y

DeLange, F., Klaassen, C. H. W., Wallace-Williams, S. E., Bovee-Geurts, P. H. M., Liu, X.-M., DeGrip, W. J., et al. (1998b). Tyrosine Structural Changes Detected during the Photoactivation of Rhodopsin. *J. Biol. Chem.* 273, 23735–23739. doi:10.1074/jbc.273.37.23735

DeLange, F., Merkx, M., Bovee-Geurts, P. H. M., Pistorius, A. M. A., and DeGrip, W. J. (1997). Modulation of the Metarhodopsin I/metarhodopsin II Equilibrium of Bovine Rhodopsin by Ionic Strength - Evidence for a Surface Charge Effect. *Eur. J. Biochem.* 243, 174–180. doi:10.1111/j.1432-1033.1997.0174a.x

Demoulin, B., Maiuri, M., Berbasova, T., Geiger, J. H., Borhan, B., Garavelli, M., et al. (2021). Control of Protonated Schiff Base Excited State Decay within Visual Protein Mimics: A Unified Model for Retinal Chromophores. *Chemistry-A Eur. J.* 27, 16389. doi:10.1002/chem.202102383

Dencher, N. A., and Heyn, M. P. (1978). Formation and Properties of Bacteriorhodopsin Monomers in the Nonionic Detergents Octyl-β-D-Glucoside and Triton X-100. *FEBS Lett.* 96, 322–326. doi:10.1016/0014-5793(78)80427-x

Derguini, F., Caldwell, C. G., Motto, M. G., Balogh-Nair, V., and Nakanishi, K. (1983). Bacteriorhodopsins Containing Cyanine Dye Chromophores - Support for the External Point-Charge Model. *J. Am. Chem. Soc.* 105, 646–648. doi:10.1021/ja00341a068

Derguini, F., and Nakanishi, K. (1986). Synthetic Rhodopsin Analogs. *Photobiochem. Photobiophys.* 13, 259–283.

Deubner, J., Coulon, P., and Diester, I. (2019). Optogenetic Approaches to Study the Mammalian Brain. *Curr. Opin. Struct. Biol.* 57, 157–163. doi:10.1016/j.sbi.2019.04.003

Devine, E. L., Oprian, D. D., and Theobald, D. L. (2013). Relocating the Active-Site Lysine in Rhodopsin and Implications for Evolution of Retinylidene Proteins. *Proc. Natl. Acad. Sci. U. S. A.* 110, 13351–13355. doi:10.1073/pnas.1306826110

Ding, X. Y., Sun, C., Cui, H. L., Chen, S. J., Gao, Y. J., Yang, Y. A., et al. (2018). Functional Roles of Tyrosine 185 during the Bacteriorhodopsin Photocycle as Revealed by *In Situ* Spectroscopic Studies. *Biochimica Biophysica Acta-Bioenergetics* 1859, 1006–1014. doi:10.1016/j.bbabio.2018.05.011

Dokukina, I., Nenov, A., Garavelli, M., Marian, C. M., and Weingart, O. (2019). QM/MM Photodynamics of Retinal in the Channelrhodopsin Chimera C1C2 with OM3/MRCI. *ChemPhotoChem* 3, 107–116. doi:10.1002/cptc.201800185

Döring, C. C., Kumar, S., Tumu, S. C., Kourtesis, I., and Hausen, H. (2020). The Visual Pigment Xenopsin Is Widespread in Protostome Eyes and Impacts the View on Eye Evolution. *Elife* 9, e55193. doi:10.7554/eLife.55193

Dörr, J. M., Scheidelaar, S., Koorengevel, M. C., Dominguez, J. J., Schäfer, M., Van Walree, C. A., et al. (2016). The Styrene-Maleic Acid Copolymer: A Versatile

Tool in Membrane Research. *Eur. Biophysics J. Biophysics Lett.* 45, 3–21. doi:10.1007/s00249-015-1093-y

Dowling, J. E. (2020). Vitamin A: its Many Roles - from Vision and Synaptic Plasticity to Infant Mortality. *J. Comp. Physiology a-Neuroethology Sens. Neural Behav. Physiology* 206, 389–399. doi:10.1007/s00359-020-01403-z

Du, W., Caicedo Burbano, P., Hellingwerf, K. J., and Branco Dos Santos, F. (2018). "Challenges in the Application of Synthetic Biology towards Synthesis of Commodity Products by Cyanobacteria via "Direct Conversion"," in *Synthetic Biology of Cyanobacteria*. Editors W. Zhang and X. Song (Gateway East, Singapore: Springer Nature Singapore Pte Ltd.), 3–26. doi:10.1007/978-981-13-0854-3_1

Duda, M., Domagalik, A., Orlowska-Feuer, P., Krzysztynska-Kuleta, O., Beldzik, E., Smyk, M. K., et al. (2020). Melanopsin: From a Small Molecule to Brain Functions. *Neurosci. Biobehav. Rev.* 113, 190–203. doi:10.1016/j.neubiorev.2020.03.012

Dunham, T. D., and Farrens, D. L. (1999). Conformational Changes in Rhodopsin - Movement of Helix F Detected by Site-specific Chemical Labeling and Fluorescence Spectroscopy. *J. Biol. Chem.* 274, 1683–1690. doi:10.1074/jbc.274.3.1683

Ebrey, T. G., and Koutalos, Y. (2001). Vertebrate Photoreceptors. *Prog. Retin. Eye Res.* 20, 49–94. doi:10.1016/s1350-9462(00)00014-8

Ehsan, M., Katsube, S., Cecchetti, C., Du, Y., Mortensen, J. S., Wang, H. Q., et al. (2020). New Malonate-Derived Tetraglucoside Detergents for Membrane Protein Stability. *ACS Chem. Biol.* 15, 1697–1707. doi:10.1021/acschembio.0c00316

Eickelbeck, D., Rudack, T., Tennigkeit, S. A., Surdin, T., Karapinar, R., Schwitalla, J. C., et al. (2020). Lamprey Parapinopsin ("UVLamP"): a Bistable UV-Sensitive Optogenetic Switch for Ultrafast Control of GPCR Pathways. *ChemBioChem* 21, 612–617. doi:10.1002/cbic.201900485

Eilers, M., Goncalves, J. A., Ahuja, S., Kirkup, C., Hirshfeld, A., Simmerling, C., et al. (2012). Structural Transitions of Transmembrane Helix 6 in the Formation of Metarhodopsin I. *J. Phys. Chem. B* 116, 10477–10489. doi:10.1021/jp3019183

Eilers, M., Ying, W. W., Reeves, P. J., Khorana, H. G., and Smith, S. O. (2002). Magic Angle Spinning Nuclear Magnetic Resonance of Isotopically Labeled Rhodopsin. *Meth. Enzymol.* 343, 212–222. doi:10.1016/s0076-6879(02)43137-0

El Khatib, S., and Atamian, A. (2019). *Evolution of Color Vision in Vertebrates*. Delhi, India: Akinik Publications, 19–42.

El-Tahawy, M. M. T., Conti, I., Bonfanti, M., Nenov, A., and Garavelli, M. (2020). Tailoring Spectral and Photochemical Properties of Bioinspired Retinal Mimics by In Silico Engineering. *Angew. Chemie-International Ed.* 59, 20619–20627. doi:10.1002/anie.202008644

Engel, A., and Gaub, H. E. (2008). Structure and Mechanics of Membrane Proteins. *Annu. Rev. Biochem.* 77, 127–148. doi:10.1146/annurev.biochem.77.062706.154450

Engelhard, C., Chizhov, I., Sieber, F., and Engelhard, M. (2018). Microbial Halorhodopsins: Light-Driven Chloride Pumps. *Chem. Rev.* 118, 10629–10645. doi:10.1021/acs.chemrev.7b00715

Engqvist, M. K. M., Mcisaac, R. S., Dollinger, P., Flytzanis, N. C., Abrams, M., Schor, S., et al. (2015). Directed Evolution of *Gloeobacter Violaceus* Rhodopsin Spectral Properties. *J. Mol. Biol.* 427, 205–220. doi:10.1016/j.jmb.2014.06.015

Erbguth, K., Prigge, M., Schneider, F., Hegemann, P., and Gottschalk, A. (2012). Bimodal Activation of Different Neuron Classes with the Spectrally Red-Shifted Channelrhodopsin Chimera C1V1 in *Caenorhabditis elegans*. *PLoS ONE* 7, e46827. doi:10.1371/journal.pone.0046827

Ernst, O. P., Lodowski, D. T., Elstner, M., Hegemann, P., Brown, L. S., and Kandori, H. (2014). Microbial and Animal Rhodopsins: Structures, Functions, and Molecular Mechanisms. *Chem. Rev.* 114, 126–163. doi:10.1021/cr4003769

Ewald, A., and Kühne, W. (1878). "Untersuchungen über den Sehpurpur," in *Untersuchungen aus dem Physiologischen Institute der Universität Heidelberg*. Editor W. Kühne, 248–290.

Farrens, D. L. (2010). What Site-Directed Labeling Studies Tell Us about the Mechanism of Rhodopsin Activation and G-Protein Binding. *Photochem. Photobiological Sci.* 9, 1466–1474. doi:10.1039/c0pp00283f

Feldman, T. B., Ivankov, O. I., Kuklin, A. I., Murugova, T. N., Yakovleva, M. A., Smitienko, O. A., et al. (2019). Small-angle Neutron and X-Ray Scattering Analysis of the Supramolecular Organization of Rhodopsin in Photoreceptor Membrane. *Biochimica Biophysica Acta-Biomembranes* 1861, 183000. doi:10.1016/j.bbamem.2019.05.022

Feng, J., Brown, M. F., and Mertz, B. (2015). Retinal Flip in Rhodopsin Activation? *Biophysical J.* 108, 2767–2770. doi:10.1016/j.bpj.2015.04.040

Feng, J., and Mertz, B. (2015). Proteorhodopsin Activation Is Modulated by Dynamic Changes in Internal Hydration. *Biochemistry* 54, 7132–7141. doi:10.1021/acs.biochem.5b00932

Feng, S., Powell, S. M., Wilson, R., and Bowman, J. P. (2013). Light-stimulated Growth of Proteorhodopsin-Bearing Sea-Ice Psychrophile *Psychroflexus Torquis* Is Salinity Dependent. *ISME J.* 7, 2206–2213. doi:10.1038/ismej.2013.97

Feng, X., Verdegem, P. J. E., Lee, Y. K., Sandström, D., Edén, M., Bovee-Geurts, P. H. M., et al. (1997). Direct Determination of a Molecular Torsional Angle in the Membrane Protein Rhodopsin by Solid-State NMR. *J. Am. Chem. Soc.* 119, 6853–6857. doi:10.1021/ja970710d

Feuda, R., Menon, A. K., and Göpfert, M. C. (2022). Rethinking Opsins. *Mol. Biol. Evol.* 39, msac033. doi:10.1093/molbev/msac033

Feuda, R., Rota-Stabelli, O., Oakley, T. H., and Pisani, D. (2014). The Comb Jelly Opsins and the Origins of Animal Phototransduction. *Genome Biol. Evol.* 6, 1964–1971. doi:10.1093/gbe/evu154

Fischer, P., Mukherjee, S., Peter, E., Broser, M., Bartl, F., and Hegemann, P. (2021). The Inner Mechanics of Rhodopsin Guanylyl Cyclase during cGMP-Formation Revealed by Real-Time FTIR Spectroscopy. *eLife* 10, e71384. doi:10.7554/eLife.71384

Fleming, J. F., Feuda, R., Roberts, N. W., and Pisani, D. (2020). A Novel Approach to Investigate the Effect of Tree Reconstruction Artifacts in Single-Gene Analysis Clarifies Opsin Evolution in Nonbilaterian Metazoans. *Genome Biol. Evol.* 12, 3906–3916. doi:10.1093/gbe/evaa015

Flytzanis, N. C., Bedbrook, C. N., Chiu, H., Engqvist, M. K. M., Xiao, C., Chan, K. Y., et al. (2014). Archaerhodopsin Variants with Enhanced Voltage-Sensitive Fluorescence in Mammalian and *Caenorhabditis elegans* Neurons. *Nat. Commun.* 5, 4894. doi:10.1038/ncomms5894

Foster, R. G., and Hankins, M. W. (2002). Non-rod, Non-cone Photoreception in the Vertebrates. *Prog. Retin. Eye Res.* 21, 507–527. doi:10.1016/s1350-9462(02)00036-8

Fotiadis, D., Jastrzebska, B., Philippsen, A., Müller, D. J., Palczewski, K., and Engel, A. (2006). Structure of the Rhodopsin Dimer: A Working Model for G-Protein-Coupled Receptors. *Curr. Opin. Struct. Biol.* 16, 252–259. doi:10.1016/j.sbi.2006.03.013

Fotiadis, D., Liang, Y., Filipek, S., Saperstein, D. A., Engel, A., and Palczewski, K. (2004). The G Protein-Coupled Receptor Rhodopsin in the Native Membrane. *FEBS Lett.* 564, 281–288. doi:10.1016/s0014-5793(04)00194-2

Fougère, M., Van Der Zouwen, C. I., Boutin, J. A., Neszvecsko, K., Sarret, P., and Ryczko, D. (2021). Optogenetic Stimulation of Glutamatergic Neurons in the Cuneiform Nucleus Controls Locomotion in a Mouse Model of Parkinson's Disease. *Proc. Natl. Acad. Sci. U. S. A.* 118, e2110934118. doi:10.1073/pnas.2110934118

Frank, M., Carlson, D. B., Hunter, M. S., Williams, G. J., Messerschmidt, M., Zatsepin, N. A., et al. (2014). Femtosecond X-Ray Diffraction from Two-Dimensional Protein Crystals. *IUCrJ* 1, 95–100. doi:10.1107/s2052252514001444

Frauenfeld, J., Löving, R., Armache, J.-P., Sonnen, A. F.-P., Guettou, F., Moberg, P., et al. (2016). A Saposin-Lipoprotein Nanoparticle System for Membrane Proteins. *Nat. Methods* 13, 345–351. doi:10.1038/nmeth.3801

Friedman, J. M. (2021). How the Discovery of Microbial Opsins Led to the Development of Optogenetics. *Cell.* 184, 5266–5270. doi:10.1016/j.cell.2021.08.022

Friedman, N., Sheves, M., and Ottolenghi, M. (1989). Model Systems for Rhodopsins: The Photolysis of Protonated Retinal Schiff-Bases, Cyanine Dye, and Artificial Cyanine-Bacteriorhodopsin. *J. Am. Chem. Soc.* 111, 3203–3211. doi:10.1021/ja00191a015

Friedrich, D., Perodeau, J., Nieuwkoop, A. J., and Oschkinat, H. (2020). MAS NMR Detection of Hydrogen Bonds for Protein Secondary Structure Characterization. *J. Biomol. NMR* 74, 247–256. doi:10.1007/s10858-020-00307-z

Fudim, R., Szczepek, M., Vierock, J., Vogt, A., Schmidt, A., Kleinau, G., et al. (2019). Design of a Light-Gated Proton Channel Based on the Crystal Structure of *Coccomyxa* Rhodopsin. *Sci. Signal.* 12, eaav4203. doi:10.1126/scisignal.aav4203

Fujimoto, K. J. (2021). Electronic Couplings and Electrostatic Interactions behind the Light Absorption of Retinal Proteins. *Front. Mol. Biosci.* 8, 752700. doi:10.3389/fmolb.2021.752700

Fujimoto, K. J., Hayashi, S., Hasegawa, J., and Nakatsuji, H. (2007). Theoretical Studies on the Color-Tuning Mechanism in Retinal Proteins. *J. Chem. Theory Comput.* 3, 605–618. doi:10.1021/ct6002687

Fujimoto, K. J., and Inoue, K. (2020). Excitonic Coupling Effect on the Circular Dichroism Spectrum of Sodium-Pumping Rhodopsin KR2. *J. Chem. Phys.* 153, 04510. doi:10.1063/5.0013642

Fujita, S., Endo, T., Ju, J.-M., Kean, E. L., and Kobata, A. (1994). Structural Studies of the N-Linked Sugar Chains of Human Rhodopsin. *Glycobiology* 4, 633–640. doi:10.1093/glycob/4.5.633

Fujiyabu, C., Sato, K., Nishio, Y., Imamoto, Y., Ohuchi, H., and Shichida, Y., T. (2022). Amino Acid Residue at Position 188 Determines the UV-Sensitive Bistable Property of Vertebrate Non-visual Opsin Opn5. *Commun. Biol.* 5, 63. doi:10.1038/s42003-022-03010-x

Fukada, Y., Shichida, Y., Yoshizawa, T., Ito, M., Kodama, A., and Tsukida, K. (1984). Studies on Structure and Function of Rhodopsin by Use of Cyclopentatrienylidene 11-*Cis*-Locked-Rhodopsin. *Biochemistry* 23, 5826–5832. doi:10.1021/bi00319a023

Furuse, M., Tamogami, J., Hosaka, T., Kikukawa, T., Shinya, N., Hato, M., et al. (2015). Structural Basis for the Slow Photocycle and Late Proton Release in *Acetabularia* Rhodopsin I from the Marine Plant *Acetabularia Acetabulum*. *Acta Crystallogr. Sect. F-Structural Biol.* D71, 2203–2216. doi:10.1107/s1399004715015722

Furutani, Y., Kandori, H., and Shichida, Y. (2003). Structural Changes in Lumirhodopsin and Metarhodopsin I Studied by Their Photoreactions at 77 K. *Biochemistry* 42, 8494–8500. doi:10.1021/bi034438y

Furutani, Y., Terakita, A., Shichida, Y., and Kandori, H. (2005). FTIR Studies of the Photoactivation Processes in Squid Retinochrome. *Biochemistry* 44, 7988–7997. doi:10.1021/bi050219w

Ganapathy, S., Bécheau, O., Venselaar, H., Frölich, S., Van Der Steen, J. B., Chen, Q., et al. (2015). Modulation of Spectral Properties and Pump Activity of Proteorhodopsins by Retinal Analogues. *Biochem. J.* 467, 333–343. doi:10.1042/bj20141210

Ganapathy, S., Kratz, S., Chen, Q., Hellingwerf, K. J., De Groot, H. J. M., Rothschild, K. J., et al. (2019). Redshifted and Near-Infrared Active Analog Pigments Based upon Archaerhodopsin-3. *Photochem. Photobiol.* 95, 959–968. doi:10.1111/php.13093

Ganapathy, S., and Liu, R. S. H. (1992). Photoisomerization of Sixteen Isomers of Retinal. Initial Product Distribution in Direct and Sensitized Irradiation. *Photochem. Photobiol.* 56, 959–964. doi:10.1111/j.1751-1097.1992.tb09718.x

Ganapathy, S., Opdam, L., Hontani, Y., Frehan, S., Chen, Q., Hellingwerf, K. J., et al. (2020). Membrane Matters: The Impact of a Nanodisc-Bilayer or a Detergent Microenvironment on the Properties of Two Eubacterial Rhodopsins. *Biochimica Biophysica Acta-Biomembranes* 1862, 183113. doi:10.1016/j.bbamem.2019.183113

Ganapathy, S., Venselaar, H., Chen, Q., De Groot, H. J. M., Hellingwerf, K. J., and De Grip, W. J. (2017). Retinal-based Proton Pumping in the Near Infrared. *J. Am. Chem. Soc.* 139, 2338–2344. doi:10.1021/jacs.6b11366

García-Nafría, J., and Tate, C. G. (2020). Cryo-Electron Microscopy: Moving beyond X-Ray Crystal Structures for Drug Receptors and Drug Development. *Annu. Rev. Pharmacol. Toxicol.* 60, 51–71.

Garczarek, F., and Gerwert, K. (2006). Functional Waters in Intraprotein Proton Transfer Monitored by FTIR Difference Spectroscopy. *Nature* 439, 109–112. doi:10.1038/nature04231

Gärtner, W. (2000). "Invertebrate Visual Pigments," in *Molecular Mechanisms in Visual Transduction*. Editors D. G. Stavenga, W. J. DeGrip, and E. N. PughJr. (Amsterdam, Netherlands: Elsevier Science Pub.), 298–388.

Gärtner, W., Ullrich, D., and Vogt, K. (1991). Quantum Yield of CHAPSO-Solubilized Rhodopsin and 3-Hydroxy-Retinal Containing Bovine Opsin. *Photochem. Photobiol.* 54, 1047–1055.

Gascón, J. A., Sproviero, E. M., and Batista, V. S. (2005). QM/MM Study of the NMR Spectroscopy of the Retinyl Chromophore in Visual Rhodopsin. *J. Chem. Theory Comput.* 1, 674–685. doi:10.1021/ct0500850

Geiser, A. H., Sievert, M. K., Guo, L. W., Grant, J. E., Krebs, M. P., Fotiadis, D., et al. (2006). Bacteriorhodopsin Chimeras Containing the Third Cytoplasmic Loop of Bovine Rhodopsin Activate Transducin for GTP/GDP Exchange. *Protein Sci.* 15, 1679–1690. doi:10.1110/ps.062192306

Gerrard, E., Mutt, E., Nagata, T., Koyanagi, M., Flock, T., Lesca, E., et al. (2018). Convergent Evolution of Tertiary Structure in Rhodopsin Visual Proteins from Vertebrates and Box Jellyfish. *Proc. Natl. Acad. Sci. U. S. A.* 115, 6201–6206. doi:10.1073/pnas.1721333115

Gerwert, K., Freier, E., and Wolf, S. (2014). The Role of Protein-Bound Water Molecules in Microbial Rhodopsins. *Biochimica Biophysica Acta-Bioenergetics* 1837, 606–613. doi:10.1016/j.bbabio.2013.09.006

Ghanbarpour, A., Nairat, M., Nosrati, M., Santos, E. M., Vasileiou, C., Dantus, M., et al. (2019). Mimicking Microbial Rhodopsin Isomerization in a Single Crystal. *J. Am. Chem. Soc.* 141, 1735–1741. doi:10.1021/jacs.8b12493

Gibson, S. K., Parkes, J. H., and Liebman, P. A. (1999). Phosphorylation Alters the pH-dependent Active State Equilibrium of Rhodopsin by Modulating the Membrane Surface Potential. *Biochemistry-USA* 38, 11103–11114. doi:10.1021/bi990411w

Giesbers, M. E., Bosman, G. J. C. G. M., Bovee-Geurts, P. H. M., and DeGrip, W. J. (2007). Introduction of a Rod Aromatic Cluster Does Not Improve the Structural Stability of the Human Green Cone Pigment. *J. Struct. Biol.* 159, 222–227. doi:10.1016/j.jsb.2007.01.010

Giesbers, M. E., Shirzad-Wasei, N., Bosman, G. J. C. G. M., and DeGrip, W. J. (2008). Functional Expression, Targeting and Ca^{2+} Signaling of a Mouse Melanopsin-eYFP Fusion Protein in a Retinal Pigment Epithelium Cell Line. *Photochem. Photobiol.* 84, 990–995. doi:10.1111/j.1751-1097.2008.00347.x

Gilhooley, M. J., Lindner, M., Palumaa, T., Hughes, S., Peirson, S. N., and Hankins, M. W. (2022). A Systematic Comparison of Optogenetic Approaches to Visual Restoration. *Mol. Ther. Methods & Clin. Dev.* 25, 111. doi:10.1016/j.omtm.2022.03.003

Gómez-Consarnau, L., Raven, J. A., Levine, N. M., Cutter, L. S., Wang, D. L., Seegers, B., et al. (2019). Microbial Rhodopsins Are Major Contributors to the Solar Energy Captured in the Sea. *Sci. Adv.* 5, eaaw8855. doi:10.1126/sciadv.aaw8855

Gong, X., Mendoza-Halliday, D., Ting, J. T., Kaiser, T., Sun, X. Y., Bastos, A. M., et al. (2020). An Ultra-sensitive Step-Function Opsin for Minimally Invasive Optogenetic Stimulation in Mice and Macaques. *Neuron* 107, 38–51. doi:10.1016/j.neuron.2020.03.032

Govorunova, E. G., Gou, Y. Y., Sineshchekov, O. A., Li, H., Wang, Y. M., Brown, L. S., et al. (2022a). Kalium Rhodopsins: Natural Light-Gated Potassium Channels. *bioRxiv*. doi:10.1101/2021.09.17.460684

Govorunova, E. G., Sineshchekov, O. A., Li, H., and Spudich, J. L. (2017). Microbial Rhodopsins: Diversity, Mechanisms, and Optogenetic Applications. *Annu. Rev. Biochem.* 86, 845–872. doi:10.1146/annurev-biochem-101910-144233

Govorunova, E. G., Sineshchekov, O. A., Li, H., Wang, Y., Brown, L. S., Palmateer, A., et al. (2021). Cation and Anion Channelrhodopsins: Sequence Motifs and Taxonomic Distribution. *mBio* 12, e0165621. doi:10.1128/mbio.01656-21

Govorunova, E. G., Sineshchekov, O. A., Li, H., Wang, Y. M., Brown, L. S., and Spudich, J. L. (2020). RubyACRs, Nonalgal Anion Channelrhodopsins with Highly Red-Shifted Absorption. *Proc. Natl. Acad. Sci. U. S. A.* 117, 22833–22840. doi:10.1073/pnas.2005981117

Govorunova, E. G., Sineshchekov, O. A., and Spudich, J. L. (2022b). Emerging Diversity of Channelrhodopsins and Their Structure-Function Relationships. *Front. Cell. Neurosci.* 15, 800313. doi:10.3389/fncel.2021.800313

Govorunova, E. G., Sineshchekov, O. A., and Spudich, J. L. (2016). Structurally Distinct Cation Channelrhodopsins from Cryptophyte Algae. *Biophysical J.* 110, 2302–2304. doi:10.1016/j.bpj.2016.05.001

Gozem, S., Luk, H. L., Schapiro, I., and Olivucci, M. (2017). Theory and Simulation of the Ultrafast Double-Bond Isomerization of Biological Chromophores. *Chem. Rev.* 117, 13502–13565. doi:10.1021/acs.chemrev.7b00177

Griffiths, J. M., Bennett, A. E., Engelhard, M., Siebert, F., Raap, J., Lugtenburg, J., et al. (2000). Structural Investigation of the Active Site in Bacteriorhodopsin: Geometric Constraints on the Roles of Asp-85 and Asp-212 in the Proton-Pumping Mechanism from Solid-State NMR. *Biochemistry* 39, 362–371. doi:10.1021/bi991106d

Grigorieff, N., Ceska, T. A., Downing, K. H., Baldwin, J. M., and Henderson, R. A. (1996). Electron-crystallographic Refinement of the Structure of Bacteriorhodopsin. *J. Mol. Biol.* 259, 393–421. doi:10.1006/jmbi.1996.0328

Grime, R. L., Logan, R. T., Nestorow, S. A., Sridhar, P., Edwards, P. C., Tate, C. G., et al. (2021). Differences in SMA-like Polymer Architecture Dictate the

Conformational Changes Exhibited by the Membrane Protein Rhodopsin Encapsulated in Lipid Nano-Particles. *Nanoscale* 13, 13519–13528. doi:10.1039/d1nr02419a

Groenendijk, G. W. T., DeGrip, W. J., and Daemen, F. J. M. (1980). Quantitative Determination of Retinals with Complete Retention of Their Geometric Configuration. *Biochim. Biophys. Acta* 617, 430–438. doi:10.1016/0005-2760(80)90009-0

Grote, M., Engelhard, M., and Hegemann, P. (2014). Of Ion Pumps, Sensors and Channels - Perspectives on Microbial Rhodopsins between Science and History. *Biochimica Biophysica Acta-Bioenergetics* 1837, 533–545. doi:10.1016/j.bbabio.2013.08.006

Gruber, E., Kabylda, A. M., Brøndsted Nielsen, M., Rasmussen, A. P., Teiwes, R., Kusochek, P. A., et al. (2022). Light Driven Ultrafast Bioinspired Molecular Motors: Steering and Accelerating Photoisomerization Dynamics of Retinal. *J. Am. Chem. Soc.* 144, 69–73. doi:10.1021/jacs.1c10752

Guimarães Backhaus, R., Fu, T., Backhaus, H., and Stroh, A. (2021). Pipeline for 2-photon All-Optical Physiology in Mouse: From Viral Titration and Optical Window Implantation to Binarization of Calcium Transients. *Star. Protoc.* 2, 101010. doi:10.1016/j.xpro.2021.101010

Gulati, S., Jastrzebska, B., Banerjee, S., Placeres, A. L., Miszta, P., Gao, S. Q., et al. (2017). Photocyclic Behavior of Rhodopsin Induced by an Atypical Isomerization Mechanism. *Proc. Natl. Acad. Sci. U. S. A.* 114, E2608–E2615. doi:10.1073/pnas.1617446114

Guo, J., Wu, Y., Gong, Z., Chen, X., Cao, F., Kala, S., et al. (2022). Photonic Nanojet-Mediated Optogenetics. *Adv. Sci.* 9, e2104140. doi:10.1002/advs.202104140

Guo, Y. (2020). Be Cautious with Crystal Structures of Membrane Proteins or Complexes Prepared in Detergents. *Crystals* 10, 86. doi:10.3390/cryst10020086

Halford, S., Freedman, M. S., Bellingham, J., Inglis, S. L., Poopalasundaram, S., Soni, B. G., et al. (2001). Characterization of a Novel Human Opsin Gene with Wide Tissue Expression and Identification of Embedded and Flanking Genes on Chromosome 1q43. *Genomics* 72, 203–208. doi:10.1006/geno.2001.6469

Hallett, F. R., Watton, J., and Krygsman, P. (1991). Vesicle Sizing. Number Distributions by Dynamic Light Scattering. *Biophys. J.* 59, 357–362. doi:10.1016/s0006-3495(91)82229-9

Han, S., Kim, S.-H., Cho, J. C., Song, J., Bleckner, G., and Jung, K.-H. (2020). Photochemical Characterization of Flavobacterial Rhodopsin: The Importance of the Helix E Region for Heat Stability. *Biochimica Biophysica Acta-Bioenergetics* 1861, 148092. doi:10.1016/j.bbabio.2019.148092

Hanai, S., Katayama, K., Imai, H., and Kandori, H. (2021). Light-induced Difference FTIR Spectroscopy of Primate Blue-Sensitive Visual Pigment at 163 K. *Biophysics Physicobiology* 18, 40–49. doi:10.2142/biophysico.bppb-v18.005

Hara, K. Y., Wada, T., Kino, K., Asahi, T., and Sawamura, N. (2013). Construction of Photoenergetic Mitochondria in Cultured Mammalian Cells. *Sci. Rep.* 3, 1635. doi:10.1038/srep01635

Hara, T., Hara, R., and Takeuchi, J. (1967). Vision in Octopus and Squid. *Nature* 214, 572–575. doi:10.1038/214572a0

Harada, Y., Senda, T., Sakamoto, T., Takamoto, K., and Ishibashi, T. (1994). Expression of octopus Rhodopsin in *Escherichia coli*. *J. Biochem. Tokyo* 115, 66–75. doi:10.1093/oxfordjournals.jbchem.a124307

Harbison, G. S., Smith, S. O., Pardoen, J. A., Courtin, J. M. L., Lugtenburg, J., Herzfeld, J., et al. (1985). Solid-state 13C NMR Detection of a Perturbed 6-S-Trans Chromophore in Bacteriorhodopsin. *Biochemistry* 24, 6955–6962. doi:10.1021/bi00345a031

Hargrave, P. A., Mcdowell, J. H., Curtis, D. R., Wang, J. K., Juszcak, E., Fong, S.-L., et al. (1983). The Structure of Bovine Rhodopsin. *Biophys. Struct. Mech.* 9, 235–244. doi:10.1007/bf00535659

Hargrave, P. A., and Mcdowell, J. H. (1992). Rhodopsin and Phototransduction - A Model System for G-Protein-Linked Receptors. *FASEB J.* 6, 2323–2331. doi:10.1096/fasebj.6.6.1544542

Hargrave, P. A. (1982). Rhodopsin Chemistry, Structure and Topography. *Prog. Retin. Res.* 1, 2–51. doi:10.1016/0278-4327(82)90003-7

Hargrave, P. A. (1977). The Amino-Terminal Tryptic Peptide of Bovine Rhodopsin. A Glycopeptide Containing Two Sites of Oligosaccharide Attachment. *Biochim. Biophys. Acta* 492, 83–94. doi:10.1016/0005-2795(77)90216-1

Haris, P. I., Robillard, G. T., Vandijk, A. A., and Chapman, D. (1992). Potential of ^{13}C and ^{15}N Labeling for Studying Protein-Protein Interactions Using Fourier Transform Infrared Spectroscopy. *Biochemistry-USA* 31, 6279–6284. doi:10.1021/bi00142a016

Hasegawa, M., Hosaka, T., Kojima, K., Nishimura, Y., Nakajima, Y., Kimura-Someya, T., et al. (2020). A Unique Clade of Light-Driven Proton-Pumping Rhodopsins Evolved in the Cyanobacterial Lineage. *Sci. Rep.* 10, 16752. doi:10.1038/s41598-020-73606-y

Hasegawa, N., Miki, K., and Takeda, K. (2018). X-ray Structure Analysis of Bacteriorhodopsin at 1.3 Ä Resolution. *Sci. Rep.* 8, 13123. doi:10.1038/s41598-018-31370-0

Hasemi, T., Kikukawa, T., Kamo, N., and Demura, M. (2016). Characterization of a Cyanobacterial Chloride-Pumping Rhodopsin and its Conversion into a Proton Pump. *J. Biol. Chem.* 291, 355–362. doi:10.1074/jbc.m115.688614

Hashimoto, S., Takeuchi, H., Nakagawa, M., and Tsuda, M. (1996). Ultraviolet Resonance Raman Evidence for the Absence of Tyrosinate in octopus Rhodopsin and the Participation of Trp Residues in the Transition to Acid Metarhodopsin. *FEBS Lett.* 398, 239–242. doi:10.1016/s0014-5793(96)01250-1

Haupts, U., Tittor, J., and Oesterhelt, D. (1999). Closing in on Bacteriorhodopsin: Progress in Understanding the Molecule. *Annu. Rev. Biophys. Biomol. Struct.* 28, 367–399. doi:10.1146/annurev.biophys.28.1.367

Havelka, W. A., Henderson, R. A., and Oesterhelt, D. (1995). Three-dimensional Structure of Halorhodopsin at 7 Å Resolution. *J. Mol. Biol.* 247, 726–738. doi:10.1016/s0022-2836(05)80151-2

Hayashi, M., Kojima, K., Sudo, Y., and Yamashita, A. (2021). An Optogenetic Assay Method for Electrogenic Transporters Using *Escherichia coli* Co-expressing Light-Driven Proton Pump. *Protein Sci.* 30, 2161–2169. doi:10.1002/pro.4154

Hayashi, S., Tajkhorshid, E., Pebay-Peyroula, E., Royant, A., Landau, E. M., Navarro, J., et al. (2001). Structural Determinants of Spectral Tuning in Retinal Proteins-Bacteriorhodopsin vs Sensory Rhodopsin II. *J. Phys. Chem. B* 105, 10124–10131. doi:10.1021/jp011362b

Hayashi, T., Yasuda, S., Suzuki, K., Akiyama, T., Kanehara, K., Kojima, K., et al. (2020). How Does a Microbial Rhodopsin RxR Realize its Exceptionally High Thermostability with the Proton-Pumping Function Being Retained? *J. Phys. Chem. B* 124, 990–1000. doi:10.1021/acs.jpcb.9b10700

Heath, G. R., Kots, E., Robertson, J. L., Lansky, S., Khelashvili, G., Weinstein, H., et al. (2021). Localization Atomic Force Microscopy. *Nature* 594, 385–390. doi:10.1038/s41586-021-03551-x

Henderson, R., and Unwin, P. N. T. (1975). Three-dimensional Model of Purple Membrane Obtained by Electron-Microscopy. *Nature* 257, 28–32. doi:10.1038/257028a0

Herwig, L., Rice, A. J., Bedbrook, C. N., Zhang, R. J. K., Lignell, A., Cahn, J. K. B., et al. (2017). Directed Evolution of a Bright Near-Infrared Fluorescent Rhodopsin Using a Synthetic Chromophore. *Cell. Chem. Biol.* 24, 415–425. doi:10.1016/j.chembiol.2017.02.008

Herzfeld, J., and Lansing, J. C. (2002). Magnetic Resonance Studies of the Bacteriorhodopsin Pump Cycle. *Annu. Rev. Biophysics Biomol. Struct.* 31, 73–95. doi:10.1146/annurev.biophys.31.082901.134233

Heymann, J. B., Müller, D. J., Mitsuoka, K., and Engel, A. (1997). Electron and Atomic Force Microscopy of Membrane Proteins. *Curr. Opin. Struct. Biol.* 7, 543–549. doi:10.1016/s0959-440x(97)80120-0

Hickey, D. G., Davies, W. I. L., Hughes, S., Rodgers, J., Thavanesan, N., Maclaren, R. E., et al. (2021). Chimeric Human Opsins as Optogenetic Light Sensitisers. *J. Exp. Biol.* 224, 240580. doi:10.1242/jeb.240580

Higuchi, A., Shihoya, W., Konno, M., Ikuta, T., Kandori, H., Inoue, K., et al. (2021). Crystal Structure of Schizorhodopsin Reveals Mechanism of Inward Proton Pumping. *Proc. Natl. Acad. Sci. U. S. A.* 118, 2016328118. doi:10.1073/pnas.2016328118

Hildebrand, P. W., Scheerer, P., Park, J. H., Choe, H.-W., Piechnick, R., Ernst, O. P., et al. (2009). A Ligand Channel through the G Protein Coupled Receptor Opsin. *PLoS ONE* 4, e4382. doi:10.1371/journal.pone.0004382

Hildebrandt, V., Polakowski, F., and Büldt, G. (1991). Purple Fission Yeast: Overexpression and Processing of the Pigment Bacteriorhodopsin in *Schizosaccharomyces pombe*. *Photochem. Photobiol.* 54, 1009–1016. doi:10.1111/j.1751-1097.1991.tb02123.x

Hillman, P., Hochstein, S., and Minke, B. (1983). Transduction in Invertebrate Photoreceptors - Role of Pigment Bistability. *Physiol. Rev.* 63, 668–772. doi:10.1152/physrev.1983.63.2.668

Hirano, T., Fujioka, N., Imai, H., Kandori, H., Wada, A., Ito, M., et al. (2006). Assignment of the Vibrational Modes of the Chromophores of Iodopsin and Bathoiodopsin: Low-Temperature Fourier Transform Infrared Spectroscopy of ^{13}C and ^{2}H-Labeled Iodopsins. *Biochemistry* 45, 1285–1294. doi:10.1021/bi0517077

Hirschi, S., Fischer, N., Kalbermatter, D., Laskowski, P. R., Ucurum, Z., Müller, D. J., et al. (2019). Design and Assembly of a Chemically Switchable and Fluorescently Traceable Light-Driven Proton Pump System for Bionanotechnological Applications. *Sci. Rep.* 9, 1046. doi:10.1038/s41598-018-37260-9

Hirschi, S., Kalbermatter, D., Ucurum, Z., Lemmin, T., and Fotiadis, D. (2021). Cryo-EM Structure and Dynamics of the Green-Light Absorbing Proteorhodopsin. *Nat. Commun.* 12, 4107. doi:10.1038/s41467-021-24429-6

Hochbaum, D. R., Zhao, Y., Farhi, S. L., Klapoetke, N. C., Werley, C. A., Kapoor, V., et al. (2014). All-optical Electrophysiology in Mammalian Neurons Using Engineered Microbial Rhodopsins. *Nat. Methods* 11, 825–833. doi:10.1038/nmeth.3000

Hoffmann, A., Hildebrandt, V., Heberle, J., and Büldt, G. (1994). Photoactive Mitochondria: *In Vivo* Transfer of a Light-Driven Proton Pump into the Inner Mitochondrial Membrane of *Schizosaccharomyces pombe*. *Proc. Nat. Acad. Sci. U. S. A.* 91, 9367–9371. doi:10.1073/pnas.91.20.9367

Hofmann, K. P. (2000). "Late Photoproducts and Signaling States of Bovine Rhodopsin," in *Molecular Mechanisms in Visual Transduction*. Editors D. G. Stavenga, W. J. DeGrip, and E. N. PughJr. (Amsterdam, Netherlands: Elsevier Science Pub.), 91–142. doi:10.1016/s1383-8121(00)80006-8

Hofmann, K. P., Scheerer, P., Hildebrand, P. W., Choe, H. W., Park, J. H., Heck, M., et al. (2009). A G Protein-Coupled Receptor at Work: the Rhodopsin Model. *Trends Biochem. Sci.* 34, 540–552. doi:10.1016/j.tibs.2009.07.005

Hofmann, L., and Palczewski, K. (2015). Advances in Understanding the Molecular Basis of the First Steps in Color Vision. *Prog. Retin. Eye Res.* 49, 46–66. doi:10.1016/j.preteyeres.2015.07.004

Hoi, K. K., Bada Juarez, J. F., Judge, P. J., Yen, H.-Y., Wu, D., Vinals, J., et al. (2021). Detergent-free Lipodisq Nanoparticles Facilitate High-Resolution Mass Spectrometry of Folded Integral Membrane Proteins. *Nano Lett.* 21, 2824–2831. doi:10.1021/acs.nanolett.0c04911

Hoischen, D., Steinmüller, S., Gärtner, W., Buss, V., and Martin, H.-D. (1997). Merocyanines as Extremely Bathochromically Absorbing Chromophores in the Halobacterial Membrane Protein Bacteriorhodopsin. *Angew. Chem. Int. Ed.* 36, 1630–1633.

Hong, F. T. (1994). "Retinal Proteins in Photovoltaic Devices," in *Molecular and Biomolecular Electronics*. Editor R. R. Birge (Washington, DC, USA: American Chemical Society), 1–27.

Hontani, Y., Broser, M., Luck, M., Weissenborn, J., Kloz, M., Hegemann, P., et al. (2020). Dual Photoisomerization on Distinct Potential Energy Surfaces in a UV-Absorbing Rhodopsin. *J. Am. Chem. Soc.* 142, 11464–11473. doi:10.1021/jacs.0c03229

Hontani, Y., Broser, M., Silapetere, A., Krause, B. S., Hegemann, P., and Kennis, J. T. M. (2017a). The Femtosecond-To-Second Photochemistry of Red-Shifted Fast-Closing Anion Channelrhodopsin PsACR1. *Phys. Chem. Chem. Phys.* 19, 30402–30409. doi:10.1039/c7cp06414d

Hontani, Y., Ganapathy, S., Frehan, S., Kloz, M., De Grip, W. J., and Kennis, J. T. M. (2019). Photoreaction Dynamics of Red-Shifting Retinal Analogues Reconstituted in Proteorhodopsin. *J. Phys. Chem. B* 123, 4242–4250. doi:10.1021/acs.jpcb.9b01136

Hontani, Y., Ganapathy, S., Frehan, S., Kloz, M., De Grip, W. J., and Kennis, J. T. M. (2018). Strong pH-dependent Near-Infrared Fluorescence in a Microbial Rhodopsin Reconstituted with a Red-Shifting Retinal Analogue. *J. Phys. Chem. Lett.* 9, 6469–6474. doi:10.1021/acs.jpclett.8b02780

Hontani, Y., Marazzi, M., Stehfest, K., Mathes, T., Van Stokkum, I. H. M., Elstner, M., et al. (2017b). Reaction Dynamics of the Chimeric Channelrhodopsin C1C2. *Sci. Rep.* 7, 7217. doi:10.1038/s41598-017-07363-w

Hope, A. J., Partridge, J. C., Dulai, K. S., and Hunt, D. M. (1997). Mechanisms of Wavelength Tuning in the Rod Opsins of Deep-Sea Fishes. *Proc. R. Soc. B-Biological Sci.* 264, 155–163. doi:10.1098/rspb.1997.0023

Hornak, V., Ahuja, S., Eilers, M., Goncalves, J. A., Sheves, M., Reeves, P. J., et al. (2010). Light Activation of Rhodopsin: Insights from Molecular Dynamics Simulations Guided by Solid-State NMR Distance Restraints. *J. Mol. Biol.* 396, 510–527. doi:10.1016/j.jmb.2009.12.003

Hosaka, T., Nomura, T., Kubo, M., Nakane, T., Fangjia, L., Sekine, S.-I., et al. (2022). Conformational Alterations in Unidirectional Ion Transport of a Light-Driven Chloride Pump Revealed Using X-Ray Free Electron Lasers. *Proc. Natl. Acad. Sci. U. S. A.* 119, e2117433119. doi:10.1073/pnas.2117433119

Hosaka, T., Yoshizawa, S., Nakajima, Y., Ohsawa, N., Hato, M., Delong, E. F., et al. (2016). Structural Mechanism for Light-Driven Transport by a New Type of Chloride Ion Pump, Nonlabens Marinus Rhodopsin-3. *J. Biol. Chem.* 291, 17488–17495. doi:10.1074/jbc.m116.728220

Hu, J. G. G., Sun, B. Q. Q., Bizounok, M., Hatcher, M. E., Lansing, J. C., Raap, J., et al. (1998). Early and Late M Intermediates in the Bacteriorhodopsin Photocycle: A Solid-State NMR Study. *Biochemistry-USA* 37, 8088–8096. doi:10.1021/bi973168e

Huang, L., Deng, H., Koutalos, Y., Ebrey, T. G., Groesbeek, M., Lugtenburg, J., et al. (1997). A Resonance Raman Study of the C=C Stretch Modes in Bovine and octopus Visual Pigments with Isotopically Labeled Retinal Chromophores. *Photochem. Photobiol.* 66, 747–754. doi:10.1111/j.1751-1097.1997.tb03219.x

Hubbard, R., Brown, P. K., and Bownds, M. D. (1971). Methodology of Vitamin A and Visual Pigments. *Meth. Enzymol.* 18C, 615–653. doi:10.1016/s0076-6879(71)18045-7

Hubbard, R., and Wald, G. (1952). Cis-trans Isomers of Vitamin A and Retinene in the Rhodopsin System. *J. General Physiology* 36, 269–315. doi:10.1085/jgp.36.2.269

Hubbell, W. L., Altenbach, C., Hubbell, C. M., and Khorana, H. G. (2003). Rhodopsin Structure, Dynamics, and Activation: A Perspective from Crystallography, Site-Directed Spin Labeling, Sulfhydryl Reactivity, and Disulfide Cross-Linking. *Adv. Protein Chem.* 63, 243–290. doi:10.1016/s0065-3233(03)63010-x

Humphreys, I. R., Pei, J. M., Baek, M., Krishnakumar, A., Anishchenko, I., Ovchinnikov, S., et al. (2021). Computed Structures of Core Eukaryotic Protein Complexes. *Science* 374, 1340.

Hunt, D. M., and Collin, S. P. (2014). "The Evolution of Photoreceptors and Visual Photopigments in Vertebrates," in *Evolution of Visual and Non-visual Pigments*. Editor D. M. Hunt (New York: Springer Science+Business Media New York), 163–217. doi:10.1007/978-1-4614-4355-1_6

Hunt, D. M., Dulai, K. S., Partridge, J. C., Cottrill, P., and Bowmaker, J. K. (2001). The Molecular Basis for Spectral Tuning of Rod Visual Pigments in Deep-Sea Fish. *J. Exp. Biol.* 204, 3333–3344. doi:10.1242/jeb.204.19.3333

Hussain, H., Du, Y., Scull, N. J., Mortensen, J. S., Tarrasch, J., Bae, H. E., et al. (2016). Accessible Mannitol-Based Amphiphiles (MNAs) for Membrane Protein Solubilisation and Stabilisation. *Chemistry-A Eur. J.* 22, 7068–7073. doi:10.1002/chem.201600533

Hussain, S., Kinnebrew, M., Schonenbach, N. S., Aye, E., and Han, S. G. (2015). Functional Consequences of the Oligomeric Assembly of Proteorhodopsin. *J. Mol. Biol.* 427, 1278–1290. doi:10.1016/j.jmb.2015.01.004

Hwa, J., Reeves, P. J., Klein-Seetharaman, J., Davidson, F. F., and Khorana, H. G. (1999). Structure and Function in Rhodopsin: Further Elucidation of the Role of the Intradiscal Cysteines, Cys-110, -185, and -187, in Rhodopsin Folding and Function. *Proc. Nat. Acad. Sci. U. S. A.* 96, 1932–1935. doi:10.1073/pnas.96.5.1932

Iizuka, A., Kajimoto, K., Fujisawa, T., Tsukamoto, T., Aizawa, T., Kamo, N., et al. (2019). Functional Importance of the Oligomer Formation of the Cyanobacterial H+ Pump Gloeobacter Rhodopsin. *Sci. Rep.* 9, 10711. doi:10.1038/s41598-019-47178-5

Ikeda, D., Furutani, Y., and Kandori, H. (2007). FTIR Study of the Retinal Schiff Base and Internal Water Molecules of Proteorhodopsin. *Biochemistry* 46, 5365–5373. doi:10.1021/bi700143g

Ikuta, T., Shihoya, W., Sugiura, M., Yoshida, K., Watari, M., Tokano, T., et al. (2020). Structural Insights into the Mechanism of Rhodopsin Phosphodiesterase. *Nat. Commun.* 11, 5605. doi:10.1038/s41467-020-19376-7

Imai, H., Hirano, T., Terakita, A., Shichida, Y., Muthyala, R. S., Chen, R.-L., et al. (1999). Probing for the Threshold Energy for Visual Transduction: Red-Shifted Visual Pigment Analogs from 3-Methoxy-3-Dehydroretinal and Related Compounds. *Photochem. Photobiol.* 70, 111–115. doi:10.1111/j.1751-1097.1999.tb01956.x

Imai, H., Imamoto, Y., Yoshizawa, T., and Shichida, Y. (1995). Difference in Molecular Properties between Chicken Green and Rhodopsin as Related to the Functional Difference between Cone and Rod Photoreceptor Cells. *Biochemistry-USA* 34, 10525–10531. doi:10.1021/bi00033a026

Imai, H., Terakita, A., Tachibanaki, S., Imamoto, Y., Yoshizawa, T., and Shichida, Y. (1997). Photochemical and Biochemical Properties of Chicken Blue-Sensitive Cone Visual Pigment. *Biochemistry-USA* 36, 12773–12779. doi:10.1021/bi970809x

Imai, Y., Inoshita, T., Meng, H. R., Shiba-Fukushima, K., Hara, K. Y., Sawamura, N., et al. (2019). Light-driven Activation of Mitochondrial Proton-Motive Force Improves Motor Behaviors in a *Drosophila* Model of Parkinson's Disease. *Commun. Biol.* 2, 424. doi:10.1038/s42003-019-0674-1

Imamoto, Y., Kandori, H., Okano, T., Fukada, Y., Shichida, Y., and Yoshizawa, T. (1989). Effect of Chloride Ion on the Thermal Decay Process of the Batho Intermediate of Iodopsin at Low Temperature. *Biochemistry* 28, 9412–9416. doi:10.1021/bi00450a025

Imamoto, Y., and Shichida, Y. (2014). Cone Visual Pigments. *Biochimica Biophysica Acta-Bioenergetics* 1837, 664–673. doi:10.1016/j.bbabio.2013.08.009

Imamoto, Y., Yoshizawa, T., and Shichida, Y. (1996). Chromophore Configuration of Iodopsin and its Photoproducts Formed at Low Temperatures. *Biochemistry* 35, 14599–14607. doi:10.1021/bi9614850

Imasheva, E. S., Balashov, S. P., Wang, J. M., and Lanyi, J. K. (2011). Removal and Reconstitution of the Carotenoid Antenna of Xanthorhodopsin. *J. Membr. Biol.* 239, 95–104. doi:10.1007/s00232-010-9322-x

Inagaki, H. K., Jung, Y., Hoopfer, E. D., Wong, A. M., Mishra, N., Lin, J. Y., et al. (2014). Optogenetic Control of *Drosophila* Using a Red-Shifted Channelrhodopsin Reveals Experience-dependent Influences on Courtship. *Nat. Methods* 11, 325–U311. doi:10.1038/nmeth.2765

Inoue, K., Del Carmen Marin, M., Tomida, S., Nakamura, R., Nakajima, Y., Olivucci, M., et al. (2019). Red-shifting Mutation of Light-Driven Sodium-Pump Rhodopsin. *Nat. Commun.* 10, 1993. doi:10.1038/s41467-019-10000-x

Inoue, K., Karasuyama, M., Nakamura, R., Konno, M., Yamada, D., Mannen, K., et al. (2021). Exploration of Natural Red-Shifted Rhodopsins Using a Machine Learning-Based Bayesian Experimental Design. *Commun. Biol.* 4, 362. doi:10.1038/s42003-021-01878-9

Inoue, K., Nomura, Y., and Kandori, H. (2016). Asymmetric Functional Conversion of Eubacterial Light-Driven Ion Pumps. *J. Biol. Chem.* 291, 9883–9893. doi:10.1074/jbc.m116.716498

Inoue, K., Reissig, L., Sakai, M., Kobayashi, S., Homma, M., Fujii, M., et al. (2012). Absorption Spectra and Photochemical Reactions in a Unique Photoactive Protein, Middle Rhodopsin MR. *J. Phys. Chem. B* 116, 5888–5899. doi:10.1021/jp302357m

Inoue, K., Sasaki, J., Morisaki, M., Tokunaga, F., and Terazima, M. (2004). Time-resolved Detection of Sensory Rhodopsin II-Transducer Interaction. *Biophysical J.* 87, 2587–2597. doi:10.1529/biophysj.104.043521

Inoue, K., Sudo, Y., Homma, M., and Kandori, H. (2011). Spectrally Silent Intermediates during the Photochemical Reactions of Salinibacter Sensory Rhodopsin I. *J. Phys. Chem. B* 115, 4500–4508. doi:10.1021/jp2000706

Inoue, K., Tahara, S., Kato, Y., Takeuchi, S., Tahara, T., and Kandori, H. (2018). Spectroscopic Study of Proton-Transfer Mechanism of Inward Proton-Pump Rhodopsin, *Parvularcula Oceani* Xenorhodopsin. *J. Phys. Chem. B* 122, 6453–6461. doi:10.1021/acs.jpcb.8b01279

Inoue, K., Tsukamoto, T., Shimono, K., Suzuki, Y., Miyauchi, S., Hayashi, S., et al. (2015). Converting a Light-Driven Proton Pump into a Light-Gated Proton Channel. *J. Am. Chem. Soc.* 137, 3291–3299. doi:10.1021/ja511788f

Inoue, K., Tsukamoto, T., and Sudo, Y. (2014). Molecular and Evolutionary Aspects of Microbial Sensory Rhodopsins. *Biochimica Biophysica Acta-Bioenergetics* 1837, 562–577. doi:10.1016/j.bbabio.2013.05.005

Inoue, K., Tsunoda, S. P., Singh, M., Tomida, S., Hososhima, S., Konno, M., et al. (2020). Schizorhodopsins: A Family of Rhodopsins from Asgard Archaea that Function as Light-Driven Inward H+ Pumps. *Sci. Adv.* 6, 2441. doi:10.1126/sciadv.aaz2441

Ito, S., Iwaki, M., Sugita, S., Abe-Yoshizumi, R., Iwata, T., Inoue, K., et al. (2018). Unique Hydrogen Bonds in Membrane Protein Monitored by Whole Mid-IR ATR Spectroscopy in Aqueous Solution. *J. Phys. Chem. B* 122, 165–170. doi:10.1021/acs.jpcb.7b11064

Iwasa, T., Colmenares, L. U., Hirata, K., Arime, Y., Nakagawa, M., Kikkawa, S., et al. (1998). ^{19}F-NMR and UV-Vis Absorption Spectroscopic Studies of Fluorinated octopus Rhodopsin and its Photoproducts. *J. Phys. Chem. A* 102, 5602–5610. doi:10.1021/jp9802477

Iyer, E. S. S., Misra, R., Maity, A., Liubashevski, O., Sudo, Y., Sheves, M., et al. (2016). Temperature Independence of Ultrafast Photoisomerization in Thermophilic Rhodopsin: Assessment versus Other Microbial Proton Pumps. *J. Am. Chem. Soc.* 138, 12401–12407. doi:10.1021/jacs.6b05002

Jacobs, G. H. (2018). Photopigments and the Dimensionality of Animal Color Vision. *Neurosci. Biobehav. Rev.* 86, 108–130. doi:10.1016/j.neubiorev.2017.12.006

Jäger, S., Lewis, J. W., Zvyaga, T. A., Szundi, I., Sakmar, T. P., and Kliger, D. S. (1997). Chromophore Structural Changes in Rhodopsin from Nanoseconds to Microseconds Following Pigment Photolysis. *Proc. Nat. Acad. Sci. U. S. A.* 94, 8557–8562. doi:10.1073/pnas.94.16.8557

Jana, S., Jung, K. H., and Sheves, M. (2020). The Chirality Origin of Retinal-Carotenoid Complex in Gloeobacter Rhodopsin: a Temperature-dependent Excitonic Coupling. *Sci. Rep.* 10, 13992. doi:10.1038/s41598-020-70697-5

Janknecht, R., Demartynoff, G., Lou, J., Hipskind, R. A., Nordheim, A., and Stunnenberg, H. G. (1991). Rapid and Efficient Purification of Native Histidine-Tagged Protein Expressed by Recombinant Vaccinia Virus. *Proc. Nat. Acad. Sci. U. S. A.* 88, 8972–8976. doi:10.1073/pnas.88.20.8972

Janssen, J. J. M., Bovee-Geurts, P. H. M., Merkx, M., and DeGrip, W. J. (1995). Histidine Tagging Both Allows Convenient Single-step Purification of Bovine Rhodopsin and Exerts Ionic Strength-dependent Effects on its Photochemistry. *J. Biol. Chem.* 270, 11222–11229. doi:10.1074/jbc.270.19.11222

Janssen, J. J. M., Mulder, W. R., DeCaluwé, G. L. J., Vlak, J. M., and DeGrip, W. J. (1991). *In Vitro* expression of Bovine Opsin Using Recombinant Baculovirus: The Role of Glutamic Acid (134) in Opsin Biosynthesis and Glycosylation. *Biochim. Biophys. Acta* 1089, 68–76. doi:10.1016/0167-4781(91)90086-2

Janssen, J. J. M., VandeVen, W. J. M., VanGroningen-Luyben, W. a. H. M., Roosien, J., Vlak, J. M., and DeGrip, W. J. (1988). Synthesis of Functional Bovine Opsin in Insect Cells under Control of the Baculovirus Polyhedrin Promotor. *Mol. Biol. Rep.* 13, 65–71. doi:10.1007/bf00539052

Janssen, J. W. H., David-Gray, Z. K., Bovee-Geurts, P. H. M., Nevo, E., Foster, R. G., and DeGrip, W. J. (2003). A Green Cone-like Pigment in the 'blind' Mole-Rat *Spalax Ehrenbergi*: Functional Expression and Photochemical Characterization. *Photochem. Photobiol. Sci.* 2, 1287–1291. doi:10.1039/b300059c

Jastrzebska, B., Palczewski, K., and Golczak, M. (2011). Role of Bulk Water in Hydrolysis of the Rhodopsin Chromophore. *J. Biol. Chem.* 286, 18930–18937. doi:10.1074/jbc.m111.234583

Ji, L. L., Ma, B. F., Meng, Q., Li, L. J., Liu, K., and Chen, D. L. (2017). Detergent-resistant Oligomeric *Leptosphaeria* Rhodopsin Is a Promising Bio-Nanomaterial and an Alternative to Bacteriorhodopsin. *Biochem. Biophysical Res. Commun.* 493, 352–357. doi:10.1016/j.bbrc.2017.09.018

Jiang, M. S., Pandey, S., and Fong, H. K. W. (1993). An Opsin Homologue in the Retina and Pigment Epithelium. *Investig. Ophthalmol. Vis. Sci.* 34, 3669–3678.

Johnson, P. J. M., Halpin, A., Morizumi, T., Brown, L. S., Prokhorenko, V. I., Ernst, O. P., et al. (2014). The Photocycle and Ultrafast Vibrational Dynamics of Bacteriorhodopsin in Lipid Nanodiscs. *Phys. Chem. Chem. Phys.* 16, 21310–21320. doi:10.1039/c4cp01826e

Johnson, P. J. M., Halpin, A., Morizumi, T., Prokhorenko, V. I., Ernst, O. P., and Miller, R. J. D. (2015). Local Vibrational Coherences Drive the Primary Photochemistry of Vision. *Nat. Chem.* 7, 980–986. doi:10.1038/nchem.2398

Jumper, J., Evans, R., Pritzel, A., Green, T., Figurnov, M., Ronneberger, O., et al. (2021). Highly Accurate Protein Structure Prediction with AlphaFold. *Nature* 596, 583–589. doi:10.1038/s41586-021-03819-2

Jun, N. Y., and Cardin, J. A. (2020). Activation of Distinct Channelrhodopsin Variants Engages Different Patterns of Network Activity. *Eneuro* 7, 0222–0218. doi:10.1523/ENEURO.0222-18.2019

Kahremany, S., Sander, C. L., Tochtrop, G. P., Kubas, A., and Palczewski, K. (2019). Z-isomerization of Retinoids through Combination of Monochromatic Photoisomerization and Metal Catalysis. *Org. Biomol. Chem.* 17, 8125–8139. doi:10.1039/c9ob01645g

Kandori, H., Inoue, K., and Tsunoda, S. P. (2018). Light-Driven Sodium-Pumping Rhodopsin: A New Concept of Active Transport. *Chem. Rev.* 118, 10646–10658. doi:10.1021/acs.chemrev.7b00548

Kandori, H. (2020). Retinal Proteins: Photochemistry and Optogenetics. *Bull. Chem. Soc. Jpn.* 93, 76–85. doi:10.1246/bcsj.20190292

Kanehara, K., Yoshizawa, S., Tsukamoto, T., and Sudo, Y. (2017). A Phylogenetically Distinctive and Extremely Heat Stable Light-Driven Proton Pump from the Eubacterium *Rubrobacter Xylanophilus* DSM 9941^{T}. *Sci. Rep.* 7, 44427. doi:10.1038/srep44427

Kaneko, A., Inoue, K., Kojima, K., Kandori, H., and Sudo, Y. (2017). Conversion of Microbial Rhodopsins: Insights into Functionally Essential Elements and Rational Protein Engineering. *Biophys. Rev.* 9, 861–876. doi:10.1007/s12551-017-0335-x

Kannan, M., Vasan, G., and Pieribone, V. A. (2019). Optimizing Strategies for Developing Genetically Encoded Voltage Indicators. *Front. Cell. Neurosci.* 13, 53. doi:10.3389/fncel.2019.00053

Kao, Y.-M., Cheng, C.-H., Syue, M.-L., Huang, H.-Y., Chen, I.-C., Yu, T.-Y., et al. (2019). Photochemistry of Bacteriorhodopsin with Various Oligomeric Statuses in Controlled Membrane Mimicking Environments: A Spectroscopic Study from Femtoseconds to Milliseconds. *J. Phys. Chem. B* 123, 2032–2039. doi:10.1021/acs.jpcb.9b01224

Karapinar, R., Schwitalla, J. C., Eickelbeck, D., Pakusch, J., Mücher, B., Grömmke, M., et al. (2021). Reverse Optogenetics of G Protein Signaling by Zebrafish Non-visual Opsin Opn7b for Synchronization of Neuronal Networks. *Nat. Commun.* 12, 4488. doi:10.1038/s41467-021-24718-0

Karasuyama, M., Inoue, K., Nakamura, R., Kandori, H., and Takeuchi, I. (2018). Understanding Colour Tuning Rules and Predicting Absorption Wavelengths of Microbial Rhodopsins by Data-Driven Machine-Learning Approach. *Sci. Rep.* 8, 15580–15511. doi:10.1038/s41598-018-33984-w

Karnik, S. S., Ridge, K. D., Bhattacharya, S. S., and Khorana, H. G. (1993). Palmitoylation of Bovine Opsin and its Cysteine Mutants in COS Cells. *Proc. Nat. Acad. Sci. U. S. A.* 90, 40–44. doi:10.1073/pnas.90.1.40

Karnik, S. S., Sakmar, T. P., Chen, H.-B., and Khorana, H. G. (1988). Cysteine Residues 110 and 187 Are Essential for the Formation of Correct Structure in Bovine Rhodopsin. *Proc. Nat. Acad. Sci. U. S. A.* 85, 8459–8463. doi:10.1073/pnas.85.22.8459

Katana, R., Guan, C. L., Zanini, D., Larsen, M. E., Giraldo, D., Geurten, B. R. H., et al. (2019). Chromophore-Independent Roles of Opsin Apoproteins in *Drosophila* Mechanoreceptors. *Curr. Biol.* 29, 2961–2969. doi:10.1016/j.cub.2019.07.036

Katanosaka, K., Tokunaga, F., Kawamura, S., and Ozaki, K. (1998). N-linked Glycosylation of *Drosophila* Rhodopsin Occurs Exclusively in the Amino-Terminal Domain and Functions in Rhodopsin Maturation. *FEBS Lett.* 424, 149–154. doi:10.1016/s0014-5793(98)00160-4

Kataoka, C., Inoue, K., Katayama, K., Béjà, O., and Kandori, H. (2019). Unique Photochemistry Observed in a New Microbial Rhodopsin. *J. Phys. Chem. Lett.* 10, 5117–5121. doi:10.1021/acs.jpclett.9b01957

Katayama, K., Furutani, Y., Imai, H., and Kandori, H. (2012). Protein-bound Water Molecules in Primate Red- and Green-Sensitive Visual Pigments. *Biochemistry* 51, 1126–1133. doi:10.1021/bi201676y

Katayama, K., Gulati, S., Ortega, J. T., Alexander, N. S., Sun, W. Y., Shenouda, M. M., et al. (2019). Specificity of the Chromophore-Binding Site in Human Cone Opsins. *J. Biol. Chem.* 294, 6082–6093. doi:10.1074/jbc.ra119.007587

Katayama, K., Nonaka, Y., Tsutsui, K., Imai, H., and Kandori, H. (2017). Spectral Tuning Mechanism of Primate Blue-Sensitive Visual Pigment Elucidated by FTIR Spectroscopy. *Sci. Rep.* 7, 4904. doi:10.1038/s41598-017-05177-4

Kathe, C., Michoud, F., Schönle, P., Rowald, A., Brun, N., Ravier, J., et al. (2021). Wireless Closed-Loop Optogenetics across the Entire Dorsoventral Spinal Cord in Mice. *Nat. Biotechnol.* 40, 198. doi:10.1038/s41587-021-01019-x

Kato, H. E., Inoue, K., Abe-Yoshizumi, R., Kato, Y., Ono, H., Konno, M., et al. (2015). Structural Basis for Na+ Transport Mechanism by a Light-Driven Na+ Pump. *Nature* 521, 48–53. doi:10.1038/nature14322

Kato, H. E., Kamiya, M., Sugo, S., Ito, J., Taniguchi, R., Orito, A., et al. (2015). Atomistic Design of Microbial Opsin-Based Blue-Shifted Optogenetics Tools. *Nat. Commun.* 6, 7177. doi:10.1038/ncomms8177

Kato, H. E., Zhang, F., Yizhar, O., Ramakrishnan, C., Nishizawa, T., Hirata, K., et al. (2012). Crystal Structure of the Channelrhodopsin Light-Gated Cation Channel. *Nature* 482, 369–374. doi:10.1038/nature10870

Katz, B., and Minke, B. (2009). *Drosophila* Photoreceptors and Signaling Mechanisms. *Front. Cell. Neurosci.* 3, 2. doi:10.3389/neuro.03.002.2009

Kaufmann, J. C. D., Krause, B. S., Adam, S., Ritter, E., Schapiro, I., Hegemann, P., et al. (2020). Modulation of Light Energy Transfer from Chromophore to Protein in the Channelrhodopsin ReaChR. *Biophysical J.* 119, 705–716. doi:10.1016/j.bpj.2020.06.031

Kaur, J., Kriebel, C. N., Eberhardt, P., Jakdetchai, O., Leeder, A. J., Weber, I., et al. (2019). Solid-state NMR Analysis of the Sodium Pump Krokinobacter Rhodopsin 2 and its H30A Mutant. *J. Struct. Biol.* 206, 55–65. doi:10.1016/j.jsb.2018.06.001

Kaushal, S., Ridge, K. D., and Khorana, H. G. (1994). Structure and Function in Rhodopsin: The Role of Asparagine-Linked Glycosylation. *Proc. Nat. Acad. Sci. U. S. A.* 91, 4024–4028. doi:10.1073/pnas.91.9.4024

Kawamura, I., Seki, H., Tajima, S., Makino, Y., Shigeta, A., Okitsu, T., et al. (2021). Structure of a Retinal Chromophore of Dark-Adapted Middle Rhodopsin as Studied by Solid-State Nuclear Magnetic Resonance Spectroscopy. *Biophysics Physicobiology* 18, 177–185. doi:10.2142/biophysico.bppb-v18.019

Kawamura, S., Gerstung, M., Colozo, A. T., Helenius, J., Maeda, A., Beerenwinkel, N., et al. (2013). Kinetic, Energetic, and Mechanical Differences between Dark-State Rhodopsin and Opsin. *Structure* 21, 426–437. doi:10.1016/j.str.2013.01.011

Kawanabe, A., Furutani, Y., Jung, K.-H., and Kandori, H. (2007). Photochromism of *Anabaena* Sensory Rhodopsin. *J. Am. Chem. Soc.* 129, 8644–8649. doi:10.1021/ja072085a

Kawasaki, Y., Konno, M., and Inoue, K. (2021). Thermostable Light-Driven Inward Proton Pump Rhodopsins. *Chem. Phys. Lett.* 779, 138868. doi:10.1016/j.cplett.2021.138868

Kazmi, M. A., Dubin, R. A., Oddoux, C., and Ostrer, H. (1996). High-level Inducible Expression of Visual Pigments in Transfected Cells. *BioTechniques* 21, 304–311. doi:10.2144/96212rr05

Kazmin, R., Rose, A., Szczepek, M., Elgeti, M., Ritter, E., Piechnick, R., et al. (2015). The Activation Pathway of Human Rhodopsin in Comparison to Bovine Rhodopsin. *J. Biol. Chem.* 290, 20117–20127. doi:10.1074/jbc.m115.652172

Khelashvili, G., and Menon, A. K. (2022). Phospholipid Scrambling by G Protein-Coupled Receptors. *Annu. Rev. Biophysics* 51, 39–61. doi:10.1146/annurev-biophys-090821-083030

Khodonov, A. A., Shevyakov, S. V., Mironova, E. V., Shvets, V. I., Alexeeva, S. G., Demina, O. V., et al. (2000). Bacteriorhodopsin Analogs, Bearing Modified Chromophore as a Basis for the Photochromic Materials. *Mol. Cryst. Liq. Cryst.* 345, 641–646. doi:10.1080/10587250008023938

Khorana, H. G., Braiman, M. S., Chao, B. H., Doi, T., Flitsch, S. L., Gilles-Gonzalez, M. A., et al. (1987). Site-specific Mutagenesis in Structure - Function Studies of Bacteriorhodopsin. *Chem. Scr.* 27B, 137–147.

Khorana, H. G., Knox, B. E., Nasi, E., Swanson, R., and Thompson, D. A. (1988). Expression of a Bovine Rhodopsin Gene in *Xenopus* Oocytes: Demonstration of Light-dependent Ionic Currents. *Proc. Nat. Acad. Sci. U. S. A.* 85, 7917–7921. doi:10.1073/pnas.85.21.7917

Khorana, H. G. (1979). Total Synthesis of a Gene. *Science* 203, 614–625. doi:10.1126/science.366749

Kikukawa, T. (2021). Unique Cl^- Pump Rhodopsin with Close Similarity to H^+ Pump Rhodopsin. *Biophysics Physicobiology* 18, 317–326. doi:10.2142/biophysico.bppb-v18.038

Kim, H.-J., Kwon, Y. D., Lee, S. Y., and Kim, P. (2012). An Engineered *Escherichia coli* Having a High Intracellular Level of ATP and Enhanced Recombinant Protein Production. *Appl. Microbiol. Biotechnol.* 94, 1079–1086. doi:10.1007/s00253-011-3779-0

Kim, H. A., Kim, H. J., Park, J., Choi, A. R., Heo, K., Jeong, H., et al. (2017). An Evolutionary Optimization of a Rhodopsin-Based Phototrophic Metabolism in *Escherichia coli*. *Microb. Cell. Factories* 16, 111. doi:10.1186/s12934-017-0725-6

Kim, S.-Y., Waschuk, S. A., Brown, L. S., and Jung, K.-H. (2008). Screening and Characterization of Proteorhodopsin Color-Tuning Mutations in *Escherichia coli* with Endogenous Retinal Synthesis. *Biochimica Biophysica Acta-Bioenergetics* 1777, 504–513. doi:10.1016/j.bbabio.2008.03.010

Kimura, Y., Vassylyev, D. G., Miyazawa, A., Kidera, A., Matsushima, M., Mitsuoka, K., et al. (1997). High Resolution Structure of Bacteriorhodopsin Determined by Electron Crystallography. *Photochem. Photobiol.* 66, 764–767. doi:10.1111/j.1751-1097.1997.tb03221.x

Kirchman, D. L., and Hanson, T. E. (2013). Bioenergetics of Photoheterotrophic Bacteria in the Oceans. *Environ. Microbiol. Rep.* 5, 188–199. doi:10.1111/j.1758-2229.2012.00367.x

Kishi, K. E., Kim, Y. S., Fukuda, M., Inoue, M., Kusakizako, T., Wang, P. Y., et al. (2022). Structural Basis for Channel Conduction in the Pump-like Channelrhodopsin ChRmine. *Cell.* 185, 1–18. doi:10.1016/j.cell.2022.01.007

Klaassen, C. H. W., and DeGrip, W. J. (2000). Baculovirus Expression System for Expression and Characterization of Functional Recombinant Visual Pigments. *Meth. Enzymol.* 315, 12–29. doi:10.1016/s0076-6879(00)15832-x

Klapoetke, N. C., Murata, Y., Kim, S. S., Pulver, S. R., Birdsey-Benson, A., Cho, Y. K., et al. (2014). Independent Optical Excitation of Distinct Neural Populations. *Nat. Methods* 11, 338–U333. doi:10.1038/nmeth.2836

Klyszejko, A. L., Shastri, S., Mari, S. A., Grubmüller, H., Müller, D. J., and Glaubitz, C. (2008). Folding and Assembly of Proteorhodopsin. *J. Mol. Biol.* 376, 35–41. doi:10.1016/j.jmb.2007.11.030

Knoot, C. J., Ungerer, J., Wangikar, P. P., and Pakrasi, H. B. (2018). Cyanobacteria: Promising Biocatalysts for Sustainable Chemical Production. *J. Biol. Chem.* 293, 5044–5052. doi:10.1074/jbc.r117.815886

Knowles, T. J., Finka, R., Smith, C., Lin, Y.-P., Dafforn, T., and Overduin, M. (2009). Membrane Proteins Solubilized Intact in Lipid Containing Nanoparticles Bounded by Styrene Maleic Acid Copolymer. *J. Am. Chem. Soc.* 131, 7484–7485. doi:10.1021/ja810046q

Knudsen, P., and Hubbell, W. L. (1978). Stability of Rhodopsin in Detergent Solutions. *Membr. Biochem.* 1, 297–322. doi:10.3109/09687687809063853

Kochendoerfer, G. G., Lin, S. W., Sakmar, T. P., and Mathies, R. A. (1999). How Color Visual Pigments Are Tuned. *Trends biochem. Sci.* 24, 300–305. doi:10.1016/s0968-0004(99)01432-2

Kojima, D., Imai, H., Okano, T., Fukada, Y., Crescitelli, F., Yoshizawa, T., et al. (1995). Purification and Low Temperature Spectroscopy of Gecko Visual Pigments Green and Blue. *Biochemistry-USA* 34, 1096–1106. doi:10.1021/bi00003a047

Kojima, D., Oura, T., Hisatomi, O., Tokunaga, F., Fukada, Y., Yoshizawa, T., et al. (1996). Molecular Properties of Chimerical Mutants of Gecko Blue and Bovine Rhodopsin. *Biochemistry* 35, 2625–2629. doi:10.1021/bi9511548

Kojima, D., Terakita, A., Ishikawa, T., Tsukahara, Y., Maeda, A., and Shichida, Y. (1997). A Novel Go-Mediated Phototransduction Cascade in Scallop Visual Cells. *J. Biol. Chem.* 272, 22979–22982. doi:10.1074/jbc.272.37.22979

Kojima, K., Kurihara, R., Sakamoto, M., Takanashi, T., Kuramochi, H., Zhang, X. M., et al. (2020a). Comparative Studies of the Fluorescence Properties of Microbial Rhodopsins: Spontaneous Emission versus Photointermediate Fluorescence. *J. Phys. Chem. B* 124, 7361–7367. doi:10.1021/acs.jpcb.0c06560

Kojima, K., Miyoshi, N., Shibukawa, A., Chowdhury, S., Tsujimura, M., Noji, T., et al. (2020c). Green-sensitive, Long-Lived, Step-Functional Anion Channelrhodopsin-2 Variant as a High-Potential Neural Silencing Tool. *J. Phys. Chem. Lett.* 11, 6214–6218. doi:10.1021/acs.jpclett.0c01406

Kojima, K., Shibukawa, A., and Sudo, Y. (2020b). The Unlimited Potential of Microbial Rhodopsins as Optical Tools. *Biochemistry* 59, 218–229. doi:10.1021/acs.biochem.9b00768

Kojima, K., Ueta, T., Noji, T., Saito, K., Kanehara, K., Yoshizawa, S., et al. (2020d). Vectorial Proton Transport Mechanism of RxR, a Phylogenetically Distinct and Thermally Stable Microbial Rhodopsin. *Sci. Rep.* 10, 282. doi:10.1038/s41598-019-57122-2

Konno, M., Inoue, K., and Kandori, H. (2021). Ion Transport Activity Assay for Microbial Rhodopsin Expressed in *Escherichia col*i Cells. *Bio-Protocol* 11, 4115. doi:10.21769/bioprotoc.4115

Kopf, A. H., Dörr, J. M., Koorengevel, M. C., Antoniciello, F., Jahn, H., and Killian, J. A. (2020). Factors Influencing the Solubilization of Membrane Proteins from *Escherichia coli* Membranes by Styrene-Maleic Acid Copolymers. *Biochimica Biophysica Acta-Biomembranes* 1862, 183125. doi:10.1016/j.bbamem.2019.183125

Kovalev, K., Astashkin, R., Gushchin, I., Orekhov, P., Volkov, D., Zinovev, E. V., et al. (2020a). Molecular Mechanism of Light-Driven Sodium Pumping. *Nat. Commun.* 11, 21371. doi:10.1038/s41467-020-16032-y

Kovalev, K., Polovinkin, V., Gushchin, I., Alekseev, A., Shevchenko, V., Borshchevskiy, V., et al. (2019). Structure and Mechanisms of Sodium-Pumping KR2 Rhodopsin. *Sci. Adv.* 5, eaav2671. doi:10.1126/sciadv.aav2671

Kovalev, K., Volkov, D., Astashkin, R., Alekseev, A., Gushchin, I., Haro-Moreno, J. M., et al. (2020b). High-resolution Structural Insights into the Heliorhodopsin Family. *Proc. Natl. Acad. Sci. U. S. A.* 117, 4131–4141. doi:10.1073/pnas.1915888117

Koyanagi, M., and Terakita, A. (2014). Diversity of Animal Opsin-Based Pigments and Their Optogenetic Potential. *Biochimica Biophysica Acta-Bioenergetics* 1837, 710–716. doi:10.1016/j.bbabio.2013.09.003

Kraack, J. P., Buckup, T., and Motzkus, M. (2011). Vibrational Analysis of Excited and Ground Electronic States of All-*Trans* Retinal Protonated Schiff-Bases. *Phys. Chem. Chem. Phys.* 13, 21402–21410. doi:10.1039/c1cp22245g

Krah, M., Marwan, W., Verméglio, A., and Oesterhelt, D. (1994). Phototaxis of *Halobacterium Salinarium* Requires a Signalling Complex of Sensory Rhodopsin I and its Methyl-Accepting Transducer HtrI. *EMBO J.* 13, 2150–2155. doi:10.1002/j.1460-2075.1994.tb06491.x

Kralj, J. M., Douglass, A. D., Hochbaum, D. R., Maclaurin, D., and Cohen, A. E. (2012). Optical Recording of Action Potentials in Mammalian Neurons Using a Microbial Rhodopsin. *Nat. Methods* 9, 90–95. doi:10.1038/nmeth.1782

Kralj, J. M., Hochbaum, D. R., Douglass, A. D., and Cohen, A. E. (2011). Electrical Spiking in *Escherichia coli* Probed with a Fluorescent Voltage-Indicating Protein. *Science* 333, 345–348. doi:10.1126/science.1204763

Krebs, A., Edwards, P. C., Villa, C., Li, J.-D., and Schertler, G. F. X. (2003). The Three-Dimensional Structure of Bovine Rhodopsin Determined by Electron Cryomicroscopy. *J. Biol. Chem.* 278, 50217–50225. doi:10.1074/jbc.M307995200

Krebs, M. P., Mollaaghababa, R., and Khorana, H. G. (1993). Gene Replacement in *Halobacterium Halobium* and Expression of Bacteriorhodopsin Mutants. *Proc. Nat. Acad. Sci. U. S. A.* 90, 1987–1991. doi:10.1073/pnas.90.5.1987

Krol, A., Lopez-Huerta, V. G., Corey, T. E. C., Deisseroth, K., Ting, J. T., and Feng, G. P. (2019). Two eARCHT3.0 Lines for Optogenetic Silencing of Dopaminergic and Serotonergic Neurons. *Front. Neural Circuits* 13, 4. doi:10.3389/fncir.2019.00004

Kropf, A. (1982). A New Detergent for the Study of Visual Pigments. *Vis. Res.* 22, 495–497. doi:10.1016/0042-6989(82)90199-7

Kropf, A. (1975). The Nature of the Chromophore-Protein Interaction in Visual Pigments as Studied by Visual Pigment Analogues. *Abstr. Annu. Meet. Biophysical Soc. Jpn.* 31, 281–282.

Kropf, A., Whittenberger, B. P., Goff, S. P., and Waggoner, A. S. (1973). The Spectral Properties of Some Visual Pigment Analogs. *Exp. Eye Res.* 17, 591–606. doi:10.1016/0014-4835(73)90088-2

Kuang, L. J., Fernandes, D. A., O'halloran, M., Zheng, W., Jiang, Y. J., Ladizhansky, V., et al. (2014). Frozen" Block Copolymer Nanomembranes with Light-Driven Proton Pumping Performance. *ACS Nano* 8, 537–545. doi:10.1021/nn4059852

Kühn, H. (1984). Interactions between Photoexcited Rhodopsin and Light-Activated Enzymes in Rods. *Prog. Retin. Res.* 3, 123–156.

Kuhne, J., Eisenhauer, K., Ritter, E., Hegemann, P., Gerwert, K., and Bartl, F. J. (2015). Early Formation of the Ion-Conducting Pore in Channelrhodopsin-2. *Angew. Chemie-International Ed.* 54, 4953–4957. doi:10.1002/anie.201410180

Kuhne, J., Vierock, J., Tennigkeit, S. A., Dreier, M.-A., Wietek, J., Petersen, D., et al. (2019). Unifying Photocycle Model for Light Adaptation and Temporal Evolution of Cation Conductance in Channelrhodopsin-2. *Proc. Natl. Acad. Sci. U. S. A.* 116, 9380–9389. doi:10.1073/pnas.1818707116

Kulkarni, R. U., and Miller, E. W. (2017). Voltage Imaging: Pitfalls and Potential. *Biochemistry* 56, 5171–5177. doi:10.1021/acs.biochem.7b00490

Kumbalasiri, T., and Provencio, I. (2005). Melanopsin and Other Novel Mammalian Opsins. *Exp. Eye Res.* 81, 368–375. doi:10.1016/j.exer.2005.05.004

Kushibiki, T., Okawa, S., Hirasawa, T., and Ishihara, M. (2014). Optogenetics: Novel Tools for Controlling Mammalian Cell Functions with Light. *Int. J. Photoenergy* 2014, 895039. doi:10.1155/2014/895039

Kusnetzow, A. K., Altenbach, C., and Hubbell, W. L. (2006). Conformational States and Dynamics of Rhodopsin in Micelles and Bilayers. *Biochemistry-USA* 45, 5538–5550. doi:10.1021/bi060101v

Kusnetzow, A. K., Dukkipati, A., Babu, K. R., Ramos, L., Knox, B. E., and Birge, R. R. (2004). Vertebrate Ultraviolet Visual Pigments: Protonation of the Retinylidene Schiff Base and a Counterion Switch during Photoactivation. *Proc. Natl. Acad. Sci. U. S. A.* 101, 941–946. doi:10.1073/pnas.0305206101

Kusnetzow, A. K., Dukkipati, A., Babu, K. R., Singh, D., Vought, B. W., Knox, B. E., et al. (2001). The Photobleaching Sequence of a Short-Wavelength Visual Pigment. *Biochemistry* 40, 7832–7844. doi:10.1021/bi010387y

Kwon, S.-K., Jun, S.-H., and Kim, J. F. (2020). Omega Rhodopsins: A Versatile Class of Microbial Rhodopsins. *J. Microbiol. Biotechnol.* 30, 633–641. doi:10.4014/jmb.1912.12010

Kwon, Y. M., Patra, A. K., Chiura, H. X., and Kim, S.-J. (2019). Production of Extracellular Vesicles with Light-Induced Proton Pump Activity by Proteorhodopsin-Containing Marine Bacteria. *MicrobiologyOpen* 8, e808. doi:10.1002/mbo3.808

Ladizhansky, V. (2017). "Advances in Solid-State NMR Studies of Microbial Rhodopsins," in *Modern Magnetic Resonance*. Editor G. A. Webb (New York City: Springer International Publishing AG), 1–19. doi:10.1007/978-3-319-28275-6_65-1

Lamarche, L. B., Kumar, R. P., Trieu, M. M., Devine, E. L., Cohen-Abeles, L. E., Theobald, D. L., et al. (2017). Purification and Characterization of RhoPDE, a Retinylidene/Phosphodiesterase Fusion Protein and Potential Optogenetic Tool from the Choanoflagellate *Salpingoeca Rosetta*. *Biochemistry* 56, 5812–5822. doi:10.1021/acs.biochem.7b00519

Lan, Y., Wang, Y., and Lu, H. (2020). Opsin 3 Is a Key Regulator of Ultraviolet A-Induced Photoageing in Human Dermal Fibroblast Cells. *Br. J. Dermatology* 182, 1228–1244. doi:10.1111/bjd.18410

Lang-Hinrichs, C., Queck, I., Büldt, G., Stahl, U., and Hildebrandt, V. (1994). The Archaebacterial Membrane Protein Bacterio-Opsin Is Expressed and N-Terminally Processed in the Yeast *Saccharomyces cerevisiae*. *Mol. Gen. Genet.* 244, 183–188. doi:10.1007/bf00283521

Lanyi, J. K. (2004). Bacteriorhodopsin. *Annu. Rev. Physiology* 66, 665–688. doi:10.1146/annurev.physiol.66.032102.150049

Larkum, A. W. D., Ritchie, R. J., and Raven, J. A. (2018). Living off the Sun: Chlorophylls, Bacteriochlorophylls and Rhodopsins. *Photosynthetica* 56, 11–43. doi:10.1007/s11099-018-0792-x

Lavington, S., and Watts, A. (2020). Lipid Nanoparticle Technologies for the Study of G Protein-Coupled Receptors in Lipid Environments. *Biophys. Rev.* 12, 1287–1302. doi:10.1007/s12551-020-00775-5

Lee, H. J., Huang, K.-C., Mei, G. X., Mamaeva, N., DeGrip, W. J., Rothschild, K. J., et al. (2019). "Pre-resonance Stimulated Raman Scattering Spectroscopy and Imaging of Membrane Potential Using Near-Infrared Rhodopsins," in *Multiphoton Microscopy in the Biomedical Sciences*. Editors M. Periasamy, P. T. C. So, and K. König (Bellingham, U.S.A: SPIE), 81. doi:10.1117/12.2506833

Lee, S., Ghosh, S., Jana, S., Robertson, N., Tate, C. G., and Vaidehi, N. (2020). How Do Branched Detergents Stabilize GPCRs in Micelles? *Biochemistry* 59, 2125–2134. doi:10.1021/acs.biochem.0c00183

Lehtinen, K., Nokia, M. S., and Takala, H. (2022). Red Light Optogenetics in Neuroscience. *Front. Cell. Neurosci.* 15, 778900. doi:10.3389/fncel.2021.778900

Lesca, E., Panneels, V., and Schertler, G. F. X. (2018). The Role of Water Molecules in Phototransduction of Retinal Proteins and G Protein-Coupled Receptors. *Faraday Discuss.* 207, 27–37. doi:10.1039/c7fd00207f

Leung, N. Y., and Montell, C. (2017). Unconventional Roles of Opsins. *Annu. Rev. Cell. Dev. Biol.* 33, 241–264. doi:10.1146/annurev-cellbio-100616-060432

Leung, N. Y., Thakur, D. P., Gurav, A. S., Kim, S. H., Di Pizio, A., Niv, M. Y., et al. (2020). Functions of Opsins in Drosophila Taste. *Curr. Biol.* 30, 1367–1379. doi:10.1016/j.cub.2020.01.068

Lewis, J. W., Hug, S. J., Wallace-Williams, S. E., and Kliger, D. S. (1990). Direct Evidence for an Equilibrium between Early Photolysis Intermediates of Rhodopsin. *J. Am. Chem. Soc.* 112, 6711–6712. doi:10.1021/ja00174a040

Lewis, J. W., Van Kuijk, F. J. G. M., Carruthers, J. A., and Kliger, D. S. (1997). Metarhodopsin III Formation and Decay Kinetics: Comparison of Bovine and Human Rhodopsin. *Vis. Res.* 37, 1–8. doi:10.1016/s0042-6989(96)00138-1

Li, H., Huang, C.-Y., Govorunova, E. G., Schafer, C. T., Sineshchekov, O. A., Wang, M. T., et al. (2019). Crystal Structure of a Natural Light-Gated Anion Channelrhodopsin. *eLife* 8, e41741. doi:10.7554/eLife.41741

Li, H., Huang, C.-Y., Govorunova, E. G., Sineshchekov, O. A., Yi, A., Rothschild, K. J., et al. (2021). The Crystal Structure of Bromide-Bound *Gt*ACR1 Reveals a Pre-activated State in the Transmembrane Anion Tunnel. *Elife* 10, 65903. doi:10.7554/elife.65903

Li, J., Edwards, P. C., Burghammer, M., Villa, C., and Schertler, G. F. X. (2004). Structure of Bovine Rhodopsin in a Trigonal Crystal Form. *J. Mol. Biol.* 343, 1409–1438. doi:10.1016/j.jmb.2004.08.090

Li, L. Z., Lu, L. H., Ren, Y., Tang, G., Zhao, Y., Cai, X., et al. (2022). Colocalized, Bidirectional Optogenetic Modulations in Freely Behaving Mice with a Wireless Dual-Color Optoelectronic Probe. *Nat. Commun.* 13, 839. doi:10.1038/s41467-022-28539-7

Liang, J., Steinberg, G., Livnah, N., Sheves, M., Ebrey, T. G., and Tsuda, M. (1994). The pK_a of the Protonated Schiff Bases of Gecko Cone and octopus Visual Pigments. *Biophys. J.* 67, 848–854. doi:10.1016/s0006-3495(94)80544-2

Lichty, J. J., Malecki, J. L., Agnew, H. D., Michelson-Horowitz, D. J., and Tan, S. (2005). Comparison of Affinity Tags for Protein Purification. *Protein Expr. Purif.* 41, 98–105. doi:10.1016/j.pep.2005.01.019

Liebel, M., Schnedermann, C., Bassolino, G., Taylor, G., Watts, A., and Kukura, P. (2014). Direct Observation of the Coherent Nuclear Response after the Absorption of a Photon. *Phys. Rev. Lett.* 112, 238301. doi:10.1103/PhysRevLett.112.238301

Liebert, A., Pang, V., Bicknell, B., Mclachlan, C., Mitrofanis, J., and Kiat, H. (2021). A Perspective on the Potential of Opsins as an Integral Mechanism of Photobiomodulation: It's Not Just the Eyes. *Photobiomodul Photomed. Laser Surg.* 40, 123–135. doi:10.1089/photob.2021.0106

Lin, J. Y., Knutsen, P. M., Muller, A., Kleinfeld, D., and Tsien, R. Y. (2013). ReaChR: a Red-Shifted Variant of Channelrhodopsin Enables Deep Transcranial Optogenetic Excitation. *Nat. Neurosci.* 16, 1499–1508. doi:10.1038/nn.3502

Lin, S. W., Kochendoerfer, G. G., Carroll, H. S., Wang, D., Mathies, R. A., and Sakmar, T. P. (1998). Mechanisms of Spectral Tuning in Blue Cone Visual Pigments - Visible and Raman Spectroscopy of Blue-Shifted Rhodopsin Mutants. *J. Biol. Chem.* 273, 24583–24591. doi:10.1074/jbc.273.38.24583

Lin, S. W., Sakmar, T. P., Franke, R. R., Khorana, H. G., and Mathies, R. A. (1992). Resonance Raman Microprobe Spectroscopy of Rhodopsin Mutants: Effect of Substitutions in the Third Transmembrane Helix. *Biochemistry-USA* 31, 5105–5111. doi:10.1021/bi00137a003

Lincereghino, J., and Cregg, J. M. (2000). Heterologous Protein Expression in the Methylotrophic Yeast *Pichia pastoris*. *FEMS Microbiol. Rev.* 24, 45–66. doi:10.1111/j.1574-6976.2000.tb00532.x

Lindner, M., Gilhooley, M. J., Peirson, S. N., Hughes, S., and Hankins, M. W. (2021). The Functional Characteristics of Optogenetic Gene Therapy for Vision Restoration. *Cell. Mol. Life Sci.* 78, 1597–1613. doi:10.1007/s00018-020-03597-6

Lips, D., Schuurmans, J. M., Branco Dos Santos, F., and Hellingwerf, K. J. (2018). Many Ways towards 'solar Fuel': Quantitative Analysis of the Most Promising Strategies and the Main Challenges during Scale-Up. *Energy & Environ. Sci.* 11, 10–22. doi:10.1039/c7ee02212c

Liu, R. S. H., and Asato, A. E. (1990). "The Binding Site of Opsin Based on Analog Studies with Isomeric, Fluorinated, Alkylated, and Other Modified Retinals," in *Chemistry and Biology of Synthetic Retinoids*. Editors M. I. Dawson and W. H. Okamura (Boca Raton, Fl, U.S.A. CRC Press), 52–75.

Liu, R. S. H., and Asato, A. E. (2003). Tuning the Color and Excited State Properties of the Azulenic Chromophore: NIR Absorbing Pigments and Materials. *J. Photochem. Photobiol. C Photochem. Rev.* 4, 179–194. doi:10.1016/j.jphotochemrev.2003.09.001

Liu, R. S. H., and Liu, J. (2011). Fluorinated Retinoids and Carotenoids. *J. Nat. Prod.* 74, 512–517. doi:10.1021/np1006394

Liu, R. S. H., Matsumoto, H., Kini, A., Asato, A. E., Denny, M., Kropf, A., et al. (1984). Seven New Hindered Isomeric Rhodopsins - A Reexamination of the Stereospecificity of the Binding-Site of Bovine Opsin. *Tetrahedron* 40, 473–482. doi:10.1016/s0040-4020(01)88435-0

Liu, Y., Cui, Y. M., Chi, H., Xia, Y., Liu, H. N., Rossiter, S. J., et al. (2019). Scotopic Rod Vision in Tetrapods Arose from Multiple Early Adaptive Shifts in the Rate of Retinal Release. *Proc. Natl. Acad. Sci. U. S. A.* 116, 12627–12628. doi:10.1073/pnas.1900481116

Liu, Y. Z., Zhang, W., Du, X. X., Liu, Y. X., Qu, J. B., Liu, X. B., et al. (2021). Genome-wide Identification of Nonvisual Opsin Family Reveals Amplification of RPE-retinal G Protein Receptor Gene (RGR) and Offers Novel Insights into Functions of RGR(s) in *Paralichthys olivaceus* (Paralichthyidae, Teleostei). *J. Exp. Zoology Part B Mol. Dev. Evol.* 334, 25–36. doi:10.1002/jez.b.22914

Locket, N. A. (1977). "Adaptations to the Deep-Sea Environment," in *The Visual System in Vertebrates*. Editor F. Crescitelli (Berlin: Springer-Verlag), 67–192.

López, S., Rodriguez, V., Montenegro, J., Saá, C., Alvarez, R., López, C. S., et al. (2005). Synthesis of *N*-Heteroaryl Retinals and Their Artificial Bacteriorhodopsins. *ChemBioChem* 6, 2078–2087. doi:10.1002/cbic.200500148

Lórenz-Fonfría, V. A., Bamann, C., Resler, T., Schlesinger, R., Bamberg, E., and Heberle, J. (2015a). Temporal Evolution of Helix Hydration in a Light-Gated Ion Channel Correlates with Ion Conductance. *Proc. Natl. Acad. Sci. U. S. A.* 112, E5796–E5804. doi:10.1073/pnas.1511462112

Lórenz-Fonfría, V. A., and Kandori, H. (2009). Spectroscopic and Kinetic Evidence on How Bacteriorhodopsin Accomplishes Vectorial Proton Transport under Functional Conditions. *J. Am. Chem. Soc.* 131, 5891–5901. doi:10.1021/ja900334c

Lórenz-Fonfría, V. A., Schultz, B.-J., Resler, T., Schlesinger, R., Bamann, C., Bamberg, E., et al. (2015b). Pre-gating Conformational Changes in the ChETA Variant of Channelrhodopsin-2 Monitored by Nanosecond IR Spectroscopy. *J. Am. Chem. Soc.* 137, 1850–1861. doi:10.1021/ja5108595

Lórenz-Fonfría, V. A., Yagi, K., Ito, S., and Kandori, H. (2021). Retinal Vibrations in Bacteriorhodopsin Are Mechanically Harmonic but Electrically Anharmonic: Evidence from Overtone and Combination Bands. *Front. Mol. Biosci.* 8, 749261. doi:10.3389/fmolb.2021.749261

Lu, Y., Zhou, X. E., Gao, X., Wang, N., Xia, R. X., Xu, Z. M., et al. (2020). Crystal Structure of Heliorhodopsin 48C12. *Cell. Res.* 30, 88–90. doi:10.1038/s41422-019-0266-0

Luck, M., Velázquez Escobar, F., Glass, K., Sabotke, M.-I., Hagedorn, R., Corellou, F., et al. (2019). Photoreactions of the Histidine Kinase Rhodopsin Ot-HKR from the Marine Picoalga *Ostreococcus Tauri*. *Biochemistry* 58, 1878–1891. doi:10.1021/acs.biochem.8b01200

Luecke, H., Schobert, B., Richter, H.-T., Cartailler, J.-P., and Lanyi, J. K. (1999). Structure of Bacteriorhodopsin at 1.55 Å Resolution. *J. Mol. Biol.* 291, 899–911. doi:10.1006/jmbi.1999.3027

Luecke, H., Schobert, B., Stagno, J., Imasheva, E. S., Wang, J. M., Balashov, S. P., et al. (2008). Crystallographic Structure of Xanthorhodopsin, the Light-Driven Proton Pump with a Dual Chromophore. *Proc. Natl. Acad. Sci. U. S. A.* 105, 16561–16565. doi:10.1073/pnas.0807162105

Lugtenburg, J., Creemers, A. F. L., Verhoeven, M. A., Van Wijk, A. a. C., Verdegem, P. J. E., Monnee, M. C. F., et al. (1999). Synthesis of ^{13}C-Labeled Carotenoids and Retinoids. *Pure Appl. Chem.* 71, 2245–2251. doi:10.1351/pac199971122245

Lugtenburg, J., Mathies, R. A., Griffin, R. G., and Herzfeld, J. (1988). Structure and Function of Rhodopsins from Solid State NMR and Resonance Raman Spectroscopy of Isotopic Retinal Derivatives. *Trends biochem. Sci.* 13, 388–393. doi:10.1016/0968-0004(88)90181-8

Luk, H. L., Bhattacharyya, N., Montisci, F., Morrow, J. M., Melaccio, F., Wada, A., et al. (2016). Modulation of Thermal Noise and Spectral Sensitivity in Lake Baikal Cottoid Fish Rhodopsins. *Sci. Rep.* 6, 38425. doi:10.1038/srep38425

Lutnaes, B. F., Kildahl-Andersen, G., Krane, J., and Liaaen-Jensen, S. (2004). Delocalized Carotenoid Cations in Relation to the Soliton Model. *J. Am. Chem. Soc.* 126, 8981–8990. doi:10.1021/ja0492541

Ma, J.-X., Kono, M., Xu, L., Das, J., Ryan, J. C., Hazard, E. S., Iii, et al. (2001). Salamander UV Cone Pigment: Sequence, Expression, and Spectral Properties. *Vis. Neurosci.* 18, 393–399. doi:10.1017/s0952523801183057

Maclaurin, D., Venkatachalam, V., Lee, H., and Cohen, A. E. (2013). Mechanism of Voltage-Sensitive Fluorescence in a Microbial Rhodopsin. *Proc. Natl. Acad. Sci. U. S. A.* 110, 5939–5944. doi:10.1073/pnas.1215595110

Maeda, A., Sasaki, J., Pfefferle, J. M., Shichida, Y., and Yoshizawa, T. (1991). Fourier Transform Infrared Spectral Studies on the Schiff Base Mode of All-Trans Bacteriorhodopsin and its Photointermediates-K and Photointermediates-L. *Photochem. Photobiol.* 54, 911–921. doi:10.1111/j.1751-1097.1991.tb02111.x

Maeda, T., Imanishi, Y., and Palczewski, K. (2003). Rhodopsin Phosphorylation: 30 Years Later. *Prog. Retin. Eye Res.* 22, 417–434. doi:10.1016/s1350-9462(03)00017-x

Mahn, M., Saraf-Sinik, I., Patil, P., Pulin, M., Bitton, E., Karalis, N., et al. (2021). Efficient Optogenetic Silencing of Neurotransmitter Release with a Mosquito Rhodopsin. *Neuron* 109, 1621–1635. doi:10.1016/j.neuron.2021.03.013

Malmerberg, E., Bovee-Geurts, P. H. M., Katona, G., Deupi, X., Arnlund, D., Wickstrand, C., et al. (2015). Conformational Activation of Visual Rhodopsin in Native Disc Membranes. *Sci. Signal.* 8, ra26. doi:10.1126/scisignal.2005646

Maly, T., Debelouchina, G. T., Bajaj, V. S., Hu, K.-N., Joo, C.-G., Mak-Jurkauskas, M. L., et al. (2008). Dynamic Nuclear Polarization at High Magnetic Fields. *J. Chem. Phys.* 128, 052211. doi:10.1063/1.2833582

Mao, J. F., Aladin, V., Jin, X. S., Leeder, A. J., Brown, L. J., Brown, R. C. D., et al. (2019). Exploring Protein Structures by DNP-Enhanced Methyl Solid-State NMR Spectroscopy. *J. Am. Chem. Soc.* 141, 19888–19901. doi:10.1021/jacs.9b11195

Mao, J. F., Do, N.-N., Scholz, F., Reggie, L., Mehler, M., Lakatos, A., et al. (2014). Structural Basis of the Green-Blue Color Switching in Proteorhodopsin as Determined by NMR Spectroscopy. *J. Am. Chem. Soc.* 136, 17578–17590. doi:10.1021/ja5097946

Marrero, H., and Rothschild, K. J. (1987). Conformational Changes in Bacteriorhodopsin Studied by Infrared Attenuated Total Reflection. *Biophys. J.* 52, 629–635. doi:10.1016/s0006-3495(87)83254-x

Marshel, J. H., Kim, Y. S., Machado, T. A., Quirin, S., Benson, B., Kadmon, J., et al. (2019). Cortical Layer-specific Critical Dynamics Triggering Perception. *Science* 365, eaaw5202. doi:10.1126/science.aaw5202

Martinez, A., Bradley, A. S., Waldbauer, J. R., Summons, R. E., and Delong, E. F. (2007). Proteorhodopsin Photosystem Gene Expression Enables Photophosphorylation in a Heterologous Host. *Proc. Natl. Acad. Sci. U. S. A.* 104, 5590–5595. doi:10.1073/pnas.0611470104

Masuda, S., Morita, E. H., Tasumi, M., Iwasa, T., and Tsuda, M. (1993). Infrared Studies of octopus Rhodopsin - Existence of a Long- Lived Intermediate and the States of the Carboxylic Group of Asp- 81 in Rhodopsin and its Photoproducts. *FEBS Lett.* 317, 223–227. doi:10.1016/0014-5793(93)81280-d

Matarèse, B. F. E., Feyen, P. L. C., De Mello, J. C., and Benfenati, F. (2019). Sub-millisecond Control of Neuronal Firing by Organic Light-Emitting Diodes. *Front. Bioeng. Biotechnol.* 7, 278. doi:10.3389/fbioe.2019.00278

Mathies, R. A., and Lugtenburg, J. (2000). "The Primary Photoreaction of Rhodopsin," in *Molecular Mechanisms in Visual Transduction*. Editors D. G. Stavenga, W. J. DeGrip, and E. N. PughJr. (Amsterdam, Netherlands: Elsevier Science Pub.), 55–90. doi:10.1016/s1383-8121(00)80005-6

Mathies, R. A., Smith, S. O., and Palings, I. (1987). "Determination of Retinal Chromophore Structure in Rhodopsins," in *Resonance Raman Spectra of Polyenes and Aromatics*. Editor T. G. Spiro (New York: John Wiley & Sons), 59–108.

Matsui, S., Seidou, M., Uchiyama, I., Sekiya, N., Hiraki, K., Yoshihara, K., et al. (1988). 4-Hydroxyretinal, a New Visual Pigment Chromophore Found in the Bioluminescent Squid, *Watasenia Scintillans*. *Biochimica Biophysica Acta* 966, 370–374. doi:10.1016/0304-4165(88)90087-6

Mccamant, D. W., Kukura, P., and Mathies, R. A. (2005). Femtosecond Stimulated Raman Study of Excited-State Evolution in Bacteriorhodopsin. *J. Phys. Chem. B* 109, 10449–10457. doi:10.1021/jp050095x

Mcdermott, A. E. (2009). Structure and Dynamics of Membrane Proteins by Magic Angle Spinning Solid-State NMR. *Annu. Rev. Biophysics* 38, 385–403. doi:10.1146/annurev.biophys.050708.133719

Mcisaac, R. S., Bedbrook, C. N., and Arnold, F. H. (2015). Recent Advances in Engineering Microbial Rhodopsins for Optogenetics. *Curr. Opin. Struct. Biol.* 33, 8–15. doi:10.1016/j.sbi.2015.05.001

Mcisaac, R. S., Engqvist, M. K. M., Wannier, T., Rosenthal, A. Z., Herwig, L., Flytzanis, N. C., et al. (2014). Directed Evolution of a Far-Red Fluorescent Rhodopsin. *Proc. Natl. Acad. Sci. U. S. A.* 111, 13034–13039. doi:10.1073/pnas.1413987111

Mckee, A. G., Kuntz, C. P., Ortega, J. T., Woods, H., Most, V., Roushar, F. J., et al. (2021). Systematic Profiling of Temperature- and Retinal-Sensitive Rhodopsin Variants by Deep Mutational Scanning. *J. Biol. Chem.* 2021, 101359. doi:10.1016/j.jbc.2021.101359

Mederos, S., Hernández-Vivanco, A., Ramírez-Franco, J., Martín-Fernández, M., Navarrete, M., Yang, A., et al. (2019). Melanopsin for Precise Optogenetic Activation of Astrocyte-Neuron Networks. *Glia* 67, 915–934. doi:10.1002/glia.23580

Mei, G. X., Cavini, C. M., Mamaeva, N., Wang, P., DeGrip, W. J., and Rothschild, K. J. (2021). Optical Switching between Long-Lived States of Opsin Transmembrane Voltage Sensors. *Photochem. Photobiol.* 97, 1001–1015. doi:10.1111/php.13428

Mei, G. X., Mamaeva, N., Ganapathy, S., Wang, P., DeGrip, W. J., and Rothschild, K. J. (2020). Analog Retinal Redshifts Visible Absorption of QuasAr Transmembrane Voltage Sensors into Near-Infrared. *Photochem. Photobiol.* 96, 55–66. doi:10.1111/php.13169

Mei, G. X., Mamaeva, N., Ganapathy, S., Wang, P., DeGrip, W. J., and Rothschild, K. J. (2018). Raman Spectroscopy of a Near Infrared Absorbing Proteorhodopsin: Similarities to the Bacteriorhodopsin O Photointermediate. *Plos One* 13, e0209506. doi:10.1371/journal.pone.0209506

Melaccio, F., Del Carmen Marín, M., Valentini, A., Montisci, F., Rinaldi, S., Cherubini, M., et al. (2016). Toward Automatic Rhodopsin Modeling as a Tool for High-Throughput Computational Photobiology. *J. Chem. Theory Comput.* 12, 6020–6034. doi:10.1021/acs.jctc.6b00367

Melyan, Z., Tarttelin, E. E., Bellingham, J., Lucas, R. J., and Hankins, M. W. (2005). Addition of Human Melanopsin Renders Mammalian Cells Photoresponsive. *Nature* 433, 741–745. doi:10.1038/nature03344

Milosevic, M. M., Jang, J., Mckimm, E. J., Zhu, M. H., and Antic, S. D. (2020). *In Vitro* Testing of Voltage Indicators: Archon1, ArcLightD, ASAP1, ASAP2s, ASAP3b, Bongwoori-Pos6, BeRST1, FlicR1, and Chi-VSFP-Butterfly. *eNeuro* 7, 0060. doi:10.1523/eneuro.0060-20.2020

Mishra, A. K., Gragg, M., Stoneman, M. R., Biener, G., Oliver, J. A., Miszta, P., et al. (2016). Quaternary Structures of Opsin in Live Cells Revealed by FRET Spectrometry. *Biochem. J.* 473, 3819–3836. doi:10.1042/bcj20160422

Misra, R., Eliash, T., Sudo, Y., and Sheves, M. (2019). Retinal-Salinixanthin Interactions in a Thermophilic Rhodopsin. *J. Phys. Chem. B* 123, 10–20. doi:10.1021/acs.jpcb.8b06795

Mitra, A. K., Miercke, L. J. W., Turner, G. J., Shand, R. F., Betlach, M. C., and Stroud, R. M. (1993). Two-dimensional Crystallization of *Escherichia Coli*-Expressed Bacteriorhodopsin and its D96N Variant: High Resolution Structural Studies in Projection. *Biophys. J.* 65, 1295–1306. doi:10.1016/s0006-3495(93)81169-x

Mitsuoka, K., Hirai, T., Murata, K., Miyazawa, A., Kidera, A., Kimura, Y., et al. (1999). The Structure of Bacteriorhodopsin at 3.0 Å Resolution Based on Electron Crystallography: Implication of the Charge Distribution. *J. Mol. Biol.* 286, 861–882. doi:10.1006/jmbi.1998.2529

Miyasaka, T., Koyama, K., and Itoh, I. (1992). Quantum Conversion and Image Detection by a Bacteriorhodopsin- Based Artificial Photoreceptor. *Science* 255, 342–344. doi:10.1126/science.255.5042.342

Molday, R. S. (1989). Monoclonal Antibodies to Rhodopsin and Other Proteins of Rod Outer Segments. *Prog. Retin. Res.* 8, 173–209.

Mollaaghababa, R., Davidson, F. F., Kaiser, C., and Khorana, H. G. (1996). Structure and Function in Rhodopsin: Expression of Functional Mammalian Opsin in *Saccharomyces cerevisiae*. *Proc. Nat. Acad. Sci. U. S. A.* 93, 11482–11486. doi:10.1073/pnas.93.21.11482

Mollevanger, L. C. P. J., Kentgens, A. P. M., Pardoen, J. A., Courtin, J. M. L., Veeman, W. S., Lugtenburg, J., et al. (1987). High-resolution Solid-State ^{13}C-NMR Study of Carbons C-5 and C-12 of the Chromophore of Bovine Rhodopsin: Evidence for a 6-S-*Cis* Conformation with Negative-Charge Perturbation Near C-12. *Eur. J. Biochem.* 163, 9–14. doi:10.1111/j.1432-1033.1987.tb10729.x

Mooney, V. L., Szundi, I., Lewis, J. W., Yan, E. C. Y., and Kliger, D. S. (2012). Schiff Base Protonation Changes in Siberian Hamster Ultraviolet Cone Pigment Photointermediates. *Biochemistry* 51, 2630–2637. doi:10.1021/bi300157r

Moraes, M. N., Monteiro De Assis, L. V., Provencio, I., and De Lauro Castrucci, A. M. (2021). Opsins outside the Eye and the Skin: a More Complex Scenario Than Originally Thought for a Classical Light Sensor. *Cell. Tissue Res.* 385, 519–538. doi:10.1007/s00441-021-03500-0

Morello, J.-P., and Bouvier, M. (1996). Palmitoylation: A Post-translational Modification that Regulates Signalling from G Protein-Coupled Receptors. *Biochem. Cell. Biol.* 74, 449–457. doi:10.1139/o96-049

Mori, A., Yagasaki, J., Homma, M., Reissig, L., and Sudo, Y. (2013). Investigation of the Chromophore Binding Cavity in the 11-*cis* Acceptable Microbial Rhodopsin MR. *Chem. Phys.* 419, 23–29. doi:10.1016/j.chemphys.2012.11.020

Morizumi, T., Ou, W.-L., Van Eps, N., Inoue, K., Kandori, H., Brown, L. S., et al. (2019). X-ray Crystallographic Structure and Oligomerization of *Gloeobacter* Rhodopsin. *Sci. Rep.* 9, 11283–1128111215. doi:10.1038/s41598-019-47445-5

Morton, R. A., and Goodwin, T. W. (1944). Preparation of Retinene *In Vitro*. *Nature* 153, 405–406. doi:10.1038/153405a0

Morton, R. A., and Pitt, G. A. J. (1957). Visual Pigments. *Fortschritte Chem. Org. Naturst.* 14, 244–316. doi:10.1007/978-3-7091-7164-6_6

Mous, S., Gotthard, G., Ehrenberg, D., Sen, S., Weinert, T., Johnson, P. J. M., et al. (2022). Dynamics and Mechanism of a Light-Driven Chloride Pump. *Science* 375, 845. doi:10.1126/science.abj6663

Moutsaki, P., Whitmore, D. H., Bellingham, J., Sakamoto, K., David-Gray, Z. K., and Foster, R. G. (2003). Teleost Multiple Tissue (Tmt) Opsin: A Candidate Photopigment Regulating the Peripheral Clocks of Zebrafish? *Mol. Brain Res.* 112, 135–145. doi:10.1016/s0169-328x(03)00059-7

Mroginski, M.-A., Adam, S., Amoyal, G. S., Barnoy, A., Bondar, A.-N., Borin, V. A., et al. (2021). Frontiers in Multiscale Modeling of Photoreceptor Proteins. *Photochem. Photobiol.* 97, 243–269. doi:10.1111/php.13372

Mukherjee, S., Hegemann, P., and Broser, M. (2019). Enzymerhodopsins: Novel Photoregulated Catalysts for Optogenetics. *Curr. Opin. Struct. Biol.* 57, 118–126. doi:10.1016/j.sbi.2019.02.003

Müller, D. J., Kessler, M., Oesterhelt, F., Möller, C., Oesterhelt, D., and Gaub, H. (2002). Stability of Bacteriorhodopsin α-helices and Loops Analyzed by Single-Molecule Force Spectroscopy. *Biophysical J.* 83, 3578–3588. doi:10.1016/S0006-3495(02)75358-7

Müller, H. (1855). Über die entoptische Wahrnemung der Netzhautgefässe, insbesondere als Beweismittel für die Lichtperception durch die nach hinten gelegene Netzhautelemente. *Verhandlungen. Physikalisch-Medizinische Gesellschaft Würzburg* 5, 411–447.

Müller, M. (1992). Proteolysis in Protein Import and Export: Signal Peptide Processing in Eu- and Prokaryotes. *Experientia* 48, 118–129.

Munro, R. A., De Vlugt, J., Ward, M. E., Kim, S. Y., Lee, K. A., Jung, K.-H., et al. (2019). Biosynthetic Production of Fully Carbon-13 Labeled Retinal in *E. coli* for Structural and Functional Studies of Rhodopsins. *J. Biomol. NMR* 73, 49–58. doi:10.1007/s10858-019-00225-9

Muradin-Szweykowska, M., Peters, A. J. M., and Lugtenburg, J. (1984). The Interaction of Bacterioopsin with 11, 14-bridged Retinals - the Synthesis of 13-demethyl-11, 14-Imino-Retinal, 13-Demethyl-N-Methyl-11, 14-imino, 13-demethyl-11, 14-Thio-Retinal, 13-demethyl-11, 14-Etheno-Retinal, 11, 14-Imino-Retinal and Their Binding with Bacterioopsin. *Recl. Des. Trav. Chim. Des. Pays-Bas* 103, 105–109.

Murakami, M., and Kouyama, T. (2008). Crystal Structure of Squid Rhodopsin. *Nature* 453, 363–U333. doi:10.1038/nature06925

Murakami, M., and Kouyama, T. (2011). Crystallographic Analysis of the Primary Photochemical Reaction of Squid Rhodopsin. *J. Mol. Biol.* 413, 615–627. doi:10.1016/j.jmb.2011.08.044

Murakami, M., and Kouyama, T. (2015). Crystallographic Study of the LUMI Intermediate of Squid Rhodopsin. *PLoS ONE* 10, e0126970. doi:10.1371/journal.pone.0126970

Musilova, Z., Cortesi, F., Matschiner, M., Davies, W. I. L., Patel, J. S., Stieb, S. M., et al. (2019). Vision Using Multiple Distinct Rod Opsins in Deep-Sea Fishes. *Science* 364, 588–592. doi:10.1126/science.aav4632

Musio, C., Santillo, S., Taddei-Ferretti, C., Robles, L. J., Vismara, R., Barsanti, L., et al. (2001). First Identification and Localization of a Visual Pigment in *Hydra* (Cnidaria, Hydrozoa). *J. Comp. Physiology A - Sens. Neural Behav. Physiology* 187, 79–81. doi:10.1007/s003590100180

Mustafi, D., Engel, A. H., and Palczewski, K. (2009). Structure of Cone Photoreceptors. *Prog. Retin. Eye Res.* 28, 289–302. doi:10.1016/j.preteyeres.2009.05.003

Na, Y.-A., Lee, J.-Y., Bang, W.-J., Lee, H. J., Choi, S.-I., Kwon, S.-K., et al. (2015). Growth Retardation of *Escherichia coli* by Artificial Increase of Intracellular ATP. *J. Industrial Microbiol. Biotechnol.* 42, 915–924. doi:10.1007/s10295-015-1609-6

Nagata, T., and Inoue, K. (2022). Rhodopsins at a Glance. *J. Cell. Sci.* 134, jcs258989. doi:10.1242/jcs.258989

Nagata, T., Koyanagi, M., Lucas, R., and Terakita, A. (2018). An All-*Trans*-Retinal-Binding Opsin Peropsin as a Potential Dark-Active and Light-Inactivated G Protein-Coupled Receptor. *Sci. Rep.* 8, 3535. doi:10.1038/s41598-018-21946-1

Nagata, T., Koyanagi, M., Tsukamoto, H., Mutt, E., Schertler, G. F. X., Deupi, X., et al. (2019). The Counterion-Retinylidene Schiff Base Interaction of an Invertebrate Rhodopsin Rearranges upon Light Activation. *Commun. Biol.* 2, 180–181189. doi:10.1038/s42003-019-0409-3

Nagel, G., Szellas, T., Huhn, W., Kateriya, S., Adeishvili, N., Berthold, P., et al. (2003). Channelrhodopsin-2, a Directly Light-Gated Cation-Selective Membrane Channel. *Proc. Natl. Acad. Sci. U. S. A.* 100, 13940–13945. doi:10.1073/pnas.1936192100

Naito, A., Makino, Y., Shigeta, A., and Kawamura, I. (2019). Photoreaction Pathways and Photointermediates of Retinal-Binding Photoreceptor Proteins as Revealed by *In Situ* Photoirradiation Solid-State NMR Spectroscopy. *Biophys. Rev.* 11, 167–181. doi:10.1007/s12551-019-00501-w

Nakagawa, M., Iwasa, T., Kikkawa, S., Takao, T., Shimonishi, Y., and Tsuda, M. (1997). Identification of Two Palmitoyl Groups in octopus Rhodopsin. *Photochem. Photobiol.* 65, 185–189. doi:10.1111/j.1751-1097.1997.tb01897.x

Nakagawa, M., Iwasa, T., Kikkawa, S., Tsuda, M., and Ebrey, T. G. (1999). How Vertebrate and Invertebrate Visual Pigments Differ in Their Mechanism of

Photoactivation. *Proc. Nat. Acad. Sci. U. S. A.* 96, 6189–6192. doi:10.1073/pnas.96.11.6189

Nakajima, Y., Pedraza-González, L., Barneschi, L., Inoue, K., Olivucci, M., and Kandori, H. (2021). Pro219 Is an Electrostatic Color Determinant in the Light-Driven Sodium Pump KR2. *Commun. Biol.* 4, 1185. doi:10.1038/s42003-021-02684-z

Nakajima, Y., Tsukamoto, T., Kumagai, Y., Ogura, Y., Hayashi, T., Song, J., et al. (2018). Presence of a Haloarchaeal Halorhodopsin-like Cl- Pump in Marine Bacteria. *Microbes Environ.* 33, 89–97. doi:10.1264/jsme2.me17197

Nakamichi, H., and Okada, T. (2006). Crystallographic Analysis of Primary Visual Photochemistry. *Angew. Chem. Int. Ed.* 45, 4270–4273. doi:10.1002/anie.200600595

Nakamura, A., Kojima, D., Imai, H., Terakita, A., Okano, T., Shichida, Y., et al. (1999). Chimeric Nature of Pinopsin between Rod and Cone Visual Pigments. *Biochemistry-USA* 38, 14738–14745. doi:10.1021/bi9913496

Nakao, S., Kojima, K., and Sudo, Y. (2021). Microbial Rhodopsins as Multi-Functional Photoreactive Membrane Proteins for Optogenetics. *Biol. Pharm. Bull.* 44, 1357–1363. doi:10.1248/bpb.b21-00544

Nakao, S., Kojima, K., and Sudo, Y. (2022). Phototriggered Apoptotic Cell Death (PTA) Using the Light-Driven Outward Proton Pump Rhodopsin Archaerhodopsin-3. *J. Am. Chem. Soc.* 144, 3771. doi:10.1021/jacs.1c12608

Nakatsuma, A., Yamashita, T., Sasaki, K., Kawanabe, A., Inoue, K., Furutani, Y., et al. (2011). Chimeric Microbial Rhodopsins Containing the Third Cytoplasmic Loop of Bovine Rhodopsin. *Biophysical J.* 100, 1874–1882. doi:10.1016/j.bpj.2011.02.054

Nakayama, T. A., and Khorana, H. G. (1991). Mapping of the Amino Acids in Membrane-Embedded Helices that Interact with the Retinal Chromophore in Bovine Rhodopsin. *J. Biol. Chem.* 266, 4269–4275. doi:10.1016/s0021-9258(20)64317-4

Nango, E., Royant, A., Kubo, M., Nakane, T., Wickstrand, C., Kimura, T., et al. (2016). A Three-Dimensional Movie of Structural Changes in Bacteriorhodopsin. *Science* 354, 1552–1557. doi:10.1126/science.aah3497

Nathans, J. (1987). Molecular Biology of Visual Pigments. *Annu. Rev. Neurosci.* 10, 163–194. doi:10.1146/annurev.ne.10.030187.001115

Nathans, J. (1992). Rhodopsin - Structure, Function, and Genetics. *Biochemistry* 31, 4923–4931. doi:10.1021/bi00136a001

Neitz, M., and Neitz, J. (1998). "Molecular Genetics and the Biological Basis of Color Vision," in *Color Vision - Perspectives from Different Disciplines*. Editors W. Backhaus and R. Kliegl (Berlin, Germany: Walter de Gruyter & Co.), 101–119.

Neumann, K., Verhoefen, M.-K., Weber, I., Glaubitz, C., and Wachtveitl, J. (2008). Initial Reaction Dynamics of Proteorhodopsin Observed by Femtosecond Infrared and Visible Spectroscopy. *Biophysical J.* 94, 4796–4807. doi:10.1529/biophysj.107.125484

Neutze, R., Brändén, G., and Schertler, G. F. X. (2015). Membrane Protein Structural Biology Using X-Ray Free Electron Lasers. *Curr. Opin. Struct. Biol.* 33, 115–125. doi:10.1016/j.sbi.2015.08.006

Nguyen, K.-A., Peuchmaur, M., Magnard, S., Haudecoeur, R., Boyère, C., Mounien, S., et al. (2018). Glycosyl-Substituted Dicarboxylates as Detergents for the Extraction, Overstabilization, and Crystallization of Membrane Proteins. *Angew. Chemie-International Ed.* 57, 2948–2952. doi:10.1002/anie.201713395

Nielsen, M. B. (2009). Model Systems for Understanding Absorption Tuning by Opsin Proteins. *Chem. Soc. Rev.* 38, 913–924. doi:10.1039/b802068j

Nikolaev, D. M., Manathunga, M., Orozco-Gonzalez, Y., Shtyrov, A. A., Omar Guerrero Martínez, Y., Gozem, S., et al. (2021). Free Energy Computation for an Isomerizing Chromophore in a Molecular Cavity via the Average Solvent Electrostatic Configuration Model: Applications in Rhodopsin and Rhodopsin-Mimicking Systems. *J. Chem. Theory Comput.* 17, 5885–5895. doi:10.1021/acs.jctc.1c00221

Nikolaev, D. M., Shtyrov, A. A., Mereshchenko, A. S., Panov, M. S., Tveryanovich, Y. S., and Ryazantsev, M. N. (2020). An Assessment of Water Placement Algorithms in Quantum Mechanics/molecular Mechanics Modeling: the Case of Rhodopsins' First Spectral Absorption Band Maxima. *Phys. Chem. Chem. Phys.* 22, 18114–18123. doi:10.1039/d0cp02638g

Nikolaev, D. M., Shtyrov, A. A., Panov, M. S., Jamal, A., Chakchir, O. B., Kochemirovsky, V. A., et al. (2018). A Comparative Study of Modern Homology Modeling Algorithms for Rhodopsin Structure Prediction. *ACS Omega* 3, 7555–7566. doi:10.1021/acsomega.8b00721

Nogly, P., Weinert, T., James, D., Carbajo, S., Ozerov, D., Furrer, A., et al. (2018). Retinal Isomerization in Bacteriorhodopsin Captured by a Femtosecond X-Ray Laser. *Science* 361, 145–151. doi:10.1126/science.aat0094

Nomura, Y., Ito, S., Teranishi, M., Ono, H., Inoue, K., and Kandori, H. (2018). Low-temperature FTIR Spectroscopy Provides Evidence for Protein-Bound Water Molecules in Eubacterial Light-Driven Ion Pumpsl. *Phys. Chem. Chem. Phys.* 20, 3165–3171. doi:10.1039/c7cp05674e

Nonaka, Y., Hanai, S., Katayama, K., Imai, H., and Kandori, H. (2020). Unique Retinal Binding Pocket of Primate Blue-Sensitive Visual Pigment. *Biochemistry* 59, 2602–2607. doi:10.1021/acs.biochem.0c00394

O'tousa, J. E. (1992). Requirement of N-Linked Glycosylation Site in *Drosophila* Rhodopsin. *Vis. Neurosci.* 8, 385–390. doi:10.1017/s0952523800004910

Oda, K., Nomura, T., Nakane, T., Yamashita, K., Inoue, K., Ito, S., et al. (2021). Time-resolved Serial Femtosecond Crystallography Reveals Early Structural Changes in Channelrhodopsin. *eLife* 10, 62389. doi:10.7554/eLife.62389

Oda, K., Vierock, J., Oishi, S., Rodriguez-Rozada, S., Taniguchi, R., Yamashita, K., et al. (2018). Crystal Structure of the Red Light-Activated Channelrhodopsin Chrimson. *Nat. Commun.* 9, 3949. doi:10.1038/s41467-018-06421-9

Oesterhelt, D., Bräuchle, C., and Hampp, N. (1991). Bacteriorhodopsin - A Biological Material for Information Processing. *Quart. Rev. Biophys.* 24, 425–478. doi:10.1017/s0033583500003863

Oesterhelt, D., and Hess, B. (1973). Reversible Photolysis of Purple Complex in Purple Membrane of *Halobacterium Halobium*. *Eur. J. Biochem.* 37, 316–326. doi:10.1111/j.1432-1033.1973.tb02990.x

Oesterhelt, D., and Stoeckenius, W. (1971). Rhodopsin-like Protein from the Purple Membrane of *Halobacterium Halobium*. *Nat. New Biol.* 233, 149–152. doi:10.1038/newbio233149a0

Oesterhelt, D. (1998). The Structure and Mechanism of the Family of Retinal Proteins from Halophilic Archaea. *Curr. Opin. Struct. Biol.* 8, 489–500. doi:10.1016/s0959-440x(98)80128-0

Ogonah, O., Shuler, M. L., and Granados, R. R. (1991). Protein Production (β-Galactosidase) from a Baculovirus Vector in *Spodoptera Frugiperda* and *Trichpolusia Ni* Cells in Suspension Culture. *Biotechnol. Lett.* 13, 265–270. doi:10.1007/bf01041482

Ogren, J. I., Yi, A., Mamaev, S., Li, H., Lugtenburg, J., DeGrip, W. J., et al. (2015). Comparison of the Structural Changes Occurring during the Primary Phototransition of Two Different Channelrhodopsins from *Chlamydomonas* Algae. *Biochemistry* 54, 377–388. doi:10.1021/bi501243y

Okada, T., Sugihara, M., Bondar, A.-N., Elstner, M., Entel, P., and Buss, V. (2004). The Retinal Conformation and its Environment in Rhodopsin in Light of a New 2.2 Å Crystal Structure. *J. Mol. Biol.* 342, 571–583. doi:10.1016/j.jmb.2004.07.044

Okano, T., Fukada, Y., Artamonov, I. D., and Yoshizawa, T. (1989). Purification of Cone Visual Pigments from Chicken Retina. *Biochemistry-USA* 28, 8848–8856. doi:10.1021/bi00448a025

Okano, T., Yoshizawa, T., and Fukada, Y. (1994). Pinopsin Is a Chicken Pineal Photoreceptive Molecule. *Nature* 372, 94–97. doi:10.1038/372094a0

Okitsu, T., Yamano, Y., Shen, Y. C., Sasaki, T., Kobayashi, Y., Morisawa, S., et al. (2020). Synthesis of One Double Bond-Inserted Retinal Analogs and Their Binding Experiments with Opsins: Preparation of Novel Red-Shifted Channelrhodopsin Variants. *Chem. Pharm. Bull.* 68, 265–272. doi:10.1248/cpb.c19-01005

Olinski, L. E., Lin, E. M., and Oancea, E. (2020). Illuminating Insights into Opsin 3 Function in the Skin. *Adv. Biol. Regul.* 75, 100668. doi:10.1016/j.jbior.2019.100668

Oppermann, J., Fischer, P., Silapetere, A., Liepe, B., Rodriguez-Rozada, S., Flores-Uribe, J., et al. (2019). MerMAIDs: a Family of Metagenomically Discovered Marine Anion-Conducting and Intensely Desensitizing Channelrhodopsins. *Nat. Commun.* 10, 3315. doi:10.1038/s41467-019-11322-6

Oprian, D. D., Asenjo, A. B., Lee, N., and Pelletier, S. L. (1991). Design, Chemical Synthesis, and Expression of Genes for the Three Human Color Vision Pigments. *Biochemistry* 30, 11367–11372. doi:10.1021/bi00112a002

Oprian, D. D., Molday, R. S., Kaufman, R. J., and Khorana, H. G. (1987). Expression of a Synthetic Bovine Rhodopsin Gene in Monkey Kidney Cells. *Proc. Nat. Acad. Sci. U. S. A.* 84, 8874–8878. doi:10.1073/pnas.84.24.8874

Ortega, J. T., and Jastrzebska, B. (2019). The Retinoid and Non-retinoid Ligands of the Rod Visual G Protein-Coupled Receptor. *Int. J. Mol. Sci.* 20, 6218. doi:10.3390/ijms20246218

Ovchinnikov, Y. A., Abdulaev, N. G., and Bogachuk, A. S. (1988a). Two Adjacent Cysteine Residues in the C-Terminal Cytoplasmic Fragment of Bovine Rhodopsin Are Palmitylated. *FEBS Lett.* 230, 1–5. doi:10.1016/0014-5793(88)80628-8

Ovchinnikov, Y. A., Abdulaev, N. G., Zolotarev, A. S., Artamonov, I. D., Bespalov, I. A., Dergachev, A. E., et al. (1988b). Octopus Rhodopsin - Amino Acid Sequence Deduced from C-DNA. *FEBS Lett.* 232, 69–72. doi:10.1016/0014-5793(88)80388-0

Owen, S. F., Liu, M. H., and Kreitzer, A. C. (2019). Thermal Constraints on *In Vivo* Optogenetic Manipulations. *Nat. Neurosci.* 22, 1061–1065. doi:10.1038/s41593-019-0422-3

Ozaki, Y., Kawashima, T., Abe-Yoshizumi, R., and Kandori, H. (2014). A Color-Determining Amino Acid Residue of Proteorhodopsin. *Biochemistry* 53, 6032–6040. doi:10.1021/bi500842w

Palczewski, K. (2012). Chemistry and Biology of Vision. *J. Biol. Chem.* 287, 1612–1619. doi:10.1074/jbc.r111.301150

Palczewski, K. (2006). G Protein-Coupled Receptor Rhodopsin. *Annu. Rev. Biochem.* 75, 743–767. doi:10.1146/annurev.biochem.75.103004.142743

Palczewski, K., Kumasaka, T., Hori, T., Behnke, C. A., Motoshima, H., Fox, B. A., et al. (2000). Crystal Structure of Rhodopsin: A G Protein-Coupled Receptor. *Science* 289, 739–745. doi:10.1126/science.289.5480.739

Palczewski, K., and Orban, T. (2013). From Atomic Structures to Neuronal Functions of G Protein-Coupled Receptors. *Annu. Rev. Neurosci.* 36, 139–164. doi:10.1146/annurev-neuro-062012-170313

Palings, I., Pardoen, J. A., Vandenberg, E. M. M., Winkel, C., Lugtenburg, J., and Mathies, R. A. (1987). Assignment of Fingerprint Vibrations in the Resonance Raman Spectra of Rhodopsin, Isorhodopsin, and Bathorhodopsin: Implications for Chromophore Structure and Environment. *Biochemistry-USA* 26, 2544–2556. doi:10.1021/bi00383a021

Panda, S., Nayak, S. K., Campo, B., Walker, J. R., Hogenesch, J. B., and Jegla, T. (2005). Illumination of the Melanopsin Signaling Pathway. *Science* 307, 600–604. doi:10.1126/science.1105121

Panda, S., Sato, T. K., De Lauro Castrucci, A. M., DeGrip, W. J., Rollag, M. D., Hogenesch, J. B., et al. (2002). Melanopsin (*Opn4*) Is Required for Circadian Phase Shifting under Low Light Conditions. *Science* 298, 2213–2216. doi:10.1126/science.1076848

Pande, C., Pande, A., Yue, K. T., Callender, R. H., Ebrey, T. G., and Tsuda, M. (1987). Resonance Raman Spectroscopy of octopus Rhodopsin and its Photoproducts. *Biochemistry* 26, 4941–4947. doi:10.1021/bi00390a009

Panneels, V., Wu, W. T., Tsai, C.-J., Nogly, P., Rheinberger, J., Jaeger, K., et al. (2015). Time-resolved Structural Studies with Serial Crystallography: A New Light on Retinal Proteins. *Struct. Dyn.* 2, 041718. doi:10.1063/1.4922774

Panzer, S., Zhang, C., Konte, T., Bräuer, C., Diemar, A., Yogendran, P., et al. (2021). Modified Rhodopsins from *Aureobasidium Pullulans* Excel with Very High Proton-Transport Rates. *Front. Mol. Biosci.* 8, 750528. doi:10.3389/fmolb.2021.750528

Park, J. H., Morizumi, T., Li, Y. F., Hong, J. E., Pai, E. F., Hofmann, K. P., et al. (2013). Opsin, a Structural Model for Olfactory Receptors? *Angew. Chemie-International Ed.* 52, 11021–11024. doi:10.1002/anie.201302374

Park, J. H., Scheerer, P., Hofmann, K. P., Choe, H.-W., and Ernst, O. P. (2008). Crystal Structure of the Ligand-free G-Protein-Coupled Receptor Opsin. *Nature* 454, 183–187. doi:10.1038/nature07063

Park, P. S.-H., Sapra, K. T., Jastrzebska, B., Maeda, T., Maeda, A., Pulawski, W., et al. (2009). Modulation of Molecular Interactions and Function by Rhodopsin Palmitylation. *Biochemistry* 48, 4294–4304. doi:10.1021/bi900417b

Passamaneck, Y. J., Furchheim, N., Hejnol, A., Martindale, M. Q., and Lüter, C. (2011). Ciliary Photoreceptors in the Cerebral Eyes of a Protostome Larva. *EvoDevo* 2, 6. doi:10.1186/2041-9139-2-6

Patel, J. S., Brown, C. J., Ytreberg, F. M., and Stenkamp, D. L. (2018). Predicting Peak Spectral Sensitivities of Vertebrate Cone Visual Pigments Using Atomistic Molecular Simulations. *Plos Comput. Biol.* 14, e1005974. doi:10.1371/journal.pcbi.1005974

Patriarchi, T., Shen, A., He, W., Baikoghli, M., Cheng, R. H., Xiang, Y. K., et al. (2018). Nanodelivery of a Functional Membrane Receptor to Manipulate Cellular Phenotype. *Sci. Rep.* 8, 3556. doi:10.1038/s41598-018-21863-3

Pebay-Peyroula, E., Neutze, R., and Landau, E. M. (2000). Lipidic Cubic Phase Crystallization of Bacteriorhodopsin and Cryotrapping of Intermediates: Towards Resolving a Revolving Photocycle. *Biochimica Biophysica Acta-Bioenergetics* 1460, 119–132. doi:10.1016/s0005-2728(00)00134-1

Pediani, J. D., Ward, R. J., Marsango, S., and Milligan, G. (2018). Spatial Intensity Distribution Analysis: Studies of G Protein-Coupled Receptor Oligomerisation. *Trends Pharmacol. Sci.* 39, 175–186. doi:10.1016/j.tips.2017.09.001

Pedraza-González, L., Barneschi, L., Padula, D., De Vico, L., and Olivucci, M. (2022). Evolution of the Automatic Rhodopsin Modeling (ARM) Protocol. *Top. Curr. Chem.* 380 (21), 21–48. doi:10.1007/s41061-022-00374-w

Pedraza-González, L., Del Carmen Marín, M., Jorge, A. N., Ruck, T. D., Yang, X. C., Valentini, A., et al. (2020). Web-ARM: A Web-Based Interface for the Automatic Construction of QM/MM Models of Rhodopsins. *J. Chem. Inf. Model.* 60, 1481–1493.

Peirson, S. N., Bovee-Geurts, P. H. M., Lupi, D., Jeffery, G., DeGrip, W. J., and Foster, R. G. (2004). Expression of the Candidate Circadian Photopigment Melanopsin (*Opn4*) in the Mouse Retinal Pigment Epithelium. *Mol. Brain Res.* 123, 132–135. doi:10.1016/j.molbrainres.2004.01.007

Penzkofer, A., Silapetere, A., and Hegemann, P. (2021). Photocycle Dynamics of the Archaerhodopsin 3 Based Fluorescent Voltage Sensor Archon2. *J. Photochem. Photobiol. B-Biology* 225, 112331. doi:10.1016/j.jphotobiol.2021.112331

Pepe, I. M., and Cugnoli, C. (1992). Retinal Photoisomerase - Role in Invertebrate Visual Cells. *J. Photochem. Photobiol. B-Biol* 13, 5–17. doi:10.1016/1011-1344(92)80035-t

Pérez, A. A., Chen, Q., Pineda Hernández, H., Branco Dos Santos, F., and Hellingwerf, K. J. (2019a). On the Use of Oxygenic Photosynthesis for the Sustainable Production of Commodity Chemicals. *Physiol. Plant.* 166, 413–427. doi:10.1111/ppl.12946

Pérez, J. H., Tolla, E., Dunn, I. C., Meddle, S. L., and Stevenson, T. J. (2019b). A Comparative Perspective on Extra-retinal Photoreception. *Trends Endocrinol. Metabolism* 30, 39–53. doi:10.1016/j.tem.2018.10.005

Pérez-Cerezales, S., Boryshpolets, S., Afanzar, O., Brandis, A., Nevo, R., Kiss, V., et al. (2015). Involvement of Opsins in Mammalian Sperm Thermotaxis. *Sci. Rep.* 5, 16146. doi:10.1038/srep16146

Perrino, A. P., Miyagi, A., and Scheuring, S. (2021). Single Molecule Kinetics of Bacteriorhodopsin by HS-AFM. *Nat. Commun.* 12, 7225. doi:10.1038/s41467-021-27580-2

Peters, L. D. M., Kussmann, J., and Ochsenfeld, C. (2020). Combining Graphics Processing Units, Simplified Time-dependent Density Functional Theory, and Finite-Difference Couplings to Accelerate Nonadiabatic Molecular Dynamics. *J. Phys. Chem. Lett.* 11, 3955–3961. doi:10.1021/acs.jpclett.0c00320

Philosof, A., and Béjà, O. (2013). Bacterial, Archaeal and Viral-like Rhodopsins from the Red Sea. *Environ. Microbiol. Rep.* 5, 475–482. doi:10.1111/1758-2229.12037

Piatkevich, K. D., Bensussen, S., Tseng, H.-A., Shroff, S. N., Lopez-Huerta, V. G., Park, D., et al. (2019). Population Imaging of Neural Activity in Awake Behaving Mice. *Nature* 574, 413–417. doi:10.1038/s41586-019-1641-1

Piatkevich, K. D., Jung, E. E., Straub, C., Linghu, C. G., Park, D., Suk, H.-J., et al. (2018). A Robotic Multidimensional Directed Evolution Approach Applied to Fluorescent Voltage Reporters. *Nat. Chem. Biol.* 14, 352–360. doi:10.1038/s41589-018-0004-9

Piechnick, R., Ritter, E., Hildebrand, P. W., Ernst, O. P., Scheerer, P., Hofmann, K.-P., et al. (2012). Effect of Channel Mutations on the Uptake and Release of the Retinal Ligand in Opsin. *Proc. Natl. Acad. Sci. U. S. A.* 109, 5247–5252. doi:10.1073/pnas.1117268109

Pieri, E., Ledentu, V., Sahlin, M., Dehez, F., Olivucci, M., and Ferré, N. (2019). CpHMD-Then-QM/MM Identification of the Amino Acids Responsible for the Anabaena Sensory Rhodopsin pH-dependent Electronic Absorption Spectrum. *J. Chem. Theory Comput.* 15, 4535–4546. doi:10.1021/acs.jctc.9b00221

Pinhassi, J., Delong, E. F., Béjà, O., González, J. M., and Pedrós-Alió, C. (2016). Marine Bacterial and Archaeal Ion-Pumping Rhodopsins: Genetic Diversity, Physiology, and Ecology. *Microbiol. Mol. Biol. Rev.* 80, 929–953. doi:10.1128/mmbr.00003-16

Plachetzki, D. C., Fong, C. R., and Oakley, T. H. (2012). Cnidocyte Discharge Is Regulated by Light and Opsin-Mediated Phototransduction. *BMC Biol.* 10, 17. doi:10.1186/1741-7007-10-17

Planchard, N., Point, E., Dahmane, T., Giusti, F., Renault, M., Le Bon, C., et al. (2014). The Use of Amphipols for Solution NMR Studies of Membrane

Proteins: Advantages and Constraints as Compared to Other Solubilizing Media. *J. Membr. Biol.* 247, 827–842. doi:10.1007/s00232-014-9654-z

Poddar, H., Heyes, D. J., Schiro, G., Weik, M., Leys, D., and Scrutton, N. S. (2022). A Guide to Time-Resolved Structural Analysis of Light-Activated Proteins. *FEBS J.* 289, 576–595. doi:10.1111/febs.15880

Polito, R., Temperini, M. E., Ritter, E., Puskar, L., Schade, U., Broser, M., et al. (2021). Conformational Changes of a Membrane Protein Determined by Infrared Difference Spectroscopy beyond the Diffraction Limit. *Phys. Rev. Appl.* 16, 014048. doi:10.1103/physrevapplied.16.014048

Polli, D., Rivalta, I., Nenov, A., Weingart, O., Garavelli, M., and Cerullo, G. (2015). Tracking the Primary Photoconversion Events in Rhodopsins by Ultrafast Optical Spectroscopy. *Photochem. Photobiological Sci.* 14, 213–228. doi:10.1039/c4pp00370e

Pope, A. L., Sanchez-Reyes, O. B., South, K., Zaitseva, E., Ziliox, M., Vogel, R., et al. (2020). A Conserved Proline Hinge Mediates Helix Dynamics and Activation of Rhodopsin. *Structure* 28, 1004–1013. doi:10.1016/j.str.2020.05.004

Popot, J.-L., Althoff, T., Bagnard, D., Banères, J.-L., Bazzacco, P., Billon-Denis, E., et al. (2011). Amphipols from A to Z. *Annu. Rev. Biophysics* 40, 379–408. doi:10.1146/annurev-biophys-042910-155219

Popp, A., Wolperdinger, M., Hampp, N., Bräuchle, C., and Oesterhelt, D. (1993). Photochemical Conversion of the O-Intermediate to 9-*Cis*-Retinal- Containing Products in Bacteriorhodopsin Films. *Biophys. J.* 65, 1449–1459. doi:10.1016/s0006-3495(93)81214-1

Porter, M. L., Blasic, J. R., Jr., Bok, M. J., Cameron, E. G., Pringle, T., Cronin, T. W., et al. (2012). Shedding New Light on Opsin Evolution. *Proc. R. Soc. B-Biological Sci.* 279, 3–14. doi:10.1098/rspb.2011.1819

Prakash, M., Murphy, J., St Laurent, R., Friedman, N., Crespo, E. L., Bjorefeldt, A., et al. (2022). Selective Control of Synaptically-Connected Circuit Elements by All-Optical Synapses. *Commun. Biol.* 5, 33. doi:10.1038/s42003-021-02981-7

Provencio, I., Jiang, G., DeGrip, W. J., Hayes, W. P., and Rollag, M. D. (1998). Melanopsin: An Opsin in Melanophores, Brain and Eye. *Proc. Nat. Acad. Sci. U. S. A.* 95, 340–345. doi:10.1073/pnas.95.1.340

Provencio, I., Rodriguez, I. R., Jiang, G., Hayes, W. P., Moreira, E. F., and Rollag, M. D. (2000). A Novel Human Opsin in the Inner Retina. *J. Neurosci.* 20, 600–605. doi:10.1523/jneurosci.20-02-00600.2000

Pushkarev, A., Inoue, K., Larom, S., Flores-Uribe, J., Singh, M., Konno, M., et al. (2018). A Distinct Abundant Group of Microbial Rhodopsins Discovered Using Functional Metagenomics. *Nature* 558, 595–599. doi:10.1038/s41586-018-0225-9

Qiu, X. D., Kumbalasiri, T., Carlson, S. M., Wong, K. Y., Krishna, V. R., Provencio, I., et al. (2005). Induction of Photosensitivity by Heterologous Expression of Melanopsin. *Nature* 433, 745–749. doi:10.1038/nature03345

Radlwimmer, F. B., and Yokoyama, S. (1997). Cloning and Expression of the Red Visual Pigment Gene of Goat (*Capra hircus*). *Gene* 198, 211–215. doi:10.1016/s0378-1119(97)00316-8

Ranganathan, R., and Stevens, C. F. (1995). Arrestin Binding Determines the Rate of Inactivation of the G Protein-Coupled Receptor Rhodopsin *In Vivo*. *Cell.* 81, 841–848. doi:10.1016/0092-8674(95)90004-7

Rath, P., Decaluwé, G. L. J., Bovee-Geurts, P. H. M., DeGrip, W. J., and Rothschild, K. J. (1993). Fourier Transform Infrared Difference Spectroscopy of Rhodopsin Mutants: Light Activation of Rhodopsin Causes Hydrogen-Bonding Changes in Residue Aspartic Acid-83 during Meta II Formation. *Biochemistry* 32, 10277–10282. doi:10.1021/bi00090a001

Rath, P., DeLange, F., DeGrip, W. J., and Rothschild, K. J. (1998). Hydrogen Bonding Changes of Internal Water Molecules in Rhodopsin during Metarhodopsin I and Metarhodopsin II Formation. *Biochem. J.* 329, 713–717. doi:10.1042/bj3290713

Rawlinson, K. A., Lapraz, F., Ballister, E. R., Terasaki, M., Rodgers, J., Mcdowell, R. J., et al. (2019). Extraocular, Rod-like Photoreceptors in a Flatworm Express Xenopsin Photopigment. *eLife* 8, e45465. doi:10.7554/eLife.45465

Reeves, P. J., Kim, J.-M., and Khorana, H. G. (2002). Structure and Function in Rhodopsin: A Tetracycline-Inducible System in Stable Mammalian Cell Lines for High-Level Expression of Opsin Mutants. *Proc. Natl. Acad. Sci. U. S. A.* 99, 13413–13418. doi:10.1073/pnas.212519199

Reeves, P. J., Klein-Seetharaman, J., Getmanova, E. V., Eilers, M., Loewen, M. C., Smith, S. O., et al. (1999). Expression and Purification of Rhodopsin and its Mutants from Stable Mammalian Cell Lines: Application to NMR Studies. *Biochem. Soc. Trans.* 27, 950–955. doi:10.1042/bst0270950

Regan, C. M., DeGrip, W. J., Daemen, F. J. M., and Bonting, S. L. (1978). Sulfhydryl Group Reactivity as a Probe of Transient Protein Conformational Changes during Rhodopsin Photolysis. *Biochim. Biophys. Acta* 537, 145–152. doi:10.1016/0005-2795(78)90609-8

Ren, Z., Ren, P. X., Balusu, R., and Yang, X. J. (2016). Transmembrane Helices Tilt, Bend, Slide, Torque, and Unwind between Functional States of Rhodopsin. *Sci. Rep.* 6, 34129. doi:10.1038/srep34129

Ridge, K. D., and Abdulaev, N. G. (2000). Folding and Assembly of Rhodopsin from Expressed Fragments. *Meth. Enzymol.* 315, 59–70. doi:10.1016/s0076-6879(00)15834-3

Ridge, K. D., Lu, Z. J., Liu, X.-M., and Khorana, H. G. (1995). Structure and Function in Rhodopsin. Separation and Characterization of the Correctly Folded and Misfolded Opsins Produced on Expression of an Opsin Mutant Gene Containing Only the Native Intradiscal Cysteine Codons. *Biochemistry-USA* 34, 3261–3267. doi:10.1021/bi00010a016

Ritchie, T. K., Grinkova, Y. V., Bayburt, T. H., Denisov, I. G., Zolnerciks, J. K., Atkins, W. M., et al. (2009). Reconstitution of Membrane Proteins in Phospholipid Bilayer Nanodiscs. *Methods Enzym.* 464, 211–231. doi:10.1016/s0076-6879(09)64011-8

Ritter, E., Zimmermann, K., Heck, M., Hofmann, K. P., and Bartl, F. J. (2004). Transition of Rhodopsin into the Active Metarhodopsin II State Opens a New Light-Induced Pathway Linked to Schiff Base Isomerization. *J. Biol. Chem.* 279, 48102–48111. doi:10.1074/jbc.m406857200

Rodgers, J., Bano-Otalora, B., Belle, M. D. C., Paul, S., Hughes, R., Wright, P., et al. (2021). Using a Bistable Animal Opsin for Switchable and Scalable Optogenetic Inhibition of Neurons. *Embo Rep.* 22, 51866. doi:10.15252/embr.202051866

Rödig, C., Chizhov, I., Weidlich, O., and Siebert, F. (1999). Time-resolved Step-Scan Fourier Transform Infrared Spectroscopy Reveals Differences between Early and Late M Intermediates of Bacteriorhodopsin. *Biophys. J.* 76, 2687–2701. doi:10.1016/S0006-3495(99)77421-7

Rohrer, B., Goletz, P. W., Znoiko, S. L., Ablonczy, Z., Ma, J.-X., Redmond, T. M., et al. (2003). Correlation of Regenerable Opsin with Rod ERG Signal in *RPE65*(-/-) Mice during Development and Aging. *Investigative Ophthalmol. Vis. Sci.* 44, 310–315. doi:10.1167/iovs.02-0567

Rost, B. R., Schneider-Warme, F., Schmitz, D., and Hegemann, P. (2017). Optogenetic Tools for Subcellular Applications in Neuroscience. *Neuron* 96, 572–603. doi:10.1016/j.neuron.2017.09.047

Rothschild, K. J., Andrew, J. R., DeGrip, W. J., and Stanley, H. E. (1976). Opsin Structure Probed by Raman Spectroscopy of Photoreceptor Membranes. *Science* 191, 1176–1178. doi:10.1126/science.1257742

Rothschild, K. J., Cantore, W. A., and Marrero, H. (1983). Fourier Transform Infrared Difference Spectra of Intermediates in Rhodopsin Bleaching. *Science* 219, 1333–1335. doi:10.1126/science.6828860

Rothschild, K. J., DeGrip, W. J., and Sanches, R. (1980). Fourier Transform Infrared Study of Photoreceptor Membrane. I. Group Assignments Based on Rhodopsin Delipidation and Reconstitution. *Biochim. Biophys. Acta* 596, 338–351. doi:10.1016/0005-2736(80)90121-2

Rothschild, K. J., Gillespie, J., and DeGrip, W. J. (1987). Evidence for Rhodopsin Refolding during the Decay of Meta II. *Biophys. J.* 51, 345–350. doi:10.1016/s0006-3495(87)83341-6

Rothschild, K. J., Marrero, H., Braiman, M. S., and Mathies, R. A. (1984). Primary Photochemistry of Bacteriorhodopsin - Comparison of Fourier-Transform Infrared Difference Spectra with Resonance Raman-Spectra. *Photochem. Photobiol.* 40, 675–679. doi:10.1111/j.1751-1097.1984.tb05359.x

Rothschild, K. J., and Marrero, H. (1982). Infrared Evidence that the Schiff Base of Bacteriorhodopsin Is Protonated: bR570 and K Intermediates. *Proc. Nat. Acad. Sci. U. S. A.* 79, 4045–4049. doi:10.1073/pnas.79.13.4045

Rothschild, K. J. (2016). The Early Development and Application of FTIR Difference Spectroscopy to Membrane Proteins: A Personal Perspective. *Biomed. Spectrosc. Imaging* 5, 231–267. doi:10.3233/bsi-160148

Rothschild, K. J., Zagaeski, M., and Cantore, W. A. (1981). Conformational Changes of Bacteriorhodopsin Detected by Fourier Transform Infrared Difference Spectroscopy. *Biochem. Biophys. Res. Commun.* 103, 483–489. doi:10.1016/0006-291x(81)90478-2

Rousso, I., Gat, Y., Lewis, A., Sheves, M., and Ottolenghi, M. (1998). Effective Light-Induced Hydroxylamine Reactions Occur with C-13 = C-14 Nonisomerizable Bacteriorhodopsin Pigments. *Biophysical J.* 75, 413–417. doi:10.1016/s0006-3495(98)77526-5

Roy, P. P., Kato, Y., Abe-Yoshizumi, R., Pieri, E., Ferré, N., Kandori, H., et al. (2018). Mapping the Ultrafast Vibrational Dynamics of All-*Trans* and 13-*cis* Retinal Isomerization in Anabaena Sensory Rhodopsin. *Phys. Chem. Chem. Phys.* 20, 30159–30173. doi:10.1039/c8cp05469j

Royant, A., Nollert, P., Edman, K., Neutze, R., Landau, E. M., Pebay-Peyroula, E., et al. (2001). X-ray Structure of Sensory Rhodopsin II at 2.1-Å Resolution. *Proc. Natl. Acad. Sci. U. S. A.* 98, 10131–10136. doi:10.1073/pnas.181203898

Rozenberg, A., Inoue, K., Kandori, H., and Béjà, O. (2021). Microbial Rhodopsins: The Last Two Decades. *Annu. Rev. Microbiol.* 75, 427–447. doi:10.1146/annurev-micro-031721-020452

Rupenyan, A., Van Stokkum, I. H. M., Arents, J. C., Van Grondelle, R., Hellingwerf, K. J., and Groot, M. L. (2008). Characterization of the Primary Photochemistry of Proteorhodopsin with Femtosecond Spectroscopy. *Biophysical J.* 94, 4020–4030. doi:10.1529/biophysj.107.121376

Rupenyan, A., Van Stokkum, I. H. M., Arents, J. C., Van Grondelle, R., Hellingwerf, K. J., and Groot, M. L. (2009). Reaction Pathways of Photoexcited Retinal in Proteorhodopsin Studied by Pump-Dump-Probe Spectroscopy. *J. Phys. Chem. B* 113, 16251–16256. doi:10.1021/jp9065289

Ruprecht, J. J., Mielke, T., Vogel, R., Villa, C., and Schertler, G. F. X. (2004). Electron Crystallography Reveals the Structure of Metarhodopsin I. *EMBO J.* 23, 3609–3620. doi:10.1038/sj.emboj.7600374

Ryazantsev, M. N., Nikolaev, D. M., Struts, A. V., and Brown, M. F. (2019). Quantum Mechanical and Molecular Mechanics Modeling of Membrane-Embedded Rhodopsins. *J. Membr. Biol.* 252, 425–449. doi:10.1007/s00232-019-00095-0

Ryba, N. J. P., Hoon, M. A., Findlay, J. B. C., Saibil, H. R., Wilkinson, J. R., Heimburg, T., et al. (1993). Rhodopsin Mobility, Structure, and Lipid-Protein Interaction in Squid Photoreceptor Membranes. *Biochemistry* 32, 3298–3305. doi:10.1021/bi00064a012

Sadaf, A., Cho, H. C., Byrne, B., and Chae, P. S. (2015). Amphipathic Agents for Membrane Protein Study. *Meth. Enzymol.* 557, 57–94. doi:10.1016/bs.mie.2014.12.021

Saint Clair, E. C., Ogren, J. I., Mamaev, S., Kralj, J. M., and Rothschild, K. J. (2012a). Conformational Changes in the Archaerhodopsin-3 Proton Pump: Detection of Conserved Strongly Hydrogen Bonded Water Networks. *J. Biol. Phys.* 38, 153–168. doi:10.1007/s10867-011-9246-4

Saint Clair, E. C., Ogren, J. I., Mamaev, S., Russano, D., Kralj, J. M., and Rothschild, K. J. (2012b). Near-IR Resonance Raman Spectroscopy of Archaerhodopsin 3: Effects of Transmembrane Potential. *J. Phys. Chem. B* 116, 14592–14601. doi:10.1021/jp309996a

Sakai, K., Imamoto, Y., Su, C.-Y., Tsukamoto, H., Yamashita, T., Terakita, A., et al. (2012). Photochemical Nature of Parietopsin. *Biochemistry* 51, 1933–1941. doi:10.1021/bi2018283

Sakai, K., Shichida, Y., Imamoto, Y., and Yamashita, T. (2022). Creation of Photocyclic Vertebrate Rhodopsin by Single Amino Acid Substitution. *eLife* 11, 75979. doi:10.7554/elife.75979

Sakmar, T. P., and Fahmy, K. (1995). Properties and Photoactivity of Rhodopsin Mutants. *Isr. J. Chem.* 35, 325–337. doi:10.1002/ijch.199500034

Sakmar, T. P., Franke, R. R., and Khorana, H. G. (1989). Glutamic Acid-113 Serves as the Retinylidene Schiff Base Counterion in Bovine Rhodopsin. *Proc. Nat. Acad. Sci. U. S. A.* 86, 8309–8313. doi:10.1073/pnas.86.21.8309

Sakmar, T. P., Menon, S. T., Marin, E. P., and Awad, E. S. (2002). Rhodopsin: Insights from Recent Structural Studies. *Annu. Rev. Biophysics Biomol. Struct.* 31, 443–484. doi:10.1146/annurev.biophys.31.082901.134348

Salcedo, E., Huber, A., Henrich, S., Chadwell, L. V., Chou, W. H., Paulsen, R., et al. (1999). Blue- and Green-Absorbing Visual Pigments of *Drosophila*: Ectopic Expression and Physiological Characterization of the R8 Photoreceptor Cell-specific Rh5 and Rh6 Rhodopsins. *J. Neurosci.* 19, 10716–10726. doi:10.1523/jneurosci.19-24-10716.1999

Salom, D., Cao, P. X., Sun, W. Y., Kramp, K., Jastrzebska, B., Jin, H., et al. (2012). Heterologous Expression of Functional G-Protein-Coupled Receptors in *Caenorhabditis elegans*. *FASEB J.* 26, 492–502. doi:10.1096/fj.11-197780

Salom, D., Jin, H., Gerken, T. A., Yu, C., Huang, L., and Palczewski, K. (2019). Human Red and Green Cone Opsins Are O-Glycosylated at an N-Terminal Ser/Thr-Rich Domain Conserved in Vertebrates. *J. Biol. Chem.* 294, 8123–8133. doi:10.1074/jbc.ra118.006835

Salom, D., Wu, N., Sun, W. Y., Dong, Z., Palczewski, K., Jordan, S., et al. (2008). Heterologous Expression and Purification of the Serotonin Type 4 Receptor from Transgenic Mouse Retina. *Biochemistry* 47, 13296–13307. doi:10.1021/bi8018527

Sanchez-Reyes, O. B., Cooke, A. L. G., Tranter, D. B., Rashid, D., Eilers, M., Reeves, P. J., et al. (2017). G Protein-Coupled Receptors Contain Two Conserved Packing Clusters. *Biophysical J.* 112, 2315–2326. doi:10.1016/j.bpj.2017.04.051

Sardet, C., Tardieu, A., and Luzzati, V. (1976). Shape and Size of Bovine Rhodopsin: A Small-Angle X-Ray-Scattering Study of A Rhodopsin-Detergent Complex. *J. Mol. Biol.* 105, 383–407. doi:10.1016/0022-2836(76)90100-5

Sarramegna, V., Muller, I., Milon, A., and Talmont, F. (2006). Recombinant G Protein-Coupled Receptors from Expression to Renaturation: A Challenge towards Structure. *Cell. Mol. Life Sci.* 63, 1149–1164. doi:10.1007/s00018-005-5557-6

Sasaki, J., Brown, L. S., Chon, Y.-S., Kandori, H., Maeda, A., Needleman, R., et al. (1995). Conversion of Bacteriorhodopsin into a Chloride Ion Pump. *Science* 269, 73–75. doi:10.1126/science.7604281

Sasaki, J., Takahashi, H., Furutani, Y., Kandori, H., and Spudich, J. L. (2011). Sensory Rhodopsin-I as a Bidirectional Switch: Opposite Conformational Changes from the Same Photoisomerization. *Biophysical J.* 100, 2178–2183. doi:10.1016/j.bpj.2011.03.026

Sasaki, K., Yamashita, T., Yoshida, K., Inoue, K., Shichida, Y., and Kandori, H. (2014). Chimeric Proton-Pumping Rhodopsins Containing the Cytoplasmic Loop of Bovine Rhodopsin. *PLoS ONE* 9, e91323. doi:10.1371/journal.pone.0091323

Sato, K., Yamashita, T., Imamoto, Y., and Shichida, Y. (2012). Comparative Studies on the Late Bleaching Processes of Four Kinds of Cone Visual Pigments and Rod Visual Pigment. *Biochemistry* 51, 4300–4308. doi:10.1021/bi3000885

Sato, K., Yamashita, T., Kojima, K., Sakai, K., Matsutani, Y., Yanagawa, M., et al. (2018a). Pinopsin Evolved as the Ancestral Dim-Light Visual Opsin in Vertebrates. *Commun. Biol.* 1, 156. doi:10.1038/s42003-018-0164-x

Sato, K., Yamashita, T., Ohuchi, H., and Shichida, Y. (2011). Vertebrate Ancient-Long Opsin Has Molecular Properties Intermediate between Those of Vertebrate and Invertebrate Visual Pigments. *Biochemistry* 50, 10484–10490. doi:10.1021/bi201212z

Sato, K., Yamashita, T., Ohuchi, H., Takeuchi, A., Gotoh, H., Ono, K., et al. (2018b). Opn5L1 Is a Retinal Receptor that Behaves as a Reverse and Self-Regenerating Photoreceptor. *Nat. Commun.* 9, 125. doi:10.1038/s41467-018-03603-3

Schafer, C. T., and Farrens, D. L. (2015). Conformational Selection and Equilibrium Governs the Ability of Retinals to Bind Opsin. *J. Biol. Chem.* 290, 4304–4318. doi:10.1074/jbc.m114.603134

Schäfer, G., Shastri, S., Verhoefen, M.-K., Vogel, V., Glaubitz, C., Wachtveitl, J., et al. (2009). Characterizing the Structure and Photocycle of PR 2D Crystals with CD and FTIR Spectroscopy. *Photochem. Photobiol.* 85, 529–534. doi:10.1111/j.1751-1097.2008.00491.x

Schapiro, I., and Ruhman, S. (2014). Ultrafast Photochemistry of Anabaena Sensory Rhodopsin: Experiment and Theory. *Biochimica Biophysica Acta-Bioenergetics* 1837, 589–597. doi:10.1016/j.bbabio.2013.09.014

Schapiro, I., Ryazantsev, M. N., Frutos, L. M., Ferré, N., Lindh, R., and Olivucci, M. (2011). The Ultrafast Photoisomerizations of Rhodopsin and Bathorhodopsin Are Modulated by Bond Length Alternation and HOOP Driven Electronic Effects. *J. Am. Chem. Soc.* 133, 3354–3364. doi:10.1021/ja1056196

Scheerer, P., Park, J. H., Hildebrand, P. W., Kim, Y. J., Krauß, N., Choe, H.-W., et al. (2008). Crystal Structure of Opsin in its G-Protein-Interacting Conformation. *Nature* 455, 497–502. doi:10.1038/nature07330

Schertler, G. F. X., and Hargrave, P. A. (1995). Projection Structure of Frog Rhodopsin in Two Crystal Forms. *Proc. Nat. Acad. Sci. U. S. A.* 92, 11578–11582. doi:10.1073/pnas.92.25.11578

Schertler, G. F. X. (2005). Structure of Rhodopsin and the Metarhodopsin I Photointermediate. *Curr. Opin. Struct. Biol.* 15, 408–415. doi:10.1016/j.sbi.2005.07.010

Schey, K. L., Papac, D. I., Knapp, D. R., and Crouch, R. K. (1992). Matrix-assisted Laser Desorption Mass Spectrometry of Rhodopsin and Bacteriorhodopsin. *Biophys. J.* 63, 1240–1243. doi:10.1016/s0006-3495(92)81699-5

Schlinkmann, K. M., and Plückthun, A. (2013). Directed Evolution of G-Protein-Coupled Receptors for High Functional Expression and Detergent Stability. *Meth. Enzymol.* 520, 67–97. doi:10.1016/b978-0-12-391861-1.00004-6

Schnedermann, C., Muders, V., Ehrenberg, D., Schlesinger, R., Kukura, P., and Heberle, J. (2016). Vibronic Dynamics of the Ultrafast All-*Trans* to 13-*cis*

Photoisomerization of Retinal in Channelrhodopsin-1. *J. Am. Chem. Soc.* 138, 4757–4762. doi:10.1021/jacs.5b12251

Schnedermann, C., Yang, X., Liebel, M., Spillane, K. M., Lugtenburg, J., Fernández, I., et al. (2018). Evidence for a Vibrational Phase-dependent Isotope Effect on the Photochemistry of Vision. *Nat. Chem.* 10, 449–455. doi:10.1038/s41557-018-0014-y

Schobert, B., Cupp-Vickery, J., Hornak, V., Smith, S. O., and Lanyi, J. K. (2002). Crystallographic Structure of the K Intermediate of Bacteriorhodopsin: Conservation of Free Energy after Photoisomerization of the Retinal. *J. Mol. Biol.* 321, 715–726. doi:10.1016/s0022-2836(02)00681-2

Schoenlein, R. W., Peteanu, L. A., Mathies, R. A., and Shank, C. V. (1991). The First Step in Vision: Femtosecond Isomerization of Rhodopsin. *Science* 254, 412–415. doi:10.1126/science.1925597

Scholz, L., and Neugebauer, J. (2021). Protein Response Effects on Cofactor Excitation Energies from First Principles: Augmenting Subsystem Time-dependent Density-Functional Theory with Many-Body Expansion Techniques. *J. Chem. Theory Comput.* 17, 6105–6121. doi:10.1021/acs.jctc.1c00551

Schreiber, M., Sugihara, M., Okada, T., and Buss, V. (2006). Quantum Mechanical Studies on the Crystallographic Model of Bathorhodopsin. *Angew. Chem. Int. Ed.* 45, 4274–4277. doi:10.1002/anie.200600585

Sekharan, S., Yokoyama, S., and Morokuma, K. (2011). Quantum Mechanical/Molecular Mechanical Structure, Enantioselectivity, and Spectroscopy of Hydroxyretinals and Insights into the Evolution of Color Vision in Small White Butterflies. *J. Phys. Chem. B* 115, 15380–15388. doi:10.1021/jp208107r

Seki, T., Isono, K., Ozaki, K., Tsukahara, Y., Shibata-Katsuta, Y., Ito, M., et al. (1998). The Metabolic Pathway of Visual Pigment Chromophore Formation in *Drosophila melanogaster* - All-*Trans* (3*S*)-3-Hydroxyretinal Is Formed from All-*Trans* Retinal via (3*R*)-3-Hydroxyretinal in the Dark. *Eur. J. Biochem.* 257, 522–527. doi:10.1046/j.1432-1327.1998.2570522.x

Seki, T., and Vogt, K. (1998). Evolutionary Aspects of the Diversity of Visual Pigment Chromophores in the Class Insecta. *Comp. Biochem. Physiol. B* 119, 53–64. doi:10.1016/s0305-0491(97)00322-2

Shao, Y. H., Mei, Y., Sundholm, D., and Kaila, V. R. I. (2020). Benchmarking the Performance of Time-dependent Density Functional Theory Methods on Biochromophores. *J. Chem. Theory Comput.* 16, 587–600. doi:10.1021/acs.jctc.9b00823

Sharma, K., Jäckel, Z., Schneider, A., Paul, O., Diester, I., and Ruther, P. (2021). Multifunctional Optrode for Opsin Delivery, Optical Stimulation, and Electrophysiological Recordings in Freely Moving Rats. *J. neural Eng.* 18, 066013. doi:10.1088/1741-2552/ac3206

Shen, C., Jin, X., Glover, W. J., and He, X. (2021). Accurate Prediction of Absorption Spectral Shifts of Proteorhodopsin Using a Fragment-Based Quantum Mechanical Method. *Molecules* 26, 4486. doi:10.3390/molecules26154486

Shen, W. L., Kwon, Y., Adegbola, A. A., Luo, J. J., Chess, A., and Montell, C. (2011). Function of Rhodopsin in Temperature Discrimination in *Drosophila*. *Science* 331, 1333–1336. doi:10.1126/science.1198904

Shen, Y., Campbell, R. E., Cote, D. C., and Paquet, M. E. (2020). Challenges for Therapeutic Applications of Opsin-Based Optogenetic Tools in Humans. *Front. Neural Circuits* 14, 41. doi:10.3389/fncir.2020.00041

Sheves, M., and Friedman, N. (1986). Influence of External Negative Charges on the Absorption Maxima of Symmetrical Cyanines. A Study with Model Compounds and Artificial Bacteriorhodopsin Pigments. *Angewandte Chemie-International Ed. Engl.* 25, 284–286. doi:10.1002/anie.198602841

Shi, L. C., Ahmed, M. a. M., Zhang, W. R., Whited, G., Brown, L. S., and Ladizhansky, V. (2009). Three-dimensional Solid-State NMR Study of a Seven-Helical Integral Membrane Proton Pump-Structural Insights. *J. Mol. Biol.* 386, 1078–1093. doi:10.1016/j.jmb.2009.01.011

Shibata, M., Inoue, K., Ikeda, K., Konno, M., Singh, M., Kataoka, C., et al. (2018). Oligomeric States of Microbial Rhodopsins Determined by High-Speed Atomic Force Microscopy and Circular Dichroic Spectroscopy. *Sci. Rep.* 8, 8262. doi:10.1038/s41598-018-26606-y

Shichida, Y., Kobayashi, T., Ohtani, H., Yoshizawa, T., and Nagakura, S. (1978). Picosecond Laser Photolysis of Squid Rhodopsin at Room and Low-Temperatures. *Photochem. Photobiol.* 27, 335–341. doi:10.1111/j.1751-1097.1978.tb07609.x

Shichida, Y. (1986). Primary Intermediates of Photobleaching of Rhodopsin. *Photobiochem. Photobiophys.* 13, 287–307.

Shichida, Y. (1990). Ultra-fast Laser Spectroscopy of Visual Pigments. *Photochem. Photobiol.* 52, 1179–1185. doi:10.1111/j.1751-1097.1990.tb08456.x

Shigeta, A., Ito, S., Inoue, K., Okitsu, T., Wada, A., Kandori, H., et al. (2017). Solid-State Nuclear Magnetic Resonance Structural Study of the Retinal-Binding Pocket in Sodium Ion Pump Rhodopsin. *Biochemistry* 56, 543–550. doi:10.1021/acs.biochem.6b00999

Shihoya, W., Inoue, K., Singh, M., Konno, M., Hososhima, S., Yamashita, K., et al. (2019). Crystal Structure of Heliorhodopsin. *Nature* 574, 132–136. doi:10.1038/s41586-019-1604-6

Shim, J.-G., Kang, N.-R., Chuon, K., Cho, S.-G., Meas, S., and Jung, K.-H. (2022). Mutational Analyses Identify a Single Amino Acid Critical for Color Tuning in Proteorhodopsins. *FEBS Lett.* 596, 784. doi:10.1002/1873-3468.14297

Shim, J.-G., Soum, V., Kang, K.-W., Chuon, K., Cho, S.-G., Kim, J.-H., et al. (2021). Discovery of a Microbial Rhodopsin that Is the Most Stable in Extreme Environments. *iScience* 24, 102620. doi:10.1016/j.isci.2021.102620

Shimamura, T., Hiraki, K., Takahashi, N., Hori, T., Ago, H., Masuda, K., et al. (2008). Crystal Structure of Squid Rhodopsin with Intracellularly Extended Cytoplasmic Region. *J. Biol. Chem.* 283, 17753–17756. doi:10.1074/jbc.c800040200

Shimono, K., Ikeura, Y., Sudo, Y., Iwamoto, M., and Kamo, N. (2001). Environment Around the Chromophore in *Pharaonis* Phoborhodopsin: Mutation Analysis of the Retinal Binding Site. *Biochimica Biophysica Acta-Biomembranes* 1515, 92–100. doi:10.1016/s0005-2736(01)00394-7

Shirzad-Wasei, N., and DeGrip, W. J. (2016). Heterologous Expression of Melanopsin: Present, Problems and Prospects. *Prog. Retin. Eye Res.* 52, 1–21. doi:10.1016/j.preteyeres.2016.02.001

Shirzad-Wasei, N., Van Oostrum, J., Bovee-Geurts, P. H. M., Kusters, L. J. A., Bosman, G. J. C. G. M., and DeGrip, W. J. (2015). Rapid Transfer of Overexpressed Integral Membrane Protein from the Host Membrane into Soluble Lipid Nanodiscs without Previous Purification. *Biol. Chem.* 396, 903–915. doi:10.1515/hsz-2015-0100

Shirzad-Wasei, N., Van Oostrum, J., Bovee-Geurts, P. H. M., Wasserman, M., Bosman, G. J. C. G. M., and DeGrip, W. J. (2013). Large Scale Expression and Purification of Mouse Melanopsin-L in the Baculovirus Expression System. *Protein Expr. Purif.* 91, 134–146. doi:10.1016/j.pep.2013.07.010

Shtyrov, A. A., Nikolaev, D. M., Mironov, V. N., Vasin, A. V., Panov, M. S., Tveryanovich, Y. S., et al. (2021). Simple Models to Study Spectral Properties of Microbial and Animal Rhodopsins: Evaluation of the Electrostatic Effect of Charged and Polar Residues on the First Absorption Band Maxima. *Int. J. Mol. Sci.* 22, 3029. doi:10.3390/ijms22063029

Sineshchekov, O. A., Govorunova, E. G., Wang, J. H., and Spudich, J. L. (2012). Enhancement of Long-Wavelength Sensitivity of Optogenetic Microbial Rhodopsins by 3, 4-dehydroretinal. *Biochemistry* 51, 4499–4506. doi:10.1021/bi2018859

Singh, M., Inoue, K., Pushkarev, A., Béjà, O., and Kandori, H. (2018). Mutation Study of Heliorhodopsin 48C12. *Biochemistry* 57, 5041–5049. doi:10.1021/acs.biochem.8b00637

Skopintsev, P., Ehrenberg, D., Weinert, T., James, D., Kar, R. K., Johnson, P. J. M., et al. (2020). Femtosecond-to-millisecond Structural Changes in a Light-Driven Sodium Pump. *Nature* 583, 314–322. doi:10.1038/s41586-020-2307-8

Smith, S. O., Aschheim, K., and Groesbeek, M. (1996). Magic Angle Spinning NMR Spectroscopy of Membrane Proteins. *Quart. Rev. Biophys.* 29, 395–449. doi:10.1017/s0033583500005898

Smith, S. O., De Groot, H. J. M., Gebhard, R., Courtin, J. M. L., Lugtenburg, J., Herzfeld, J., et al. (1989). Structure and Protein Environment of the Retinal Chromophore in Light-Adapted and Dark-Adapted Bacteriorhodopsin Studied by Solid-State NMR. *Biochemistry* 28, 8897–8904. doi:10.1021/bi00448a032

Smith, S. O., De Groot, H. J. M., Gebhard, R., and Lugtenburg, J. (1992). Magic Angle Spinning NMR Studies on the Metarhodopsin II Intermediate of Bovine Rhodopsin: Evidence for an Unprotonated Schiff Base. *Photochem. Photobiol.* 56, 1035–1039. doi:10.1111/j.1751-1097.1992.tb09726.x

Smith, S. O. (2021). Deconstructing the Transmembrane Core of Class A G Protein-Coupled Receptors. *Trends Biochem. Sci.* 46, 1017. doi:10.1016/j.tibs.2021.08.006

Smith, S. O., Myers, A. B., Mathies, R. A., Pardoen, J. A., Winkel, C., Vandenberg, E. M. M., et al. (1985). Vibrational Analysis of the All-Trans Retinal Protonated Schiff Base. *Biophys. J.* 47, 653–664. doi:10.1016/s0006-3495(85)83961-8

Smith, S. O. (2010). Structure and Activation of the Visual Pigment Rhodopsin. *Annu. Rev. Biophysics* 39, 309–328. doi:10.1146/annurev-biophys-101209-104901

Smitienko, O. A., Feldman, T. B., Petrovskaya, L. E., Nekrasova, O. V., Yakovleva, M. A., Shelaev, I. V., et al. (2021). Comparative Femtosecond Spectroscopy of Primary Photoreactions of *Exiguobacterium Sibiricum* Rhodopsin and *Halobacterium Salinarum* Bacteriorhodopsin. *J. Phys. Chem. B* 125, 995–1008. doi:10.1021/acs.jpcb.0c07763

Smitienko, O. A., Nekrasova, O. V., Kudriavtsev, A. V., Yakovleva, M. A., Shelaev, I. V., Gostev, F. E., et al. (2017). Femtosecond and Picosecond Dynamics of Recombinant Bacteriorhodopsin Primary Reactions Compared to the Native Protein in Trimeric and Monomeric Forms. *Biochemistry-Moscow* 82, 490–500. doi:10.1134/S0006297917040113

Sneskov, K., Olsen, J. M. H., Schwabe, T., Hättig, C., Christiansen, O., and Kongsted, J. (2013). Computational Screening of One- and Two-Photon Spectrally Tuned Channelrhodopsin Mutants. *Phys. Chem. Chem. Phys.* 15, 7567–7576. doi:10.1039/c3cp44350g

Sonar, S., Liu, X.-M., Lee, C.-P., Coleman, M., He, Y.-W., Pelletier, S., et al. (1995). Site-directed Isotope Labeling and FT-IR Spectroscopy: The Tyr 185/Pro 186 Peptide Bond of Bacteriorhodopsin Is Perturbed during the Primary Photoreaction. *J. Am. Chem. Soc.* 117, 11614–11615. doi:10.1021/ja00151a041

Song, Y. Z., Cartron, M. L., Jackson, P. J., Davison, P. A., Dickman, M. J., Zhu, D., et al. (2020). Proteorhodopsin Overproduction Enhances the Long-Term Viability of *Escherichia coli*. *Appl. Environ. Microbiol.* 86, 02087–02019. doi:10.1128/AEM.02087-19

Soni, B. G., and Foster, R. G. (1997). A Novel and Ancient Vertebrate Opsin. *FEBS Lett.* 406, 279–283. doi:10.1016/s0014-5793(97)00287-1

Spooner, P. J. R., Sharples, J. M., Goodall, S. C., Bovee-Geurts, P. H. M., Verhoeven, M. A., Lugtenburg, J., et al. (2004). The Ring of the Rhodopsin Chromophore in a Hydrophobic Activation Switch within the Binding Pocket. *J. Mol. Biol.* 343, 719–730. doi:10.1016/j.jmb.2004.08.049

Spudich, J. L., Sineshchekov, O. A., and Govorunova, E. G. (2014). Mechanism Divergence in Microbial Rhodopsins. *Biochimica Biophysica Acta-Bioenergetics* 1837, 546–552. doi:10.1016/j.bbabio.2013.06.006

Spudich, J. L., Yang, C.-S., Jung, K.-H., and Spudich, E. N. (2000). Retinylidene Proteins: Structures and Functions from Archaea to Humans. *Annu. Rev. Cell. Dev. Biol.* 16, 365–392. doi:10.1146/annurev.cellbio.16.1.365

Sridharan, S., Gajowa, M. A., Ogando, M. B., Jagadisan, U. K., Abdeladim, L., Sadahiro, M., et al. (2022). High-performance Microbial Opsins for Spatially and Temporally Precise Perturbations of Large Neuronal Networks. *Neuron* 110, 1–17. doi:10.1016/j.neuron.2022.01.008

Srinivasan, S., Ramon, E., Cordomí, A., and Garriga, P. (2014). Binding Specificity of Retinal Analogs to Photoactivated Visual Pigments Suggest Mechanism for Fine-Tuning GPCR-Ligand Interactions. *Chem. Biol.* 21, 369–378. doi:10.1016/j.chembiol.2014.01.006

Standfuss, J., Xie, G. F., Edwards, P. C., Burghammer, M., Oprian, D. D., and Schertler, G. F. X. (2007). Crystal Structure of a Thermally Stable Rhodopsin Mutant. *J. Mol. Biol.* 372, 1179–1188. doi:10.1016/j.jmb.2007.03.007

Stavenga, D. G., Oberwinkler, J., and Postma, M. (2000). "Modeling Primary Visual Processes in Insect Photoreceptors," in *Molecular Mechanisms in Visual Transduction*. Editors D. G. Stavenga, W. J. DeGrip, and E. N. PughJr. (Amsterdam, Netherlands: Elsevier Science Pub.), 527–574. doi:10.1016/s1383-8121(00)80013-5

Steinhoff, H.-J., Mollaaghababa, R., Altenbach, C. A., Khorana, H. G., and Hubbell, W. L. (1995). Site Directed Spin Labeling Studies of Structure and Dynamics in Bacteriorhodopsin. *Biophys. Chem.* 56, 89–94. doi:10.1016/0301-4622(95)00019-t

Stenkamp, R. E. (2008). Alternative Models for Two Crystal Structures of Bovine Rhodopsin. *Acta Crystallogr. d-biol. Cryst.* 64, 902–904. doi:10.1107/s0907444908017162

Steward, L. E., and Chamberlin, A. R. (1998). Protein Engineering with Nonstandard Amino Acids. *Meth. Mol. Biol.* 77, 325–354. doi:10.1385/0-89603-397-X:325

Struts, A. V., Salgado, G. F. J., Tanaka, K., Krane, S., Nakanishi, K., and Brown, M. F. (2007). Structural Analysis and Dynamics of Retinal Chromophore in Dark and Metal States of Rhodopsin from ^{2}H NMR of Aligned Membranes. *J. Mol. Biol.* 372, 50–66. doi:10.1016/j.jmb.2007.03.046

Stubbs, G. W., Smith, H. G., and Litman, B. J. (1976). Alkyl Glucosides as Effective Solubilizing Agents for Bovine Rhodopsin - A Comparison with Several Commonly Used Detergents. *Biochim. Biophys. Acta* 426, 46–56. doi:10.1016/0005-2736(76)90428-4

Su, C.-Y., Luo, D.-G., Terakita, A., Shichida, Y., Liao, H.-W., Kazmi, M. A., et al. (2006). Parietal-eye Phototransduction Components and Their Potential Evolutionary Implications. *Science* 311, 1617–1621. doi:10.1126/science.1123802

Subramaniam, S., Lindahl, I., Bullough, P. A., Faruqi, A. R., Tittor, J., Oesterhelt, D., et al. (1999). Protein Conformational Changes in the Bacteriorhodopsin Photocycle. *J. Mol. Biol.* 287, 145–161. doi:10.1006/jmbi.1999.2589

Sudo, Y., Ihara, K., Kobayashi, S., Suzuki, D., Irieda, H., Kikukawa, T., et al. (2011). A Microbial Rhodopsin with a Unique Retinal Composition Shows Both Sensory Rhodopsin II and Bacteriorhodopsin-like Properties. *J. Biol. Chem.* 286, 5967–5976. doi:10.1074/jbc.m110.190058

Sudo, Y., Okazaki, A., Ono, H., Yagasaki, J., Sugo, S., Kamiya, M., et al. (2013). A Blue-Shifted Light-Driven Proton Pump for Neural Silencing. *J. Biol. Chem.* 288, 20624–20632. doi:10.1074/jbc.m113.475533

Sugimoto, T., Katayama, K., and Kandori, H. (2021). Role of Thr82 for the Unique Photochemistry of TAT Rhodopsin. *Biophysics Physicobiology* 18, 108–115. doi:10.2142/biophysico.bppb-v18.012

Sun, H., Gilbert, D. J., Copeland, N. G., Jenkins, N. A., and Nathans, J. (1997). Peropsin, a Novel Visual Pigment-like Protein Located in the Apical Microvilli of the Retinal Pigment Epithelium. *Proc. Nat. Acad. Sci. U. S. A.* 94, 9893–9898. doi:10.1073/pnas.94.18.9893

Sun, Y., Li, M. J., Cao, S., Xu, Y., Wu, P., Xu, S., et al. (2022). Optogenetics for Understanding and Treating Brain Injury: Advances in the Field and Future Prospects. *Int. J. Mol. Sci.* 23, 1800. doi:10.3390/ijms23031800

Suzuki, E., Katayama, E., and Hirosawa, K. (1993). Structure of Photoreceptive Membranes of Drosophila Compound Eyes as Studied by Quick-Freezing Electron Microscopy. *J. Electron Microsc.* 42, 178–184.

Suzuki, K., Del Carmen Marín, M., Konno, M., Bagherzadeh, R., Murata, T., and Inoue, K. (2022). Structural Characterization of Proton-Pumping Rhodopsin Lacking a Cytoplasmic Proton Donor Residue by X-Ray Crystallography. *J. Biol. Chem.* 298, 101722. doi:10.1016/j.jbc.2022.101722

Tahara, S., Kuramochi, H., Takeuchi, S., and Tahara, T. (2019a). Protein Dynamics Preceding Photoisomerization of the Retinal Chromophore in Bacteriorhodopsin Revealed by Deep-UV Femtosecond Stimulated Raman Spectroscopy. *J. Phys. Chem. Lett.* 10, 5422–5427. doi:10.1021/acs.jpclett.9b02283

Tahara, S., Singh, M., Kuramochi, H., Shihoya, W., Inoue, K., Nureki, O., et al. (2019b). Ultrafast Dynamics of Heliorhodopsins. *J. Phys. Chem. B* 123, 2507–2512. doi:10.1021/acs.jpcb.9b00887

Tahara, S., Takeuchi, S., Abe-Yoshizumi, R., Inoue, K., Ohtani, H., Kandori, H., et al. (2015). Ultrafast Photoreaction Dynamics of a Light-Driven Sodium-Ion-Pumping Retinal Protein from *Krokinobacter Eikastus* Revealed by Femtosecond Time-Resolved Absorption Spectroscopy. *J. Phys. Chem. Lett.* 6, 4481–4486. doi:10.1021/acs.jpclett.5b01994

Takayama, R., Kaneko, A., Okitsu, T., Tsunoda, S. P., Shimono, K., Mizuno, M., et al. (2018). Production of a Light-Gated Proton Channel by Replacing the Retinal Chromophore with its Synthetic Vinylene Derivative. *J. Phys. Chem. Lett.* 9, 2857–2862. doi:10.1021/acs.jpclett.8b00879

Tam, B. M., and Moritz, O. L. (2009). The Role of Rhodopsin Glycosylation in Protein Folding, Trafficking, and Light-Sensitive Retinal Degeneration. *J. Neurosci.* 29, 15145–15154. doi:10.1523/jneurosci.4259-09.2009

Tan, P., He, L., Huang, Y., and Zhou, Y. (2022). Optophysiology: Illuminating Cell Physiology with Optogenetics. *Physiol. Rev.* 102, 1263. doi:10.1152/physrev.00021.2021

Tanaka, T., Singh, M., Shihoya, W., Yamashita, K., Kandori, H., and Nureki, O. (2020). Structural Basis for Unique Color Tuning Mechanism in Heliorhodopsin. *Biochem. Biophysical Res. Commun.* 533, 262–267. doi:10.1016/j.bbrc.2020.06.124

Tansley, K. (1931). The Regeneration of Visual Purple: its Relation to Dark Adaptation and Night Blindness. *J. Physiology* 71, 442–458. doi:10.1113/jphysiol.1931.sp002749

Tarttelin, E. E., Bellingham, J., Hankins, M. W., Foster, R. G., and Lucas, R. J. (2003). Neuropsin (Opn5): A Novel Opsin Identified in Mammalian Neural Tissue. *FEBS Lett.* 554, 410–416. doi:10.1016/s0014-5793(03)01212-2

Tarttelin, E. E., Fransen, M. P., Edwards, P. C., Hankins, M. W., Schertler, G. F. X., Vogel, R., et al. (2011). Adaptation of Pineal Expressed Teleost Exo-Rod Opsin to Non-image Forming Photoreception through Enhanced Meta II Decay. *Cell. Mol. Life Sci.* 68, 3713–3723. doi:10.1007/s00018-011-0665-y

Tastan, O., Dutta, A., Booth, P. J., and Klein-Seetharaman, J. (2014). Retinal Proteins as Model Systems for Membrane Protein Folding. *Biochimica Biophysica Acta-Bioenergetics* 1837, 656–663. doi:10.1016/j.bbabio.2013.11.021

Tavanti, F., and Tozzini, V. (2014). A Multi-Scale-Multi-Stable Model for the Rhodopsin Photocycle. *Molecules* 19, 14961–14978. doi:10.3390/molecules190914961

Terakita, A., Koyanagi, M., Tsukamoto, H., Yamashita, T., Miyata, T., and Shichida, Y. (2004). Counterion Displacement in the Molecular Evolution of the Rhodopsin Family. *Nat. Struct. Mol. Biol.* 11, 284–289. doi:10.1038/nsmb731

Terakita, A. (2005). The Opsins. *Genome Biol.* 6, 213. doi:10.1186/gb-2005-6-3-213

Tian, Y., Yang, S., Nagel, G., and Gao, S. Q. (2022). Characterization and Modification of Light-Sensitive Phosphodiesterases from Choanoflagellates. *Biomolecules* 12, 88. doi:10.3390/biom12010088

Tkatch, T., Greotti, E., Baranauskas, G., Pendin, D., Roy, S., Nita, L. I., et al. (2017). Optogenetic Control of Mitochondrial Metabolism and Ca^{2+} Signaling by Mitochondria-Targeted Opsins. *Proc. Natl. Acad. Sci. U. S. A.* 114, E5167–E5176. doi:10.1073/pnas.1703623114

Toba, Y., and Hanawa, I. (1985). Photoreceptor Sensitivity as a Function of Rhodopsin Content in the Isolated Bullfrog Retina. *Jpn. J. Physiology* 35, 483–494. doi:10.2170/jjphysiol.35.483

Tomida, S., Ito, S., Mato, T., Furutani, Y., Inoue, K., and Kandori, H. (2020). Infrared Spectroscopic Analysis on Structural Changes Around the Protonated Schiff Base upon Retinal Isomerization in Light-Driven Sodium Pump KR2. *Biochimica Biophysica Acta-Bioenergetics* 1861, 148190. doi:10.1016/j.bbabio.2020.148190

Tomida, S., Kitagawa, S., Kandori, H., and Furutani, Y. (2021). Inverse Hydrogen-Bonding Change between the Protonated Retinal Schiff Base and Water Molecules upon Photoisomerization in Heliorhodopsin 48C12. *J. Phys. Chem. B* 125, 8331–8341. doi:10.1021/acs.jpcb.1c01907

Tomobe, K., Yamamoto, E., Kholmurodov, K., and Yasuoka, K. (2017). Water Permeation through the Internal Water Pathway in Activated GPCR Rhodopsin. *PLoS ONE* 12, e0176876. doi:10.1371/journal.pone.0176876

Townson, S. M., Chang, B. S. W., Salcedo, E., Chadwell, L. V., Pierce, N. E., and Britt, S. G. (1998). Honeybee Blue-And Ultraviolet-Sensitive Opsins: Cloning, Heterologous Expression in *Drosophila*, and Physiological Characterization. *J. Neurosci.* 18, 2412–2422. doi:10.1523/jneurosci.18-07-02412.1998

Tribet, C., Audebert, R., and Popot, J.-L. (1996). Amphipols: Polymers that Keep Membrane Proteins Soluble in Aqueous Solutions. *Proc. Nat. Acad. Sci. U. S. A.* 93, 15047–15050. doi:10.1073/pnas.93.26.15047

Tsai, C.-J., Marino, J., Adaixo, R., Pamulal, F., Muehle, J., Maeda, S., et al. (2019). Cryo-EM Structure of the Rhodopsin-Gαι-Bγ Complex Reveals Binding of the Rhodopsin C-Terminal Tail to the Gβ Subunit. *Elife* 8, 46041. doi:10.7554/elife.46041

Tsujimura, M., and Ishikita, H. (2020). Insights into the Protein Functions and Absorption Wavelengths of Microbial Rhodopsins. *J. Phys. Chem. B* 124, 11819–11826. doi:10.1021/acs.jpcb.0c08910

Tsujimura, M., Noji, T., Saito, K., Kojima, K., Sudo, Y., and Ishikita, H. (2021). Mechanism of Absorption Wavelength Shifts in Anion Channelrhodopsin-1 Mutants. *Biochimica Biophysica Acta-Bioenergetics* 1862, 148349. doi:10.1016/j.bbabio.2020.148349

Tsukamoto, H., Szundi, I., Lewis, J. W., Farrens, D. L., and Kliger, D. S. (2011). Rhodopsin in Nanodiscs Has Native Membrane-like Photointermediates. *Biochemistry* 50, 5086–5091. doi:10.1021/bi200391a

Tsukamoto, H., and Terakita, A. (2010). Diversity and Functional Properties of Bistable Pigments. *Photochem. Photobiological Sci.* 9, 1435–1443. doi:10.1039/c0pp00168f

Tsukamoto, T., Mizutani, K., Hasegawa, T., Takahashi, M., Honda, N., Hashimoto, N., et al. (2016). X-ray Crystallographic Structure of Thermophilic Rhodopsin - *Implications For High Thermal Stability and Optogenetic Function*. *J. Biol. Chem.* 291, 12223–12232. doi:10.1074/jbc.m116.719815

Tsunoda, S. P., Ewers, D., Gazzarrini, S., Moroni, A., Gradmann, D., and Hegemann, P. (2006). H^+-pumping Rhodopsin from the Marine Alga *Acetabularia*. *Biophysical J.* 91, 1471–1479. doi:10.1529/biophysj.106.086421

Tsunoda, S. P., Sugiura, M., and Kandori, H. (2021). "Molecular Properties and Optogenetic Applications of Enzymerhodopsins," in *Optogenetics: Light-Sensing Proteins and Their Applications in Neuroscience and beyond*. Editors H. Yawo, H. Kandori, A. Koizumi, and R. Kageyama. 2nd ed (Singapore: Springer), 153–165. doi:10.1007/978-981-15-8763-4_9

Tu, C.-H., Yi, H.-P., Hsieh, S.-Y., Lin, H.-S., and Yang, C.-S. (2018). Overexpression of Different Types of Microbial Rhodopsins with a Highly Expressible Bacteriorhodopsin from *Haloarcula Marismortui* as a Single Protein in *E. coli*. *Sci. Rep.* 8, 14026. doi:10.1038/s41598-018-32399-x

Tutol, J. N., Lee, J., Chi, H. C., Faizuddin, F. N., Abeyrathna, S. S., Zhou, Q., et al. (2021). A Single Point Mutation Converts a Proton-Pumping Rhodopsin into a Red-Shifted, Turn-On Fluorescent Sensor for Chloride. *Chem. Sci.* 12, 5655–5663. doi:10.1039/d0sc06061e

Ueta, T., Kojima, K., Hino, T., Shibata, M., Nagano, S., and Sudo, Y. (2020). Applicability of Styrene-Maleic Acid Copolymer for Two Microbial Rhodopsins, RxR and HsSRI. *Biophysical J.* 119, 1760–1770. doi:10.1016/j.bpj.2020.09.026

Urner, L. H., Liko, I., Yen, H.-Y., Hoi, K.-K., Bolla, J. R., Gault, J., et al. (2020). Modular Detergents Tailor the Purification and Structural Analysis of Membrane Proteins Including G Protein-Coupled Receptors. *Nat. Commun.* 11, 564. doi:10.1038/s41467-020-14424-8

Valdez-Lopez, J. C., Petr, S. T., Donohue, M. P., Bailey, R. J., Gebreeziabher, M., Cameron, E. G., et al. (2020). The C-Terminus and Third Cytoplasmic Loop Cooperatively Activate Mouse Melanopsin Phototransduction. *Biophysical J.* 119, 389–401. doi:10.1016/j.bpj.2020.06.013

Van Der Steen, R., Biesheuvel, P. L., Mathies, R. A., and Lugtenburg, J. (1986). Retinal Analogs with Locked 6-7 Conformations Show that Bacteriorhodopsin Requires the 6-S-*Trans* Conformation of the Chromophore. *J. Am. Chem. Soc.* 108, 6410–6411. doi:10.1021/ja00280a060

Van Eps, N., Caro, L. N., Morizumi, T., Kusnetzow, A. K., Szczepek, M., Hofmann, K. P., et al. (2017). Conformational Equilibria of Light-Activated Rhodopsin in Nanodiscs. *Proc. Natl. Acad. Sci. U. S. A.* 114, E3268–E3275. doi:10.1073/pnas.1620405114

VanAken, T., Foxall-Vanaken, S., Castleman, S., and Ferguson-Miller, S. (1986). Alkyl Glycoside Detergents: Synthesis and Applications to the Study of Membrane Proteins. *Methods Enzym.* 125, 27–35. doi:10.1016/s0076-6879(86)25005-3

Varma, N., Mutt, E., Mühle, J., Panneels, V., Terakita, A., Deupi, X., et al. (2019). Crystal Structure of Jumping Spider Rhodopsin-1 as a Light Sensitive GPCR. *Proc. Natl. Acad. Sci. U. S. A.* 116, 14547–14556. doi:10.1073/pnas.1902192116

Verdegem, P. J. E., Bovee-Geurts, P. H. M., DeGrip, W. J., Lugtenburg, J., and De Groot, H. J. M. (1999). Retinylidene Ligand Structure in Bovine Rhodopsin, Metarhodopsin I, and 10-methylrhodopsin from Internuclear Distance Measurements Using ^{13}C-Labeling and 1-D Rotational Resonance MAS NMR. *Biochemistry-USA* 38, 11316–11324. doi:10.1021/bi983014e

Verhoefen, M.-K., Schäfer, G., Shastri, S., Weber, I., Glaubitz, C., Mäntele, W., et al. (2011). Low Temperature FTIR Spectroscopy Provides New Insights in the pH-dependent Proton Pathway of Proteorhodopsin. *Biochimica Biophysica Acta-Bioenergetics* 1807, 1583–1590. doi:10.1016/j.bbabio.2011.09.001

Verhoeven, M. A., Bovee-Geurts, P. H. M., De Groot, H. J. M., Lugtenburg, J., and DeGrip, W. J. (2006). Methyl Substituents at the 11- or 12-position of Retinal Profoundly and Differentially Affect Photochemistry and Signalling Activity of Rhodopsin. *J. Mol. Biol.* 363, 98–113. doi:10.1016/j.jmb.2006.07.039

Verhoeven, M. A., Creemers, A. F. L., Bovee-Geurts, P. H. M., DeGrip, W. J., Lugtenburg, J., and De Groot, H. J. M. (2001). Ultra-high-field MAS NMR Assay of a Multispin Labeled Ligand Bound to its G-Protein Receptor Target in the Natural Membrane Environment: Electronic Structure of the Retinylidene Chromophore in Rhodopsin. *Biochemistry* 40, 3282–3288. doi:10.1021/bi0023798

Vierock, J., Rodriguez-Rozada, S., Dieter, A., Pieper, F., Sims, R., Tenedini, F., et al. (2021). BiPOLES Is an Optogenetic Tool Developed for Bidirectional Dual-Color Control of Neurons. *Nat. Commun.* 12, 4527. doi:10.1038/s41467-021-24759-5

Villette, V., Chavarha, M., Dimov, I. K., Bradley, J., Pradhan, L., Mathieu, B., et al. (2019). Ultrafast Two-Photon Imaging of a High-Gain Voltage Indicator in Awake Behaving Mice. *Cell.* 179, 1590–1609. doi:10.1016/j.cell.2019.11.004

Vissers, P. M. a. M., Bovee-Geurts, P. H. M., Portier, M. D., Klaassen, C. H. W., and DeGrip, W. J. (1998). Large-scale Production and Purification of the Human Green Cone Pigment: Characterization of Late Photo-Intermediates. *Biochem. J.* 330, 1201–1208. doi:10.1042/bj3301201

Vissers, P. M. a. M., and DeGrip, W. J. (1996). Functional Expression of Human Cone Pigments Using Recombinant Baculovirus: Compatibility with Histidine Tagging and Evidence for N-Glycosylation. *FEBS Lett.* 396, 26–30. doi:10.1016/0014-5793(96)01064-2

Vlasov, A. V., Maliar, N. L., Bazhenov, S. V., Nikelshparg, E. I., Brazhe, N. A., Vlasova, A. D., et al. (2020). Raman Scattering: From Structural Biology to Medical Applications. *Crystals* 10, 38–3149. doi:10.3390/cryst10010038

Vöcking, O., Leclère, L., and Hausen, H. (2021). The Rhodopsin-Retinochrome System for Retinal Re-isomerization Predates the Origin of Cephalopod Eyes. *BMC Ecol. Evol.* 21, 1–141. doi:10.1186/s12862-021-01939-x

Vogel, R., Mahalingam, M., Lüdeke, S., Huber, T., Siebert, F., and Sakmar, T. P. (2008). Functional Role of the "Ionic Lock" - an Interhelical Hydrogen-Bond Network in Family a Heptahelical Receptors. *J. Mol. Biol.* 380, 648–655. doi:10.1016/j.jmb.2008.05.022

Vogel, R., Sakmar, T. P., Sheves, M., and Siebert, F. (2007). Coupling of Protonation Switches during Rhodopsin Activation. *Photochem. Photobiol.* 83, 286–292. doi:10.1562/2006-06-19-ir-937

Vogeley, L., Sineshchekov, O. A., Trivedi, V. D., Sasaki, J., Spudich, J. L., and Luecke, H. (2004). *Anabaena* Sensory Rhodopsin: A Photochromic Color Sensor at 2.0 Å. *Science* 306, 1390–1393. doi:10.1126/science.1103943

Vogt, A., Guo, Y., Tsunoda, S. P., Kateriya, S., Elstner, M., and Hegemann, P. (2015). Conversion of a Light-Driven Proton Pump into a Light-Gated Ion Channel. *Sci. Rep.* 5, 16450. doi:10.1038/srep16450

Vogt, A., Silapetere, A., Grimm, C., Heiser, F., Möller, M. A., and Hegemann, P. (2019). Engineered Passive Potassium Conductance in the KR2 Sodium Pump. *Biophysical J.* 116, 1941–1951. doi:10.1016/j.bpj.2019.04.001

Vogt, K., and Kirschfeld, K. (1984). Chemical Identity of the Chromophores of Fly Visual Pigment. *Naturwissenschaften* 71, 211–213. doi:10.1007/bf00490436

Volkov, O., Kovalev, K., Polovinkin, V., Borshchevskiy, V., Bamann, C., Astashkin, R., et al. (2017). Structural Insights into Ion Conduction by Channelrhodopsin 2. *Science* 358, eaan8862. doi:10.1126/science.aan8862

Vought, B. W., Dukkipati, A., Max, M., Knox, B. E., and Birge, R. R. (1999). Photochemistry of the Primary Event in Short-Wavelength Visual Opsins at Low Temperature. *Biochemistry-USA* 38, 11287–11297. doi:10.1021/bi990968b

Vought, B. W., Salcedo, E., Chadwell, L. V., Britt, S. G., Birge, R. R., and Knox, B. E. (2000). Characterization of the Primary Photointermediates of *Drosophila* Rhodopsin. *Biochemistry* 39, 14128–14137. doi:10.1021/bi001135k

Wada, A., Fujioka, N., Tanaka, Y., and Ito, M. (2000). A Highly Stereoselective Synthesis of 11Z-Retinal Using Tricarbonyliron Complex. *J. Org. Chem.* 65, 2438–2443. doi:10.1021/jo9916030

Wada, T., Shimono, K., Kikukawa, T., Hato, M., Shinya, N., Kim, S.-Y., et al. (2011). Crystal Structure of the Eukaryotic Light-Driven Proton-Pumping Rhodopsin, *Acetabularia* Rhodopsin II, from Marine Alga. *J. Mol. Biol.* 411, 986–998. doi:10.1016/j.jmb.2011.06.028

Wagner, M. J., Savall, J., Hernandez, O., Mel, G., Inan, H., Rumyantsev, O., et al. (2021). A Neural Circuit State Change Underlying Skilled Movements. *Cell.* 184, 3731–3747. doi:10.1016/j.cell.2021.06.001

Wagner, N. L., Greco, J. A., Ranaghan, M. J., and Birge, R. R. (2013). Directed Evolution of Bacteriorhodopsin for Applications in Bioelectronics. *J. R. Soc. Interface* 10, 201301971. doi:10.1098/rsif.2013.0197

Wald, G., and Brown, P. K. (1953). The Molar Extinction of Rhodopsin. *J. General Physiology* 37, 189–200. doi:10.1085/jgp.37.2.189

Wald, G. (1935). Carotenoids and the Visual Cycle. *J. General Physiology* 19, 351–371. doi:10.1085/jgp.19.2.351

Wald, G. (1953). The Biochemistry of Vision. *Annu. Rev. Biochem.* 22, 497–526. doi:10.1146/annurev.bi.22.070153.002433

Wald, G. (1968). The Molecular Basis of Visual Excitation. *Nature* 219, 800–807. doi:10.1038/219800a0

Walter, J. M., Greenfield, D., and Liphardt, J. (2010). Potential of Light-Harvesting Proton Pumps for Bioenergy Applications. *Curr. Opin. Biotechnol.* 21, 265–270. doi:10.1016/j.copbio.2010.03.007

Wand, A., Gdor, I., Zhu, J. Y., Sheves, M., and Ruhman, S. (2013). Shedding New Light on Retinal Protein Photochemistry. *Annu. Rev. Phys. Chem.* 64, 437–458. doi:10.1146/annurev-physchem-040412-110148

Wang, N., Wang, M. T., Gao, Y. Y., Ran, T. T., Lan, Y. L., Wang, J., et al. (2012). Crystallization and Preliminary X-Ray Crystallographic Analysis of a Blue-Light-Absorbing Proteorhodopsin. *Acta Crystallogr. Sect. F-Structural Biol. Cryst. Commun.* 68, 281–283. doi:10.1107/s1744309111043612

Wang, S. L., Munro, R. A., Shi, L. C., Kawamura, I., Okitsu, T., Wada, A., et al. (2013). Solid-state NMR Spectroscopy Structure Determination of a Lipid-Embedded Heptahelical Membrane Protein. *Nat. Methods* 10, 1007–1012. doi:10.1038/nmeth.2635

Wang, Y.-J., Bovee-Geurts, P. H. M., Lugtenburg, J., and DeGrip, W. J. (2004). Constraints of the 9-methyl Group Binding Pocket of the Rhodopsin Chromophore Probed by 9-halogeno Substitution. *Biochemistry* 43, 14802–14810. doi:10.1021/bi048404h

Wang, Y., Li, Y., Xu, T., Shi, Z. Y., and Wu, Q. (2015). Experimental Evidence for Growth Advantage and Metabolic Shift Stimulated by Photophosphorylation of Proteorhodopsin Expressed in *Escherichia coli* at Anaerobic Condition. *Biotechnol. Bioeng.* 112, 947–956. doi:10.1002/bit.25504

Wang, Z. Y., Asenjo, A. B., and Oprian, D. D. (1993). Identification of the Cl^- Bbinding Site in the Human Red and Green Color Vision Pigments. *Biochemistry-USA* 32, 2125–2130. doi:10.1021/bi00060a001

Warrant, E. J., and Locket, N. A. (2004). Vision in the Deep Sea. *Biol. Rev.* 79, 671–712. doi:10.1017/s1464793103006420

Warrant, E. J., and Mciintyre, P. D. (1993). Arthropod Eye Design and the Physical Limits to Spatial Resolving Power. *Prog. Neurobiol.* 40, 413–461. doi:10.1016/0301-0082(93)90017-m

Watari, M., Ikuta, T., Yamada, D., Shihoya, W., Yoshida, K., Tsunoda, S. P., et al. (2019). Spectroscopic Study of the Transmembrane Domain of a Rhodopsin-Phosphodiesterase Fusion Protein from a Unicellular Eukaryote. *J. Biol. Chem.* 294, 3432–3443. doi:10.1074/jbc.ra118.006277

Weinert, T., Skopintsev, P., James, D., Dworkowski, F., Panepucci, E., Kekilli, D., et al. (2019). Proton Uptake Mechanism in Bacteriorhodopsin Captured by Serial Synchrotron Crystallography. *Science* 365, 61–65. doi:10.1126/science.aaw8634

Weingart, O. (2007). The Twisted C11=C12 Bond of the Rhodopsin Chromophore - A Photochemical Hot Spot. *J. Am. Chem. Soc.* 129, 10618–10619. doi:10.1021/ja071793t

Weissbecker, J., Boumrifak, C., Breyer, M., Wiessalla, T., Shevchenko, V., Mager, T., et al. (2021). The Voltage Dependent Sidedness of the Reprotonation of the Retinal Schiff Base Determines the Unique Inward Pumping of Xenorhodopsin. *Angew. Chemie-International Ed.* 60, 23010–23017. doi:10.1002/anie.202103882

Werner, K., Lehner, I., Dhiman, H. K., Richter, C., Glaubitz, C., Schwalbe, H., et al. (2007). Combined Solid State and Solution NMR Studies of α, ε-^{15}N Labeled Bovine Rhodopsin. *J. Biomol. NMR* 37, 303–312. doi:10.1007/s10858-007-9143-0

Wickstrand, C., Dods, R., Royant, A., and Neutze, R. (2015). Bacteriorhodopsin: Would the Real Structural Intermediates Please Stand up? *Biochimica Biophysica Acta-General Subj.* 1850, 536–553. doi:10.1016/j.bbagen.2014.05.021

Wietek, J., Beltramo, R., Scanziani, M., Hegemann, P., Oertner, T. G., and Wiegert, J. S. (2015). An Improved Chloride-Conducting Channelrhodopsin for Light-Induced Inhibition of Neuronal Activity *In Vivo*. *Sci. Rep.* 5, 14807. doi:10.1038/srep14807

Wijffels, R. H., Kruse, O., and Hellingwerf, K. J. (2013). Potential of Industrial Biotechnology with Cyanobacteria and Eukaryotic Microalgae. *Curr. Opin. Biotechnol.* 24, 405–413. doi:10.1016/j.copbio.2013.04.004

Williams, R. H., Tsunematsu, T., Thomas, A. M., Bogyo, K., Yamanaka, A., and Kilduff, T. S. (2019). Transgenic Archaerhodopsin-3 Expression in Hypocretin/Orexin Neurons Engenders Cellular Dysfunction and Features of Type 2 Narcolepsy. *J. Neurosci.* 39, 9435–9452. doi:10.1523/jneurosci.0311-19.2019

Wright, P., Rodgers, J., Wynne, J., Bishop, P. N., Lucas, R. J., and Milosavljevic, N. (2021). Viral Transduction of Human Rod Opsin or Channelrhodopsin Variants to Mouse on Bipolar Cells Does Not Impact Retinal Anatomy or Cause Measurable Death in the Targeted Cells. *Int. J. Mol. Sci.* 22, 13111. doi:10.3390/ijms222313111

Wright, W., Gajjeraman, S., Batabyal, S., Pradhan, S., Bhattacharya, S., Mahapatra, V., et al. (2017). Restoring Vision in Mice with Retinal Degeneration Using Multicharacteristic Opsin. *Neurophotonics* 4, 041505. doi:10.1117/1.nph.4.4.049801

Xu, C., Wang, R. X., Yang, Y. F., Xu, T. Y., Li, Y., Xu, J., et al. (2020). Expression of OPN3 in Lung Adenocarcinoma Promotes Epithelial-Mesenchymal Transition and Tumor Metastasis. *Thorac. Cancer* 11, 286–294. doi:10.1111/1759-7714.13254

Xu, Y. X., Peng, L. X., Wang, S. C., Wang, A. Q., Ma, R. R., Zhou, Y., et al. (2018). Hybrid Indicators for Fast and Sensitive Voltage Imaging. *Angew. Chemie-International Ed.* 57, 3949–3953. doi:10.1002/anie.201712614

Yaguchi, M., Jia, X., Schlesinger, R., Jiang, X., Ataka, K., and Heberle, J. (2022). Near-Infrared Activation of Sensory Rhodopsin II Mediated by NIR-To-Blue Upconversion Nanoparticles. *Front. Mol. Biosci.* 8, 782688. doi:10.3389/fmolb.2021.782688

Yalouz, S., Senjean, B., Günther, J., Buda, F., O'brien, T. E., and Visscher, L. (2021). A State-Averaged Orbital-Optimized Hybrid Quantum-Classical Algorithm for a Democratic Description of Ground and Excited States. *Quantum Sci. Technol.* 6, 024004. doi:10.1088/2058-9565/abd334

Yamashita, T., Ohuchi, H., Tomonari, S., Ikeda, K., Sakai, K., and Shichida, Y. (2010). Opn5 Is a UV-Sensitive Bistable Pigment that Couples with Gi Subtype of G Protein. *Proc. Natl. Acad. Sci. U. S. A.* 107, 22084–22089. doi:10.1073/pnas.1012498107

Yamashita, T., Ono, K., Ohuchi, H., Yumoto, A., Gotoh, H., Tomonari, S., et al. (2014). Evolution of Mammalian Opn5 as a Specialized UV-Absorbing Pigment by a Single Amino Acid Mutation. *J. Biol. Chem.* 289, 3991–4000. doi:10.1074/jbc.m113.514075

Yamashita, T. (2020). Unexpected Molecular Diversity of Vertebrate Nonvisual Opsin Opn5. *Biophys. Rev.* 12, 333–338. doi:10.1007/s12551-020-00654-z

Yan, E. C. Y., Ganim, Z., Kazmi, M. A., Chang, B. S. W., Sakmar, T. P., and Mathies, R. A. (2004). Resonance Raman Analysis of the Mechanism of Energy Storage and Chromophore Distortion in the Primary Visual Photoproduct. *Biochemistry* 43, 10867–10876. doi:10.1021/bi0400148

Yang, X., Manathunga, M., Gozem, S., Léonard, J., Andruniów, T., and Olivucci, M. (2022). Quantum-classical Simulations of Rhodopsin Reveal Excited-State Population Splitting and its Effects on Quantum Efficiency. *Nat. Chem.* 14, 441. doi:10.1038/s41557-022-00892-6

Yasuda, S. I., Akiyama, T., Kojima, K., Ueta, T., Hayashi, T., Ogasawara, S., et al. (2022). Development of an Outward Proton Pumping Rhodopsin with a New Record in Thermostability by Means of Amino Acid Mutations. *J. Phys. Chem. B* 126, 1004. doi:10.1021/acs.jpcb.1c08684

Ye, S. X., Huber, T., Vogel, R., and Sakmar, T. P. (2009). FTIR Analysis of GPCR Activation Using Azido Probes. *Nat. Chem. Biol.* 5, 397–399. doi:10.1038/nchembio.167

Ye, S. X., Zaitseva, E., Caltabiano, G., Schertler, G. F. X., Sakmar, T. P., Deupi, X., et al. (2010). Tracking G-Protein-Coupled Receptor Activation Using Genetically Encoded Infrared Probes. *Nature* 464, 1386–1U14. doi:10.1038/nature08948

Yee, D. C., Shlykov, M. A., Västermark, A., Reddy, V. S., Arora, S., Sun, E. I., et al. (2013). The Transporter-Opsin-G Protein-Coupled Receptor (TOG) Superfamily. *FEBS J.* 280, 5780–5800. doi:10.1111/febs.12499

Yeh, V., Lee, T.-Y., Chen, C.-W., Kuo, P.-C., Shiue, J., Chu, L.-K., et al. (2018). Highly Efficient Transfer of 7TM Membrane Protein from Native Membrane to Covalently Circularized Nanodisc. *Sci. Rep.* 8, 13501. doi:10.1038/s41598-018-31925-1

Yi, A., Li, H., Mamaeva, N., De Cordoba, R. E. F., Lugtenburg, J., DeGrip, W. J., et al. (2017). Structural Changes in an Anion Channelrhodopsin: Formation of the K and L Intermediates at 80 K. *Biochemistry* 56, 2197–2208. doi:10.1021/acs.biochem.7b00002

Yi, A., Mamaeva, N., Li, H., Spudich, J. L., and Rothschild, K. J. (2016). Resonance Raman Study of an Anion Channelrhodopsin: Effects of Mutations Near the Retinylidene Schiff Base. *Biochemistry* 55, 2371–2380. doi:10.1021/acs.biochem.6b00104

Yizhar, O., Fenno, L. E., Davidson, T. J., Mogri, M., and Deisseroth, K. (2011). Optogenetics in Neural Systems. *Neuron* 71, 9–34. doi:10.1016/j.neuron.2011.06.004

Yokoyama, S. (1995). Amino Acid Replacements and Wavelength Absorption of Visual Pigments in Vertebrates. *Mol. Biol. Evol.* 12, 53–61. doi:10.1093/oxfordjournals.molbev.a040190

Yokoyama, S. (2000). Molecular Evolution of Vertebrate Visual Pigments. *Prog. Retin. Eye Res.* 19, 385–419. doi:10.1016/s1350-9462(00)00002-1

Yokoyama, S., and Yokoyama, R. (2000). "Comparative Molecular Biology of Visual Pigments," in *Molecular Mechanisms in Visual Transduction*. Editors D. G. Stavenga, W. J. DeGrip, and E. N. PughJr. (Amsterdam, Netherlands: Elsevier Science Pub.), 257–296. doi:10.1016/s1383-8121(00)80009-3

Yoshida, K., Yamashita, T., Sasaki, K., Inoue, K., Shichida, Y., and Kandori, H. (2017). Chimeric Microbial Rhodopsins for Optical Actvation of Gs-Proteins. *Biophysics physicobiology* 14, 183–190. doi:10.2142/biophysico.14.0_183

Yoshizawa, T., and Kandori, H. (1991a). Primary Photochemical Events in the Rhodopsin Molecule. *Prog. Retin. Res.* 11, 33–55. doi:10.1016/0278-4327(91)90023-u

Yoshizawa, T., and Kuwata, O. (1991b). Iodopsin, a Red-Sensitive Cone Visual Pigment in the Chicken Retina. *Photochem. Photobiol.* 54, 1061–1070. doi:10.1111/j.1751-1097.1991.tb02130.x

Yoshizawa, T. (1984). Photophysiological Functions of Visual Pigments. *Adv. Biophysics* 17, 5–67. doi:10.1016/0065-227x(84)90024-8

Yoshizawa, T., and Wald, G. (1967). Photochemistry of Iodopsin. *Nature* 214, 566–571. doi:10.1038/214566a0

Yoshizawa, T., and Wald, G. (1963). Pre-lumirhodopsin and the Bleaching of Visual Pigments. *Nature* 197, 1279–1286. doi:10.1038/1971279a0

Young, R. W. (1976). Visual Cells and the Concept of Renewal. *Investig. Ophthalmol. Vis. Sci.* 15, 700–725.

Yu, H., Siewny, M. G. W., Edwards, D. T., Sanders, A. W., and Perkins, T. T. (2017). Hidden Dynamics in the Unfolding of Individual Bacteriorhodopsin Proteins. *Science* 355, 945–949. doi:10.1126/science.aah7124

Yu, N., Huang, L., Zhou, Y. B., Xue, T., Chen, Z. G., and Han, G. (2019). Near-Infrared-Light Activatable Nanoparticles for Deep-Tissue-Penetrating Wireless Optogenetics. *Adv. Healthc. Mater.* 8, 1801132. doi:10.1002/adhm.201801132

Yu, S. M., Mcquade, D. T., Quinn, M. A., Hackenberger, C. P. R., Krebs, M. P., Polans, A. S., et al. (2000). An Improved Tripod Amphiphile for Membrane Protein Solubilization. *Protein Sci.* 9, 2518–2527. doi:10.1110/ps.9.12.2518

Yun, J.-H., Li, X. X., Park, J.-H., Wang, Y., Ohki, M., Jin, Z. Y., et al. (2019). Non-cryogenic Structure of a Chloride Pump Provides Crucial Clues to Temperature-dependent Channel Transport Efficiency. *J. Biol. Chem.* 294, 794–804. doi:10.1074/jbc.ra118.004038

Yun, J.-H., Li, X. X., Yue, J. N., Park, J.-H., Jin, Z. Y., Li, C. F., et al. (2021). Early-stage Dynamics of Chloride Ion-Pumping Rhodopsin Revealed by a Femtosecond X-Ray Laser. *Proc. Natl. Acad. Sci. U. S. A.* 118, 2020486118. doi:10.1073/pnas.2020486118

Yun, J.-H., Ohki, M., Park, J.-H., Ishimoto, N., Sato-Tomita, A., Lee, W., et al. (2020). Pumping Mechanism of NM-R3, a Light-Driven Bacterial Chloride Importer in the Rhodopsin Family. *Sci. Adv.* 6, eaay204. doi:10.1126/sciadv.aay2042

Zabelskii, D., Alekseev, A., Kovalev, K., Rankovic, V., Balandin, T., Soloviov, D., et al. (2020). Viral Rhodopsins 1 Are an Unique Family of Light-Gated Cation Channels. *Nat. Commun.* 11, 5707. doi:10.1038/s41467-020-19457-7

Zabelskii, D., Dmitrieva, N., Volkov, O., Shevchenko, V., Kovalev, K., Balandin, T., et al. (2021). Structure-based Insights into Evolution of Rhodopsins. *Commun. Biol.* 4, 821. doi:10.1038/s42003-021-02326-4

Zhang, J. Y., Choi, E. H., Tworak, A., Salom, D., Leinonen, H., Sander, C. L., et al. (2019). Photic Generation of 11-Cis-Retinal in Bovine Retinal Pigment Epithelium. *J. Biol. Chem.* 294, 19137–19154. doi:10.1074/jbc.ra119.011169

Zhang, L., Salom, D., He, J. H., Okun, A., Ballesteros, J., Palczewski, K., et al. (2005). Expression of Functional G Protein-Coupled Receptors in Photoreceptors of Transgenic *Xenopus laevis*. *Biochemistry* 44, 14509–14518. doi:10.1021/bi051386z

Zhang, L., Wang, K., Ning, S., Pedersen, P. A., Duelli, A. S., and Gourdon, P. E. (2022). Isolation and Crystallization of the D156C Form of Optogenetic ChR2. *Cells* 11, 895. doi:10.3390/cells11050895

Zhang, M., Gui, M., Wang, Z.-F., Gorgulla, C., Yu, J. J., Wu, H., et al. (2021a). Cryo-EM Structure of an Activated GPCR-G Protein Complex in Lipid Nanodiscs. *Nat. Struct. Mol. Biol.* 28, 258–267. doi:10.1038/s41594-020-00554-6

Zhang, S. S., Zheng, S. N., Sun, J. H., Zeng, X. X., Duan, Y. K., Luan, G. D., et al. (2021). Rapidly Improving High Light and High Temperature Tolerances of Cyanobacterial Cell Factories through the Convenient Introduction of an AtpA-C252f Mutation. *Front. Microbiol.* 12, 647164. doi:10.3389/fmicb.2021.647164

Zhang, T., Cao, L.-H., Kumar, S., Enemchukwu, N. O., Zhang, N., Lambert, A., et al. (2016). Dimerization of Visual Pigments *In Vivo*. *Proc. Natl. Acad. Sci. U. S. A.* 113, 9093–9098. doi:10.1073/pnas.1609018113

Zhang, X. M., Yokoyama, T., and Sakamoto, M. (2021b). Imaging Voltage with Microbial Rhodopsins. *Front. Mol. Biosci.* 8, 738829. doi:10.3389/fmolb.2021.738829

Zhang, Y., Iwasa, T., Tsuda, M., Kobata, A., and Takasaki, S. (1997). A Novel Monoantennary Complex-type Sugar Chain Found in octopus Rhodopsin: Occurrence of the Galβ1->3Fuc Group Linked to the Proximal *N*-Acetylglucosamine Residue of the Trimannosyl Core. *Glycobiology* 7, 1153–1158. doi:10.1093/glycob/7.8.1153

Zhao, D. Y., Pöge, M., Morizumi, T., Gulati, S., Van Eps, N., Zhang, J. Y., et al. (2019). Cryo-EM Structure of the Native Rhodopsin Dimer in Nanodiscs. *J. Biol. Chem.* 294, 14215–14230. doi:10.1074/jbc.ra119.010089

Zhao, Z. L., Wang, P., Xu, X. L., Sheves, M., and Jin, Y. D. (2015). Bacteriorhodopsin/Ag Nanoparticle-Based Hybrid Nano-Bio Electrocatalyst for Efficient and Robust H_2 Evolution from Water. *J. Am. Chem. Soc.* 137, 2840–2843. doi:10.1021/jacs.5b00200

Zhou, H.-X., and Cross, T. A. (2013). Influences of Membrane Mimetic Environments on Membrane Protein Structures. *Annu. Rev. Biophysics* 42, 361–392. doi:10.1146/annurev-biophys-083012-130326

Zhou, Y., Ding, M. Q., Duan, X. D., Konrad, K. R., Nagel, G., and Gao, S. Q. (2021). Extending the Anion Channelrhodopsin-Based Toolbox for Plant Optogenetics. *Membranes* 11, 287–281212. doi:10.3390/membranes11040287

Zou, L., Tian, H. H., Guan, S. L., Ding, J. F., Gao, L., Wang, J. F., et al. (2021). Self-assembled Multifunctional Neural Probes for Precise Integration of Optogenetics and Electrophysiology. *Nat. Commun.* 12, 5871–58715879. doi:10.1038/s41467-021-26168-0

Zundel, G. (1988). "Hydrogen-bond Systems as Proton Wires Formed by Side Chains of Proteins and by Side Chains and Phosphates," in *Transport through Membranes: Carriers, Channels and Pumps*. Editor A. Pullman (Dordrecht, Netherlands: Kluwer Academic Publishers), 409–420. doi:10.1007/978-94-009-3075-9_27

Conflict of Interest: The authors declare that the research was conducted in the absence of any commercial or financial relationships that could be construed as a potential conflict of interest.

Publisher's Note: All claims expressed in this article are solely those of the authors and do not necessarily represent those of their affiliated organizations, or those of the publisher, the editors and the reviewers. Any product that may be evaluated in this article, or claim that may be made by its manufacturer, is not guaranteed or endorsed by the publisher.

frontiers | Frontiers in Chemistry

ORIGINAL RESEARCH
published: 13 September 2022
doi: 10.3389/fchem.2022.877618

Synthesis and Biological Evaluation of Termini-Modified and Cyclic Variants of the Connexin43 Inhibitor Peptide5

Sin Hang Crystal Chan[1], *Jarred M. Griffin*[2], *Connor A. Clemett*[2], *Margaret A. Brimble*[1,3,4], *Simon J. O'Carroll*[2]* *and Paul W. R. Harris*[1,3,4]*

[1]School of Chemical Sciences, The University of Auckland, Auckland, New Zealand, [2]Centre for Brain Research, Department of Anatomy and Medical Imaging, Faculty of Medical and Health Sciences, University of Auckland, Auckland, New Zealand, [3]School of Biological Sciences, The University of Auckland, Auckland, New Zealand, [4]Maurice Wilkins Centre for Molecular Biodiscovery, The University of Auckland, Auckland, New Zealand

Peptide5 is a 12–amino acid mimetic peptide that corresponds to a region of the extracellular loop 2 (EL2) of connexin43. Peptide5 regulates both cellular communication with the cytoplasm (hemichannels) and cell-to-cell communication (gap junctions), and both processes are implicated in neurological pathologies. To address the poor *in vivo* stability of native peptide5 and to improve its activity, twenty-five novel peptide5 mimetics were designed and synthesized. All the analogues underwent biological evaluation as a hemichannel blocker and as a gap junction disruptor, and several were assessed for stability in human serum. From this study, it was established that several acylations on the *N*-terminus were tolerated in the hemichannel assay. However, the replacement of the L-Lys with an *N*-methylated L-Lys to give H-VDCFLSRPTE-*N*-MeKT-OH showed good hemichannel and gap junction activity and was more stable in human serum. The cyclic peptide variants generally were not tolerated in either the hemichannel and gap junction assay although several possessed outstanding stability in human serum.

Keywords: connexin43, gap junctions, hemichannels, peptide5, peptide mimetics

OPEN ACCESS

Edited by:
John D. Wade,
University of Melbourne, Australia

Reviewed by:
Richard J Clark,
The University of Queensland, Australia
Thomas Handley,
University of Melbourne, Australia

***Correspondence:**
Simon J. O'Carroll
s.ocarroll@auckland.ac.nz
Paul W. R. Harris
paul.harris@auckland.ac.nz

Specialty section:
This article was submitted to Chemical Biology, a section of the journal Frontiers in Chemistry

Received: *16 February 2022*
Accepted: *20 May 2022*
Published: *13 September 2022*

Citation:
Crystal Chan SH, Griffin JM, Clemett CA, Brimble MA, O'Carroll SJ and Harris PWR (2022) Synthesis and Biological Evaluation of Termini-Modified and Cyclic Variants of the Connexin43 Inhibitor Peptide5. Front. Chem. 10:877618. doi: 10.3389/fchem.2022.877618

1 INTRODUCTION

Connexin43 (Cx43) is a member of the gap junction protein family and is found widely throughout the body (Oyamada et al., 2005). Cx43 plays a crucial role in tissue function, allowing cell-to-cell communication via the formation of gap junctions (Márquez-Rosado et al., 2012). Connexin proteins are membrane-bound proteins that consist of cytoplasmic N- and C-termini, four transmembrane domains, a cytoplasmic loop, and two highly conserved extracellular loops (EL1 and EL2) (Ribeiro-Rodrigues et al., 2017). Within the cell membrane, six connexin proteins oligomerize to form a connexon, and connexons on adjacent cell membranes align and dock via EL1 and EL2 to form an intercellular gap junction channel (Li et al., 1996). The gap junctions allow for the movement of ions and other small molecules between cells, which is crucial for cell function and survival (Krysko et al., 2005). Within the central nervous system, Cx43 gap junctions form a syncytium and provide a high degree of cell-to-cell communication, especially in endothelial and glial cells (Sarrouilhe et al., 2017). The injury or inflammation of the central nervous system leads to the upregulation and opening of unopposed connexons (hemichannels) (Xing et al., 2019). This creates a conduit between the intra- and extra-cellular environment allowing the movement of water and small molecules. The opening of connexin hemichannels negatively impacts a cell's ability to osmoregulate (Quist et al., 2000;

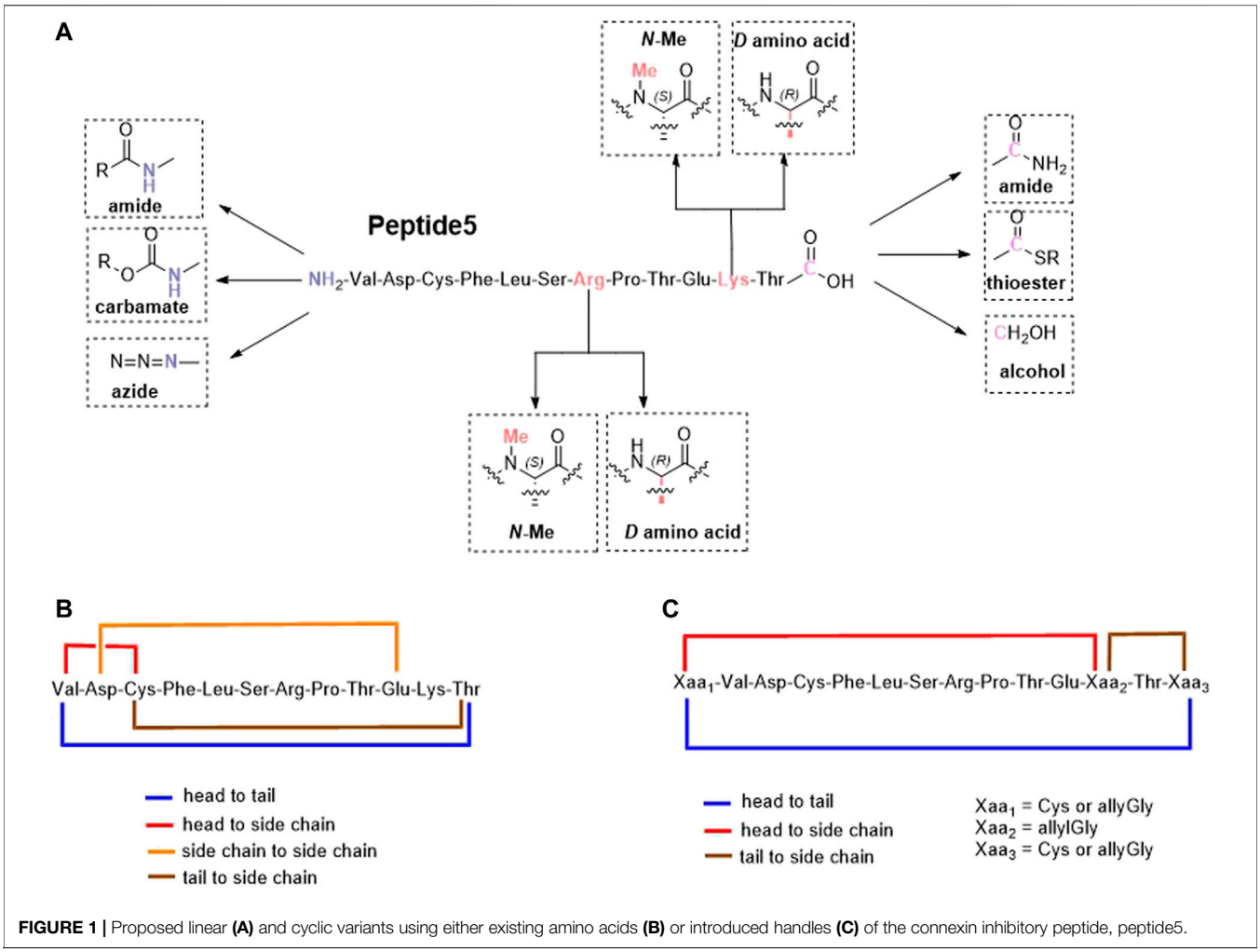

FIGURE 1 | Proposed linear **(A)** and cyclic variants using either existing amino acids **(B)** or introduced handles **(C)** of the connexin inhibitory peptide, peptide5.

Rodríguez-Sinovas et al., 2007; Danesh-Meyer et al., 2012), leading to cell edema (Quist et al., 2000), excitotoxic neuronal cell death (Froger et al., 2010), glial cell activation (Li et al., 1996), vascular hemorrhage (De Bock et al., 2011), and ultimately the spread of secondary damage (Davidson et al., 2013.; Decrock et al., 2015). The opening of Cx43 hemichannels has been shown to be a major contributor to a number of CNS pathologies including retinal ischemia–reperfusion injury (Danesh-Meyer et al., 2012), spinal cord injury (O'Carroll et al., 2008; O'Carroll et al., 2013; Tonkin et al., 2015), preterm ischemia and asphyxiation (Davidson et al., 2012; Davidson et al., 2014), and infection (Eugenin et al., 2011). As such, targeting Cx43 hemichannels has potential as a treatment for neurological conditions.

One approach to target Cx43 hemichannels has been the use of peptidomimetics that target the EL1 and EL2 extracellular loops of Cx43 (gap26, gap27, and peptide5) (Evans, 2015) or intracellular regions of the protein (gap19, ACT-1) (D'hondt et al., 2013). The extracellular targeting of peptide5, H_2N-VDCFLSRPTEKT-CO_2H (O'Carroll et al., 2008), has been shown to selectively target either hemichannels or gap junctions in a concentration-dependent manner, with concentrations as low as 5 μM selectively inhibiting hemichannels and higher concentrations (e.g., 500 μM), inhibiting both gap junctions and hemichannels *in vitro*. This ability to selectively target pathological hemichannels whilst not interfering with the normal function of gap junctions presents the opportunity for therapeutic applications and Peptide5 has shown benefit in reducing inflammation, vascular breakdown, neuronal survival, and improved functional outcomes in a number of models of CNS injury such as brain ischemia–reperfusion injuries (Davidson et al., 2012, 2014), retinal injury and disease (Danesh-Meyer et al., 2012; Guo et al., 2016; Mugisho et al., 2019; Kuo et al., 2020), and spinal cord injury (O'Carroll et al., 2013; Mao et al., 2017). Despite these advances, further work is required to maximize both the efficacy and serum stability of peptide5-based therapeutic candidates to demonstrate their potential as agents to treat human diseases. Generally speaking, short native, unmodified peptides (< 20 amino acids) are rapidly cleared or degraded *in vivo* due to the action of proteases and/or filtration by the kidneys. The peptides are also limited in that they are unable

to cross cell membranes due to polar functional groups and low lipophilicity leading to low bioavailability. A variety of chemical modifications have been employed to render peptides more suitable for human therapeutics (Muttenthaler et al., 2021) including lipidation (Zhang and Bulaj, 2012), glycosylation (van Witteloostuijn et al., 2016), cyclization (Bechtler and Lamers, 2021), and modification of individual amino acids (Gentilucci et al., 2010); these improvements are exemplified by the ever-increasing clinical application of peptides for use in cancer, infectious diseases, and diabetes (D'Aloisio et al., 2021; de la Torre and Albericio, 2020).

We report herein our efforts in designing, synthesizing, and evaluating 25 novel linear and cyclic peptide5 analogues (**Figure 1**) as inhibitors of connexin hemichannels and gap junctions as well as assessing their stability in human serum. All peptides were readily generated via solid-phase peptide synthesis. It was found that most of the modifications to peptide5 resulted in the loss of activity in both a hemichannel inhibition assay and a gap junction dye spread assay. Several linear peptide5 analogs exhibiting *N*-terminal acylation did show activity comparable to peptide5 in their ability to block hemichannels, while all the cyclic peptide5 congeners failed to demonstrate significant hemichannel activity compared to the peptide5 control. Several D- or *N*-methylated variants of linear peptide5 were both shown to have gap junction activity similar to that of peptide5 and were significantly more stable in human serum.

2 RESULTS

In our previous studies on peptide5 (**1**), we constructed a 42-peptide library of *S*-lipidated linear analogues modified at six different amino acid positions (Yang et al., 2020) that were informed by the results of our preliminary alanine scan study (Kim et al., 2017a). While it was shown that lipidation at certain residues was tolerated and, in some cases improved connexon hemichannel blocking, (rat) serum stability of the lipidated peptides was not improved relative to peptide5 which had a short half-life of just 5 min. This suggested that the individual amino acids are responsible for the degradation of peptide5 and that modification of specific amino acids was required to improve the stability, whilst maintaining connexin blocking activity.

Lipidation is only one of several methods employed to improve the stability, permeability, and half-life of peptides that include the incorporation of non-canonical amino acids, D- and *N*-methylated amino acids, and modification of the C- and *N*-termini including cyclization (Erak et al., 2018). Cyclization, in particular, is also known to rigidify the peptide backbone, reducing the number of possible conformers and promoting binding to its intended target (Philippe et al., 2021). An exquisite example of this is the FDA-approved macrocyclic peptide cilengitide which displayed a 10-fold increase in binding compared to its linear form. (Kumagai et al., 1991). Based on the aforementioned considerations, we proposed to synthesize peptide5 analogues as depicted in **Figure 1**. These analogues included modification of both the C- and

TABLE 1 | A summary of all linear and cyclic variants of the connexon43 inhibitor peptide. Peptide5 prepared. The chemical changes are highlighted in bold.

Number	Structure
1 (Peptide5)	H_2N-VDCFLSRPTEKT-CO_2H
2	**CH_3CH_2OCO**-NH-VDCFLSRPTEKT-CO_2H
3	**$(CH_3)_2CH_2CH_2OCO$**-NH-VDCFLSRPTEKT-CO_2H
4	**PhCO**-NH-VDCFLSRPTEKT-CO_2H
5	**$CH_3CH_2CH_2CO$**-NH-VDCFLSRPTEKT-CO_2H
6	**N_3**-VDCFLSRPTEKT-CO_2H
7	H_2N-VDCFLSRPTE-***N*-Me-K**T-CO_2H
8	H_2N-VDCFLS-***N*-Me-R**PTEKT-CO_2H
9	H_2N-VDCFLSRPTE**k**T-CO_2H
10	H_2N-VDCFLS**r**PTEKT-CO_2H
11	**CH_3CH_2OCO**-NH-VDCFLSRPTEKT-**$CONH_2$**
12	**$(CH_3)_2CH_2CH_2OCO$**-NH-VDCFLSRPTEKT-**$CONH_2$**
13	**PhCO**-NH-VDCFLSRPTEKT-**$CONH_2$**
14	**$CH_3CH_2CH_2CO$**-NH-VDCFLSRPTEKT-**$CONH_2$**
15	H_2N-VDCFLSRPTEKT-**CH_2OH**
16	H_2N-VDCFLSRPTEKT-**$COSCH_2CH_2Gly\text{-}CO_2H$**
21	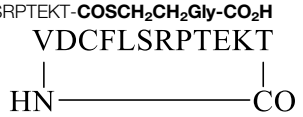
22	
25	
28	
32	
34	
37	
39	
40	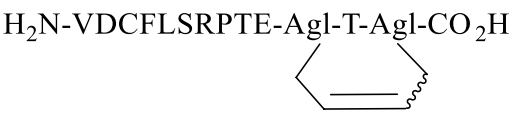
42	

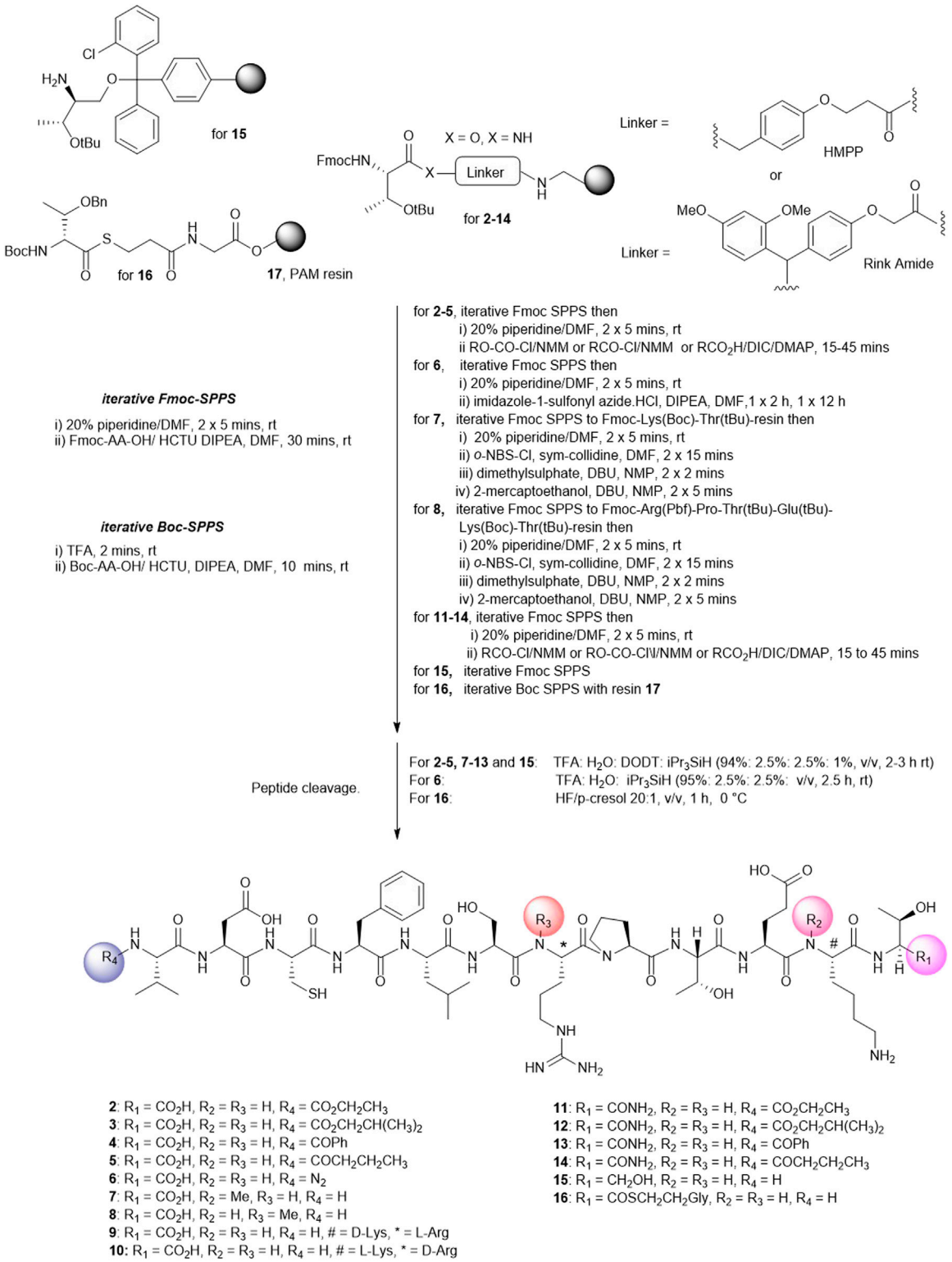

FIGURE 2 | Solid phase synthesis strategy to prepare linear Peptide5 analogues modified at the C- and Ntermin and D and N-Me variants.

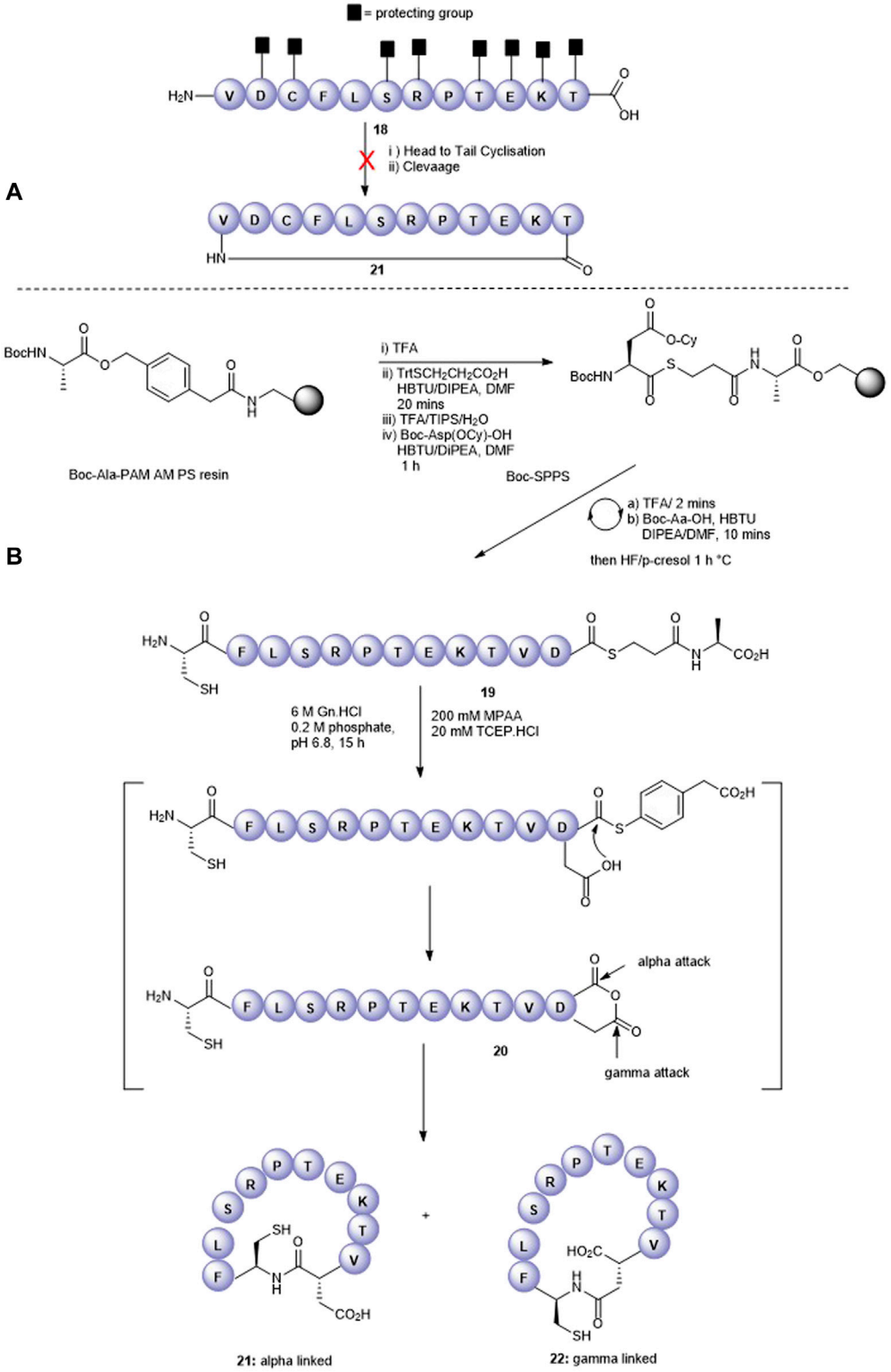

FIGURE 3 | Unsuccessful cyclization attempt to prepare cyclic peptide5 **21 (A)** and the successful strategy employing native chemical ligation **(B)**.

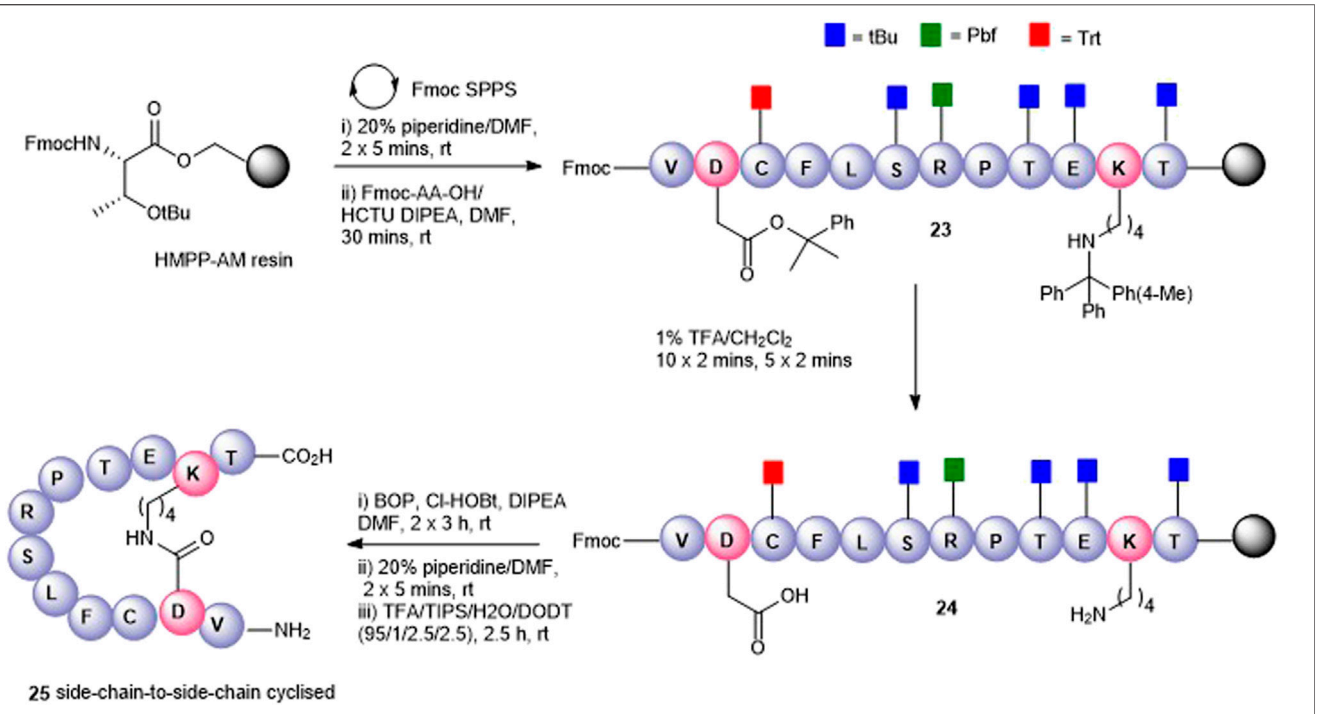

FIGURE 4 | Synthesis of the Asp2-Lys11 side-chain–to–side-chain cyclized peptide5 (**25**).

N-termini and replacement of enzymatically susceptible Arg and Lys by their D- and *N*-methylated variants. The cyclic peptide5 analogues were prepared using the side chains and the C- and *N*-termini already present in the primary sequence or employing introduced chemical handles to affect cyclization.

2.1 Synthesis of linear peptides modified at the C- and *N*-termini, and incorporation of non-proteogenic amino acids

We commenced by designing and synthesizing a set of linear peptides that 1) were modified at the *N*-terminus by acylation or by converting the amine group to an azide; 2) replaced the C terminal carboxy group with a carboxamide and capping of the *N*-terminus by acylation; 3) replaced the trypsin-susceptible amino acids, Arg-7 and Lys-11 with their D- or *N*-methylated congeners; and 4) replaced the C terminal carboxy group with a carboxamide, a thioester, or an alcohol. The synthesis of these sixteen analogues is depicted in **Figure 2**. These modifications were in line with our alanine scan data which demonstrated that replacement of each amino acid by alanine had little effect on gap junction uncoupling (Kim et al., 2017b).

The analogues of Peptide5 capped at the N-terminus (**2–5**) were readily prepared on Fmoc-Thr (tBu) esterified hydroxymethylphenoxypropionic acid (HMPP) linker functionalized on aminomethyl polystyrene resin. Following the peptide chain assembly, the final Fmoc group was removed and the N-terminal amino group reacted with either ethyl chloroformate/*N*-methylmorpholine (NMM), isobutyl chloroformate/NMM, benzoyl chloride/NMM, or butyric acid in the presence of the acylating reagents diisoproylcarbodiimide (DIC)/catalytic dimethylaminopyridine (DMAP) to effect amidation. In all cases, a single treatment was required, and all compounds were recovered in >95% purity following HPLC purification (see **Supplementary Material**).

For azide analogue **6**, the azide transfer reagent, imidazole-1-sulfonyl azide.HCl (Goddard-Borger and Stick, 2007), reacted directly with the *N*-terminal amino group of the resin-bound peptide. In this case, two treatments were required for complete conversion, and importantly, no thiol scavenger (DODT) was used for the peptide cleavage cocktail to mitigate the potential reduction of the azide to the amine.

N-methylated Arg-7 and Lys-11 peptides (**7** and **8**) could be accessed by adopting the on-resin *N*-methylation protocol developed by Kessler (Chatterjee et al., 2012). Following Fmoc removal at the amino acid site of putative N-methylation, the amino group was nosylated affording a sulfonamide. Methylation of the sulfonamide (dimethylsulfate/DBU) and removal of the nosyl group (2-mecaptoethanol/DBU) yielded the *N*-methylated peptides. The elongation of the peptide sequence, resin cleavage, and HPLC purification gave **7** and **8** in high purity. No difficulties were encountered when coupling the subsequent Fmoc amino acid to the sterically

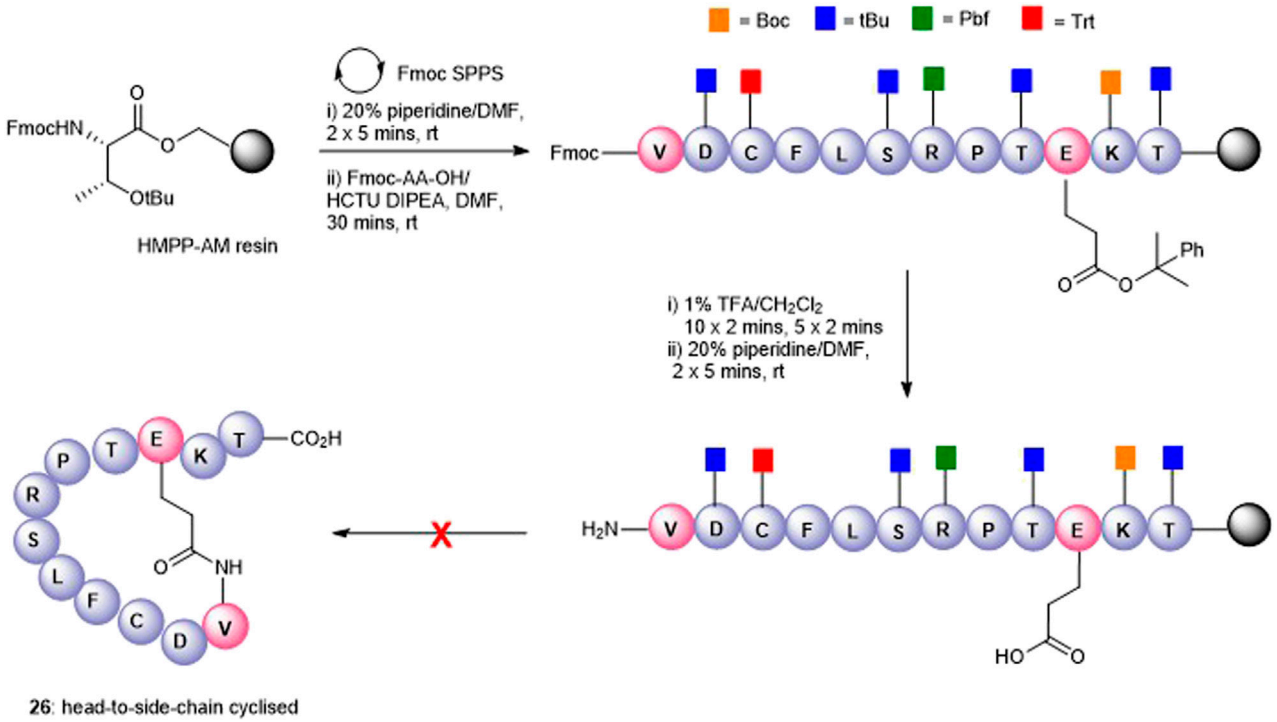

FIGURE 5 | Unsuccessful synthesis of Glu10-Val1 side-chain-to-head cyclized peptide5 **26**.

hindered, resin-bound *N*-methylated amino acid. For the synthesis of peptide5 containing D-amino acids at Lys-11 (**9**) and Arg-7 (**10**), Fmoc-D-Lys (Boc)-OH or Fmoc-D-Arg (Pbf)-OH was used at the appropriate positions during the Fmoc SPPS assembly.

Finally, the peptide analogues modified at the C-terminus (**11**–**16**) were prepared on the appropriate linker resin. Carboxamides (**11**–**14**) were assembled on a Rink amide linker using Fmoc SPPS and were *N*-terminally modified according to the protocols outlined for peptides **2**–**5**. C-terminal alcohol **15** was directly accessible from the 2-chlorotrityl resin functionalized with *tert*-butyl–protected Fmoc-threoninol using Fmoc SPPS. Thioester **16** was best prepared using the thioester generating resin **17** (Camarero et al., 2000) and employing Boc SPPS to avoid aminolysis of the thioester linkage, a known concern when employing piperidine as an Fmoc deblocking reagent during Fmoc synthesis (Li et al., 1998).

2.1.1 Synthesis of Cyclic Peptides Using Pre-Existing Amino Acids

We next attempted to cyclize the C- and *N*-termini of the maximally side-chain–protected peptide **18** to obtain cyclic analogue **21**. In turn, protected peptide **18** was prepared on the hyper acid-labile 2-chloro trityl resin (**Figure 3A**). However, using HBTU or BOP-Cl/DMAP as condensation reagents was unsuccessful and none of the expected head-to-tail cyclic products was detected after side-chain deprotection and LC-MS analysis. This is most likely due to the difficult cyclization site that contains the bulky, secondary amino acids, valine and threonine. We therefore repositioned the cyclization site to the Asp-Cys junction as we anticipated that using native chemical ligation (NCL) (Dawson et al., 1994), the chemoselective amide bond-forming reaction between a cysteinyl peptide and peptide thioester would furnish the desired cyclic peptide **21** (**Figure 3B**).

The linear thioester precursor, CFLSRPTEKTVD-COS-CH_2CH_2Ala-OH **19**, was prepared satisfactorily using Boc SPPS and then directly subjected to NCL conditions (0.2 M phosphate, 6 M Gn.HCl, 20 mM TCEP.HCl, and 200 mM 4-mercaptophenyl acetic acid [MPAA]) for 15 h which afforded a separable mixture (2:1) of the desired cyclic product **21** (calc $(M + H)^+$ 1378.6, found 1378.4) and undesired product **22** (calc $(M + H)^+$ 1378.6, found 1378.5) (**Figure 3B**). This was not unexpected as ligation between Asp and Cys has been reported (Villain et al., 2003) to result in the formation of the unnatural β amide bond as a by-product (20%–30%) (Dang et al., 2013) by the formation of an intermediate succinic anhydride **20** which can undergo aminolysis at either carbonyl group. Fortunately, in the present work, the undesired isomeric by-product **22** was easily separated from the desired product **21** using RP-HPLC.

Having successfully prepared the head-to-tail cyclic variant of peptide5 (**21**), we next focused on constraining the peptide via its

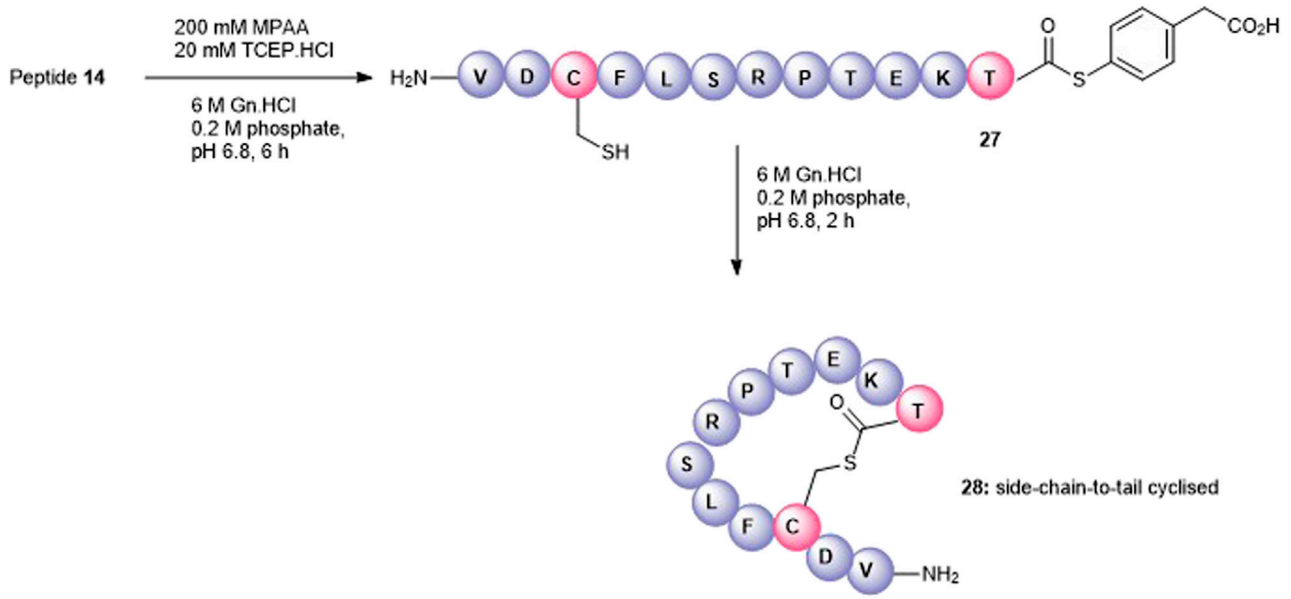

FIGURE 6 | Synthesis of the Cys3-Thr12 thioester-linked side-chain-to-tail cyclized peptide5 (**28**).

amino acid side chains. An alanine scan (Kim et al., 2017a) revealed that all amino acids could be modified with no significant loss in gap junction uncoupling, although some replacements abolished hemichannel blocking activity. We first pursued the preparation of an amide linkage between Asp and Lys (**Figure 4**). This is most easily accomplished on the solid support whereby the pseudo-dilution effect minimizes unwanted dimerization or oligomerization that prevails under solution-phase conditions. Furthermore, the coupling reaction can be conveniently monitored by the Kaiser test that determines any free primary amines.

To maximize synthetic efficiency, the 4-methyltriphenylmethyl (Mtt)– and 2-phenylisopropyl (2-Ph^{i}Pr)–protecting groups were used on the Lys and Glu side chains, respectively, as these can be removed simultaneously with diluted TFA, selectively unmasking the amine and carboxylic acid functionalities for subsequent lactamisation leaving other side-chain–protecting groups unmodified. Thus, resin-bound peptide **23** was assembled by Fmoc SPPS on Fmoc-Thr (O^{t}Bu)-HMPP resin using 20% piperidine in DMF for Fmoc removal and HCTU/DIPEA for coupling. Orthogonally protected Fmoc-Lys (Mtt)-OH and Fmoc-Asp(O-2-Ph^{i}Pr) were incorporated uneventfully and the Mtt and 2-Ph-^{i}Pr side-chain–protecting groups both cleaved upon repetitive treatments with 1% TFA in CH_2Cl_2 to give **24**. The key macrolactamization step was then explored on resin using PyBOP/Cl-HOBt, DIC/HOAt, DIC/Oxyma, or BOP/Cl-HOBt as condensation reagents. Employing PyBOP- or DIC-based couplings led to aspartimide formation (PyBOP), no reaction or incomplete reaction (DIC/HOAt), or a complex mixture (DIC/Oxyma). PyBOP/Cl-HOBt (2 × 3 h) proved to be the optimal coupling reagents and affording the desired cyclic peptide **25** in >90% conversion as judged by LC-MS (calc $(M + H)^+$ 1378.6, found 1378.6) that was easily purified by RP-HPLC.

The attempts to form the head-to-side-chain macrolactamisation **26** by on-resin coupling of the *N*-terminal amino group and the side-chain carboxylic acid of Glu using the orthogonal protecting strategy as described above met with failure (**Figure 5**). Extensive oligomerization was observed using several different coupling conditions and the use of a lower loading resin, or PEG-based resins had little effect on the success of the reaction.

Satisfactorily, a side-chain-to-tail mode of macrocyclization was effected by the selective condensation of Cys with the C-terminal threonyl aryl thioester at neutral pH (**Figure 6**). The precursor and less reactive alkyl thioester, **14**, was quantitatively transformed into the more reactive aryl thioester **27** (calc $(M+2H)^{2+}$ 773.8, found 773.4) using the water-soluble aryl thiol, MPAA (Johnson and Kent, 2006) at pH 6.5 after 6 h and isolated by SPE. We anticipated that at neutral pH in the absence of added thiols, the cysteine thiol would undergo transthioesterfication with the activated C-terminus in an irreversible manner. Thus, **27** (2 mM) was dissolved in 0.2 M phosphate/6 M Gn.HCl, at pH = 6.7, and the cyclization was monitored by RP-HPLC. After 2 h, the linear polypeptide was quantitatively converted into the side-chain-to-tail macrocyclic thiolactone **28** (calc $(M+2H)^{2+}$ 689.8, found 689.4) as the sole product that was easily recovered by RP-HPLC.

2.1.2 Synthesis of Cyclic Peptides Using Introduced Handles

Disulfide bonds, the covalent linkage formed between two cysteines, are naturally occurring structure-stabilizing motifs

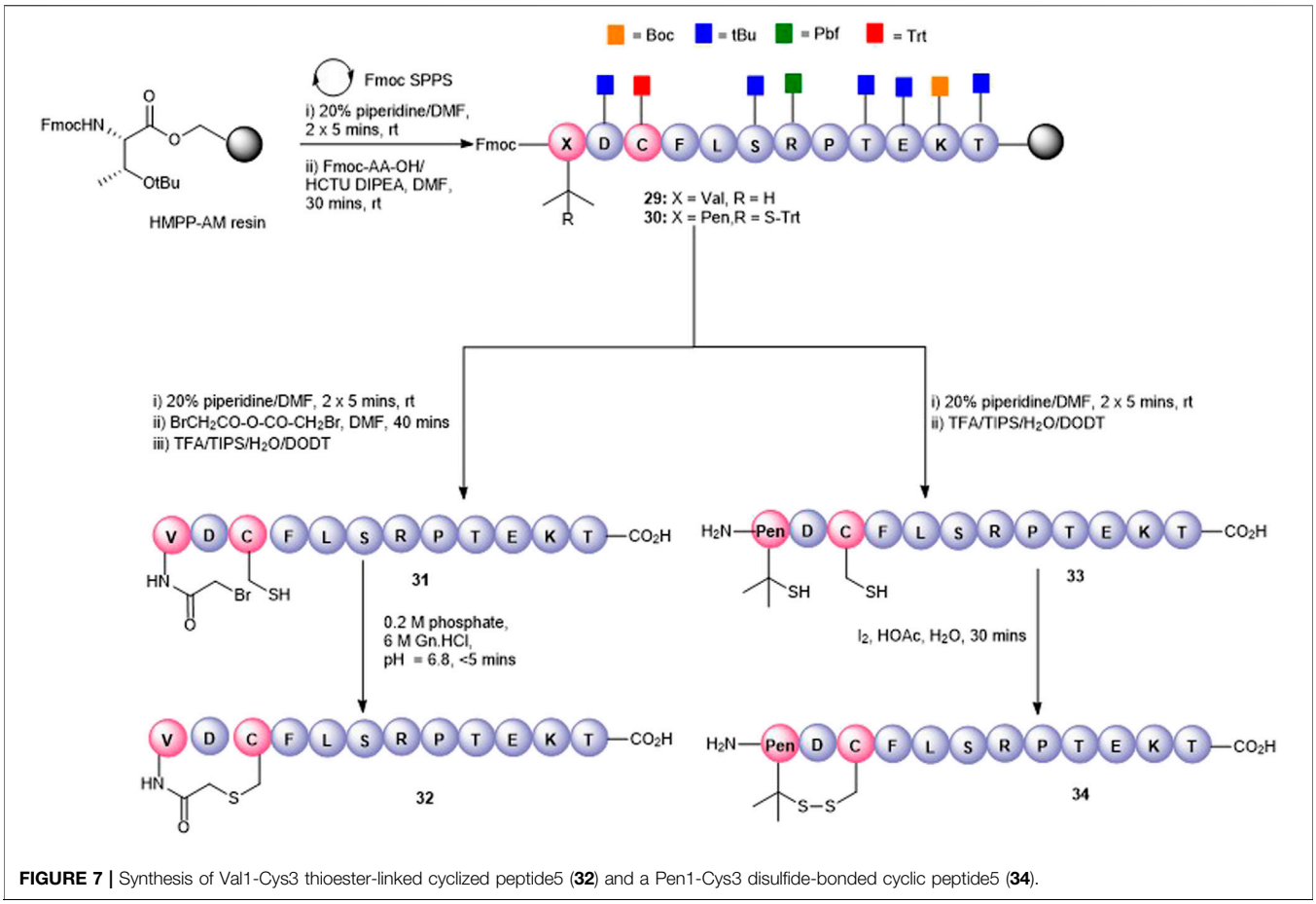

FIGURE 7 | Synthesis of Val1-Cys3 thioester-linked cyclized peptide5 (**32**) and a Pen1-Cys3 disulfide-bonded cyclic peptide5 (**34**).

that are important for maintaining the structure and function of proteins and peptides. Not surprisingly, they have been also been employed for peptide cyclization to confer structural rigidity on synthetic peptides, leading to higher affinity to target receptors (Góngora-Benítez et al., 2014). Peptide5 contains a single cysteine residue (Cys3) that could be used as a cyclization handle, though our alanine scanning data suggested that this residue could not be altered without some loss of hemichannel activity. However, the *N*-terminal valine (Val1) residue could be modified as the substitution of Val1 to Ala caused little effect in activity (Kim et al., 2017b) in both hemichannel and gap junction assays. Furthermore, a truncated peptide5, SRPTEKT, was equally effective as a gap junction inhibitor, suggesting that the *N*-terminal residues, VDCFL, could be modified. Therefore, we used Cys3 to 1) create a thioether bridge by intramolecular chemo-selective alkylation of Cys-SH with the *N*-terminus capped with a 2-bromoacetyl group or 2) to form a disulfide bond between Cys-SH and β,β-dimethylcysteine (penicillamine, Pen) introduced as a substitute for Val1. A disulfide-linked head-to-tail cyclic peptide was also proposed by introducing a cysteine adjacent to both the C- and *N*-termini as cyclization handles enabling subsequent oxidation to the disulfide.

The thioether macrocycle (**32**, **Figure 7**) was prepared by acylation of the resin-bound *N*-terminus (**29**) with bromoacetic acid anhydride (Robey and Fields, 1989), followed by cleavage from the resin to afford the *N*-bromoacetylated peptide **31** (calc $(M+2H)^{2+}$ 759.2, found 758.3). Spontaneous cyclization then took place by exposing the crude peptide to an aqueous buffer (pH = 6.9) to afford the thioether **32** (calc $(M+2H)^{2+}$ 717.8, found 718.4) in 20% yield.

To effect the disulfide head-to-side-chain–linked macrocycle (**34**, **Figure 7**), commercially available Fmoc-Pen (Trt)-OH was coupled with the resin-bound peptide in lieu of Fmoc-Val to afford **30**. Following final Fmoc removal and recovery of the peptide by cleavage from the resin, the crude peptide (**33**) was subjected to several oxidative folding conditions. Stirring in aqueous buffer (0.1 M tris, pH = 7.9) at room temperature or heating at 37°C gave no reaction or undesired by-products. Using 4,4′-dithiodipyridine (DTDP) in DMSO or the more reactive 5,5′-dithiobis-(2-nitrobenzoic acid) (DTNB) in 4:1 HOAc:water gave mostly unoxidized peptide after 24 h and unknown by-products. Employing I_2 in 4:1 HOAc:water resulted in quantitative conversion to the expected disulfide **34** (calc. $M+2H)^{2+}$ 713.8, found 713.4) which was consistent with the expected loss of 2 Da.

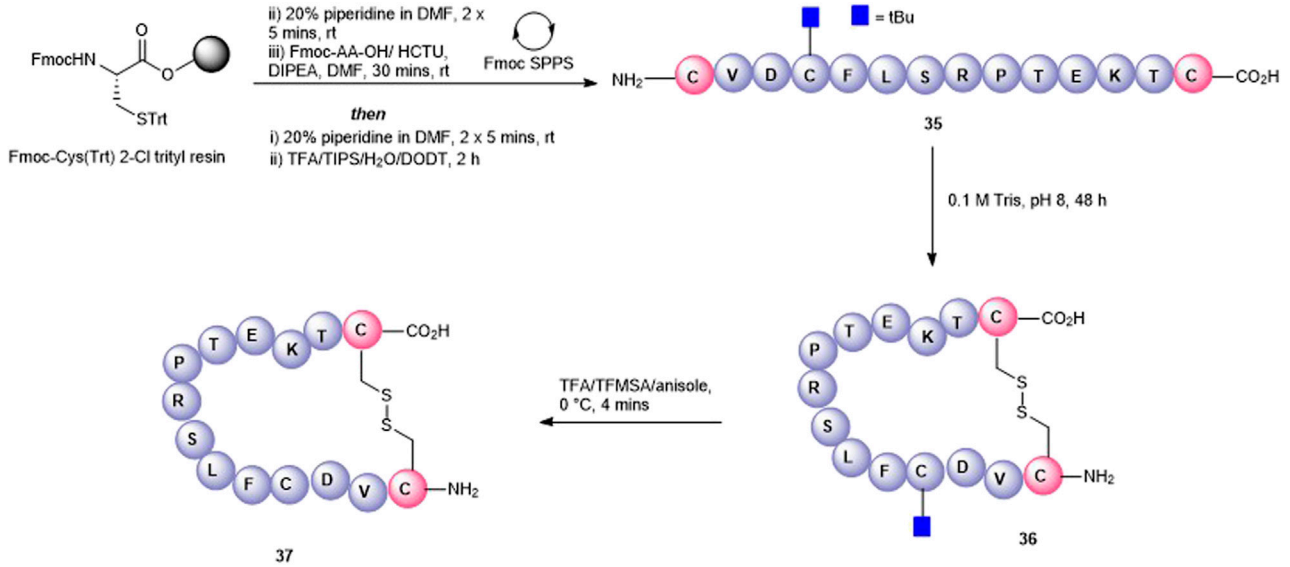

FIGURE 8 | Synthesis of a disulfide-linked head-to-tail macrocycle **37** via introduction of Cys at the C- and *N*-termini.

Finally, a disulfide head-to-tail peptide5 analogue (**37, Figure 8**) was accessed from peptide **35** prepared on a 2-chlorotrityl resin. In this case, Cys3 required orthogonal protection on the sulfhydryl so that the disulfide bond between the two Cys at either end of the peptide could be formed selectively. In contrast to the oxidation of **33**, oxidation of **35** proceeded readily in the air (0.1 M Tris buffer, pH = 8.1) with no exogenous reagents required to afford **36** (calc $(M+2H)^{2+}$ 825.9, found 825.5). A noticeable shift in HPLC retention time (see SI) was observed for the disulfide-containing peptide **36** compared to the free thiol-containing peptide **35**. The subsequent unmasking of Cys3 with TFA/TFMSA afforded **37** (calc. $(M+2H)^{2+}$ 800.9, found 800.4) in 22% yield.

Olefin metathesis has been demonstrated as an exquisite way to prepare cyclic peptides containing all carbon bridges (coined "stapling") (Miller et al., 1996) and is most often used to stabilize alpha-helical peptides (Schafmeister et al., 2000). In our case, we employed olefin metathesis to prepare three further cyclic peptide5 variants; a head-to-tail analogue **39**, a head-to-side chain analogue **42**, and a tail-to-side-chain analogue **40**. Fmoc-(*S*)-allylGly (AgI), a commercially available chiral alkenyl amino acid, was employed to introduce the required olefin at positions adjacent to the *N*- and C-termini and at Lys-11, a position known to tolerate substitution in gap junction unblocking.

The head-to-tail cyclic variant **39** was obtained through ring-closing metathesis (RCM) of peptidyl-resin **38** containing two allylglycine (Agl) residues adjacent to the *N*- and C-terminal amino acids using 30 mol% Hoveyda-Grubbs' II catalyst in DMF/CH_2Cl_2 100°C for 2 h (**Figure 9**). These conditions had previously been employed by us in the synthesis of carba analogues of dianthin G (Amso et al., 2016). The side-chain–protecting groups were removed using the standard TFA cleavage cocktail to afford crude product. Although the expected product **39** was observed by HPLC and MS (calc $[M + H]^+$ 1561.8 found 1560.0), the complicated HPLC profile precluded subsequent purification. The reaction conditions were modified to two 1-h treatments at 100°C using fresh 30 mol% Hoveyda-Grubbs' II catalyst in each instance. This resulted in a better HPLC profile and the cyclic product (**39**) was easily purified.

A tail-to-side-chain carba analogue (**40**) was prepared by RCM of peptidyl resin (**41**) containing an allylGly at the C-terminus and at Lys11 (**Figure 10**). A single treatment using 30 mol% Hoveyda–Grubbs' II catalyst at 100°C for 2 h afforded the cyclized side-chain–protected product which upon cleavage from the resin and side-chain deprotection using the TFA cocktail yielded the cyclic RCM product **40** (calc $[M + H]^+$ 1433.7, found 1433.5) which was recovered by semi-preparative HPLC. The clean HPLC profile in this instance may be reflective of the smaller macrocyclic ring formed in this analogue.

Finally, a head-to-side-chain variant (**42**) was accessed through RCM of peptidyl resin **43** containing an allylGly at Lys11 and adjacent to the *N*-terminus (**Figure 10**). In this case, two 1-h treatments at 100°C each in the presence of 30 mol% Hoveyda–Grubbs' II catalyst were required for complete conversion to the desired macrocycle **42**. Following resin cleavage, an extremely clean HPLC chromatogram was observed (see SI) with the MS of the major peak being consistent for **42** (calc $[M + H]^+$ 1434.7, found 1434.6).

For the three carba analogues **39**, **42**, and **40** obtained by RCM, it was postulated that a mixture of *E* and *Z* isomers were present. No attempt was made to determine the *E*/*Z* ratio or to separate

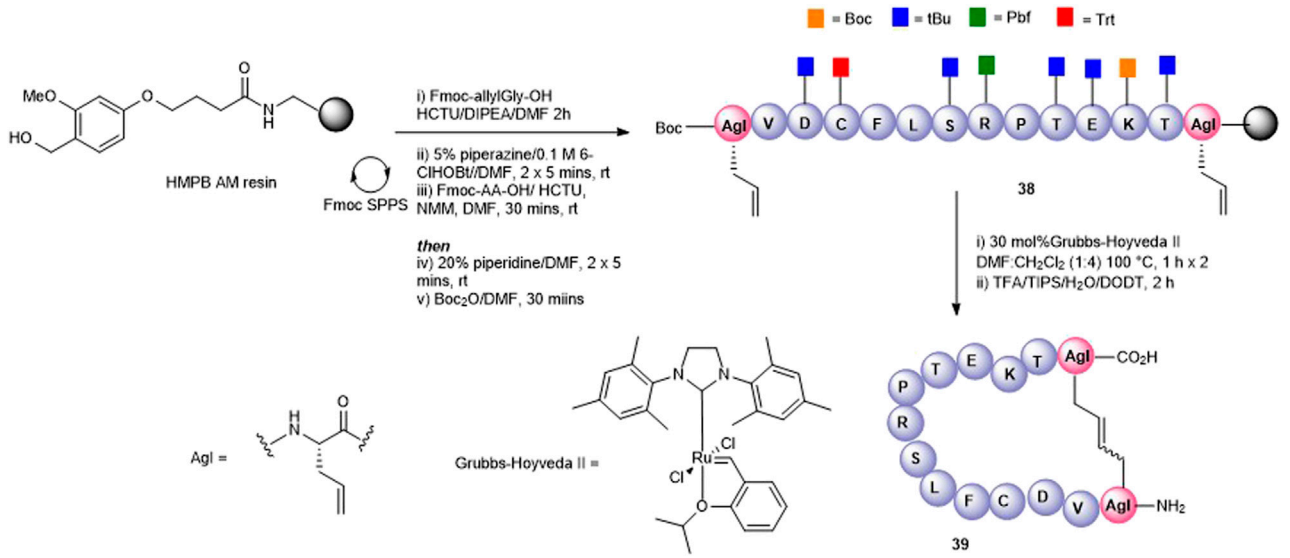

FIGURE 9 | Synthesis of an all-carba head-to-tail macrocycle **37** via the introduction allylGly (Agl) at the C- and *N*-termini and ring-closing metathesis.

out each individual isomer, and the analogues underwent biological testing as the presumed *E/Z* mixture.

2.2 Biological assay of linear and cyclic peptides to inhibit gap junctions and hemichannel opening

To test the effect of the peptide modifications on peptide5 (**1**) activity against hemichannels, a model of ischemic insult on a cell culture model of the brain microvasculature was used to induce Cx43 hemichannel opening and ATP release (**Supplementary Material**, Method 4). The cells were incubated in hypoxic-acidic ion-shifted ringers (HAIR) solution to generate disrupted pH and ion balance leading to ATP leak from the cells, which can be sampled and quantified luminometrically using a commercially available firefly luciferase assay (Molecular Probes). Consistent with our previous study, treatment with HAIR solution induced an approximately three-fold increase of ATP in the culture medium. The peptide5 (**1**) treatment caused a reduction of ATP release over untreated HAIR controls (49.4 ± 6.9%; p = <0.001. One-way ANOVA, Dunnet's multiple comparisons post-hoc test) as did carbenoxolone (Cbx; 42.5 ± 3.4%; p = <0.001), an inhibitor of both Cx43 hemichannels and gap junctions (**Figure 11**).

Of the 15 linear analogues (**2**–**16**) of peptide5 (**1**) tested, the majority of these modifications did not reduce the release of ATP to comparable levels as peptide5 (**1**) (**Figure 11**) although generally, any modification to the native peptide5 (**1**) resulted in reduced or abolished activity. The addition of either an isobutyloxycarbonyl (**3**) or butanoyl (**5**) group lead to a statistically significant reduction in ATP release (52.6 ± 1.3%; p < 0.05 and 57.3 ± 12.4%; p < 0.05, respectively), equaling the efficacy of peptide5 (**1**) (**Figure 11**). Peptide **7** also appeared to reduce ATP release to a similar level as Peptide5 (**1**), but due to limited peptide, this could only be used for two experimental repeats and was not found to be statistically significant. Other *N*-terminal modifications involving the addition of an ethyloxycarbonyl (**2**), benzoyl (**4**), or masking of the amine as an azide (**6**) did not reduce ATP release compared to HAIR control, and ATP release from cells treated with modified peptide **6** was significantly increased compared to peptide5 (**1**). C-terminal modifications involving the removal of the carbonyl group (**15**) or using a thioester (**16**) also did not reduce ATP release. The addition of a C-terminal amide group (peptides **11**–**14**) in conjunction with the *N*-terminal modifications used for peptides **2**–**5** did not reduce ATP release compared to HAIR, demonstrating the addition of a C-terminal amide group prevents the reduction in ATP release observed with peptides **3** and **5**. Substitution of the lysine and arginine amino acids with an *N*-methyl-lysine (**7**), *N*-methyl-arginine (**8**), D-lysine (**9**), or D-arginine (**10**) did not reduce ATP release compared to HAIR-treated cells, and ATP release from cells treated with modified peptide **10** was significantly increased compared to peptide5 (**1**). None of the cyclic variants reduced the ATP levels (**Figure 11**). Rather, several of these showed a complete lack of activity compared to peptide5 (**28, 32, 34,** and **37**; p < 0.05). However, a number of the peptides (**28**, **32**, **34**, and **37**) showed significantly increased ATP release compared to peptide5 (**1**). This indicated that cyclization of peptide5 critically hinders the hemichannel blocking activity.

We next investigated the ability of peptide5 variants to inhibit gap junctional communication using a scrape loading assay. In this assay, the cells in culture are loaded with a dye (Lucifer Yellow dilithium salt (LY), M.W. 457.25 Da) of molecular size (<1 kDa) that is able to transit through the

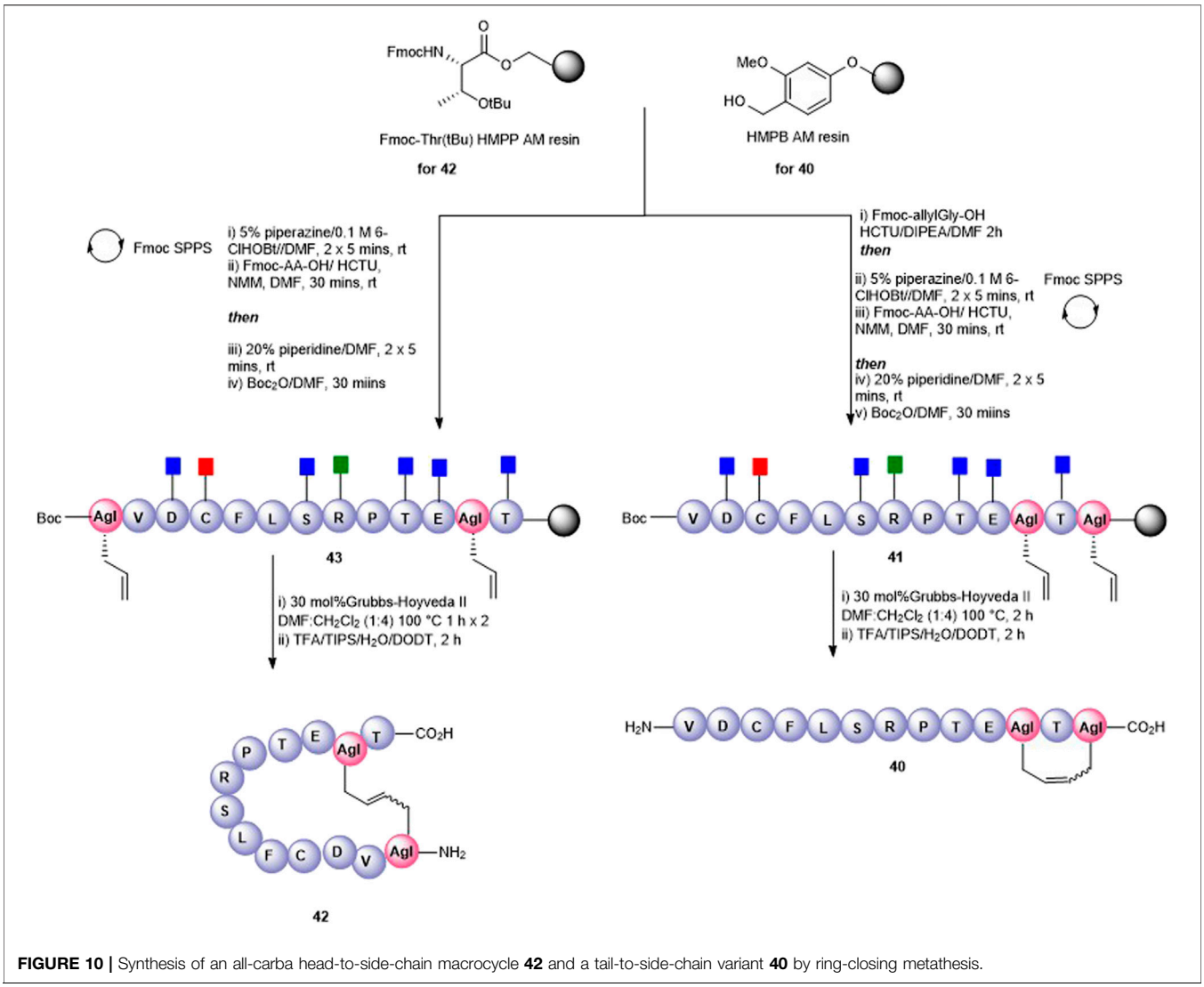

FIGURE 10 | Synthesis of an all-carba head-to-side-chain macrocycle **42** and a tail-to-side-chain variant **40** by ring-closing metathesis.

gap junctions and the degree of dye spread is then measured by counting the number of cells that contain LY (**Supplementary Material**, Method 4) [1]. Consistent with our previous study, peptide5 (**1**) and Cbx reduced the degree of dye spread following incubation with LY (56.16 ± 2.1%; $p < 0.0001$ and 16.2 ± 1.1%; $p < 0.0001$, respectively) compared to the untreated controls (**Figure 12**). Of the 15 linear analogues (**2**–**16**) of peptide5 (**1**) tested, two reduced LY dye spread. These were peptide **7**, containing an *N*-methyl lysine substitution, and **9**, containing a D-lysine substitution which caused a statistically significant reduction in the number of LY-positive cells (64.3 ± 7.2%; $p < 0.001$ and 74.7 ± 10.4%; $p < 0.01$, respectively), and these were not statistically different from peptide5. The corresponding peptides with *N*-methyl arginine (**8**) and D-arginine (**10**) did not reduce the degree of dye spread compared to control, and dye spread in cells treated with modified peptide **10** was significantly increased compared to peptide5 (**1**). A number of additional peptides including those with *N*-modifications (**2**, **4**, and **6**), C-modification (**15**), and a C-terminal amide group in conjunction with the *N*-terminal modifications (**11** and **14**) also showed significantly increased dye spread relative to peptide5 (**1**).

Of the 8 cyclic peptides tested, peptides **25** and **32** caused a statistically significant reduction in the number of LY-positive cells (61.7 ± 5.9%; $p < 0.001$ and 68.0 ± 3.0%; $p < 0.01$, respectively) compared to control that was not statistically different from peptide5 (**1**) (**Figure 12**), while peptides **34** and **42** had levels of dye spread that were significantly greater than that observed with peptide5 (**1**).

2.3 Serum Stability of Selected Analogs

One of the limitations of using peptide5 (**1**) as a therapeutic is its poor half-life. The half-lives of peptide therapeutics can be significantly improved by *N*- and C-terminal functional group masking, cyclization, and conversion of susceptible amide

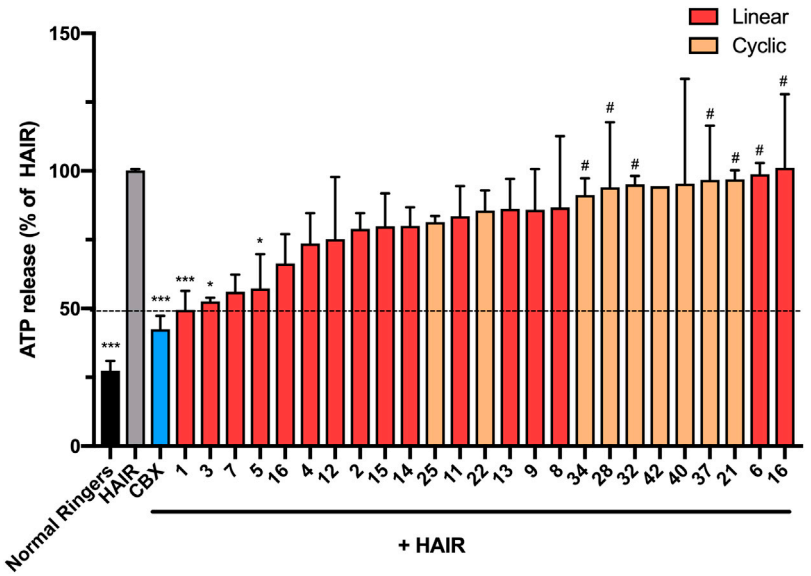

FIGURE 11 | *N*-terminal, C-terminal, and cyclic modifications affect peptide5 (1) function against ischemic injury–induced ATP release from hCMVEC cells *in vitro*. *N*-terminal modified peptides **3** and **5** displayed efficacy equaling peptide5 ($^{*}p < 0.05$, $^{***}p < 0.001$, respectively). N-terminal modified peptide **6** and the D-arginine–containing peptide **10** equaled the ATP release of the HAIR control indicating a complete lack of activity ($^{\#}p < 0.05$). None of the cyclic peptides led to a reduction in ATP release that was significantly different from HAIR control, and a number of peptides (**34**, **28**, **32**, and **37**) demonstrated a level of ATP release significantly greater than peptide5, indicating loss of function of these peptides, $^{\#}p < 0.05$. All values represent the mean, SEM. One-way ANOVA, Dunnett's comparison test against HAIR (*) or peptide5 (#).

bonds using D- or *N*-methylated amino acids, and these methods have been successfully used to progress peptides to the clinic (Yao et al., 2018; Khatri et al., 2019). Our previous studies of lipidated peptide5 demonstrated that the native sequence was completely degraded in rat serum in less than 5 min (Yang et al., 2020). In the present work, we instead employed the more relevant human serum and established that peptide5 (**1**) was relatively stable and degraded completely within 10 h. We then evaluated the *N*-methylated variants **7** and **8**, D amino acid variants **9** and **10**, and the two carbo cyclic peptides **39** and **42**. Each peptide was incubated with 25% aq. human serum at 37°C, and 6 aliquots were extracted within 48 h. The stability of each peptide upon exposure to human serum was then analyzed via analytical RP HPLC, and the amount of peptide still present at each time point was recorded relative to t = 0 h. The results are presented in **Figure 13**.

N-methylated peptides, **7** and **8**, showed a similar degradation profile to peptide5 (**1**), although the rate of degradation was slower. Peptide5 (**1**) containing either a D-Arg or D-Lys showed good stability with *ca.* 30% remaining after 48 h suggesting that Ser-L-Arg and Glu-L-Lys sites were susceptible to enzymatic cleavage and that replacement with the D amino acids conferred improved stability. The side-chain-to-tail carba peptide5 analogue **39** exhibited good stability over 48 h, but the head-to-tail analogue **42**, was extremely resistant to enzymatic degradation, and *ca.* 90% of the peptide remained intact at the completion of the experiment.

2.4 Discussion

Our goal was to apply a peptidomimetic strategy to improve the half-life of connexin channel inhibitor peptide5 (**1**), whist maintaining its ability to bind to connexin hemichannels and to moderate gap junctions. In the hemichannel assay, *N*-lipidated peptide5 analogues with short alkyl lipids (**3** and **5**) showed the comparable ability of peptide5 to block ATP release whilst an *N*-terminal azido (**6**) or D-Arg (**10**) variants were both poor at blocking hemichannels. This suggests that only certain *N*-terminal modifications are tolerated. Thus, whereas a short *N*-terminal lipid may interact with the lipid membrane to anchor peptide5 (**1**), the conversion of the amino group to an azide was detrimental, suggesting that the *N*-terminal amino group is important. At physiological pH, the amine group is protonated; when acylated or present as an azide, the positive charge is lost which may be compensated by the lipid at the *N*-terminus that can bind to the lipid membrane. The D-Arg substitution (**10**) also resulted in poor activity in the hemichannel assay. Given that alanine scan data showed that L-Arg could be substituted by L-Ala, this would suggest a stereochemical requirement as well as an interaction of the guanidyl group present in Arg for effective peptide5 (**1**) binding. Of the cyclic peptides prepared, none were able to reduce ATP lost to a level seen with the Cbx control or with peptide5 (**1**). While this may be logical given that we have shown that alanine substitutions at Asp2, Cys3, Leu5, Arg7, Pro8, and Lys11 were not tolerated in this assay, the head-to-tail cyclic amide analogues **21** and **22** and the disulfide cyclic variant **37** retain all side-chain functionality. This

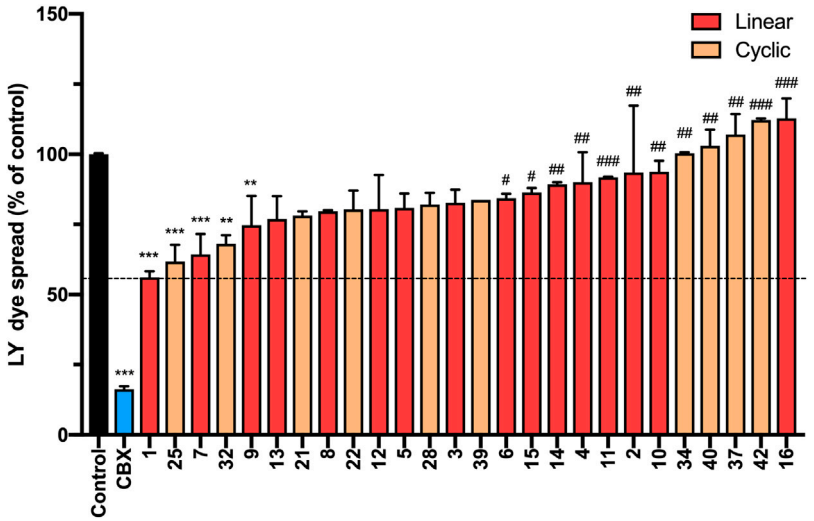

FIGURE 12 | *N*-terminal, C-terminal, and cyclic modifications affect peptide5 (1) function against gap junctional coupling in hCMVEC cells *in vitro*. Positive LY dye transfer between coupled gap junction channels is represented as a percentage of the untreated control. LY dye transfer was significantly reduced compared to untreated control following treatment with Cbx or peptide5 (**1**) (****$p < 0.0001$). The peptides substituted with an *N*-methyl lysine (**7**) or D-lysine (**9**) prevented the spread of LY to a level comparable to peptide5 (1) (**$p < 0.01$, ***$p < 0.001$, respectively). A number of modified peptides demonstrated a level of LY dye transfer significantly greater than peptide5 and not different from control, indicating complete loss of function of these peptides, $^{\#}p < 0.05$. The cyclic peptides **25** and **32** significantly reduced LY transfer compared to control but not peptide5 **$p < 0.01$, ***$p < 0.001$. The cyclic peptides **40**, **34**, and **42** demonstrated a level of LY dye transfer significantly greater than peptide5 and not different from control, indicating loss of function of these peptides, $^{\#\#\#}p < 0.001$, $^{\#\#\#\#}p < 0.0001$. All values represent the mean, SEM. One-way ANOVA, Dunnett's comparison test against control (*) or peptide5 (#).

suggests that a less rigid linearized sequence is optimal for binding to Cx43.

In the gap junction assay, both an *N*-MeLys (**7**) and a D-Lys (**9**) substitution resulted in gap junction uncoupling comparable to that of peptide5 (**1**), and both exhibited improved human serum stability relative to peptide5. It should be noted that the *N*-Me-Lys congener (**7**) also appeared effective in the hemichannel assay and was the next best analogue after the *N*-lipidated analogues **3** and **5**. The incorporation of a D-Arg resulted in poor activity in line with the hemichannel data, thus confirming that an L-Arg is critical for both hemichannel blocking and gap junction uncoupling.

Examination of the cyclic peptides to inhibit the gap junctions revealed that side-chain Asp4-Lys11, side-chain–cyclized peptide **25**, and Cys3-Val1 cyclic peptide **32** were not as effective as peptide5 (**1**) but were better than most other cyclic peptides. As detailed in our alanine scan data, all positions in peptide5 (**1**) were able to be modified without adversely affecting gap junction blocking. However, given that the other cyclic compounds were poor, this suggests that positioning and composition of the cycle are important. The disulfide-containing cyclic compound **37** which retains all the side-chain amino acid functionality as well as the amino and carboxylate groups at the *N*- and C-termini, respectively, was a poor gap junction inhibitor as was the all-carba analogue **42**. Both **42** and **37** contain significantly larger macrocyclic rings compared to **25** and **32**, indicative of a preference for a smaller ring size to be optimal for cyclic variants of peptide5 (**1**). Nonetheless, the results demonstrated herein establish that cyclic variants of peptide5 (**1**) are able to retain some gap junction activity which was not the case for hemichannel blocking.

The goal of increasing the half-life of peptide5 whilst retaining activity has been met. The simple substitution of L- and D-Arg with D- or *N*-Me amino acids overall improved their stability. The half-life of peptide5 is estimated from **Figure 13** to be *ca.* 2–3 h; its D-Arg congener was 5-fold higher with 50% remaining after 14–15 h, and the D-Lys peptide, 4-fold higher than peptide5 with 50% remaining after 12–13 h. Whilst not as noticeable, the *N*-Me-Lys variant also showed a modest increase in stability relative to peptide5. The cyclic all-carba analogues **39** and **42** were the most stable in human serum. These peptides are the most chemically modified with a 4-atom carbon bridge linking the peptide backbone with an additional rigidifying double bond. While this improved their stability, this was at the expense of both hemichannel and gap junction activity. There may therefore be scope to examine other stapling methodologies that include less rigid structures.

3 CONCLUSION

The abovementioned data have highlighted that a linearized peptide5 is the key design principle to ensure dual hemichannel and connexin activity. In the linear peptide5 analogues prepared, only those that had a small modification at the *N*-terminus, namely, an isobutyloxycarbonyl or butanoyl functional group, exhibited similar activity to

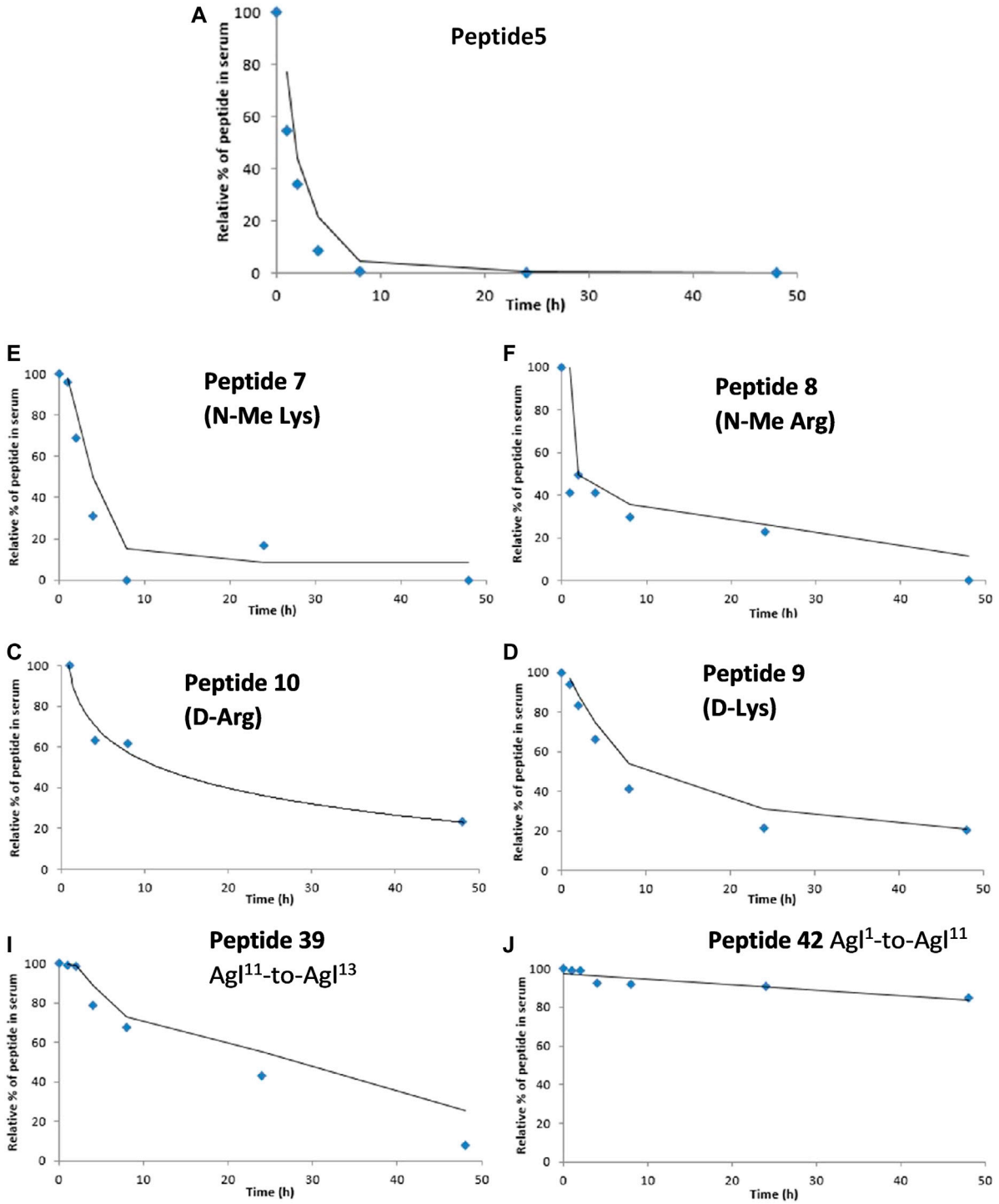

FIGURE 13 | Degradation studies of peptide5 and selected analogues in 25% human serum at 37°C via monitoring by HPLC at 210 nm.

peptide5 in the hemichannel assay. The only other exception was an *N*-MeLys replacement for the canonical L-Lys; remarkably, a D-Arg substitution for L-Arg abolished hemichannel activity completely, corroborating the sensitive relationship between individual amino acid substitutions and loss of activity. Converting the linear sequence to cyclic analogues containing several different cyclization modes was not tolerated in the hemichannel assay although an Asp-Lys side-chain–cyclized peptide performed well in the gap junction assay. Further work focusing on the development of peptide-based mimetics of peptide5 (**1**) should thus concentrate on the modification of the linear peptide5 sequences containing an *N*-acylated terminus or an *N*-alkylated Lys rather than cyclic variants.

DATA AVAILABILITY STATEMENT

The original contributions presented in the study are included in the article/**Supplementary Material**; further inquiries can be directed to the corresponding authors.

AUTHOR CONTRIBUTIONS

SCC designed and performed the peptide synthesis and peptide stability. JG and CC designed and performed the biological assays. MB oversaw the peptide synthesis. SJO designed and oversaw the biological assays and co-wrote the manuscript. PWH designed and performed the peptide synthesis and co-wrote the manuscript.

FUNDING

The authors wish to thank the Maurice Wilkins Centre for Molecular Biodiscovery for financial support.

SUPPLEMENTARY MATERIAL

The Supplementary Material for this article can be found online at: https://www.frontiersin.org/articles/10.3389/fchem.2022.877618/full#supplementary-material

REFERENCES

Amso, Z., Kowalczyk, R., Park, Y.-E., Watson, M., Lin, J.-m., Musson, D. S., et al. (2016). Synthesis and *In Vitro* Bone Cell Activity of Analogues of the Cyclohexapeptide Dianthin G. *Org. Biomol. Chem.* 14, 6231–6243. doi:10.1039/C6OB00983B

Bechtler, C., and Lamers, C. (2021). Macrocyclization Strategies for Cyclic Peptides and Peptidomimetics. *RSC Med. Chem.* 12, 1325–1351. doi:10.1039/D1MD00083G

Camarero, J. A., Adeva, A., and Muir, T. W. (2000). 3-thiopropionic Acid as a Highly Versatile Multidetachable Thioester Resin Linker. *Lett. Pept. Sci.* 7, 17–21. doi:10.1007/bf02443557

Chatterjee, J., Laufer, B., and Kessler, H. (2012). Synthesis of N-Methylated Cyclic Peptides. *Nat. Protoc.* 7, 432–444. doi:10.1038/nprot.2011.450

D'Aloisio, V., Dognini, P., Hutcheon, G. A., and Coxon, C. R. (2021). PepTherDia: Database and Structural Composition Analysis of Approved Peptide Therapeutics and Diagnostics. *Drug Discov. Today* 26, 1409–1419. doi:10.1016/j.drudis.2021.02.019

Danesh-Meyer, H. V., Kerr, N. M., Zhang, J., Eady, E. K., O'Carroll, S. J., Nicholson, L. F. B., et al. (2012). Connexin43 Mimetic Peptide Reduces Vascular Leak and Retinal Ganglion Cell Death Following Retinal Ischaemia. *Brain* 135, 506–520. doi:10.1093/brain/awr338

Dang, B., Kubota, T., Mandal, K., Bezanilla, F., and Kent, S. B. H. (2013). Native Chemical Ligation at Asx-Cys, Glx-Cys: Chemical Synthesis and High-Resolution X-Ray Structure of ShK Toxin by Racemic Protein Crystallography. *J. Am. Chem. Soc.* 135, 11911–11919. doi:10.1021/ja4046795

Davidson, J. O., Drury, P. P., Green, C. R., Nicholson, L. F., Bennet, L., and Gunn, A. J. (2014). Connexin Hemichannel Blockade Is Neuroprotective after Asphyxia in Preterm Fetal Sheep. *PLoS One* 9, e96558. doi:10.1371/journal.pone.0096558

Davidson, J. O., Green, C. R., B. Nicholson, L. F., O'Carroll, S. J., Fraser, M., Bennet, L., et al. (2012). Connexin Hemichannel Blockade Improves Outcomes in a Model of Fetal Ischemia. *Ann. Neurol.* 71, 121–132. doi:10.1002/ana.22654

Dawson, P. E., Muir, T. W., Clark-Lewis, I., and Kent, S. B. H. (1994). Synthesis of Proteins by Native Chemical Ligation. *Science* 266, 776–779. doi:10.1126/science.7973629

De Bock, M., Culot, M., Wang, N., Bol, M., Decrock, E., De Vuyst, E., et al. (2011). Connexin Channels Provide a Target to Manipulate Brain Endothelial Calcium Dynamics and Blood-Brain Barrier Permeability. *J. Cereb. Blood Flow. Metab.* 31, 1942–1957. doi:10.1038/jcbfm.2011.86

de la Torre, B. G., and Albericio, F. (2020). Peptide Therapeutics 2.0. *Molecules* 25, 2293. doi:10.3390/molecules25102293

Decrock, E., De Bock, M., Wang, N., Bultynck, G., Giaume, C., Naus, C. C., et al. (2015). Connexin and Pannexin Signaling Pathways, an Architectural Blueprint for CNS Physiology and Pathology? *Cell. Mol. Life Sci.* 72, 2823–2851. doi:10.1007/s00018-015-1962-7

D'hondt, C., Iyyathurai, J., Wang, N., Gourdie, R. G., Himpens, B., Leybaert, L., et al. (2013). Negatively Charged Residues (Asp378 and Asp379) in the Last Ten Amino Acids of the C-Terminal Tail of Cx43 Hemichannels Are Essential for Loop/tail Interactions. *Biochem. Biophysical Res. Commun.* 432, 707–712. doi:10.1016/j.bbrc.2013.01.066

Erak, M., Bellmann-Sickert, K., Els-Heindl, S., and Beck-Sickinger, A. G. (2018). Peptide Chemistry Toolbox - Transforming Natural Peptides into Peptide Therapeutics. *Bioorg. Med. Chem.* 26, 2759–2765. doi:10.1016/j.bmc.2018.01.012

Eugenin, E. A., Clements, J. E., Zink, M. C., and Berman, J. W. (2011). Human Immunodeficiency Virus Infection of Human Astrocytes Disrupts Blood-Brain Barrier Integrity by a Gap Junction-dependent Mechanism. *J. Neurosci.* 31, 9456–9465. doi:10.1523/JNEUROSCI.1460-11.2011

Evans, W. H. (2015). Cell Communication across Gap Junctions: a Historical Perspective and Current Developments. *Biochem. Soc. Trans.* 43, 450–459. doi:10.1042/BST20150056

Froger, N., Orellana, J. A., Calvo, C.-F., Amigou, E., Kozoriz, M. G., Naus, C. C., et al. (2010). Inhibition of Cytokine-Induced Connexin43 Hemichannel Activity in Astrocytes Is Neuroprotective. *Mol. Cell. Neurosci.* 45, 37–46. doi:10.1016/j.mcn.2010.05.007

Gentilucci, L., De Marco, R., and Cerisoli, L. (2010). Chemical Modifications Designed to Improve Peptide Stability: Incorporation of Non-natural Amino Acids, Pseudo-peptide Bonds, and Cyclization. *Curr. Pharm. Des.* 16, 3185–3203. doi:10.2174/138161210793292555

Goddard-Borger, E. D., and Stick, R. V. (2007). An Efficient, Inexpensive, and Shelf-Stable Diazotransfer Reagent: Imidazole-1-Sulfonyl Azide Hydrochloride. *Org. Lett.* 9, 3797–3800. doi:10.1021/ol701581g

Góngora-Benítez, M., Tulla-Puche, J., and Albericio, F. (2014). Multifaceted Roles of Disulfide Bonds. Peptides as Therapeutics. *Chem. Rev.* 114, 901–926. doi:10.1021/cr400031z

Guo, C. X., Mat Nor, M. N., Danesh-Meyer, H. V., Vessey, K. A., Fletcher, E. L., O'Carroll, S. J., et al. (2016). Connexin43 Mimetic Peptide Improves Retinal Function and Reduces Inflammation in a Light-Damaged Albino Rat Model. *Invest. Ophthalmol. Vis. Sci.* 57, 3961–3973. doi:10.1167/iovs.15-16643

Johnson, E. C. B., and Kent, S. B. H. (2006). Insights into the Mechanism and Catalysis of the Native Chemical Ligation Reaction. *J. Am. Chem. Soc.* 128, 6640–6646. doi:10.1021/Ja058344i

Khatri, B., Nuthakki, V. R., and Chatterjee, J. (2019). "Strategies to Enhance Metabolic Stabilities," in *Cyclic Peptide Design*. Editor G. Goetz (New York, NY: Springer New York), 17–40. doi:10.1007/978-1-4939-9504-2_2

Kim, Y., Griffin, J. M., Harris, P. W. R., Chan, S. H. C., Nicholson, L. F. B., Brimble, M. A., et al. (2017a). Characterizing the Mode of Action of Extracellular Connexin43 Channel Blocking Mimetic Peptides in an *In Vitro* Ischemia Injury Model. *Biochimica Biophysica Acta (BBA) - General Subj.* 1861, 68–78. doi:10.1016/j.bbagen.2016.11.001

Kim, Y., Griffin, J. M., Harris, P. W. R., Chan, S. H. C., Nicholson, L. F. B., Brimble, M. A., et al. (2017b). Characterizing the Mode of Action of Extracellular Connexin43 Channel Blocking Mimetic Peptides in an *In Vitro* Ischemia Injury Model. *Biochimica Biophysica Acta (BBA) - General Subj.* 1861 (2), 68–78. doi:10.1016/j.bbagen.2016.11.001

Krysko, D. V., Leybaert, L., Vandenabeele, P., and D'Herde, K. (2005). Gap Junctions and the Propagation of Cell Survival and Cell Death Signals. *Apoptosis* 10, 459–469. doi:10.1007/s10495-005-1875-2

Kumagai, H., Tajima, M., Ueno, Y., Giga-Hama, Y., and Ohba, M. (1991). Effect of Cyclic RGD Peptide on Cell Adhesion and Tumor Metastasis. *Biochem. Biophysical Res. Commun.* 177, 74–82. doi:10.1016/0006-291X(91)91950-H

Kuo, C., Green, C. R., Rupenthal, I. D., and Mugisho, O. O. (2020). Connexin43 Hemichannel Block Protects against Retinal Pigment Epithelial Cell Barrier Breakdown. *Acta Diabetol.* 57, 13–22. doi:10.1007/s00592-019-01352-3

Li, H., Liu, T. F., Lazrak, A., Peracchia, C., Goldberg, G. S., Lampe, P. D., et al. (1996). Properties and Regulation of Gap Junctional Hemichannels in the Plasma Membranes of Cultured Cells. *J. Cell Biol.* 134, 1019–1030. doi:10.1083/jcb.134.4.1019

Li, X., Kawakami, T., and Aimoto, S. (1998). Direct Preparation of Peptide Thioesters Using an Fmoc Solid-phase Method. *Tetrahedron Lett.* 39, 8669–8672. doi:10.1016/s0040-4039(98)01868-1

Mao, Y., Tonkin, R. S., Nguyen, T., O'Carroll, S. J., Nicholson, L. F. B., Green, C. R., et al. (2017). Systemic Administration of Connexin43 Mimetic Peptide Improves Functional Recovery after Traumatic Spinal Cord Injury in Adult Rats. *J. Neurotrauma* 34, 707–719. doi:10.1089/neu.2016.4625

Márquez-Rosado, L., Solan, J. L., Dunn, C. A., Norris, R. P., and Lampe, P. D. (2012). Connexin43 Phosphorylation in Brain, Cardiac, Endothelial and Epithelial Tissues. *Biochimica Biophysica Acta (BBA) - Biomembr.* 1818, 1985–1992. doi:10.1016/j.bbamem.2011.07.028

Miller, S. J., Blackwell, H. E., and Grubbs, R. H. (1996). Application of Ring-Closing Metathesis to the Synthesis of Rigidified Amino Acids and Peptides. *J. Am. Chem. Soc.* 118, 9606–9614. doi:10.1021/ja961626l

Mugisho, O. O., Green, C. R., Squirrell, D. M., Bould, S., Danesh-Meyer, H. V., Zhang, J., et al. (2019). Connexin43 Hemichannel Block Protects against the Development of Diabetic Retinopathy Signs in a Mouse Model of the Disease. *J. Mol. Med.* 97, 215–229. doi:10.1007/s00109-018-1727-5

Muttenthaler, M., King, G. F., Adams, D. J., and Alewood, P. F. (2021). Trends in Peptide Drug Discovery. *Nat. Rev. Drug Discov.* 20, 309–325. doi:10.1038/s41573-020-00135-8

O'Carroll, S. J., Alkadhi, M., Nicholson, L. F. B., and Green, C. R. (2008). Connexin43 Mimetic Peptides Reduce Swelling, Astrogliosis, and Neuronal Cell Death after Spinal Cord Injury. *Cell Commun. Adhesion* 15, 27–42. doi:10.1080/15419060802014164

O'Carroll, S. J., Gorrie, C. A., Velamoor, S., Green, C. R., and Nicholson, L. F. B. (2013). Connexin43 Mimetic Peptide Is Neuroprotective and Improves Function Following Spinal Cord Injury. *Neurosci. Res.* 75, 256–267. doi:10.1016/j.neures.2013.01.004

O. Davidson, J., R. Green, C., Bennet, L., F.B. Nicholson, L., Danesh-Meyer, H., J. O'Carroll, S., et al. (2013). A Key Role for Connexin Hemichannels in Spreading Ischemic Brain Injury. *Curr. Drug Targets* 14, 36–46. doi:10.2174/13894501380480647 9

Oyamada, M., Oyamada, Y., and Takamatsu, T. (2005). Regulation of Connexin Expression. *Biochimica Biophysica Acta (BBA) - Biomembr.* 1719, 6–23. doi:10.1016/j.bbamem.2005.11.002

Philippe, G. J. B., Craik, D. J., and Henriques, S. T. (2021). Converting Peptides into Drugs Targeting Intracellular Protein-Protein Interactions. *Drug Discov. Today* 26, 1521–1531. doi:10.1016/j.drudis.2021.01.022

Quist, A. P., Rhee, S. K., Lin, H., and Lal, R. (2000). Physiological Role of Gap-Junctional Hemichannels. *J. Cell Biol.* 148, 1063–1074. doi:10.1083/jcb.148.5.1063

Ribeiro-Rodrigues, T. M., Martins-Marques, T., Morel, S., Kwak, B. R., and Girão, H. (2017). Role of Connexin 43 in Different Forms of Intercellular Communication - Gap Junctions, Extracellular Vesicles and Tunnelling Nanotubes. *J. Cell Sci.* 130, 3619–3630. doi:10.1242/jcs.200667

Robey, F. A., and Fields, R. L. (1989). Automated Synthesis of N-Bromoacetyl-Modified Peptides for the Preparation of Synthetic Peptide Polymers, Peptide-Protein Conjugates, and Cyclic Peptides. *Anal. Biochem.* 177, 373–377. doi:10.1016/0003-2697(89)90068-7

Rodríguez-Sinovas, A., Cabestrero, A., López, D., Torre, I., Morente, M., Abellán, A., et al. (2007). The Modulatory Effects of Connexin 43 on Cell Death/survival beyond Cell Coupling. *Prog. Biophysics Mol. Biol.* 94, 219–232. doi:10.1016/j.pbiomolbio.2007.03.003

Sarrouilhe, D., Dejean, C., and Mesnil, M. (2017). Connexin43- and Pannexin-Based Channels in Neuroinflammation and Cerebral Neuropathies. *Front. Mol. Neurosci.* 10, 320. doi:10.3389/fnmol.2017.00320

Schafmeister, C. E., Po, J., and Verdine, G. L. (2000). An All-Hydrocarbon Cross-Linking System for Enhancing the Helicity and Metabolic Stability of Peptides. *J. Am. Chem. Soc.* 122, 5891–5892. doi:10.1021/Ja000563a

Tonkin, R. S., Mao, Y., Oâ€™Carroll, S. J., Nicholson, L. F. B., Green, C. R., Gorrie, C. A., et al. (2015). Gap Junction Proteins and Their Role in Spinal Cord Injury. *Front. Mol. Neurosci.* 7, 102. doi:10.3389/fnmol.2014.00102

van Witteloostuijn, S. B., Pedersen, S. L., and Jensen, K. J. (2016). Half-Life Extension of Biopharmaceuticals Using Chemical Methods: Alternatives to PEGylation. *ChemMedChem* 11, 2474–2495. doi:10.1002/cmdc.201600374

Villain, M., Gaertner, H., and Botti, P. (2003). Native Chemical Ligation with Aspartic and Glutamic Acids asC-Terminal Residues: Scope and Limitations. *Eur. J. Org. Chem.*, 2003, 3267–3272. doi:10.1002/ejoc.200300032

Xing, L., Yang, T., Cui, S., and Chen, G. (2019). Connexin Hemichannels in Astrocytes: Role in CNS Disorders. *Front. Mol. Neurosci.* 12, Available at: https://www.frontiersin.org/article/10.3389/fnmol.2019.00023 (Accessed May 11, 2022). doi:10.3389/fnmol.2019.00023

Yang, S.-H., Clemett, C. A., Brimble, M. A., O'Carroll, S. J., and Harris, P. W. R. (2020). Synthesis and Biological Evaluation of S-Lipidated Lipopeptides of a Connexin 43 Channel Inhibitory Peptide. *RSC Med. Chem.* 11, 1041–1047. doi:10.1039/D0MD00172D

Yao, J.-F., Yang, H., Zhao, Y.-Z., and Xue, M. (2018). Metabolism of Peptide Drugs and Strategies to Improve Their Metabolic Stability. *Curr. Drug. Metab.* 19, 892–901. doi:10.2174/1389200219666180628171531

Zhang, L., and Bulaj, G. (2012). Converting Peptides into Drug Leads by Lipidation. *Curr. Med. Chem.* 19, 1602–1618. doi:10.2174/092986712799945003

Conflict of Interest: The authors declare that the research was conducted in the absence of any commercial or financial relationships that could be construed as a potential conflict of interest.

Publisher's Note: All claims expressed in this article are solely those of the authors and do not necessarily represent those of their affiliated organizations, or those of the publisher, the editors, and the reviewers. Any product that may be evaluated in this article, or claim that may be made by its manufacturer, is not guaranteed or endorsed by the publisher.

Advantages of publishing in Frontiers

OPEN ACCESS
Articles are free to read for greatest visibility and readership

FAST PUBLICATION
Around 90 days from submission to decision

HIGH QUALITY PEER-REVIEW
Rigorous, collaborative, and constructive peer-review

TRANSPARENT PEER-REVIEW
Editors and reviewers acknowledged by name on published articles

Frontiers
Avenue du Tribunal-Fédéral 34
1005 Lausanne | Switzerland

Visit us: www.frontiersin.org
Contact us: frontiersin.org/about/contact

REPRODUCIBILITY OF RESEARCH
Support open data and methods to enhance research reproducibility

DIGITAL PUBLISHING
Articles designed for optimal readership across devices

FOLLOW US
@frontiersin

IMPACT METRICS
Advanced article metrics track visibility across digital media

EXTENSIVE PROMOTION
Marketing and promotion of impactful research

LOOP RESEARCH NETWORK
Our network increases your article's readership